DISSERTATION

REGIONAL SELENIUM CYCLING IN AN IRRIGATED AGRICULTURAL GROUNDWATER SYSTEM: CONCEPTUALIZATION, MODELING, AND MITIGATION

Submitted by

Ryan T. Bailey

Department of Civil and Environmental Engineering

In partial fulfillment of the requirements

For the Degree of Doctor of Philosophy

Colorado State University

Fort Collins, Colorado

Summer 2012

Doctoral Committee:

Advisor: Timothy K. Gates
Co-Advisor: Domenico A. Baù

Mazdak Arabi
Michael J. Ronayne
Liwang Ma

ABSTRACT

REGIONAL SELENIUM CYCLING IN AN IRRIGATED AGRICULTURAL GROUNDWATER SYSTEM:
CONCEPTUALIZATION, MODELING, AND REMEDIATION

Selenium (Se) is an element that occurs naturally as a trace constituent in geologic formations and associated soils and, although an essential nutrient for animals and humans, can prove detrimental to health at high concentrations. Over the previous decades, the presence of either deficient or elevated concentrations of Se in groundwater, surface water, and associated plants and cultivated crops has emerged as a serious issue in many regions of the world, including the United States, northern and western Europe, the Middle East, and East Asia.

Regardless of the nature of concern regarding Se, whether concentrations are deficient or elevated in water supplies and cultivated crops, there is a basic need for a thorough description of the movement and chemical processes of Se within a dynamic soil-aquifer system influenced by agricultural practices, and for the development of numerical simulation tools that allow these processes to be simulated in assessing baseline conditions and exploring remediation best-management practices (BMPs). While the individual processes controlling Se speciation, transformation, and movement within soil systems have been well documented, their synthesis into a comprehensive numerical model of Se fate and transport within an alluvial aquifer system influenced by agricultural practices has not yet been realized.

This dissertation presents the development of a numerical model that can simulate the fate and transport of Se species in irrigation-influenced agricultural soil and groundwater systems at a regional scale. The model was developed by first, linking RT3D, modified to handle multi-species reactive transport in variably-saturated porous media, to MODFLOW, which uses the

UZF1 (Unsaturated Zone Flow) package to simulate groundwater flow in the unsaturated zone; and second, developing an Se reaction module for RT3D that accounts for the cycling, chemical activity, and transport of Se species in regional-scale agricultural soil and groundwater systems. The module also accounts for the influence of other chemical species such as dissolved oxygen and nitrate (NO_3). The resulting model, referred to as UZF-RT3DAG, is applied to a 50,600 ha regional site in the Lower Arkansas River Valley (LARV) in southeastern Colorado for the years 2006 through 2009. Using the calibrated model, multiple BMPs for remediation of Se contamination in the LARV are investigated. These strategies include decreasing annual loading of nitrogen fertilizer, decreasing species concentration in canal water, decreasing applied volume of irrigation water, and increasing chemical activity within riparian areas.

Research results are presented through a series of published and submitted articles and modeling results that outline the progression of model development and model application. Results of the BMP scenario testing indicate that alternative land-management practices can have a significant impact in decreasing the concentration of dissolved Se in groundwater by up to 5-8% as well as mass loadings of Se to the Arkansas River by as much as 20-30%. Practices also have a significant impact on decreasing NO_3 concentrations and loadings by up to 50% and 45%, respectively. As the alluvial aquifer in the LARV is similar to other Se-contaminated aquifer systems, the results of this research are pertinent to the assessment and remediation of Se contamination world-wide.

ACKNOWLEDGEMENTS

The author would like to thank his advisor Dr. Timothy K. Gates and his co-advisor Dr. Domenico A. Baù for their continued encouragement and overall excellent methods of mentorship. They have been great mentors throughout the course of the research, providing guidance and allowing independence. The author would like to acknowledge the support and assistance from the members of his committee, Drs. Mazdak Arabi, Michael J. Ronayne, and Liwang Ma, particularly to Dr. Arabi for his exceptional encouragement and assistance in completing critical components of the research. Special thanks also to fellow graduate students and colleagues during the previous four years, including Eric Morway, Keith Morse, Joy Labadie, Brent Cody, Greg Steed, and André Dozier. This research was made possible through the cooperation of more numerous participating farmers in the Lower Arkansas River Valley in southeastern Colorado, and with funding from the Nonpoint Source Program of the Colorado Department of Public Health and Environment and the Colorado Agricultural Experiment Station. Special thanks to Randy Ristau, Greg Naugle, and Lucia Muchado of CDPHE for their attention and support. Thanks to Dr. William Hunter of the ARS – USDA in Fort Collins, CO, for providing laboratory access and equipment, and to both Dr. Hunter and Robin Montenieri for expert technical assistance in the laboratory studies. Thanks also to Dr. Ardell Halverson of ARS-USDA and to Dr. Michael Bartolo at the Arkansas Valley Research Center for their general support and for providing access to research plots for soil sampling.

Most importantly, the author acknowledges the tremendous support of his wife, Jamie, and of their four daughters, Emma, Marta, Jane, and Nellie. Without their support and encouragement the attainment of this degree would not have been possible. The last four years have been full of joy.

PREFACE

The research described in this dissertation involves the fate and transport of selenium (Se) in the Lower Arkansas River Valley (LARV) in southeastern Colorado, and provides a key component of implementing best-management practices within the LARV in regards to water quantity and water quality. Field, laboratory, and numerical modeling studies were performed to conceptualize and simulate the chemical transport of Se in an agricultural groundwater system, as well as explore potential remediation schemes through scenario testing and analysis. The author was responsible for a portion of the field work, the work in the laboratory, and the development of the numerical modeling code that simulates the cycling and reactive transport of Se in regional-scale irrigated agricultural groundwater systems. The model also has the capabilities of simulating the reactive transport of dissolved oxygen (O_2) and the cycling and reactive transport of nitrogen (N) species due to the strong dependence of Se on O_2 and nitrate (NO_3). The author was not responsible for the development of the groundwater flow model and simulation.

The conceptualization of Se fate and transport and the development of the numerical modeling code is documented in two published journal articles (Chapters 2 and 3), one article that is in review (Chapter 4), and one article that soon will be submitted (Chapter 5). The application of the model to a 50,600-ha study site within the LARV and the use of the model to explore best-management practices in regards to remediation of Se and NO_3 are presented in Chapters 6 and 7, respectively. Major conclusions and avenues of future research are summarized in Chapter 8. Three appendices also are included to provide supplemental field and modeling results.

DEDICATION

For my wife Jamie
and our children Emma, Marta, Jane, Nellie, and the little one on the way

For their tremendous love and support

TABLE OF CONTENTS

LIST OF TABLES

CHAPTER 6 TABLES

CHAPTER 7 TABLES

LIST OF FIGURES

CHAPTER 1 FIGURES

CHAPTER 2 FIGURES

CHAPTER 3 FIGURES

CHAPTER 4 FIGURES

CHAPTER 5 FIGURES

CHAPTER 6 FIGURES

CHAPTER 7 FIGURES

LIST OF APPENDICES

CHAPTER 1

LITERATURE REVIEW AND RESEARCH OVERVIEW

1.1 THE SELENIUM PROBLEM

Selenium (Se) is an essential micro-nutrient for animals and human, although high concentrations and bio-accumulation can prove detrimental to both animal and human health (Winkel et al., 2012). The dietary requirement of Se contrasted with the risk of over-consumption has led researchers to term Se as the "double-edged sword" element (Conde and Alaejos, 1997; Fernández-Martínez and Charlet, 2009) and an "essential toxin" (Stolz et al., 2002), with a narrow range of daily intake between dietary deficiency and toxic over-consumption for both animal and human populations (Levander and Burk, 2006).

For humans, the narrow range between dietary deficiency and toxicity is 40 µg day^{-1} to 400 µg day^{-1} (Levander and Burk, 2006). Insufficient uptake of Se is reportedly the cause of the Keshan disease, a deterioration of the function of the heart muscle (Beck et al., 2003) and has been linked to diseases such as endemic liver cancer and fluorosis (Peng et al., 1995) and increased risk of cardiovascular death and cancer (Alfthan et al., 1995; Aro et al., 1998). Schwarz and Folz (1957) also demonstrated that an appropriate daily uptake of Se can protect against liver degeneration. Daily intake exceeding the upper level of 400 µg day^{-1}, however, can lead to selenosis, with symptoms of gastrointestinal disorders, hair loss, sloughing of nails, and neurological damage and extreme cases resulting in cirrhosis of the liver and death.

Effects of insufficient uptake of Se in animal populations include metabolic damage and white-muscle disease, among others (Kishchak, 1998). In Finland, insufficient Se uptake in animal populations led to muscular dystrophy and other disorders, with the prescribed remedy to add Se to commercial animal feeds (Aro et al., 1998). In contrast, the negative biological effects of Se at toxic concentrations include retardation of growth and development of the organism, negative effects on the nervous system, inhibition of tissue breathing, and decreases in enzyme activity (Kischcak, 1998), resulting in numerous mortalities and deformities. "Alkali disease" (i.e., selenosis) in large animals, first reported by an army surgeon stationed in the Nebraska Territory in the mid-nineteenth century, was identified to be a cause of Se by Moxon (1937). In the Colorado River basin, declines in fish populations have been linked to Se contamination in river water (Hamilton, 1998), and Skorupa (1998) outlines twelve case studies documenting fish and waterfowl Se poisoning in California, Utah, Colorado, Wyoming, Texas, North Carolina, and Sweden. Lemly (1998), in discussing the pathology of Se poisoning in fish, reported that range of appropriate Se uptake for fish as between 0.5 $\mu g\ g^{-1}$ dry weight and 3.0 $\mu g\ g^{-1}$ dry weight, although these values are approximate.

Perhaps the most famous case of Se poisoning among waterfowl is the case of Kesterson Reservoir, a drainage reservoir collecting agricultural drainage water in the San Joaquin Valley, California, that also served as a Pacific byway for migratory birds and a wildlife habitat. Beginning in 1983, scientists reported a high incidence of death and deformities among water fowl (Flury et al., 1997) with elevated Se concentrations found in aquatic organisms such as fish and invertebrates. As discussed in Section 1.2, the results of this discovery and subsequent investigation into the cause of the Se contamination led to comprehensive field studies that

illuminated the cause of Se contamination in Kesterson Reservoir, the western United States, and other regions of the world.

1.2 SELENIUM IN GEO-HYDROLOGIC SYSTEMS

As a trace constituent in all igneous rocks Se is present in all soils (Byers, 1937), and the crustal concentration of Se has been estimated at approximately 0.05 to 0.09 mg kg^{-1} (Wang and Gao, 2001). The spatial distribution of Se in geologic formations and associated soils, however, is dependent on the geologic history of a given region. Significantly high Se concentrations, for example, occur mostly in marine shale that was deposited during the Cretaceous period, with Se substituting for S in pyrite (FeS_2) to form seleno-pyrite ($FeSe_2$) (Bye and Lund, 1982; Logan et al., 1987). Se-bearing shale has been studied and documented in Finland (Alfthan et al., 1995), Norway (Bye and Lund, 1982), Japan (Mizutani et al., 2001), and many parts of the western United States (e.g., Presser et al., 1994). Associated shale-derived soils such as those found in Colorado and other western states tend to have high (2 to 10 mg kg^{-1}) soil Se concentrations whereas the Northwest, Southeast, and Great Lake states have concentrations below 0.05 mg kg^{-1} (Kubota et al., 1967).

The results of the study of Kesterson Reservoir, as well as other studies worldwide (e.g., Seiler, 1995), concluded that the occurrence of Se contamination is a function of this geologic history, as well as hydrologic conditions and land management practices, of a given geographic region. In the case of Kesterson Reservoir, it was determined that irrigation water collected Se derived from marine shales forming the bedrock that underlies the alluvial aquifers, with resulting drainage water containing toxic concentrations of Se (Seiler, 1995). Other studies also correlated Se contamination with geologic formations and associated soils. For example, corn

grown in soils derived from Se-rich carbonaceous shale led to Se toxicity among human populations (Yang and Xia, 1995). Also, the Kashin-Beck disease reported by Wang and Gao (2001) in China and the diseases reported by Aro et al. (1998) in Finland resulted from Se-deficient soils, a function of the local geology.

The case of Kesterson Reservoir prompted a large-scale field study through the National Irrigation Water Quality Program (NIWQP) to determine if Se contamination conditions could occur elsewhere in irrigated regions of the western United States. Between 1986 and 1993, 26 regions in 14 states in the western United States, shown in Figure 1-1A, were studied in regards to groundwater and surface water in alluvial stream-aquifer systems. Due to the presence of Se in marine sedimentary rocks, which form the near-surface bedrock beneath 805,000 km^2 of land in the 17 contiguous western states (Seiler, 1997) (Figure 1-1B), all 14 of the study areas determined to be seleniferous (i.e., Se concentration in surface water in and downstream of study areas) are associated with marine sedimentary rocks, as shown in Figure 1-2. Results indicated also that Se contamination occurs only in arid and semi-arid climates.

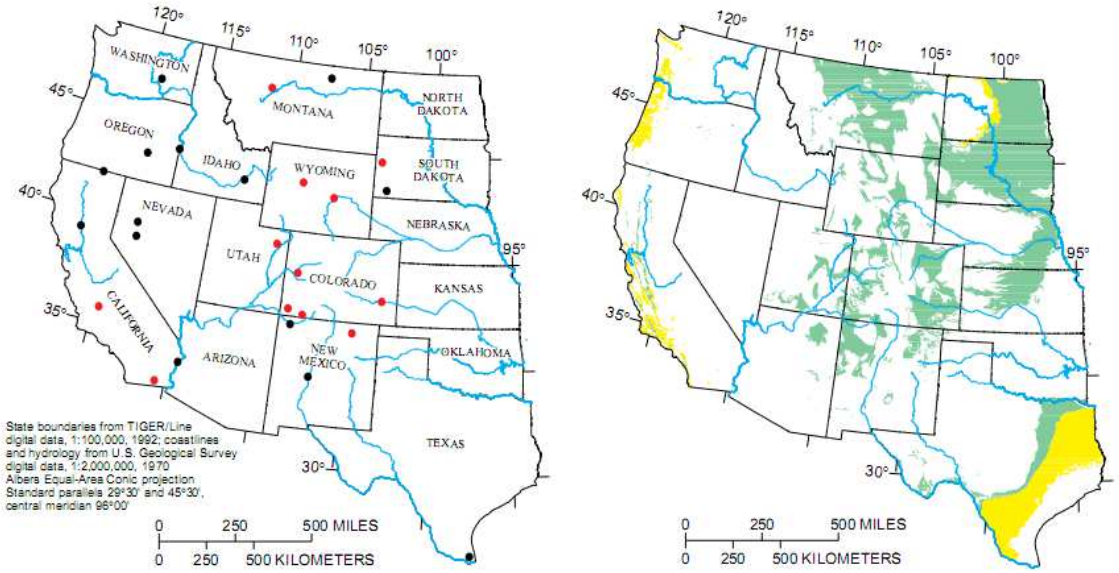

Figure 1- 1. (A) Locations of study states in the NIWQP and (B) Spatial distribution of Upper Cretaceous (green) and Tertiary (yellow) marine sedimentary deposits. From Seiler (1997).

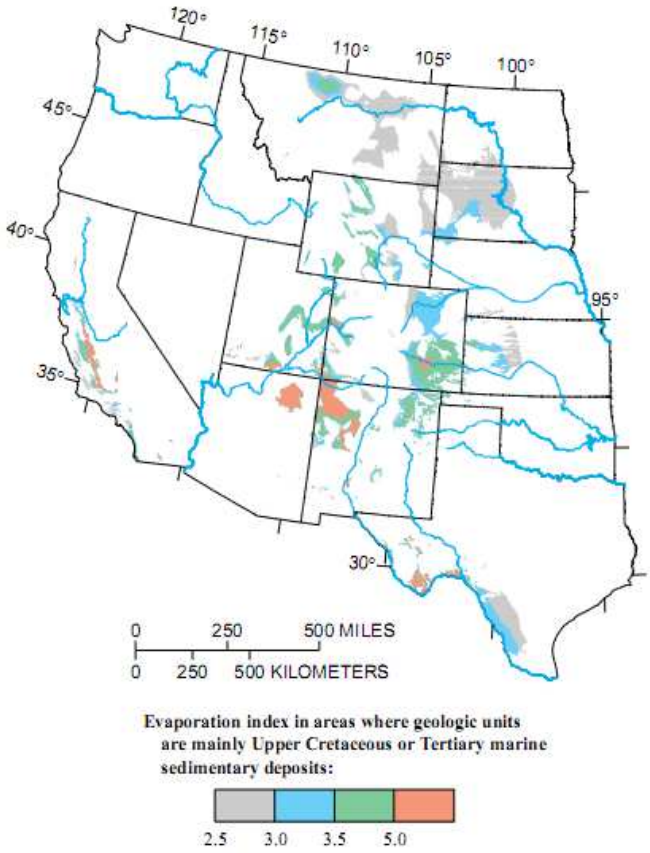

Figure 1- 2. Locations of regions in the western United States that are susceptible to irrigation-induced Se contamination. From Seiler (1997).

Se contamination in these areas is a result of the release of Se from $FeSe_2$ through chemical reduction of oxidative species such as dissolved oxygen (O_2) and nitrate (NO_3) (Wright, 1999; Fernández-Martínez and Charlet, 2009; Stillings and Amacher, 2010). The mobilized Se is transported through the aquifer and discharged to nearby surface water bodies. Problems are exacerbated in irrigated systems due to the presence of O_2- and NO_3-laden water and the increased rate of groundwater flow and discharge to adjacent surface water bodies.

To determine the geographic areas of potential occurrence and frequency Se-related diseases for both human and animal populations, an assessment of the spatial distribution, mobilization,

transport, and fate of Se in geologic formations, soils, and associated waters must be performed at the watershed scale. Within a given watershed, an understanding of the fate and transport of Se in the subsurface soil-aquifer system is essential due to (i) the mobilization of Se occurring typically at near-surface shale or the bedrock shale-aquifer interface, (ii) the rate of Se release from shale dependent on the rate of transport of O_2 and NO_3 through the aquifer and subsequent arrival at the bedrock-aquifer interface, (iii) the speciation, transport, and crop uptake of Se that occurs in the root zone in the shallow subsurface layers, which governs the leaching of Se to the saturated zone of the aquifer, (iv) the use of pumped groundwater for domestic animals and for drinking water for municipalities, and (v) the role of the aquifer as a large buffer reservoir between the water infiltrating at the ground surface and the groundwater discharged to surface water.

1.3 INVESTIGATING THE FATE AND TRANSPORT OF SELENIUM IN SOIL AND GROUNDWATER SYSTEMS

As a result of the Kesterson Reservoir tragedy, numerous studies regarding the occurrence, mobilization, and chemical fate and transport of Se in soil and aquifer systems were undertaken. These studies, along with others worldwide, provided important knowledge regarding the chemistry, speciation, and fate and transport of Se in soil-aquifer systems.

Numerous studies have documented the speciation of Se and associated oxidation-reduction (redox) reactions and the conditions of occurrence (e.g., Macy et al., 1989; Oremland et al., 1990; Martens and Suarez, 1997; Fernández-Martínez and Charlet, 2009), the sorption of mobile Se species (Ahlrichs and Hossner, 1987; Balisterieri and Chao, 1987), and the release of Se from Se-bearing pyrite into groundwater in the presence of O_2 (Stillings and Amacher, 2010) and NO_3

(Wright, 1999). Numerous investigators (e.g., Losi and Frankenberger, 1998; Guo et al., 1999) also have analyzed the kinetics of such systems.

Field and laboratory studies also have been conducted to determine the potential fate and transport of Se in soil profiles. Neal and Sposito (1991) analyzed agricultural soil collected from the western San Joaquin Valley, CA to study the effect of irrigation practices and carbon (C) on Se leaching. Guo et al. (1999) performed Se displacement experiments to evaluate redox reactions and Se leaching in saturated soil columns. Results from both studies indicated that chemical reduction of mobile Se forms to immobile forms would occur with additions of C to the soil or the soil water, and hence decrease the amount of leaching. Gao et al (2000) constructed a flow-through wetland system in the San Joaquin Valley and studied the Se speciation and accumulation in the system's waters and sediments to determine the potential for Se removal. They concluded that significant Se removal was possible, with chemical reduction and immobilization the major sink of dissolved Se. Zhang and Moore (1997) found similar results for wetland sediments in a lake in Montana.

Additional field studies have been conducted to investigate the cause of high Se concentrations in groundwater. Deverel and Fujii (1988) and Deverel and Millard (1988) evaluated samples of shallow groundwater in irrigated areas of the western San Joaquin Valley to determine the source and cause of high Se concentrations in groundwater. Results from their studies indicated that high Se concentrations in shallow groundwater are strongly influenced by the geologic sources of the alluvial soil material as well as hyper-concentration due to evaporation from shallow water tables.

Results from both Neal and Sposito (1991) and Guo et al. (1999) indicated that Se would be chemically reduced and immobilized in the upper layers of the soil profile, particularly if

adequate amounts of C are present. These results, however, neglect the influence of other species in the soil water and groundwater. As a redox-sensitive species, Se depends on the succession of terminal e^--accepting processes (Korom, 1992; McMahon and Chapelle, 2008), and is consumed after the concentrations O_2 and NO_3 have been decreased to a certain threshold value (Weres et al., 1990; Oremland et al., 1990; Benson, 1998). Hence, the presence of O_2 and NO_3 inhibits the chemical reduction of mobile Se and thus induces Se leaching (Fio et al., 1991). Incorporating the influence of O_2 and NO_3 likely would alter substantially the results of Neal and Sposito (1991) and Guo et al. (1999).

A key component of Se fate and transport in the soil system, and hence the influence on Se leaching, is the cycling of organic and inorganic Se. Studies have documented the cycle of Se in the plant-soil system (Shrift, 1964) similar to the cycle of nitrogen (N), C, and S. Plant uptake (Bisbjerg and Gissel-Nielsen, 1969; Logan et al., 1987; Ajwa et al., 1998; Milne, 1998), conversion to organic Se within the plant (Wang and Gao, 2001; Sors et al., 2005), and mineralization of organic Se in the soil to inorganic, mobile forms of Se (Logan et al., 1987; Ajwa et al., 1998; Budjdos et al., 2000) have been reported.

Due to the complex dynamics of Se transformation processes, the use of numerical reactive transport models is an appealing approach in analyzing the state of the system and system processes as well as for scenario analysis. Numerical modeling studies involving Se fate and transport have thus far been confined to one-dimensional (1D) soil profile models and simplified two-dimensional (2D) vertical profile models. For the majority of the studies, Se transport in saturated or unsaturated conditions is subject to sorption processes, redox reactions, or both in a 1D soil column in a laboratory setting (Table 1-1). For most studies only sorption, employing equilibrium sorption isotherms, has been simulated. Forcing terms such as inflow rate and

concentration of influent have been kept very basic. None have taken into account the influence of other species, such as O_2 and NO_3, on Se processes. Incorporation of redox reactions was first included by Lui and Narasimhan (1994) in a modeling study of the vertical movement of Se in the aquifer underlying the Kesterson reservoir. Guo et al. (1999) simulated the reduction and equilibrium sorption of mobile Se species in saturated soil columns, with reduction rates and sorption terms estimated through calibration.

Table 1- 1. Summary of characteristics included in Se Numerical Modeling Studies

Study	Model Dim.	Sat-urated	Unsat.	Sorption		Redox	Volatil.	Plant Uptake	Org. Matter Decay
				SeO_4	SeO_3				
Alemi et al. 1988	1D	x		x					
Fio et al. 1991	1D	x		x	x				
Alemi et al. 1991	1D		x	x	x				
Liu and Narasimhan 1994	1D	x				x			
Guo et al. 1999	1D	x		x	x	x	x		
Mirbagheri et al. 2008	1D		x	x	x	x	x	x	x
Tayfur et al. 2010	2D		x	x	x	x	x	x	x

More recently, Mirbagheri et al. (2008), in a 1D model, incorporated a more complete suite of the processes involving Se species in the unsaturated zone, including advective-dispersive transport, sorption, redox reactions, volatilization, mineralization and immobilization, and plant uptake of Se. Mineralization and immobilization are simulated using first-order rate constants. In a similar study, Tayfur et al. (2010) employed a 2D finite element model to simulate Se transport in both saturated and unsaturated soil zones, considering the same processes as Mirbagheri et al. (2008). The model was applied to two soil profiles 300 cm in depth, with four observations of Se for each profile. For both studies, reactions were simulated using simple first-order kinetics, without taking into account the influence of organic carbon, required for reduction reactions to proceed, and other species inhibiting the reactions from occurring.

Of the modeling studies shown in Table 1-1, only Guo et al. (1999) investigated land-management alternatives using a calibrated Se model, although to a very limited degree. Using a calibrated 1D Se leaching model, water application rates of 1, 2, and 5 cm day-1 were investigated, with results indicating that Se could be retained in the upper layers of the soil profile even under high infiltration rates. However, as previously mentioned their study neglected the influence of other higher-redox species and hence provided unrealistic results in an agricultural setting. Remediation schemes such as permeable reactive barriers have been recommended for Se remediation (e.g., Bureau of Reclamation, 2006), although potential benefits have not yet been investigated in a model application to a study site.

1.4 RELATED MODELING STUDIES

1.4.1 Related Models as a Guide for Selenium Transport Model

Although Se fate and transport modeling has been restricted to 1D and simple 2D domains, other modeling studies dealing with redox-sensitive species and nutrient cycles provide a framework for modeling Se fate and transport in large-scale aquifer systems. Studies simulating the fate and transport of redox-sensitive species such as NO_3 and SO_4 include Frind et al. (1990), Molénat and Gascuel-Odoux (2002), and Conan et al. (2003), among others (e.g., Shamrukh et al., 2001). The majority of these studies simulate reduction reactions as first-order kinetic processes, with several employing the Monod or dual-Monod kinetic approach with sequential reduction processes as specified by Widdowson et al. (1988), Kindred and Celia (1989), and Kinzelbach et al. (1991), where (i) the rate of the kinetic reaction depends on the relative abundance of both the e^- acceptor and the e^- donor, and (ii) the reactions are dependent on the presence of other redox-sensitive species, with inhibition occurring for lower-redox species.

Nutrient cycling simulation models for large-scale systems include the NITS (Nitrogen Transformation) module (Birkinshaw and Ewen, 2000a) of the spatially-distributed river catchment modeling system SHETRAN (Ewen et al., 2000) as well as the study performed by Wriedt and Rode (2006) in their study of NO_3 transport in a catchment system.

1.4.2 Simulating Fate and Reactive Transport of Multiple Species in Variably-Saturated Subsurface Systems

Of the available models capable of simulating the fate and transport of species in subsurface systems of multiple dimensions, such as VS2DT (Healy, 1990), TRAN3D (Gambolati et al., 1994), RT3D (Clement, 1997), MT3DMS (Zheng and Wang, 1999), SHETRAN (Ewen et al., 2000), MIN3P (Mayer et al., 2002), HYDRUS (2D/3D) (Simunek et al., 2006), MODFLOW-SURFACT (Panday and Huyakorn, 2008), PHAST (Parkhurst et al., 2010), SUTRA (Voss and Provost, 2010), only a select few (SHETRAN, MIN3P, MODFLOW-SURFACT) provide for multiple interacting species in variably-saturated transport systems. The capacity of a model to simulate water flow and chemical transport in the root zone and underlying unsaturated zone in of vital importance for simulating the fate and transport of species in agriculturally-influenced aquifers. This is especially true for species, such as Se and NO_3, that are redox-sensitive and that are cycled through the soil-plant system.

These few models, however, are hampered by a reliance on groundwater flow simulators that solve the full Richards equation for variably-saturated flow, and hence are limited in spatial and temporal applications due to high computational burden. Furthermore, only SHETRAN contains a module for N cycling and transport. The Soil and Water Assessment Tool (SWAT) (Neitsch et al., 2011), although designed for assessment of nutrient transport and the impact of land management practices in large-scale watersheds, treats groundwater flow in a simplified manner

inconsistent with the requirements for Se fate and transport in subsurface systems. Specifically, the model partitions the aquifer into a shallow unconfined aquifer and a confined deep aquifer, with the former contributing flow to the main channel of the catchment and the latter assumed to discharge water to surface water bodies at locations outside of the watershed.

1.4.3 Methods of Model Calibration

Fate and transport models for groundwater systems typically require a large number of parameters (e.g., rate constants for chemical reactions) for the included physical and chemical processes. Various methods have been employed to provide or estimate parameter values for a model. Typically, a single value for each parameter is estimated or taken from the literature and applied to the entire model domain (e.g., Frind et al., 1990; Conan et al., 2003; Wreidt and Rode, 2006). Values are taken from previously-performed field studies (Frind et al., 1990; Conan et al., 2003), from published literature or geochemical databases (e.g., Heatwole and McCray, 2007) or through trial and error techniques during the modeling processes to match observed and simulated species concentration at points in the aquifer (Lu et al., 1999; Shamrukh et al., 2001). In a few selected cases, automated parameter estimation techniques have been used. For example, van Breukelen et al. (2004) used the nonlinear optimization program PEST (Doherty, 2005) to estimate model parameters in a 1D leaching scenario by comparing simulated and observed species concentrations. Some studies (Almasri and Kaluarachchi, 2007) attempted automated calibration before resorting to manual trial-and-error methods. For other studies, as in the application of the NITS nitrogen cycling module to a small watershed in the United Kingdom (Birkinshaw and Ewen, 2000b) or the application of an MT3DMS model to simulate NO_3 transport in France (Molénat and Gascuel-Odoux, 2002), parameter estimation was not performed.

Although a comparison between simulated and observed concentrations at points within the aquifer often is used in calibration of reactive transport models, such a procedure often is not practical or feasible (Konikow, 2011). Whereas gradual spatial variations of hydraulic head between points of measurement (i.e., observation wells) lend to straight-forward calibration of groundwater flow models and reproduction of point observations, field measurements of concentration can vary drastically in magnitude in space and time and hence present a stiff challenge to reproduce point measurements via parameter estimation. Furthermore, scaling issues arise when comparing point observations in the field (e.g., samples from small-diameter observation wells) to finite-difference cell averaged values provided by numerical models. For large-scale study sites, this may result in comparing point values to spatial areas the size of cultivated fields or larger (Ledoux et al., 2007). Hence, as discussed further by Konikow (2011), reproducing major trends and locally-averaged values should be the aim of transport models rather than reproducing point-measured concentrations. This is reflected to some degree in the work of Almasri and Kaluarachchi (2007) in a 388 km^2 aquifer Washington state, who used time-averaged measurements of NO_3 concentration (although still at specific observation wells in the aquifer) to estimate denitrification rates, and the work of Ledoux et al. (2007) in a 95,560 km^2 in the Seine basin in north-central France, who used comparisons between the probability distribution of simulated and computed values of NO_3 concentration.

1.4.4 Investigating Alternative Land-Management Practices

The objective of many modeling studies is the use of the model, calibrated and tested for accuracy under historical conditions, to investigate the impact of alternative cultivation, land-use, and water management practices on concentrations and mass loadings to surface water. For agricultural watersheds, typically the reduction in loadings of nutrients (N and phosphorus P) and

sediments from the aquifer to the stream are used as indicators of improvement and remediation. Alternative management schemes typically explore reduction in nutrient application, reduction in applied irrigation water, changes in land-use and cultivation practices, and implementation of riparian buffer zones.

To cite briefly several small-scale studies, Garcet et al. (2002) used a deterministic N-balance model to explore the impact on NO_3 leaching for 77 scenarios of fertilizer loading patterns and crop rotation for fields in central Belgium using the WAVE model, and El-Sadek et al. (2001) used a similar model to investigate NO_3 transport within the soil profile under various fertilizer loadings. Ma et al. (1998) explored the influence of manure application reduction on NO_3 leaching. For large-scale systems, Molénat and Gascuel-Odoux (2002) in France, Vaché et al. (2002) in Iowa, Conan et al. (2003) in France, Chaplot et al. (2004) in central Iowa, Almasri and Kaluarachchi (2007) in Washington state, Ledoux et al. (2007) in France, Sahu and Gu (2009) in Iowa, Sood and Ritter (2011) in Delaware, Lee et al. (2010) in South Korea, and Zhang et al. (2012) in China explored the impact of reduction in applied N fertilizer on N loads to streams. Chaplot et al. (2004) decreased current N applications by 20, 40, and 60%, Ledoux et al. (2007) by 20%, Almasri and Kaluarachchi (2007) by 40%, Lee et al. (2010) by 30%, and Conan et al. (2003) decreased N manure application by 19%. These values of decrease are consistent with the reports of Babcock and Blackmer (1992) and Trachtenberg and Ogg (1994), who report that farmers apply a fertilizer loading that is generally 24-38% higher than the demand of the crop.

A reduction in applied irrigation water also has been investigated for its influence on nutrient loading, although this typically has been explored only at the field scale. For example, Buchleiter et al. (1995) and Ma et al. (1998) investigated the impact of over-irrigation and reduced irrigation, respectively, for single cultivated fields. Rong and Xuefeng (2011), for a field

experiment in China, evaluated the effect of irrigation application rates on NO_3 in the soil profile, using a 25% reduction in traditional irrigation rates.

The implementation of riparian buffer zones and their impact on reducing nutrient loads to streams has been studied extensively in both field and modeling experiments. As a source of organic carbon, these buffer zones provide an ideal condition for chemical reduction reactions (e.g., denitrification) that can remove dissolved nutrients from the groundwater before discharging to surface water (Spruill, 2000). Field studies generally quantify the removal of nutrient mass as well as the required width of the buffer zones. For example, Heathwaite et al. (1998) found that the use of buffer strips reduced N export in surface runoff by 94%, Spruill (2000) found that NO_3 concentrations were 95% lower in buffer areas than non-buffer areas, and the study of Hefting and Klein (1998) in The Netherlands showed a 95% decrease in NO_3 concentration in the groundwater flowing through the riparian buffer zone, with numerous others also showing favorable results (e.g., Anbumoazhi et al., 2005; Hefting et al., 2005).

In modeling studies, Sahu and Gu (2009), in their study on a 51.3 km^2 watershed in Iowa, indicated that a 30% reduction in N load could be achieved by establishing a watershed vegetation buffer. Lee et al. (2010) investigated the use of a 30-60 m wide riparian buffer system, Sood and Ritter (2011) explored providing grassland riparian zones, and Zhang et al. (2012) explored establishing riparian vegetation buffers, with a resulting 13.9% decrease in N loads. Vaché et al. (2002) found that combinations of riparian buffers, engineering wetlands, filter strips, and rotational grazing potentially could reduce current loadings of NO_3 by 54 to 75%, with the conclusion that traditional approaches to improving water quality will have little to no impact.

In recognition that several years to decades may be required for BMPs to provide a change in loadings to streams due to the long travel time of groundwater, simulations exploring alternative management scenarios typically are run for one or more decades using system inputs (e.g., rainfall, climate variables, irrigation application, etc.) that are both reflective of watershed conditions and also capture the temporal variability of climate. For example, Garcet et al. (2002) and El-Sadek et al. (2001) used simulation runs of 30 years in their field-scale studies, and Conan et al. (2003), Chaplot et al. (2004) and Ledoux et al. (2007) used 15-year, 32-year, and 45-year forecast simulations, respectively. Almasri and Kaluarachchi (2007) and Zhang et al. (2012) both used simulation periods of 10 years.

1.5 ADDRESSING RESEARCH GAPS

In summary, Se species are redox-sensitive and subject to the overall cycle of Se in soil and aquifer systems. Numerous investigators have documented processes, rates of processes, and the influence of other species, such as O_2 and NO_3, on these processes. Several modeling studies have been undertaken to study Se fate and transport, each in a simplified soil profile setting with measurement data limited to that profile. None, however, have included the influence of other species on Se transformations in the Se cycle, and none have attempted to apply the Se cycle at scales larger than soil profiles. Furthermore, the development of numerical models capable of simulating the fate and transport of species and nutrients at the regional scale requires methods to efficiently and accurately estimate the spatially-variable parameter values required by the models. In order to provide a working tool that simulates the fate and transport of Se in a regional-scale aquifer system driven by regional hydrologic processes and localized land

management practices, i.e., to develop a tool that can accurately investigate best-management practices, the objectives of this research effort are:

(i) Development of a conceptual model of the cycle of Se in an agricultural groundwater system through field and laboratory studies. The processes of Se transformation will be influenced by other species and, as such, the cycles and processes affecting these other species will be included. Specifically, these species include O_2 and N species.

(ii) Development of a numerical reactive transport model capable of simulating a) reactive transport in both the unsaturated and saturated zones, with the required forcing terms, and b) the cycle of Se and other nutrients on a local and regional scale. For a), the principal concern besides accuracy is the efficiency and speed in the solution of the groundwater flow simulation as compared to other variably-saturated transport models. For b), the model requires testing in localized settings (i.e., soil profile) to ensure the accuracy of the nutrient cycling and chemical reaction module.

(iii) Development of a parameter estimation methodology that allows spatially-variable parameter values to be estimated in a regional aquifer setting. *A priori* estimates of parameter values are based on frequency distributions of parameter values compiled from the literature.

(iv) Application of the developed variably-saturated, reactive transport model of Se species to a regional-scale, agricultural alluvial aquifer system. This application includes model calibration, model testing, and scenario testing in which selected BMPs will be analyzed for Se and NO_3 remediation in the groundwater as well as mass loadings of Se and NO_3 to surface water. Model calibration is performed using concentration values averaged in space and time, with additional comparisons

performed between observed and simulated values to determine if the model is able to reproduce the global statistics of the observed measurements as well as observed inter-species relationships. In regards to scenario testing, of prime importance is the influence of other species on the fate and transport of Se within these BMPs.

The prime motivation for these research objectives is the Se contamination problem in the alluvial stream-aquifer system of the Lower Arkansas River Valley (LARV) in southeastern Colorado which serves as a reference system for data collection, data analysis, and numerical modeling. The LARV is an ideal setting for application sine since (i) it is a designated seleniferous river basin, as determined through the NIWQP (Seiler, 1997) (Figure 1-3), (ii) all river segments have been identified as impaired for Se by the Colorado Department of Public Health and Environment (CDPHE), (iii) it has been monitored for both hydrologic and chemical species components during the last decade by Colorado State University, hence yielding an extensive dataset of measured groundwater and surface water species concentrations, and (iv) a groundwater flow model for the Upstream Study Region has been constructed, calibrated, and tested. It is important to note that although the model herein is applied to a region with Se contamination, the model equally could be applied to a region of Se deficiency, and hence used to investigate land-management practices to increase the concentration of Se in groundwater and soils. This fulfills the main objective of this dissertation in providing a tool that simulates the fate and transport Se in regional groundwater systems regardless of the nature of the Se problem.

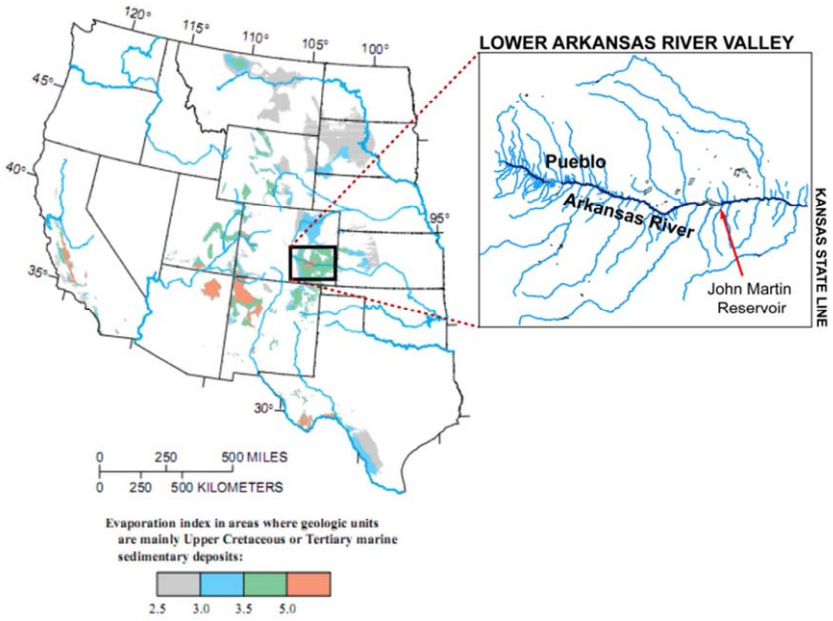

Figure 1- 3. Lower Arkansas River Valley (LARV) in southeastern Colorado in association with the Se contamination problem areas identified by the National Irrigation Water Quality Program (NIWQP) (Seiler, 1997).

The results of these research objectives are organized according to the following chapters, with each chapter building on results of the previous chapter:

- Chapter 2 presents results of field and laboratory work aimed at first, investigating the presence of Se in the groundwater and bedrock shale of the LARV and second, investigating the influence of O_2 and NO_3 on near-surface chemical processes as well as chemical processes at the bedrock-aquifer interface.
- Chapter 3 presents the use of the Ensemble Kalman Filter (Evensen, 1994) to provide estimates of spatially-variable first-order rate constants in an aquifer system. As such, it provides a new methodology for estimating model parameters in large-scale chemically active aquifer systems. The methodology is used in the small-scale modeling study in Chapter 5. Although not used as a parameter estimation methodology for the regional-

scale model presented in Chapter 6, results could be used in regional-scale reactive transport simulations wherein the reaction rates strongly influence the resulting species concentration in groundwater.

- Chapter 4 outlines the development of UZF-RT3D, a numerical model capable of simulating the reactive transport of multiple chemically-interactive species in large-scale, variably-saturated aquifer systems. The model couples the Unsaturated Zone Flow (UZF1) package (Niswonger et al., 2006) of MODFLOW (Harbaugh, 2005), designed for large-scale systems, with RT3D (Reactive Transport in 3 Dimensions) (Clement, 1997), originally designed only for reactive transport in the saturated zone of the aquifer. The chapter outlines the modification of RT3D to handle reactive transport in the unsaturated zone, the linkage with MODFLOW-UZF1, and test simulations to verify the accuracy of the model and explore advantages over other available models.
- Using the results of Chapter 2-4, Chapter 5 presents the development of a Selenium reaction module to be used with UZF-RT3D and its application to a field study site. The chapter outlines the key features of Se fate and transport in agricultural groundwater systems and the method by which they are incorporated into a reaction module within UZF-RT3D. The resulting model is referred to as UZF-RT3DAG to denote its use in agricultural systems. All pertinent chemical reactions and system sources/sinks as reported in the published literature are accounted for, including the influence of O_2 and N species on the chemical reactions involving Se species as presented in Chapter 2. The model is tested against data collected at field test plots at the CSU Arkansas Valley Research Center in Rocky Ford, CO, and uses the methodology described in Chapter 3 to estimate selected model parameters.

- Chapter 6 builds upon the results in Chapter 5 and presents the application of UZF-RT3DAG and accompanying Se reaction module to the 50,600-ha regional-scale stream-aquifer system within the Upstream Study Region of the LARV. Besides the near-surface root zone processes described in Chapter 5, the large-scale processes included in the model in Chapter 6 are shown in Figure 1-4. Such processes include canal seepage, spatially-variable application rates of irrigation water, spatially-variable loading of fertilizer, 3D groundwater flow and reactive transport, mass exchange between the groundwater and surface water, and autotrophic reduction of O_2 and NO_3 in the vicinity of shale and resulting release of Se from $FeSe_2$. Sensitivity analysis and parameter estimation is performed for the time period January 1 2006 to March 31 2008 using space- and time-averaged groundwater concentrations of O_2, NO_3, and Se and mass loadings of Se to the Arkansas River, and model testing is performed for the time period April 1 2008 to October 31 2009.
- Chapter 7 summarizes the use of the calibrated and tested model of the Upstream Study Region to investigate BMPs in regards to the remediation of Se contamination. Results of the BMPs on remediation of NO_3 contamination also are reported. Practices investigated included reduced irrigation, reduced fertilizer loadings, a decrease in the species concentration in canal water, enhanced chemical reduction in the riparian zones to represent the implementation of riparian buffer zones, and several combinations of these practices. The duration of simulation periods and applied hydrologic forcing terms are chosen to characterize historical climate variability.
- Chapter 8 presents major findings, conclusions, and avenues of future research.

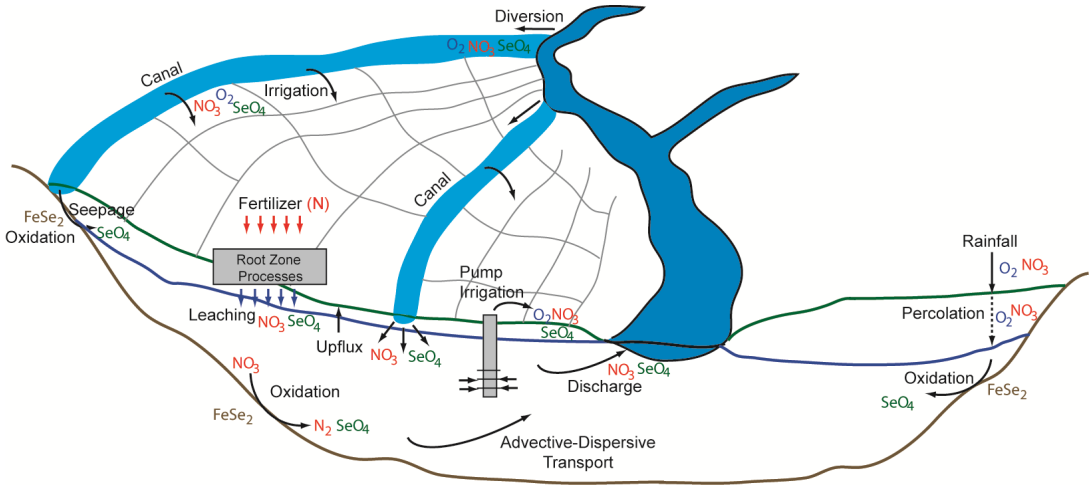

Figure 1- 4. Conceptual model of the fate and transport of O_2, NO_3, and SeO_4 in an irrigated stream-aquifer system subject to agricultural activities (e.g., irrigation and fertilize loading).

Several appendices are included for completeness of the research performed:

- Appendix A contains a full description of the UZF-RT3DAG model, with a description of reaction packages, explanation of model subroutines, and explanation of example input files.
- Appendix B contains additional information and results from the application of UZF-RT3DAG to the Upstream Study Region. These results include aerial photographs of the region, complete listing of field data used in model calibration, and point comparisons between observed and simulated concentrations of species at all 93 observation wells in the Upstream Study Region.
- Appendix C contains detailed results of the Sensitivity Analysis performed in Chapter 6 and discusses system processes and system inputs that likely require further investigation or appropriate management techniques to control and remediate Se contamination.

- Appendices D, E, and F are published or submitted journal articles that present the methodology of using data assimilation to estimate parameters in both hydrologic and solute reactive transport systems. Specifically, these papers present the development and application of an Ensemble Smoother to estimate the spatial distribution of hydraulic conductivity and chemical reaction rate constants. Although these methods were not used in the application of UZF-RT3DAG to the LARV, they are included here as a demonstration of potential use for parameter estimation in catchment systems.

    - Appendix D:
      Bailey, R.T., and D.A. Baù (2010), Ensemble Smoother assimilation of hydraulic head and return flow data to estimate hydraulic conductivity, *Water Resour. Res.*, 46, W12543, doi:10.1029/2010WR009147.

    - Appendix E:
      Bailey, R.T., and D.A. Baù (2012), Estimating geostatistical parameters and spatially-variable hydraulic conductivity within a catchment system using an ensemble smoother, *Hydrol. Earth Syst. Sci.*, 16, 287-304.

    - Appendix F:
      Bailey, R.T., Baù, D.A., and T.K. Gates (2012), Estimating spatially-variable rate constants of denitrification in irrigated agricultural groundwater systems using an ensemble smoother, *J. Hydrol.*, submitted in revised form June 2012.

CHAPTER 2

THE INFLUENCE OF NITRATE ON SELENIUM IN IRRIGATED AGRICULTURAL GROUNDWATER SYSTEMS[1]

2.0 SUMMARY Selenium (Se) contamination of groundwater is an environmental concern, especially in areas where aquifer systems are underlain by Se-bearing geologic formations such as marine shale. This study examined the influence of nitrate (NO_3) on Se species in irrigated soil and groundwater systems and presents results from field and laboratory studies that further clarify this influence. Inhibition of selenate (SeO_4) reduction in the presence of NO_3 and the oxidation of reduced Se from shale by autotrophic denitrification were investigated. Groundwater sampling from piezometers near an alluvium-shale interface suggest that SeO_4 present in the groundwater was due in part to autotrophic denitrification. Laboratory shale oxidation batch studies indicate that autotrophic denitrification is a major driver in the release of SeO_4 and sulfate. Similar findings occurred for a shale oxidation flow-through column study, with 70% and 31% more reduced Se and S mass, respectively, removed from the shale material in the presence of NO_3 than in its absence. A final laboratory flow-through column test was performed with shallow soil samples to assess the inhibition of SeO_4 reduction in the presence of NO_3, with results suggesting that a concentration of NO_3 of approximately 5 mg L^{-1} or greater will diminish the reduction of SeO_4. Although not trivial, the inclusion of the fate and transport

[1] As published in the Journal of Environmental Quality, Ryan T. Bailey, William J. Hunter, Timothy K. Gates Used with permission, from Journal of Environmental Quality 41:783-792 (2012).

of NO_3 and other oxidants such as dissolved oxygen is imperative when studying or simulating the fate and transport of Se species in soil and groundwater systems.

2.1 INTRODUCTION

An element that naturally occurs as a trace constituent in geologic formations and associated soils, selenium (Se) is an essential nutrient for animals and humans, although high concentrations and bio-accumulation can prove detrimental to health. These two effects have led to Se being termed an "essential toxin" [Stolz et al., 2002] and the "double-edged sword" element [Fernández-Martínez and Charlet, 2009], with a narrow range between dietary deficiency (<40 $\mu g\ day^{-1}$) and toxic levels (>400 $\mu g\ day^{-1}$) [Levander and Burk, 2006] for humans. Over the previous three decades, the presence of either deficient or elevated concentrations of Se in ground waters, surface waters, and associated plants and cultivated crops has emerged as a serious issue in the United States [Seiler, 1995; Seiler, 1997; Gates, 2009; Hudak, 2010], northern and western Europe [Bye and Lund, 1982; Aro et al., 1998; Alfthan et al., 1995], the Middle East [Afzal et al., 2000; Kuisi et al., 2010], and East Asia [Mizutani et al., 2001; Zhang et al., 2008]. Toxic concentrations in surface water bodies fed by contaminated aquifer systems have led to deformities and death among water fowl [Flury et al., 1997] and fish populations [Hamilton, 1998; Skorupa, 1998].

Regardless of the nature of concern regarding Se, whether concentrations are either at deficient or toxic levels in water supplies and habitats and in cultivated crops, there is a basic need for information on the movement of and chemical processes that influence Se within a dynamic soil-aquifer system influenced by agricultural practices. The transport and transformation of Se species in soil and groundwater systems have been well-documented

[Fernández-Martínez and Charlet, 2009], with efforts principally guided towards remediation schemes that eliminate Se from the groundwater solution through oxidation-reduction (redox) and sorption processes.

However, the study of the fate and transport of Se species is incomplete without an understanding of the effects of higher-redox species such as dissolved oxygen (O_2) and nitrate (NO_3) on Se. These effects include (i) inhibition of the chemical reduction of toxic forms of Se [Masscheleyn et al., 1989; Oremland et al., 1989; Weres et al., 1990; Sposito et al., 1991; White et al., 1991; Zhang and Moore, 1997], and (ii) the release of Se from shale due to the autotrophic reduction of oxidative species [Wright, 1999; Fernandez-Martinez and Charlet, 2009; Stillings and Amacher, 2010].

For the former process, inhibition of reduction allows toxic forms of Se to remain in solution, leading to enhanced leaching and transport to surface water bodies. Studies investigating the fate and transport of Se in soil systems often neglect the influence of O_2 and NO_3 on Se speciation and transformation [e.g., Guo et al., 1999], and hence predict the reduction and immobilization of Se in agricultural soils when in fact Se would remain in solution and be leached due to the presence of O_2 and/or NO_3. For the process of autotrophic reduction, O_2-rich and/or NO_3-rich groundwater coming into contact with shale present either in the shallow or deep subsurface layers oxidize reduced Se to mobile forms.

In this report we present a short review of Se transport and transformations in soil and aquifer systems and examine the influence of NO_3 on these processes. We also present results from field and laboratory work that lend insight into these influences within an irrigated agricultural groundwater system. Surface soil and bedrock shale samples taken from an irrigated region within the Lower Arkansas River Basin (LARB) in southeastern Colorado were collected for

analysis, and piezometers were installed near the alluvium-bedrock shale interface for groundwater sampling. Soil surface samples were used in flow-through column studies to determine the influence of NO_3 on Se transformations; bedrock shale samples were used to determine the release of Se in O_2- and NO_3-rich water; and groundwater samples from the piezometers were used to determine the *in situ* relationship between NO_3 and Se.

2.1.1 Se chemistry and conceptual model of transport in an irrigated agricultural groundwater system

Se is present in nature primarily in the four oxidation states of +6 (selenate SeO_4), +4 (selenite SeO_3), 0 (elemental selenium Se), and -2 (selenide Se^{2-}). Selenide occurs in many forms, such as the organic selenomethionine (SeMet), the gaseous Dimethyl-selenide (DMSe , a product of the volatilization of SeMet), and solid Se found in geologic formations in the form of seleno-pyrite ($FeSe_2$), in which Se substitutes for sulfur (S) in pyrite (FeS_2) [Bye and Lund, 1982] or as other Se-bearing species [Ryser et al., 2005]. Soluble species of Se include SeO_4, one of the most toxic of the Se species, SeO_3, and SeMet, whereas Se^0 and other forms of Se^{2-} are insoluble and hence immobile unless suspended. Due to the biogeochemistry of Se and its dependence on redox conditions Se speciation is largely dependent on local environmental conditions, although SeO_4 has been reported to account for approximately 90% to 95% of soluble Se in oxygenated agricultural waters [Masscheleyn et al., 1989; Gates et al., 2009]. Toxicity of most forms of Se^{2-} is strong, although it has been reported that the toxicity of gaseous DMSe is 500 to 700 times less than that of SeO_4 [Calderone et al., 1990; Stork et al., 1999].

The movement of soluble Se species in soil and aquifer systems is governed by (i) redox reactions, which control the speciation of Se, and (ii) sorption processes, which retard the advective transport of the species (Figure 2-1). SeO_4, with the highest oxidation state, is reduced

to SeO_3, which can then be reduced to either Se^0, SeMet, or various selenides depending on pH. Both processes are mediated by microbial populations [Macy et al., 1989; Oremland et al., 1990; Zhang and Moore, 1997] and are depicted by the following chemical reactions:

$$CH_2O + 2SeO_4^{2-} \rightarrow CO_2 + 2SeO_3^{2-} + H_2O \quad (1)$$

$$CH_2O + SeO_3^{2-} + 2H^+ \rightarrow CO_2 + Se_{(s)} + 2H_2O \quad (2)$$

where $Se_{(s)}$ and CH_2O represent elemental Se and a generic organic carbon compound, respectively. The requirements for Se reduction to proceed are similar to those listed by Korom [1992] for heterotrophic denitrification, and include (i) the presence of microbial populations possessing the appropriate metabolic capacity, (ii) suitable electron (e^-) donors, (iii) the presence of e^- acceptors, which in this case are SeO_4 or SeO_3, and (iv) restricted availability of O_2. Also, SeO_4 can be produced through oxidation of residual Se by O_2 or NO_3 (Figure 2-1), for example in the oxidation of $FeSe_2$ within geologic formations:

$$2FeSe_2 + 7O_2 + 2H_2O \rightarrow 2Fe^{2+} + 4SeO_4^{2-} + 4H^+ \quad (3)$$

$$5FeSe_2 + 14NO_3^- + 4H^+ \rightarrow 5Fe^{2+} + 10SeO_4^{2-} + 7N_2 + 2H_2O \quad (4)$$

These reactions are analogous to those in which FeS_2 is oxidized by O_2 or NO_3 to produce sulfate (SO_4) [Frind et al., 1990; Pauwels et al., 1998]:

$$5FeS_2 + 14NO_3^- + 4H^+ \rightarrow 5Fe^{2+} + 10SO_4^{2-} + 7N_2 + 2H_2O \quad (5)$$

The processes depicted by Equations (3) and (4) are likely the cause of Se contamination of surface water in regions underlain by marine sedimentary rocks such as shale. The National Irrigation Water Quality Program study, conducted between 1986 and 1993 in 26 irrigated regions within 14 states of the western United States, demonstrated that toxic levels of Se

concentration in agricultural drainage waters typically occur when irrigated aquifer systems are underlain by marine shales [Seiler, 1995, 1997].

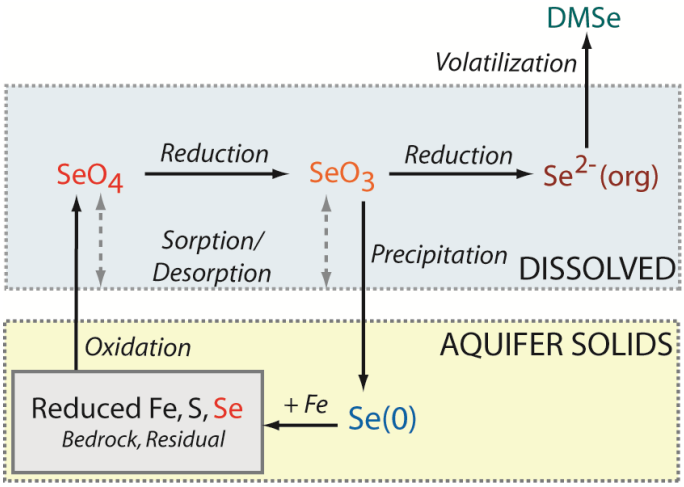

Figure 2- 1. Oxidation-reduction transformations of Se species in a soil and groundwater system.

Methods of removing soluble Se species from environmental waters include (i) reducing SeO_4, which sorbs weakly[Ahlrichs and Hossner 1987; Neal and Sposito, 1989] to SeO_3, which sorbs strongly [Ahlrichs and Hossner, 1987; Balistrieri and Chao, 1987] via the process in Equation (1), (ii) reducing SeO_3 to immobile elemental Se^0, as in Equation (2), or (iii) reducing SeO_3 to SeMet, which is then volatilized to DMSe [Calderone et al., 1990; Flury et al., 1997; Frankenberger and Arshad, 2001]. Due to the succession of terminal e^--acceptor processes [Korom, 1992; McMahon and Chapelle, 2008], however, each of these mitigation pathways is inhibited by the presence of higher-redox species such as O_2 and NO_3. With O_2 and NO_3 present in the system, SeO_4 remains in the dissolved phase and undergoes transport through the groundwater system, although Oremland et al. [1999] observed simultaneous reduction of NO_3 and SeO_4, and Oremland et al. [1990] posited a lower "threshold" concentration at which both NO_3 and SeO_4 reduction can occur simultaneously. This also was suggested by the data

presented by Gates et al. [2009], with a NO_3 concentration of approximately 10 mg L^{-1} (or about 2.3 mg L^{-1} as NO_3-N) below which SeO_4 reduction should proceed.

Hence, in an agricultural groundwater system where O_2 and NO_3 are present in the subsurface due to infiltrating irrigation water and seepage from earthen canals and NO_3 is prevalent due to fertilizer and mineralization of crop residue, SeO_4 entering the aquifer system via irrigation water and canal seepage has a tendency to enter the saturated zone through leaching. Furthermore, leached O_2 and NO_3 coming into contact with outcropped or bedrock shale liberates additional SeO_4 into the aquifer through the oxidation of reduced Se, presumably in the form of $FeSe_2$ or other Se-bearing minerals.

2.2 MATERIALS AND METHODS

2.2.1 Piezometer Installation and Groundwater Sampling

Nine piezometer wells at six locations were installed June 2009 within the Upstream Study Region [Gates et al., 2009] in southeastern Colorado, a 50,400-ha region that is part of an on-going extensive investigation of the irrigated stream-aquifer system of the LARB and is located upstream from John Martin Reservoir (Figure 2-2). The six locations were situated along a groundwater flow path, from the highest-contour canal, the Rocky Ford Highline Canal, to the Arkansas River, a distance of ~7.5 km.

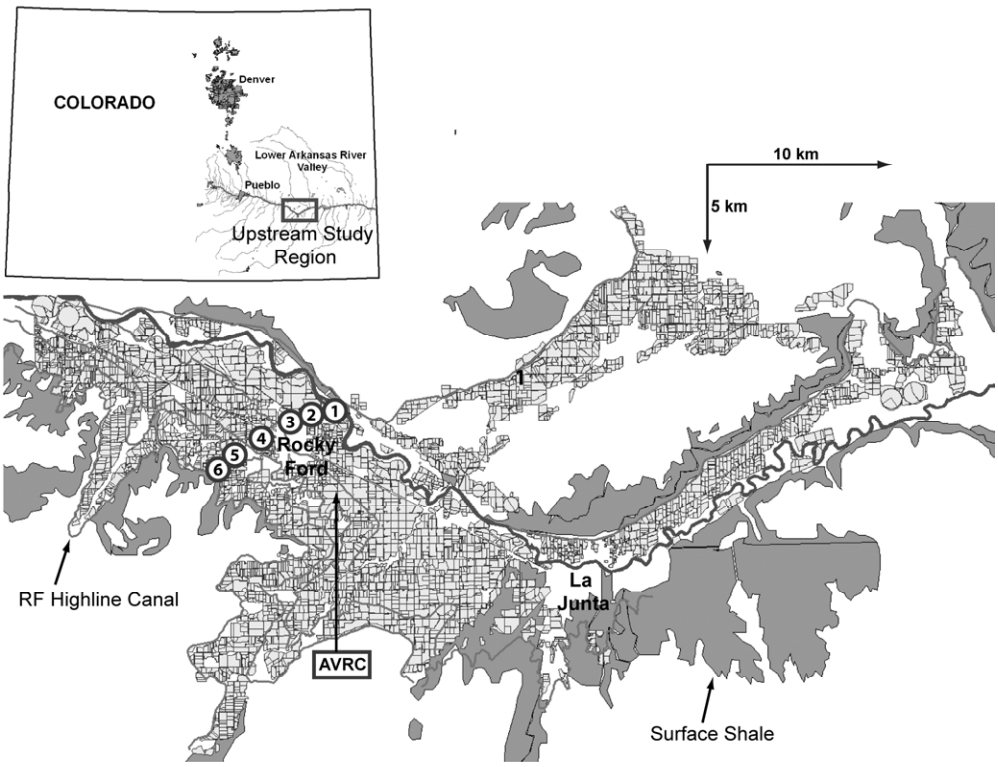

Figure 2- 2. Upstream Study Region [Gates et al., 2009] within the Lower Arkansas River Basin in southeastern Colorado, showing the locations of the six piezometer placement sites as well as the Arkansas Valley Research Center, where soil was collected for analysis. Surface shale is shaded in gray. The Arkansas River is depicted in a dark gray line, and irrigation canals are depicted in light gray lines.

The piezometer wells were installed by Layne Christensen Company using the AP 1000 Percussion Hammer Drill. Upon drilling to the desired depth, 5.08-cm diameter PVC risers were placed within the borehole, with a 1.52-m screen at the base. A filter pack, composed of Colorado silica sand, was placed around the PVC from the base of the borehole to two feet above the top of the screen. After pre-developing the well using a surge block and bailer, a 1-m vertical section of bentonite chips was added to the top of the filter pack to act as a primary annular seal, followed by a portland cement secondary annular seal from the top of the bentonite chips to the ground surface. The surface was sealed using concrete and a flush mount manhole cover. The metal casing used to drill the boreholes was decontaminated between each drilling event.

The depth to bedrock at Sites 1, 2, 3, 4, 5 and 6 (see Figure 2-2) are 9.8 m, 12.8 m, 6.7 m, 13.7 m, 15.7 m, and 12.2 m, respectively. At each site a piezometer was installed with the screen positioned just above the alluvium-bedrock interface. At sites 2, 3, and 4 a second, adjacent piezometer was installed with the screen positioned at the approximate vertical midpoint between the ground surface and the bedrock. For all sites a clay loam layer extended from the ground surface to 2.5 to 5.0 m below the ground surface. For sites 1, 2, 3, and 4, gravelly alluvium extended from the base of the clay loam layer to a 0.50 to 0.75-m thick section of weathered shale atop the shale bedrock, whereas for sites 5 and 6 a tight yellow clay formation extended to the shale.

Groundwater was sampled from each piezometer well during the following sampling events: 25 August 2009, 28 September 2009, 19 October 2009, 29 December 2009, 6 April 2010, 17 June 2010, 8 September 2010, and 1 December 2010. Well purging and groundwater extraction was conducted using a low-flow QED Sample Pro^{TM} bladder pump [Gates et al. 2009] and samples for NO_3 and Se were filtered through disposable in-line 0.003 m^2 0.45 µm capsule filters. Samples for Se were taken in a 0.12 L plastic (polypropylene or polyethylene) bottle, while samples for NO_3 were taken in 0.25 L plastic bottles. Samples for Se were preserved at pH < 2 by adding ~0.005 L of 10% ultra-pure nitric acid (HNO_3) in reagent water per liter of sample (~0.00625 L per 0.12 L sample bottle) prior to sample collection. All samples were stored on ice. Field blanks were taken once per day before sample collection to insure that sample contamination had not occurred in the field. Field duplicates for groundwater also were gathered to assess the field sampling and analytical process.

Samples were analyzed for Se at the Olson Biochemistry Laboratories at South Dakota State University in Brookings, SD (USEPA certified) using Official Methods of Analysis of AOAC

International, 17th Edition, test number 996.16 Selenium in Feeds and Premixes, Fluorometric Method. This method determines the concentration of selenite as Se (SeO_3-Se). Total recoverable Se is determined by reducing all forms of selenium within the sample to $SeO_3$with hydrochloric (HCl) acid. The concentration of SeO_4-Se was estimated by subtracting the concentration of SeO_3-Se before adding HCl from the concentration of SeO_3-Se after adding HCl. Detection limit was 0.4 $\mu g\ L^{-1}$. Samples for NO_3 analysis were analyzed by Ward Laboratories, Inc. in Kearney, NE using the standard USEPA method [1983, Method 353.2].

2.2.2 Shale Analysis and Oxidation Study

Samples of shale were collected from the bottom of the borehole at each of the six sites during the drilling process, placed on ice, and transported to the Agricultural Research Service (ARS) laboratories at the USDA Natural Resources Research Center in Fort Collins, CO for storage. Samples were air-dried, ground to a particle size of ~0.75 mm and then sent to Olson lab for analysis of Se mass. Se mass was determined by pre-digesting the samples using nitric and perchloric acids, with an aliquot of the pre-digest analyzed according to AOAC 996.16. Samples for sites 1-6 contained mass concentrations ($\mu g\ g^{-1}$) of 5.15, 1.04, 2.33, 7.15, 4.70, and 3.77, respectively.

At site 4 (13.7 m depth), *in situ* samples were collected using a split-spoon sampler, placed on ice and transported to the ARS laboratories for storage. These samples were used for table-top batch and flow-through column oxidation studies for analysis of the release of SeO_4 from the shale in the presence of oxygenated solutions. The release of SO_4 was also analyzed since oxidation of FeS_2 also was expected to occur.

For the batch study, three different buffer solutions were used. The first solution contained O_2, the second contained a NO_3-N concentration of 19.2 $mg\ L^{-1}$, and the third was depleted of

both. All three solutions were composed of 225 mL of very hard reconstituted water [Greenburg et al., 1992], 4.5 mL of phosphorus stock solution (68 g L^{-1} of KH_2PO_4), and 200 µL of Hoagland's trace elements [Blankendaal et al., 1972] in order to preserve the microbial population in the shale samples. The first solution was exposed to the atmosphere to bring the O_2 concentration to equilibrium. For the latter two, the solution was de-oxygenated by (i) bringing the solution to a boil, (ii) applying a vacuum for 2 minutes, (iii) sparging with nitrogen (N_2) for 4-5 minutes, with steps (i) through (iii) repeated 3 times, followed by (iv) placing the solution in a BBL GasPak 150 anaerobic jar made anaerobic via GasPak™ pouches (Becton, Dickinson and Company, Cockeville, MD, USA) within a N_2 glove bag (Aldrich® AtmosBag, Sigma-Aldrich Co., St. Louise, MO, USA). After 3 days, the solution was transferred to 250 mL bottles within the glove bag, and 7 g of shale sample added. Bottles were prepared in duplicate.

Sampling from the O_2, NO_3, and control (*Ct*) bottles was performed immediately upon adding the shale sample to the solution, as well as at Days 1, 2, 4, 8, and 16. Sampling was performed within the glove bag by placing the anaerobic jar inside the glove bag and purging the bag three times with N_2 gas before opening the anaerobic jar. In between sample dates the anaerobic jar was placed on an Innova incubator orbital shaker (New Brunswick, Edison, NJ, USA) operated at 28°C and 100 rpm. The NO_3 and SO_4 content of the subsamples were measured by suppressed ion chromatography. The analytical system consisted of a Shimadzu (Kyoto, Japan) LC-10 high-pressure liquid chromatograph, an Alltech (Deerfield, IL, USA) DS-Plus auto-suppressor and a Shimadzu CDD-6 conductivity detector. The elution buffer, pumped at a flow rate of 1 mL min^{-1}, was 0.19 mM sodium bicarbonate and 0.55 mM sodium carbonate. The analytical column was a 250 by 2.6 mm Serasep AN-1 obtained from Alltech. The

remainder of the sample was sent to the Olson lab for analysis of total Se, SeO_3-Se, and SeO_4-Se using the procedure described previously for groundwater sample analysis.

For the column study, a NO_3 solution and a de-oxygenated control solution were pumped through columns containing shale samples. The solutions were prepared in the manner described for the batch study. The shale samples were ground, sieved to 1 mm, and homogenized. 40 g of shale sample was placed in 2.54 by 15 cm glass columns, with a 2.5-cm sand filter on top and bottom of the shale particles to prevent clogging of the influent and effluent tubing. A subsample of the homogenized sample was analyzed separately to determine pre-experiment concentrations. The NO_3 and *Ct* solutions, contained in an anaerobic chamber within a glove bag to prevent O_2 contamination, were pumped using a Gilson (Middleton, WI) Minipuls 3 Peristaltic pump through the columns at a rate of 0.8 mL hr^{-1} to simulate slow groundwater flow. Pumping continued for 760 hours (31.67 days), after which the shale material within the columns was divided lengthwise into 3 sections, air-dried, and analyzed for sorbed SeO_4-Se, sorbed SeO_3-Se, residual Se, and residual S.

For sorption, 10 mL of a 0.1 M K_2HPO_4 (9.5 g L^{-1} of PO_4) solution was added to a subsample of the air-dried shale material, with the strong sorbing behavior of PO_4 assumed to displace sorbed SeO_4 and SeO_3 [Fio et al., 1991; Guo et al., 2000]. The solution was placed in a 15-mL centrifuge tube with 1 g of air-dried shale material, shaken on a Burrell (Pittsburg, PA) wrist-shaker for 24 hours, and centrifuged 1620 xg for 15 min. The supernatant was analyzed for total Se, SeO_3-Se, and SeO_4-Se at the Olson lab. Total Se and total S in the dry sample were analyzed at the Olson lab using the methodology described earlier in this section. Residual Se was calculated as the difference between the total Se mass in the dry sample and the combined sorbed

SeO_3-Se and SeO_4-Se mass. The same procedure was performed for the subsample to determine the total mass lost from the shale material.

2.2.3 NO_3-SeO_4 interaction in shallow soil

Top soil was collected from a recently-harvested corn plot at the Colorado State University Arkansas Valley Research Center (AVRC) (Figure 2-2) in October 2009. The silty clay soil (fine-silty, mixed, calcareous) [Halvorson et al., 2005] was sampled using a hand auger, placed on ice, and transported to the ARS laboratories for storage. The soil was air-dried for 5 days, sieved to between 0.42 and 2.0 mm, and packed into three 2.54 by 15 cm glass columns, with a 2.5-cm sand filter on the top and bottom of the soil. The columns were flushed from below with a 0.05 M NaCl solution at a flow rate of 0.66 cm hr^{-1} for 5 days to displace and remove any soluble and sorbed Se species [Guo et al., 1999]. Columns were drained for 10 days, re-saturated with the 0.05 M NaCl solution and, after verifying that steady-state solutions had been achieved, a NO_3-SeO_4 solution was applied. For all three columns the influent solution contained 75 µM SeO_4-Se (5.92 mg L^{-1} SeO_4-Se). The solution for the first column contained no NO_3; the solution for the second contained 94 µM NO_3-N (1.32 mg L^{-1} NO_3-N and 5.84 mg L^{-1} NO_3), and the solution for the third contained 800 µM NO_3-N (11.2 mg L^{-1} NO_3-N and 49.6 mg L^{-1} NO_3). Following Guo et al. [1999], an upflow pumping procedure was used to reduce preferential flow along the column's annular wall.

Effluent from the three columns was collected using a fraction collector (Spectra/Chrom CF1, Houston, TX) with collection vials rotated every hour. After 23.5 hours of pumping (31 mL of influent solution), the NaCl solution was re-applied to displace NO_3 and the mobile Se species. Pumping was stopped at hour 66 after NO_3 and the mobile Se species had been purged from the top of the column. NO_3-N, SeO_4-Se, and SeO_3-Se in the effluent were analyzed using

the ion chromatograph. After pumping was stopped, the column soils were air-dried, and sorbed SeO_4-Se, sorbed SeO_3-Se, and residual Se were analyzed using the same procedure as in the shale oxidation column study.

2.3 RESULTS AND DISCUSSION

2.3.1 Groundwater Sampling

The concentration of SeO_4-Se in the groundwater samples from the nine piezometers from the eight sampling events is shown in Figure 2-3A in relation to the concentration of NO_3-N. The correlation between NO_3-N and SeO_4-Se (log-log) can be seen in Figure 2-3A, with higher values of SeO_4-Se typically associated with higher values of NO_3-N. The r^2 value for the log-log relationship is 0.67, statistically significant at $\alpha = 0.05$. A similar relationship between NO_3-N and total dissolved Se (predominantly SeO_4) was found by Wright [1999] for groundwater and surface water samples in areas underlain by shale in western Colorado and between NO_3 and total dissolved Se (predominantly SeO_4) by Gates et al. [2009] for the LARB in southeastern Colorado. Concentrations of SeO_4-Se and NO_3-N were by far the highest in the piezometer at site 6, with average values of 2508 $\mu g\ L^{-1}$ and 25.9 $mg\ L^{-1}$, respectively.

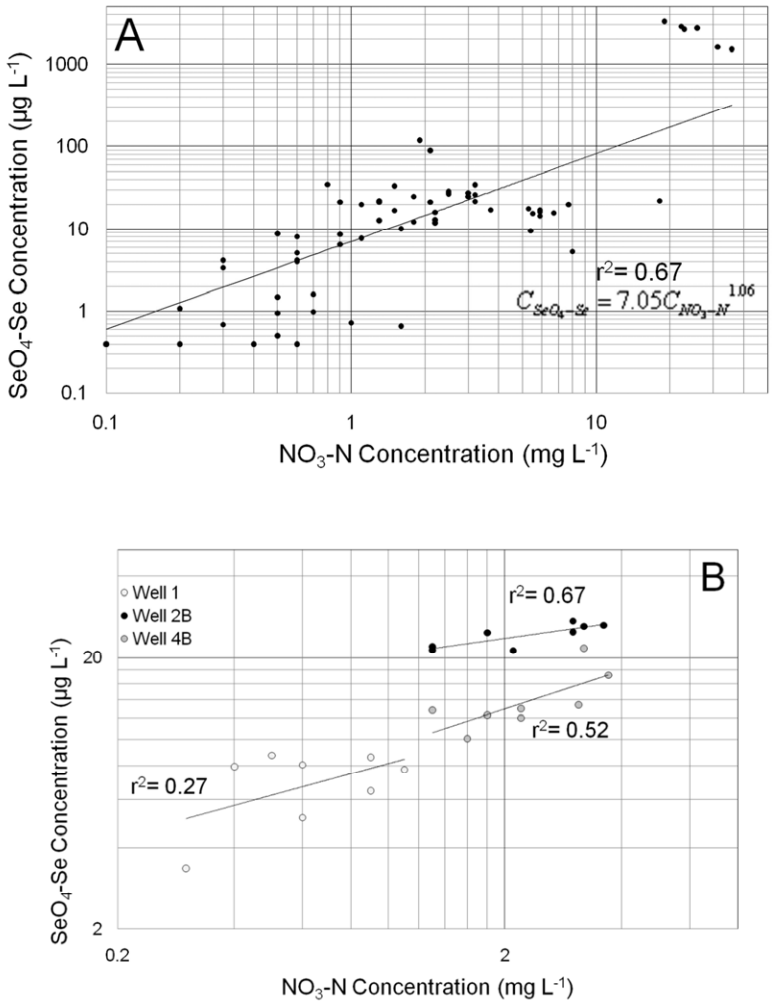

Figure 2- 3. The concentration of SeO_4-Se (µg L^{-1}) in groundwater samples from the eight sampling times in relation to the concentration of NO_3-N (mg L^{-1}) for (A) all piezometer wells and (B) three pieozometer wells located at the alluvium-bedrock shale interface.

SeO_4-Se constituted ~93% of soluble Se. As HNO_3, a strong oxidizing agent, was used to preserve Se in groundwater samples during shipment, oxidation of SeO_3 to SeO_4 during shipment may have occurred, thus over-estimating the *in situ* SeO_4 groundwater concentration. However, since filtration is assumed to remove the majority of bacterial cells, and since samples are stored on ice microbial oxidation, if any, would proceed at a very low rate. Analysis of field blanks verified that sampling equipment had not been contaminated. Average absolute difference between original and duplicate samples was below 1.4%.

The relationship between NO_3-N and SeO_4-Se (log-log) is illustrated further in Figure 2-3B for individual piezometers (Site 1, Site 2, Site 4) located at the alluvium-bedrock shale interface. Values of r^2 for Well 2B and Well 4B are 0.67 and 0.52, respectively (significant at $\alpha = 0.05$; correlation in Well 1 is not significant), suggesting that the relationship between NO_3-N and SeO_4-Se is due to autotrophic oxidation of reduced Se [see Equation (4)]. A further indication that this process is not due merely to a general change in groundwater chemistry is seen in Figures 4A and 4B, which reveal non-significant relationships between NO_3-N and other groundwater constituents (Na, K, Ca, Mg, $CaCO_3$, Cl, HCO_3, B, SO_4-S) at Well 2B and Well 4B, respectively. Although a product of FeS_2 oxidation, the amount of SO_4-S released likely is negligible compared to the high background mass of SO_4-S in the regional groundwater system [Gates et al., 2009], and hence a significant measurable relationship does not occur between NO_3-N and SO_4-S.

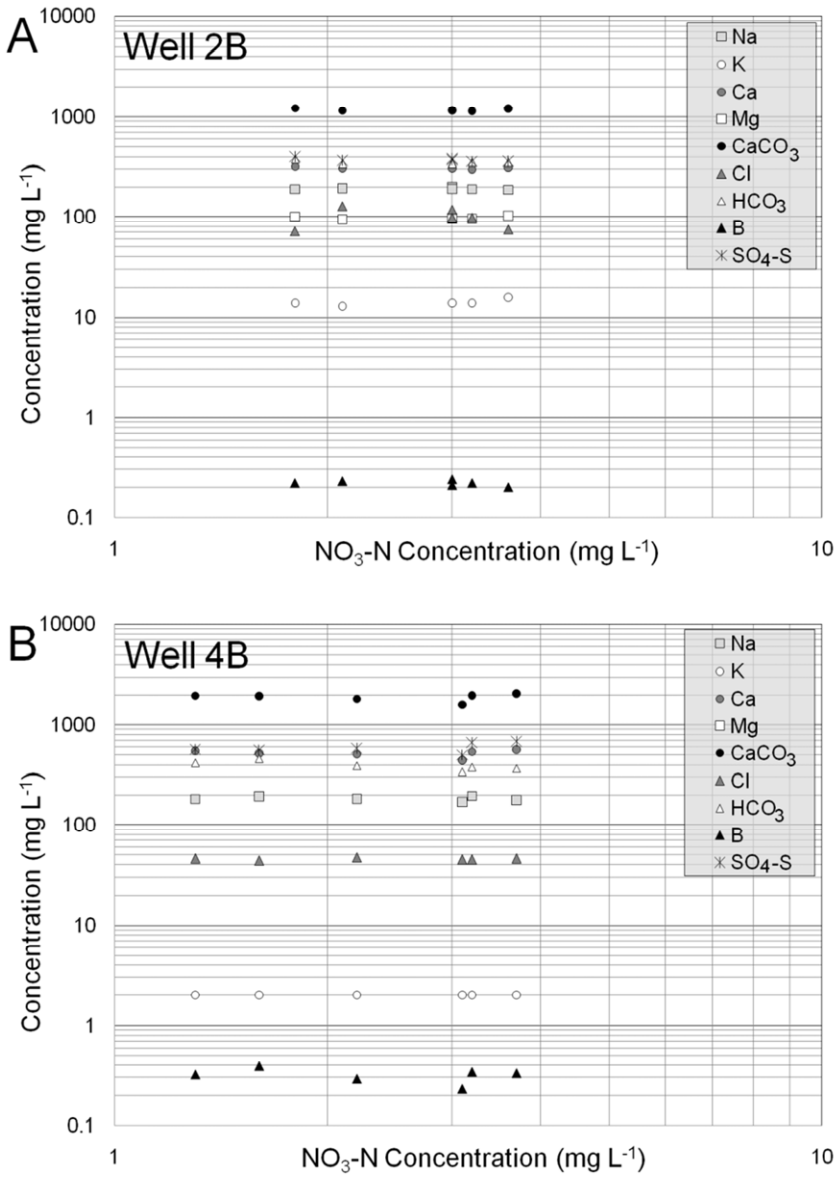

Figure 2- 4. The concentration of NO_3-N (mg L^{-1}) in groundwater samples in relation to other groundwater constituents for (A) Well 2B and (B) Well 4B at the alluvium-bedrock shale interface.

2.3.2 Shale Oxidation Batch Study

2.3.2.1 *Qualitative Analysis*

The batch oxidation study also demonstrates the influence that NO_3 has on the release of reduced Se from bedrock shale. Figure 2-5 shows the concentration of SO_4-S, SeO_4-Se, and SeO_3-Se at

each of the 6 sampling times in each of the duplicate O_2, NO_3, and *Ct* bottles. Dotted lines in Figure 2-5 differentiate the duplicates. The production of SO_4-S follows an exponential production towards an upper limit, with the O_2 bottles producing more SO_4-S (average concentration on day 16 = 425.5 mg L^{-1}), followed by the NO_3 bottles (331.3 mg L^{-1}) and then the *Ct* bottles (261.7 mg L^{-1}) (Figure 2-5A).

A similar pattern was seen for the production of SeO_4-Se (Figure 2-5B). Following assumed initial dissolution or desorption of both SeO_4 and SeO_3 from the shale during the first two days (see Figures 2-5B and 2-5C), the average concentration of total Se on Day 4 in the O_2, NO_3, and *Ct* bottles is 32.1, 28.0, and 21.6 µg L^{-1}, respectively. Due to the presence of O_2 and the sequence of e^- acceptors, the produced SeO_4-Se in the O_2 bottles stays in solution through the 16 days. During Days 1 through 8 a portion of the dissolved Se was comprised of SeO_3-Se (Figure 2-5C), which then either was sorbed or further oxidized to SeO_4-Se by Day 16. After Day 2 the dissolved Se in the *Ct* bottles was reduced, since there were no inhibiting e^- acceptors present in the solution, although contamination of O_2 into the first *Ct* bottle seemed to occur between Days 2 and 4. This is evidenced by (i) a high value of SeO_4-Se on Day 4 for the first *Ct* bottle (Figure 2-5B), (ii) the large scatter between the Se values on Day 4 (Figures 2-5B and 2-5C) and Day 8 (Figure 2-5C) for the two *Ct* bottles (Figures 2-5B and 2-5C), and (iii) the presence of SeO_4-Se in the first *Ct* bottle on Day 8, when SeO_4-Se in the other *Ct* bottle, as well as the two NO_3 bottles, has been completely depleted.

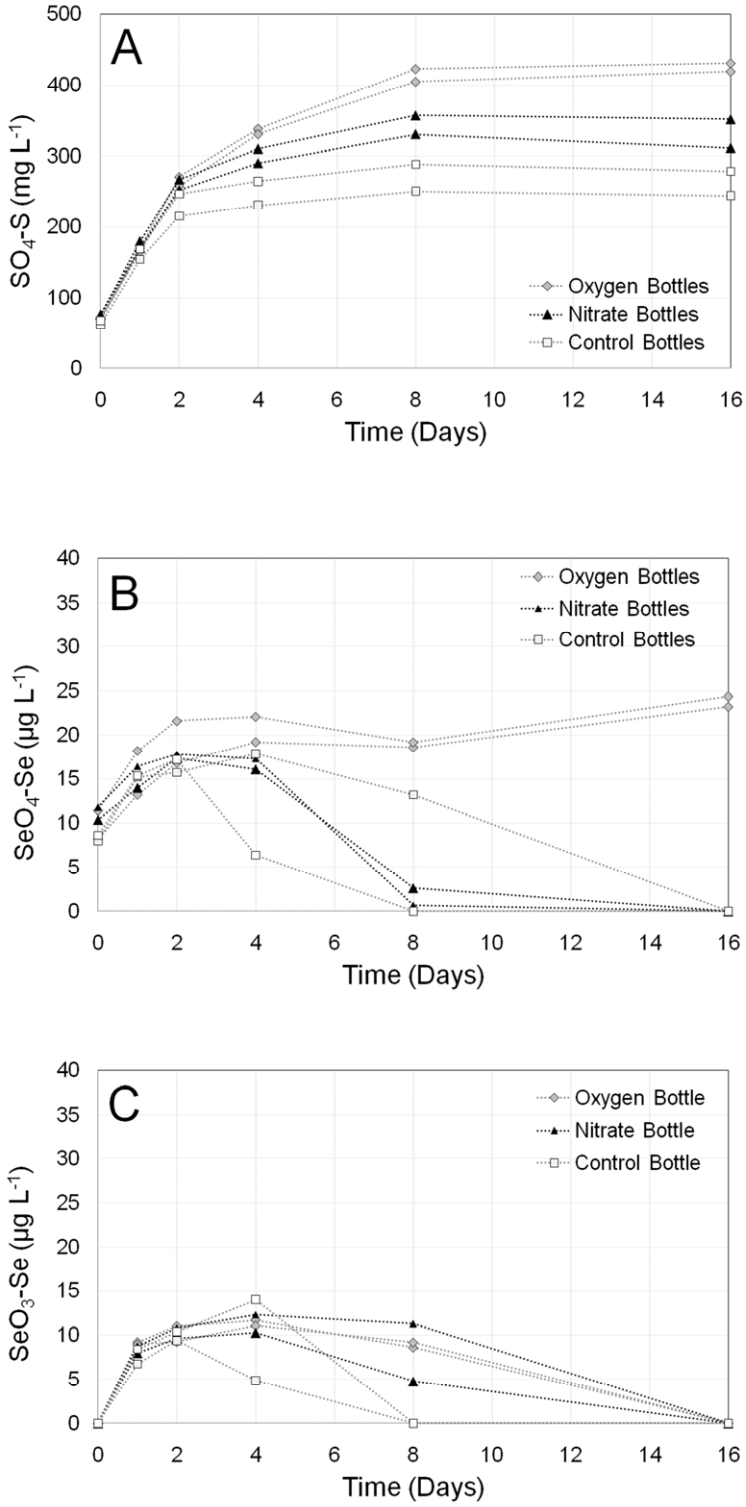

Figure 2- 5. Concentration of (A) SO_4-S (B) SeO_4-Se, and (C) SeO_3-Se at sampling times during the shale oxidation batch study in the O_2-solution, NO_3-solution, and Control bottles.

Within the NO_3 bottles, production of SeO_4 and SeO_3 was followed by reduction. The sequence of reduction is further elucidated in Figures 2-6A and 2-6B, which show the concentration of both NO_3-N (mg L^{-1}) and the Se species (µg L^{-1}) in both of the NO_3 bottles for each of the sampling times. On Day 16 NO_3, SeO_4-Se, and SeO_3-Se all have a concentration of 0 in both bottles.

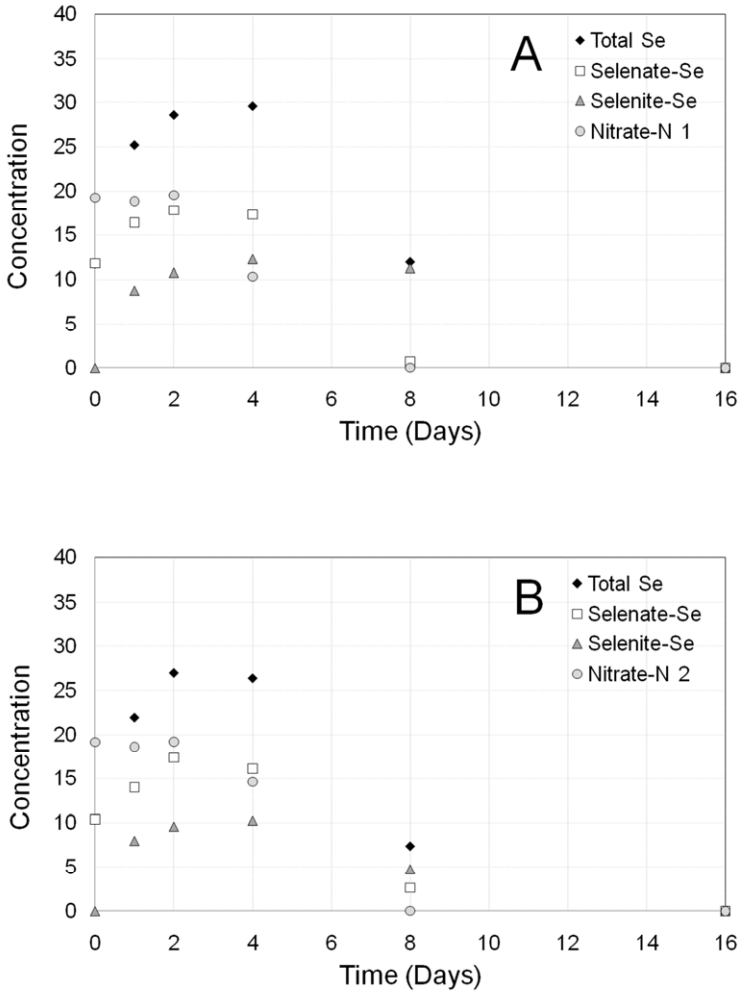

Figure 2- 6. Concentration of total Se, SeO_4-Se, SeO_3-Se, and NO_3-N in (A) the first NO_3-solution bottle and (B) the second NO_3-solution bottle. Concentrations of NO_3 are in mg L^{-1}, whereas concentrations for Se species are in µg L^{-1}.

The following sequence of events is assumed to have occurred for both bottles:

- Between Days 0 and 2, NO_3-N concentration was steady, with any SeO_3 and SeO_4 in solution due to dissolution from the shale.
- Between Days 2 and 4 NO_3, as the dominant *e*- acceptor, begins to be reduced. However, the NO_3-N concentration was still high enough that SeO_4 was not yet influenced.
- Between Days 4 and 8, NO_3 was depleted and the NO_3-N concentration became low enough for SeO_4 reduction to commence. This was further evidenced through the production of SeO_3-Se, which on Day 8 makes up all of the dissolved Se.
- Between Days 8 and 16, with NO_3 and SeO_4 depleted, SeO_3 became the dominant *e*- acceptor until it was depleted by day 16 (Figure 2-5C). SO_4 was no longer produced (Figure 2-5A) since NO_3 had been depleted.
- Between Days 8 and 16, with NO_3 and SeO_4 depleted, and with SeO_3 depleted some-time between days 8 and 16, SO_4 became the dominant e- acceptor, and began to deplete by Day 16 in the NO_3 bottles (Figure 2-5A).

Overall, the (i) preservation of SeO_4 in solution until the concentration of NO_3 dropped to a low value, (ii) depletion of SeO_3 once the concentration of SeO_4 dropped to a low value, and (iii) small depletion of SO_4 between Days 8 and 16 (9.5% and 3.4% average decrease in the *Ct* and NO_3 bottles, respectively) are indicators of the process of sequential reduction of *e*- acceptors. The inclusion of PO_4, a strong competitor with SeO_4 and SeO_3 for surface sorption sites, in the P stock solution used in solution preparation may have prevented SeO_4 and SeO_3 sorption from occurring, hence providing an enhanced dissolved concentration. Since SeO_4 is a weak sorbent this primarily would affect SeO_3. However, the PO_4 concentration in the solution is

approximately one-tenth of the generally accepted concentration used to displace SeO_4 and SeO_3 in laboratory studies (see previous sections). Furthermore, SeO_3 experiences a steady decline in concentration (Figure 2-5C) indicative of reduction kinetics. Therefore, the influence of PO_4 probably is not considerable.

2.3.2.2 *Quantitative Analysis*

Using a first-order reaction kinetic model in the differential and associated integrated forms of $\frac{dC_i}{dt} = \lambda C_i$ and $C_i(t) = C_i(t_0)e^{\lambda t}$, respectively, the first-order rate constant λ [T^{-1}] is estimated for the production of SO_4-S, the production of SeO_4-Se, and the depletion of NO_3. The variable C_i denotes the concentration of constituent *i* under consideration.

For the production of SO_4-S, which corresponds to the chemical reaction represented in Equation (5), average values of λ are 0.054, 0.062, and 0.082 day^{-1} for the *Ct*, NO_3, and O_2 bottles, respectively. For the autotrophic reduction of NO_3, the value of λ, termed λ_{auto}, was -0.157 d^{-1} for the first NO_3 solution bottle and -0.067 d^{-1} for the second bottle. This also corresponds to Equation (5) since the mass of NO_3 reduced according to the oxidation of $FeSe_2$ represented in Equation (4) is negligible in comparison. These values are shown in Figure 2-7A in relation to estimated values of λ_{auto} from other denitrification studies [Frind et al., 1990; Pauwels et al., 1998; McMahon et al., 1999].

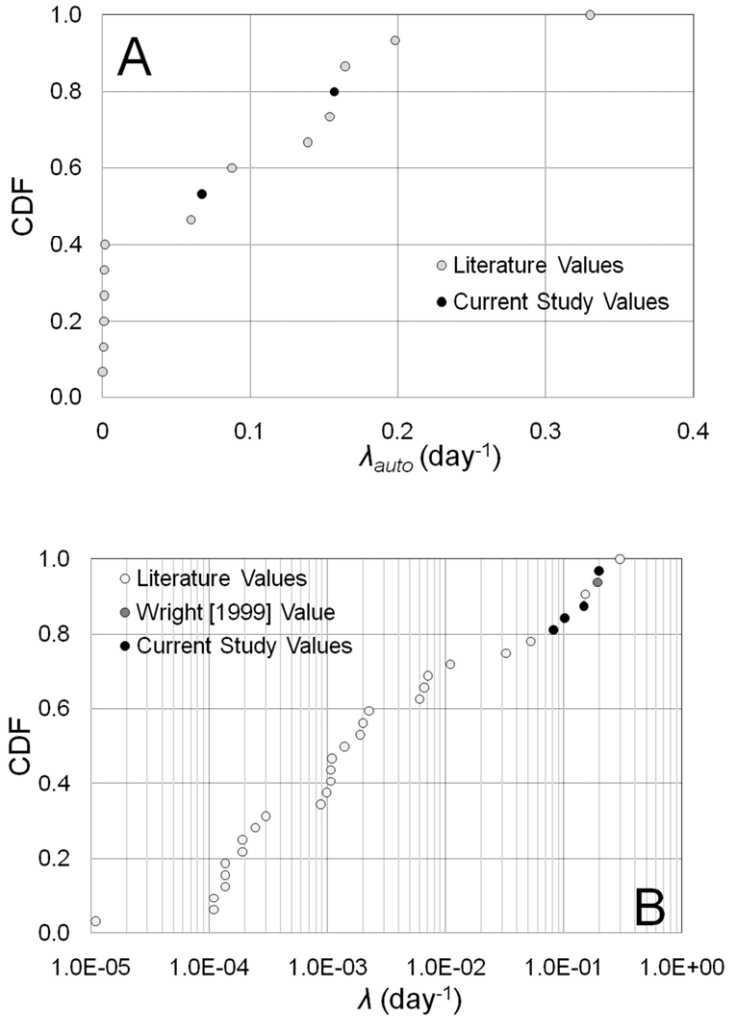

Figure 2- 7. Empirical cumulative distributive function (CDF) for first-order rate constants for (A) autotrophic denitrification and (B) Se oxidation. Rates estimated during this study are shown in red.

It should be noted that the reduction of NO_3 occurs only between Days 2 and 8 (Figures 2-6A and 2-6B), and thus the production of SO_4-S due to autotrophic denitrification only occurred during the same time period. This is further confirmed through a stoichiometric mass balance between the mass of N consumed and the mass of S produced, according to Equation (5). According to Equation (5), the ratio of S produced to N consumed is equal to 1.64 (320.65 g / 196.0 g). For the first NO_3 bottle, the mass of N depleted is equal to 4.40 mg, whereas the mass of S produced between Days 2 and 8 is 6.76 mg, resulting in an S:N ratio of 1.54. For the second

NO_3 bottle, the S:N ratio is 1.24, for an average of 1.39. Hence, the calculated values of λ for SO_4-S production encompass both presumably initial non-oxidative dissolution of the shale as well as the oxidation of FeS_2. If only the data points from Days 2, 4, and 8 are used to calculate λ, then the resulting average values of λ are 0.025, 0.045, and 0.072 d^{-1} for the *Ct*, NO_3, and O_2 bottles, respectively.

For the production of SeO_4-Se, and taking only the first three data points during which production occurred, the average values of λ are 0.092 and 0.173 d^{-1} for the NO_3 and O_2 bottles, respectively. These are similar to the value of 0.193 d^{-1} calculated using the first four data points from the NO_3 = 100 mg L^{-1} bottles in the study performed by Wright [1999]. These values are shown in Figure 2-7B in relation to estimated values of λ from other Se oxidation studies [Zawislanski and Zavarin, 1996; Losi and Frankenberger, 1998; Dowdle and Oremland, 1998; Stillings and Amacher, 2010]. Computed rates are within the range reported in the published literature, although on the higher end.

2.3.3 Shale Oxidation Column Study

Table 2-1 contains the components of Se mass (sorbed Se, residual Se) in the shale material before and after the solution was pumped through the column in order to determine the mass of reduced Se that was released from the shale material during the experiment. The first column in Table 2-1 is the total Se mass concentration (µg g^{-1}) in each section of both the NO_3 and *Ct* column; the second and third columns contain the mass concentration of sorbed SeO_3-Se and sorbed SeO_4-Se, respectively, and the fourth column contains the mass concentration of the residual Se, calculated as the difference between the total Se and the sorbed Se. The fifth column is total reduced Se mass in each section (µg), column six is the total reduced Se mass for the

entire shale column, and the last column shows the mass of reduced Se that was lost during the 760 hours of solution pumping, through a comparison of the final and initial reduced Se mass.

Table 2- 1. Components of Se mass in the shale column sections, demonstrating the loss of mass in the shale material during the flow-through column experiment.

Section	Total Se µg g^{-1}	Sorbed SeO_3-Se µg g^{-1}	Sorbed SeO_4-Se µg g^{-1}	Reduced Se µg g^{-1}	Reduced Se µg	Total Reduced Se µg	Total Reduced Se Lost µg
INITIAL MASS							
All	5.08	0.29	0.35	4.45	177.92	**177.92**	-
FINAL MASS							
NO_3 TOP	3.64	0.08	0.11	3.45	46.02		
NO_3 MID	4.41	0.07	0.09	4.25	56.68	**153.61**	24.31
NO_3 BOT	4.07	0.10	0.15	3.82	50.92		
Ct TOP	4.27	0.09	0.13	4.05	54.00		
Ct MID	4.84	0.09	0.11	4.65	61.96	**163.59**	14.33
Ct BOT	3.74	0.06	0.10	3.57	47.64		

Notice that the majority of the initially sorbed SeO_3-Se and SeO_4-Se mass (total = 0.64 µg g^{-1}) has been displaced. Also, notice that 69.8% more reduced Se mass was removed in the NO_3 column (24.31 µg removed) than in the *Ct* column (14.33 µg removed). The effect of oxidation by NO_3 also can be seen through an analysis of the reduced S mass, as shown in Table 2-2. In the NO_3 column 0.18 g of reduced S mass was removed from the shale column, compared to 0.13 g from the *Ct* column, for a difference of 30.9%. A decrease in reduced Se and S mass in the *Ct* column is likely due to either some type of non-oxidative dissolution and/or the contamination of the influent solution with O_2 and subsequent O_2 autotrophic reduction and Se oxidation according to Equation (3).

Table 2- 2. Comparison of reduced S mass in the shale columns before and after the solution pumping.

Section	Total S µg g^{-1}	Total S µg	Total S g	Mass Lost g
INITIAL MASS				
All	11780	471200	**0.47**	-
FINAL MASS				
NO_3 TOP	6265	83533		
NO_3 MID	8080	107733	**0.29**	0.18
NO_3 BOT	7580	101067		
Ct TOP	8623	114973		
Ct MID	9432	125760	**0.34**	0.13
Ct BOT	7040	93867		

2.3.4 Shallow Soil Column Study

The break-through curve (BTC) of SeO_4 in the effluent for each of the three soil columns, using the normalized value of $C_{SeO_4} / \left(C_{SeO_4}\right)_0$, is shown in Figure 2-8, along with the BTC for NO_3 in the third column (initial C_{NO_3-N} = 11.2 mg L^{-1}). NO_3 in the second column (initial C_{NO_3-N} = 1.32 mg L^{-1}) was depleted before leaving the soil column. Table 2-3 contains the percentage of the total Se mass introduced into the column for each mass balance component (effluent, sorbed Se, reduced Se) for the three columns. The gray-filled slots in Table 2-3 correspond to components of Se mass that are a result of SeO_4 reduction, following the pathways of (i) SeO_4 reduction to SeO_3, followed by sorption of SeO_3, and (ii) SeO_4 reduction to SeO_3, which was then reduced to residual Se.

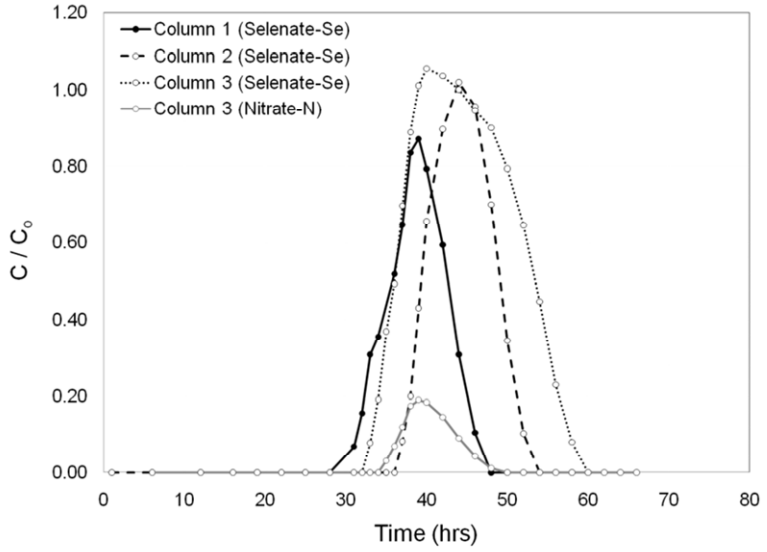

Figure 2- 8. Break-through curves for SeO_4 for the three soil columns, and the break-through curve for NO_3 for the third soil column (influent NO_3-N concentration = 11.2 mg L^{-1}).

Table 2- 3. Percentage of the total influent mass of Se attributed to each mass balance component.

			Percentage of total influent mass of Se (mg)					
Column	**NO_3-N** *mg L^{-1}*	**Total Se In**	**Effluent SeO_4-Se**	**Effluent SeO_3-Se**	**Sorbed SeO_4-Se**	**Sorbed SeO_3-Se**	**Reduced Se**	**Total**
Column 1	0.0	**0.14**	33.2%	0.0%	27.6%	2.0%	30.6%	**93.5%**
Column 2	1.32	**0.10**	43.3%	0.0%	32.1%	2.5%	8.1%	**86.0%**
Column 3	11.2	**0.14**	75.5%	0.0%	27.1%	1.1%	5.0%	**108.7%**

Gray fill = Product from Reduction of SeO_4

Notice in Table 2-3 that the mass of SeO_4-Se leaving the soil column in the effluent, in relation to the mass of SeO_4-Se entering the column in the influent, is least for column 1 (33.2%), followed by column 2 (43.3%) and then by column 3(75.5%). This is reflected in the areas under the BTC of SeO_4-Se for each column (Figure 2-8). Most importantly, the mass of reduced Se in relation to the mass of SeO_4-Se entering the column in the influent is much higher for column 1 (30.6%), where NO_3 is absent, than for column 2 (8.1%) and column 3 (5.0%). Furthermore, the mass of SeO_4-Se reduction products (sorbed SeO_3-Se + reduced Se) accounts

for 32.6% of the influent Se mass in column 1, followed by only 10.6% for column 2 and 6.1% for column 3. Even though the influent NO_3-N concentration for column 2 was approximately one-tenth the influent NO_3-N concentration for column 3, the percentage of influent SeO_4-Se mass that was reduced is only slightly increased, indicating the inhibition of SeO_4 reduction in the presence of NO_3. With the percentage of reduced Se mass slightly higher for column 2 than for column 3, the threshold NO_3-N concentration at which the microbial population jointly reduced NO_3 and SeO_4 may be posited above 1.32 mg L^{-1} (5.84 mg L^{-1} NO_3). This result is in general agreement with the groundwater sampling data and analysis presented by Gates et al. [2009] for the LARB.

The stronger capacity for SeO_4 reduction exhibited in column 1 is further demonstrated in Figure 2-9, which shows the mass of reduced Se in the top, middle, and bottom sections of the three columns. For each section, the reduced Se mass is much less for columns 2 and 3 than for column 1. For column 3, there is no residual Se in the bottom section of the column, since the high NO_3-N concentration prevents the reduction of the incoming SeO_4. However, as the solution migrates upward through the soil column, NO_3 was reduced, and eventually lowered to a concentration at which SeO_4 also was reduced. Hence, the reduced Se mass in the middle and top sections for column 3 were similar to that in column 2.

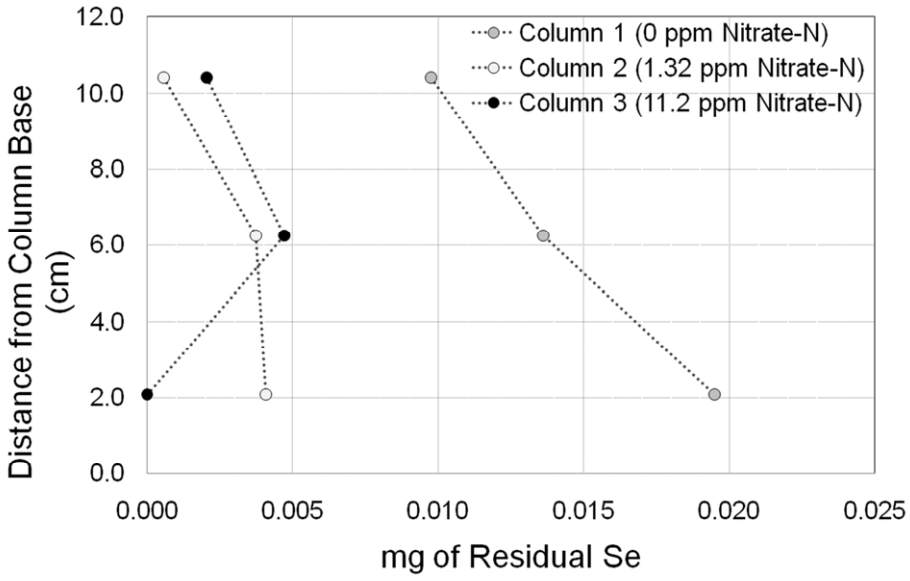

Figure 2- 9. Mass of reduced Se in the top, middle, and bottom sections of the three columns in the NO_3-SeO_4 soil column study.

2.4 CONCLUSION

Field groundwater sampling and laboratory experiments conducted in this study have strengthened the premise that oxidative species such as NO_3 have a significant influence on the fate and transport of Se species in soil and groundwater systems. Results show that under high-redox conditions, represented in this study by the presence of NO_3, SeO_4 can be released from Se-bearing shale and also can be kept in solution through inhibition of chemical reduction to SeO_3, hence inhibiting mitigation of Se contamination.

Failure to account for the presence of O_2 and NO_3 in Se subsurface fate and transport studies may result in an overall non-conservative and harmful approach, since such studies will (i) over-estimate the rate of SeO_4 reduction in soil and groundwater systems and (ii) neglect the introduction of SeO_4 into the groundwater system through oxidation of reduced Se species present in shale and other geologic formations. This is especially important in irrigated

agricultural areas, where NO_3 is present in abundance due to the application of inorganic and organic N fertilizers and the recharging flows that result from excess irrigation application and canal seepage. Furthermore, some strategies currently being used to mitigate NO_3 contamination itself, such as autotrophic denitrification in the presence of shale, may exacerbate the Se contamination problem for a given aquifer system. These strategies must be reconciled, which almost certainly must include reducing fertilizer application using optimized management strategies that maintain acceptable crop yield. Since an accurate depiction of the fate and transport of NO_3 in soil and groundwater systems generally requires an accounting of various components of the N cycle, the inclusion of NO_3 in Se fate and transport studies is not a trivial undertaking. However, accurate results and interventions for successful mitigation generally will be reached only when this is carried out.

CHAPTER 3

ESTIMATING SPATIALLY-VARIABLE FIRST-ORDER RATE CONSTANTS IN GROUNDWATER REACTIVE TRANSPORT SYSTEMS[2]

3.0 SUMMARY Numerical reactive transport models are often used as tools to assess aquifers contaminated with reactive groundwater solutes as well as investigating mitigation scenarios. The ability to accurately simulate the fate and transport of solutes, however, is often impeded by a lack of information regarding the parameters that define chemical reactions. In this study, we employ a steady-state Ensemble Kalman Filter (EnKF), a data assimilation algorithm, to provide improved estimates of a spatially-variable first-order rate constant λ through assimilation of solute concentration measurement data into reactive transport simulation results. The methodology is applied in a steady-state, synthetic aquifer system in which a contaminant is leached to the saturated zone and undergoes first-order decay. Multiple sources of uncertainty are investigated, including hydraulic conductivity of the aquifer and the statistical parameters that define the spatial structure of the parameter field. For the latter scenario, an iterative method is employed to identify the statistical mean of λ of the reference system. Results from all simulations show that the filter scheme is successful in conditioning the λ ensemble to the

[2] As published in the Journal of Contaminant Hydrology 122 (2011) 104-121, Ryan T. Bailey, Domenico A. Baù, Copyright by Elsevier B.C., Reprinted with Permission.

reference λ field. Sensitivity analyses demonstrate that estimation of the λ values is dependent on the number of concentration measurements assimilated, the locations from which the measurement data are collected, the error assigned to the measurement values, and the correlation length of the λ fields.

3.1 INTRODUCTION

In recent decades, computational models have been used with increasing frequency in an evolving effort to accurately assess the fate and movement of groundwater constituents in contaminated local and regional aquifer systems. For prediction purposes as well as assessment of best-management practices, the migration of contaminants in aquifer systems through advection and dispersion processes, as well as reactions with the aquifer matrix and other groundwater constituents, must be characterized accurately. Of prime importance is the characterization of chemical reaction processes, which often play a major, if not dominating, role in the fate of the contaminant. As such, reaction rates that govern these chemical processes must be accurately identified.

In an ongoing effort to include chemical reactions in simulation models, mass transport numerical models with capabilities of simulating one or more equilibrium or time-dependent physical and biological chemical reactions have been developed and used extensively. In many cases, the procedure involves simulating the microbial-mediated oxidation-reduction reactions involving contaminants in an aquifer system. For example, *Frind et al.* [1990] used first-order kinetics to simulate the oxidation of pyrite (FeS_2) and release of sulfate through autotrophic reduction of nitrate. In other studies, such as in *Widdowson et al.* [1988] and *Kindred and Celia*

[1989], and more recently in *Clement et al.* [1998], *Schafer et al.* [1998] and *Brun and Engesgaard* [2002], Monod kinetics describing oxidation-reduction reactions are coupled with biomass equations that account for the growth and death of microbial populations mediating the reactions.

The performance of the models, however, is dependent on the values assigned to the large number of input parameters required for simulation, which are often not known with certainty, a problem recognized in hydrologic model applications in general [*Hendricks Franssen et al.*, 2003; *Liu and Gupta*, 2007]. In transport models, a list of the required parameters include first-order rate constants used in simulating first-order kinetic reactions, sorption isotherm parameters, half-saturation coefficients for Monod kinetics, inhibition constants for sequential consumption of electron acceptors, and microbial growth and death rates for biochemical processes. As discussed by *Kinzelbach et al.* [1990] and cited by *Korom* [1992] in his review of denitrification in the saturated aquifer zone, the predictive abilities of groundwater quality models are limited due to insufficient knowledge regarding fate and transport parameters, rather than any technical fault of the models. Furthermore, for models simulating reaction kinetics, the simulated system is often most sensitive to the rate constant used [*Lu et al.*, 1999; *Almasri and Kaluarachchi*, 2007; *Heatwole and McCray*, 2007].

Due to difficulties in quantifying chemical reaction parameters in a large aquifer setting [*Heatwole and McCray*, 2007], modeling studies have relied on a variety of methods to populate the list of input parameter values required by the numerical model. Such methods include (i) using parameter values determined from field tests, (ii) using model calibration methods, wherein parameter values are methodically adjusted until the difference between the model output and selected field observations decreases below an acceptable tolerance, (iii) selecting

representative values from the published literature, and (iv) performing Monte Carlo simulations in which each realization of the ensemble utilizes a different parameter value from a specified frequency distribution.

Frind et al. [1990], in their modeling study of autotrophic denitrification and sulfate reduction in the Fuhrberg aquifer in northern Germany, used first-order decay rate constants determined from an earlier field study in the same aquifer by *Boettcher et al.* [1989]. Similarly, *Molenat and Gascuel-Odoux* [2002], in a modeling study of denitrification in an aquifer in French Brittany, used a first-order autotrophic denitrification rate constant based on the findings of a field study conducted by *Pauwels et al.* [1998]. However, a rate constant describing heterotrophic denitrification in the upper horizon of the aquifer was fixed at an arbitrary value. Values from the study of *Pauwels et al.* [1998] were also used by *Conan et al.*, [2003] in a modeling study of the same region. In the absence of site-specific studies on reaction kinetics of the solute being modeled, other modeling studies have used model calibration techniques to determine the parameter values. *Lu et al.* [1999], in their study on the reactive transport and degradation of dissolved BTEX (benzene, toluene, ethyl benzene and xylene) compounds through microbial-mediated electron-acceptor processes, adjusted first-order rate constants of aerobic respiration, denitrification, Fe(III) reduction, sulfate reduction, and methanogenesis until model-calculated solute plumes agreed reasonably well with field measurements. *Almasri and Kaluarachchi* [2007], in modeling nitrate transport in an agricultural watershed, carried out calibration of the model by methodically altering the first-order denitrification rate until the simulated nitrate concentration at certain reference points matched the observed nitrate concentration values within an acceptable tolerance. A similar procedure was performed by

Shamrukh et al. [2001] in a modeling study of nitrogen and phosphorous fertilizer transport in the Nile Valley Aquifer in Egypt.

A third set of modeling studies use fixed parameter values taken from the published literature and geochemical databases [e.g., *Schafer and Therrien*, 1995; *Ray and Jain*, 1999; *Lee et al.*, 2006; *Wreidt and Rode*, 2006; *Heatwole and McCray*, 2007]. This method typically poses accuracy problems, since environmental factors influencing chemical reactions are generally site-dependent [*Pauwels et al.*, 1998]. Moreover, some studies utilize reported rate constants of biochemical processes differing from those in the modeled region, as is the case with *Ray and Jain* [1999] using the autotrophic denitrification rate constant reported in *Frind et al.* [1990] in their study of heterotrophic reduction of nitrate. In stochastic (or Monte Carlo) transport simulations, an ensemble of modeling realizations is run, with each simulation using a different parameter value in order to address and quantify the sensitivity of the model response to parameter uncertainty in the system. For example, *McNab and Dooher* [1998] used Monte Carlo simulation to model the degradation of fuel hydrocarbon in an aquifer system, with the selected first-order biodegradation rates sampled from a log-normal distribution assembled from the literature.

For each of the described methods, a single value for each parameter is estimated or taken from the literature and applied to the entire model domain. However, reaction kinetics are dependent on a number of factors such as temperature, rate of groundwater flow, density of microbial population, and concentration of electron acceptors and donors, each of which vary in time and space according to local environmental conditions [*Schafer et al.*, 1998]. As such, local environmental conditions often affect the rate at which a reaction proceeds [*Hill*, 1996; *Ray and Jain*, 1999; *Conan et al.*, 2003; *Almasri and Kaluarachchi*, 2007], particularly in an agricultural

setting where solute transport and chemical reaction parameters in the aquifer are strongly linked with land management practices. As discussed by *Hill* [1996] in a study of denitrification processes in riparian zones, high rates of nitrate reduction can occur in localized hot spots, creating a highly heterogeneous distribution of rate constants. Monod and dual-Monod kinetics, in which the rate constant is varied according to the microbial population and concentration of reactants, have been employed to deal with the dependency of the rate constant on surrounding environmental conditions [e.g., *Widdowson et al.*, 1988; *Kindred and Celia*, 1989; *Clement et al.*, 1998; *Lee et al.*, 2006]. However, these methods require the assignment of several parameters to simulate the reactive transport of the contaminants, all of which must be accurately estimated. And furthermore, spatial variability of the microbial population density and chemical reactants are also often not known with certainty for a given aquifer system [*von der Heide et al.*, 2008].

In the absence of knowledge concerning the spatial heterogeneity of reactive transport parameters, inverse modeling techniques present an intriguing solution to estimate the spatial distribution of these parameters, and may provide improved accuracy to reactive transport simulation models. These techniques, which often involve optimization algorithms or covariance-based (methods aimed at minimizing the variance of the error) techniques to determine the distribution of parameters given field measurement data, have been extensively used in both flow and transport modeling studies. For example, in groundwater flow inverse models spatial heterogeneities of hydraulic conductivity or transmissivity of an aquifer system are estimated given system response measurements of variables that are influenced by these heterogeneities, such as hydraulic head and groundwater travel time [e.g., *Hendricks Franssen et al.*, 2003; *Chen and Zhang*, 2006]. Optimization techniques, in which an objective function is defined and minimized in a least-squares approach, include the pilot point method [*RamaRao et*

al., 1995], the self-calibrated method [*Gomez-Hernandez et al.*, 2003], and the representer method [*Valstar et al.*, 2004]. Covariance-based routines, in which the correlation between the parameter and system response variables is employed to correct the parameter values, include the cokriging method [*Ahmed and Marsily*, 1993], the iterative cokriging method [*Yeh et al.*, 1995], and Kalman Filter and Ensemble Kalman Filter methods, in which the system state is augmented to include the parameter values [*Hantush and Marino*, 1997; *Chen and Zhang*, 2006]. Inverse modeling methods have also been used in contaminant transport models, although estimation of spatially-variable parameters has thus far been limited to longitudinal and transverse dispersivities [*Wagner*, 1992; *Giacobbo et al.*, 2002; *Liu et al.*, 2008] and non-equilibrium sorption rates along a single flow path [*Mishra et al., 1999*; *Vugrin et al.*, 2007]. None have addressed the estimation of multi-dimensional spatially-variable parameters in reactive transport models.

An advantage of the optimization methods is the built-in constraint requiring that the state equations, and hence the physical laws of the aquifer system, be satisfied, a condition not always guaranteed in the covariance-based methods [*Hendricks Franssen and Kinzelbach*, 2008; *Wang et al.*, 2009]. However, computational burden of the optimization methods may be overwhelming, making covariance-based methods such as the Ensemble Kalman Filter (EnKF) [*Evensen*, 1994] appealing. Derived from the original Kalman Filter [*Kalman*, 1960], a data assimilation method in which prior information from a theoretical system (i.e., the numerical model) is merged with information from the actual system (i.e., field measurement data) to produce a corrected, posterior system estimate, the EnKF is a Monte Carlo scheme that represents uncertainty of the theoretical system state via an ensemble of model realizations [*Evensen*, 1994]. Merging of the model simulation results with measurement data is performed

through an update algorithm that spreads information from measurement locations to non-measurements locations according to the spatial covariance of simulation results. Assimilation of measurement data occurs sequentially through time whenever data becomes available, although the update algorithm can be applied to steady-state conditions to provide a one-time correction of the model state. The EnKF routine has been used in transport modeling studies to estimate the distribution of solute concentration in an aquifer system [*Zou and Parr*, 1995; *Kollat et al.*, 2008; *Chang and Latif*, 2010], and dispersivity values [*Wagner*, 1992; *Giacobbo et al.*, 2002; *Liu et al.*, 2008].

In this paper, we investigate the feasibility of using inverse modeling procedures to estimate the spatial distribution of a chemical reaction parameter within an aquifer system. Specifically, the EnKF method is used to estimate the spatial heterogeneity of a first-order kinetic rate constant for a chemical reaction affecting the fate of a groundwater solute. Using the EnKF update algorithm, measurements of the reactive solute concentration are used to condition the spatial distribution of steady-state solute concentration as well as the first-order rate constant. Since only the steady-state solution of the system is considered, the EnKF update algorithm is run only once, allowing the algorithm to be written off-line from the model simulation code.

The applicability of the method is demonstrated using a synthetic two-dimensional steady-state flow and transport simulation, in which a generic reactive solute is introduced to the aquifer system through leaching and subsequently transported via advection and dispersion while undergoing kinetic first-order decay. Several system scenarios are considered in order to demonstrate the flexibility of the methodology. These include (1) aquifer with uniform hydraulic conductivity (K), (2) aquifer in which K is spatially-variable and not known with certainty, and (3) aquifer in which the mean value of the reference rate-constant field is not known with

certainty. This last scenario employs the EnKF in an iterative sequence to converge upon the mean value of the reference field. Sensitivity analyses are also undertaken to gain insights into the performance of the update algorithm as a function of concentration measurement error, number of measurements, measurement location, and correlation length of the rate-constant fields. Several complicating factors of the aquifer system (hydraulic head boundary conditions, groundwater recharge, and concentration of the leaching solute) are assumed constant in this study in order to determine the applicability of the methodology. In general, the uncertain nature of these factors would be included in a complete sensitivity analysis, and will be pursued in future studies.

3.2 STEADY-STATE ENSEMBLE KALMAN FILTER AND ESTIMATION OF SYSTEM PARAMETERS

3.2.1 Ensemble Kalman Filter Methodology

The Ensemble Kalman Filter (EnKF) is a data assimilation algorithm based on Bayesian statistics and the Monte Carlo method, in which a prior system state is merged with measurement data to produce a corrected, posterior system state [*Evensen,* 2003]. This blending of model simulation results and measurement data follows a forecast-update cycle, with the forecast obtained by Monte Carlo model simulation and the update, or correction, of the system occurring whenever measurements become available. In the *forecast* step, the state vector $\boldsymbol{X}$ of the system is estimated through stochastic model simulation from an initial time t to a time $t+\Delta t$ at which measurement data is available, given the uncertain parameters $\boldsymbol{P}$, the forcing terms $\boldsymbol{q}$, and the boundary conditions $\boldsymbol{b}$ of the model domain:

$$\boldsymbol{X}^{f}_{t+\Delta \mathrm{t}} = \boldsymbol{\Phi}(\boldsymbol{P}; \boldsymbol{X}_t; \boldsymbol{q}_t; \boldsymbol{b}_t) + \boldsymbol{\epsilon}_{t+\Delta t} \quad (1)$$

where $\boldsymbol{\Phi}$ represents the solution to the mathematical model, i.e. a groundwater flow or solute reactive transport model, $\boldsymbol{\epsilon}_{t+\Delta t}$ represents model structural errors, and $\boldsymbol{X}^{f}_{t+\Delta t}$ [*n x nmc*] is the forecasted estimate of the state, with *n* denoting the number of computational grid cells in the model domain and *nmc* the number of realizations in the ensemble. Uncertainty in the predicted system state is achieved using the Monte Carlo method by assigning each model simulation in the ensemble a set of randomly sampled values for the parameters, forcing terms, or boundary conditions.

At time $t+\Delta t$, *m* measurements are collected from the true system, perturbed with a Gaussian error with assigned variance to represent uncertainty in the measured data value, and assimilated into the forecasted state estimate $\boldsymbol{X}^{f}_{t+\Delta t}$ to generate a posterior estimate $\boldsymbol{X}^{u}_{t+\Delta t}$ [*n x nmc*], according to the following update algorithm:

$$\boldsymbol{X}^{u}_{t+\Delta t} = \boldsymbol{X}^{f}_{t+\Delta t} + \boldsymbol{K}_{t+\Delta t}\left(\boldsymbol{D}_{t+\Delta t} - \boldsymbol{H}\boldsymbol{X}^{f}_{t+\Delta t}\right) \tag{2}$$

where $\boldsymbol{D}_{t+\Delta t}$ [*m x nmc*] holds the perturbed measurement data and $\boldsymbol{H}$ [*m x n*] contains binary constants (0 or 1) that allows the product $\boldsymbol{H}\boldsymbol{X}^{f}_{t+\Delta t}$ to hold model simulation results at measurement locations. The difference ($\boldsymbol{D}_{t+\Delta t}$ - $\boldsymbol{H}\boldsymbol{X}^{f}_{t+\Delta t}$) is the residual matrix $\boldsymbol{R}$ [*m x nmc*], and holds the residuals between the measured values and the predicted values, signifying the error in the model simulations when compared with the true state. The structure of the update equation thus supplies an update value for each grid cell in the model domain based on the addition of the model-forecasted value and a correction value provided by the measurement data. For scenarios in which only the steady-state solution of the system is desired, the time $t+\Delta t$ represents the time at which steady-state conditions are achieved, and hence the model states $\boldsymbol{X}^{f}_{t+\Delta t}$ and $\boldsymbol{X}^{u}_{t+\Delta t}$ represent the predicted and corrected model states, respectively, under steady conditions.

The matrix $\boldsymbol{K}$ [*n x m*] is referred to as the Kalman Gain matrix and serves the dual purpose of (i) weighting the corrections given to the forecasted values and (ii) spreading information of the true system state from measurement locations to non-measurement locations, and has the following structure:

$$\boldsymbol{K} = \boldsymbol{C}^f \boldsymbol{H}^T \left(\boldsymbol{H} \boldsymbol{C}^f \boldsymbol{H}^T + \boldsymbol{P} \right)^{-1} \tag{3}$$

where $\boldsymbol{C}^f$ [*n x n*] is the forecast error covariance matrix associated with the model forecast $\boldsymbol{X}^f_{t+1}$, defined as:

$$\boldsymbol{C}^f = \frac{\left(\boldsymbol{X}^f_{t+\Delta t} - \overline{\boldsymbol{X}} \right) * \left(\boldsymbol{X}^f_{t+\Delta t} - \overline{\boldsymbol{X}} \right)^T}{nmc - 1} \tag{4}$$

where each column of $\overline{\boldsymbol{X}}$ [*n* x *nmc*] holds the average value of the ensemble at each model cell. As such, $\boldsymbol{C}^f$ holds the spatial correlation between all grid cell values, with positive correlation between two model locations occurring when ensemble values vary from their respective ensemble means in the same manner. The deviation of the model values from the average ensemble value at each grid cell also provides an indication of the uncertainty associated with the forecasted system state. $\boldsymbol{P}$ [*m x m*] is the measurement error covariance matrix associated with the perturbed measurements contained in $\boldsymbol{D}_{t+\Delta t}$, and is obtained as:

$$\boldsymbol{P} = \frac{\boldsymbol{E} * \boldsymbol{E}^T}{nmc - 1} \tag{5}$$

where the matrix $\boldsymbol{E}$ [*m x nmc*] holds the ensemble of perturbations assigned to the *m* measurements. As such, $\boldsymbol{P}$ represents the spread in the errors assigned to the measurements, and signifies the departure of the assimilated measurement values from the measurement value collected from the "true" system state. Measurement errors contained in $\boldsymbol{E}$ are assumed to be independent. However, off-diagonal terms in the matrix $\boldsymbol{P}$ receive small values due to the fact that measurement error statistics are represented with a finite number of perturbations.

In general terms, $\boldsymbol{HC}^{\boldsymbol{f}}\boldsymbol{H}^{T}$ represent the variance, or uncertainty, of the model forecast at measurement locations, while $\boldsymbol{P}$ represents the uncertainty of the measurement data. In regards to Equation (3), as $\boldsymbol{P}$ approaches zero (the null matrix), signifying high confidence in the measurement data, the value of $\boldsymbol{K}$ increases, and the residual in Equation (2) is weighted more heavily. In contrast, as $\boldsymbol{C}^{\boldsymbol{f}}$ approaches zero, signifying high confidence in the model forecast, the value of $\boldsymbol{K}$ decreases, and the residual is weighted less heavily. The model forecast values thus receive little to no correction from the measurement data. As discussed by *Evensen and van Leeuwen* [2000], Equations (2) and (3) are obtained by maximizing the likelihood function $f(\boldsymbol{X}_{t+\Delta t}|\boldsymbol{D}_1, \boldsymbol{D}_2, \boldsymbol{D}_3, \ldots, \boldsymbol{D}_{t+\Delta t})$, which represents the conditional probability of the state $\boldsymbol{X}$ at time $t + \Delta t$ given the measurements collected until that time.

The formulation of $\boldsymbol{K}$ also allows the update routine in Equation (2) to spread measurement information from measurement locations to locations throughout the model domain. Upon computing Equation (3), the Kalman Gain matrix has the dimensions [n x m] where the spatial correlation between the i^{th} grid cell value in the model domain and the value from a grid cell where the j^{th} measurement is contained in each $\boldsymbol{K}_{i,j}$ element. Each row in $\boldsymbol{K}$ corresponds to a different grid cell, and the elements in the row contain the spatial correlation between the model value of the grid cell and the model values of grid cells where measurements are located. When $\boldsymbol{K}$ is multiplied by the matrix $\boldsymbol{R}$ (Equation (2)), which holds the residuals between the observed and model-predicted values at measurement cells, a correction term for each ensemble member of each i^{th} grid cell is computed by:

$$\sum_{j=1}^{m} K_{i,j} R_j \tag{6}$$

which, when added to the predicted value according to Equation (2), will provide an updated grid cell value conditioned by nearby measurement information, with each residual weighted according to the spatial correlation between model value of the grid cell and the model value of the corresponding measurement cell. Hence, every measurement value is used to condition every grid cell value in the model domain, tempered by the degree to which the grid cell values are correlated with the values at measurement cells. As such, the influence of measurement information is felt throughout the model domain. For systems in which there is significant spatial correlation of the variables, a few well-placed measurements are able to effectively condition the system.

With correction terms provided to non-measurement cells using the residuals at measurement cells, the update algorithm of Equation (2) operates similar to an interpolation scheme [*McLaughlin*, 2002], with measurement information used to provide estimated system state values at non-measurement locations. However, the degree of spreading of measurement information is dependent on the correlation of grid cell values provided by the numerical model simulation, which presents a state of the system that honors the physical laws inherent in model state equations. The prior information (i.e., spatial patterns of calculated system state response variables, such as hydraulic head for a groundwater flow model or a solute concentration distribution for a transport model) is hence a vital part of the system update and provides information about the system that could not be captured with stand-alone measurement data. Thus, the model simulation results are improved upon by the measurement information, and the measurement information is improved upon by the information about the system contained in the simulation results.

Efficient algorithms to implement the update routine of Equation (2) have been presented by *Burgers et al.* [1998], *Keppenne* [2000], and *Evensen* [2003]. The numerical strategy employed by *Keppenne* [2000], which does not require the explicit assemblage of the forecast covariance matrix $\boldsymbol{C}^f$, was used in this study.

3.2.2 Parameter Estimation using the EnKF

Any values incorporated into the system state matrix $\boldsymbol{X}^f_{t+\Delta t}$ have the potential to be corrected by assimilating measurement data, provided that spatial correlation exists between the variables to be conditioned and the data. For numerical models, the parameters supplied to the model (e.g., hydraulic conductivity, seepage velocity, longitudinal and transverse dispersivity) dictate the behavior of, and hence are significantly correlated with, the model response variables (e.g., hydraulic head, solute concentration). As such, parameter values used in the forecast step can be incorporated into the system state matrix $\boldsymbol{X}^f_{t+1}$, and conditioned in the update equation (Equation (2)) by system response measurement data. This conditioning provides an updated spatial distribution of parameter values that approaches the system state from which the measurements were collected. Conditioning parameters through data assimilation is a powerful tool since the model itself, rather than just model results, as in *Zou and Parr* [1995] and *Chang and Latif* [2010], are corrected to reflect the internal workings of the actual system.

In the data assimilation framework described in Section 2.1, uncertainty in the actual parameters $\boldsymbol{P}$ of the system is accounted for by generating an ensemble of spatially-distributed parameter fields, with each field covering the extent of the model domain. Each field is then used by the numerical model to produce a corresponding distribution of the model response variable. When measurement data are available, the state matrix $\boldsymbol{X}^f_{t+\Delta t}$ is assembled with model response variables and augmented to include parameter variables, yielding a forecast covariance matrix $\boldsymbol{C}^f$

that contains spatial cross-covariance submatrices between the model response variable and the model parameters:

$$\boldsymbol{C}^{f}{}_{t}(\boldsymbol{X}_{(S)}, \boldsymbol{X}_{(P)}) = \frac{\boldsymbol{X}^{Dev}{}_{t_{(S)}} * \boldsymbol{X}^{Dev}{}_{t_{(P)}}{}^{T}}{nmc - 1} \quad (7)$$

Where $\boldsymbol{X}^{Dev}{}_{t(S)}$ [n x nmc] holds the deviation of each model response grid cell value from the grid cell ensemble mean, and $\boldsymbol{X}^{Dev}{}_{t(P)}$ [e x nmc] holds the deviation of each grid cell parameter value from the ensemble mean, where e is the number of grid cells to which the parameter variable is assigned. Equation (7) defines the correlation between response and parameter forecast values at all model locations, allowing response measurement information to correct the parameter values throughout the model domain according to Equation (6).

3.2.3 Estimation of First-Order Rate Constants using the EnKF

Based on the methodology presented in Sections 2.1 and 2.2, this section describes the process of estimating the spatial distribution of a first-order rate constant λ [T^{-1}] using a reactive transport model for the forecast step and the update algorithm described by Equation (2) for the update step. Spatial variability of the rate constant is assumed to be a function of environmental factors such as soil type and chemistry, electron donor distribution, or spatial variability of microbial population density and in this study is assumed to be time-invariant.

The general forecast-update process is shown in Figure 3-1. An ensemble of random log-λ fields is generated using a sequential Gaussian simulation algorithm called SKSIM developed by *Baú and Mayer* [2008]. According to this model, the spatial distribution of log-λ is characterized by a normal distribution using an exponential covariance model in the log domain:

$$\log \lambda = Y_{\lambda} = N\left(\mu_{Y_{\lambda}}; \sigma_{Y_{\lambda}}\right); \quad (8)$$

$$cov_{Y_\lambda,Y_\lambda}(d) = \sigma_{Y_\lambda}^2 . \exp\left(\sqrt{\sum_{i=1}^{2} \frac{d_i^2}{l_i^2}}\right)$$

where μ_{Y_λ} and σ_{Y_λ} are the mean and standard deviation of the log-λ distribution, d_i are the components of the distance vector **d**, and l_is are the spatial correlation scales in the coordinate directions. Correlation of λ in space is assumed to result from spatial correlation of environmental factors due to land management practices and environmental conditions. A lognormal distribution was chosen for λ due to the reported lognormality of first-order reaction rate constants [*Parkin and Robinson*, 1989; *McNab and Dooher*, 1998; *Heatwole and McCray*, 2007]. As stated by *Parkin and Robinson* [1989] in their study on denitrification, this is predicted by the law of proportionate effects, which states that lognormal distributions result from multiplicative operations on the random variables (e.g., microbial population density, electron donor distribution, soil properties) that govern the rate constant.

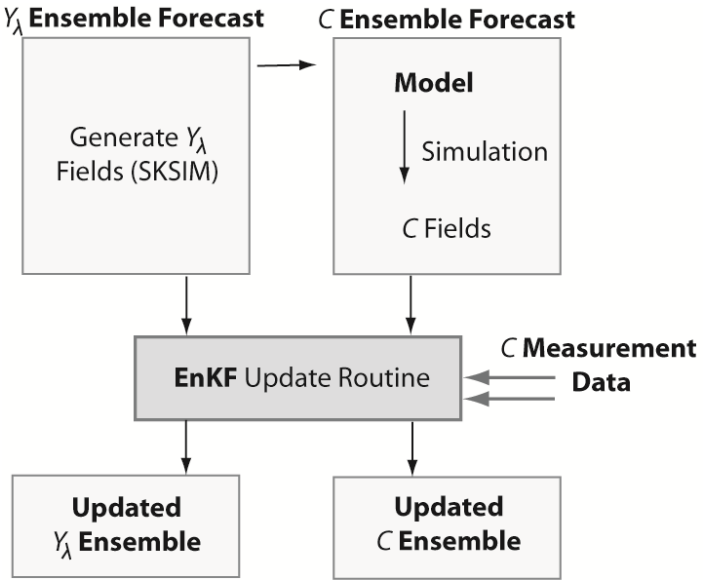

Figure 3- 1. Forecast-update routine process for the Ensemble Kalman Filter, for a system in which both concentration *C* and first-order rate constant Y_λ values are conditioned by *C* measurement data. The forecast step includes an ensemble of estimated Y_λ and *C* fields

Applications of the method to actual aquifer systems would require site measurements to estimate the structure of the covariance model, with the number of measurements determined by the areal extent of the study site. However, as this study is purely hypothetical, the structure of the random Y_λ fields is framed by specified values of the geostatistical parameters μ_{Y_λ}, σ_{Y_λ}, and l_i as is described in Section 3. However, the scenario presented in Section 3.3 investigates the performance of the EnKF update algorithm when one or more of these parameters are not known *a priori*.

Upon running SKSIM, each of the *n* grid cells of each realization of the ensemble is assigned a unique Y_λ value, which is spatially correlated with Y_λ values of surrounding grid cells according to the specified correlation model. Taken together, the ensemble of generated Y_λ fields represents the prior information of the system parameters $\boldsymbol{P}$. The system scenario presented in Section 3.2, in which the aquifer hydraulic conductivity is uncertain and spatially-variable, will use an ensemble of hydraulic conductivity *K* fields also constructed using SKSIM, with specified values of the geostatistical parameters μ_{Y_K}, σ_{Y_K}, and l_i.

Using a steady-state flow field from a groundwater flow model and defining the location and loading rate of the solute contaminant entering the aquifer system, each Y_λ field is then used by a reactive transport model to produce a corresponding field of solute concentration. These model simulations are encompassed in Equation (1). The Reactive Transport in Three Dimensions (RT3D) [*Clement*, 1997] numerical model, which simulates the reactive transport of one or more species in a multi-dimensional saturated aquifer environment, is used in this study. RT3D solves the following system of advection-dispersion-reaction (ADR) equations:

$$R\frac{\partial C_k}{\partial t} = -\frac{\partial}{\partial x_i}(v_i C_k) + \frac{\partial}{\partial x_i}\left(D_{ij}\frac{\partial C_k}{\partial x_i}\right) + \frac{q_s}{n}C_{s_k} + r \quad k = 1,2,\dots,m \tag{9}$$

where m is the total number of aqueous-phase species, C_k is the concentration of the k^{th} species [ML^{-3}], D_{ij} is the hydrodynamic dispersion coefficient [L^2T^{-1}], v is the pore velocity [LT^{-1}], n is the soil porosity, q_s is the volumetric flux of water representing sources and sinks of the species [T^{-1}], C_s is the concentration of the source or sink [ML^{-3}], and r represents the rate of all reactions that occur in the aqueous phase for the k^{th} species [ML^3T^{-1}]. Values for v are calculated from hydraulic head and flux values computed deterministically by a three-dimensional groundwater flow model such as MODFLOW [*McDonald and Harbaugh*, 1988]. In this study it is assumed that the ADR equation shown in Equation (9) is an accurate representation of solute reactive transport in an aquifer system, and hence the error term $\boldsymbol{\epsilon}_{t+\Delta t}$ in Equation (1) is neglected.

The numerical model RT3D uses a reaction operator-split (OS) numerical scheme [*Yeh and Tripathy*, 1989; *Clement et al.*, 1998] that solves the advection, dispersion and source-sink mixing portions of Equation (9) for a single transport time step, whereupon the reaction portion is solved using an ordinary differential equation solver. As such, any number of user-defined reaction equations can be incorporated into the model. In this study, first-order kinetics is assumed to govern the decay of a generic groundwater constituent according to the following rate law:

$$r = \frac{\partial C_k}{\partial t} = -\lambda C_k \tag{10}$$

where λ is the spatially-variable first-order rate constant [T^{-1}]. Each reactive transport simulation is run until steady-state conditions are achieved, in which calculated grid cell solute concentration values no longer change with time.

The update step (Figure 3-1) is performed at a time $t + \Delta t$ at which the concentration distribution of the solute has reached steady-state conditions, and consists of the following steps:

(1) The forecast system state matrix $\boldsymbol{X}^{f}_{t+\Delta t}$ is populated with the parameter values Y_{λ} and model-calculated steady-state concentration values C from each grid cell for each model simulation of the ensemble. The dimensions of $\boldsymbol{X}^{f}_{t+\Delta t}$ are thus [$(2n)\ x\ nmc$].

(2) Measurements are collected from the true system state. A coefficient of variation is assigned to the measurement values and used to perturb each measurement value with a Gaussian error, resulting in an ensemble of measurement values that is normally distributed around the measurement value. For example, assigning a coefficient of variation of 0.100 to a C measurement value of 100 mg L^{-1} results in an ensemble of measurement values ranging from 67.6 to 120.3 (Figure 3-2), with 69 out of the 100 values within 10.0% of the original measurement value. Each of the 100 perturbed measurement values is then assigned to a different model realization.

(3) The EnKF update algorithm is run, resulting in an ensemble of C and Y_{λ} fields that are conditioned by the C measurement data.

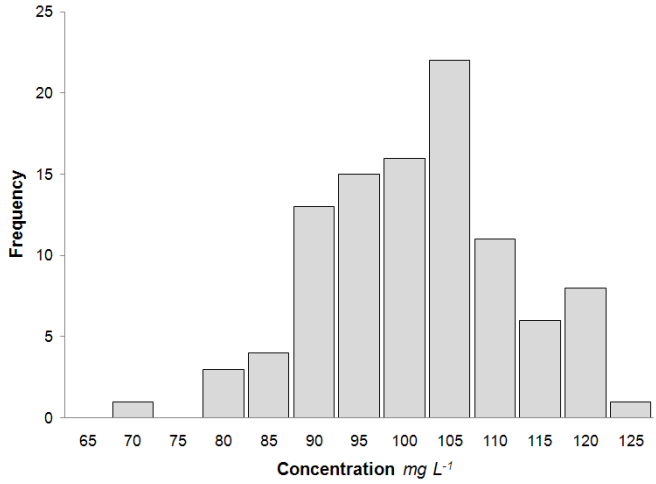

Figure 3- 2. Frequency distribution of 100 perturbed measurements for an original C measurement value of 100 mg L^{-1}, using a coefficient of variation of 0.10.

In order to test the accuracy of the method, measurement data are collected from a known reference state of Y_{λ} and C, generated using SKSIM and RT3D, respectively. Once the C and Y_{λ}

ensembles have been updated, the performance of the update routine is analyzed by comparing the forecasted and updated ensembles to this reference state via the following four performance parameters:

$$EE_i = \left|\bar{X}_i - X_{i,true}\right| \quad (i = 1, \dots, n) \tag{11}$$

$$EP_i = \frac{1}{nmc}\sum_{j=1}^{nmc}\left|X_{i,j} - \bar{X}_i\right| \quad (i = 1, \dots, n) \tag{12}$$

$$AE(\boldsymbol{X}) = \frac{1}{nmc * n}\sum_{j=1}^{nmc}\sum_{i=1}^{n}\left|X_{i,j} - X_{i,true}\right| \tag{13}$$

$$AEP(\boldsymbol{X}) = \frac{1}{nmc * n}\sum_{j=1}^{nmc}\sum_{i=1}^{n}\left|X_{i,j} - \bar{X}_i\right| \tag{14}$$

where $\bar{X}_i$is the ensemble mean of the i^{th} grid cell, $X_{i,true}$ is the reference "true" value of the i^{th} grid cell, and $X_{i,j}$ is the variable value of the i^{th} grid cell of the j^{th} ensemble realization. Equations (11) and (12) are calculated on a cell-by-cell basis, whereas Equations (13) and (14) provide values for the entire model domain. Equations (11) and (13) provide measures of the accuracy of the ensemble in relation to the reference state, and Equations (12) and (14) indicate the precision of the ensemble values, i.e. the "spread" of the values around the ensemble mean. When plotted on the model domain, the ensemble error (*EE*) displays the relative degrees of conditioning to the reference values $X_{i,true}$ and the ensemble precision (*EP*) displays the spread around the ensemble mean $\bar{X}_i$ for each cell. The absolute error (*AE*) accounts for the total deviation of the ensemble values from the reference state, comparing the model state values $X_{i,j}$ to the true value $X_{i,true}$ at each grid cell in the model domain, and the average ensemble precision (*AEP*) accounts

for the total deviation of the ensemble from the ensemble mean $\bar{X}_i$ at each grid cell. Ideally, the *AE* and *AEP* values of the updated ensembles are significantly lower than the forecasted values, with the spread of the values at each grid cell minimized and the ensemble mean at each grid cell approaching the value from the reference state.

3.3 REACTIVE TRANSPORT SIMULATIONS AND ESTIMATION OF λ

Three system scenarios will be considered in this section. In the first scenario, the hydraulic conductivity of the aquifer is assumed to be homogeneous; in the second scenario, the hydraulic conductivity of the aquifer is assumed to be uncertain, and is characterized by an ensemble of hydraulic conductivity fields defined by the geostatistical parameters μ_{Y_K}, σ_{Y_K}, and l_i; and in the third scenario, the actual mean value of λ in the reference field is not known *a priori*. In the latter case, the statistical parameter μ_{Y_λ} used to construct the prior λ fields are different from those of the reference λ field. For this last scenario, the same hydraulic conductivity uncertainty used in the second scenario is used to define the flow fields.

The same model domain, boundary conditions, and solute-leaching concentration are used for each of the three scenarios. The model domain is 510 m west-east and 310 m north-south with 10 m by 10 m grid cells, resulting in 1581 grid cells. The aquifer has a saturated thickness of 10 m, and the two-dimensional steady-state flow field is simulated with constant-head boundaries of 100 m and 95 m assigned along the north and south edges of the domain, respectively, with impermeable boundaries along the west and east edges. A constant recharge value of 0.005 m day^{-1}, representing deep percolation, was assigned to each grid cell.

For the reactive transport simulation, longitudinal and transverse dispersivity values were set to 10 m, and solute with concentration 1000 mg L^{-1} is "leached" to each cell with the deep

percolation. It is assumed that the solute is not subject to sorption processes. Each realization was run to 1000 days (2.74 years), at which time steady-state conditions were achieved. An additional RT3D simulation was run using the prescribed actual distribution of Y_λ to produce a reference C field from which measurements were collected for data assimilation, and against which the updated Y_λ and C ensembles could be compared.

3.3.1 Aquifer with Uniform Hydraulic Conductivity

3.3.1.1 Model Forecast

In the first scenario, hydraulic conductivity was set to 10 m day^{-1} throughout the model domain, resulting in the same flow field for each of the reactive transport realizations. The ensemble of nmc = 100 Y_λ fields was generated using mean μ_{Y_λ} of -2.52 (log day^{-1}), standard deviation σ_{Y_λ} of 0.707 (log day^{-1}), and correlation length (l_x=l_y) of 250 m, resulting in λ values ranging from 8.61 x 10^{-6} day^{-1} to 2.02 day^{-1}, which fall within published values for first-order reaction rates [e.g., *Korom* 1992; *Heatwole and McCray*, 2007]. The reference Y_λ field shown in Figure 3-3A was generated using the same parameters, displaying pockets of high (white), average (gray), and low (black) reactivity. In particular, a region of low reactivity is located in the south-southwest region of the aquifer, and a region of high reactivity is located in the south-southeast region. The *AE* and *AEP* values for the Y_λ forecast ensemble are 0.697 and 0.574, respectively. Notice that the corresponding C reference field (Figure 3-3B) has high solute concentrations in regions of low Y_λ values, and vice versa. This correlation between the Y_λ values and the resulting solute concentration C allows conditioning of the Y_λ fields by C measurements in the EnKF scheme. The forecast ensemble mean of C for every grid cell is shown in Figure 3-4A, while the ensemble precision (*EP*) at every grid cell, calculated using Equation (12), is shown in Figure 3-4B. The larger spread of C values in the southern portion of the field is a

factor of the high hydraulic gradient, which acts to advect and disperse the solute through the aquifer more thoroughly, as well as the fact that there is more solute mass in the southern portion of the aquifer (see Figure 3-4A). The *AE* and *AEP* values for the *C* forecast ensemble were 143.1 and 120.2, respectively.

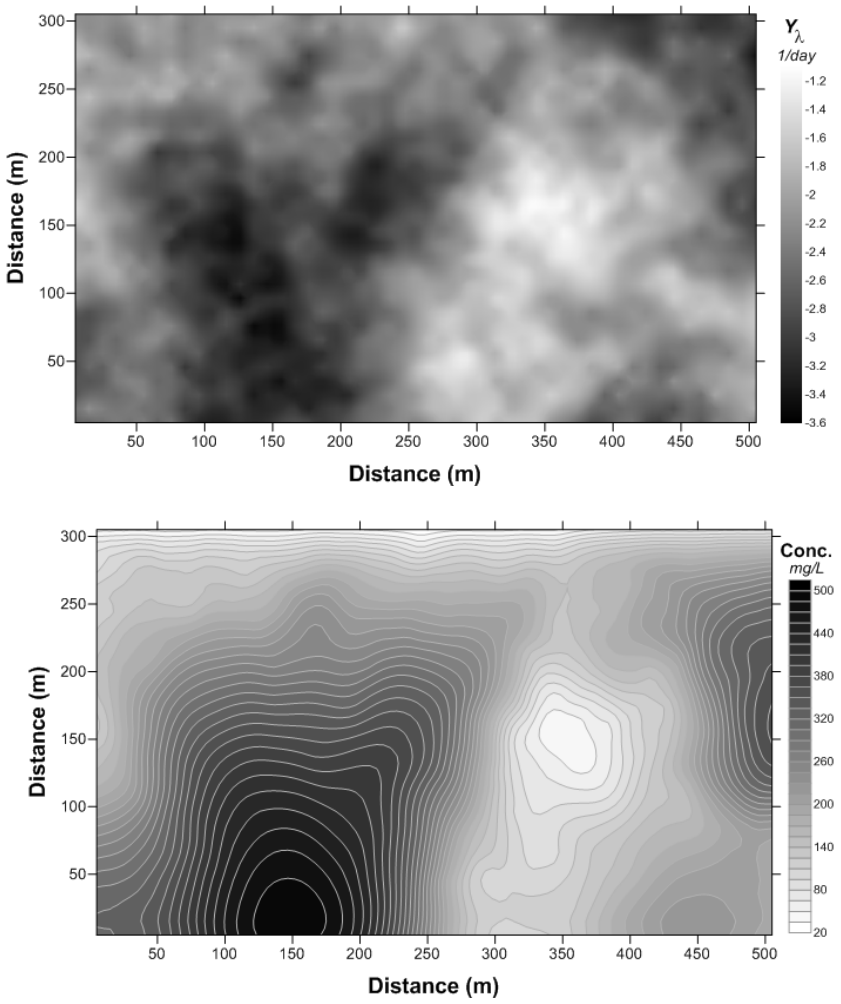

Figure 3- 3. A) Reference first-order rate constant Y_λ field, and (B) Resulting reference field for solute concentration *C*.

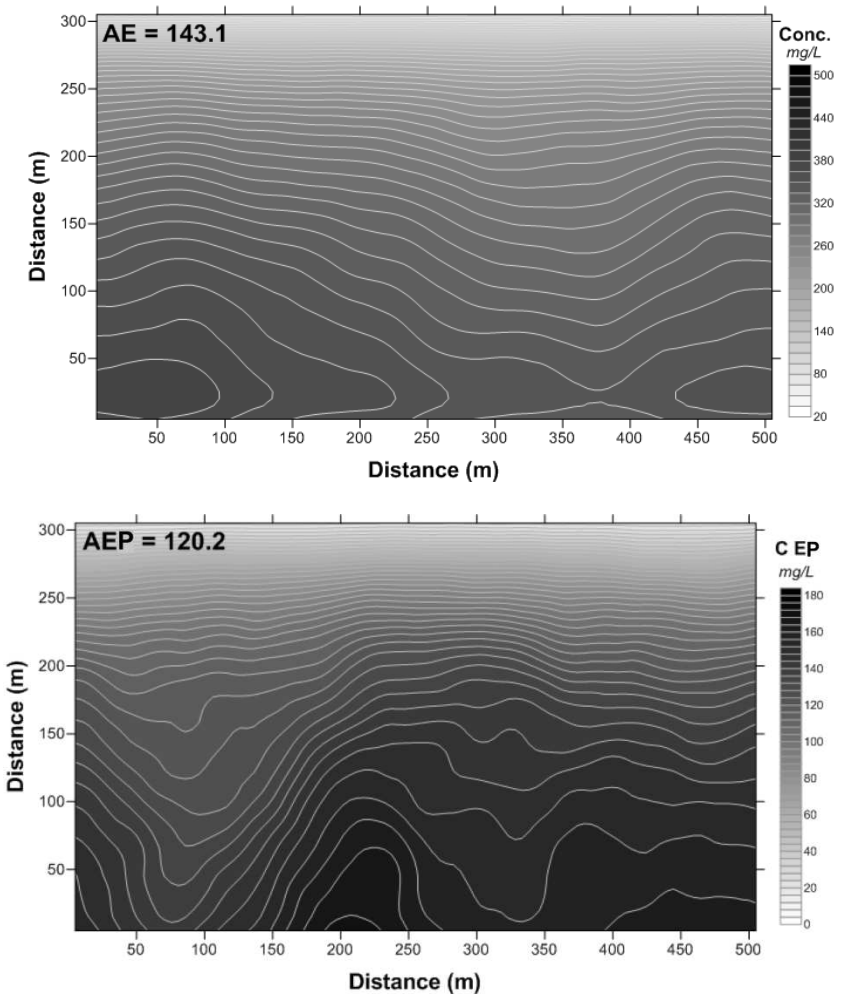

Figure 3- 4. (A) Mean and (B) Precision (EP) of the forecasted *C* ensemble at every model grid cell, with corresponding *AE* and *AEP* values.

3.3.1.2 Update of the *C* and λ Ensembles

The forecast ensembles of *C* and Y_λ were updated using *C* measurements collected from 12 locations, as shown in Figure 3-5. The updated *C* ensemble shows considerable improvement from the forecasted *C* ensemble, with the ensemble mean at every grid cell (Figure 3-5A) approaching the reference *C* field (see Figure 3-3B) and the spread of the ensemble reduced (Figure 3-5B), particularly in the vicinity of the measurement locations. Using the performance parameters of Equations (13) and (14), the *AE* and *AEP* values of the updated *C* ensemble were

44.3 and 23.4, a reduction of 69.0% and 80.5%, respectively, from the forecast values of 143.1 and 120.2.

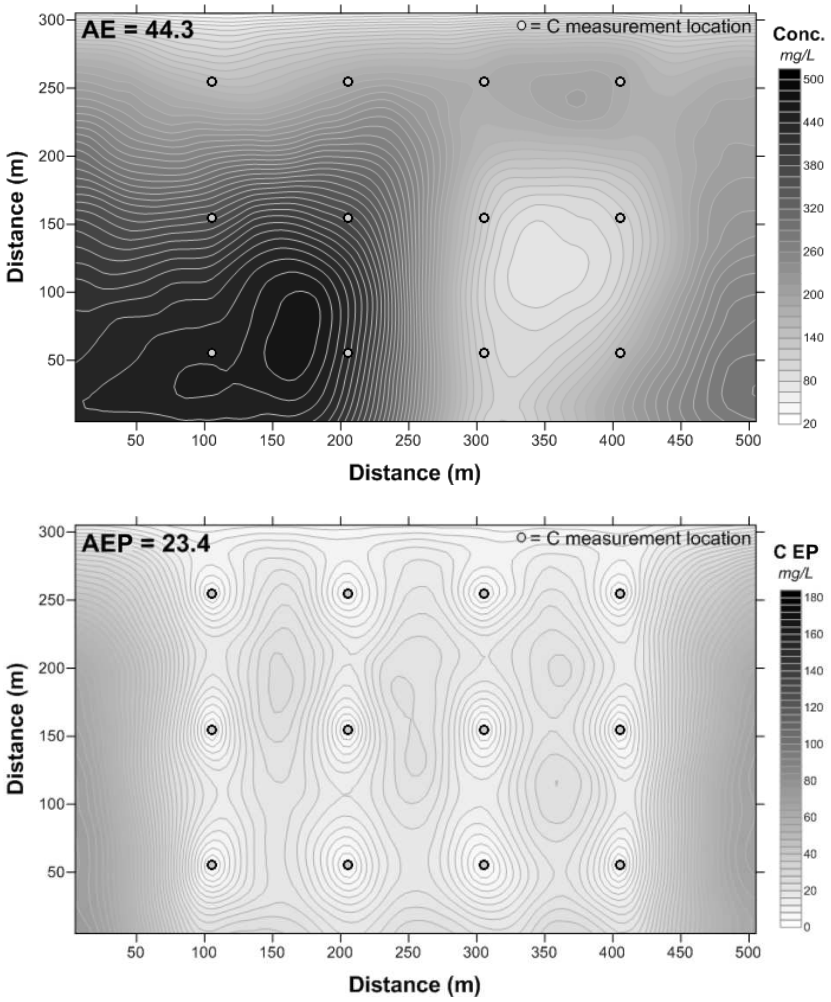

Figure 3- 5. (A) Mean and (B) Precision (EP) of the updated *C* ensemble at every model grid cell, with corresponding *AE* and *AEP* values. Locations of measurements are shown with gray circles. Compare to the forecasted ensemble mean and ensemble precision in Figure 3-4, and the reference *C* field in Figure 3-3B.

Similar improvements, although to a lesser degree, occurred for the Y_λ ensemble. When four *C* measurements are assimilated, the updated Y_λ ensemble (Figure 3-6A) is able to capture the major patterns of the reference Y_λ field (see Figure 3-3A), with a high reactivity zone on the east side of the field and a low reactivity zone on the west side of the field. The *AE* value for this scenario is 0.511, a reduction of 26.7% from the forecast value of 0.697. However, when twelve

C measurements are assimilated (Figure 3-6B), the updated Y_λ ensemble has a much stronger resemblance with the reference Y_λ field, with an *AE* value of 0.386, an improvement from the forecast ensemble of 44.6%.

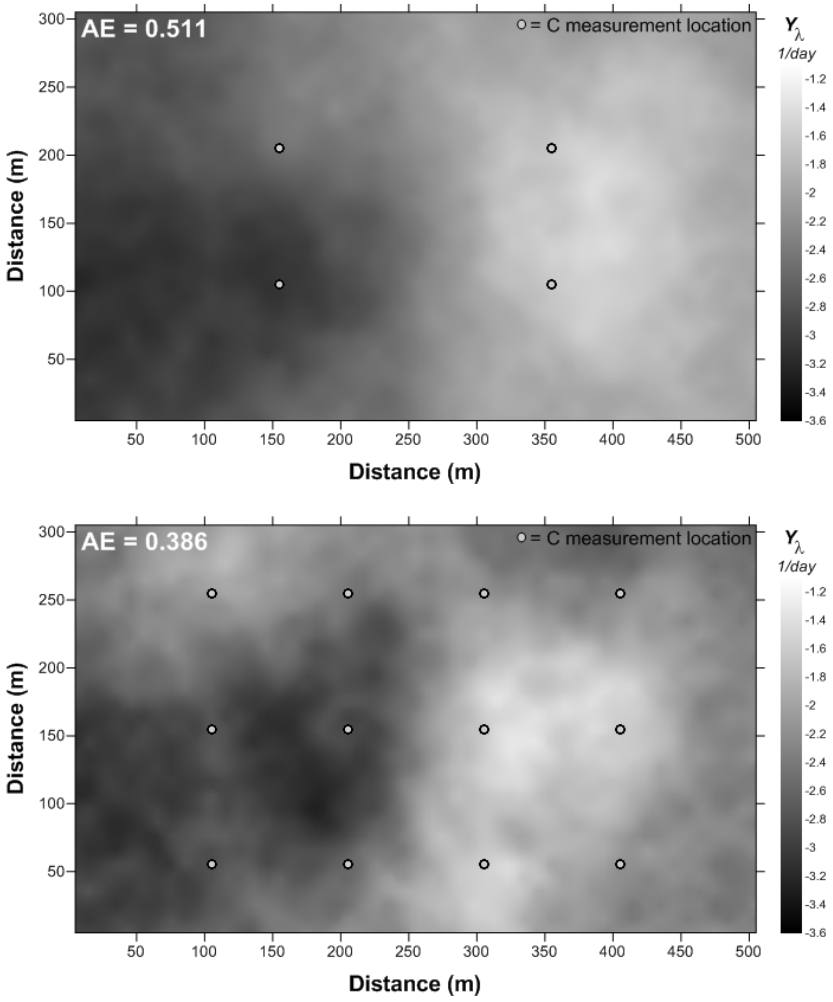

Figure 3- 6. Mean of the updated Y_λ ensemble at every model grid cell when (A) 4 *C* measurements are assimilated, with measurement locations shown in gray circles, and when (B) 12 *C* measurements are assimilated. Compare to the reference Y_λ field in Figure 3-3A.

Using 12 *C* measurements, the updated ensemble precision of the Y_k values (Figure 3-7B) shows marked improvement from the forecasted ensemble spread (Figure 3-7A), with the *AEP* values being reduced from 0.564 to 0.254, an improvement of 54.9%. This can also be seen in Figure 3-8, which shows the histogram of the ensemble of forecasted and updated Y_λ values at

the cell centered at the location (355m,155m), which is halfway between cells where *C* measurements were taken. The updated ensemble has a reduced variance from the forecast ensemble, and an ensemble mean closer to the reference Y_k value. For cells closer to a measurement cell, the variance would be even smaller, since cells closest to measurement cells receive enhanced conditioning (see Figure 3-7B).

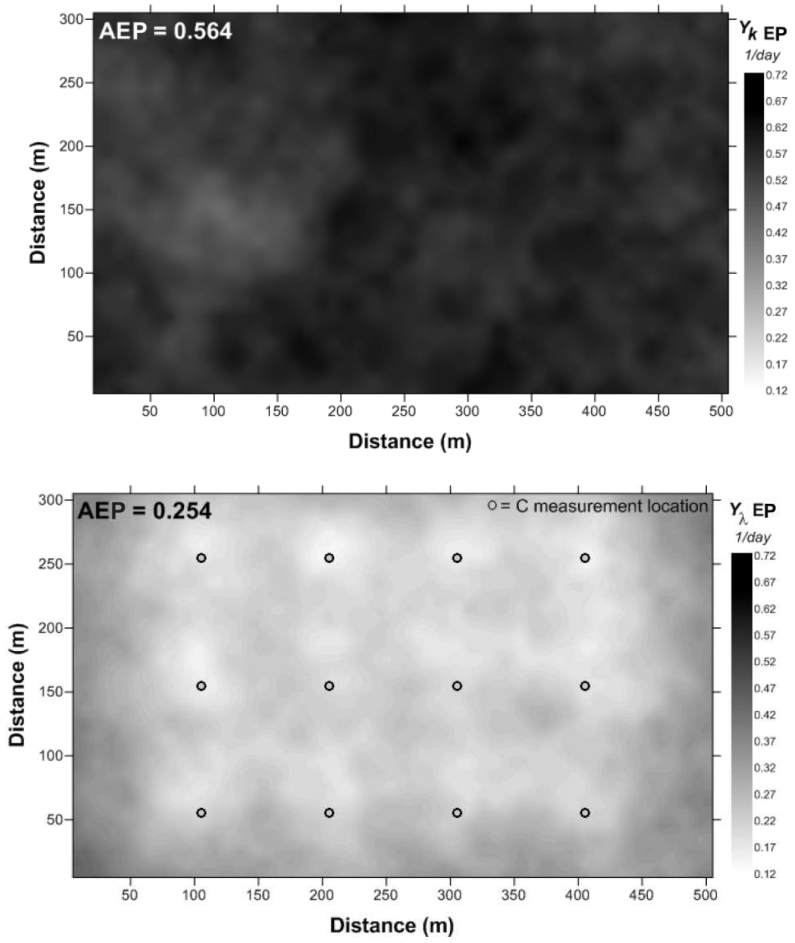

Figure 3- 7. Ensemble precision of the (A) forecasted Y_λ ensemble and the (B) updated Y_λ ensemble, at every model grid cell, when 12 *C* measurements are assimilated.

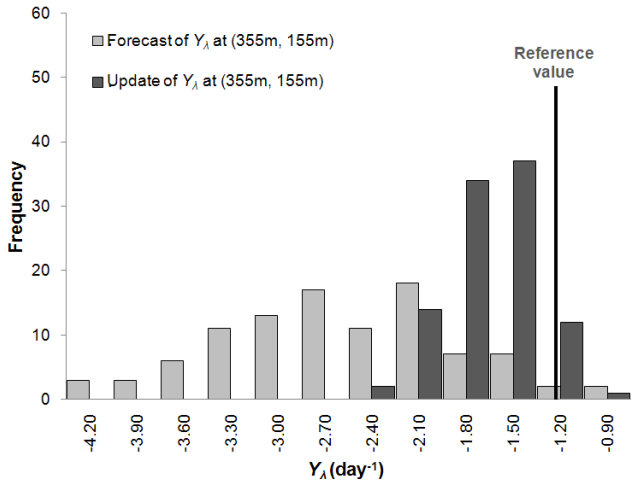

Figure 3- 8. Forecast and update ensembles of Y_λ values at cell centered at (355m,155m), located between *C* measurement cells.

3.3.1.3 Sensitivity Analysis

Additional update algorithm runs were carried out to quantify the sensitivity of the update routine to the coefficient of variation assigned to the measurement data, the number of *C* measurements assimilated, and the location of the measurements. The results of this analysis, which consisted of 16 scenarios, are shown in Table 3-1. The coefficient of variation ranged from 0.00 to 1.00 (Scenarios 1 through 7); the number of *C* measurements assimilated ranged from 1 to 20 (Scenarios 8 through 13); and measurements were taken from a west-east line in the northern (Scenario 14), central (Scenario 15), and southern (Scenario 16) portions of the aquifer. Results are shown in Table 3-1.

Table 3- 1. Sensitivity of performance parameters to measurement coefficient of variation, number of *C* measurements assimilated, and the location of the measurements, for the case of uniform hydraulic conductivity.

				AE *(C)*		***AEP*** *(C)*		***AE*** *(Y_λ)*		***AEP*** *(Y_λ)*	
Scenario	**Analysis**	**Num Meas** *C*	**Coeff Var** *C*	***AE*** *C*	**% Reduct**	***AEP*** *C*	**% Reduct**	***AE*** *Y_λ*	**% Reduct**	***AEP*** *Y_λ*	**% Reduct**
Forecast	-	-	-	**143.1**	-	**120.2**	-	**0.697**	-	**0.564**	-
1	*C* Measurement Error	12	**0.000**	**44.3**	69.0%	**23.4**	80.5%	**0.386**	44.7%	**0.254**	54.9%
2		12	**0.100**	**50.0**	65.0%	**29.4**	75.6%	**0.399**	42.7%	**0.273**	51.7%
3		12	**0.200**	**60.9**	57.4%	**35.9**	70.1%	**0.433**	37.9%	**0.295**	47.7%
4		12	**0.300**	**69.9**	51.1%	**41.5**	65.5%	**0.466**	33.2%	**0.314**	44.4%
5		12	**0.500**	**82.0**	42.7%	**50.3**	58.2%	**0.511**	26.6%	**0.344**	39.1%
6		12	**0.750**	**91.1**	36.3%	**58.5**	51.3%	**0.546**	21.7%	**0.373**	36.6%
7		12	**1.000**	**96.7**	32.4%	**64.6**	46.3%	**0.567**	18.7%	**0.394**	36.6%
8	Number of *C* Measurements	**1**	0.000	**119.6**	16.4%	**76.3**	36.5%	**0.620**	11.1%	**0.441**	21.8%
9		**2**	0.000	**93.6**	34.6%	**58.7**	51.2%	**0.576**	17.4%	**0.390**	31.0%
10		**4**	0.000	**79.9**	44.2%	**48.1**	60.0%	**0.511**	26.7%	**0.346**	38.7%
11		**8**	0.000	**49.5**	65.4%	**29.0**	75.9%	**0.403**	42.2%	**0.279**	50.6%
12		**12**	0.000	**44.3**	69.0%	**23.4**	80.5%	**0.386**	44.7%	**0.254**	54.9%
13		**20**	0.000	**45.0**	68.5%	**22.8**	81.1%	**0.386**	44.6%	**0.251**	55.6%
14	Meas. Location*	4	**North**	**101.0**	29.4%	**61.0**	49.3%	**0.557**	20.1%	**0.381**	32.5%
15		4	**Middle**	**71.6**	49.9%	**42.9**	64.3%	**0.511**	26.7%	**0.347**	38.6%
16		4	**South**	**65.4**	54.3%	**44.5**	63.0%	**0.479**	31.4%	**0.344**	39.1%

* Coefficient of Variation for scenarios 14, 15, and 16 is 0.00

When a coefficient of variation of 0.10 (Table 3-1, Scenario 1) is used, the updated *AE* value for the *C* ensemble is 50.0, a 65.0% reduction from the forecast value of 143.1. The Y_λ ensemble has an *AE* value of 0.399, a 42.7% reduction from the forecast value of 0.697. Even with a coefficient of variation of 1.00 (Table 3-1, Scenario 7), the updated *AE* values for the *C* and Y_λ ensembles are reduced 32.4% and 18.7%, respectively, from the forecast *AE* value. The update routine is quite sensitive to the number of *C* measurements assimilated, as the *AE* value is reduced from 119.6 to 45.0 for the *C* ensemble and 0.620 to 0.386 for the Y_λ ensemble when 1 measurement (Table 3-1, Scenario 8), taken from the grid cell centered at the location (255m, 155m), and 20 measurements (Table 3-1, Scenario 13) are assimilated, respectively. However, the *AE* value is decreased only slightly when more than 8 measurements (Table 3-1, Scenario 11) are used.

Further scenarios were run to investigate the sensitivity of the update routine to measurement location (Table 3-1, Scenarios 14-16). As seen in Table 3-1, the largest improvement in the AE value for both the C and Y_λ ensembles occurs when the four measurements are collected from the south section (AE value of 65.4). This area experiences a much larger variation in concentration values between the model realizations (see Figure 3-4B), signifying a high level of uncertainty in the forecast ensemble. Minimizing the variation of these values through the use of measurement data provides a larger improvement in the updated C ensemble than if the measurement data were collected in an area with small variation, highlighting the fact that measurement data is more valuable in situations where knowledge about the field variable is more uncertain.

3.3.2 Aquifer with Uncertain Hydraulic Conductivity

Since transport of solutes is highly dependent on the flow field, and since flow fields are often not known with certainty for a given aquifer, this section deals with estimating the spatial distribution of Y_λ given uncertainty in the spatial distribution of hydraulic conductivity. Using the same model set-up and reference Y_λ field as in Section 3.1, an ensemble of nmc = 100 Y_K fields were created using the geostatistical parameter values μ_{Y_K} = -3.94, σ_{Y_K} = 0.274, and l_i = 250 m, resulting in a range of K values from 0.864 m day^{-1} to 118.3 m day^{-1}. These Y_K fields were used to produce an ensemble of 100 flow fields, with each realization serving as the flow field for a corresponding reactive transport simulation. The reference Y_K field (Figure 3-9), together with the reference Y_λ field shown in Figure 3-3A, produced the reference C field from which measurements were taken. This procedure is somewhat equivalent to increasing the uncertainty in the prior distribution of Y_λ, since uncertainty in both K and λ produce a prior C ensemble that has a much larger spread of values.

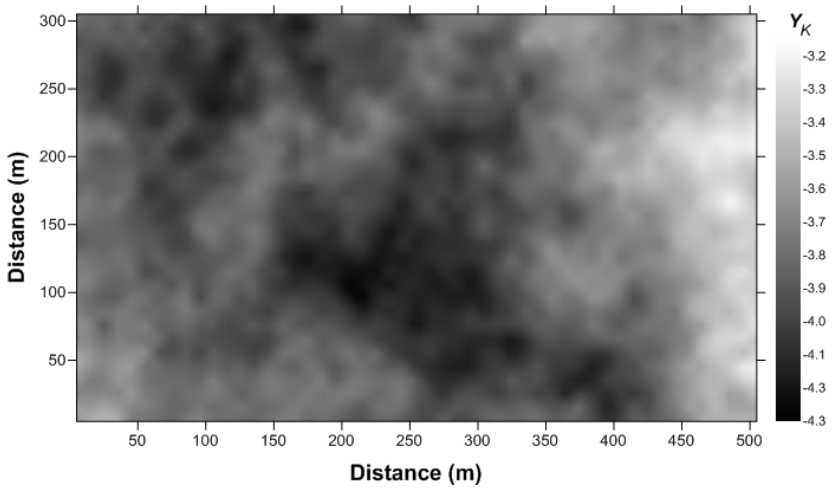

Figure 3- 9. Reference hydraulic conductivity field, created using geostatistical parameter values $\boldsymbol{\mu_{Y_K}}$ = -3.94, $\boldsymbol{\sigma_{Y_K}}$ = 0.274, and l_i = 250 m.

The updated Y_λ ensemble, conditioned by 12 *C* measurements from the reference *C* field, is shown in Figure 3-10. Notice that the conditioning is less pronounced than in the case of uniform hydraulic conductivity (Section 3.1), with the *AE* and *AEP* values reduced by 33.4% (0.697 to 0.464) and 45.6% (0.564 to 0.307), respectively, as compared to 44.7% and 54.9% for the case of uniform *K* presented in Section 3.1. This is also seen in Figure 3-11, which shows the reduction of *AE* with an increasing number of *C* measurements for the two cases of uniform and uncertain *K*. In both cases, the departure of the Y_λ ensemble from the reference state is reduced with an increase in the number of *C* measurements. However, the reduction in error is less pronounced for the case in which *K* is uncertain, since in this case the *C* field produced by the simulations is dependent on the spatial distribution of both *K* and λ. This will be discussed further in Section 4.

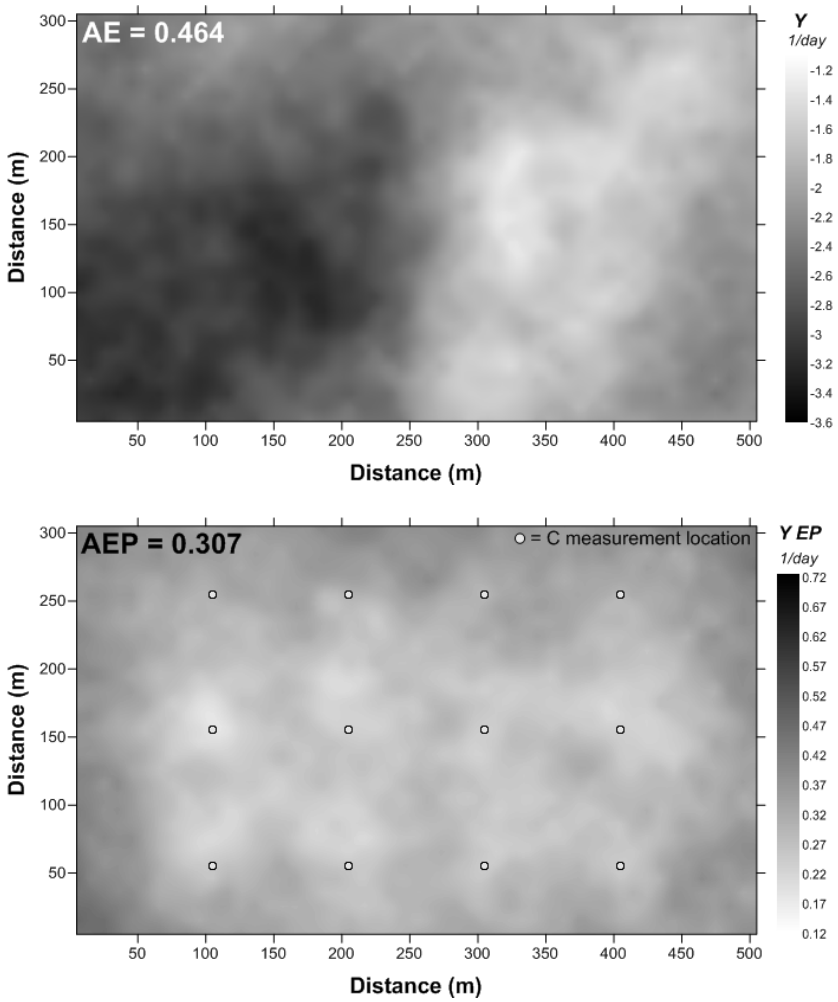

Figure 3- 10. (A) Mean of the updated Y_λ ensemble at every model grid cell and (B) Ensemble Precision of the updated Y_λ ensemble using 12 *C* measurements in an aquifer with uncertain, spatially-variable hydraulic conductivity. Compare (A) to the reference Y_λ field shown in Figure 3-3A.

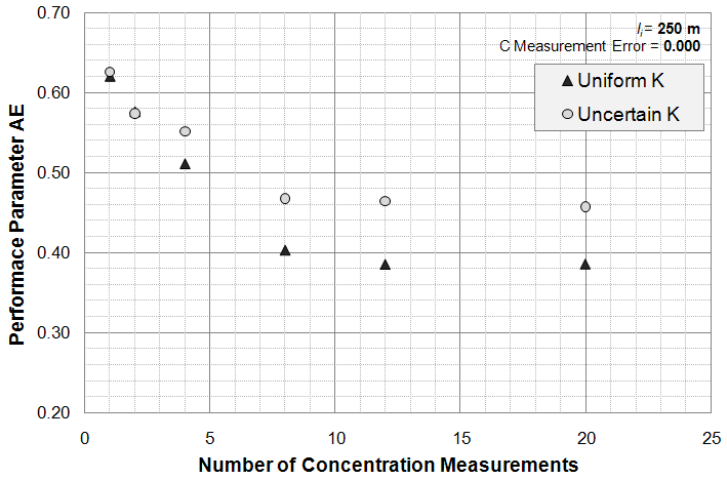

Figure 3- 11. AE of the updated Y_λ ensemble using various number of C measurements, for cases of uniform hydraulic conductivity and uncertain, spatially-variable hydraulic conductivity.

Similar to the case in Section 3.1, additional runs of the update algorithm were conducted, with similar results for C measurement error (not shown). In addition, the sensitivity of the update algorithm to the correlation length used in creating the prior Y_λ ensemble was investigated. Results are shown in Table 3-2. Three correlation lengths (l_i = 50m, 150m, and 250m) were used, with the corresponding *AE* and *AEP* values of the forecast C and Y_λ ensembles shown in the first three rows of the table. For each correlation length used, an ensemble of Y_λ fields and corresponding model-simulated C fields were created and conditioned using 12 C measurements from a reference C field. As seen in Table 3-2, the ability for the C measurement data to condition the Y_λ ensemble decreases with decreasing correlation length. For example, the *AE* value is decreased by only 16.4% (0.812 to 0.679) when l_i = 50 m, compared to a decrease of 33.4% when l_i = 250 m. Similar patterns were seen for the C ensemble. This is further seen in Figure 3-12, which shows the reference Y_λ field (Figure 3-12A) and the mean of the updated Y_λ ensemble at every cell (Figure 3-12B), with the conditioning to the reference field much weaker than when l_i = 250 m (see Figure 3-6B).

Table 3- 2. Sensitivity of performance parameters to correlation length of the Y_λ fields, for the case of uncertain, spatially-variable hydraulic conductivity

					AE *(C)*		***AEP*** *(C)*		***AE*** *(Y_λ)*		***AEP*** *(Y_λ)*	
Scen.	**Analysis**	**Num Meas** *C*	**Coeff Var** *C*	**Corr. Length** Y_λ	***AE*** *C*	**% Reduct**	***AEP*** *C*	**% Reduct**	***AE*** Y_λ	**% Reduct**	***AEP*** Y_λ	**% Reduct**
	-	-	-	250	**180**	-	**159.4**	-	**0.697**	-	**0.564**	-
Forecast	-	-	-	150	**170.7**	-	**146.6**	-	**0.741**	-	**0.561**	-
	-	-	-	50	**139**	-	**108.6**	-	**0.812**	-	**0.561**	-
1	Corr. Length	12	0	**250**	**47.6**	73.60%	**31.7**	80.10%	**0.464**	33.40%	**0.307**	45.60%
2		12	0	**150**	**55.6**	67.40%	**37.9**	74.20%	**0.514**	30.60%	**0.341**	39.30%
3		12	0	**50**	**67.9**	51.10%	**47.7**	56.10%	**0.679**	16.40%	**0.455**	18.80%

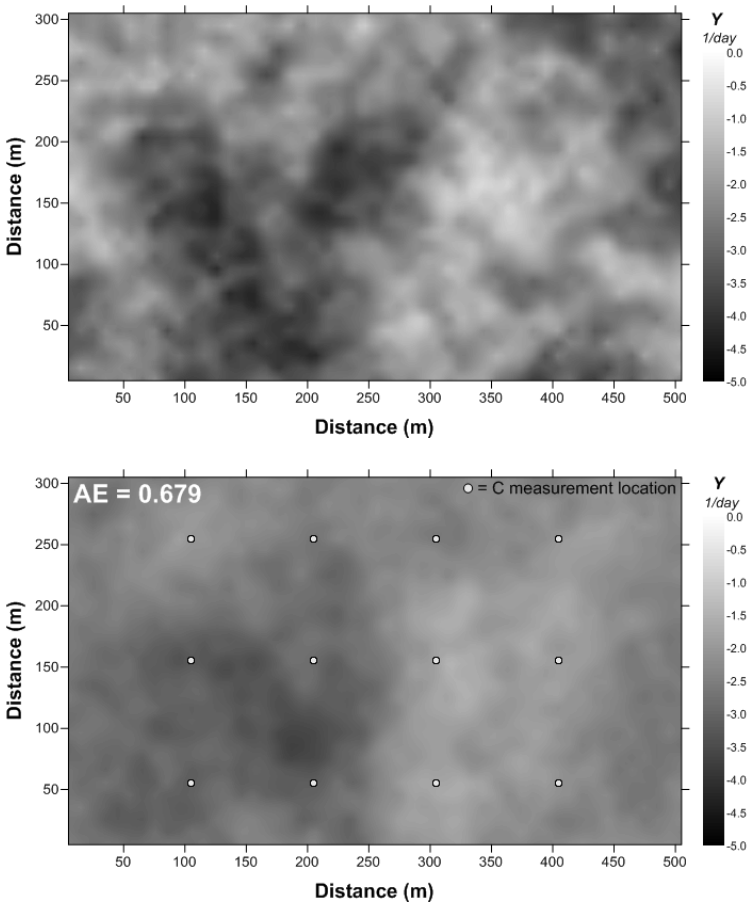

Figure 3- 12. (A) Reference field of Y_λ using a correlation length l_i = 50 m, and (B) Mean of the updated Y_λ ensemble at every model grid cell using 12 *C* measurements in an aquifer with uncertain hydraulic conductivity.

3.3.3 Estimation of λ in Aquifer of Unknown Reactivity

For the preceding two cases (Sections 3.1 and 3.2), it is assumed that the spatial statistical parameters of Y_λ (μ_{Y_λ}, σ_{Y_λ}, and l_i) are known *a priori*. However, this is generally not the case, and hence it is important to investigate the usefulness of the EnKF update scheme in cases where the statistical parameters of the prior Y_λ ensemble differ from those of the target Y_λ reference field. That is, the magnitude (μ_{Y_λ}), the range (σ_{Y_λ}) or the degree of spatial correlation of the rate constant (l_i) in the aquifer system is not known with certainty.

To do so, a scenario was developed in which the reactivity of the soil in the actual aquifer system is much more intense than what is initially assumed in the reactive transport model. Specifically, the reference Y_λ field was given a value of μ_{Y_λ} (-1.593, corresponding to λ = 0.026 day^{-1}) that is one order of magnitude higher than the initial value provided to the forecast ensemble (-2.523, corresponding to λ = 0.003 day^{-1}). Creating a reference *C* field from the reference Y_λ field, and assimilating 12 *C* measurements from the reference field, the *AE* was reduced from 1.074 for the forecast Y_λ ensemble to 0.554, a reduction of 48.4%. The *AEP* value was reduced from 0.564 to 0.307, a reduction of 45.6%.

In order to further bring the Y_λ ensemble into conformity with the Y_λ reference field, an iterative scheme was used as follows. Following the first update using the 12 *C* measurements, a simple inference analysis was employed to calculate the μ_{Y_λ} and σ_{Y_λ} of the updated Y_λ ensemble. Using these new values, SKSIM was run to create a new Y_λ ensemble, which was then updated by the same *C* measurements from the reference field. This process was repeated three times. As can been seen in Table 3-3, in which results of the three iterations are shown, the *AE* and *AEP* values are further reduced and the μ_{Y_λ} of the Y_λ ensemble further approaches the true μ_{Y_λ} with each additional iteration. From the forecast ensemble to the updated ensemble after the third

iteration, the error of the μ_{Y_λ} value is reduced from 58.4% to 6.5%. This reduction is further seen in Figure 3-13, which plots the ensemble mean of Y_λ along the row of cells located 155 m from the south boundary of the aquifer. As can been seen in Figure 3-13, the Y_λ values increasingly approach the true values with each additional iteration.

Table 3- 3. Performance parameters and mean of the Y_λ ensemble for each iteration of the EnKF-iteration scheme, showing the convergence of the updated Y_λ ensemble to the mean Y_λ of the reference system.

	C		Y_λ			
ITERATION	***AE***	***AEP***	***AE***	***AEP***	μ_{Y_λ}	**Error**
Forecast	234.572	159.415	1.074	0.564	**-2.523**	**58.4%**
1	37.838	31.726	0.554	0.307	**-1.974**	**23.9%**
2	27.105	21.627	0.443	0.228	**-1.791**	**12.5%**
3	22.677	15.743	0.392	0.186	**-1.697**	**6.5%**
REFERENCE	-	-	-	-	**-1.593**	-

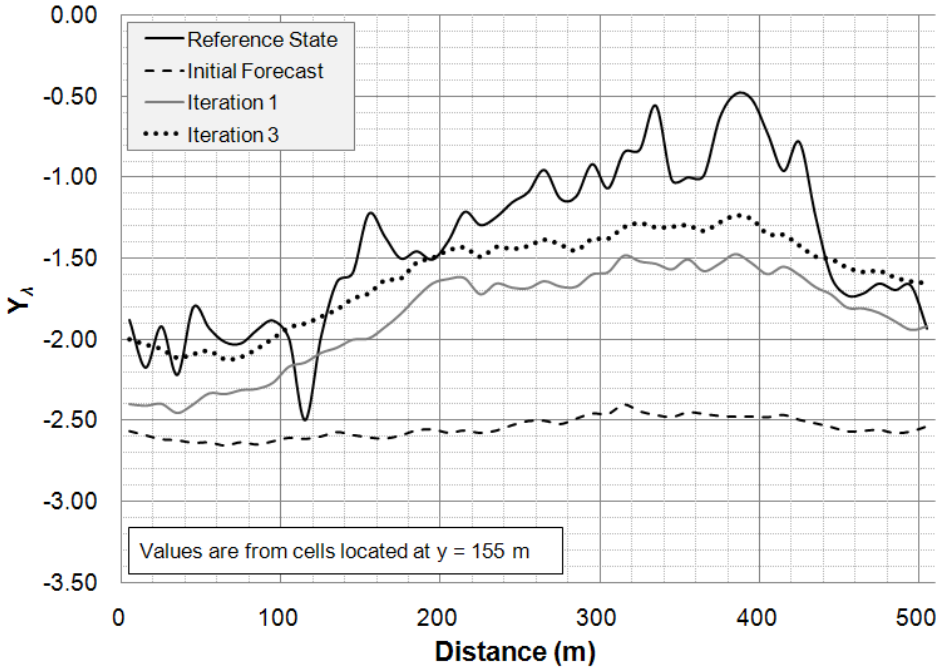

Figure 3- 13. Mean of the updated Y_λ ensemble for grid cells located at y = 155 m for the forecast, and the first and third iterations as compared to the reference state.

3.4 DISCUSSION

From results presented in Section 3, the EnKF update routine is shown to be quite successful in using C measurement data to condition the Y_k ensemble to the reference Y_k field. Sensitivity analyses demonstrated that the degree of conditioning is dependent on (i) the number of C measurements assimilated, (ii) the coefficient of variation assigned to the measurement, (iii) the location of the measurement data, and (iv) the correlation length of the Y_k forecast ensemble. In general (see Tables 3-1 and 3-2), the quality of the updated C and Y_λ ensembles, defined by the performance parameters *AE* and *AEP*: improved as the number of assimilated C measurements increased, although improvement was negligible when the number of measurements exceeded eight; improved as measurements were taken from areas of low solute concentration certainty; declined as the coefficient of variation assigned to the measurement values increased; and increased with increasing correlation length assigned to the Y_λ forecast ensembles.

Although the *AE* and *AEP* values increase as the measurement value coefficient of variation is increased (see Section 3.1), the increase is acceptable for the measurement error considered. The perturbed measurements resulting from assigning a coefficient of variation of 0.10 to a C measurement value of 183.6 mg L^{-1}, taken from the cell centered at the location (205m, 255m), are shown in Figure 3-14. Values range from 140.0 to 231.7 mg L^{-1}, with 69.0% of the values within 10.0% of the original measurement value. Even with this level of uncertainty in the measurement value, the *AE* value is 0.399, an increase of only 3.37% from the condition in which no measurement error is assigned. As such, the update algorithm appears to be rather insensitive to measurement errors that would typically occur in field sampling events.

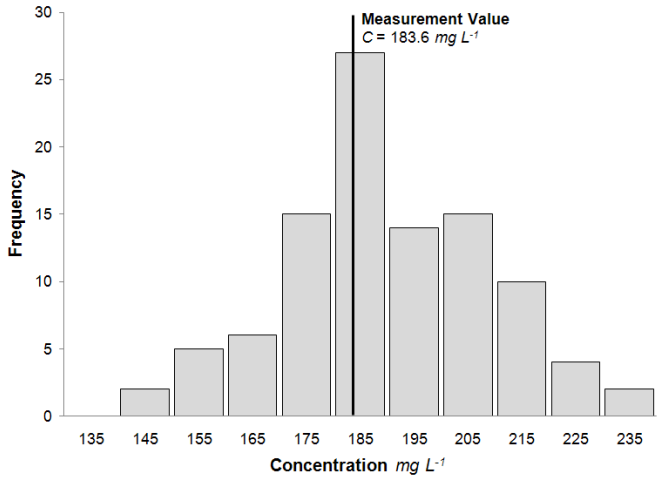

Figure 3- 14. Frequency distribution of 100 perturbed measurements for the original *C* measurement value of 183.6 mg L^{-1}, using a coefficient of variation of 0.10.

Although global values of *AE* and *AEP* were reported for the results in Sections 3.1 to 3.3, the degree of conditioning was spatially-dependent. As seen in Figure 3-15, which shows the Ensemble Error (*EE*) distribution across the domain for the results presented in Section 3.2, the deviation of the Y_λ ensemble mean from the reference Y_λ value is relatively even across the entire model domain, although higher deviation values occur in areas of low reactivity (see Figure 3-3A), signifying that conditioning to low rate-constant values is poor when compared with conditioning to high rate-constant values. Low-order rate constants, such as those found in the south-southwest and northeast portions of the aquifer, minimally affect the concentration of the solute when compared with high-order rate constants. This in turn prevents significant correlation to be established between the first-order rate constant and the solute concentration, and hence the correction provided to the Y_λ value by the *C* measurement is not as great.

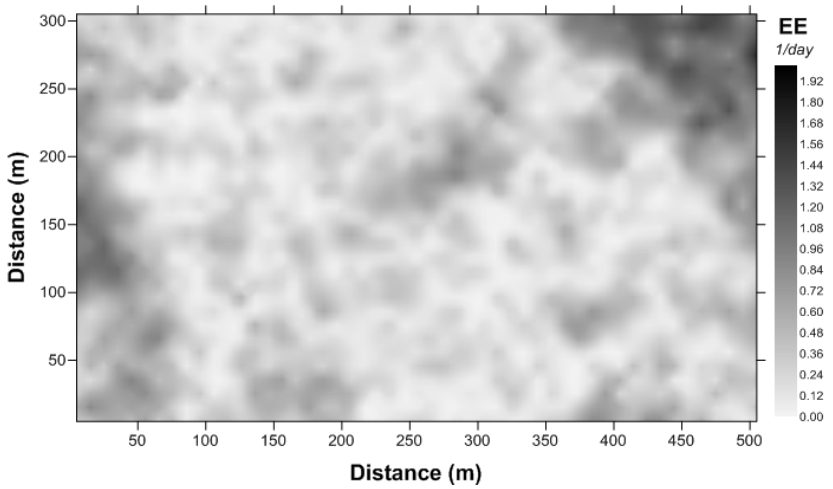

Figure 3- 15. Ensemble Error (EE) of the updated Y_λ ensemble at every model grid cell using 12 *C* measurements in an aquifer with uncertain hydraulic conductivity.

The correlation length of the forecast Y_λ ensemble has a large influence on the ability of *C* measurement data to condition the spatial distribution of Y_λ values, with superior conditioning occurring for large correlation lengths (see Table 3-2). This is expected, as corrections made to the forecasted Y_λ values in the EnKF scheme depend on the spatial correlation between *C* and Y_λ. Y_λ fields that are highly spatially-correlated produce *C* fields that are also highly spatially-correlated. As such, large pockets of Y_λ and *C* values are correlated, and hence information from assimilated *C* measurement data is correlated to, and thus can condition, a high number of surrounding Y_λ cell values. Information from *C* measurements values can thus be "spread" further throughout the model domain. Similar conclusions on the importance of correlation length in estimating aquifer parameters were also drawn by *Chen and Zhang* [2006].

As evidenced by the results of Sections 3.1 and 3.2, and in reference to Figure 3-11, the mean of the updated Y_λ ensemble approaches the reference Y_λ field more proficiently in the case of uniform *K* than that of uncertain, spatially-variable *K*. This results from the fact that the simulated *C* field is dependent on both *K* and λ, and in the case of uncertain *K* the *C* field is dependent on the spatial distribution of both. That is, *C* measurement values are correlated to

both K and λ, and hence only a portion of the resulting C value can be attributed to λ while the other portion is attributed to K. For example, a pocket of low K, which produces a high residence time of the solute, would allow the solute to undergo substantial decay even if the rate-constant λ were low. On the other hand, a pocket of high K, which produces a low residence time of the solute, would prevent the solute from undergoing substantial decay, even if the rate-constant λ were high.

As such, only a portion of the information contained in the assimilated C measurement values can be used to estimate the spatial distribution of λ, while the remaining portion can be used to estimate the spatial distribution of K. If the μ_{Y_K} forecast ensemble is included in the EnKF update scheme, and hence is allowed to be conditioned by the C measurement data, the AE of the Y_K ensemble if reduced from 0.281 to 0.230, a reduction of 18.3%. Of course, for the case of estimating the spatial distribution of K using solute concentration data, a system in which the fate and transport of the solute was governed by pure advection-dispersion processes, without the influence of chemical reactions, would allow C to more strongly condition K. These results are not shown in the Figures, as estimation of K is out of the scope of this work.

Results of Section 3.3, in which the uncertain, mean value of the true rate-constant field was approximated using an iterative EnKF technique, suggest that the methodology proposed in this paper is applicable to real-world sites in which the distributional properties of the first-order rate constant field are unknown and need to be accurately estimated. For a true application to real-world aquifer systems, however, other factors assumed constant in this study (initial and boundary conditions, sources and sinks of fluid and solute) would need to be characterized, as well as taking into account the time-dependent nature of the hydraulic head and solute concentration fields.

As such, further implementations for real-world applications would include first, identifying the spatially-variable *K* field through field measurements as well as assimilation of hydraulic head and solute concentration measurement data into transient flow simulation results [e.g., *Gailey et al.*,1991; *Franssen et al.*, 2003], in which the uncertainty of the initial conditions, boundary conditions, and inputs in space and time (e.g., groundwater recharge) are properly characterized [e.g., *Hendricks Franssen and Kinzelbach*, 2008]. Once the *K* field, and hence the flow field, is identified, the rate-constant field could be identified using the methodology presented in this paper, again with the uncertainty of the solute initial conditions and input history appropriately characterized. At both steps, the EnKF update routine would be run in an iterative scheme, similar to the one proposed in Section 3.3, to identify the distributional parameters (mean, standard deviation, correlation length) that describe the spatial structure of the parameter fields.

In general, computational burden of the EnKF update routine is extremely affordable. Overall CPU time to generate the forecast ensembles was approximately 18 minutes, with 8 minutes to run SKSIM and 10 minutes to run the ensemble of RT3D simulations. CPU time required to run the EnKF update routine, with a $\boldsymbol{X}^{f}_{k+1}$ matrix of dimension of [(1581*2) x 100], was approximately 1.24 seconds, or 0.115% of the forecast CPU time.

3.5 CONCLUSIONS

The Ensemble Kalman Filter (EnKF), a Bayesian statistical data assimilation algorithm that merges Monte Carlo model simulation results with measurement data to produce an updated system state, was implemented and employed in a synthetic aquifer system under steady flow and transport conditions to estimate the spatial distribution of a first-order rate constant λ. Using

the reactive transport model RT3D to provide an estimate of the spatial distribution of solute concentration *C* within the system, assimilating measurements of solute concentration *C* was successful in not only conditioning the *C* ensemble to the reference *C* field, but also in conditioning the spatially-variable first-order rate constant λ to the reference λ field. Conditioning was found to be most sensitive to the number of *C* measurements assimilated and the correlation length of the λ fields. Overall, conditioning of the λ ensemble is successful when the λ values significantly affect the concentration field.

The influence of uncertain aquifer hydraulic conductivity *K* was also investigated, as was the ability of the update routine to condition to the reference state if the spatial statistical parameters, such as the mean value of λ field, are not known *a priori*. In the former scenario, conditioning to the reference λ field was inferior to the case of uniform *K* since the *C* measurement data was correlated to the spatial distribution of both λ and *K*, although conditioning was still satisfactory. In the latter case, an iterative scheme was employed to converge upon the true mean value of the λ field, and results demonstrate that the EnKF scheme could be successfully employed in real-world applications in which the spatial statistical parameters that describe the parameter fields are not known with certainty.

As a first step in developing methodologies to determine spatially-variable chemical reaction parameters in contaminated aquifer systems, these results demonstrate the promising applicability of the EnKF routine, especially when considering the low computational burden. As seen in this study, a principle advantage of the EnKF routine is the ability to include a number of correlated system variables, whether response or parameter variables, into the forecast system state matrix. Hence, any variable in the system influenced by the parameter variable may serve to condition the parameter values to actual field conditions.

Future work could hence involve utilizing other system response variables to condition the first-order rate constant as well as using results from transient simulations, in which measurement data could be sequentially assimilated at multiple simulation times, to condition the set of uncertain system parameters. Other potential uses of the methodology include applications to specific chemical reactions, as well as incorporating uncertain forcing terms such as infiltration and recharge from precipitation and irrigation events and accompanying solute leaching loads, with the end goal of applying the scheme to real-world coupled flow and transport systems.

CHAPTER 4

MODELING VARIABLY-SATURATED MULTI-SPECIES REACTIVE TRANSPORT WITH MODFLOW-UZF AND RT3D

4.0 SUMMARY A numerical model was developed that is capable of simulating multi-species reactive transport in variably-saturated porous media. This model consists of a modified version of the reactive transport model RT3D that is linked to the Unsaturated-Zone Flow (UZF1) package and MODFLOW. Referred to as UZF-RT3D, the model is tested against published analytical benchmarks as well as other published contaminant transport models, such as the U.S. Geological Survey's VS2DT and SUTRA, and the coupled flow and transport modeling system of CATHY and TRAN3D. Comparisons in one-dimensional (1D), two-dimensional (2D) and three-dimensional (3D) variably-saturated systems are explored. Whereas the 1D and 2D test cases are included to verify the correct implementation of variably-saturated transport in UZF-RT3D, the 3D test cases and additional scenarios are included to demonstrate the usefulness of the code in terms of model run-time and the usefulness of the code in handling the reaction kinetics of multiple interacting species in variably-saturated subsurface systems. Because UZF1 relies on a kinematic-wave approximation for unsaturated flow that neglects the diffusive terms

in Richards equation, UZF-RT3D can be used for large-scale aquifer systems for which the UZF1 formulation is reasonable, i.e., capillary-pressure gradients can be neglected and soil parameters can be treated as homogeneous. Decreased model run-time and the ability to include site-specific chemical species and chemical reactions make UZF-RT3D an attractive model for efficient simulation of multi-species reactive transport in variably-saturated large-scale subsurface systems.

4.1 INTRODUCTION

A thorough understanding of water movement and the fate and transport of chemical species and nutrients in the shallow unsaturated zone is imperative due to its control on the transformation, removal, and leaching of chemical species, especially in agricultural settings. However, the complex physical and chemical processes that occur in such systems (e.g., nonlinear flow patterns and nonlinear kinetic chemical reactions) as well as the accounting of chemical sources and sinks for the system, renders such an analysis prohibitive without the use of physically-based multi-species (i.e., interactions between selected species) and multi-component (i.e., mixed kinetic systems subject to thermodynamic constraints) reactive transport models (Mayer et al., 2002). These models allow for the inclusion of chemical reactions and the interaction of multiple solutes, in conjunction with the environmental factors that govern these relationships (e.g., soil water content and temperature, microbial population density, and electron- (e^-) acceptor and e^--donor concentration), and multiple sources and sinks of solute mass, such as from infiltrating precipitation and irrigation water, seepage from irrigation canals, organic and inorganic fertilizer, nutrient uptake by crops, solute upflux from shallow water tables, and oxidative dissolution of consolidated and unconsolidated material.

The development of reactive transport codes has been an on-going research focus during the past two decades. Initially, numerical models capable of simulating reactive transport of multiple species in groundwater were limited to the zone of saturated porous media (e.g., Rubin, 1983; RT3D, Clement et al., 1997a; PHT3D, Prommer et al., 2003; PHAST, Parkhurst et al., 2004; Parkhurst et al., 2010) with the advective-dispersive processes coupled to chemical reactions described by equilibrium and/or kinetic relationships. RT3D (Reactive Transport in 3 Dimensions) is an especially useful model, being integrated with MODFLOW (Harbaugh, 2005) and allowing the use of pre-defined (e.g., sequential decay reactions, microbial growth and transport) or user-defined sets of kinetically-controlled reactions with the option of Monod and dual-Monod kinetics (e.g., Clement et al., 1997b; Lee et al., 2006; Wriedt and Rode, 2006). It has most commonly been used to simulate the interaction of species in the saturated zone, for example the biodegradation of hydrocarbons via the sequential reduction of e^- acceptors such as dissolved oxygen, nitrate, Fe(II), and sulfate (Clement et al., 1998) or the sequential decay of chlorinated solvents such as PCE and its daughter products TCE, DCE, and VC (Johnson et al., 2006). In such systems, the decay or production of species' mass according to kinetic rate laws are dependent on the concentration of other reactive solutes, and hence require an implicit ordinary differential equation (ODE) solver as utilized by RT3D.

In recent years, reactive transport models have been developed to extend simulation capability to variably-saturated porous media. Typically, these models have been designed for one-dimensional (1D) systems (e.g, HYDRUS-1D, Simunek et al., 1998; RZWQM, Ma et al., 2000; HP1, Jacques and Simunek, 2005; RICH-PHREEQC, Wissmeier and Barry, 2010) or two-dimensional (2D) systems (e.g., VS2DT, Healy, 1990; HYDRUS (2D/3D), Simunek et al., 2006), and are applied in 1D soil profiles or 2D vertical profiles at the field scale. Models for

three-dimensional (3D) variably-saturated systems also have been designed in recent years, for example MIN3P (Mayer et al., 2002), SUTRA (Voss and Provost, 2003, 2010), HYDRUS (2D/3D) (Simunek et al., 2006), the flow-transport coupled system of the catchment flow model CATHY (Bixio et al., 2000; Camporese et al., 2009) and TRAN3D (Gambolati et al., 1994), and the proprietary code MODFLOW-SURFACT (Panday and Huyakorn, 2008). SUTRA and CATHY-TRAN3D are limited to single-species reactive transport. MODFLOW-SURFACT was linked to MT3D (Zheng and Wang, 1999) to simulate variably-saturated flow and transport, and included the reaction package of RT3D to simulate the decay of hydrocarbons.

Similar to the 1D and 2D models, however, these 3D models solve the full Richards equation for variably-saturated flow, and hence are limited in applications due to a burdensome computational expense. As an alternative to solving the full Richards equation, the Unsaturated-Zone Flow (UZF1) package (Niswonger et al., 2006) developed for MODFLOW-NWT, a Newton formulation for MODFLOW-2005 (Harbaugh, 2005; Niswonger et al., 2011) assumes vertical homogeneity of the unsaturated zone and neglects the diffusive term in Richards equation, resulting in the kinematic wave equation for vertical unsaturated flow, with the Brooks-Corey formulation used to define the relationships between water content and variably-saturated hydraulic conductivity. MODFLOW-UZF1 requires less computational effort than the afore-mentioned models that solve the full Richards equation, and therefore provides an appealing approach to simulating variably-saturated groundwater flow in large-scale aquifer systems wherein the assumptions inherent in the UZF1 formulation, i.e., neglect of capillary pressure gradients and vertical homogeneity of the unsaturated zone, can be assumed. Hence, tradeoffs exists between the speed of UZF1 and the accuracy of Richards equation-based

approaches, although accuracy with the latter requires detailed knowledge of the spatial distribution of soil parameters.

Morway et al. (2012) present the linkage of MODFLOW-UZF1 with MT3DMS (Zheng and Wang, 1999) for multi-species advective-dispersive-reactive (with reactions limited to single species only) transport. MODFLOW-UZF1, however, has yet to be linked with a multi-species reactive transport model that accounts for interacting species. The ability to incorporate the dependence of chemical reaction rates on the presence of other reactive chemical species is a vital component in numerous chemical transport systems.

In this paper, we present the modification of RT3D to simulate multi-species reactive transport in variably-saturated subsurface systems by linking it with MODFLOW-UZF1. RT3D was chosen as the base code due to i) its wide-spread use when the simulation of interacting chemical species is required, ii) its ability to handle multiple reactive solutes and inter-species chemical kinetics, iii) the option of implementing user-defined kinetic chemical reactions and developing new reaction modules, and iv) its linkage with MODFLOW and hence inclusion in the readily-accessible suite of MODFLOW-related codes. The resulting model, hereafter referred to as UZF-RT3D, incorporates the advantages of both models (i.e., lower computational burden due to the kinematic-wave equation for simulating unsaturated flow and simulation of multiple interacting species). This paper is focused on testing UZF-RT3D through a series of benchmarks to demonstrate the linkage with MODFLOW-UZF1, verify the implementation of the variably-saturated transport processes within RT3D, and provide a general assessment of computational effort required as compared to other models. Testing of UZF-RT3D is performed through comparisons to the published analytical model of van Genuchten (1981) as well as to simulated results from the published models VS2DT (1D and 2D systems), SUTRA (3D system) and

CATHY-TRAN3D (3D system). Comparisons are made for both steady and unsteady flow systems with reactive chemical species. Further 3D simulations are included to demonstrate the flexibility of the model. Whereas the 1D and 2D test cases are provided to verify the accurate development of UZF-RT3D, the 3D test case and additional scenarios highlights the advantages of UZF-RT3D, i.e., reduced run-time and the ability to simulate the interaction of multiple reactive species in both the unsaturated and saturated zones.

4.2 DEVELOPMENT OF UZF-RT3D

The numerical model RT3D simulates the reactive transport of one or more species in a multi-dimensional saturated aquifer environment by solving finite-difference (FD) approximations of a system of advection-dispersion-reaction (ADR) equations, with one ADR equation for each chemical species (Clement, 1997; Clement et al., 1998). Assuming rigid porous media, linear equilibrium sorption, and saturated conditions, the system of ADR equations is:

$$\phi \frac{\partial C_k}{\partial t} = -\phi \frac{\partial}{\partial x_i}\left(v_i C_k\right) + \phi \frac{\partial}{\partial x_i}\left(D_{ij} \frac{\partial C_k}{\partial x_j}\right) + q_s C_{s_k} - \rho_b \frac{\partial \overline{C}_k}{\partial t} + \phi r \quad k = 1, 2, \ldots, m \tag{1}$$

where m is the total number of aqueous-phase species, C_k is the concentration of the k^{th} species $[M_f L_f^{-3}]$ where f denotes the fluid phase, D_{ij} is the hydrodynamic dispersion coefficient $[L^2T^{-1}]$, v is the average seepage velocity $[L_bT^{-1}]$, ϕ is the soil porosity $[L_f^3 L_b^{-3}]$ and b denotes the bulk phase, q_s is the volumetric flux of water representing sources and sinks of the species $[L_f^3 T^{-1} L_b^{-3}]$, C_{s_k} is the concentration of the source or sink $[M_f L_f^{-3}]$, r represents the rate of all reactions that occur in the aqueous phase for the k^{th} species $[M_f L_f^{-3} T^{-1}]$, ρ_b is the bulk density of the porous

media [$M_b L_b^{-3}$], and $\overline{C}_k$ is the concentration of the k^{th} species sorbed on solids[$M_f M_b^{-1}$]. To simplify Equation (1), the retardation factor R_k [-], equal to 1 + ($\rho_b K_{d_k}$)/ϕ for linear sorption where K_{d_k} is the partitioning coefficient [$L_f^{-3} M_b$] for the k^{th} species and is equal to $\overline{C}_k / C_k$, is incorporated to yield:

$$\frac{\partial C_k}{\partial t} R_k = -\frac{\partial}{\partial x_i}\left(v_i C_k\right) + \frac{\partial}{\partial x_i}\left(D_{ij}\frac{\partial C_k}{\partial x_j}\right) + \frac{q_s C_{s_k}}{\phi} + r \qquad k = 1, 2, \ldots, m \tag{2}$$

Rate laws for *r* describing the decay or production of species according to simple, Monod, or dual-Monod kinetics and in relation to the concentration of other species can be simulated. Saturated thicknesses, groundwater flow velocities, and volumetric flux of water into and out of the model domain are supplied by the three-dimensional groundwater flow model MODFLOW through a flow-transport link file. The system of ADR equations are solved for the change in C_k using the operator-split (OS) numerical scheme (Clement, 1997; Yeh and Tripathy, 1989) either partially or in full. In the partial OS scheme, an iterative solver is used to solve the change in C_k implicitly due to advection-dispersion-source-sink, whereupon the change in concentration due to kinetic rate laws is calculated using an ODE solver. In the full OS scheme (i.e., fully-explicit scheme), Equation (2) is separated into four distinct equations, one each for advection, dispersion, source-sink mixing, and chemical reactions, with each equation solved for the change in C_k (Clement et al., 1998). Fully-explicit formulation requires stability constraints on the length of the transport time-step, whereas the implicit scheme does not (Zheng and Wang, 1999).

In the remainder of this section, Equation (2) is reformulated to describe multi-species reactive transport in a variably-saturated aquifer environment and the solution procedures are described. Variably-saturated transport processes were implemented in UZF-RT3D for both the fully-explicit and the implicit schemes. Morway et al. (2012) describes the implementation of the

implicit scheme, and only the implementation of the explicit scheme is presented here. By replacing the porosity term ϕ in Equation (1) with volumetric water content θ [L_f^3 L_b^{-3}], the system of ADR equations for simulating multi-species reactive transport under variable saturation is:

$$\frac{\partial(C_k\theta)}{\partial t} = -\frac{\partial}{\partial x_i}(\theta v_i C_k) + \frac{\partial}{\partial x_i}\left(\theta D_{ij}\frac{\partial C_k}{\partial x_j}\right) + q_s C_{s_k} - \rho_b \frac{\partial \overline{C}_k}{\partial t} + \theta r \quad k = 1, 2, \ldots, m \tag{3}$$

where θ is a function of time and space and hence placed inside the time and space derivatives. Bringing the aqueous-solid surface sorption term to the left-hand side (Vanderborght et al., 2005) and multiplying it by $\partial(C_k\theta)/\partial(C_k\theta)$ yields:

$$\frac{\partial(C_k\theta)}{\partial t} + \rho_b \frac{\partial(C_k\theta)}{\partial t}\frac{\partial \overline{C}_k}{\partial(C_k\theta)} = -\frac{\partial}{\partial x_i}(\theta v_i C_k) + \frac{\partial}{\partial x_i}\left(\theta D_{ij}\frac{\partial C_k}{\partial x_j}\right) + q_s C_{s_k} + \theta r \quad k = 1, 2, ..., m \tag{4}$$

which can be simplified to

$$\frac{\partial(C_k\theta)}{\partial t}\left(1 + \rho_b \frac{\partial \overline{C}_k}{\partial(C_k\theta)}\right) = -\frac{\partial}{\partial x_i}(\theta v_i C_k) + \frac{\partial}{\partial x_i}\left(\theta D_{ij}\frac{\partial C_k}{\partial x_j}\right) + q_s C_{s_k} + \theta r \quad k = 1, 2, ..., m \tag{5}$$

Substitution of the following expression of R_k

$$R_k = 1 + \rho_b \frac{\partial \overline{C}_k}{\partial(C_k\theta)} \tag{6}$$

into Equation (5) yields

$$\frac{\partial(C_k\theta)}{\partial t} R_k = -\frac{\partial}{\partial x_i}(\theta v_i C_k) + \frac{\partial}{\partial x_i}\left(\theta D_{ij}\frac{\partial C_k}{\partial x_j}\right) + q_s C_{s_k} + \theta r \quad k = 1, 2, ..., m \tag{7}$$

To solve Equation (7) in the fully-explicit scheme, UZF-RT3D employs the full OS numerical scheme in terms of species mass. Substituting the mass per bulk porous media volume M_{f_k} of the

k^{th} species in the fluid phase for $C_k\theta$, Equation (7) is divided into four distinct equations to solve for the change in M_{f_k} : the advection equation,

$$\left(\frac{\partial M_{f_k}}{\partial t}\right)_{ADV} = -\frac{1}{R_k}\frac{\partial}{\partial x_i}\left(\theta v_i C_k\right) \qquad k = 1, 2, ..., m \tag{8a}$$

the dispersion equation,

$$\left(\frac{\partial M_{f_k}}{\partial t}\right)_{DSP} = \frac{1}{R_k}\frac{\partial}{\partial x_i}\left(\theta D_{ij}\frac{\partial C_k}{\partial x_j}\right) \qquad k = 1, 2, ..., m \tag{8b}$$

the source-sink mixing equation,

$$\left(\frac{\partial M_{f_k}}{\partial t}\right)_{SSM} = \frac{q_s C_{s_k}}{R_k} \qquad k = 1, 2, ..., m \tag{8c}$$

and the reaction equation,

$$\left(\frac{\partial M_{f_k}}{\partial t}\right)_{RCT} = \frac{\theta r}{R_k} \qquad k = 1, 2, ..., m \tag{8d}$$

Equations (8a), (8b), and (8c) are solved sequentially using explicit FD methods to calculate the changes in M_{f_k} for each of the *m* species due to advection, dispersion, and source-sink mixing, whereupon Equation (8d) is solved simultaneously for all *m* species using an ODE solver. Equation (8d) assumes that chemical reactions occur only in the aqueous phase. For immobile species, only the reaction equation in the form of $\left(\partial M / \partial t\right) = r_s$ is solved, with r_s representing the rate of all reactions that occur in the solid phase *s*. R_k is equal to 1 + ($\rho_b K_{d_k}$)/θ since Equation (8) is solved explicitly and uses θ only from the current time step. The implicit scheme was implemented in a similar fashion to Morway et al. (2012), the difference being that the chemical

reaction term for all species is solved simultaneously using the OS scheme once the change in C_k due to advection, dispersion, and source-sink mixing has been solved implicitly for each species.

Other modifications made to RT3D to implement variably-saturated transport with 1D downward flow in the unsaturated zone include reading and storing UZF1-specific flow output data, modifications to subroutines within the advection and source-sink mixing packages to handle new data arrays, and changes to RT3D input files to incorporate data required for variably-saturated transport. Volumetric fluxes of infiltrating water are used in conjunction with specified solute concentration values to calculate the mass of each species entering the model domain via infiltrating water at the ground surface. As a function of θ, R_k is recalculated at the beginning of each flow time step. These modifications constitute the Variably-Saturated Transport (VST) package for UZF-RT3D, which can be turned off to revert to the original RT3D functionality.

4.3 DESCRIPTION OF TESTING AND NUMERICAL EXPERIMENTS

Testing of UZF-RT3D was made through a number of comparisons to both an analytical benchmark model and to simulation results from published numerical models. Although the 1D and 2D simulations also can be performed by the newly-developed UZF-MT3DMS code (Morway et al., 2012), they are presented to verify the accurate linkage and implementation of UZF-RT3D. The simulation details are summarized in Table 1. The fully-explicit scheme was used for the 1D and 2D simulations, whereas the implicit scheme was used for the 3D simulations. The analytical model is a solution published by van Genuchten (1981) to the following single-species steady-state flow (i.e. θ and v_i remain constant in time and space) version of Equation (7) wherein the subscript k has been dropped to indicate a single species

$$\frac{\partial C}{\partial t} R = -v_i \frac{\partial C}{\partial x_i} + D_{ij} \frac{\partial^2 C}{\partial x_i} + q_s C_s - \mu C \tag{9}$$

using the following initial and boundary conditions:

$$C(x,0) = C_i \tag{10a}$$

$$C(0,t) = \begin{cases} C_0 & 0 < t < t_0 \\ 0 & t > t_0 \end{cases} \tag{10b}$$

where C_i is the initial solute concentration, C_0 is the solute concentration of infiltrating water and t_0 is the time at which the infiltrating water no longer contains solute mass. In Equation (9) the reaction term is represented by a first-order kinetic reaction with a decay constant μ [T^{-1}]. For Scenario 1, a 200 cm 1D soil profile system is used to test simulation results of UZF-RT3D against the van Genuchten solution. For the first set of tests, longitudinal dispersivity values α_L equal to 0.1, 1.0, 2.5, 5.0, and 10.0 cm were used, and t_o was set to 1 day. For the second set of tests, various combinations of R (ranging from 1.0 to 5.0) and μ (ranging from 0.0 to 0.2 d^{-1}) were used, and α was set equal to 2.5 cm.

For Scenario 2, UZF-RT3D is tested against VS2DT in a 500 cm 1D silt soil profile system for unsteady flow conditions with μ equal to 0.005 d^{-1}, with daily precipitation and potential ET values as specified in Vanderborght et al. (2005) (see also Morway et al., 2012). Scenario 3 uses the same precipitation and ET values as Scenario 2 for a sandy profile with μ equal to 0.05. The parameters used for the silt and sandy profiles are shown in Table 4-1. For both unsteady flow scenarios, C_i was set to 100 g m_f^{-3} for the top 20 cm of the profile and 0 g m_f^{-3} elsewhere, and C_0 was set to 0.0 g m_f^{-3}.

Table 4- 1. Summary of simulation set-up and parameter values for testing UZF-RT3D against analytical and numerical simulation benchmarks.

Scenario	**1**	**2**	**3**	**4**	**5**
Benchmark Model	van Genuchten Analytical	VS2DT	VS2DT	VS2DT	SUTRA, TRAN3D
Flow Condition	Steady	Unsteady	Unsteady	Steady	Unsteady
Dimension	1	1	1	2	3
Simulation time t	45 d	2 yr	2 yr	30 d	5 yr
Cell Length ΔX	-	-	-	-	25 m
Cell Height ΔY	-	-	-	0.25 m	25 m
Cell Length ΔZ	1 cm	1 cm	1 cm	0.25 m	0.5 m
Domain Length	-	-	-	-	1000 m
Domain Width	-	-	-	10 m	300 m
Domain Thickness	200 cm	500 cm (Silt)	500 cm (Sand)	5 m	45 m
Porosity ϕ	0.43	0.485	0.351	0.45	0.35
Initial θ	0.38	0.231	0.08	0.1	0.1
K_h	-	-	-	See Table 4-2	5 m d^{-1}
K_v	5 cm d^{-1}	22.5 cm d^{-1}	4000 cm d^{-1}	See Table 4-2	5 m d^{-1}
van Genuchten α	-	-	-	-	1.65
van Genuchten n	-	-	-	-	2
Brooks-Corey λ	-	1.82	1.82	2	-
Bubbling Pressure h_b	-	75 cm	16 cm	-0.15 m	-
Brooks-Corey ε	14.5	4.1	3.873	4	4
Inflow Rate q	5 cm d^{-1}	Daily	Daily	See Table 4-2	Monthly
Long. Disp. α_L	0.1 to 10 cm	5.0 cm	1.0 cm	See Table 4-2	2 m
Trans. Disp. α_T	-	-	-	See Table 4-2	0.2 m
R	1 to 5	-	-	-	-
Decay Rate μ	-	0.005 d^{-1}	0.05 d^{-1}	See Table 4-2	0.001 d^{-1}

For Scenario 4, UZF-RT3D is tested against VS2DT in a 10 m by 5 m 2D vertical-plane aquifer, as shown in Figure 4-1A. Infiltrating water is specified across the full length of the ground surface, with an influx of species mass occurring along a central 2.5 m-long segment of the ground surface. Hydraulic conductivity, inflow rate, initial position of the water table, longitudinal (α_L) and transverse (α_T) dispersivity, and μ were varied across eight test simulations, as summarized in Table 4-2, with Test 1 designated as the baseline simulation. Parameters modified in the other seven tests from those in Test 1 are bolded in Table 4-2. Each simulation was run for 30 days. Hydraulic head is specified as 2.0 m on both sides of the domain, except for the fifth test simulation that simulates a high water table and has a specified hydraulic head of

4.0 m on both sides of the domain. C_i throughout the model domain was set to 0 g m_f^{-3} and C_0 was set to 1.0 g m_f^{-3}.

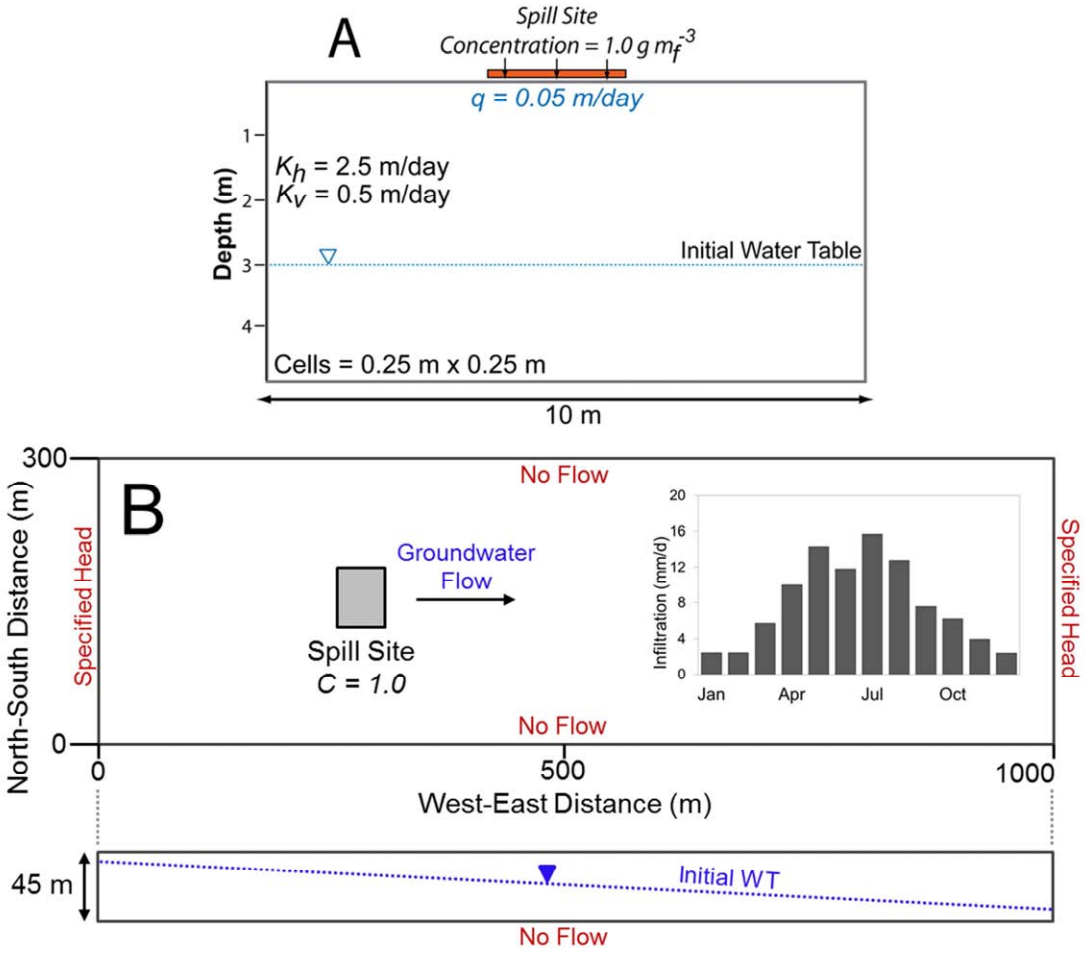

Figure 4- 1. Conceptualization of (A) 2D vertical profile aquifer system and (B) 3D aquifer system. For the 2D system, eight test simulations are performed with varying flow and transport model parameters with results compared against VS2DT. For the 3D system, monthly infiltration is specified during a 5-year simulation with results compared against SUTRA and CATHY-TRAN3D.

Table 4- 2. Details for the 2D aquifer system test simulations, belonging to Scenario 4 shown in Table 4-1. The measure of agreement with VS2DT, as indicated by R^2 values, is shown in the far-right column.

Test	Description	Figure	α_L m	α_T m	μ day^{-1}	K_{sat} m day^{-1}	Initial WT depth m	q m day^{-1}	R^2
1	Baseline Conditions	4A	0.5	0.2	0.0	2.5	3.0	0.05	0.996
2	Low Rate Constant	4B	0.5	0.2	**0.005**	2.5	3.0	0.05	0.998
3	Mid Rate Constant	4C	0.5	0.2	**0.05**	2.5	3.0	0.05	0.998
4	High Rate Constant	4D	0.5	0.2	**0.5**	2.5	3.0	0.05	0.999
5	High Water Table	4E	0.5	0.2	0.05	2.5	**1.0**	0.05	0.991
6	Low Inflow Rate	4F	0.5	0.2	0.05	2.5	3.0	**0.005**	0.998
7	High K_{Sat}	4G	0.5	0.2	0.05	**10.0**	3.0	0.05	0.993
8	Low Dispersivity	4H	**0.1**	**0.04**	0.05	2.5	3.0	0.05	0.999

For Scenario 5, UZF-RT3D is tested against SUTRA and CATHY-TRAN3D in a 300 m by 1000 m by 45 m 3D aquifer, as shown in Figure 4-1B, with a species spill site located in the western portion of the system. Groundwater flow direction is west to east, with constant hydraulic head specified as 41 m, 44 m, 5 m, 1 m, in the southwest, northwest, northeast, and southeast corners of the aquifer, respectively, with the specified hydraulic head varying linearly along the western and eastern edges of the aquifer. The resulting flow field provides 1D leaching of species mass through a shallow unsaturated zone (~ 5 m), followed by lateral species plume migration in the saturated zone due to the imposed hydraulic gradient. No-flow boundaries were specified for the northern and southern edges of the aquifer, as well as at the aquifer base. Spatial discretization was set at 25 m and 0.5 m in the horizontal and vertical directions, respectively.

Each simulation is run for 5 years, with infiltration varying on a monthly basis (see Figure 4-1B). Relationships of $K_r(\psi)$ and $S_w(\psi)$ for SUTRA, CATHY, and MODFLOW-UZF1, where K_r is relative hydraulic conductivity [-], S_w is relative saturation [-], and ψ is pressure head [L], were specified using the formulations of van Genuchten (1980), van Genuchten and Nielsen (1985), and Brooks and Corey (1966), respectively. The parameter values for these formulations, shown in Table 4-1, were selected to provide a reasonable match between the water retention curves. C_i

throughout the model domain was set to 0 g m_f^{-3} and C_0 was set to 1.0 g m_f^{-3}. The first-order decay rate μ is set to 0.001 day^{-1}. Daily time steps were used for both the flow and transport solutions.

Assessment of the agreement between UZF-RT3D and the benchmark simulations was made through a comparison of concentration profiles, contour plots, and concentration break-through curves (BTC); and on the basis of the coefficient of determination R^2 (Vanderborght et al., 2005):

$$R^2 = 1 - \frac{\sum_i (u_i - b_i)^2}{\sum_i (b_i)^2 - \frac{\left(\sum_i b_i\right)^2}{N}} \tag{11}$$

where N is either the number of grid cells in the model domain in the case of concentration profiles and contour plots or the number of time series data points for a BTC, and u_i and b_i are the concentration values of the ith grid cell for the UZF-RT3D and benchmark solutions, respectively. As Scenarios 1-4 provide an adequate suite of test cases for verifying the correct implementation of variably-saturated transport processes in UZF-RT3D, and due to differences in solution strategies (finite difference vs. finite element) as well as the location of species mass sources (cell-centered vs. nodal) for the 3D models, point-by-point comparisons for Scenario 5 are not compared using Equation (15). Rather, a general assessment in terms of species plume migration and overall computational effort is provided for Scenario 5.

Two additional scenarios using the same model domain as shown in Figure 4-1B are included to demonstrate the usefulness of UZF-RT3D in terms of (i) possible computational savings and (ii) the reactive transport of multiple interacting species. For (i), the 45-m aquifer depth is

discretized using layer thicknesses of 0.5 m, 1.0 m and 3.0 m in successive simulations, with results from the simulations compared to demonstrate the sustained accuracy when employing a coarse discretization scheme that is prohibitive for accurate flow-transport modeling systems employing Richards' equation for the flow solution. Constant hydraulic head is specified as 37 m, 41 m, 5 m, 1 m, in the respective corners of the aquifer, to enable the top layer in the 3.0-m discretization simulation to be completely within the unsaturated zone.

For (ii), a system of multiple, interacting species is employed similar to that of Kim et al. (2004) in their study of the reactive transport of organic and nitrogen species in a variably-saturated subsurface system. The defined reaction package includes the nitrification of ammonium *NH4* to nitrite *NO2* and then to nitrate *NO3*, the chemical reduction of dissolved oxygen *O2*, the denitrification of *NO3*, and the oxidation of dissolved organic carbon *DOC* through the reduction of both *O2* and *NO3*. *O2* and *NO3* are both e^- acceptors with preferential chemical reduction in the order of *O2* and *NO3*, hence establishing sequential reduction kinetics wherein denitrification does not proceed at an appreciable rate until C_{O_2} is below a specified threshold value, termed the *O2* inhibition constant I_{O_2} [$M\ L_f^{-3}$].

The rate laws for the reactions of nitrification, *O2* reduction, and denitrification are specified using dual-Monod expressions wherein the rate of reaction is dependent on the presence of the chemical reactants as well as the presence of inhibitive e^- acceptors:

$$r_{NH_4} = -\mu_{NH_4} C_{NH_4} \left(\frac{C_{NH_4}}{K_{NH_4} + C_{NH_4}} \right) \left(\frac{C_{O_2}}{K_{O_2} + C_{O_2}} \right) \tag{12a}$$

$$r_{O_2} = -\mu_{O_2} C_{O_2} \left(\frac{C_{O_2}}{K_{O_2} + C_{O_2}} \right) \left(\frac{C_{DOC}}{K_{DOC} + C_{DOC}} \right) \tag{12b}$$

$$r_{NO_3} = -\mu_{NO_3} C_{NO_3} \left(\frac{C_{NO_3}}{K_{NO_3} + C_{NO_3}} \right) \left(\frac{C_{DOC}}{K_{DOC} + C_{DOC}} \right) \left(\frac{I_{O_2}}{I_{O_2} + C_{O_2}} \right) \tag{12c}$$

where K_{NH_4}, K_{O_2}, and K_{NO_3} are the Monod half-saturation constants [$M_f L_f^{-3}$]. In this species system, *NH4* is consumed via nitrification, *NO2* is produced via nitrification, *O2* is consumed via nitrification and through chemical reduction, *NO3* is produced through nitrification of *NH4* and consumed through denitrification, and *DOC* is consumed during the chemical reduction of both *O2* and *NO3*. A north-south line source of *O2*, *NO3*, *NH4*, *NO2*, and *DOC* (6.0, 2.0, 10.0, 2.0, and 8.0 g m_f^{-3}, respectively) in the infiltrating water is specified at a distance of 162.5 m from the western edge of the aquifer. I_{O_2} is set to 1.0 g m_f^{-3}, and K_{NH_4}, K_{O_2}, and K_{NO_3} are set to 2.0, 2.0, and 1.0 g m_f^{-3}, respectively. To further demonstrate the flexibility of the RT3D code, spatially-variable first-order kinetic rate constants are specified, with the parameter field generated using the geostatistical model SKSIM (Baù and Mayer, 2008), a sequential Kriging Gaussian simulation algorithm, wherein the mean and standard deviation of a logarithmic distribution and spatial correlation scales are specified. Lognormality of first-order reactions has been reported in the literature (e.g., Parkin and Robinson, 1989). For this example, the mean, standard deviation, and correlation scale are set to 0.001 d^{-1}, 0.30 d^{-1}, and 100 m, respectively. The resulting field of spatially-variable rate constants is multiplied by four to establish the field of μ_{NH_4} values and by two to establish the field of μ_{O_2} and μ_{NO_3} values.

A key feature of the reaction system, and one which is necessary when simulating processes that are *O2*-dependent such as the sequential degradation of e^- acceptors or the bioattenuation of

petroleum hydrocarbons, is the inclusion of a reaeration term that supplies O_2 to the saturated zone via gaseous diffusion from the ambient atmosphere through the unsaturated zone. The inclusion of such a term prevents the simulation of rapid O_2 degradation and subsequent onset of anaerobic processes when in reality the presence of O_2 in the saturated zone may persist due to replenishment of O_2 via the unsaturated zone. Based on results from Neale et al. (2000) and Neale et al. (2002), the groundwater reaeration equation used in the reaction package accounts for soil type (in the form of porosity ϕ), water content θ, the thickness of the unsaturated zone z, and the difference between the saturation concentration of O_2 in groundwater, $C_{O_2(aq),sat}$, and the present O_2 concentration, $C_{O_2(aq)}$, and is given by (Neale et al., 2002):

$$\frac{dC_{O_2}}{dt} = \frac{D_s}{z^2}\left(C_{O_2(aq),sat} - C_{O_2(aq)}\right) \tag{13}$$

where the diffusion coefficient of O_2 in porous media D_s is a function of ϕ and θ (Millington and Quirk, 1961):

$$D_s = D_o \frac{\theta_a^{10/3}}{\phi^2} \tag{14}$$

where D_o is the diffusion coefficient of O_2 in air [L^2T^{-1}], with values ranging between 1.52 and 1.99 m^2d^{-1}, and $\theta_a = \phi - \theta$ is the volumetric air content of the porous media in the unsaturated zone. The five-year simulation is run both with and without the inclusion of the reaeration term. It should be noted that the flow-transport system neglects the supply of O_2 to the pore water in the unsaturated zone via gaseous transport. Depletion of O_2 in the unsaturated zone thus may be over-estimated, although likely not to a great extent when applying the model to areas where infiltrating water introduces a large mass flux of O_2 into the unsaturated zone (e.g., irrigated areas).

4.4 RESULTS AND DISCUSSION

4.4.1 One-Dimensional and Two-Dimensional Test Simulation Results

Results for the two sets of tests for Scenario 1 are shown in Figures 4-2A and 4-2B, respectively, with accompanying R^2 values. As with simulation results presented in the following sections for the 2D and 3D systems, mass balance error for all UZF-RT3D simulations is less than 0.005%. Figure 4-2A shows the concentration profile of the species after 10 days for the five dispersivity values. Reasonable matches (R^2 values between 0.925 and 0.989) between UZF-RT3D and the analytical solution occur, with the largest difference occurring for the case of α_L = 0.1 cm due to numerical dispersion at the concentration front and an under-prediction of the peak concentration. These values compare well to the R^2 values for the suite of numerical models tested against an analytical solution in a comparable simulation set-up in Vanderborght et al. (2005). For example, for the case of α_L = 0.1 cm the HYDRUS, MACRO, MARTHE, and WAVE models had R^2 values of 0.82, 0.98, 0.97, and 0.64, respectively, and for the case of α_L = 1.0 these same models had R^2 values of 0.95, 0.998, 0.997, and 0.78, respectively. Figure 4-2B shows the concentration profile of the species after 10 days for the second set of tests, and in general the R^2 values again are very good (0.969 to 0.986) with slight numerical dispersion occurring at the concentration front.

Figure 4-3 shows results for Scenarios 2 and 3. Figures 4-3A and 4-3B show the BTC of the solute at depths of 25, 50, 100, and 150 cm for the silt and sand profiles, respectively. Good R^2 values are attained for the BTC comparisons, with generally a slight under-prediction of the solute concentration. The under-prediction is more noticeable for the sandy profile, which uses α_L = 1.0 cm (compared to α_L = 5.0 cm for the silt profile). Differences between the solutions of VS2DT and UZF-RT3D result from the distinct approaches in simulating the solution of

infiltrating fronts, i.e., using the kinematic wave approximation vs. solving Richards' equation. This difference is seen in Figure 4-3A for the BTC at 100 cm depth, and is expected because UZF1 neglects the diffusive terms of Richards equation and instead simulates a sharp wetting front.

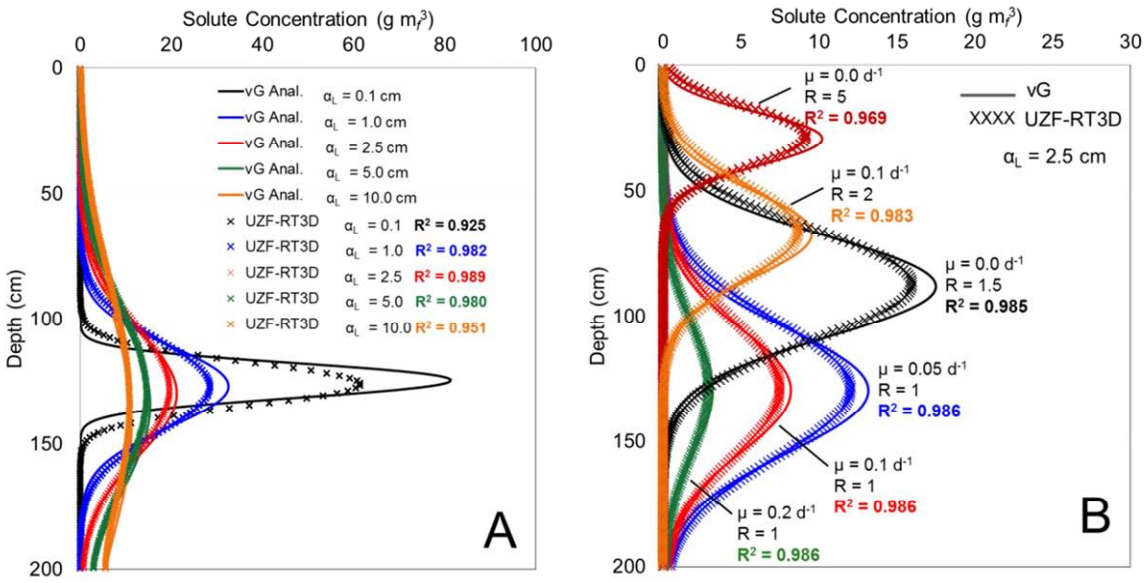

Figure 4- 2. Simulation results of UZF-RT3D and the van Genuchten (1981) analytical model for a 200-cm soil profile, showing (A) species concentration profile after 10 days for five dispersivity values (α_L = 0.1 cm, 1 cm, 2.5 cm, 5.0 cm, and 10.0 cm) and (B) species concentration profile after 10 days for various retardation coefficients (R) and first-order rate constants (μ). R^2 values are presented to provide a quantitative measure of agreement between UZF-RT3D and the analytical solution.

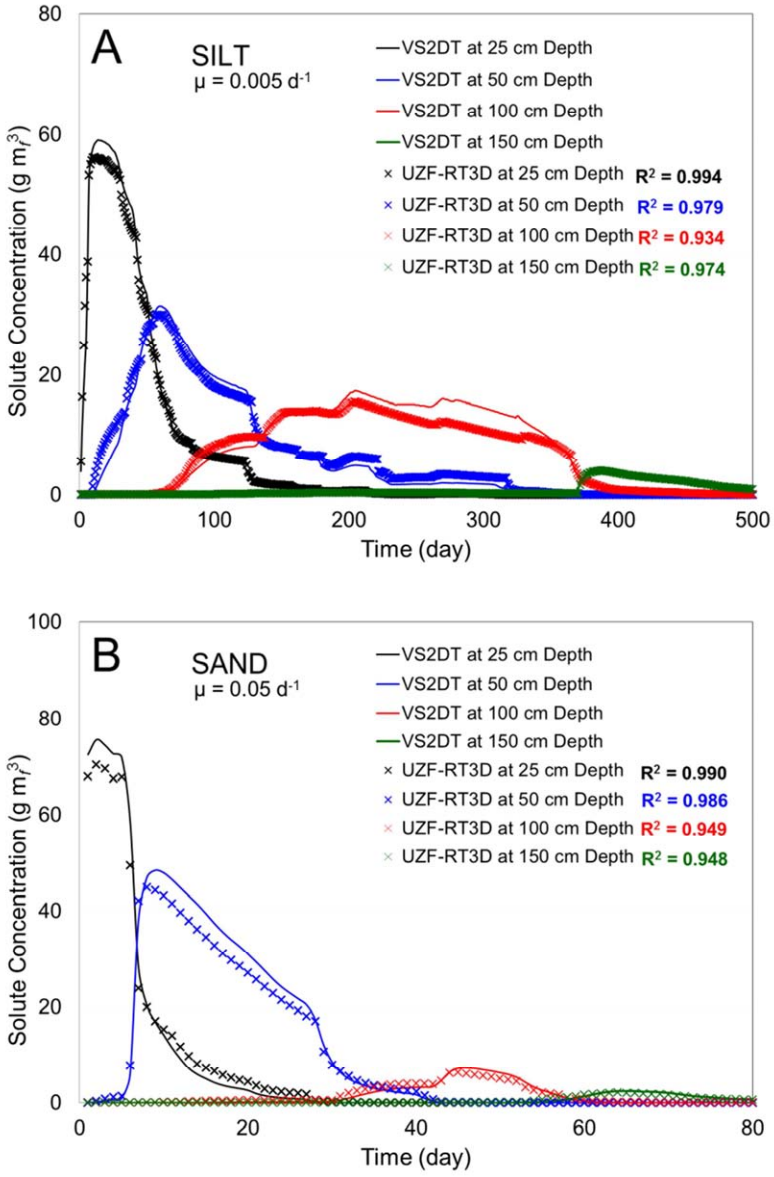

Figure 4- 3. Simulation results of UZF-RT3D and VS2DT for the 500-cm soil profile 1D unsteady flow scenario, showing simulated solute concentrations at four depths (25, 50, 100, and 150 cm) for the (A) silt profile with μ = 0.005 d^{-1}, and (B) sand profile with μ = 0.05 d^{-1}.

As seen in Figure 4-2A and 4-3B, low values of dispersivity (e.g., α_L = 0.1 cm and 1.0 cm in Scenario 1, α_L = 1.0 cm in Scenario 3) compared to the grid cell height (1.0 cm) results in numerical dispersion. However, this problem is not expected to occur when a fine model grid is used or when the dispersivity is adequately large (Zheng and Wang, 1999). Such is the case in Scenario 1 where α_L = 2.5, 5.0, and 10 cm, and in Scenario 2 where α_L = 5.0 cm.

Contour plots comparing simulation results of UZF-RT3D and VS2DT for each of the eight test simulations of Scenario 4 are shown in Figure 4-4. Excellent matches between water table elevations calculated by MODFLOW-UZF1 and VS2DT are shown in Morway et al. (2012) for a similar test scenario, and only water table elevations produced by MODFLOW-UZF1 are shown here. The agreement of the concentration fields of UZF-RT3D and VS2DT for the eight test simulations is excellent, with R^2 values ranging from 0.991 to 0.999 (see Table 4-2). As seen in Figures 4-4A, 4-4B, 4-4C, 4-4E, and 4-4G, agreement between concentration fields is slightly lower below the water table than above the water table. These discrepancies likely are caused by differences in water table elevation and mounding as calculated by the different flow solutions.

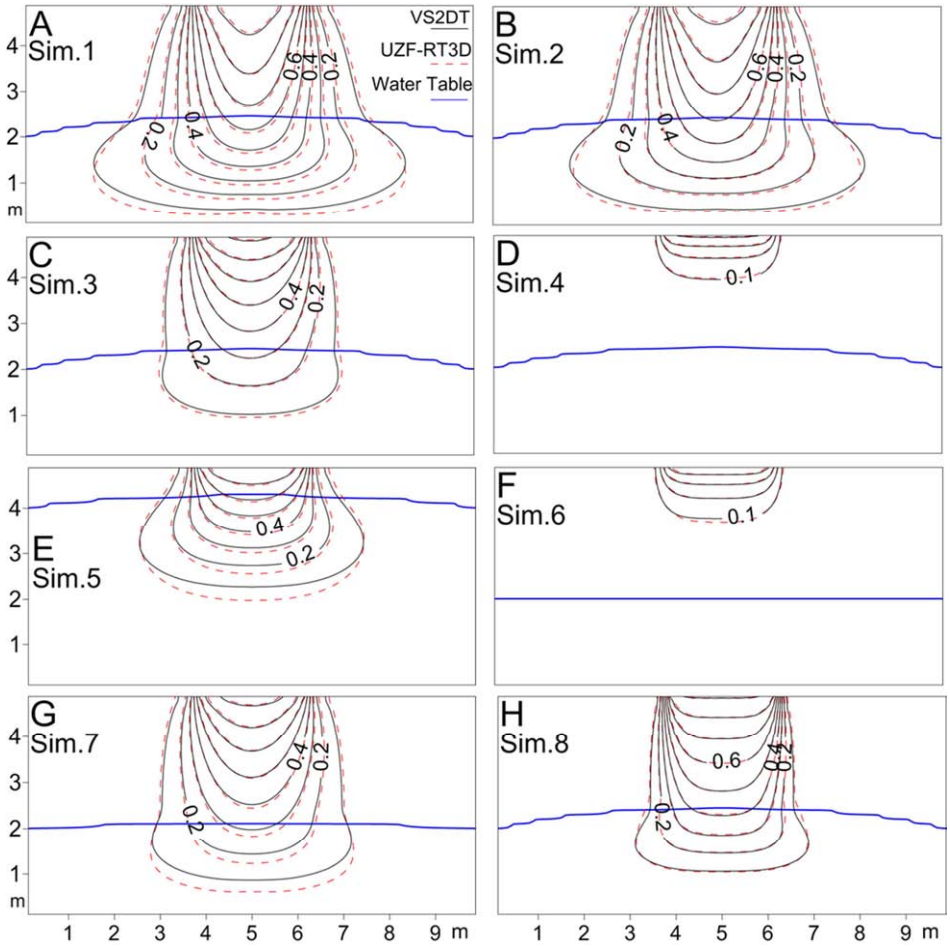

Figure 4- 4. Species concentration contour plots for the eight 2D test simulations described in Table 4-2. VS2DT results are shown in a solid black line, UZF-RT3D results are shown in a dashed red line, and water table elevation is displayed in a blue line. R^2 values comparing UZF-RT3D to VS2DT are presented in Table 4-2.

4.4.2 Three-Dimensional Test Simulation Results

Figure 4-5 shows the results of UZF-RT3D, SUTRA, and CATHY-TRAN3D for Scenario 5. Figure 4-5A shows a comparison of the simulated plume migration after five years at the cross-section located 162.5 m from the southern edge of the aquifer, and Figure 4-5B shows the plume migration in plan view after five years at an elevation of 30.25 m above the aquifer base. The spatial distribution of θ as simulated by UZF1 is shown in Figure 4-5A, and the water table simulated by SUTRA and CATHY for each column nodes is represented by blue and red circles, respectively.

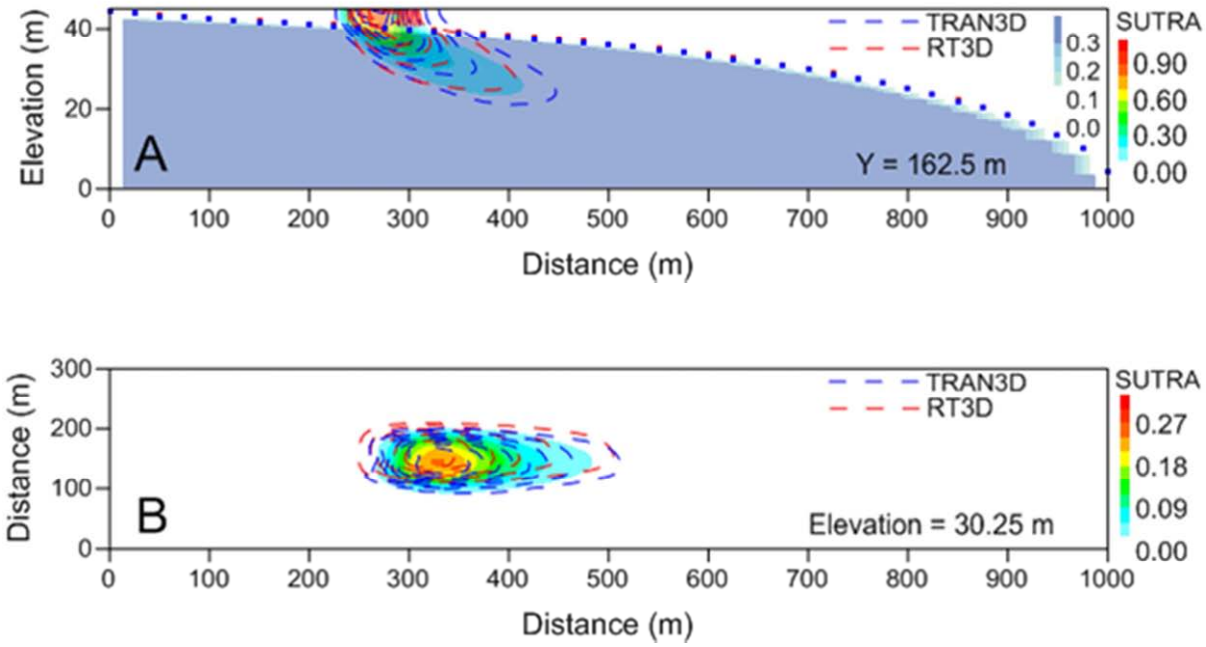

Figure 4- 5. Comparison of plume migration at 1825 days of SUTRA, CATHY-TRAN3D, and UZF-RT3D simulations for (A) the cross-section located at Y = 162.5 m and (B) the areal section at Z = 30.25 m. The water content θ from the UZF simulation is shown in blue contours, whereas the water table elevation at each column of nodes for the SUTRA and CATHY simulations are shown in blue and red squares, respectively.

For both comparisons, the plume migration is similar for each of the three models, although the plume simulated by TRAN3D is more dispersive than the plume for UZF-RT3D, and both are more dispersive than the plume simulated by SUTRA. A main difference between the plume

migration simulated by SUTRA and by UZF-RT3D stems from the location of species mass sources (cell-centered for the finite difference grid vs. nodal for the finite element mesh) for the respective models. This is seen in Figure 4-5B, where the plume simulated by UZF-RT3D is offset to the north by about 12.5 m (the difference between mass input locations for a cell-centered and nodal mass input scheme when cell size is 25 m).

Run-times for UZF-RT3D are promising when compared with CATHY-TRAN3D and SUTRA. Total CPU (Central Processing Unit) time to run UZF-RT3D on an Intel® Core™ i7-2600 CPU @ 3.40GHz desktop computer was 34.1 min (7.6 min for UZF1 and 26.5 min for RT3D), as compared to 64.5 minutes for CATHY-TRAN3D (38.3 min for CATHY and 26.1 min for TRAN3D) and 178.4 min for SUTRA. In comparing UZF-RT3D to CATHY-TRAN3D, the time savings are achieved through the use of UZF1 (7.6 min) as compared to CATHY (38.3 min). It should be noted, however, that the simulation was designed to provide a hydrogeologic setting that conforms to the assumptions inherent in the UZF1 formulation, i.e., homogeneity of soil parameters in the unsaturated zone.

It also should be noted that an exhaustive suite of comparisons (e.g., varying boundary conditions, initial conditions, forcing terms, etc.) has not been attempted, and hence the report of CPU times is not an attempt to provide a complete comparison between the models. Rather, they provide a general sense of the efficient solution provided by UZF-RT3D. A further demonstration of the potential computational savings for systems conforming to the assumptions in the UZF1 formulation is the successive use of 0.5 m, 1.0 m, and 3.0 m layer thicknesses for the aquifer depth discretization, with results shown in Figure 4-6. The plume migration after five years for each of the simulations is shown in a color scheme, a dashed blue line, and a dashed red line, respectively. The water elevation is identical for all three cases. Total CPU time for the first,

second, and third cases were 34.6 min (7.6 min for UZF and 27.0 min for RT3D), 18.2 min (3.5 min for UZF and 14.7 min for RT3D), and 6.2 min (1.0 min for UZF and 5.2 min for RT3D), respectively. As can be seen in the figure, the extent of the plume is very similar for all three simulations, with the plume from the third case slightly different than the first two. The decrease in computational burden for the third case, however, likely compensates for the slight decrease in accuracy.

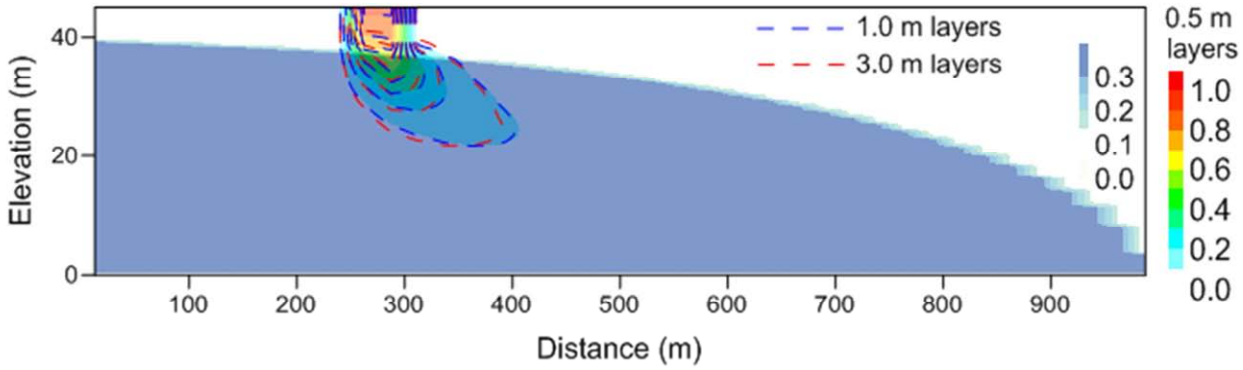

Figure 4- 6. Comparison of plume migration for the three UZF-RT3D simulations with varying vertical grid cell discretization (0.5 m, 1.0 m, and 3.0 m cell thicknesses).

4.4.3 Multi-Species Simulation Results

Figures 4-7 and 4-8 show results from the multi-species simulation in areal extent and profile view, respectively, and demonstrate the interactive behavior of the five simulated species as specified in Equations (12a-c) and the influence of the reaeration term as defined by Equations (13) and (14). The extent of the water table is the same as in Figure 4-6, and chemical reactions occur as the species are leached through the ~8-m thick unsaturated zone and then transported in the saturated zone. Figure 4-7 shows the generated base first-order rate constant field (top pane), and the resulting extent of the NH_4 (second pane), NO_3 (third pane), and O_2 (fourth pane) plumes after five years for the simulation that does not include the reaeration term, at an elevation of 30

m above the aquifer base. Notice that for NH_4 the spatial distribution of concentration is directly related to the spatial distribution of the rate constant of nitrification, with areas of higher and lower concentration occurring in the vicinity of lower and higher rate constants, respectively. As a product of nitrification, C_{NO_3} is hence higher in the southern portion of the plume where the rate of nitrification is highest, and lower in the northern portion of the plume where the rate of nitrification is lowest.

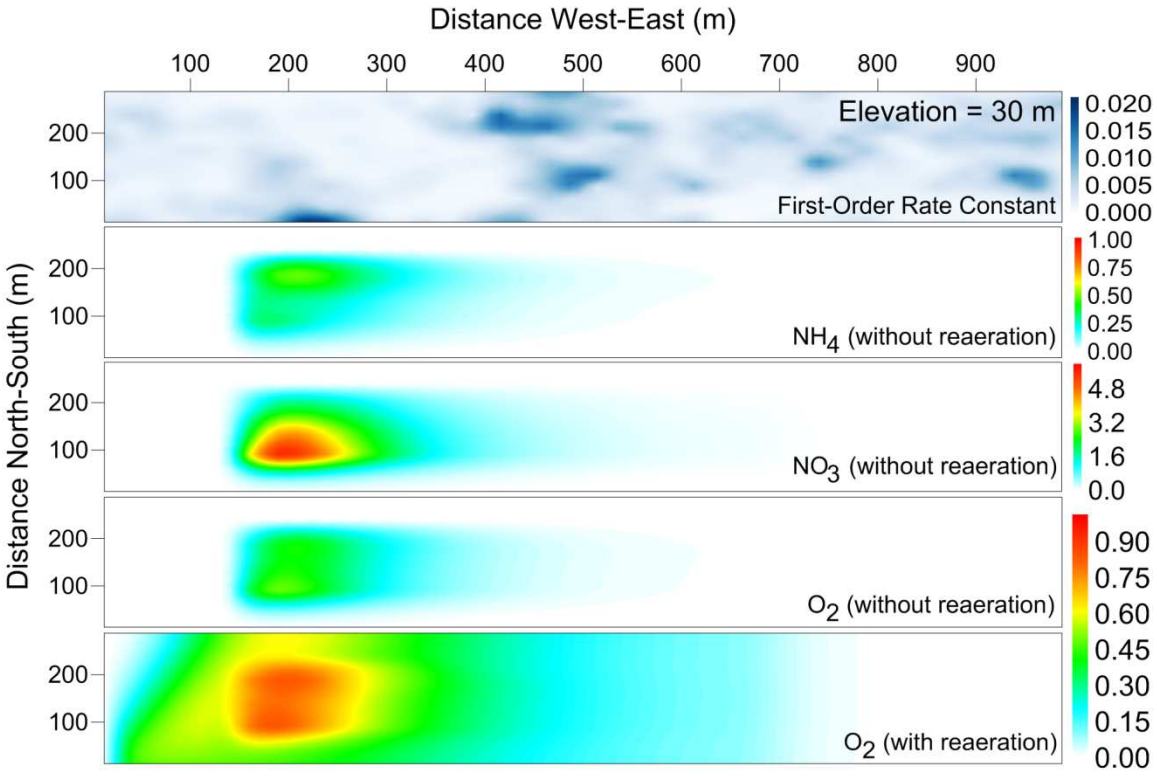

Figure 4- 7. Contour plot of the spatially-varying base rate constant (top pane), followed by plan views at elevation 30 m of plume migration after five years at Z = 30 m for NH_4, NO_3 (simulation without reaeration), O_2 without reaeration, and O_2 with reaeration.

The interaction between the species is further demonstrated in Figure 4-8, which shows the vertical extent of the species plumes at a cross-section located 87.5 m from the southern edge of the aquifer. NH_4 (top pane), with an input concentration of 10.0 g m_f^{-3} in the infiltrating water, is

consumed whereas both NO_2 (second pane) and NO_3 (third pane) are produced to result in concentrations much higher than the input concentrations (2.0 g m_f^{-3} for both). Due to the inhibitive presence of O_2, NO_3 does not undergo extensive denitirification and is transported freely through the saturated zone.

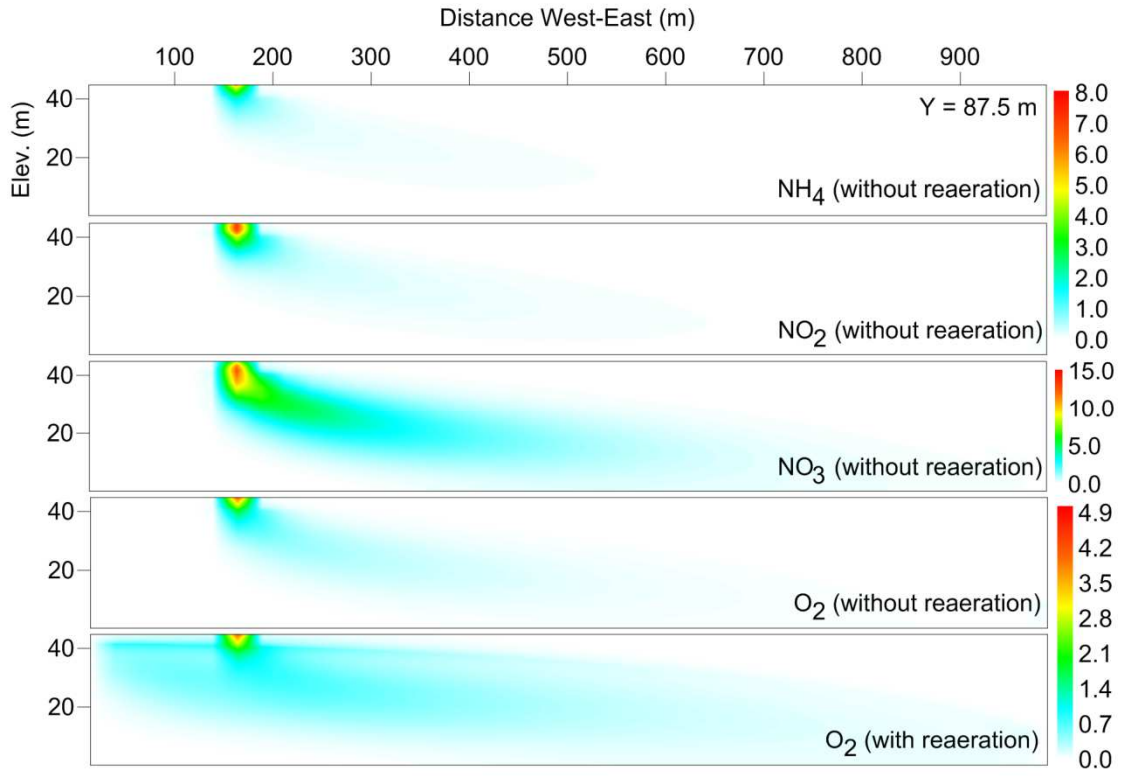

Figure 4- 8. Cross-section view of plume migration after five years at Y = 87.5 m for O_2 (simulations without and with reaeration) and NO_3 (simulations without and with reaeration).

The O_2 plume for the simulation with the reaeration term is shown in the bottom panes of both Figures 4-7 and 4-8, and when compared with the fourth panes from each figure demonstrates the significance of including reaeration to the saturated zone via gaseous diffusion. In Figure 4-7, the areal extent of the O_2 plume is much more pronounced, and in Figure 4-8 the supply of O_2 to regions of the saturated zone outside the spill site area is evident, with higher concentrations of O_2 occurring in locations where the unsaturated zone is shallow (i.e., the

western portion of the aquifer). For the simulation set-up, NO_3 only enters the system at the specified north-south line source and hence is not affected by the increased O_2 concentration in other sections of the saturated zone. However, for systems where non-point sources of nitrogen are an important source of NO_3 to the subsurface, such as in agricultural settings, the inclusion of the reaeration term will have an important influence on NO_3 as O_2 inhibits denitrification throughout the aquifer system.

4.5 CONCLUSIONS

The numerical model UZF-RT3D is presented for simulating the reactive transport of multiple interacting species in variably-saturated subsurface systems. A number of simulations in variably-saturated 1D, 2D, and 3D soil profile and aquifer systems were used to introduce and test simulation capabilities of UZF-RT3D. Tests were made against an analytical solution as well as a suite of published variably-saturated flow and transport models (VS2DT, SUTRA, CATHY-TRAN3D). Further simulations were used to demonstrate the usefulness and flexibility of UZF-RT3D in terms of computational effort and possible species and reaction scenarios. Qualitative and quantitative assessments of agreement between UZF-RT3D and the benchmark models were made, with satisfactory agreement attained for all scenarios. Future amendments to UZF-RT3D may include modification of other advection solution options included in RT3D, such as the method of characteristics, an upstream finite-difference scheme, or an implicit solution using Newton linearization.

Whereas the 1D and 2D test cases demonstrated the accuracy of UZF-RT3D, the 3D test case and additional scenarios aimed at demonstrating the usefulness and flexibility of the UZF-RT3D model, i.e., the computational efficiency of employing the kinematic-wave approximation for

unsaturated flow, and the use of user-defined, site-specific kinetic reactions for chemically interactive species.

To the first point, comparisons between UZF-RT3D, SUTRA, and the coupled CATHY-TRAN3D system demonstrate that, for the conceptual model adopted, UZF-RT3D yielded improved run-times. This was further shown through an assessment of grid discretization in the vertical direction and demonstrated the sustained accuracy in the flow and reactive transport solution for large cell sizes (e.g., 1.0 to 3.0 m layer thicknesses) and hence significant saving in model CPU time. It should be noted, however, that providing an exact comparison of CPU times between the models was not the aim of this study, as a comprehensive set of comparison tests was not carried out, but rather to demonstrate the potential advantage of UZF-RT3D in large-scale systems; and, that the conceptual model of the 3D test case was designed to suit the capabilities of UZF1, i.e., homogeneous soil parameters. The fate and transport of chemical species in variably-saturated subsurface systems that do not conform to these assumptions most likely should be investigated using Richards equation-based models.

To the second point, UZF-RT3D offers a platform for a number of applications not originally possible with the original RT3D functionality, e.g., leaching of nutrients and other chemical species in soil profiles, particularly when the reaction kinetics of a given species are dependent on the presence of other species, as in the case of sequential reduction of e^- acceptors. The 3D multi-species reactive transport scenario demonstrated these features in simulating the interactive behavior of chemical species during leaching in the unsaturated and lateral plume migration in the saturated zone. A reaeration term, in which O_2 is supplied to the saturated zone via gaseous diffusion in the unsaturated zone, is included for systems simulating the fate and transport of O_2 and O_2-dependent species and reactions, although O_2 is not supplied directly to the pore water in

the unsaturated zone. A final, important point is the inclusion of UZF-RT3D into the suite of models available to the worldwide community of MODFLOW.

Combined with the computational advantages of UZF1, UZF-RT3D is an attractive option for multi-species reactive transport in large-scale variably-saturated flow systems wherein the unsaturated zone plays an important role in the movement and transformation of chemical species over last landscapes, such as in agricultural watersheds. Modular packages currently are being developed to simulate the fate and transport of certain nutrients and chemical species in agricultural systems, and will be used in the development of a regional-scale (10^5 ha) model to assess alternatives for mitigating selenium and nitrate pollution in the irrigated stream-aquifer system of Colorado's Lower Arkansas River Valley.

CHAPTER 5

MODEL FOR SIMULATING THE REACTIVE TRANSPORT OF SELENIUM SPECIES IN AGRICULTURAL GROUNDWATER SYSTEMS

5.0 SUMMARY Selenium (Se) contamination in environmental systems has become a major issue in many regions world-wide during the previous decades, with both elevated and deficient Se concentrations in groundwater, surface water, soils and associated cultivated crops reported. In an effort to provide a tool for assessing baseline conditions and exploring remediation strategies, this paper presents a numerical model, referred to as UZF-RT3DAG, capable of simulating the reactive transport of Se species in large-scale variably-saturated groundwater systems influenced by agricultural practices. Developed by incorporating a Se reaction module into the multi-species, variably-saturated reactive transport model UZF-RT3D, model features include near-surface Se cycling due to agricultural practices, oxidation-reduction reactions, and the inclusion of a nitrogen (N) cycle and reaction module due to the dependence of Se transformation and speciation on the presence of nitrate (NO_3). Although the primary motivation is applying the model to large-scale systems, this paper presents applications to agricultural soil profile systems in order to corroborate the near-surface module processes that are vital in estimating mass loadings to the saturated zone in reginal fate and transport studies. The first

application tests the N module, whereas the second application jointly tests the Se and N modules for test plots receiving varying rates of fertilizer. Results indicate that the model is successful in reproducing observed measurements of Se and NO_3 concentrations, particularly in lower soil layers and hence in regards to leaching. For one scenario, the Ensemble Kalman Filter (EnKF) is used to condition model parameters using observed field data, indicating the usefulness of the EnKF in real-world reactive transport systems.

5.1 INTRODUCTION

Selenium (Se) is an element that naturally occurs as a trace constituent in geologic formations and associated soils, crops, and water bodies. Although an essential micro-nutrient for humans and animals (Combs et al., 1986; Aro et al., 1998) elevated concentrations and bio-accumulation have proven detrimental to human and animal health (Schwarz and Foltz, 1957; Flury et al., 1997; Aro et al., 1998). The narrow range between dietary deficiency (<40 $\mu g\ day^{-1}$) and toxic levels (>400 $\mu g\ day^{-1}$) (Levander and Burk, 2006) for humans has led to Se being termed “double-edged sword element” (Fernández-Martínez and Charlet, 2009) and an “essential toxin” (Stolz et al., 2002).

Se, as a trace constituent in all igneous rocks, is present in all soils (Byers, 1937), particularly in irrigated agricultural aquifer systems underlain by or adjacent to shale formations containing seleno-pyrite ($FeSe_2$) (Seiler, 1995; Seiler, 1997; Gates et al., 2009) wherein mobile forms of Se are released through oxidation-reduction (redox) processes (Wright, 1999; Stillings and Amacher, 2010; Bailey et al., 2012a). Mobile forms of Se are transported through aquifer systems to either shallow soil zones or surface water discharge points, with transport tempered

by possible sorption and chemical reduction processes that lead to immobilized, volatilized, and/or precipitated forms of Se. These processes, however, are inhibited by the presence of oxygenated groundwater species such as dissolved oxygen (O_2) and nitrate (NO_3) (Oremland et al., 1989; Weres et al., 1990; White et al., 1991; Zhang and Moore, 1997). Once accumulated in the shallow soil and root zone in agricultural regions, due to either transport through the aquifer or deposited within irrigation water, Se is subject to cycling in the plant-soil system similar to other elements such as nitrogen (N), phosphorus (P), and sulfur (S) (Shrift, 1964; Stolz et al., 2002).

During the last half-century, the presence of elevated Se concentrations in groundwater, surface waters, and associated crops has garnered serious concern in the United States (Seiler, 1997; Gates, 2009; Hudak, 2010), the Middle East (Afzal et al., 2000; Kuisi et al., 2010), and East Asia (Mizutani et al., 2001; Zhang et al., 2008). Deformities and death among water fowl and fish populations have been caused by toxic concentrations of Se in surface waters fed by contaminated aquifer systems (Flury et al., 1997; Hamilton, 1998; Skorupa, 1998), with the specific negative biological effects including nervous system defects, inhibition of tissue breathing, and decrease in enzyme activity (Kishchak, 1998). According to the National Irrigation Water Quality Program (NIWQP), areas of Se contamination of surface waters occur when irrigated aquifer systems are underlain by marine shales (Seiler, 1995, 1997), suggesting that Se contamination is due to the release of mobile Se forms from shale material. This result has been supported by field and laboratory work (Wright, 1999; Stillings and Amacher, 2010; Bailey et al., 2012a), with the work by Wright (1999) and Bailey et al. (2012a) concluding that NO_3, present in aquifer due to over-fertilization, can release Se from seleno-pyrite contained in the shale.

In several regions of the world, however, Se deficiency in soils and associated cultivated crops has been reported to be linked with diseases affecting both animal (Aro et al., 1998; Kishchak, 1998;) and human (Schwarz and Foltz, 1957; Alfthan et al., 1995; Peng et al., 1995; Wang and Gao, 2001) populations. For example, studies suggested a relationship between low Se uptake in human populations and increased risk of cardiovascular death and cancer in Finland (Alfthan et al., 1995; Aro et al., 1998). In such regions, supplementation of fertilizers with Se has been recommended. Other remedies include enhancing Se-rich crops from regions of natural Se-enriched soils for distribution and consumption in Se-deficient regions (Gerla et al., 2011). Both of these remedies are aligned with the recommendation of the American Dietetic Association (2001) that the intake of nutrients should occur through the regular consumption of food products (Gerla et al., 2011).

Regardless of the nature of concern regarding Se, there is a basic need for tools that allow the processes governing Se fate and transport in agricultural groundwater systems to be simulated in assessing baseline conditions and exploring remediation schemes. Due to the complex dynamics of Se transformation processes, the dependence of transformation processes on other chemical species, and the numerous time-dependent system sources and sinks of Se in an agricultural system, the use of numerical reactive transport models is an appealing approach for the development of such tools. Numerical modeling studies involving Se fate and transport thus far have been confined to one-dimensional (1D) soil profile models (Alemi et al., 1988; Fio et al., 1991; Alemi et al., 1991; Liu and Narasimhan, 1994; Guo et al., 1999; Mirbagheri et al., 2008) and a small-scale two-dimensional (2D) vertical profile model (Tayfur et al., 2010). For the majority of the studies, Se transport in saturated or unsaturated conditions is subject to sorption processes, redox reactions, or both in a 1D soil column in a laboratory setting. For most studies

only sorption, employing equilibrium sorption isotherms, has been simulated. Forcing terms such as inflow rate and concentration of influent have been kept very basic, and none have taken into account the influence of other species such as NO_3 and hence probably over-estimate the chemical reduction potential for soil systems in a given agricultural setting.

More recently, Mirbagheri et al. (2008), in a 1D model, incorporated a more complete suite of the processes involving Se species in the unsaturated zone, including advective-dispersive transport, sorption, redox reactions, volatilization, mineralization and immobilization, and plant uptake of Se. Mineralization and immobilization are simulated using first-order rate constants. In a similar study, Tayfur et al. (2010) employed a small-scale 2D vertical cross-section finite element model to simulate Se transport in both saturated and unsaturated soil zones, considering the same processes as Mirbagheri et al. (2008). The model was applied to two soil profiles 300 cm in depth, with four observations of Se for each profile. For both studies, reactions were simulated using simple first-order kinetics, without taking into account the influence of organic carbon (OC) (required for chemical reduction reactions to proceed), the influence of other chemical species, and the redox reactions governing the release of Se from marine shale. Furthermore, the cycling of Se through input of crop residue and fertilizer and the general decomposition of Se in soil organic matter was not simulated.

Although Se fate and transport modeling has been restricted to 1D and simple 2D domains, modeling studies dealing with other redox-sensitive species and nutrient cycles provide a framework for modeling Se fate and transport in a more complex aquifer system at larger scales. Studies simulating the fate and transport of redox-sensitive species such as NO_3 and SO_4 include Frind et al. (1990), Molenat and Gascuel-Odoux (2002), and Conan et al. (2003), among many others (e.g., Shamrukh et al., 2001). The majority of these studies simulate reduction reactions as

first-order kinetic processes, with several employing the Monod or dual-Monod kinetic approach with sequential reduction processes as specified by Widdowson et al. (1988), Kindred and Celia (1989), and Kinzelbach et al. (1991), where (i) the rate of the kinetic reaction depends on the relative abundance of both the electron (e^-) acceptor and the e^- donor, and (ii) the reactions are dependent on the presence of other redox-sensitive species, with inhibition occurring for lower-redox species. Nitrogen cycling simulation models (Johnsson et al., 1987; Gusman and Mariño, 1999; Birkinshaw and Ewen, 2000) provide a framework for nutrient cycling.

Of critical importance in reactive transport models is first, the identification of parameters that govern the simulated species concentration, and second, the estimation of values for these parameters. Targeted parameters often are kinetic rate constants since simulated concentrations of reactive species frequency are most sensitive to the rate constant used (Lu et al., 1999; Heatwole and McCray, 2007). Besides employing field tests to determine rate constants (e.g., Frind et al., 1990; Molenat and Gascuel-Odoux, 2002; Conan et al., 2003), other studies systematically adjusted rate constants until simulated and field-observed concentrations agreed within an acceptable tolerance. An appealing approach to parameter estimation is the Ensemble Kalman Filter (EnKF) (Evensen, 1994), a Bayesian-based data assimilation strategy. The method uses a set of Monte Carlo simulations to establish the prior probability density function (pdf) of the system state (forecast step), with data from the true system used to correct the system state and provide a posterior pdf of the system state (update step).Values of identified sensitive parameters are included in the system to allow measured values of system-response variables (i.e., species concentration) to condition the parameter values. Although tested in a synthetic aquifer setting (Bailey and Baù, 2011), the methodology has yet to be used in a real-world setting for reactive transport in soil and groundwater systems.

The objective of this study is to present the development and application of a numerical reactive transport model capable of simulating the fate and transport of Se in multi-dimensional variably-saturated groundwater systems. The model, referred to as UZF-RT3DAG, is developed by incorporating a Se cycling and reaction module to the recently-developed multi-species, reactive transport model UZF-RT3D (Bailey et al., 2012b) that includes 1D downward flow and 3D flow in the unsaturated and saturated zones, respectively. The Se module includes all pertinent components for applications to agricultural groundwater systems, including Se cycling, accompanying N cycling in order to simulate the fate and transport of NO_3, Monod and dual-Monod formulation of redox reactions, and system sources and sinks such as fertilizer, irrigation water, and canal seepage. Although the intended use of the model is for regional-scale aquifer systems wherein marine shale is a major source of Se, the application of the model in this study is limited to 1D soil systems in order to corroborate the cycling processes, redox reactions, and system sources/sinks that have been included in the model. Specifically, a time-series of observed NO_3 concentrations in soil water underlying a cultivated field is used to test the N module, whereupon observed NO_3 and Se concentrations along a soil profile are used to test the Se module as well provide further testing of the N module. This study also presents the use of a data assimilation method, the Ensemble Kalman Filter (EnKF), to provide conditioning of the parameter values in the latter test case.

5.2 SE FATE AND TRANSPORT IN AGRICULTURAL GROUNDWATER SYSTEMS

Se is present in nature primarily in the four oxidation states of +6 (selenate SeO_4), +4 (selenite SeO_3), 0 (elemental selenium Se), and -2 (selenide Se^{2-}). Selenide occurs in many forms, such as organic selenomethionine (SeMet), gaseous Dimethyl-selenide (DMSe , a product

of the volatilization of SeMet), and solid Se found in geologic formations in the form of seleno-pyrite ($FeSe_2$), in which Se substitutes for S in pyrite (FeS_2) (Bye and Lund, 1982), or as other Se-bearing species (Ryser et al., 2005). Soluble species of Se include SeO_4, a weak sorbent (Ahlrichs and Hossner 1987) and one of the most toxic of the Se species, SeO_3, a strong sorbent (Balistrieri and Chao, 1987), and SeMet, whereas Se^0 and other forms of Se^{2-} are insoluble and hence immobile unless suspended. In oxygenated agricultural waters, SeO_4 has been reported to account for 90% to 95% of soluble Se (Masscheleyn et al., 1989; Gates et al., 2009; Gerla et al., 2011) and hence is the principal target in Se contamination remediation.

The transport of Se species in soil and aquifer systems is controlled by redox and sorption reactions. The following microbially-mediated (Oremland et al., 1990) chemical reduction reactions reduce SeO_4 to SeO_3 and SeO_3 to either mobile SeMet or immobile Se^0 (Bailey et al., 2012a):

$$CH_2O + 2SeO_4^{2-} \rightarrow CO_2 + 2SeO_3^{2-} + H_2O \quad (1a)$$

$$CH_2O + SeO_3^{2-} + 2H^+ \rightarrow CO_2 + Se_{(s)} + 2H_2O \quad (1b)$$

where $Se_{(s)}$ and CH_2O represent elemental Se and a generic OC compound, respectively. SeMet can then be volatilized to non-toxic DMSe (Calderone et al., 1990; Frankenberger and Arshad, 2001). The system requirements for Se reduction to proceed include (i) the presence of microbial populations possessing the appropriate metabolic capacity, (ii) the presence of e^- donors such as OC, and (iii) restricted availability of O_2 and NO_3 due to the succession of terminal e^--acceptor processes. SeO_4 can be released from seleno-pyrite contained in marine shale through oxidation of residual Se via autotrophic reduction of O_2 or NO_3 according to the following chemical reactions (Bailey et al., 2012a):

$$2FeSe_2 + 7O_2 + 2H_2O \rightarrow 2Fe^{2+} + 4SeO_4^{2-} + 4H^+ \quad (2a)$$

$$5FeSe_2 + 14NO_3^- + 4H^+ \rightarrow 5Fe^{2+} + 10SeO_4^{2-} + 7N_2 + 2H_2O \quad (2b)$$

Possible mitigation pathways of SeO_4 remediation, all of which include reduction to SeO_3, Se^0, or SeMet, are inhibited by the presence of O_2 and NO_3. However, Oremland et al. (1990), Gates et al. (2009), and Bailey et al. (2012a) each suggested a concentration of NO_3 at which NO_3 reduction and SeO_4 reduction can occur simultaneously.

Similar to other nutrients, Se is taken up by crop rooting systems (e.g., Bisbjerg and Gissel-Nielsen, 1969; Logan et al., 1987; Johnson, 1991; Ajwa et al., 1998), distributed throughout the plant structure, and then deposited back to the soil either through decaying root mass or above-ground crop material (i.e., stover) not removed at harvest. The decaying crop mass, as a part of the soil organic matter pool, can be mineralized to inorganic species of Se (i.e., SeO_4 or SeO_3) (Bañuelos and Meek, 1990; Budjdos et al., 2000; Dhillon et al., 2007; Stavridou et al., 2011), which then are either sorbed, reduced, leached through the soil profile, or taken up by the crop

during the next growing season. Immobilization, whereby the microbes convert inorganic Se to organic Se to satisfy cellular Se requirements, has also been reported (Ajwa et al., 1998). SeO_4 and SeO_3 are the predominant species taken up by crops, although SeMet also can be used by crops (Abrams et al., 1990; Williams and Mayland, 1992; Sager, 2006). In general, SeO_4 is taken up at higher rates than SeO_3 (Sors et al., 2005), with Bisbjerg and Gissel-Nielsen (1969) and Sager (2006), respectively, reporting that SeO_4 is taken up from soil by plants up to 8 and 10 times more effectively than SeO_3. Overall, the rate of Se uptake is affected principally by concentration of Se in the soil water (Wan et al., 1988).

Including appropriate system sources and sinks, the conceptual model of Se fate and transport in an agricultural soil and groundwater system is presented in Figure 5-1. All redox reactions as discussed previously in this section are included. Cycling of carbon (C), N, and Se are based on conceptual models of C and N cycling as presented by Johnsson et al. (1987) and Birkinshaw and Ewen (2000). For C, N, and Se, the model includes three immobile, solid-phase species that contribute to the composition of soil organic matter (litter *L* (fast-decomposing), humus *H* (slow-decomposing), manure *M*), with C species included due to the dependence of N mass transfer on C mass transfer, with the dependence governed by C/N ratios of soil organic matter and microbial populations. At harvest the dead root mass is incorporated into the litter pool, and at plowing the remaining root mass and after-harvest stover is incorporated into the litter pool, upon which decomposition of the organic matter occurs with associated production of CO_2 as an indicator of the availability of OC as e^- donors for redox reactions to proceed. Mineralization of organic matter to inorganic species and immobilization of inorganic species to organic matter also occurs.

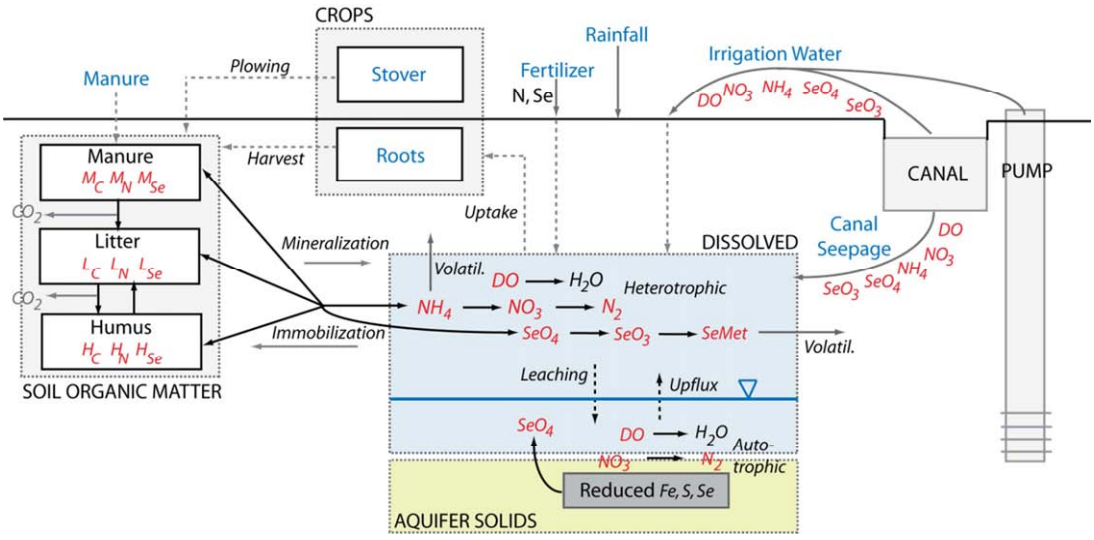

Figure 5- 1. Conceptual model of fate and transport of selenium, carbon, and nitrogen solid-phase and dissolved-phase species in an irrigated agricultural soil and groundwater system. Species' mass enters the system via fertilizer, irrigation water, and aquifer-stream exchange (e.g., canal seepage). Chemical reactions include organic matter decomposition, mineralization/immobilization, heterotrophic and autotrophic chemical reduction, volatilization, and sorption.

The model also includes six mobile, dissolved-phase species: O_2, NH_4-N, NO_3-N, SeO_4-Se, SeO_3-Se, and SeMet, of which NH_4, SeO_4, and SeO_3 can sorb. For simplicity of notation, NH_4-N, NO_3-N, SeO_4-Se, SeO_3-Se will be written as NH_4, NO_3, SeO_4, SeO_3 throughout the remainder of this paper. Redox reactions are dependent on species concentration, concentration of e^- donors, soil temperature, soil moisture, and presence of higher-redox species. Uptake of the mobile species occurs throughout the growing season. System sources include root and stover mass, which is dependent on the amount taken up during the previous growing season, fertilizer, irrigation water, canal seepage, and possibly upflux from a shallow water table. Species mass reaching the base of the root zone undergoes leaching through the underlying soil profile, and upon reaching the water table is transported through the aquifer via advection and further influenced by sorption and redox reactions. A reaeration term that supplies O_2 mass to the saturated zone via gaseous diffusion through the unsaturated zone is also included (Bailey et al.,

2012b), although this is term is not used in this study since the water table is below the soil profiles.

5.3 MODEL DEVELOPMENT

5.3.1 Multi-Species Reactive Transport in Variably-Saturated Flow Systems

The base reactive transport model for the Se and N modules is UZF-RT3D (Bailey et al., 2012b), which was developed by linking a version of RT3D (Clement, 1997; Clement et al., 1998), modified to handle variably-saturated reactive transport, with the Unsaturated-Zone Flow (UZF1) package (Niswonger et al., 2006) developed for MODFLOW-NWT (Niswonger et al., 2011), a Newton formulation for MODFLOW-2005 (Harbaugh, 2005). UZF1 assumes vertical homogeneity of the unsaturated zone and neglects the diffusive term in the Richards equation, hence requiring less computational effort than models that solve the full Richards equation and providing an attractive approach to simulating variably-saturated flow and transport in large-scale aquifer systems. Using 1D downward flow in the unsaturated zone, evapotranspiration (ET) from both the saturated and unsaturated zones, 3D flow in the saturated zone provided, and flow sources and sinks provided by MODFLOW-UZF1, UZF-RT3D solves the following system of advection-dispersion-reaction (ADR) equations for dissolved-phase and solid-phase species using the operator-split strategy (Yeh and Tripathy, 1989; Clement, 1997; Bailey et al., 2012b):

$$\frac{\partial (C_k \theta)}{\partial t} R_k = -\frac{\partial}{\partial x_i}(\theta v_i C_k) + \frac{\partial}{\partial x_i}\left(\theta D_{ij} \frac{\partial C_k}{\partial x_j}\right) + q_f C_{f_k} + \theta r_f \qquad k = 1, 2, ..., m \tag{3a}$$

$$\frac{\partial (C_l \varepsilon)}{\partial t} = \alpha_l P_s + \varepsilon r_s \qquad l = 1, 2, ..., n \tag{3b}$$

where *m* and *n* are the total number of dissolved-phase and solid-phase species, respectively; C_k and C_l are the concentration of the k^{th} dissolved-phase species [$M_f L_f^{-3}$] and l^{th} solid-phase species [$M_s L_s^{-3}$], respectively, where *f* denotes the fluid phase and *s* denotes the solid phase; D_{ij} is the hydrodynamic dispersion coefficient [L^2T^{-1}]; *v* is the pore velocity [L_bT^{-1}] provided by MODFLOW-UZF1; ϕ is the soil porosity [$L_f^3 L_b^{-3}$] with *b* denoting the bulk phase; θ is the volumetric water content [$L_f^3 L_b^{-3}$]; ε is the volumetric solid content [$L_s^3 L_b^{-3}$] with *s* denoting the solid phase and is equal to $1-\phi$; q_f is the volumetric flux of water representing sources and sinks [$L_f^3 T^{-1} L_b^{-3}$]; C_{f_k} is the concentration of the source or sink for the k^{th} dissolved-phase species [$M_f L_f^{-3}$]; P_s represents the mass application rate of all solid-phase sources mass inputs for the l^{th} solid-phase species [$M_s L_b^{-3}$] with α_l the fraction of P_s attributed to species *l* [-]; r_f and r_s represent the rate of all reactions that occur in the dissolved-phase and solid-phase for the k^{th} species [$M_f L_f^3 T^{-1}$] and l^{th} species [$M_s L_s^3 T^{-1}$]; and R_k is the retardation factor for the k^{th} dissolved-phase species, equal to $1 + (\rho_b K_{d_k})/\theta$, where ρ_b is the bulk density of the porous media [$M_b L_b^{-3}$] and $K_{d,k}$ is the partitioning coefficient for the k^{th} species [$L_f^{-3} M_b$].

5.3.2 Selenium and Nitrogen Modules

Using the form of the ADR equation (Equation 3a) and the conceptual model in Figure 5-1, the following equations are written for the Se dissolved-phase species:

$$\frac{\partial\left(C_{SeO_4}\theta\right)}{\partial t}R_{SeO_4} = -\frac{\partial}{\partial x_i}\left(\theta v_i C_{SeO_4}\right)+\frac{\partial}{\partial x_i}\left(\theta D_{ij}\frac{\partial C_{SeO_4}}{\partial x_j}\right)+q_f C_{f_{SeO_4}}+F_{SeO_4}-U_{SeO_4}+\varepsilon\left(r_{s,Se}^{min}-r_{s,Se}^{imm}\right) + \theta\left(r_{f,SeO_4}^{auto}-r_{f,SeO_4}^{het}\right) \quad (4a)$$

$$\frac{\partial\left(C_{SeO_3}\theta\right)}{\partial t}R_{SeO_3} = -\frac{\partial}{\partial x_i}\left(\theta v_i C_{SeO_3}\right)+\frac{\partial}{\partial x_i}\left(\theta D_{ij}\frac{\partial C_{SeO_3}}{\partial x_j}\right)+q_f C_{f_{SeO_3}}-U_{SeO_3} + \theta\left(r_{f,SeO_4}^{het}-r_{f,SeO_3}^{het(Se_s)}-r_{f,SeO_3}^{het(SeMet)}\right) \quad (4b)$$

$$\frac{\partial\left(C_{SeMet}\theta\right)}{\partial t} = -\frac{\partial}{\partial x_i}\left(\theta v_i C_{SeMet}\right)+\frac{\partial}{\partial x_i}\left(\theta D_{ij}\frac{\partial C_{SeMet}}{\partial x_j}\right)+q_f C_{f_{SeMet}}-U_{SeMet}+\theta\left(r_{f,SeO_3}^{het(SeMet)}-r_{f,SeMet}^{het}\right) \quad (4c)$$

where the volumetric flow rate for each of the MODFLOW-UZF1 sources/sinks (e.g., aquifer-stream exchange, pumping, infiltrating water at the ground surface) and the accompanying species concentration for each of the sources/sinks are contained in the terms q_f and C_f, respectively; F is the inorganic fertilizer application [$M_f L_b^{-3} T^{-1}$]; U is the potential uptake rate [$M_f L_b^{-3} T^{-1}$]; *min* and *imm* signify mineralization and immobilization, respectively; *auto* and *het* represent autotrophic and heterotrophic chemical reduction, respectively. Mathematical expressions for terms are presented in Section 3.3. Similar equations are written for NH_4, NO_3, and O_2:

$$\frac{\partial\left(C_{NH_4}\theta\right)}{\partial t}R_{NH_4} = -\frac{\partial}{\partial x_i}\left(\theta v_i C_{NH_4}\right)+\frac{\partial}{\partial x_i}\left(\theta D_{ij}\frac{\partial C_{NH_4}}{\partial x_j}\right)+q_f C_{f_{NH_4}}+F_{NH_4}-U_{NH_4}+\varepsilon\left(r_{s,N}^{min}-r_{s,N}^{imm}\right) + \theta\left(-r_f^{nit}-r_f^{vol}\right) \quad (5a)$$

$$\frac{\partial\left(C_{NO_3}\theta\right)}{\partial t} = -\frac{\partial}{\partial x_i}\left(\theta v_i C_{NO_3}\right)+\frac{\partial}{\partial x_i}\left(\theta D_{ij}\frac{\partial C_{NO_3}}{\partial x_j}\right)+q_f C_{f_{NO_3}}+F_{NO_3}-U_{NO_3} + \theta\left(r_f^{nit}-r_{f,NO_3}^{het}-r_{f,NO_3}^{auto}\right) \quad (5b)$$

$$\frac{\partial\left(C_{O_2}\theta\right)}{\partial t} = -\frac{\partial}{\partial x_i}\left(\theta v_i C_{O_2}\right)+\frac{\partial}{\partial x_i}\left(\theta D_{ij}\frac{\partial C_{O_2}}{\partial x_j}\right)+q_f C_{f_{O_2}}+\theta\left(-r_{f,O_2}^{het}-r_{f,O_2}^{auto}\right) \quad (6)$$

Following the pattern established for C and N cycling in soil systems (e.g., Birkinshaw and Ewen, 2000), the following equations are written in the form of Equation 3b for the Se solid-phase L_{Se}, H_{Se}, and M_{Se}, with similar equations (not shown) implemented for C and N cycling:

$$\frac{\partial\left(C_{L_{Se}}\varepsilon\right)}{\partial t} = \alpha_{Rt,Se}P_{Rt} + \alpha_{St,Se}P_{St} + \varepsilon\left(r^{dec}_{s,Se(H\rightarrow L)} + r^{dec}_{s,Se(M\rightarrow L)} + r^{dec}_{s,Se(L\rightarrow L)} - r^{dec}_{s,Se(L)}\right) + \varepsilon\left(r^{imm}_{s,Se(L)} - r^{min}_{s,Se(L)}\right) \quad (7a)$$

$$\frac{\partial\left(C_{H_{Se}}\varepsilon\right)}{\partial t} = \varepsilon\left(r^{dec}_{s,Se(L\rightarrow H)} - r^{dec}_{s,Se(H)}\right) + \varepsilon\left(r^{imm}_{s,Se(H)} - r^{min}_{s,Se(H)}\right) \quad (7b)$$

$$\frac{\partial\left(C_{M_{Se}}\varepsilon\right)}{\partial t} = M_{Se} - \varepsilon r^{dec}_{s,Se(M)} + \left(r^{imm}_{s,Se(M)} - r^{min}_{s,Se(M)}\right) \quad (7c)$$

where P_{Rt} and P_{St} are the application rates of root and after-harvest stover mass, respectively; $\alpha_{Rt,Se}$ and $\alpha_{St,Se}$ the portions of the root and stover mass attributed to Se, respectively; *dec* signifies organic matter decomposition; and *L*, *H*, and *M*, respectively, represent the litter, humus, and manure pool, with the arrow representing the direction of mass flow.

5.3.3 Definition of Mass-Balance Terms

5.3.3.1 Selenium and Nitrogen Sources and Sinks

Additions of Se and N mass consist of inorganic fertilizer application *F*, organic fertilizer application *M*, incorporation of root mass P_{Rt} into the litter pool at harvest and plowing events, and incorporation of stover mass P_{St} into the litter pool (within the specified plowing depth d_{pw}) at plowing events at the end of the growing season. Se and N mass also enter/leave the system via infiltrating water, aquifer-stream exchange, groundwater pumping, and drainage. Fertilizer loadings are applied to the top soil layers and can be split between application times. For perennial crops, the number of years of application during the perennial cycle is specified. For

incorporation of dead root mass, the fraction of live roots at harvest (i.e., the fraction that is incorporated at plowing) is specified.

As the rate of Se uptake is affected principally by concentration of Se in the soil water (Wan et al., 1988), it is simulated using first-order kinetics:

$$\begin{aligned} U_{SeO_4} &= \lambda_{up,Se} C_{SeO_4} \\ U_{SeO_3} &= \frac{\lambda_{up,Se}}{\gamma_{up}} C_{SeO_3} \\ U_{SeMet} &= \lambda_{up,Se} C_{SeMet} \end{aligned} \tag{8}$$

where $\lambda_{up,Se}$ is the Se uptake first-order rate constant [T^{-1}] and γ_{up} is the SeO_4-SeO_3 uptake ratio and signifies the effectiveness of the crop to take up SeO_4 as opposed to SeO_3 [-]. For N, daily uptake is calculated using a logistic equation (Johnsson et al., 1987) that accounts for the relative rate of uptake during stages of the growing season, with the daily uptake divided between NH_4 and NO_3 according to the relative concentration of each.

For both Se and N, the calculated rate of uptake is distributed across a profile of grid cells according to the depth and mass distribution of the root system using the depth-distribution function of Neitsch et al. (2005), with the time-dependent rooting depth calculated using a logistic equation similar to the one used in calculating daily N uptake. Maximum seasonal uptake values Se_{up} and N_{up} [ML_b^{-2}] are specified, with seasonal deficits tracked and subtracted from the amount of Se and N placed back into the soil through root and stover material in order to maintain mass balance (Wreidt and Rode, 2006). For each crop type included, the planting day, harvest day, plowing day, fertilizer loading and timing, potential seasonal uptake, maximum rooting depth $d_{rt,max}$ [L], mass of roots and stover, and constants defining the root growth and daily uptake rate are specified. For perennial crops, incorporation of root and stover mass occurs only at the end of perennial cycle.

5.3.3.2 Selenium and Nitrogen Transformation Processes

Rates of decomposition, mineralization, immobilization, and redox reactions are tempered according to soil moisture and soil temperature [T] through the inclusion of an environmental factor E [-] that has the form $E = E_\theta E_T$, where E_θ and E_T are the normalized microbial activities [-] as a function of θ and soil T, respectively. Values of E_θ for nitrification, mineralization, and denitrification for varying degrees of saturation are based on the work of Brady and Weil (1996) and the values found in Birkinshaw and Ewen (2000). For all other reactions the E_θ values for nitrification are adopted, which are similar to those in Birkinshaw and Ewen (2000) for generic reactions. Values of E_T are calculated as (Johnsson et al., 1987):

$$E_T = E_\theta + (\beta_{10})^{\frac{(T_Z - T_B)}{10}} \tag{9}$$

where T_z (^{o}C) is the soil T below the ground surface, β_{10} [-] is the factor change in rate for a 10-degree change in soil T, and T_B (^{o}C) is the base soil T at which E_T = 1, and hence no effect on the reaction rate. Values of T_z are calculated using the approach of Wreidt and Rode (2006) where T_Z in the top (0-50 cm depth), middle (50-250 cm depth), and deep soil layers (below 250 cm depth) is influenced by damped daily air temperatures (average of preceding 3 days), damped annual cycle (average of preceding 60 days), and the mean annual temperature (average of preceding 365 days), respectively.

Mathematical expressions for organic matter decomposition reactions can be written using first-order kinetics (van Veen and Paul, 1981; Birkinshaw and Ewen, 2000). Such expressions for decomposition of L_C, H_C, M_C, L_N, H_N, and M_N are contained elsewhere (e.g., Birkinshaw and Ewen, 2000), and only expressions for L_{Se}, H_{Se}, M_{Se} will be presented. Microbial populations are assumed to reside only in the litter pool (Johnsson et al., 1987). A final assumption is that decomposed mass is transferred via three pathways: to the pool of destination, to the microbial

mass within the litter pool, and to CO_2 that is used for microbial energy. Rate expressions defining the decomposition of L_{Se}, H_{Se}, M_{Se} and inter-pool mass transfers are:

$$
\begin{aligned}
r_{s,Se(H)}^{dec} &= \lambda_H C_{H_{Se}} E \\
r_{s,Se(H\to L)}^{dec} &= \lambda_H \left(C_{H_{Se}} / H_{C/Se} \right) f_e E \\
r_{s,Se(M)}^{dec} &= \lambda_M C_{M_{Se}} E \\
r_{s,Se(M\to L)}^{dec} &= \lambda_M \left(C_{M_{Se}} / B_{C/Se} \right) E \\
r_{s,Se(L)}^{dec} &= \lambda_L C_{L_{Se}} E \\
r_{s,Se(L\to H)}^{dec} &= \lambda_L \left(C_{L_{Se}} / B_{C/Se} \right) f_e f_h E \\
r_{s,Se(L\to L)}^{dec} &= \lambda_L \left(C_{L_{Se}} / B_{C/Se} \right) f_e \left(1 - f_h \right) E
\end{aligned}
\qquad (10)
$$

where λ_L, λ_H, λ_M are the first-order rate constants for litter, humus, and manure decomposition [T^{-1}], respectively; f_e is the synthesis efficiency constant (Johnsson et al., 1987) and defines the fraction of decomposed mass that reaches the destination pool [-], or in other words the fraction (1-f_e) is converted to CO_2; f_h is the humification factor [-] and represents the portion of decomposed mass that is transferred to the humus pool, and $H_{C/Se}$ and $B_{C/Se}$ are humus and microbial population C/Se ratios, similar to the C/N ratios used in Birkinshaw and Ewen (2000). The process of L_{Se} decomposition includes an internal cycle, since Se incorporated into microbial biomass stays in L_{Se} under the assumption that microbes reside only in L_{Se}.

Decomposed Se mass is transferred to H_{Se}, L_{Se} through incorporation of microbial biomass, or, if there is any remaining, to SeO_4 through mineralization. However, if the requirement of Se for microbial growth is not satisfied through the decomposition of available organic Se, than SeO_4 mass is immobilized to organic Se. The difference between the total Se mass transferred and the Se mass incorporated into H_{Se} and the microbial biomass define mineralization and immobilization, with these processes occurring if the amount is positive and negative, respectively:

$$\lambda_L E\left(C_{L_{Se}} - \frac{C_{L_{Se}} f_e f_h}{H_{C/Se}} - \frac{C_{L_{Se}} f_e}{B_{C/Se}}\right)\begin{cases} > 0 = r_{s,Se(L)}^{min} \\ < 0 = r_{s,Se(L)}^{imm} \end{cases}$$

$$\lambda_M E\left(1 - \frac{f_e}{B_{C/Se}}\right)\begin{cases} > 0 = r_{s,Se(M)}^{min} \\ < 0 = r_{s,Se(M)}^{imm} \end{cases} \quad (11)$$

$$\lambda_H C_{H_{Se}} E\left(\frac{1}{H_{C/Se}} - \frac{f_e}{B_{C/Se}}\right)\begin{cases} > 0 = r_{s,Se(H)}^{min} \\ < 0 = r_{s,Se(H)}^{imm} \end{cases}$$

Similar equations are included for N (Birkinshaw and Ewen, 2000).

The rate law expressions for heterotrophic reduction of O_2, NO_3, SeO_4, SeO_3, and SeMet using Monod terms are written as:

$$r_{f,O_2}^{het} = \lambda_{O_2}^{het} C_{DO}\left(\frac{C_{O_2}}{K_{O_2} + C_{O_2}}\right)\left(\frac{CO_{2,prod}}{K_{CO_2} + CO_{2,prod}}\right)E \quad (12a)$$

$$r_{f,NO_3}^{het} = \lambda_{NO_3}^{het} C_{NO_3}\left(\frac{C_{NO_3}}{K_{NO_3} + C_{NO_3}}\right)\left(\frac{CO_{2,prod}}{K_{CO_2} + CO_{2,prod}}\right)\left(\frac{I_{O_2}}{I_{O_2} + C_{O_2}}\right)E \quad (12b)$$

$$r_{f,SeO_4}^{het} = \lambda_{SeO_4}^{het} C_{SeO_4}\left(\frac{CO_{2,prod}}{K_{CO_2} + CO_{2,prod}}\right)\left(\frac{I_{O_2}}{I_{O_2} + C_{O_2}}\right)\left(\frac{I_{NO_3}}{I_{NO_3} + C_{NO_3}}\right)E \quad (12c)$$

$$r_{f,SeO_3}^{het(Se_s)} = \lambda_{SeO_3}^{het(Se_s)} C_{SeO_3}\left(\frac{CO_{2,prod}}{K_{CO_2} + CO_{2,prod}}\right)\left(\frac{I_{O_2}}{I_{O_2} + C_{O_2}}\right)\left(\frac{I_{NO_3}}{I_{NO_3} + C_{NO_3}}\right)E \quad (12d)$$

$$r_{f,SeO_3}^{het(SeMet)} = \lambda_{SeO_3}^{het(SeMet)} C_{SeO_3}\left(\frac{CO_{2,prod}}{K_{CO_2} + CO_{2,prod}}\right)\left(\frac{I_{O_2}}{I_{O_2} + C_{O_2}}\right)\left(\frac{I_{NO_3}}{I_{NO_3} + C_{NO_3}}\right)E \quad (12e)$$

$$r_{f,SeMet}^{het} = \lambda_{SeMet}^{het} C_{SeMet}\left(\frac{CO_{2,prod}}{K_{CO_2} + CO_{2,prod}}\right)\left(\frac{I_{O_2}}{I_{O_2} + C_{O_2}}\right)\left(\frac{I_{NO_3}}{I_{NO_3} + C_{NO_3}}\right)E \quad (12f)$$

where K_j is the Monod half-saturation constant for species j [$M_f L_f^{-3}$]; I_{O_2} and I_{NO_3} are the O_2 and NO_3 inhibition constants [$M_f L_f^{-3}$] signifying the species concentration at which lower-redox species can undergo appreciable rates of reduction; and $CO_{2,prod}$ is the total amount of CO_2 produced during decomposition of L_C, H_C, M_C and is used as an indicator of available OC for microbial consumption (Birkinshaw and Ewen, 2000). It is calculated as:

$$CO_{2,prod} = \left[\lambda_L C_{L_C} (1 - f_e) + \lambda_H C_{H_C} (1 - f_e) + \lambda_M C_{M_C} (1 - f_e) \right] E \tag{13}$$

Assuming that FeS_2 is in limitless supply in any adjacent shale material, the rate law expressions for autotrophic reduction of O_2 and NO_3 are:

$$r_{f,O_2}^{auto} = \lambda_{O_2}^{auto} C_{O_2} \left(\frac{C_{O_2}}{K_{O_2} + C_{O_2}} \right) \tag{14a}$$

$$r_{f,NO_3}^{auto} = \lambda_{NO_3}^{auto} C_{NO_3} \left(\frac{C_{NO_3}}{K_{NO_3} + C_{NO_3}} \right) \left(\frac{I_{O_2}}{I_{O_2} + C_{O_2}} \right) \tag{14b}$$

The mass of Se released during these two reactions is dependent on the portion of autotrophically -reduced O_2 or NO_3 that contributes to the production of SeO_4, and is dependent on the stoichiometry of Equation (2) and the ratio of S to Se in the shale material:

$$r_{f,SeO_4}^{auto} = r_{f,O_2}^{auto} \left(\frac{1}{\xi} \right) Y_{Se:O_2} + r_{f,NO_3}^{auto} \left(\frac{1}{\xi} \right) Y_{Se:NO_3} \tag{15}$$

where $Y_{Se:O_2}$ is the mass of Se produced for O_2 consumed in Equation (2a), $Y_{Se:NO_3}$ is the mass of Se produced for NO_3 consumed in Equation (2b), and ξ is the ratio of S to Se in the shale material. This last term is included since autotrophic reduction of O_2 and NO_3 release both S and Se from shale. Referring to Equation (2), $Y_{Se:O_2}$ is equal to 1.41 (315.84 g / 224.0 g) and $Y_{Se:NO_3}$ is equal to 4.03 (789.6 g / 196.0 g).

5.3.4 Parameter Estimation using the Ensemble Kalman Filter

The parameter estimation scheme developed by Bailey and Baù (2011) for chemical reaction parameters is employed in this study to estimate the model parameters within UZF-RT3DAG using observed concentration values. A more in-depth presentation of the EnKF update scheme and parameter estimation framework in a solute reactive transport setting is provided in Bailey and Baù (2011), and only a brief discussion and the main equations are presented here.

In a straightforward application for solute transport systems, i.e., data assimilation methodologies such as the EnKF are used to update the spatial distribution of concentration using values of concentration observed in the field at observation wells. This is done by merging the results of a stochastic set of model simulations with the observed values. The merging is performed according to (i) the level of confidence placed in the observed values as opposed to the variability of values simulated by the stochastic simulation, and (ii) the spatial covariance between model results, with the ability therefore to spread information from the observation points to spatial areas between the observation points. Hence, if the model result is corrected by the observed value at an observation point, and the model result at that point is correlated with model results in the spatial area surrounding the observation point, then the model values within this area will receive a correction similar in magnitude to the correction at the observation point. In a parameter estimation framework, the temporal and spatial correlation between a model parameter (e.g., chemical reaction rate) and the simulated solute concentration will allow observations of solute concentration to also condition the parameter value.

Using a set of Monte Carlo simulations, in which initial conditions, forcing terms, and parameters are stochastically varied, the system state $\mathbf{X}_t^f$ (n x nmc) at a given time t is estimated, where f indicates *forecast*, n is the number of computational points (i.e., grid cells), and nmc is

the number of realizations in the ensemble. In the update step, *m* field-observed values from the true system are assimilated into $\mathbf{X}_t^f$ to obtain the updated, corrected system state $\mathbf{X}_t^u$ via the following update algorithm:

$$\mathbf{X}_t^u = \mathbf{X}_t^f + \frac{\mathbf{C}_t^f \mathbf{H}^T}{\mathbf{H}\mathbf{C}_t^f \mathbf{H}^T + \mathbf{P}_t}\left(\mathbf{D}_t - \mathbf{H}\mathbf{X}_t^f\right) \tag{16}$$

where $\mathbf{D}_t$ (*m* x *nmc*) holds the measurement data, with data being perturbed if incorporation of measurement error is desired; **H** (*m* x *n*) contains binary constants (0 or 1) resulting in the matrix product $\mathbf{H}\mathbf{X}_t^f$ holding model results at measurement locations; and $\mathbf{C}_t^f$ (*n* x *n*) and $\mathbf{P}_t$ (*m* x *m*) are the prediction error covariance and measurement error covariance matrices, respectively. Correction to the predicted values are governed by the residual between the model values and measurement data as well as the relative error associated with each contained in $\mathbf{C}_t^f$ and $\mathbf{P}_t$, respectively.

Any information from the system (e.g., parameters, forcing terms) can be included in $\mathbf{X}_t^f$ and, if significant correlation exists with the measurement data, can be conditioned to reflect a system that produces the measurement data. For a more in-depth presentation of the EnKF and parameter estimation in a solute transport setting, see Bailey and Baù (2011). In this study, observed C_{SeO_4} and C_{NO_3} in soil profiles underlying cultivated field plots are used to condition system parameters and forcing terms. Once updated parameters are obtained, the ensemble is re-run to obtain updated comparisons between model and observed values.

5.4 MODEL APPLICATION

5.4.1 Testing of N module

The processes incorporated in the N module are tested by comparing simulation results with data trends provided by Johnsson et al. (1987), in which dissolved *N* was monitored in a soil profile of irrigated barley plots from 1981 to 1983 at the Kjettslinge test site in central Sweden. The growing season of 1981 was warm and wet, with enhanced irrigation amounts and associated drainage, followed by relatively dry growing seasons during 1982 and 1983. Two fields were monitored: one without fertilizer, and the other on which 120 kg ha^{-1} of NO_3 fertilizer was applied on May 20 of each year. The fertilizer was assumed to dissolve at a rate of 0.15 d^{-1}. For both fields and for all three years, planting, harvest, and plow days were May 6, August 25, and October 16, respectively. All crop parameter values for field conditions and cropping practices, as well as estimated parameter values for chemical reactions, are as provided in Johnsson et al. (1987), and are summarized in Table 5-1. No further calibration was performed. Initial C_{NO_3} for the unfertilized and fertilized fields was approximately 1.0 and 2.0 g m_b^{-3}, respectively.

Table 5- 1. Agricultural management, crop, and chemical reaction parameter symbols, units, and values for the model application to the barley test plots in Sweden (column 3) and the corn test plot soil profiles at the Arkansas Valley Research Center (column 4). For the model application to the AVRC, the parameters that are estimated using the EnKF method as described in Section 5.4.2.3 are highlighted in gray.

Parameter	Units	Barley Test 1	Corn Test 2
Agricultural Management & Parameters			
Planting Day	-	6-May	27-Apr
Harvest Day	-	25-Aug	10-Oct
Plowing Day	-	16-Oct	7-Nov
d_{pw}	m	1.0	1.0
F_{NH_4}	kg ha^{-1}	0	56.2 / 280.8 *
F_{NO_3}	kg ha^{-1}	120	0
P_{Rt}	kg ha^{-1}	750	500
$\alpha_{Rt,Se}$	-	-	2.2 x 10^{-6}
$\alpha_{Rt,N}$	-	0.016	0.016
P_{St}	kg ha^{-1}	500	5616
$\alpha_{St,Se}$	-	-	1.3 x 10^{-6}
$\alpha_{St,N}$	-	0.008	0.008
Crop Parameters			
Se_{up}	g ha^{-1}	-	10.8
N_{up}	kg ha^{-1}	150	225

$\lambda_{up,Se}$	d^{-1}	-	0.01
γ_{up}	-	-	10
$d_{rt,max}$	m	1.0	1.22
Chemical Reaction Parameters			
General			
β_{10}	-	3.0	2.5
T_B	^{0}C	20.0	20.0
K_{d,NH_4}	-	3.5	7.0
Organic Matter Decomposition			
λ_H	d^{-1}	0.00007	0.003
λ_L	d^{-1}	0.035	0.25
f_e	-	0.5	0.5
f_h	-	0.2	0.2
$H_{C/Se}$	-	-	1.23×10^5
$B_{C/Se}$	-	-	1.75×10^5
$H_{C/N}$	-	12	12
$B_{C/N}$	-	8	8
Oxidation-Reduction			
$\lambda_{SeO_4}^{het}$	d^{-1}	-	0.04
$\lambda_{SeO_3}^{het(Se_s)}$	d^{-1}	-	0.08
$\lambda_{SeO_3}^{het(SeMet)}$	d^{-1}	-	0.08
λ_{SeMet}^{het}	d^{-1}	-	0.02
ξ	-	-	3000
λ_{nit}	d^{-1}	0.2	0.2
λ_{vol}	d^{-1}	-	0.1
$\lambda_{NO_3}^{het}$	d^{-1}	0.1	0.3
K_{NO_3}	g m_f^{-3}	10	10
I_{NO_3}	g m_f^{-3}	-	0.5
$\lambda_{O_2}^{het}$	d^{-1}	-	5.0
I_{O_2}	g m_f^{-3}	-	1.0
K_{O_2}	g m_f^{-3}	-	1.0
K_{CO_2}	g m_f^{-3}	-	0.75

* Treatment N1 = 56.2, Treatment N2 = 280.8

denotes conditioned parameter in EnKF scheme

Using the provided monthly infiltrated and drainage depths, soil water content and soil temperature, observed initial C_{NO_3} (g m_b^{-3}), and the indicated crop and reaction parameters, the fluctuation of C_{NO_3} during the three years was simulated using UZF-RT3DAG. Due to the lack of precise data regarding the transport of heat and water flux between the textural layers, a single 1.0 m grid cell was used for the model domain, with the infiltration and drainage rates applied to

the top and bottom of the cell. Furthermore, soil water content and soil temperature were tabulated on a monthly rather than a daily basis. Daily time steps were used.

Results from the simulation were compared to observed C_{NO_3} of the top soil layer for the unfertilized and fertilized plots, and are shown in Figure 5-2. Despite the simplifications of the implemented data in the simulation, the overall magnitude and trend of the observed C_{NO_3} are achieved. For the fertilized plot, simulated C_{NO_3} (i) increases accurately upon addition of fertilizer on May 20 of each year, (ii) decreases during the fall of 1981, when wet climatic conditions allowed for high rates of infiltration and subsequent high rates of drainage, allowing NO_3 to be drained from the soil layer, and (iii) increases during the fall of 1982 and 1983, when dry conditions prevented substantial drainage from occurring, thus allowing C_{NO_3} to increase due to continuing nitrification of NH_4.

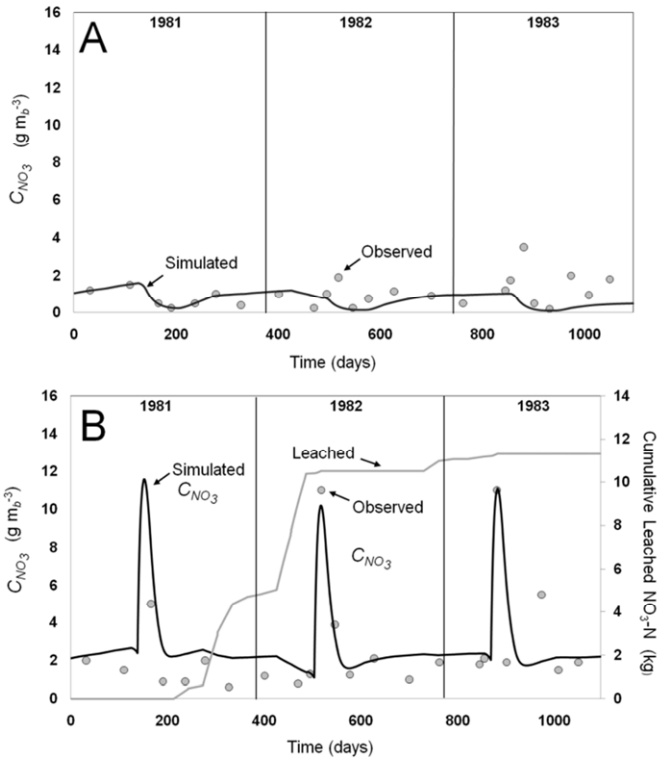

Figure 5- 2. Comparison between observed and predicted (using UZF-RT3DAG) concentrations of NO_3 during 1981-1983 for the (A) unfertilized and (B) fertilized barley plots at the Kjettslinge test site in central Sweden.

Observed and predicted concentrations are shown in gray circles and solid black lines, respectively. The cumulative leached mass of NO_3 is shown in (B) with a gray solid line.

Sources of error include the coarse approximation of the system by using a single layer, an underestimation of water flow from the surface layer to lower layers, and an underestimation of water movement in the lower profile as reported by Johnsson et al. (1987). Items (ii) and (iii) also are reflected in the plot of cumulative leaching, shown in Figure 5-2B, in which the majority of the leaching occurs before the 1982 growing season. Figure 5-3 shows the NO_3 mass-balance term values for each daily time step of the simulation, with fertilizer application and crop uptake in kg, and nitrification, denitrification, and leaching in g. Totals for the 3-year period for each of the terms are 197.1 kg, 204.2 kg, 31.6 kg, 9.3 kg, and 11.3 kg, respectively. During the winter months, when soil temperature approaches 0.0 ^{o}C, mass transferred due to nitrification and denitrification approaches zero.

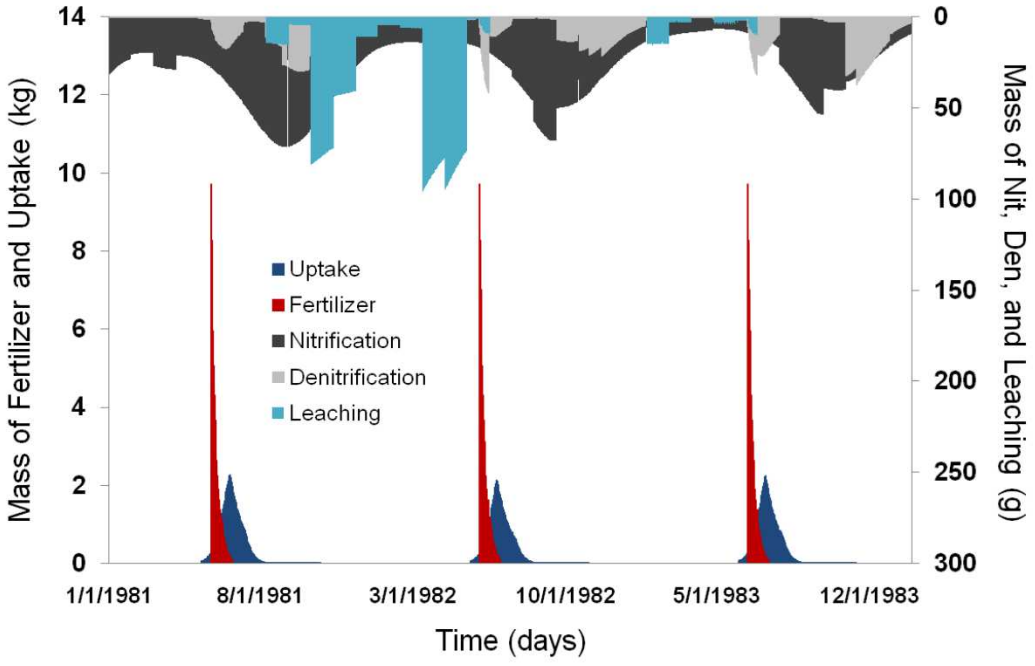

Figure 5- 3. Mass associated with each NO_3 mass-balance term for each day of the 1981-1983 simulation for the fertilized barley plot.

5.4.2 Joint Testing of Selenium and Nitrogen modules

5.4.2.1 Site Description and Data Collection

Soil samples were collected from recently-harvested corn test plots at the Colorado State University Arkansas Valley Research Center (AVRC) in Rocky Ford, CO in October 2009. The test plots had received varying rates of NH_4 fertilizer loading, with fertilizer applied seven days before planting (April 27 2009). Irrigation from a nearby canal was applied 9 times from June 17 to August 10, with an approximate applied depth of 9.5 cm. Tail water fraction was approximately 0.05, representative of the regional trend (Gates et al., 2012) and the typically higher efficiencies of irrigation application at the AVRC. The measured water table depth at the AVRC typically exceeds 5 m, resulting in negligible upflux to the soil root zone. Timing of irrigation events and values of C_{SeO_4}, C_{NH_4}, C_{NO_3}, and C_{O_2} in the irrigation water for each event are shown in Table 5-2. C_{NH_4} and C_{NO_3} were measured directly from the applied irrigation water, whereas C_{SeO_4} and C_{O_2} were not measured directly and hence are estimated from samples taken from the nearby Rocky Ford Canal.

Table 5- 2. Summary of 9 irrigation events during the 2009 growing season for the corn test plots, showing the infiltrated depths (0.0895 m for all events), and concentration of *SeO_4-Se*, *NH_4-N*, *NO_3-N*, and *O_2* in the irrigation water.

Irrigation Event	Date	*SeO_4-Se* * µg m_f^{-3}	*NH_4-N* g m_f^{-3}	*NO_3-N* g m_f^{-3}	*O_2* g m_f^{-3}
1	6/17/2009	8.100	0.098	1.310	8.740
2	6/23/2009	8.100	0.065	0.937	8.740
3	6/29/2009	8.100	0.052	1.000	8.740
4	7/04/2009	8.100	0.063	1.140	8.740
5	7/10/2009	7.310	0.072	1.180	7.560
6	7/17/2009	7.310	0.060	1.500	7.560
7	7/20/2009	7.310	0.039	1.340	7.560
8	7/31/2009	7.310	0.075	1.610	7.560
9	8/10/2009	7.310	0.065	1.610	7.560
Applied (m)	0.0942				
TW Fraction	0.05				
Infiltrated (m)	0.0895				

* Sampled from nearby Rocky Ford Canal

Soil was sampled at depths of 0.15 m, 0.30 m, 0.61 m, 0.91 m, 1.22 m, 1.52 m, and 1.83 m from four plots, two receiving a fertilizer loading of 56.2 kg ha^{-1} (Treatment N1) and the other two a loading of 280.8 kg ha^{-1} (Treatment N2). Soil was sampled using a hand auger, placed on ice, and transported to the Agricultural Research Service (ARS) laboratories at the USDA Natural Resources Research Center in Fort Collins, CO. C_{SeO_4} and C_{NO_3} in the soil water were analyzed using saturated paste extracts. Soil samples were air-dried, ground to pass through a 2-mm sieve, and brought to saturation to create a saturated paste, upon which a 80 kPa vacuum was applied to extract the soil water.

One subsample was sent to the Olson Biochemistry Laboratories at South Dakota State University in Brookings, SD (USEPA certified) for analysis of C_{SeO_4} using Official Methods of Analysis of AOAC International, 17th Edition, test number 996.16 Selenium in Feeds and Premixes, Fluorometric Method. A separate subsample was analyzed for C_{NO_3} using suppressed ion chromatography, consisting of a Shimadzu (Kyoto, Japan) LC-10 high-pressure liquid chromatograph, an Alltech (Deerfield, IL, USA) DS-Plus auto-suppressor and a Shimadzu CDD-6 conductivity detector. The elution buffer, pumped at a flow rate of 1 mL min^{-1}, was 0.19 mM sodium bicarbonate and 0.55 mM sodium carbonate. The analytical column was a 250 by 2.6 mm Serasep AN-1 obtained from Alltech. Results are shown in Table 5-3. Notice that the values of C_{SeO_4} vary significantly between the two test plots for each fertilizer treatment level, whereas the values of C_{NO_3} are more comparable.

It should be noted that air-drying and sieving may alter the speciation of Se in the soil through redox reactions and volatization (Fio et al., 1991), although soil samples were unsaturated and hence the changes in Se speciation probably are negligible (Fio et al., 1991). In general, however, measurements of solute concentration using saturated paste extracts should be

treated cautiously, with moderate values of coefficient of variation reported for solution extract methodologies (Kleinman et al., 2001).

Table 5- 3. Observed concentrations of *SeO_4-Se* and *NO_3-N* at the seven depths in the soil profile for the two test plots receiving the N1 fertilizer treatment level (56.2 kg h^{-1}) and the two test plots receiving the N2 fertilizer treatment level (280.8 kg ha^{-1}).

NH_4 Applied kg ha^{-1}	**Plot ID**	**Depth** m	**SeO_4-Se µg m_f^{-3}**	**NO_3-N g m_f^{-3}**
56.2	N1 Plot 1	0.15	39.11	20.12
		0.30	26.62	13.41
		0.61	21.17	5.24
		0.91	22.38	6.91
		1.22	25.26	5.29
		1.52	22.95	4.15
		1.83	39.60	3.65
56.2	N1 Plot 2	0.15	42.53	28.81
		0.30	30.53	14.82
		0.61	24.39	10.61
		0.91	16.63	11.51
		1.22	13.51	11.71
		1.52	12.70	8.43
		1.83	7.95	11.26
280.8	N2 Plot 1	0.15	22.61	22.05
		0.30	24.05	13.92
		0.61	28.24	11.98
		0.91	16.10	10.63
		1.22	21.03	5.14
		1.52	16.03	5.82
		1.83	14.44	5.38
280.8	N2 Plot 2	0.15	11.42	18.37
		0.30	31.89	19.97
		0.61	27.51	11.58
		0.91	15.71	18.24
		1.22	16.43	13.07
		1.52	1.77	7.54
		1.83	11.48	8.78

5.4.2.2 System Forecast

The system forecast consists of simulating the Se-N system for the four test plots described in Section 4.2.1 using a Monte Carlo approach, with initial conditions, forcing terms, and system

parameters varied over prescribed ranges. Ranges were either determined from the literature or provided by Michael Bartolo at the AVRC (personal communication, June 2010).

Forcing terms and parameters for the flow regime consist of daily precipitation, infiltrated irrigation water from the 9 irrigation events, daily ET, soil porosity ϕ (0.45), hydraulic conductivity (0.15 m d^{-1}), residual water content θ_r (0.20), Brooks-Corey exponent ε (-) (5.0), and the ET extinction depth (1.22 m). ET was calculated using the ASCE standardized reference ET equation (Allen et al., 2005) with climatic data measured at the AVRC weather station. Alfalfa was used as the reference crop, with corn crop coefficients supplied by Allen and Wright (2002). Daily precipitation, daily ET, and daily values for the corn crop coefficient are shown in Figure 5-4. The depth of infiltrated water, the daily reference ET rates, and the crop coefficient all were perturbed with a CV of 0.20 in the forecast Monte Carlo simulation.

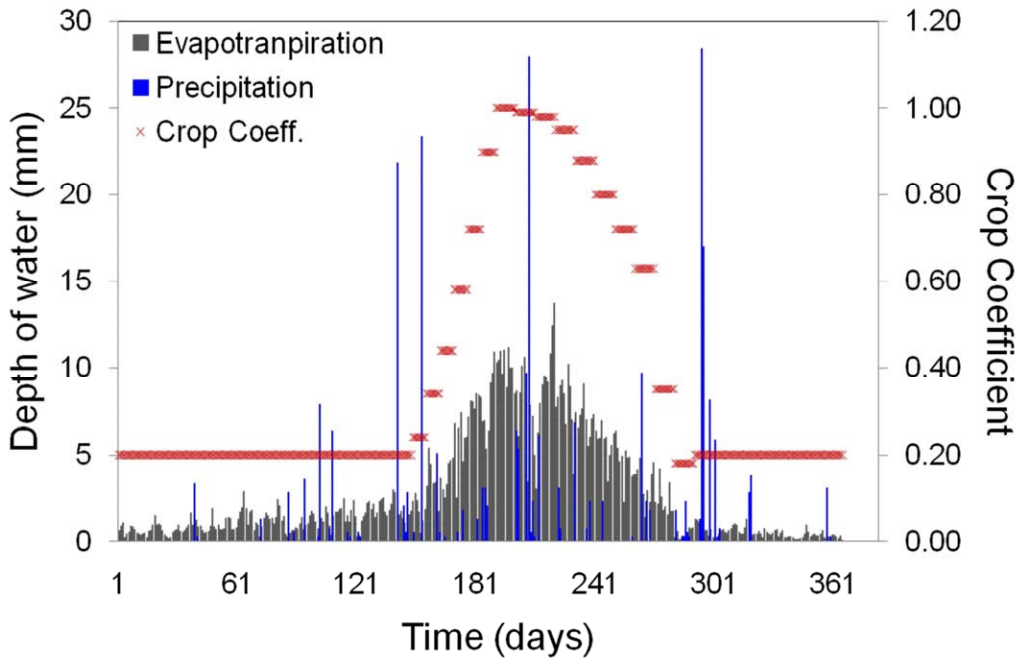

Figure 5- 4. Measured daily precipitation, daily corn crop coefficients, and calculated daily evapotranspiration (using the ASCE standardized reference ET equation) using alfalfa as a reference crop and the corn crop coefficients.

Values for C_{SeO_4} and C_{O_2} in the irrigation water ($C_{SeO_4,irrig}$ and $C_{O_2,irrig}$) are perturbed (CV = 0.20) since they are taken from a nearby canal and hence not known with certainty for the irrigation water supplied on the test plots, whereas C_{NH_4} and C_{NO_3} were measured in the applied irrigation water and hence are treated deterministically. A value of 0.20 for the CV was deemed adequate to provide a reasonable distribution of concentration values as compared to other data sampled during field work in the LARV.

The 1D profile finite-difference grid was constructed to include one cell for each depth of sampling in order to easily compare model results with observed data. The ensemble included 300 realizations, with each realization run for 9 years (using the 2009 data) to establish steady seasonal variation in species concentration and unbiased initial conditions, whereupon the final year was run to establish the fluctuation of species concentration during 2009. Daily time steps were used. Since no apparent differences exist between the forcing terms and parameters between the plots receiving the same fertilizer loading, only one ensemble was run for each of the two fertilizer treatment levels.

Results from a representative realization are shown in Figure 5-5, 5-6, and 5-7. Figure 5-5 shows the achieved steady seasonal variation during the combined 10-year period for L_C, L_N, and L_{Se}. Figure 5-6 shows simulated daily mass-balance term values, in µg and g, for Se and N, respectively. Figure 5-7 presents scatter-plots of the C_{NO_3} - C_{SeO_4} relationship at layers 4 and 7 in the soil profile (depths of 0.91 m and 1.83 m, respectively). Relationships (R^2 values of 0.65 and 0.39, respectively) are similar to relationships found by Gates et al. (2009) for groundwater samples in the region surrounding the AVRC, indicating the model is correctly capturing the dependence of C_{SeO_4} on C_{NO_3} and the associated correlation. Generally, however, relationships in Gates et al. (2009) are non-linear.

Figures 5-8A and 5-8C show the forecast ensemble and ensemble mean for C_{NO_3} and C_{SeO_4} for the entire 365-day period of 2009 for layer 1, respectively for Treatment N2. For C_{NO_3}, replenishment of N mass occurs at the beginning of the growing season due to nitrification of the applied NH_4 fertilizer. For C_{SeO_4}, on the other hand, Se mass does not enter the system via fertilizer application, and replenishment of Se mass occurs at a later period due to Se mass supplied in the irrigation water.

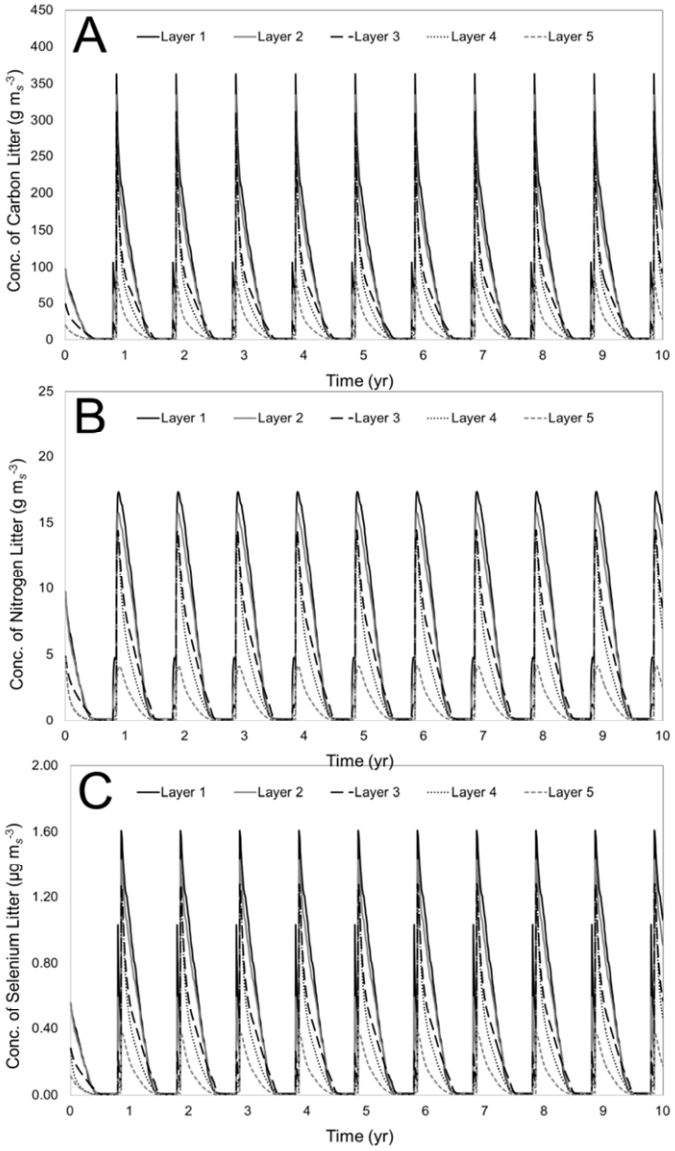

Figure 5- 5. Seasonal variation of (A) Carbon litter L_C concentration, (B) Nitrogen litter L_N concentration, and (C) Selenium litter L_{Se} concentration during 10-year spin-up period for the top five layers in the model grid, demonstrating the achievement of steady seasonal variations.

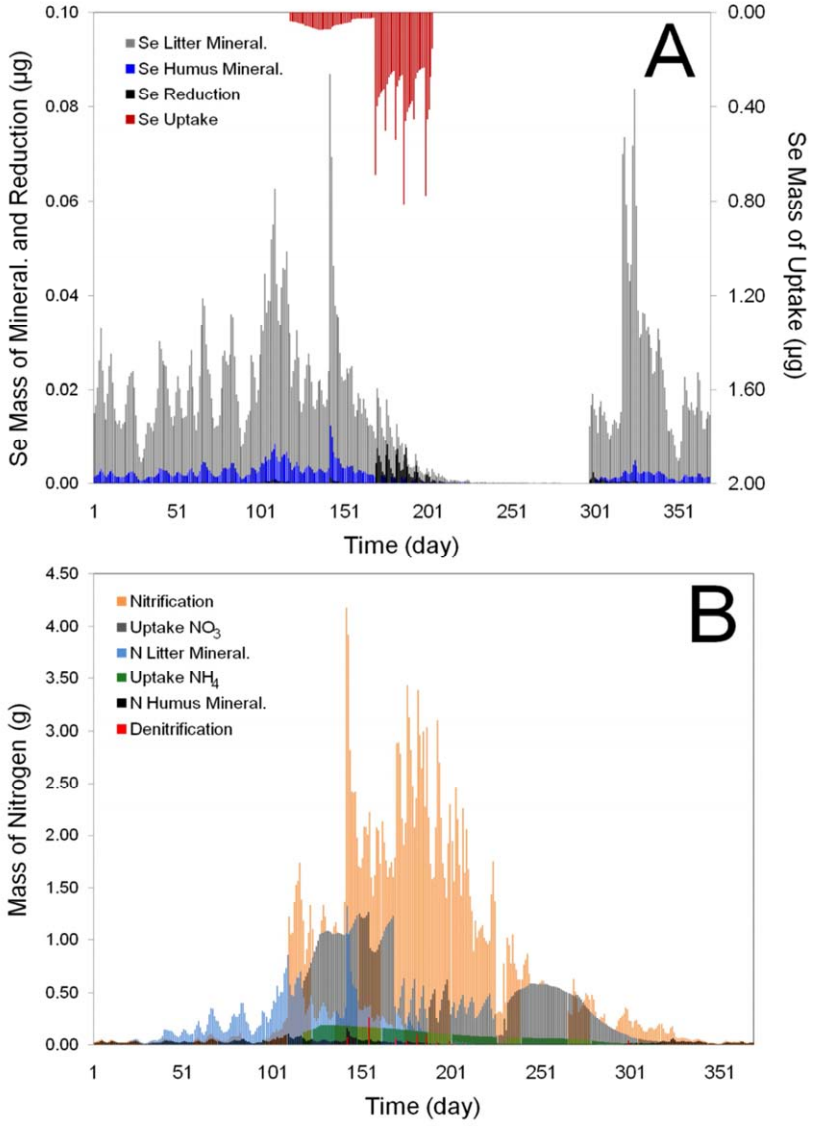

Figure 5- 6. Daily mass transfer of selected mass-balance terms for (A) Se and (B) N. Mass balance terms for Se are shown in µg, whereas those for N are shown in g. For Se, the process of root uptake is the dominant process of mass transfer, where nitrification is the dominant process for N.

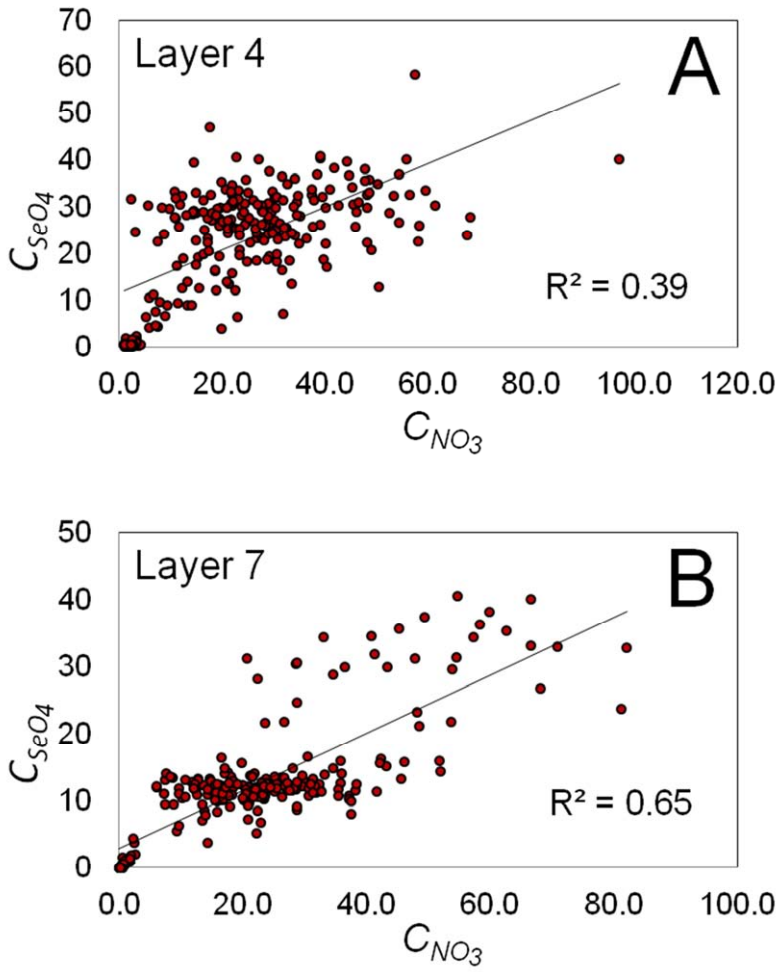

Figure 5- 7. Plot of the C_{NO_3} vs. C_{SeO_4} relationship for (A) Layer 4 and (B) Layer 7 in the model grid.

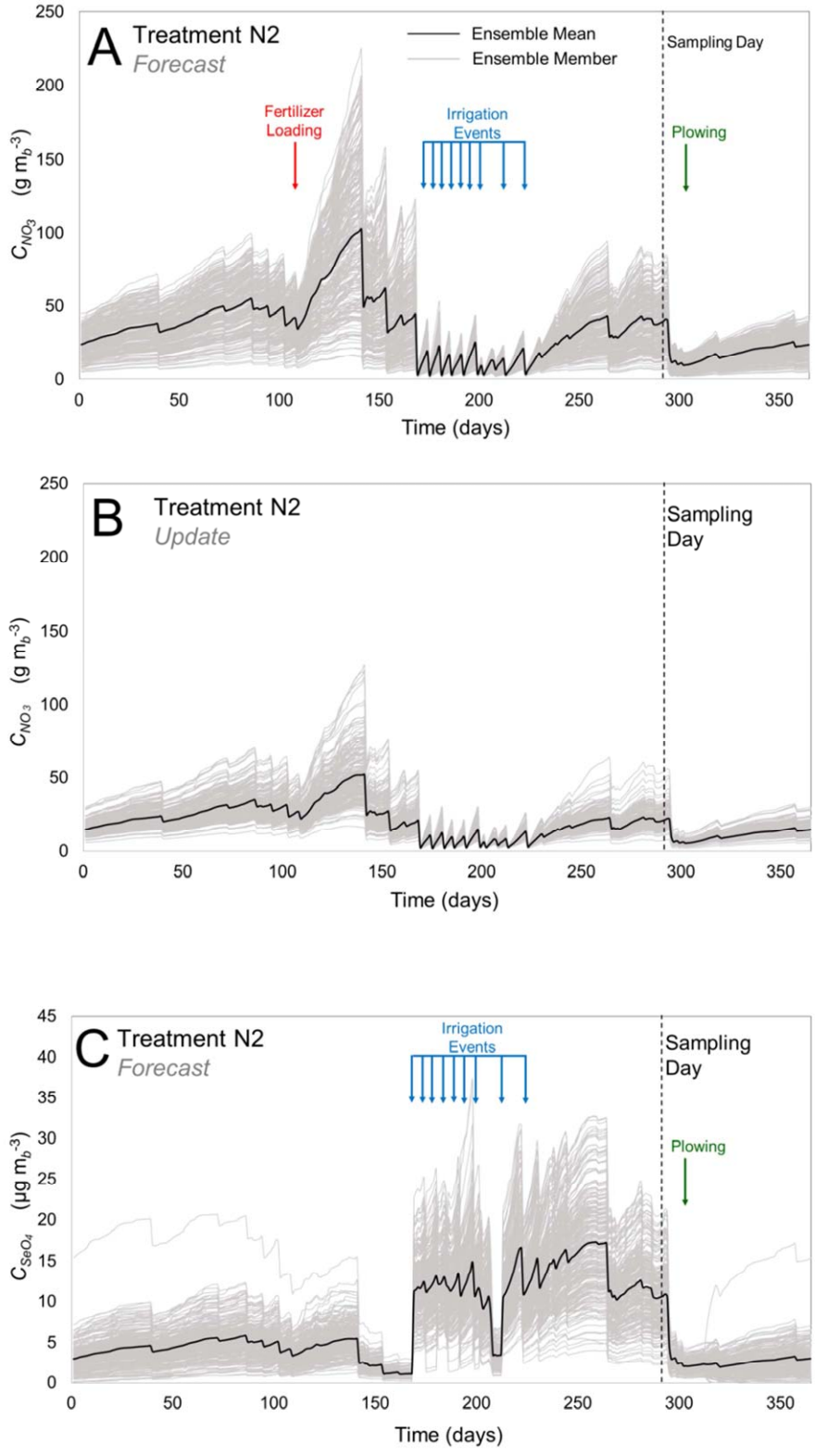
A
Treatment N2
Forecast
Ensemble Mean
Ensemble Member
Sampling Day
Fertilizer Loading
Irrigation Events
Plowing
C_{NO_3} (g m_b^{-3})
Time (days)
B
Treatment N2
Update
Sampling Day
C_{NO_3} (g m_b^{-3})
Time (days)
C
Treatment N2
Forecast
Irrigation Events
Sampling Day
Plowing
C_{SeO_4} (µg m_b^{-3})
Time (days)

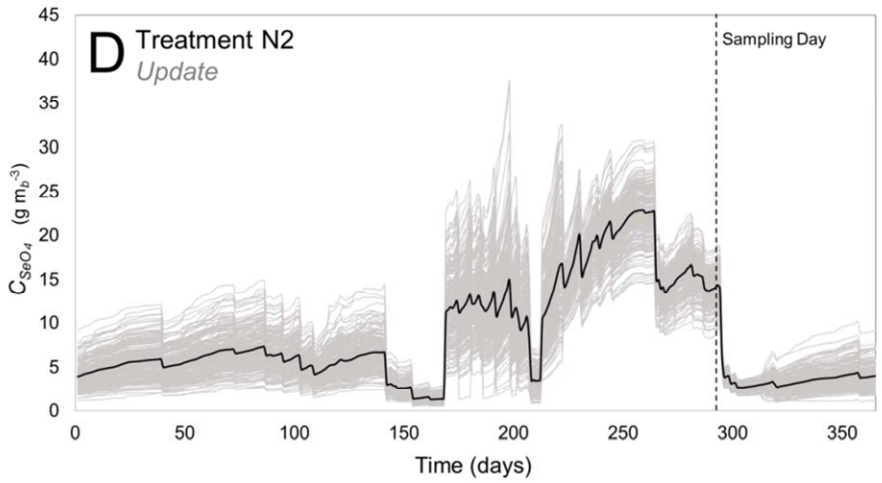

Figure 5- 8. Simulated fluctuation of species concentration in the top layer of the soil profile for (A) the forecast ensemble of C_{SeO_4}, (B) the updated ensemble of C_{SeO_4}, (C) the forecast ensemble of C_{NO_3}, and (D) the updated ensemble of C_{NO_3}. The updated ensembles use parameters estimated from observation data and the EnKF update scheme. For each plot the member simulations of the ensemble are depicted by light gray lines and the ensemble mean is depicted by a solid black line.

Figures 5-9A and 5-9C show the forecast ensemble and ensemble mean for each grid layer on the sampling day (day 292) as compared to the observed values for the two plots receiving Treatment N1, for C_{SeO_4} and C_{NO_3}, respectively. Figures 5-10A and 5-10C show similar results for Treatment N2. For Treatment N1, the ensemble realizations consistently under-predict C_{NO_3}, with the observed C_{NO_3} values relatively consistent between the two test plots. For C_{SeO_4} the model realizations under-predict the observed C_{SeO_4} values in the upper layers but approach the observed values in the lower layers, although the observed values for the two test plots vary drastically in the lower layers. For Treatment N2, realizations consistently over-predict C_{NO_3}, whereas the realizations under-predict C_{SeO_4} in the upper layers and are relatively consistent with C_{SeO_4} in the lower layers. Once again, however, the observed values of C_{SeO_4} for the two test plots are significantly different.

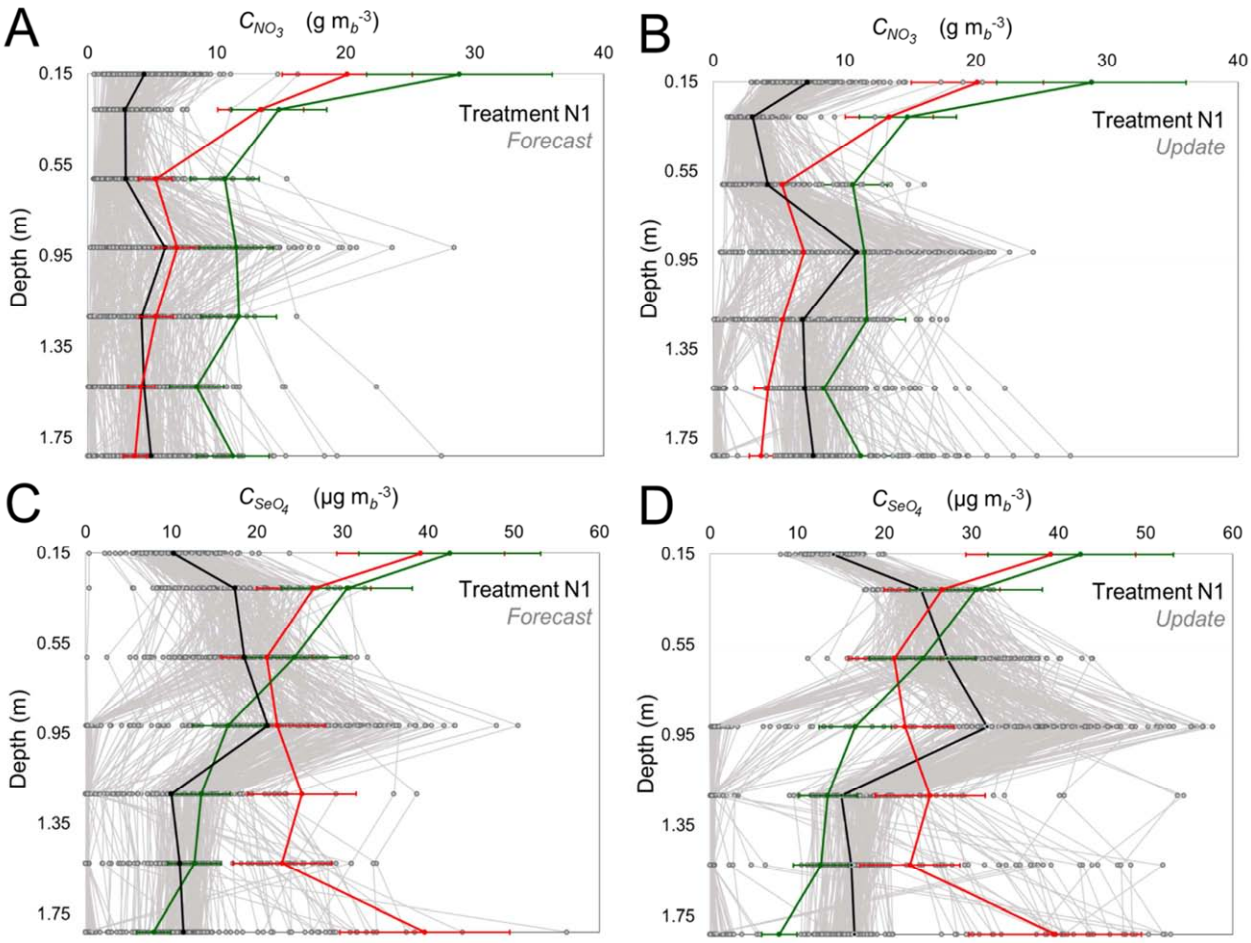

Figure 5- 9. Simulated concentration in the soil profile after 292 days with accompanying observation data for the fields receiving the N1 fertilizer treatment level (56.2 kg ha^{-1}) for (A) the forecast ensemble of C_{NO_3} (B) the updated ensemble of C_{NO_3} (C) the forecast ensemble of C_{SeO_4}, and (D) the updated ensemble of C_{SeO_4}. The observation data from the first and second test plots are shown in green and red, respectively, with 1-σ error bars, and the ensemble mean of each simulated ensemble is shown in black.

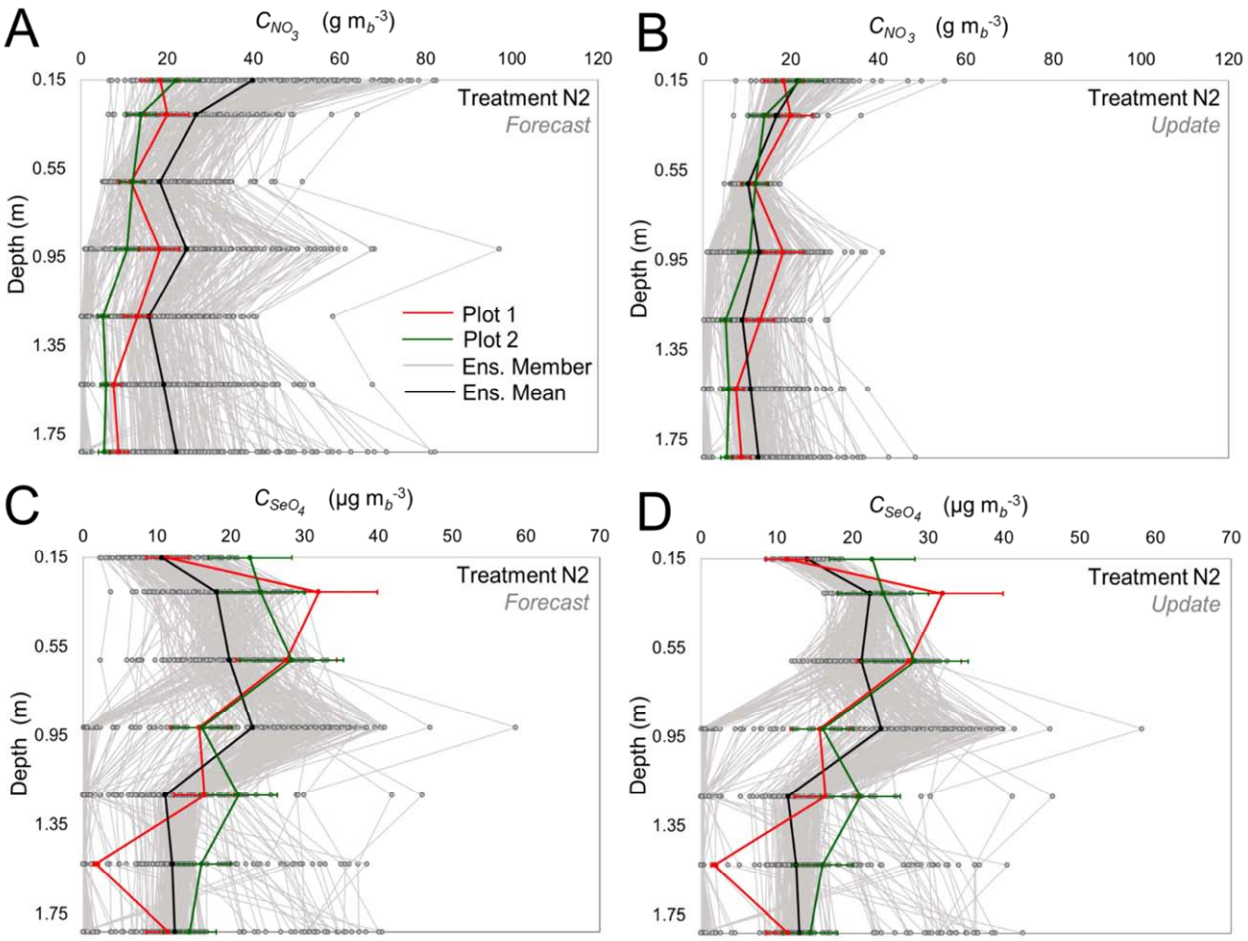

Figure 5- 10. Simulated concentration in the soil profile after 292 days with accompanying observation data for the fields receiving the N2 fertilizer treatment level (280.8 kg ha^{-1}) for (A) the forecast ensemble of C_{NO_3} (B) the updated ensemble of C_{NO_3} (C) the forecast ensemble of C_{SeO_4}, and (D) the updated ensemble of C_{SeO_4}. The observation data from the first and second test plots are shown in green and red, respectively, with 1-σ error bars, and the ensemble mean of each simulated ensemble is shown in black.

For the observed values of C_{SeO_4} and C_{NO_3} shown in Figures 5-9 and 5-10, 1-σ error bars are included to exhibit errors associated with obtaining the observed concentration values via laboratory analysis. For example, Kleinman et al. (2001) reported CV values for saturated paste extracts to range between 0.11 and 0.70, and the CV associated with the fluorometric technique for C_{SeO_4} determination has been reported to be 0.05 (Mueller Price and Gates, 2008). Using a lower value (0.20) from the range reported by Kleinman et al. (2001) and adding it to 0.05 for water sample analysis, a CV value of 0.25 was assigned to each observed value.

5.4.2.3 System Update

Model results for the ensemble were compared with C_{SeO_4} and C_{NO_3} at the sampling day for each test plot and each sampling depth. A scatter-plot analysis was used to identify influential parameters and forcing terms that could be conditioned using the observed values of C_{SeO_4} and C_{NO_3} shown in Table 5-3. Figure 5-11 shows scatter-plots of relationships between C_{SeO_4}, C_{NO_3}, and selected parameters for the Treatment N2 ensemble. For C_{NO_3}, the principal governing parameters are λ_{nit} for layer 1 (R^2 = 0.77, positive correlation), and N_{up} for layer 3 (R^2 = 0.46, negative correlation), with slight influence from $d_{rt,max}$ for layer 3 (R^2 = 0.05, negative correlation) and P_{St} for layer 4 (R^2 = 0.03, positive correlation). For C_{SeO_4}, $C_{SeO_4,irrig}$ has the strongest influence (R^2 = 0.71, positive correlation), with influences also $\lambda_{SeO_4}^{het}$ from in layer 3 (R^2 = 0.19, negative correlation), and Se_{up} in layer 4 (R^2 = 0.19, negative correlation). A similar procedure was used to identify sensitive parameters for the Treatment N1 ensemble.

Using these results, observed values of C_{SeO_4} and C_{NO_3} were used to condition λ_{nit}, N_{up}, $d_{rt,max}$, P_{St}, $C_{SeO_4,irrig}$, $\lambda_{SeO_4}^{het}$, and Se_{up} using the EnKF update algorithm in Equation (16). The ensemble mean of the updated parameter values are shown in Table 5-4. It should be noted that the observed values assimilated in the EnKF scheme were the average of the two test plots receiving the same fertilizer treatment. Figure 5-12 shows the frequency distribution for the ensemble of forecasted and updated values for λ_{nit}, N_{up}, $\lambda_{SeO_4}^{het}$, and $C_{SeO_4,irrig}$. Notice that only slight change occurs for N_{up} and $\lambda_{SeO_4}^{het}$, with large change occurring for λ_{nit} and $C_{SeO_4,irrig}$.

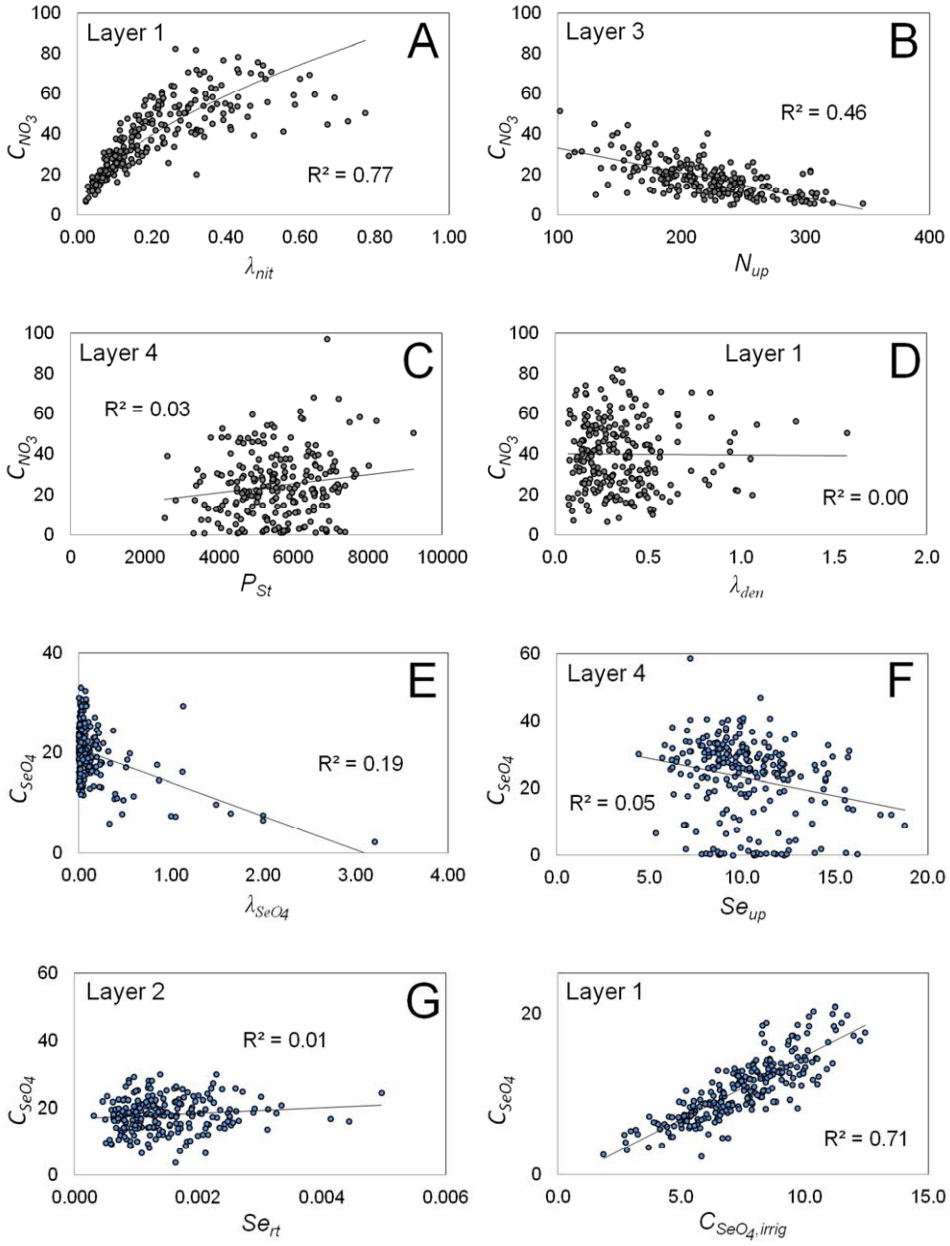

Figure 5- 11. Selected scatter-plot relationships between C_{NO_3} and (A) λ_{nit}, (B) N_{up}, (C) P_{St}, (D) λ_{den} and between C_{SeO_4} and (E) λ_{SeO_4}, (F) Se_{up}, (G), Se_{rt}, and (H) $C_{SeO_4,irrig}$ using the ensemble of model forecast simulations. Such plots are used to determine which parameters are most influential on simulated C_{SeO_4} and C_{NO_3}, and hence which parameters are conditioned in the EnKF update scheme using the observation data.

Table 5- 4. The parameter value used in the forecast ensemble and the resulting updated parameter value using the observed data and the EnKF update scheme. If the parameter is assumed to be the same for the fields of both treatment N1 and N2, then only one updated value is obtained. If, on the other hand, the parameter value is assumed to vary between the fields, then an updated value is obtained for both treatment levels (N1 and N2).

	Forecast		*Update Ensemble Mean*	
Parameter	**Value**	**CV**	**Treatment N1**	**Treatment N2**
$C_{SeO_4,irrig}$	See Table 5-2	2.0	-	9.77
$\alpha_{Rt,Se}$	2.2×10^{-6}	0.2	-	1.5×10^{-6}
P_{St}	5616	0.2	5855	5478
Se_{up}	10.8	0.1	10.47	10.5
N_{up}	225	0.2	-	245
$d_{rt,max}$	1.22	0.2	1.17	1.28
K_{d,NH_4}	7.0	0.2	10.9	-
λ_{SeO_4}	0.04	0.5	0.023	0.023
λ_{nit}	0.2	0.2	1.04	0.08

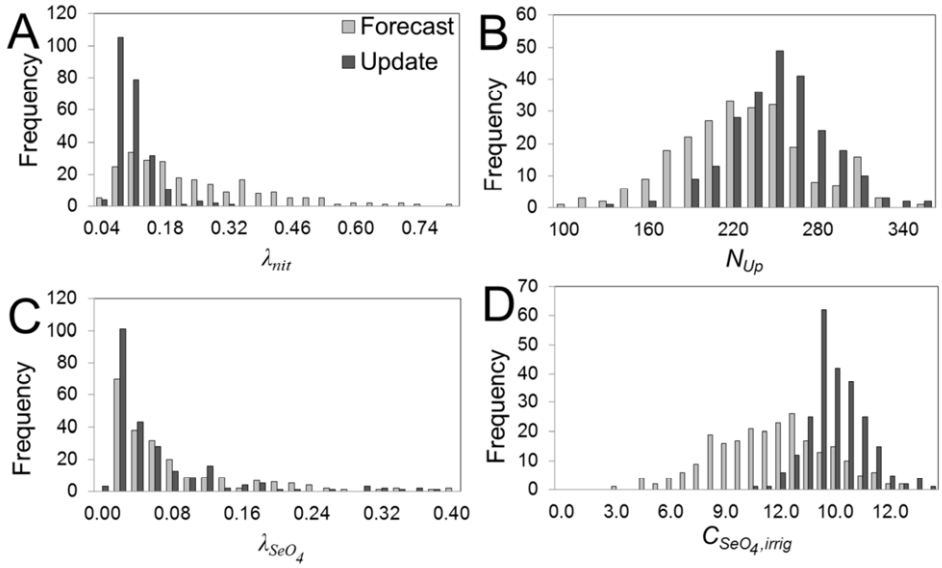

Figure 5- 12. Forecasted and updated frequency distribution for the ensemble of parameter values for (A) λ_{nit}, (B) N_{up}, (C) λ_{SeO_4}, and (D) $C_{SeO_4,irrig}$, demonstrating the influence of conditioning the parameters using the observed values of C_{SeO_4} and C_{NO_3}.

Using the update ensemble of parameter values and forcing term values, the 300-simulation Treatment N1 and Treatment N2 ensembles were re-run. It should be noted that the same updated ensemble of $C_{SeO_4,irrig}$ achieved using the Treatment N2 data was used in the re-run of the Treatment N1 ensemble as well, since it is assumed that the irrigation water used on the four test plots has the same $C_{SeO_4,irrig}$.

An example of the comparison between the forecast and update ensemble, and as they compare to the observed values, is shown in Figure 5-13 for layer 1 of the model for Treatment N2. In Figure 5-13A, the updated ensemble of C_{NO_3} is much closer in value to the observed values of C_{NO_3} for the two test plots. This is reflected in Figure 5-10B, which shows the updated ensemble along the soil profile. The ensemble spread is much less as compared to the forecasted ensemble in Figure 5-10A, and the ensemble mean is very close to the two observed C_{NO_3} profiles. The decrease in ensemble spread is also seen in Figure 5-8B. In quantitative terms, the sum of the squared errors between the ensemble mean and the observed C_{NO_3} values improved from 2118.3 to 196.8 from the forecast to the updated ensembles, a decrease of 90.7%. Less success was achieved with the Treatment N1 plots, as the update ensemble is not able to capture the high C_{NO_3} in the upper layers (Figure 5-9B). However, the ensemble values were increased in the lower layers to capture the average of the observed C_{NO_3} values. For Treatment N1, the sum of the squared errors between the ensemble mean and the observed C_{NO_3} values improved from 1319.3 to 1014.0 from the forecast to the updated ensemble, a decrease of 23.1%.

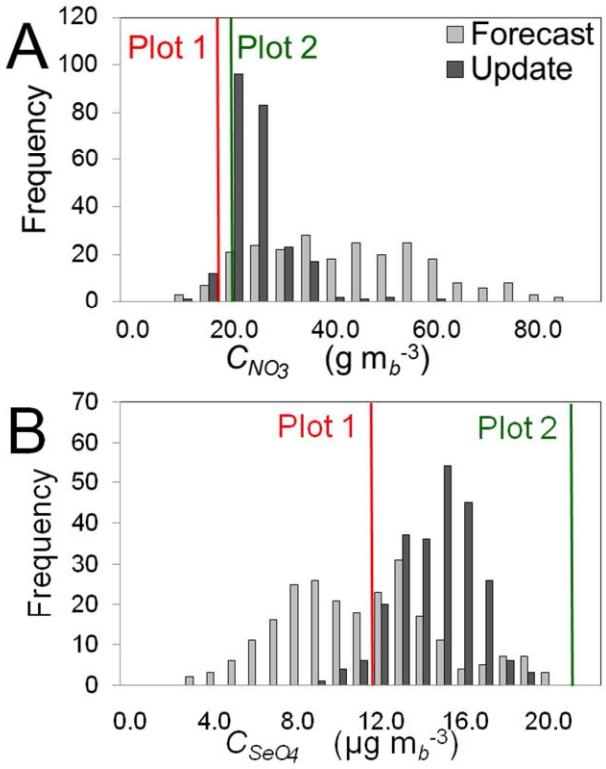

Figure 5- 13. Frequency distribution of the forecasted and updated ensemble of simulation results in the top layer of the soil profile for (A) C_{NO_3} and (B) C_{SeO_4}. The observed values of C_{NO_3} and C_{SeO_4} in the top layer are shown in red and green for the first and second test plots. Results are shown for the two plots receiving the N2 fertilizer treatment level.

In Figure 5-13B, the updated ensemble of C_{SeO_4} is much closer in value to the average of the observed values of C_{SeO_4} for the two test plots. However, as seen in Figure 5-10D, improvement in the ensemble along the soil profile only occurs in the upper layers where $C_{SeO_4,irrig}$ has a strong influence, with an accompanied decrease in the ensemble spread. The decrease in ensemble spread is also seen in Figure 5-8D. However, improvement in the lower layers could not be expected since the forecast ensemble already captures the approximate pattern of the two test plots (Figure 5-10C). In quantitative terms, the sum of the squared errors between the ensemble mean and the observed C_{SeO_4} values improved from 854.6 to 635.6 from the forecast to the

updated ensembles, a decrease of 25.6%. Similar to the case for C_{NO_3}, the high observed values of C_{SeO_4} in the upper layers in the Treatment N1 plots could not be achieved by the updated ensemble, particularly since $C_{SeO_4,irrig}$ was not conditioned using Treatment N1 C_{SeO_4} values. However, the ensemble values in the second and third layers show an improved match with the observed values compared to the forecast ensemble, and the ensemble values in the lower layers have been increased to capture the approximate average of the observed values. For Treatment N1, the sum of the squared errors between the ensemble mean and the observed C_{SeO_4} values improved from 3387.8 to 2602.3 from the forecast to the updated ensemble, a decrease of 23.2%.

In general, the results are encouraging in regards to the improved match between model-calculated and observed values of C_{SeO_4} and C_{NO_3} for the four test plots using the updated ensembles, especially when considering (i) the error associated with establishing the observed data through field sampling and laboratory analysis and (ii) the lack of agreement between observed C_{SeO_4} for plots receiving the same fertilizer treatment. In regards to (ii), conditioning parameters and forcing terms to match two disparate observed concentration profiles is not possible given the lack of information regarding other environmental and cultivation factors that vary on a small spatial scale. For the C_{NO_3} comparison for the Treatment N1 plots, the model underestimates by a large degree the observed C_{NO_3} values in both test plots. This is expected, since a lower fertilizer loading (56.2 kg ha^{-1}) provided to the model produces much lower values of C_{NO_3} in the upper layers (Figure 5-9A) than for Treatment N2 (Figure 5-10A). However, the observed C_{NO_3} values are opposite of what is expected in the field, with higher values of C_{NO_3} in the Treatment N1 plots, and hence likely were affected by factors not included in the model.

In regards to a fundamental objective of this study, i.e. to determine if the Se and N module for UZF-RT3DAG is able to provide accurate estimates of species leaching to the saturated zone for a regional-scale reactive transport simulations, of utmost importance is the concentration values at the base of the soil profiles. As can be seen in Figures 5-9 and 5-10, the matches between the ensemble mean of the updated ensemble and the observed concentrations are reasonable, with the ensemble mean approximately equal to the average of the observed values from the two test plots.

For the Treatment N1 plots, the squared error for the C_{SeO_4} and C_{NO_3} values improved from 158.0 to 55.0 and 6.89 to 0.01 from the forecast to the updated ensembles, a decrease of 65.2% and 99.9%, respectively. For the Treatment N2 plots, the squared error for the C_{SeO_4} and C_{NO_3} values improved from 0.56 to 0.03 and 216.6 to 28.4, a decrease of 95.3% and 86.9%, respectively. This agreement occurs even for soil profiles where matches between model-calculated values and observed values are somewhat poor in the upper soil layers (see Figures 5-9B, 5-9D, and 5-10D).

5.5 CONCLUSION

A numerical reactive transport model capable of simulating the fate and transport of Se in multi-dimensional variably-saturated groundwater systems was presented and applied to 1D soil profile systems to corroborate the accuracy of the incorporated processes. The model, referred to as UZF-RT3DAG, was constructed through the development of a Se cycling and reaction module for the recently-developed UZF-RT3D model, and includes an accompanying N cycling

and reaction module due to the dependence of Se transformation and speciation on the presence of NO_3.

The model was applied to 1D soil profile systems to corroborate the correctness of the incorporated processes and to explore the ability of the near-surface cycling and chemical reactions to provide accurate estimates of leaching to the saturated zone when the model is employed in a large-scale agriculturally-influenced aquifer setting. In a first application, the N module was able to accurately reproduce a 3-year time series of NO_3 concentration in the near-surface soil water for unfertilized and fertilizer plots. In a second application, the Se and N modules were tested against observed concentrations of SeO_4 and NO_3 with depth for soil profiles in four test plots. Using the EnKF to condition parameters and forcing terms, the updated parameter values were able to produce an ensemble with mean values that matched to a reasonable degree the observed concentration values. Identified sensitive parameters include the rate of chemical reduction of SeO_4, $\lambda_{SeO_4}^{het}$, seasonal uptake of SeO_4, Se_{up}, concentration of SeO_4 in the irrigation water, $C_{SeO_4,irrig}$, rate of nitrification, λ_{nit}, maximum rooting depth, $d_{rt,max}$, and seasonal uptake of N, N_{up}. Model-calculated and observed values matched particularly well in the deepest soil layer (1.83 m), indicating that leaching is accurately depicted. Results in general demonstrate the usefulness and applicability of the EnKF in conditioning reaction rates and other parameters in subsurface reactive transport systems.

Although the autotrophic reduction processes and associated release of SeO_4 from pyrite-bearing shale were not included in this study, they are expected to be a principal component of SeO_4 fate and transport in regional-scale aquifer systems associated with marine shale bedrock and outcrops. Such systems exist in many alluvial of the world, one of which is the Lower

Arkansas River Valley in southeastern Colorado, where Se contamination problems have arisen and significant SeO_4-NO_3 relationships have been observed.

CHAPTER 6

APPLICATION OF UZF-RT3DAG TO THE IRRIGATED GROUNDWATER SYSTEM OF THE LOWER ARKANSAS RIVER VALLEY, SOUTHEASTERN COLORADO

6.1 INTRODUCTION

The UZF-RT3DAG model described in Chapter 5 and was applied to the Upstream Study Region (Gates et al., 2009), a 50,600 ha (125,000 ac) area of the irrigated stream-aquifer system of the Lower Arkansas River Valley (LARV) in southeastern Colorado in an overall effort to provide a tool capable of exploring best-management practices for Se and N mitigation. The model was applied for the years 2006-2009, with January 1 2006 through March 31 2008 comprising the period of model calibration and April 1 2008 through October 31 2009 comprising the period of model testing (i.e., validation). Model calibration consisted of comparing model results with field-observed groundwater concentrations of O_2, NO_3, and SeO_4, as well as mass loadings of Se from the aquifer to the Arkansas River. Following model testing, the model was applied to various land- and water-management scenarios to investigate their effect on groundwater concentrations and mass loadings to the Arkansas River. In light of the discussion by Konikow (2011) regarding calibration of transport models, and as discussed in Chapter 1, groundwater concentrations are compared using space- and time-averaged values rather than point-by-point comparisons.

Following a brief summary of the UZF-RT3DAG model in Section 6.2, the climate, geology, field monitoring network and associated field measurement data, and calibrated groundwater

flow model of the Upstream Study Region of the LARV is summarized in Section 6.3. The UZF-RT3DAG model set-up, model spin-up and calibration, and model testing for the Upstream Study Region is described in Section 6.4. Model calibration and model testing is accomplished through comparison of model results with observed values of spatially-averaged groundwater concentration and mass loadings to the Arkansas River. Chapter 7 summarizes the set-up and results of the land management scenarios investigation using the calibrated model. Similar to Chapter 5, NO_3 and SeO_4 throughout this chapter refer to NO_3-N and SeO_4-Se.

6.2 UZF-RT3DAG MODEL

6.2.1 Se and N Reactive Transport in Groundwater Systems

The UZF-RT3DAG model as described in Chapter 5 simulates the fate and reactive transport of Se and N species in an irrigated agricultural groundwater systems, and accounts for appropriate sources and sinks of species mass (fertilizer, irrigation water, canal seepage, regional lateral groundwater fluxes, crop residue from roots and after-harvest stover, uptake during the growing season), key chemical reactions (oxidation-reduction, mineralization/ immobilization, organic matter decomposition, volatilization), and the environmental component that control these reactions (soil temperature, soil moisture, presence of electron e^- donors).

The conceptualization of the large-scale fate and transport of O_2, NO_3, and SeO_4 in an alluvial groundwater system is shown in Figure 1-4, with main system inputs, outputs, and processes including application of canal irrigation water and pumped irrigation water, fertilizer application and species leaching, transport through the saturated zone of the aquifer due to hydraulic gradients, and discharge and exchange with canals, streams, and rivers. Upflux from

shallow water tables also occurs, potentially leading to hyper-concentration of species in the unsaturated zone. The cycling and transport of carbon (C), Se, and N species in the root zone and upper layers of the soil profile are comprised by "Root Zone Processes" shown in Figure 1-4, and are discussed thoroughly in Chapter 5.

Whereas Chapter 5 summarized the application of UZF-RT3DAG to soil profiles, this chapter summarizes the application of UZF-RT3DAG to a large-scale (50,600 ha) irrigated agricultural groundwater system. Model components considered in this chapter that were not pertinent to the modeling effort described in Chapter 5 include the spatial distribution of surface and bedrock shale; the cultivation of a number of crops throughout the model domain; the spatial distribution of cultivated fields and the mapping of these fields to model grid cells, with the possibility of portions of multiple fields residing in a single grid cell; the application of both canal irrigation water and pumped irrigation water, with the possibility of fields residing in a single grid cell receiving irrigation water from either source; and the availability of a large set of measured groundwater concentrations of O_2, NO_3, and SeO_4 for comparison with model results.

For the fate and transport of Se species, of utmost importance is the inclusion and representation of Se oxidation from shale ($FeSe_2$) (Figure 1-4) which in many aquifer systems can play a vital role in the overall control of Se concentration in groundwater and nearby surface water bodies (Seiler, 1995; Seiler, 1997; Gates et al., 2009). The oxidation of residual Se was not considered in the application of UZF-RT3DAG to the soil profiles of the Arkansas Valley Research Center (AVRC) summarized in Chapter 5, but, due to the presence of numerous shale outcrops as well as shale constituting the bedrock underlying the alluvial aquifer, is of prime importance in the application to the regional-scale groundwater systems of the Lower Arkansas River Valley (LARV).

6.2.2 Numerical Code Development

The implementation of Se and N cycling and reactive transport into the UZF-RT3D model is described in Chapter 5. Details regarding the framework of UZF-RT3DAG, including descriptions of the newly-developed Nutrient Cycling (NTR) and IRG (Irrigation) packages and associated input files and subroutines, are contained in Appendix A. The description of the linkage between MODFLOW-UZF (Niswonger et al., 2006) and RT3D is described in Chapter 4.

In addition to the processes described in Chapter 5, two key processes are added in the application of the UZF-RT3DAG model to the LARV. First, the autotrophic reduction of O_2 and NO_3 and resulting oxidation of residual Se is included due to the pervasive presence of shale in the LARV either in outcrop or bedrock form. As described in Appendix A, Se oxidation from FeSe2 in the shale material occurs if the cell contains O_2 and/or NO_3 and if any of the surrounding six cells contain shale. Second, and with a direct influence on the first, the reaeration term described in Chapter 4 regarding O_2 fate and transport has been included, and hence supplies O_2 mass to the saturated zone via gaseous diffusion through the unsaturated zone. Hence, more O_2 is available in the saturated zone for Se oxidation than would be the case if the reaeration term were not included.

6.2.3 Limitations and Assumptions of the UZF-RT3DAG model

Limitations of the UZF-RT3DAG model are discussed throughout this chapter, but are summarized here for conciseness. Limitations result principally from (1) treating the aquifer as the control system and (2) treating the growth and death of crops using logistical equations and average seasonal values.

In regards to (1), all fluid flow and chemical processes occurring beyond the boundary of the aquifer, e.g., surface water flow and chemical transport, overland flow and chemical transport, are not simulated explicitly but rather treated as boundary conditions or mass sources/sinks to the aquifer system. Whereas mass loadings from the aquifer to surface water bodies is determined using simulated groundwater flows and groundwater concentrations, the concentrations of chemical species in canal seepage, river seepage, and applied irrigation water contributing to mass loadings from surface water to the aquifer are specified using measured concentration values from field sampling events. Whereas species' concentrations were sampled at multiple locations along the Arkansas River, and hence the species' concentration in the river seepage from the river channel to the aquifer varies along the reach of the river, only one species' concentration value per sampling event is available for each canal. These concentrations can vary considerably in time (see Table 6-11), hence indicating that frequent sampling events are required to provide an accurate representation of the boundary conditions. The species' concentration is thus assumed to be uniform along the reach of the canal.

The exclusion of surface transport processes is particularly notable in regards to scenario analysis (presented in Chapter 7). First, the impact of implementing BMPs only can be analyzed in regards to groundwater concentrations and mass loadings to surface water bodies rather than in regard to changes in species' concentration in surface water. Second, the surface water species' concentrations and associated mass loadings from surface water to the aquifer are not coupled to the influence of the BMPs on the groundwater concentrations and mass loadings to the surface water. For example, mass loadings of Se and N to the Arkansas River in the upstream portion of the river reach modify the species' concentration in the river water, and hence directly influence the amount of species mass loaded to the aquifer in the case of river seepage in

downstream sections of the river reach. The model, however, cannot account for this change in species' concentration. Similar model shortcomings occur for the handling of species' concentration in canal water, which likely will vary along the length of the canal in response to, for example, mass loadings from upland surface drainage of cultivated fields as a result of changes in applied fertilizer loadings.

In regards to (2), root growth and daily crop nutrient uptake during the growing season and the mass of crop roots and after-harvest stover incorporated into the pool of soil organic matter at the end of the growing season are specified as crop parameters rather than as output variables from a plant growth simulation model. For example, plant growth models simulate the root mass throughout the growing, with this mass incorporated into the soil organic matter during plowing events. In UZF-RT3DAG, however, the root mass at the end of the growing season is based on average seasonal values from historical events. While greatly simplifying the inclusion of crop life cycles and their influence on the amount of nutrient uptake and soil organic matter concentrations, doing so assumes that crop growth patterns are identical for each growing season during the model simulation period, and therefore assumes that the climatic and land management variables governing the growth of the crop (e.g., water availability, soil conditions, fertilizer application, air temperature and humidity) also remain unchanged from year to year.

These simplifications are acceptable, however, since (i) the model is shown to be capable of describing accurately the daily and seasonal fluctuation of species' concentrations, as summarized in the application of UZF-RT3DAG to the barley fields as described in Chapter 5 ; (ii) they provide typically an adequate imitation of the mass of nutrients taken up and the mass of roots and stover when averaged over the spatial extent of the model domain if employed in a large-scale system (Wreidt and Rode, 2006); (iii) sensitivity analysis of UZF-RT3DAG (shown

in Appendix C) demonstrates that the crop parameters used to define root growth, nutrient uptake, and root and after-harvest stover mass are not as influential on resulting groundwater species' concentrations as other model parameters; and (iv) crop parameters are treated stochastically in order to account for uncertainty as well as to provide spatial heterogeneity.

Similar to the exclusion of surface transport processes, the inclusion of crop growth simplifications is notable in regards to scenario analysis, presented in Chapter 7. Of particular note are the scenarios investigating the management scheme of reducing fertilizer loadings by certain percentages. The model does not link root growth with the availability of nutrients (i.e., through the addition of fertilizer into the soil) and, as such, the crop parameters describing root growth and amount of root and stover mass remain unchanged across the scenarios. For situations wherein root growth would be affected by a decrease in seasonal fertilizer loading, the model overestimates the amount of nutrients taken up by the crops and hence provides an underestimation of the leaching of nutrients, the resulting concentration in the saturated zone, and the mass loadings to surface water bodies.

Other assumptions in the simulated physical processes in UZF-RT3DAG are that (i) rates of chemical reactions proceed according to first-order kinetics, i.e., that the rate of reaction is dependent on the concentration of the species, (ii) that the rates of reaction are tempered through the availability of other reactants in the chemical reaction, e.g., that heterotrophic reduction of O_2, NO_3, and Se species is dependent on the presence of organic carbon, and (iii) that microbial populations required for microbial-mediated reactions to proceed are present in a limitless supply. In practice, the model does not simulate the growth and death of microbial populations, and does not account for the distribution of various microbial species responsible for different reaction types. These assumptions, however, are inherent in other models that successfully have

been applied to study sites (e.g., Johnson et al., 1987; Birkinshaw and Ewen, 2000; Wreidt and Rode, 2006). Another limitation is that the model does not account for competition of SeO_3 with PO_4, a strong sorbent, for sorption to soil surface sites, since the cycling of phosphorus (P) is not accounted for in the model. The inclusion of P into UZF-RT3DAG, however, is an objective for future studies.

6.3 UPSTREAM STUDY REGION OF THE LARV

6.3.1 Climate and Geology, and Cultivation Practices of the LARV

The site of model application within the LARV, termed the Upstream Study Region (Gates et al., 2009) due to its position upstream from John Martin Reservoir, is shown in Figure 6-1. The boundary of the model domain is shown with a black line, and encompasses an area of 50,600-ha (125,000 acres), of which 26,400 ha (65,300 acres) are irrigated. As discussed in Chapter 1, the site is an ideal setting since (i) it is a designated seleniferous river basin, as determined through the NIWQP (Seiler, 1997), (ii) all river segments have been identified as impaired for Se by the CDPHE, (iii) it has been monitored for both hydrologic and chemical species components during the last decade by Colorado State University, hence yielding an extensive dataset of measured groundwater and surface water species concentrations, and (iv) a groundwater flow model for the Upstream Study Region has been constructed, calibrated, and tested.

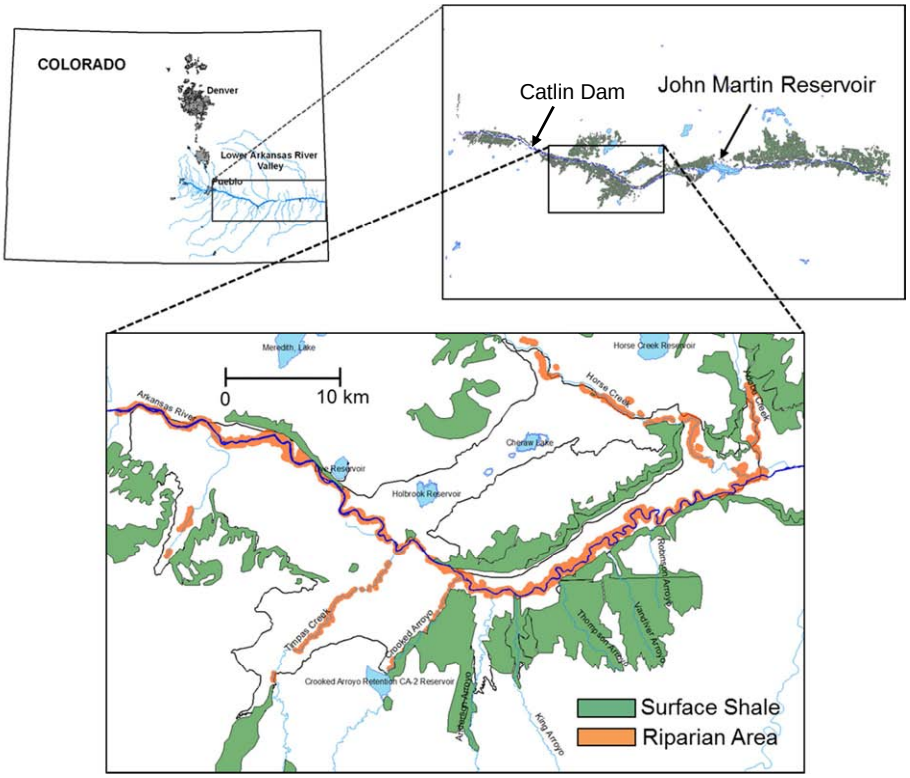

Figure 6- 1. Location and surface features of the Upstream Study Region of the Lower Arkansas River Valley in southeastern Colorado, showing extent of surface shale (within 2 m of ground surface), natural water bodies (Arkansas River, tributaries, and lakes), and riparian areas along the Arkansas River and its tributaries.

The climate is semi-arid, with average monthly temperatures and month precipitation ranging from -1 ^{o}C and 0.7 cm during the winter months, respectively, to 25 ^{o}C and 5.0 cm during the summer months. The LARV has been intensively irrigated for more than 100 years, and has served as one of the most productive agricultural areas for the state of Colorado. The Arkansas River (Figure 6-1), originating from snowmelt in the upper Arkansas River Valley northwest of Pueblo, CO, has a flow pattern typical of snowmelt-derived rivers with high flows in the spring and low flows in the late summer and fall. The discharge of the Arkansas River measured at Catlin Dam (Figure 6-1) between January 1 1964 and December 31 2009 is shown in Figure 6-2, with a maximum value of 518.2 $m^3 s^{-1}$ (June 18 1965), a minimum value of 0.00 $m^3 s^{-1}$, and an average value of 18.3 $m^3 s^{-1}$.

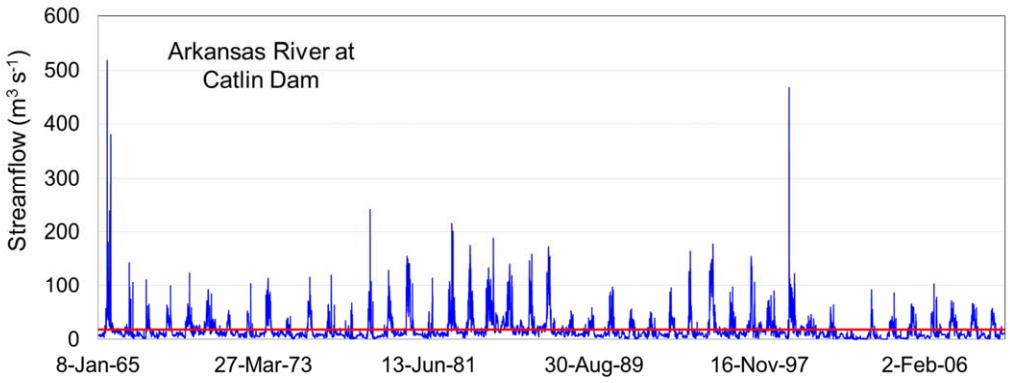

Figure 6- 2. Daily discharge (m^3 s^{-1}) of Arkansas River at Catlin Dam from 01-01-2965 to 12-31-2009. The average discharge during the period if 18.3 m^3 s^{-1}, shown in red.

Alfalfa is the dominant crop, followed by sorghum, corn, grass/pasture, wheat, melons, onion, oats, sunflower, and soybeans. Melons and onions, as the principal cash crops, receive the most irrigation water per unit cultivated area. The growing season commences mid to late-March and ends in early November, with un-lined irrigation canals receiving water from the Arkansas River during the period of March 15th to November 15th. Irrigation water is derived from either one of six principal irrigation canals (Rocky Ford Highline, Catlin, Otero, Rocky Ford Ditch, Fort Lyon, and Holbrook) or ground water pumps, as shown in Figure 6-3. The command areas associated with each canal, i.e., the collection of cultivated fields that receive irrigation water from the same canal, are shown in Figure 6-4. Due to over-irrigation, canal seepage, and poor drainage resulting in salinization and waterlogging, the region has experienced a decrease in crop productivity (Burkhalter and Gates, 2005; Morway and Gates, 2012).

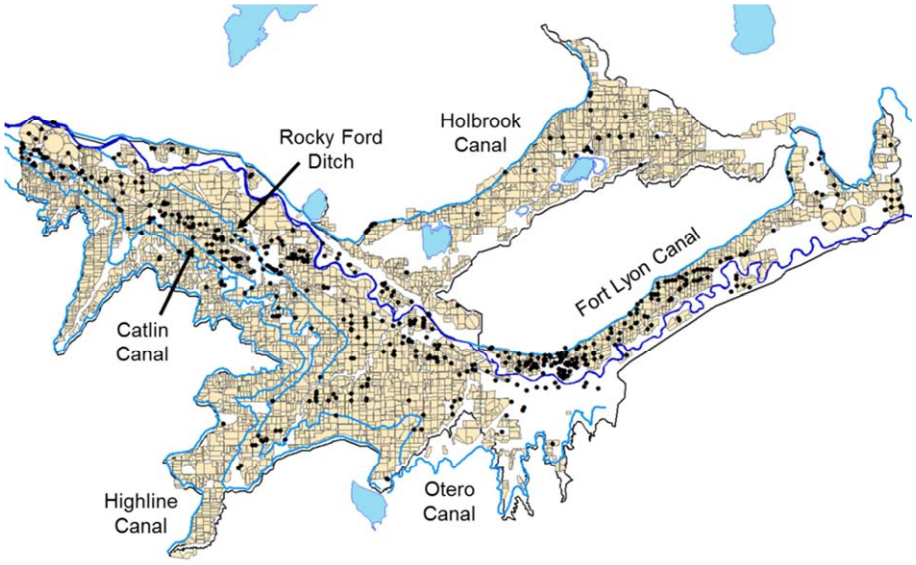

Figure 6- 3. Irrigation system of the Upstream Study Region, with the Arkansas River shown in dark blue, irrigation canals shown in light blue, pumping wells shown in black circles, and cultivated fields shown in tan.

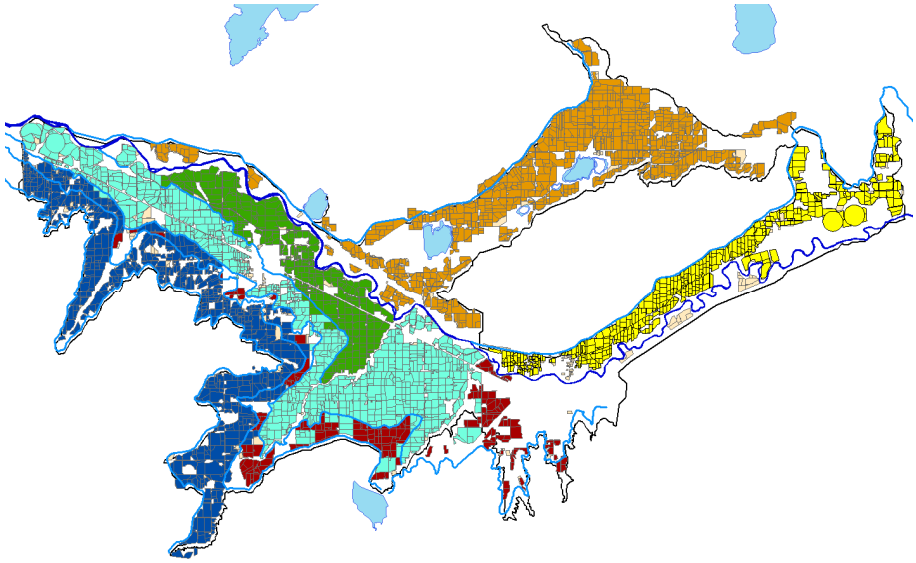

Figure 6- 4. Commmad areas of the Upstream Study Region, with fields receiving irrigation water from the Highline, Otero, Catlin, Rocky Ford Ditch, Holbrook, and Fort Lyon canals shown in dark blue, maroon, light blue, green, orange, and yellow.

The amount and distribution of cultivated crops in the Upstream Study Region are representative of the LARV. In terms of spatial extent, alfalfa is the dominant crop, followed by sorghum, corn, grass/pasture, wheat, melons, onion, oats, sunflower, and soybeans. The crop

type cultivated for each field in 2006, provided by the Farm Service Agency in Rocky Ford, CO, is shown in Figure 6-5, with the percentage of total land area occupied by each crop type for 2006 through 2009 shown in Figure 6-6. Notice that the portion of the region occupied by fallow areas increases each year over this period.

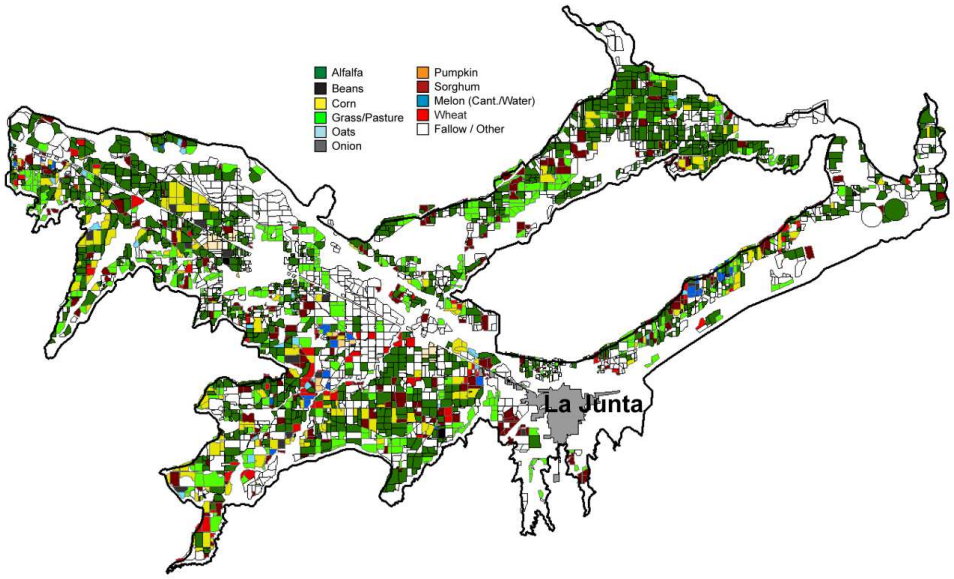

Figure 6- 5. Crop type for each cultivated field for the year 2006, according to records of the Farm Service Agency located in Rocky Ford, CO.

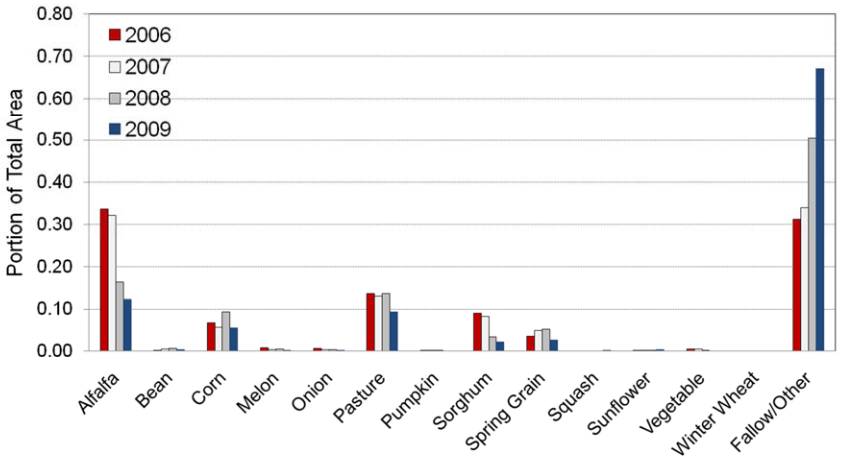

Figure 6- 6. Portion of total area of the Upstream Study Region attributed to each crop type for each year from 2006 to 2009.

The designation of the region as seleniferous is likely due to the preponderance of shale. The alluvial aquifer in the LARV, which ranges from approximately 4 to 34 m in thickness (Figure 6-7), is underlain by Cretaceous shale (Seiler, 1997) (Pierre Shale, Niobrara Shale, Carlisle Shale, Graneros Shale) (Scott, 1968; Sharps, 1976) in both solid and weathered form. In the Upstream Study Region, the aquifer is underlain principally by Niobrara Shale, followed by Greenhorn Limestone, Carlile Shale, and Graneros Shale. Shale formations, predominantly Niobrara and Carlisle shale, residing within approximately 1.5 m of the ground surface also have been delineated, as shown in Figure 6-1. Aerial photos showing shale outcrops in relation to the irrigation canals within the Upstream Study Region are shown in Appendix B.

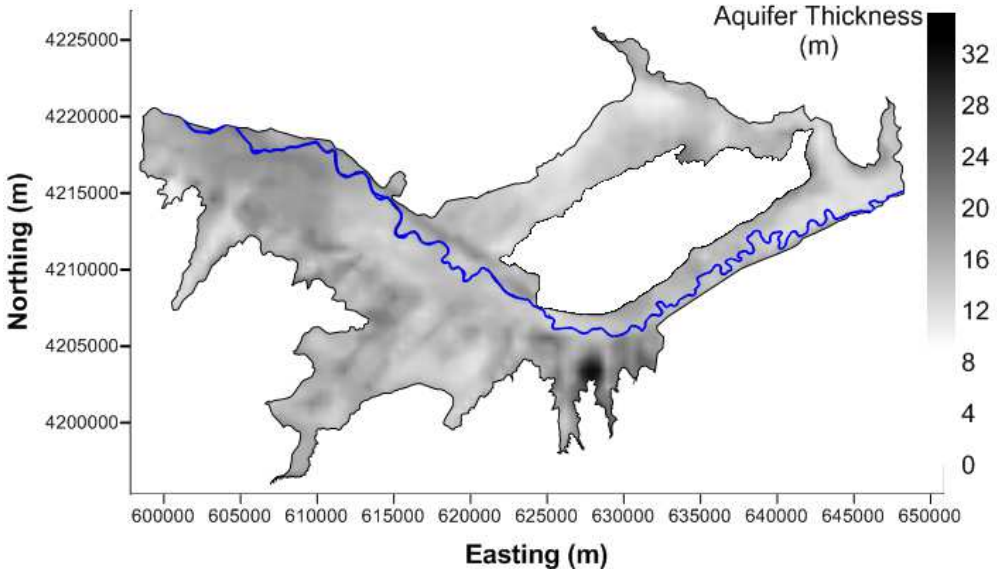

Figure 6- 7. Thickness of the aquifer throughout the Upstream Study Region. Aquifer thickness ranges approximately from 4 m to 34 m.

6.3.2 Monitoring Network and Field Measurements

Water samples, from which concentrations of O_2, NO_3, SeO_4, SeO_3, and other irrigation salts have been measured, have been taken in the Upstream Study Region since the growing season of 2006. Samples were taken routinely from about 45 groundwater observation wells, four locations in tributaries and drains, and 10 locations along the river. Sampling events from 2006 through 2009 include June 2006, May 2007, October 2007, March 2008, June 2008, August 2008, January 2009, May 2009, and July 2009. For several of these events samples from an additional 61 observation wells also were taken. Figure 6-8 shows the location of the groundwater observation wells (black targets) and the surface water sampling points (red triangles).

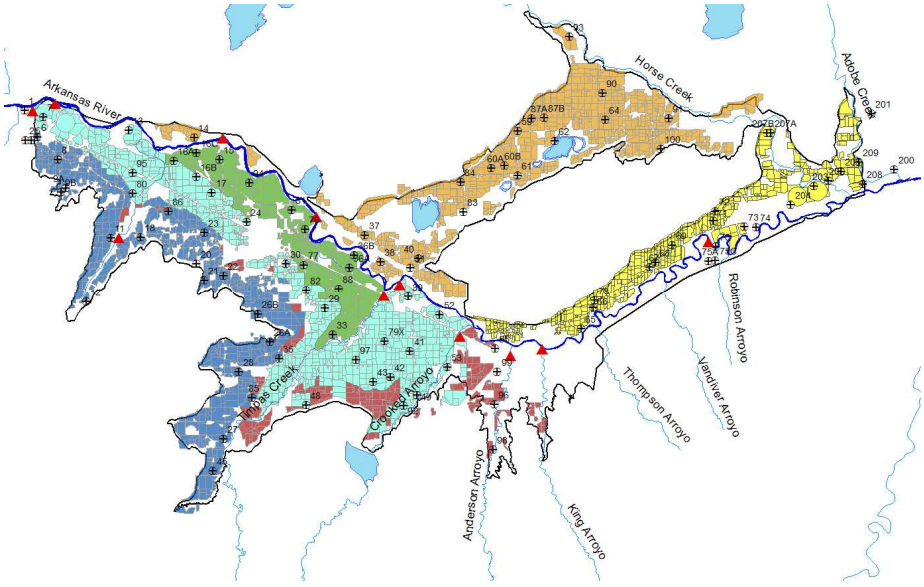

Figure 6- 8. Location of groundwater observations wells (black targets) and surface water sampling points (red triangles) in the Upstream Study Region from which water samples were taken and analyzed for species concentrations.

Samples for NO_3 and Se were filtered through disposable in-line 0.003 m^2 0.45 µm capsule filters. Samples for Se were taken in a 0.12 L plastic (polypropylene or polyethylene) bottle, while samples for NO_3 were taken in 0.25 L plastic bottles. Samples for Se were preserved at pH < 2 by adding ~0.005 L of 10% ultra-pure nitric acid (HNO_3) in reagent water per liter of sample

(~0.00625 L per 0.12 L sample bottle) prior to sample collection. All samples were stored on ice. Samples for NO_3 analysis were analyzed by Ward Laboratories, Inc. in Kearney, NE using the standard USEPA method [1983, Method 353.2]. Samples were analyzed for Se at the Olson Biochemistry Laboratories at South Dakota State University in Brookings, SD (USEPA certified) using Official Methods of Analysis of AOAC International, 17th Edition, test number 996.16 Selenium in Feeds and Premixes, Fluorometric Method. This method determines the concentration of selenite as Se (SeO_3-Se). Total recoverable Se is determined by reducing all forms of selenium within the sample to $SeO_3$with hydrochloric (HCl) acid. The concentration of SeO_4-Se was estimated by subtracting the concentration of SeO_3-Se before adding HCl from the concentration of SeO_3-Se after adding HCl. Detection limit was 0.4 $\mu g\ L^{-1}$.

A complete listing of the measured O_2, NO_3, and SeO_4 concentrations from the observation wells for the 9 sampling events is contained in Appendix B. Average species concentrations also were calculated according to command area, with the wells located within a given command area shown in Figure 6-8. Summaries of the average groundwater concentrations, as well as the number of samples per command area for each sampling event, are contained in Tables 6-1 to 6-6. Tables 6-1 and 6-2 contain the average concentrations and sampling tallies for O_2, respectively; Tables 6-3 and 6-4 the average concentrations and tallies for NO_3; and Tables 6-5 and 6-6 the average concentrations and tallies for SeO_4.

The values of groundwater concentration have further been grouped into a “model calibration” average as well as a “model testing” average. The “model calibration” average includes all concentration values during the first four sampling events, which corresponds to the period of model calibration (January 1 2006 through March 31 2008), and the “model testing” average includes values during the final five sampling events, corresponding to the period of

model testing (April 1 2008 through October 31 2009). These values establish practical target concentration values for model calibration and subsequent model testing, discussed in detail in Section 6.3.3.

Table 6- 1. Average concentration (mg L^{-1}) of O_2 from groundwater observation wells in the Upstream Study Region, grouped according to canal command area, and further grouped according to first four sampling events (CALIB Period AVG) and final five sampling events (TEST Period AVG). The latter two are used for model calibration and model testing.

Canal	6/19/06	5/23/07	10/6/07	3/20/08	CALIB Period AVG	6/23/08	8/14/08	1/15/09	5/14/09	7/22/09	TEST Period AVG
Highline	3.36	3.68	1.46	2.74	**2.81**	2.81	2.13	2.35	2.39	2.1	**2.36**
Otero						4.17	3.85				
Catlin	2.81	1.54	1.9	2.84	**2.27**	2.72	1.41	2.58	2.48	2.49	**2.34**
RFDitch	3.88	3.77	2.87	2.96	**3.37**	2.04	6.88	5.01	3.1	2.74	**3.95**
FortLyon	2.5	2.11	2.6	2.97	**2.55**	4.05	1.62	3.39	2.28	2.69	**2.81**
Holbrook	2.91	2.42	2.34	2.13	**2.45**	2.54	0.96	1.45	2.5	2.51	**1.99**
Clear	0.73	2.44	1.08	3.06	**1.83**	3.26	0.24	0.8	1.11	1.55	**1.39**

Table 6- 2. The number of samples from each command areas analyzed for O_2, for each of the 9 sampling events. The total for the first four sampling events (CALIB Period TALLY) and the final five sampling events (TEST Period TALLY) according to canal command area also are shown.

Canal	6/19/06	5/23/07	10/6/07	3/20/08	CALIB Period TALLY	6/23/08	8/14/08	1/15/09	5/14/09	7/22/09	TEST Period TALLY
Highline	8	11	9	9	**37**	16	13	9	9	9	**56**
Otero						2	2				
Catlin	8	8	8	8	**32**	14	8	6	8	8	**44**
RFDitch	2	2	2	2	**8**	6	1	1	2	2	**12**
FortLyon	9	8	7	3	**27**	5	4	3	2	2	**16**
Holbrook	7	7	7	6	**27**	12	6	7	7	5	**37**
Clear	2	3	3	2	**10**	4	1	1	3	3	**12**

Table 6- 3. Average concentration (mg L^{-1}) of NO_3 from groundwater observation wells in the Upstream Study Region, grouped according to canal command area.

Canal	6/19/06	5/23/07	10/6/07	3/20/08	CALIB Period AVG	6/23/08	8/14/08	1/15/09	5/14/09	7/22/09	TEST Period AVG
Highline	17.61	8.95	5.38	3.32	**8.81**	2.84	2.69	3.36	2.33	4.1	**3.06**
Otero						0.95	0.9				
Catlin	8.99	12.42	15.37	11.34	**12.03**	4.93	5.6	11.23	5.05	3.88	**6.14**
RFDitch	7.4	3.55	6.55	3.3	**5.2**	3.33	4.1	5.9	2.9	2.65	**3.78**
FortLyon	4.27	2.52	5.23	2.93	**3.74**	1.51	1.73	1.23	1.8	1.67	**1.59**
Holbrook	1.71	2.37	3.97	1.5	**2.39**	1.73	5.02	6.1	3.53	1.16	**3.51**
Clear	2.25	2.5	3.65	4	**3.1**	2.9	2.1	3.55	8.6	3.93	**4.22**

Table 6- 4. The number of samples from each canal command areas analyzed for NO_3, for each of the 9 sampling events.

Canal	6/19/06	5/23/07	10/6/07	3/20/08	CALIB Period TALLY	6/23/08	8/14/08	1/15/09	5/14/09	7/22/09	TEST Period TALLY
Highline	6	11	10	9	**36**	17	14	9	10	10	**60**
Otero						2	2				
Catlin	7	8	6	8	**29**	15	8	7	8	8	**46**
RFDitch	1	2	2	2	**7**	7	1	1	2	2	**13**
FortLyon	6	9	7	3	**25**	9	4	4	3	3	**23**
Holbrook	7	7	7	6	**27**	14	7	7	7	5	**40**
Clear	2	3	2	1	**8**	4	1	2	3	3	**13**

Table 6- 5. Average concentration ($\mu g\ L^{-1}$) of SeO_4 from groundwater observation wells in the Upstream Study Region, grouped according to canal command area.

Canal	6/19/06	5/23/07	10/6/07	3/20/08	CALIB Period AVG	6/23/08	8/14/08	1/15/09	5/14/09	7/22/09	TEST Period AVG
Highline	208.77	86.81	25.42	54.52	**93.88**	39.38	41.17	71.91	38.83	49.48	**48.15**
Otero						16.65	16.35				
Catlin	86.88	55.08	231.23	111.2	**121.1**	29.77	32.77	237.55	73.19	62.26	**87.11**
RFDitch	9.2	13.95	10.21	10.18	**10.89**	14.07	13.8	20.3	8.99	9.11	**13.26**
FortLyon	19.48	26.69	14.57	6.45	**16.8**	24.38	8.83	3.01	4.75	4.99	**9.19**
Holbrook	31.66	50.93	54.03	39.93	**44.14**	50.91	119.77	63.1	24.39	15.8	**54.79**
Clear	18.2	418.7	29.65	26.9	**123.36**	25.43	7.18	25.02	127.57	33.9	**43.82**

Table 6- 6. The number of samples from each canal command areas analyzed for SeO_4, for each of the 9 sampling events.

Canal	6/19/06	5/23/07	10/6/07	3/20/08	CALIB Period TALLY	6/23/08	8/14/08	1/15/09	5/14/09	7/22/09	TEST Period TALLY
Highline	9	11	10	9	**39**	17	14	9	10	10	**60**
Otero						2	2				
Catlin	9	8	6	8	**31**	15	8	7	8	8	**46**
RFDitch	2	2	2	2	**8**	7	1	1	2	2	**13**
FortLyon	9	9	7	3	**28**	9	4	4	3	3	**23**
Holbrook	7	7	7	6	**27**	14	7	7	7	5	**40**
Clear	2	3	2	1	**8**	4	1	2	3	3	**13**

Notice that only four samples were taken from Otero command area throughout 2006-2009. Limited samples also were collected from the Rocky Ford Ditch command area. During the first four sampling events, only 8, 7, and 8 samples of O_2, NO_3, and SeO_4 were taken, respectively, whereas during the final five sampling events only 12, 13, and 13 samples of O_2, NO_3, and SeO_4 were taken. The average concentrations of the species reported for the Rocky Ford Ditch command area should hence be treated with caution as the number of samples does not allow for accurate statistical analysis. This also is true for the Outside Area, with only 10, 8, and 8 samples of O_2, NO_3, and SeO_4, respectively, for the first four sampling events and 12, 13, and 13 samples of O_2, NO_3, and SeO_4 for the final five sampling events.

Measured concentrations of SeO_4 in surface water samples from the Arkansas River and its tributaries were used in a mass-balance study by Keith Morse, a graduate student at Colorado State University, to calculate the approximate mass loadings of Se in the Arkansas River not accounted for by loading from the tributaries. Using surface water flow rates and estimated Se concentrations, based upon periodic measurements, at the upstream and downstream ends of the Upstream Study Region as well as at tributaries within the study region, values of daily mass loading (kg) of Se within the Arkansas River were determined for January 1 2006 to October 31 2009. Using the loading values from the tributaries, the values of unaccounted-for daily mass loading (kg) of Se for the entire reach of the Arkansas River within the Upstream Study Region also were calculated, and are shown in Figure 6-9. It is assumed that the majority of the unaccounted-for mass loading is attributed to loading from the aquifer to the Arkansas River. These values are used in conjunction with the average groundwater concentrations shown in Tables 6-1, 6-3, 6-5 to perform model parameter estimation and model testing, as described in

Section 6.3.5. As the values shown in Figure 6-9 represent the total unaccounted-for daily mass loading in the Arkansas River, they provide a maximum value of mass loading from the aquifer.

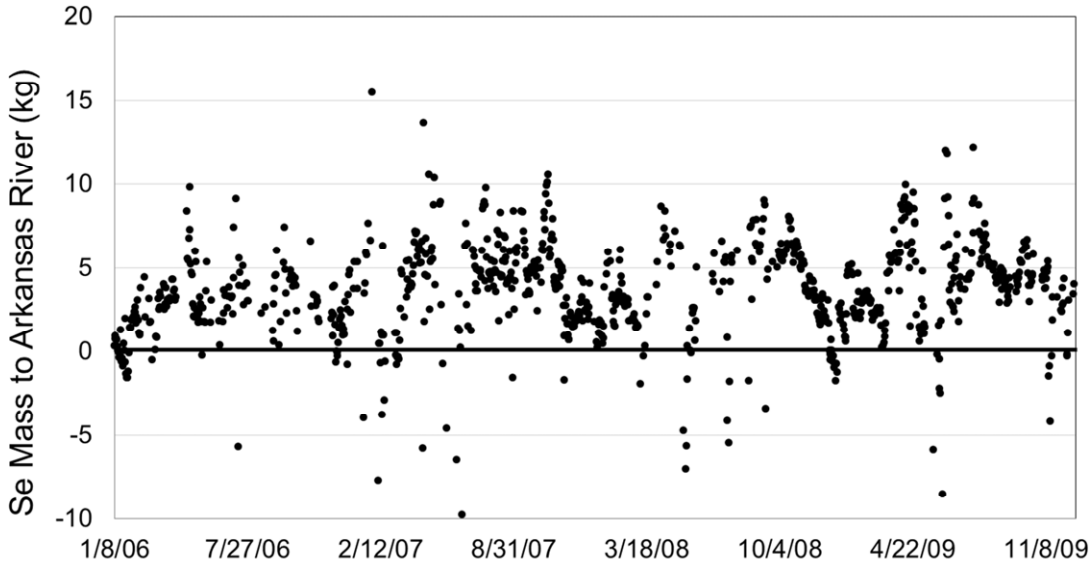

Figure 6- 9. Daily mass loading of Se (kg) along the reach of the Arkansas River within the Upstream Study Region that is not accounted for by loadings from the measured river tributaries. It is assumed that these loadings primarily are a result of mass loadings from the aquifer to the Arkansas River.

6.3.3 Groundwater Flow Model of the Upstream Study Region

The groundwater flow model of the Upstream Study Region was constructed, calibrated, and tested as described in Gates et al. (2012) and Morway and Gates (2012) using MODFLOW-UZF (Niswonger et al., 2006). Horizontal cell dimensions are 250 m by 250 m, resulting in grid cells with spatial areas comparable to dimensions of irrigated fields. The finite-difference surface grid for the model domain is shown in Figure 6-10, with the inset figure showing the contour of the ground elevation, with black and white representing 1345 m and 1195 m, respectively.

The alluvial aquifer is divided into two layers, with a third layer constituting the bedrock (Morway and Gates, 2012). Applied irrigation water is based on crop type as well as on gauged diversion data obtained from the State Engineer's Office (SEO), with timing of water application based on the following hierarchy: melons and onion receive water on a weekly basis; corn, oats, and pumpkin receive water on either a bi-weekly or tri-weekly basis; and alfalfa, grass/pasture, sorghum and wheat receive water either every four, five, six, or seven weeks, subject to availability. Stress periods, which coincided with flow time steps, are one week. Groundwater pumping also was supplied by the SEO. The model was calibrated for the years 1999 through 2007 using UCODE (Hill and Tiedeman, 2007) with hydraulic conductivity and specific yield modified until an acceptable deviation between observed and calculated water table elevations and return flows of groundwater to the Arkansas River was achieved (Gates et al., 2012; Morway and Gates, 2012). The spatial distribution of hydraulic conductivity (m/wk) and specific yield for layer 1 of the calibrate flow model are shown in Figure 6-11. For use in this study, the simulation time period of the groundwater flow model was extended through October 31 2009. To do so, canal diversion data, ground water pumping data, and crop type for 2008 and 2009 were gathered.

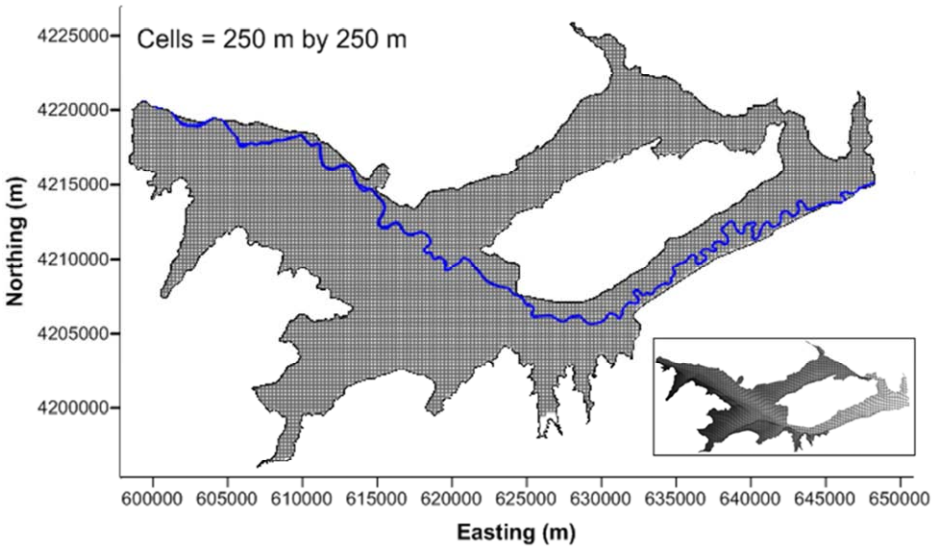

Figure 6- 10. Finite-difference surface grid of the Upstream Study Region groundwater flow model, as described in Morway and Gates (2012). Grid cell dimensions are 250 m by 250 m. A three-dimensional representation of the ground surface is shown in the inset figure.

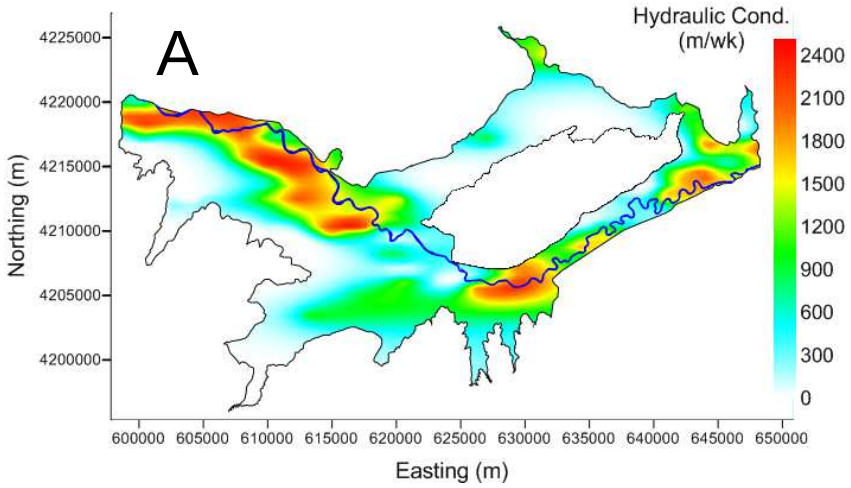

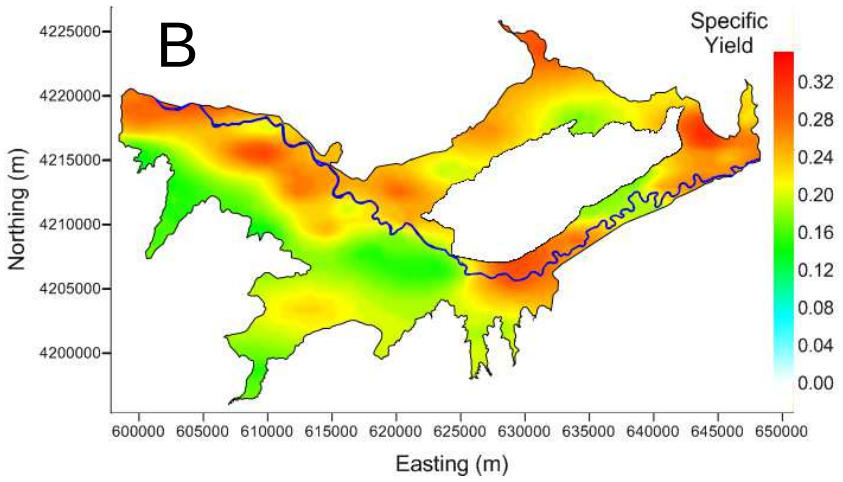

Figure 6- 11. Spatial distribution of (A) hydraulic conductivity (m/wk) and (B) specific yield as calculated through an automated parameter estimation process, with water table elevation and groundwater discharge to the Arkansas River used as calibration targets.

Examples of the flow model simulation results are shown in Figures 6-12 to 6-15. Figure 6-12 shows the flux of infiltrating water (m/week) for January 1 2006 and July 9 2006, and Figure 6-13 shows the simulated volumetric water content for the same two dates, demonstrating the influence of irrigation water on the hydrologic conditions of the system. Figure 6-14 shows the simulated water table elevation and associated vectors describing the direction of groundwater flow for one of the weeks of the simulation. Figure 6-15 shows an example plot of flow volumes discharged to the Arkansas River from the aquifer (positive values) or seeped from the Arkansas River to the aquifer (negative values) for each grid cell along the path of the Arkansas River for one of the weeks of the simulation. High negative values indicate river water seeped to the aquifer due to high rates of pumping at clusters of adjacent pumping wells.

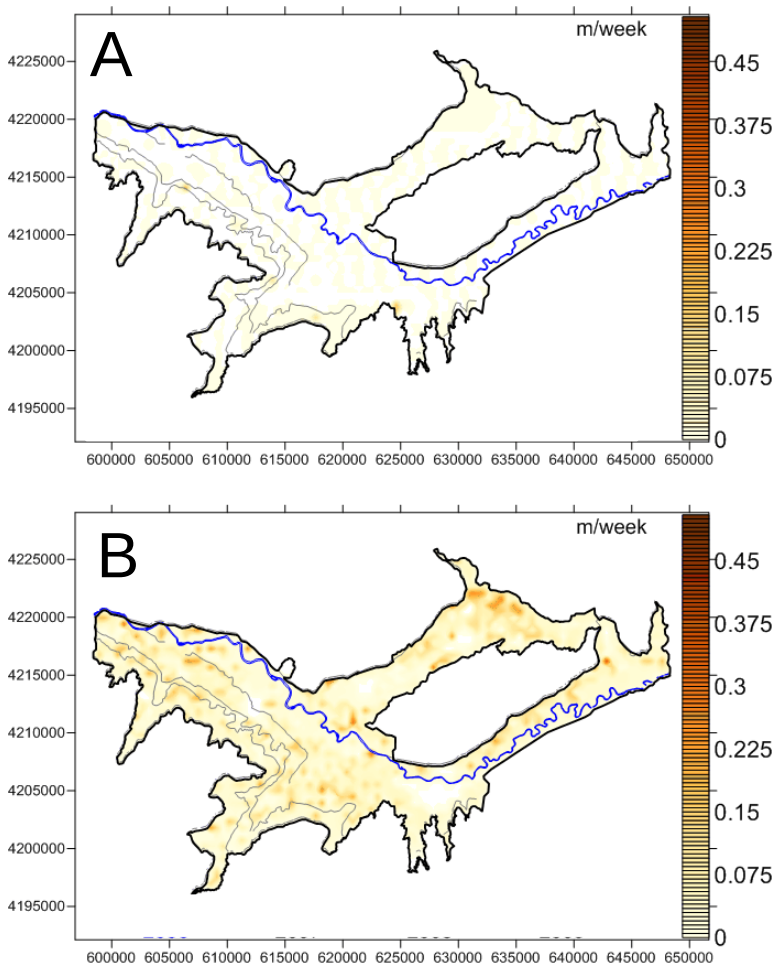

Figure 6- 12. Specified flux of infiltrating water (m/week) for (A) January 1 2006 and (B) July 9 2006 for the groundwater flow model.

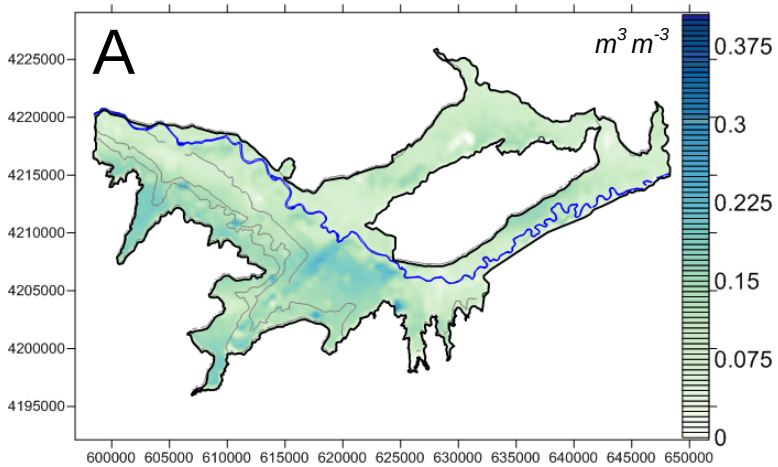

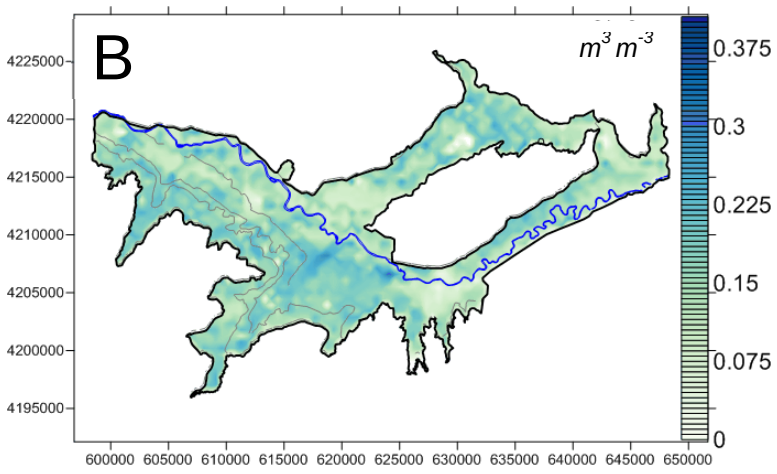

Figure 6- 13. Simulated volumetric water content in layer 1 of the groundwater flow model for (A) January 1 2006 and (B) July 9 2006.

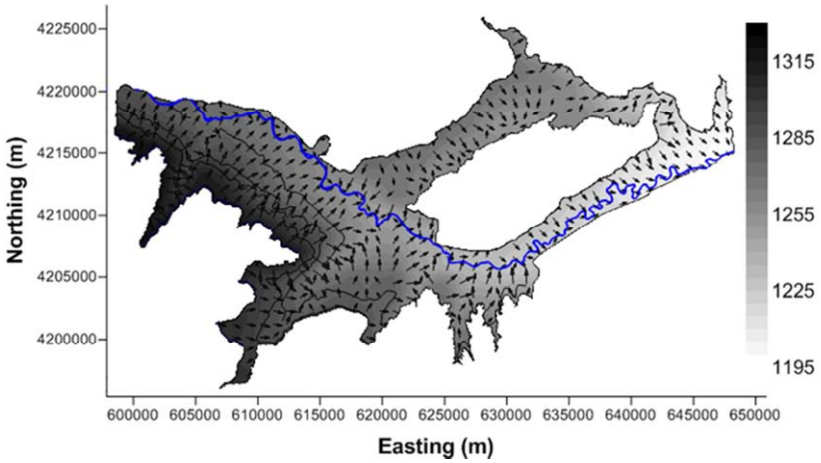

Figure 6- 14. Average simulated water table elevation and associated groundwater flow vectors all weeks of the groundwater flow simulation.

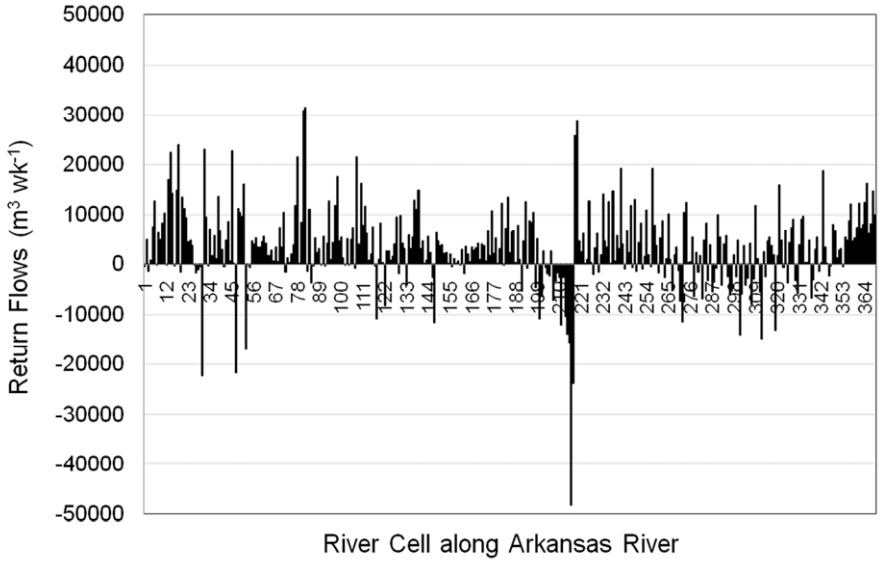

Figure 6- 15. Flow volumes discharged from the aquifer to the Arkansas River (positive values) or seeped from the Arkansas River to the aquifer (negative values) for each grid cell along the length of the Arkansas River, averaged over the weeks of the simulation.

6.4 APPLICATION OF UZF-RT3DAG TO THE LARV

This section describes the application of the UZF-RT3DAG model to the Upstream Study Region in regards to model set-up, model calibration, and model testing. Section 6.4.1 describes the set-up of the model in regards to model domain discretization and specification of sources, sinks, and chemical reaction parameters. Section 6.4.2 describes the process used to estimate model parameters and presents results of model calibration and model testing. The period of model calibration is January 1 2006 through March 31 2008, with groundwater concentrations and mass loadings from four sampling events used to condition model parameters. The subsequent period of model testing is April 1 2008 through October 31 2009, wherein groundwater concentrations and mass loadings from five samplings events are used to test model results.

6.4.1 Model Set-Up

Explanation of the set-up of the RT3DAG simulation for the Upstream Study Region is summarized in the following four sub-sections. The first section provides details regarding the 3D finite-difference grid used in the simulation and the method by which the volumetric flow rates from the groundwater flow model are applied. The second section describes the methods by which species' mass is added to or removed from the subsurface system via cultivation practices (e.g., fertilizer, root mass and stover mass, crop uptake, irrigation water). The third section outlines the method of mass exchange between the groundwater and surface water (e.g., canal seepage, aquifer-Arkansas River interaction). The fourth and concluding section provides information regarding the chemical reactions that act on the species mass within the system.

6.4.1.1 Spatial and Temporal Discretization Scheme

The finite-difference surface grid for the reactive transport simulation using RT3DAG is the same grid used for the groundwater flow simulation, with grid cell dimensions of 250 m by 250 m in the horizontal directions. The vertical cell discretization, however, was modified to use seven grid layers rather than the original three used by Morway and Gates (2012) to simulate localized chemical reactions and physical processes, particularly in the vicinity of the root zone (e.g., root growth and corresponding nutrient uptake, incorporation of dead root mass and stover mass). The top four layers are comprised in the original first layer, the next two layers are contained in the original second layer, and the third layer, representing the bedrock shale, is the same as the original third layer. The aquifer depth discretization for both the groundwater flow and reactive transport models is shown in Figure 6-16 with associated layer thicknesses. The top two layers, comprising the root zone, each have a thickness of 0.5 m, followed by a third layer with a thickness of 1.0 m. The thickness of the fourth layer depends on the elevation of the

bottom of the fourth layer, and the fifth and sixth layers are of equal thickness, each comprising half of the original second layer. Layer 4 corresponds to the depth at which groundwater samples were taken from the observation wells (see Section 6.3.2). Hence, model results from layer 4 are compared with the observed groundwater concentrations during model calibration and model testing, as described in Section 6.4.2.

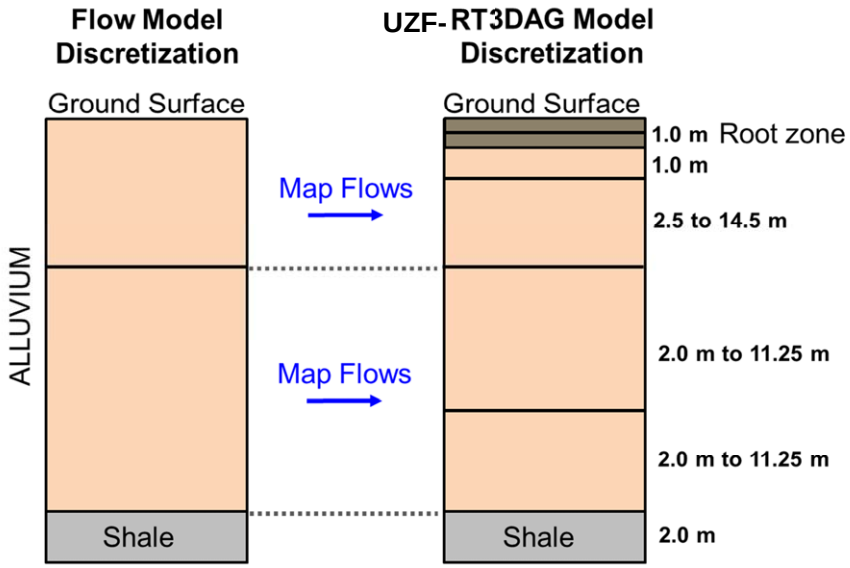

Figure 6- 16. Discretization of the aquifer depth for both the groundwater flow model (left) and the UZF-RT3DAG model (right). Three layers were used in the flow model, and seven are used in the UZF-RT3DAG model, with fine discretization occurring in the vicinity of the root zone.

In order to preserve the groundwater flow field as established through the calibration procedure performed by Gates et al. (2012) and Morway and Gates (2012), the volumetric flow rates and volumes of water sources and groundwater sinks are mapped from the three-layer grid to the seven-layer grid using the following rules:

- Volumetric water content is mapped directly, with values from the original first layer given to layers 1-4 and values from the original second layer given to layers 5-6

- The flux of infiltrated water for the original first layer is given to the first layer of the new grid, to preserve the infiltration of water at the ground surface; for all other layers, the flux of infiltrated water is mapped according to the layer thicknesses of the new grid, e.g., the infiltrated flux in the first layer of the original grid is divided and given to the top four layers in the new grid according to the thicknesses of the four layers
- The saturated thickness for each layer of the seven-layer grid is calculated using the location of the water table in the three-layer grid
- Volumetric flow rates in the horizontal directions are mapped according to the location of the water table in the three-layer grid, i.e., a layer in the new grid does not receive lateral flows if the water table is below the bottom of the layer
- For vertical flow rates in the upward direction, i.e., flowing from the second layer to the first layer in the original grid, the flow is added only to the fourth layer in the new grid
- Pumping volumes are assigned to layer 5 in the new grid (assigned to layer 2 in the original grid)
- Layers corresponding to designated river cells (cells that exchange water between the aquifer and surface water bodies) are determined in accordance with the bed of the surface water channel (canal, tributary, or Arkansas River)

Volumes of water for each type of flow and source/sink for both the original three-layer and the new seven-layer flow fields were tracked and compared in order to verify that water volume was conserved during the mapping procedure. When read into RT3DAG, the volumetric flow rates and sources/sinks were divided by 7 to convert from weekly rates to daily rates. As such, the daily flow rates and sources/sinks used in UZF-RT3DAG remain constant during a given week. Daily time steps are used in UZF-RT3DAG.

In addition to the limitations of UZF-RT3DAG described in Section 6.2.3, the application of the model to the Upstream Study Region results in further limitations due to the adopted schemes of spatial and temporal discretization described in this section. Using weekly time steps prevents short-duration hydrologic events (e.g., rainfall events) from influencing the hydrologic patterns of the aquifer system, and the spatial discretization adopted in the lateral direction often results in portions of multiple irrigated fields residing within a single grid cell, hence requiring the use of weighting schemes. Having a finer grid discretization would allow more grid cells to contain portions of only one cultivated field. However, as geometric outlines of fields are not conducive to aligning with outlines of grid cells, weighting of crop parameters will always be a necessity. Furthermore, the use of two layers in the groundwater flow model to discretize the aquifer depth results in a thick top layer that prevents the simulation of localized evapotranspiration due to spatially-varying crop root mass.

The adopted temporal and spatial discretization schemes, however, are consistent with the spatio-temporal scale of observed field data and with the aim of capturing regional trends rather than point-by-point predictions. Furthermore, the adopted discretization schemes provide reasonable run-times for the groundwater flow and UZF-RT3DAG simulations.

6.4.1.2 Crop Parameters

Parameters governing the management, growth and accompanying nutrient uptake, and death are provided for each crop type. These parameters are described in detailed in Chapter 5 as well as Appendix A. For the Upstream Study Region, the crop types and corresponding crop parameters are contained in Tables 6-7 to 6-10. Table 6-7 contains parameters concerning crop cultivation (planting, harvesting, plowing, root mass and stover mass); Table 6-8 contains parameters concerning root growth, Table 6-9 contains parameters concerning nitrogen fertilizer

and crop uptake, and Table 6-10 contains parameters concerning selenium root mass, stover mass, fertilizer, and crop uptake. Average crop parameters were supplied either by Dr. Michael Bartolo at the AVRC (Bartolo, personal communication) or obtained from the literature (e.g., Johnsson et al., 1987; Birkinshaw and Ewen, 2000; see Chapter 5). Figure 6-17 shows the scheduling of cultivation practices (fertilizer loading, planting, irrigation application, harvesting, plowing) for a typical growing season. Typically, 40% of the annual fertilizer load is applied one week before planting, with the remaining 60% applied six weeks after planting.

Each surface grid cell receives a set of crop parameter values depending on the crop type cultivated during the current growing season with the possibility that crop type may change from year to year. See Figure 6-5 for the crop type of each cultivated field in the Upstream Region for the 2006 growing season. In the event that portions of multiple cultivated fields reside in a single grid cell, a weighting scheme is used to calculate composite crop parameter values according to the spatial area of each field contained within the grid cell. This weighting scheme is described in detail in Appendix A. A similar weighting scheme is used to determine the concentration of chemical species in infiltrating water for each grid cell, since each field contained within a grid cell may have a different source of irrigation water (e.g., canal water, pumped aquifer water) with accompanying species mass, and hence a composite species concentration must be determined. This process is described in detail in Appendix A.

Table 6- 7. General crop parameters for each crop type cultivated in the Upstream Study Regions. Variable names and description are given in Appendix A.

CROP	*PLDY* -	*HVTP* -	*FYR* -	*HVDY* -	*PGDY* -	d_{pw} m	P_{Rt} kg ha^{-1}	*CBRT* -	P_{St} kg ha^{-1}	*CBST* -	*FLR* -
Alfalfa	120	5	3	273	293	1.0	500.0	0.4	561.6	0.4	0.8
Bean	140	1	1	273	293	0.8	500.0	0.3	561.6	0.3	0.0
Corn	121	1	1	298	318	1.0	500.0	0.4	5616	0.4	0.0
Melon	135	1	1	222	242	1.0	500.0	0.4	561.6	0.4	0.0
Onion	79	1	1	258	278	1.0	500.0	0.4	561.6	0.4	0.0
Pasture	242	5	3	273	293	1.0	500.0	0.4	0	0.4	0.8
Pumpkin	152	1	1	273	293	1.0	500.0	0.4	561.6	0.4	0.0
Sorghum	140	1	1	288	308	1.0	500.0	0.4	1684.8	0.4	0.0
Spring Grain	91	1	1	196	216	1.0	500.0	0.4	1684.8	0.4	0.0
Squash	140	1	1	206	226	1.0	500.0	0.4	561.6	0.4	0.0
Sunflower	152	1	1	283	303	1.0	500.0	0.4	561.6	0.4	0.0
Vegetable	115	1	1	242	262	1.0	500.0	0.4	561.6	0.4	0.0
Winter Wheat	273	1	1	186	206	1.0	500.0	0.4	1684.8	0.4	0.0
Clear	0	0	0	0	0	0.0	0.0	0.0	0	0.0	0.0

Table 6- 8. Root growth parameters for each crop type. Variable names and description are given in Appendix A.

CROP	$d_{rt,max}$ m	*RTB* -	*RTC* -	*RBETA* -
Alfalfa	1.83	0.1	0.05	5
Bean	0.91	0.05	0.05	5
Corn	1.22	0.07	0.05	5
Melon	1.22	0.1	0.07	5
Onion	0.46	0.05	0.05	5
Pasture	0.91	0.05	0.05	5
Pumpkin	0.91	0.08	0.06	5
Sorghum	0.91	0.1	0.05	5
SpringGrain	0.91	0.1	0.07	5
Squash	0.91	0.05	0.1	5
Sunflower	0.91	0.05	0.06	5
Vegetable	0.91	0.05	0.06	5
WinterWheat	0.91	0.05	0.06	5
Clear	0	0	0	0

Table 6- 9. Nitrogen fertilizer and crop uptake parameters for each crop type. Variable names and description are given in Appendix A.

CROP	*CNRT* -	*CNST* -	F_{NO_3} kg ha^{-1}	F_{NH_4} kg ha^{-1}	F_{Urea} kg ha^{-1}	N_{up} kg ha^{-1}	*NB* -	*NC* -	*NBETA* -
Alfalfa	25	50	0	22.4	0.0	22.4	1.0	0.08	5
Bean	25	45	0	140.0	0.0	84.2	1.0	0.08	5
Corn	70	50	0	252.0	0.0	224.6	2.0	0.06	5
Melon	25	50	0	112.0	0.0	112.3	2.0	0.10	5
Onion	25	50	0	140.0	0.0	78.6	1.3	0.06	5
Pasture	70	50	0	0.0	140.0	112.3	1.2	0.06	5
Pumpkin	25	50	0	140.0	0.0	84.2	1.0	0.08	5
Sorghum	70	50	0	0.0	112.0	112.3	1.0	0.07	5
SpringGrain	70	50	0	0.0	112.0	112.3	2.0	0.09	5
Squash	25	50	0	140.0	0.0	84.2	3.0	0.12	5
Sunflower	25	50	0	140.0	0.0	84.2	2.0	0.11	5
Vegetable	25	50	0	140.0	0.0	84.2	2.0	0.11	5
WinterWheat	70	50	0	0.0	112.0	112.3	2.0	0.09	5
Clear	0	0	0	0.0	0.0	0	0.0	0	0

Table 6- 10. Selenium fertilizer, root, stover, and crop uptake parameters for each crop type. Variable names and description are given in Appendix A.

CROP	*SEST* -	*SERT* -	F_{Se} g ha^{-1}	Se_{up} g ha^{-1}
Alfalfa	0.000	0.0002	0.0	1.30
Bean	0.000	0.0001	0.0	0.30
Corn	0.001	0.0022	0.0	10.80
Melon	0.000	0.0001	0.0	1.30
Onion	0.000	0.0001	0.0	2.70
Pasture	0.003	0.0053	0.0	10.70
Pumpkin	0.000	0.0001	0.0	2.70
Sorghum	0.001	0.0022	0.0	10.40
SpringGrain	0.001	0.0022	0.0	8.70
Squash	0.000	0.0001	0.0	2.00
Sunflower	0.000	0.0001	0.0	0.10
Vegetable	0.000	0.0001	0.0	2.70
WinterWheat	0.001	0.0022	0.0	8.70
Clear	0.000	0.0000	0.0	0.00

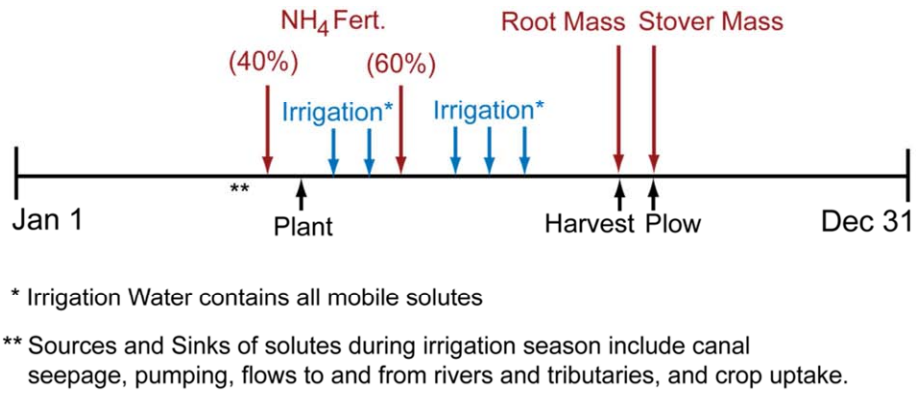

Figure 6- 17. Scheduling of fertilizer loading, planting, irrigation water application, harvesting, and plowing during a typical growing season. Root mass and stover mass are incorporated into the pool of soil organic matter during the harvest and plowing events, respectively.

Values of selected parameters (planting day, harvest day, N fertilizer loading, root mass, stover mass, Se root content, Se stover content) are perturbed stochastically to provide uncertainty in the parameter values and establish spatial heterogeneity in cultivation practices throughout the Upstream Study Region. Values for Se root content and Se stover content were generated from a lognormal distribution, whereas all others were generated using a normal distribution. Values of coefficient of variation (CV) are specified for each of the selected parameters, with values of 0.02, 0.01, 0.05, 0.10, 0.10, 0.05, and 0.05 used for planting day, planting day, harvest day, N fertilizer loading, root mass, stover mass, Se root content, and Se stover content, respectively. CV values were chosen to provide a reasonable range of parameter values. Resulting frequency distributions over fields for planting day, annual N fertilizer loading, and stover mass for a typical model-simulated cropping season are shown in Figure 6-18. The spatial distribution of annual N fertilizer loading (kg/ha) and applied stover mass (kg/ha) in the model domain for the 2006 growing season are shown in Figure 6-19. Notice the high values of N fertilizer loading and stover mass in areas of corn cultivation (comparing Figure 6-19 to Figure 6-5).

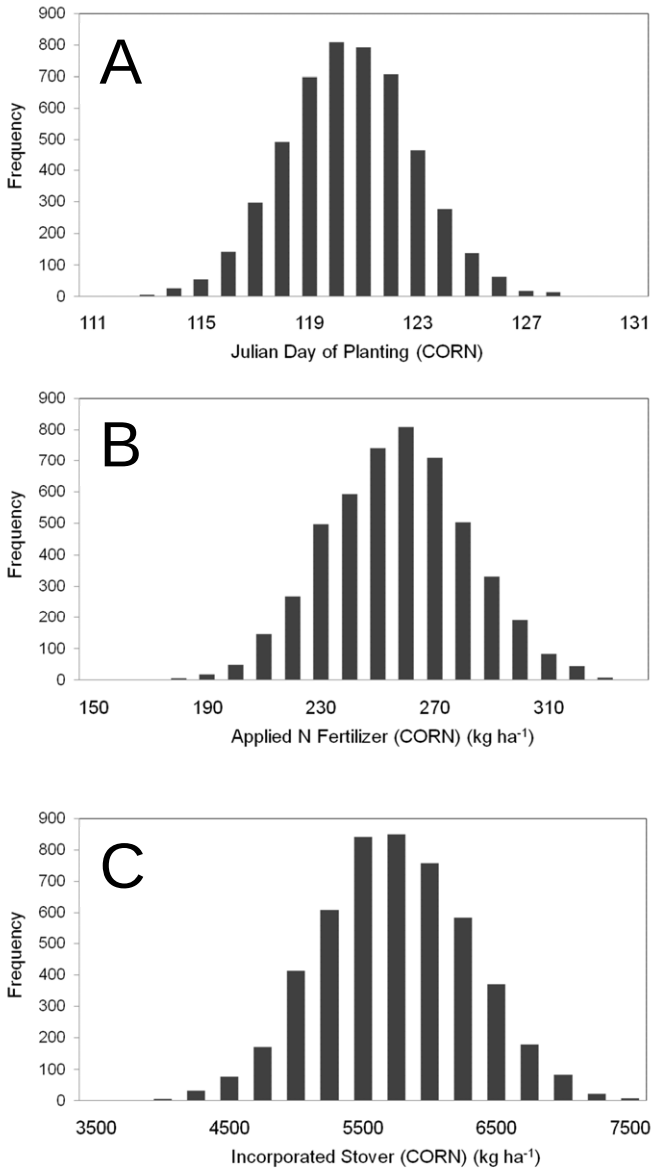

Figure 6- 18. Frequency distribution over fields of (A) corn planting day, (B) annual corn fertilizer loading, and (C) corn after-harvest stover mass for the Upstream Study. Values were generated from a normal distribution.

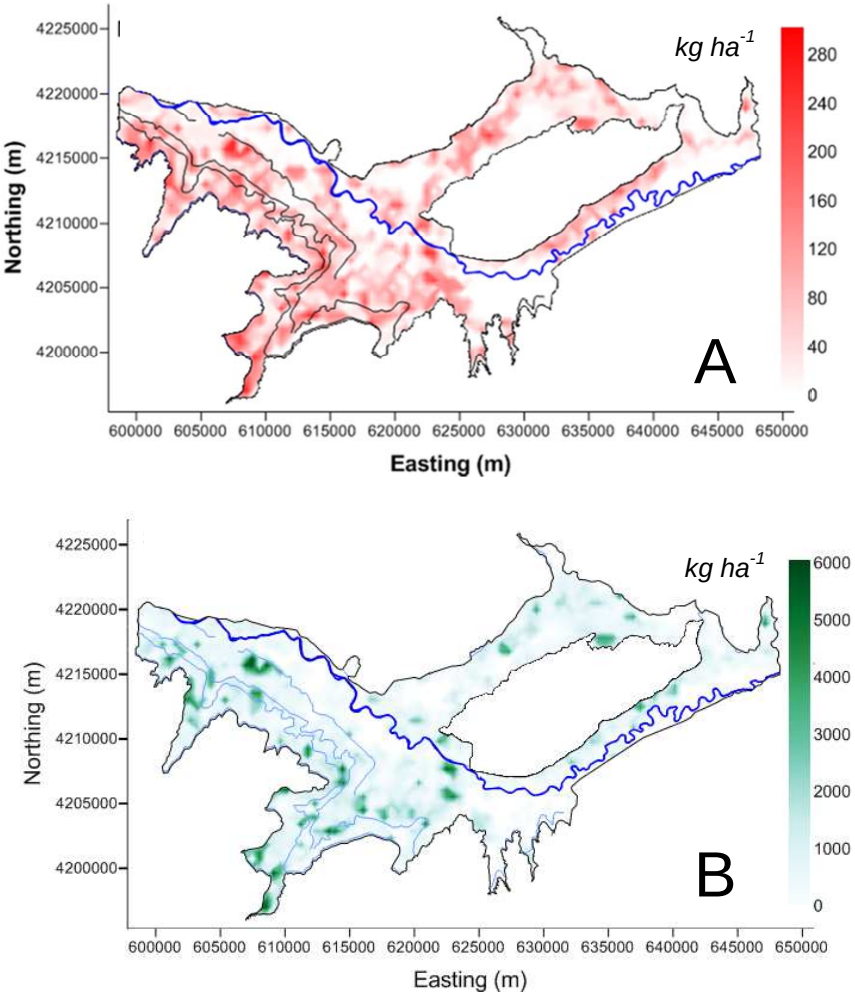

Figure 6- 19. Spatial distribution of (A) N fertilizer (kg/ha) and (B) incorporated stover (kg/ha) for the 2006 growing season.

6.4.1.3 Species Mass Exchange via Groundwater-Surface Water Interaction

The mass of each species brought into or removed from the subsurface system via groundwater-surface water interaction is calculated for the cells designated as River cells in the MODFLOW-UZF simulation of Morway and Gates (2012). For the case of groundwater discharge to surface water, the simulated species concentration in the grid cell is used in conjunction with the simulated volumetric flow rate to calculate the mass of each species removed from the aquifer and loaded to the surface water body. For the case of surface water

seepage to the aquifer, the species concentration in the surface water is used with the simulated volumetric flow rate to calculate the mass of species entering the aquifer.

For the latter case, the concentration of each species in the surface water must be specified. As the model does not simulate chemical transport in surface water, field measurements are used to specify species concentration in the canals and the Arkansas River. Details regarding this process are provided in Appendix A. For this simulation, field measurements are available for the following dates: June 20 2006, May 24 2007, October 11 2007, May 20 2008, June 26 2008, August 14 2008, January 17 2009, May 14 2009, and July 22 2009.

For the canals, the species concentration at the canal diversion point on the Arkansas River is used, with the species concentration assumed to be constant along the length of the canal (see Section 6.2.3 regarding model limitations). The species concentrations for each canal for each of the 9 sampling events are presented in Table 6-11, showing the discontinuous change in time of the concentration values. Notice that concentrations for NH_4, SeO_3, and SeMet are 0.00 for each canal and for each sampling event. For the Arkansas River, species' concentrations are available for each of the 9 sampling events at 9 sampling points along the reach of the river within the model domain. For the Arkansas River tributaries (Patterson Hollow, Timpas Creek, Crooked Arroyo, Anderson, Horsecreek, and Adobe Creek), one measurement of species concentration is available for all or most of the 9 sampling events.

Table 6- 11. Concentration of mobile species in each canal for each sampling event of 2006-2009, . Concentrations for O_2, NH_4, NO_3, and N_2 are given in mg L^{-1}, and concentrations for SeO_4, SeO_3, and SeMet are given in µg L^{-1}.

6/20/06	O_2	NH_4	NO_3	N_2	SeO_4	SeO_3	SeMet
Highline	7.43	0.00	1.20	0.00	2.63	0.00	0.00
Otero	7.43	0.00	1.20	0.00	3.28	0.00	0.00
Catlin	7.78	0.00	0.67	0.00	3.60	0.00	0.00
Rocky Ford	7.40	0.00	0.86	0.00	4.17	0.00	0.00
Fort Lyon	7.43	0.00	1.20	0.00	3.92	0.00	0.00
Holbrook	7.43	0.00	1.20	0.00	4.83	0.00	0.00
5/24/07							
Highline	9.57	0.00	1.33	0.00	4.50	0.00	0.00
Otero	9.57	0.00	1.33	0.00	4.99	0.00	0.00
Catlin	10.15	0.00	1.05	0.00	5.40	0.00	0.00
Rocky Ford	9.76	0.00	2.00	0.00	5.60	0.00	0.00
Fort Lyon	9.57	0.00	1.33	0.00	5.47	0.00	0.00
Holbrook	9.57	0.00	1.33	0.00	6.15	0.00	0.00
10/11/07							
Highline	9.67	0.00	1.32	0.00	8.92	0.00	0.00
Otero	9.67	0.00	1.32	0.00	8.92	0.00	0.00
Catlin	9.57	0.00	1.43	0.00	9.50	0.00	0.00
Rocky Ford	9.79	0.00	1.33	0.00	9.27	0.00	0.00
Fort Lyon	9.67	0.00	1.32	0.00	8.92	0.00	0.00
Holbrook	9.67	0.00	1.32	0.00	8.92	0.00	0.00
3/20/08							
Highline	9.44	0.00	1.88	0.00	6.23	0.00	0.00
Otero	9.44	0.00	1.88	0.00	8.32	0.00	0.00
Catlin	10.18	0.00	1.71	0.00	9.90	0.00	0.00
Rocky Ford	9.51	0.00	1.62	0.00	10.47	0.00	0.00
Fort Lyon	9.44	0.00	1.88	0.00	10.35	0.00	0.00
Holbrook	9.44	0.00	1.88	0.00	13.28	0.00	0.00
6/26/08							
Highline	7.71	0.00	0.60	0.00	2.57	0.00	0.00
Otero	7.71	0.00	0.60	0.00	3.09	0.00	0.00
Catlin	7.71	0.00	0.60	0.00	3.35	0.00	0.00
Rocky Ford	8.08	0.00	0.60	0.00	3.87	0.00	0.00
Fort Lyon	7.71	0.00	0.60	0.00	3.60	0.00	0.00
Holbrook	7.71	0.00	0.60	0.00	4.34	0.00	0.00
8/14/08							
Highline	9.32	0.00	2.00	0.00	6.00	0.00	0.00
Otero	9.32	0.00	2.00	0.00	8.74	0.00	0.00
Catlin	9.55	0.00	1.70	0.00	10.20	0.00	0.00
Rocky Ford	9.27	0.00	1.70	0.00	11.80	0.00	0.00
Fort Lyon	9.32	0.00	2.00	0.00	11.40	0.00	0.00
Holbrook	9.32	0.00	2.00	0.00	15.23	0.00	0.00
1/17/09							
Highline	13.22	0.00	2.87	0.00	14.71	0.00	0.00
Otero	13.22	0.00	2.87	0.00	14.71	0.00	0.00
Catlin	12.50	0.00	3.30	0.00	16.90	0.00	0.00
Rocky Ford	13.32	0.00	2.90	0.00	13.30	0.00	0.00
Fort Lyon	13.22	0.00	2.87	0.00	14.71	0.00	0.00
Holbrook	13.22	0.00	2.87	0.00	14.71	0.00	0.00
5/14/09							
Highline	8.58	0.00	1.09	0.00	6.72	0.00	0.00
Otero	8.58	0.00	1.09	0.00	7.14	0.00	0.00
Catlin	8.67	0.00	1.20	0.00	7.54	0.00	0.00
Rocky Ford	8.74	0.00	1.20	0.00	8.10	0.00	0.00
Fort Lyon	8.58	0.00	1.09	0.00	7.54	0.00	0.00
Holbrook	8.58	0.00	1.09	0.00	8.13	0.00	0.00
7/22/09							
Highline	8.52	0.00	0.90	0.00	6.10	0.00	0.00
Otero	8.52	0.00	0.90	0.00	6.10	0.00	0.00
Catlin	8.52	0.00	0.90	0.00	6.10	0.00	0.00
Rocky Ford	7.56	0.00	1.20	0.00	7.31	0.00	0.00
Fort Lyon	8.52	0.00	0.90	0.00	6.10	0.00	0.00
Holbrook	8.52	0.00	0.90	0.00	6.10	0.00	0.00

6.4.1.4 Chemical Reaction Parameters

A list of parameters for the chemical reactions and associated values are presented in Table 6-12. The parameters are grouped according to affected species: General reaction parameters, for C species and O_2; Nitrogen reaction parameters, for N species; and Selenium reaction parameters, for Se species. The parameter values listed in Table 6-12 are derived from the published literature (e.g., Johnsson et al., 1987; Tokanuga et al., 1997; Guo et al., 2000; Lee et al., 2006) and are used in pre-calibration simulations and sensitivity analysis simulations presented in Section 6.4.2. Values can be either spatially-constant or spatially-variable. In the pre-calibration simulations, the values are treated as spatially-constant. They are varied spatially during model calibration according to canal command area. As discussed in Chapter 4, a reaeration term is also included that supplies O_2 mass to the saturated zone via gaseous diffusion from the ambient atmosphere through the unsaturated zone. However, the supply of O_2 mass to the pore water in the unsaturated zone via gaseous transport is not included.

The first-order rate constant λ values represent the maximum rate of reaction for a given chemical reaction. As described in Chapter 5, these rates are tempered according to (i) concentration of species, (ii) concentration of other reactant species, (iii) the presence of e^- donors for reactions of chemical reduction, (iv) the presence of inhibiting, higher-redox species, and (v) soil temperature and soil water content. The measured daily average air temperature at the Rocky Ford climatic station at the AVRC, used in the model to calculate soil temperature using the method described in Chapter 5, is shown in Figure 6-20A. The percentage of maximum microbial activity as a function of percent soil saturation for mineralization, denitrification, and general chemical reactions is shown in Figure 6-20B.

As described in Chapter 5, available dissolved organic carbon for microbial-mediated chemical reduction reactions is quantified according to the amount of carbon dioxide (CO_2) released during organic matter decomposition, which in the model occurs only under cultivated fields. Hence, for non-cultivated riparian zones (see Figure 6-1) the presence of organic carbon is not used as a factor in tempering the rate constants λ.

Table 6- 12. Parameters for chemical reactions involving General species (C species, O_2), N species, and Se species. Variable names and description are given in Appendix A.

General		Nitrogen		Selenium	
λ_L	0.25	I_{O_2}	1.0	$B_{C/Se}$	122.5
λ_H	0.003	I_{NO_3}	0.5	$H_{C/Se}$	175
f_e	0.5	$B_{C/N}$	8.0	$\lambda_{SeO_4}^{het}$	0.02
f_h	0.2	$H_{C/N}$	12	$\lambda_{SeO_3}^{het(Se_s)}$	0.02
K_{CO_2}	0.75	λ_{nit}	0.8	$\lambda_{SeO_3}^{het(SeMet)}$	0.02
K_{O_2}	1.0	λ_{vol}	0.1	λ_{SeMet}^{het}	0.02
$\lambda_{O_2}^{het}$	2.0	K_{NO_3}	10	K_{Se}	1000
$\lambda_{O_2}^{auto}$	0.1	$\lambda_{NO_3}^{het}$	0.1	K_{d,SeO_3}	0.10
		$\lambda_{NO_3}^{auto}$	0.01		
		K_{d,NH_4}	3.50		

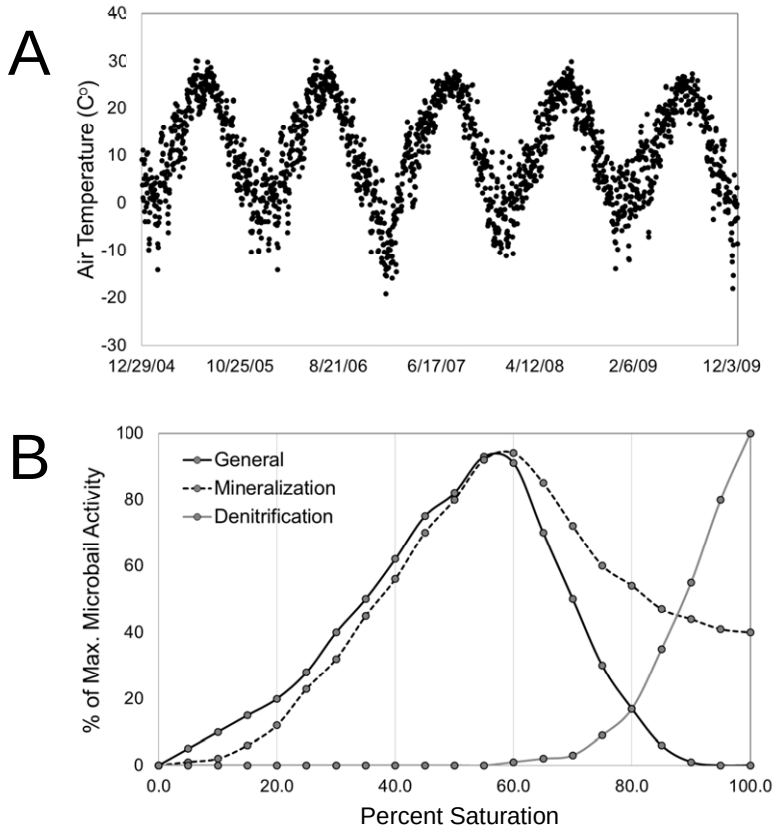

Figure 6- 20. System variables influencing the rate of reaction of microbial-mediated chemical reactions - (A) Daily average air temperature as measured at the Rocky Ford climatic station at the Arkansas Valley Research Center, and (B) Percent of maximum microbial activity as a function of percent soil saturation, demonstrating the dependence of microbial-mediated chemical reactions on the presence/absence of soil water.

In order to account for the autotrophic reduction of O_2 and NO_3 in the presence of shale and the resulting release of SeO_4 into the groundwater, the spatial distribution of bedrock shale as well as shale near the ground surface needs to be delineated and mapped to the grid cells. During field sampling it also was recognized that a yellow clay material (presumably weathered shale) located in certain portions of the aquifer also contained residual Se as well as released vast amounts of SeO_4 into the groundwater (see Chapter 2). Yellow clay hence is treated as shale in the model application.

To designate grid cells as shale, yellow clay, or alluvium, the spatial distribution of near-surface shale shown in Figure 6-1, along with known locations of yellow clay using borehole

data, is mapped onto the model grid. Furthermore, the bottom layer of the grid comprises the bedrock and hence also is designated as shale. Using the 3-layer grid of Morway and Gates (2012), the resulting material type for each grid cell for each of the three layers is shown in Figure 6-21, with the shale material designated as Niobrara, Carlisle, or Graneros. Greenhorn Limestone also is present, and is treated as shale since it too contains $FeSe_2$. The material type for each layer is then mapped to the seven-layer grid using the system shown in Figure 6-16. The material type for each grid cell in the model domain is read into RT3DAG, and used to determine locations of autotrophic reduction of O_2 and NO_3. Autotrophic reduction proceeds within a given cell if any adjacent cell has a shale material type, with the possibility of multiple shale cells surrounding the cell. Reaction rate laws for these processes are given in Chapter 5.

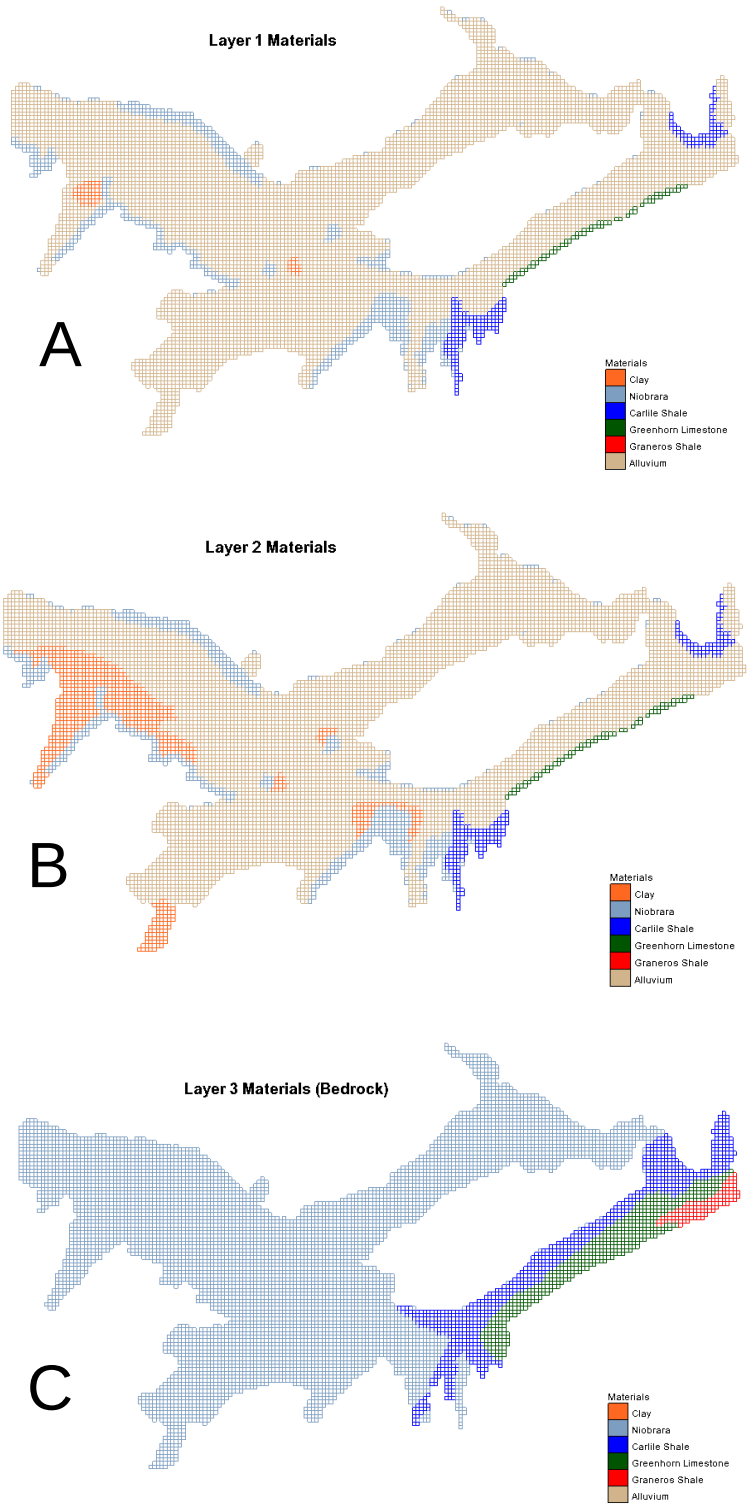

Figure 6- 21. Material types (shale, yellow clay, or alluvium) for the three layers in the grid layering in Morway and Gates (2012). Shale consists of the Niobrara, Carlisle, and Graneros formations as well as Greenhorn Limestone. The layer material types are mapped to the 7-layer grid using the process shown in Figure 6-16.

6.4.2 Model Results

Using the information regarding the species mass sources and sinks and chemical reactions, the model is used to simulate species groundwater concentrations and mass loadings to surface water bodies for the years 2006-2009. In order to achieve concentration values that are in dynamic equilibrium with the system, a 20-year spin-up simulation is run to provide spatial distributions of species concentrations as initial conditions for the 2006-2009 simulation. Using a spin-up simulation to achieve equilibrium often is used in hydrologic modeling studies (e.g., Rodell et al., 2005). In this study, the seasonal forcing terms (applied irrigation water, fertilizer loading, etc.) from 2006 were used for each year of the 20-year period in order to achieve steady seasonal fluctuations in species concentrations. Initially the required length of the spin-up simulation, i.e., the simulation length required to achieve a dynamic equilibrium in species concentration fluctuation and mass loadings to surface water, was not known. However, using successive 10-year simulations, with the end of one simulation providing the initial conditions for the next 10-year simulation, it was concluded that 20 years is an adequate simulation period to achieve dynamic equilibrium.

Model-response targets used to estimate model parameters include spatio-temporal averages of groundwater concentrations and mass exchange of Se between the aquifer and the Arkansas River. For the first, groundwater concentrations are averaged for each of the four sampling events of the calibration period according to command area, as described in Section 6.3.2. For the second, mass exchange between the aquifer and the Arkansas River is summed along the length of the river within the model domain, also described in Section 6.3.2. Although not a target for calibration, time-series comparisons between observed NO_3 and SeO_4 concentrations and corresponding grid-cell calculated concentrations for each of the 93 observation wells are

presented in Appendix B to demonstrate that the model is able to produce cell-by-cell results that are similar in magnitude and range to observed point values.

For additional model corroboration, supplementary comparisons between observed and simulated species concentrations in the groundwater are performed at the scale of the model domain. These are designated as global comparisons, and are included to verify that the model captures the large-scale system behavior identified through analysis of field measurements. These global measures include (i) the relationship between NO_3 and SeO_4 concentration in groundwater, (ii) the portion of dissolved Se in groundwater attributed to SeO_4 (with the remaining attributed to SeO_3), and (ii) frequency distributions of NO_3 and SeO_4 concentration in the groundwater. For each global measure, concentration values are grouped according to either the calibration period or the testing period.

6.4.2.1 Estimation of Model Parameters

This section provides details regarding the method of parameter estimation using observed concentrations and mass loadings during the 2006-2008 calibration period. In summary, the methodology includes a combination of automated calibration and manual calibration, with the PEST (Parameter ESTimation) software (Doherty, 2007) used for automated calibration. An iterative approach using both the 20-year spin-up simulation and the 2006-2008 simulation was used in the model calibration procedure due to the dependence of initial concentrations on the parameter values used in the spin-up simulation. The overall procedure is explained in detail in the following sections, and is summarized here as well as in Figure 6-22:

(i) Establish initial set of initial conditions for the 2006-2008 simulation using a 20-year spin-up simulation

(ii) Use sensitivity analysis for 2006-2008 simulation to identify influential parameters

(iii) Use PEST to provide initial set of estimated parameters, with parameter values assigned to each command area and groundwater concentrations averaged according to command area

(iv) Re-run the 20-year spin-up with the new parameter values to establish new set of initial conditions, with comparisons made between to the estimated exchange of Se mass between the aquifer and Arkansas River. The spin-up simulation was re-run using different values of $\lambda_{SeO_4}^{het}$ until the mass loadings at the end of the 20-year simulation matched well with the range of observed daily mass loadings during the 2006-2008 time period.

Steps (iii) and (iv) are repeated in an iterative fashion until both groundwater concentrations and mass loadings simulated by the model compare to a satisfactory degree with observed values. Initial attempts to include Se mass loadings as a target in the automated calibration step proved unsuccessful due to the large scatter and the lack of spatial variability in the observed mass loading values. Mass loadings thus were not included in step (iii).

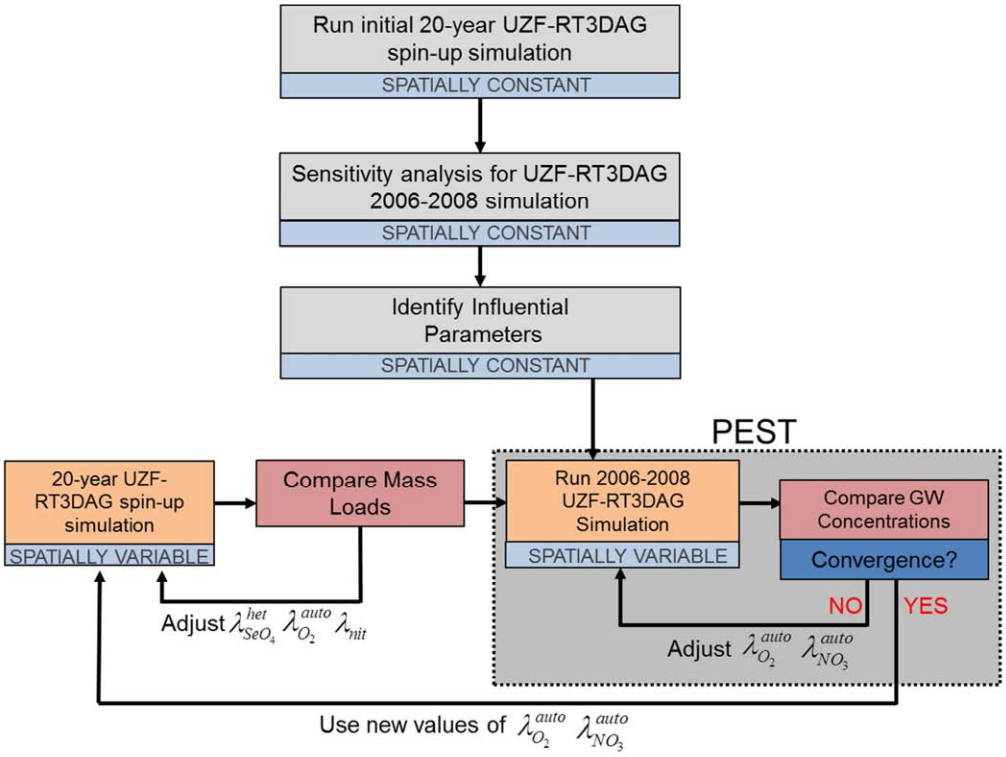

Figure 6- 22. Method for initialization model simulation and performing estimation of UZF-RT3DAG model parameters.

6.4.2.1.1 Preliminary Set of Initial Concentrations for the 2006-2008 Simulation

Following the procedure outlined in Figure 6-22, the first step in the model calibration process consisted of establishing a preliminary set of initial concentrations throughout the model domain for each species for the 2006-2008 simulation. This was achieved through a 20-year spin-up simulation in which the flow and cropping patterns for the year 2006 were repeated for 20 years, with the parameter values contained in Tables 6-7, 6-8, 6-9, 6-10, and 6-12 used for the crop and chemical reaction parameters. Chemical reaction parameters were spatially-constant. Each grid layer was given an initial concentration for each species at the beginning of the 20-year spin-up simulation. These values were taken from modeling studies in the literature (e.g.,

Birkinshaw and Ewen, 2000a) as well as results from soil water samples at the AVRC as described in Chapter 5. Values for selected species are shown in Table 6-13. Concentrations of organic species such as L_N and L_{Se} (litter pool concentration of N and Se) have values greater than 0.0 only for grid layers within the root zone. Initial concentrations for each grid cell for the beginning of the 20-year spin-up simulation were assigned according to amount of cultivation, i.e., the concentration values in Table 6-13 were scaled according to the ratio of spatial area occupied by cultivated fields to the spatial area of the grid cell. This process was adopted in order to prevent unrealistic species concentrations in non-cultivated areas. Examples of the achieved equilibrium for both groundwater concentrations and mass loadings to surface water are shown in Section 6.4.2.1.4 when the final spin-up simulation results are shown.

Table 6- 13. Initial values of concentration for selected species for each layer of the grid.

Model Layer	O_2 mg L^{-1}	L_N g m_s^{-3}	NH_4 mg L^{-1}	NO_3 mg L^{-1}	L_{Se} g m_s^{-3}	SeO_4 µg L^{-1}
1	5.00	10.00	1.00	7.00	0.57	40.00
2	2.00	2.00	0.50	4.00	0.11	20.00
3	2.00	2.00	0.50	4.00	0.11	20.00
4	1.00	0.00	0.50	4.00	0.00	20.00
5	1.00	0.00	0.00	2.00	0.00	20.00
6	1.00	0.00	0.00	2.00	0.00	20.00
7	0.00	0.00	0.00	0.00	0.00	0.00

6.4.2.1.2 Identification of Influential Parameters using Sensitivity Analysis

Using the set of concentrations from the end of the 20-year spin-up simulation as the initial concentrations for the model calibration period, a sensitivity analysis was run on the 2006-2008 simulation using the FAST (Fourier Amplitude Sensitivity Test) (Cukier et al., 1973) method to determine the influence of selected parameters and system sources/sinks on model results. Parameters and sources/sinks to be tested for influence were selected due to their supposed

influence on C_{NO_3} and C_{SeO_4} in groundwater, leaching of NO_3 and SeO_4 in the upper grid layers, and mass loadings of NO_3 and SeO_4 to the Arkansas River.

Selected source/sink terms include NH_4 fertilizer, seasonal N uptake, seasonal Se uptake, and C_{NO_3} and C_{SeO_4} in surface water. Selected chemical reaction parameters include the rates of litter pool decomposition, λ_L; humus pool decomposition, λ_H; autotrophic reduction of O_2 in the presence of shale, $\lambda_{O_2}^{auto}$; autotrophic reduction of NO_3 in the presence of shale, $\lambda_{NO_3}^{auto}$; nitrification, λ_{nit}; NH_4 volatilization, λ_{vol}; and heterotrophic reduction of NO_3, $\lambda_{NO_3}^{het}$; and heterotrophic reduction of SeO_4, $\lambda_{SeO_4}^{het}$. A total of 1053 simulations were run to analyze the influence of all 13 parameters and source/sink terms. For each simulation the parameter values were perturbed around an average value, with the average values contained in Tables 6-7 to 6-10. All parameters were perturbed using a CV of 0.2 except for the surface water concentration of NO_3 and SeO_4, which were perturbed using a CV of 0.3. CV values were determined by comparing the resulting spread of parameter values to values found in the literature and from field data in the LARV. Chemical reaction parameters were perturbed according to a lognormal distribution, whereas all others were perturbed according to a normal distribution.

Resulting C_{NO_3} and C_{SeO_4} in groundwater from each of the 1053 simulations were spatially-averaged globally (across the entire model domain), according to command area, and according to crop type. The latter two were included to determine if parameter influences varied according to irrigation and cultivation patterns. For example, to see if parameters in corn-cultivated areas influenced simulated NO_3 concentrations differently than in alfalfa-cultivated areas. Concentrations also were averaged temporally, with concentrations averaged across the dormant season, the growing season, and over the entire year for each year of the simulation. Mass

loadings of NO_3 and SeO_4 to the Arkansas River also were processed for each simulation to determine parameter influence.

A limited number of results are shown in this chapter, with additional results shown in Appendix C. Results are presented using global sensitivity plots, with the first-order sensitivity index, S_i (the main effect of the parameter on the change in model output), along the abscissa and the interaction effect, S_{t_i} (effect of the parameter on the change in model output due to interaction with other parameters), along the ordinate. The parameter labels shown in Figures 6-23 to 6-25 are defined in Appendix C. Figure 6-23 shows the results for C_{NO_3} in groundwater averaged across the entire model domain during the years 2006 and 2007, with λ_{nit}, C_{NO_3} of surface water, and $\lambda_{NO_3}^{auto}$ governing simulated C_{NO_3} in groundwater. The parameter λ_{nit} has a stronger influence in 2007 relative to $\lambda_{NO_3}^{auto}$ and C_{NO_3} of surface water than in 2006. Similar plots are shown for C_{SeO_4} in groundwater during 2006 and 2007 in Figure 6-24, with $\lambda_{O_2}^{auto}$ clearly dominating the resulting concentration. The influence of parameters, however, can vary locally within the model domain. For example, $\lambda_{NO_3}^{auto}$ has a stronger influence than $\lambda_{O_2}^{auto}$ on both C_{NO_3} and C_{SeO_4} in groundwater within the Catlin canal command area for the year 2007, as shown in Figure 6-25. This likely is due to the high number of fields within the Catlin canal command area that cultivate corn, and hence a larger loading of N fertilizer and a higher concentration of NO_3 in the groundwater, relative to the other command areas.

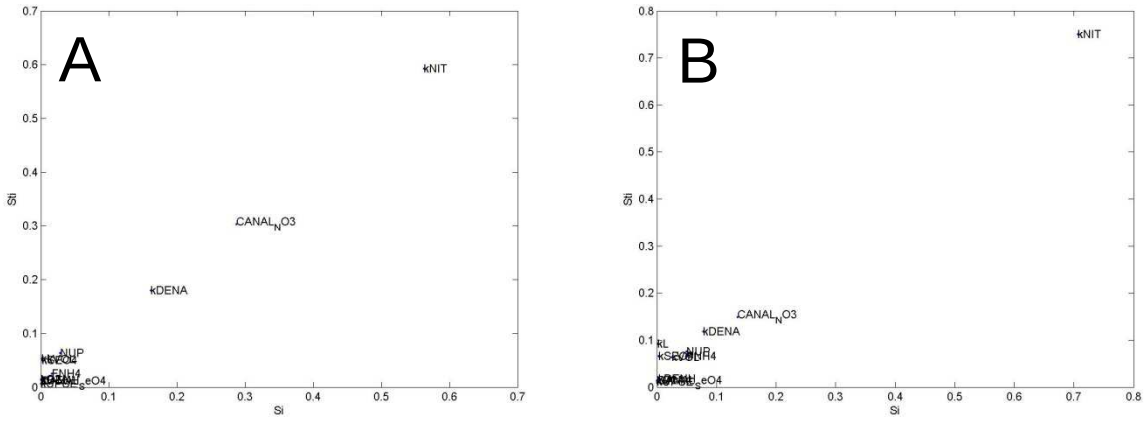

Figure 6- 23. Global sensitivity of plots for model domain-averaged NO_3 groundwater concentration for (A) 2006 and (B) 2007.

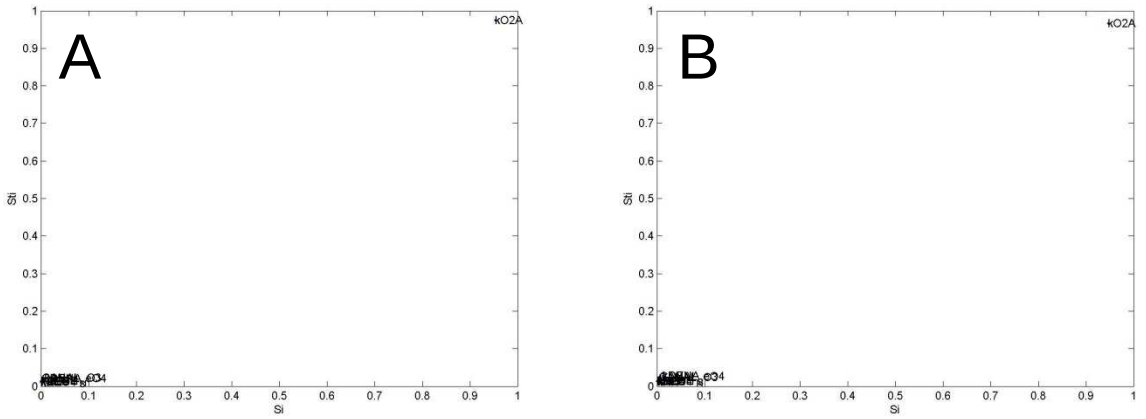

Figure 6- 24. Global sensitivity of plots for model domain-averaged SeO_4 groundwater concentration for (A) 2006 and (B) 2007.

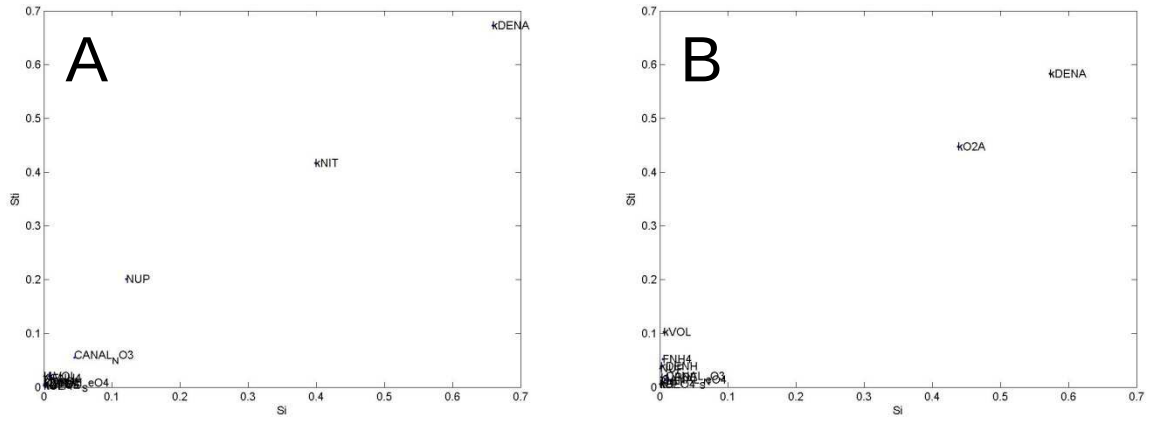

Figure 6- 25. Global sensitivity of plots for (A) NO_3 and (B) SeO_4 groundwater concentrations within the Catlin canal command area for the year 2007.

These results indicate that, on the scale of the model domain or the scale of a command area, λ_{nit} , $\lambda_{O_2}^{auto}$, and $\lambda_{NO_3}^{auto}$ can be modified to yield simulated groundwater concentrations and mass loadings that compare favorably with observed data. The results of such an exercise are presented in the following section.

Additional results showing the influence of the parameters on groundwater concentration, mass leaching, and mass loading to surface water according to the entire model domain, the individual command areas, and crop type are presented in Appendix C. Results lend valuable insight into system processes and system inputs that require investigation or appropriate management techniques to control mass transfer and accumulation of NO_3 and SeO_4 in the aquifer and adjoining surface water bodies.

6.4.2.1.3 Using PEST to estimate Command Area Chemical Reaction Parameters

Values of the parameters λ_{nit}, $\lambda_{O_2}^{auto}$, and $\lambda_{NO_3}^{auto}$, identified to be most influential on C_{NO_3} and C_{SeO_4} in groundwater, were assigned to each command area and estimated with PEST using the command area average values of C_{NO_3} and C_{SeO_4} in groundwater shown in Tables 6-3 and 6-5. PEST minimizes the objective function, which in this simulation is defined as the sum of squared deviations between model predictions and observations. During each iteration of the PEST simulation, the model was run once for each included parameter in order to calculate the parameter covariance matrix, upon which model results were compared to observed values and a new parameter was identified for the next iteration. The PEST simulation would terminate upon convergence to a minimal objective function.

Sensitivity indices also are calculated at each iteration, with the indices for the first iteration of the PEST simulation shown in Figure 6-26 for C_{SeO_4}. As seen in the figure, $\lambda_{O_2}^{auto}$ has overall a stronger influence on C_{SeO_4} than $\lambda_{NO_3}^{auto}$, although $\lambda_{NO_3}^{auto}$ has a strong influence in the Catlin command area. This also was seen in Figure 6-25. As expected, $\lambda_{O_2}^{auto}$ and $\lambda_{NO_3}^{auto}$ have stronger influences in command areas that contain large amounts of shale. Initial PEST runs indicated that λ_{nit} did not have a sufficient influence on C_{NO_3} to modify the command area λ_{nit} rates during the 2006-2008 simulation. However, as discussed in Section 6.4.1.2.4 the λ_{nit} rates did influence C_{NO_3} during the spin-up simulation and hence were used in a manual calibration.

For this initial run of PEST, the objective function was minimized from 30,601 to 4,037 after 8 iterations. The initial and final values of $\lambda_{O_2}^{auto}$ and $\lambda_{NO_3}^{auto}$ for each command area are shown in Table 6-14, and the initial, PEST-derived, and final values of simulated C_{SeO_4} in the groundwater

averaged for each command area are shown in Table 6-15. Final values were determined by modifying PEST-derived values during a re-run of the 20-year spin-up simulation. The initial, PEST-derived, and final values for C_{NO_3} and C_{O_2} (Tables 6-16 and 6-17) for the PEST run are the same for each command area since $\lambda_{O_2}^{auto}$ and $\lambda_{NO_3}^{auto}$, although significantly affecting C_{SeO_4}, have a negligible influence on C_{NO_3} and C_{O_2} when averaging concentration values over each command area.

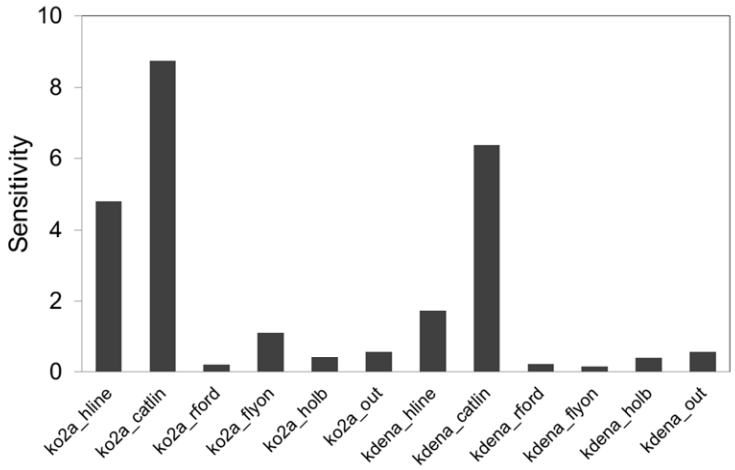

Figure 6- 26. Sensitivity index of $\lambda_{O_2}^{auto}$, and $\lambda_{NO_3}^{auto}$ for C_{SeO_4} in groundwater as computed by PEST. ko2a variables refer to $\lambda_{O_2}^{auto}$, and kdena variables refer to $\lambda_{NO_3}^{auto}$ for the command areas.

Table 6- 14. Initial, PEST-derived, and final values of $\lambda_{O_2}^{auto}$, $\lambda_{NO_3}^{auto}$, λ_{nit}, and $\lambda_{SeO_4}^{het}$ for each command area. The final values were determined by modifying the PEST-derived values during a re-run of the 20-year spin-up simulation.

Parameter	Command	Pre-PEST	PEST	Final
$\lambda_{O_2}^{auto}$	Highline	0.10000	0.70280	0.45000
	Catlin	0.10000	3.00000	3.00000
	Rocky Ford	0.10000	0.00012	0.00012
	Fort Lyon	0.10000	0.00010	0.00010
	Holbrook	0.10000	0.10801	0.04000
	Outside	0.10000	0.49179	0.01000
$\lambda_{NO_3}^{auto}$	Highline	0.01000	0.00032	0.00032
	Catlin	0.01000	1.00000	1.00000
	Rocky Ford	0.01000	0.00018	0.00018
	Fort Lyon	0.01000	0.00028	0.00028
	Holbrook	0.01000	0.30308	0.30308
	Outside	0.01000	0.00998	0.00998
λ_{nit}	Highline	0.80000	0.80000	1.50000
	Catlin	0.80000	0.80000	2.00000
	Rocky Ford	0.80000	0.80000	1.00000
	Fort Lyon	0.80000	0.80000	0.80000
	Holbrook	0.80000	0.80000	0.20000
	Outside	0.80000	0.80000	0.40000
$\lambda_{SeO_4}^{het}$	-	0.02000	0.02000	0.02000

Table 6- 15. SeO_4 concentration averages for each command area

Command	Observed	Pre-PEST*	PEST	Final
Highline	93.9	93.9	95.2	93.4
Catlin	121.1	17.6	96.4	118.1
Rocky Ford	10.9	51.3	68.4	167.9
Fort Lyon	16.8	141.1	27.7	17.9
Holbrook	44.1	78.6	44.2	54.5
Outside	123.4	163.6	123.1	65.5

*Using initial 20-year spin-up simulation for initial conditions

Table 6- 16. NO_3 concentration averages for each command area

Command	Observed	Pre-PEST*	PEST	Final
Highline	7.99	3.5	3.5	5.6
Catlin	11.90	1.7	1.7	2.2
Rocky Ford	4.89	2.7	2.7	3.1
Fort Lyon	3.75	3.2	3.2	3.6
Holbrook	2.42	5.7	5.7	6.0
Outside	2.91	4.8	4.8	4.3

*Using initial 20-year spin-up simulation for initial conditions

Table 6- 17. O_2 concentration averages for each command area

Command	Observed	Pre-PEST*	PEST	Final**
Highline	2.8	0.7	0.7	2.0
Catlin	2.3	1.9	1.9	3.6
Rocky Ford	3.4	1.7	1.7	4.2
Fort Lyon	2.5	2.3	2.3	3.7
Holbrook	2.5	4.8	4.8	6.4
Outside	1.8	3.3	3.3	3.6

*Using initial 20-year spin-up simulation for initial conditions

**Including reaeration term in the reaction system

6.4.2.1.4 Additional Parameter Value Modification Using Spin-up Simulation

Using the values of $\lambda_{O_2}^{auto}$ and $\lambda_{NO_3}^{auto}$ derived from the PEST simulation, the 20-year spin-up simulation is re-run to allow these new parameter values to impact the initial conditions of the 2006-2008 simulation. If this process is not undertaken, i.e. if the parameter values used in the spin-up simulation are different than those used in the 2006-2008 simulation, then the dynamic equilibrium achieved during the spin-up simulation may not occur during the 2006-2008 simulation, with species concentrations either increasing or decreasing to obtain a new steady seasonal fluctuation. It also was recognized that $\lambda_{O_2}^{auto}$, which governs the release of SeO_4 from shale, had a strong influence on the loading of SeO_4 mass to the Arkansas River, particularly for command areas with grid cells adjacent to the river (e.g., Holbrook and the outside area). Hence, values for this parameter were modified during the re-run of the spin-up simulation, as shown in Figure 6-22. It also should be noted that the reaeration term, described in Chapter 4, was included in the model at this point of the parameter estimation process. With more O_2 supplied to the saturated zone and hence more O_2 available for oxidation of residual Se from shale, values of $\lambda_{O_2}^{auto}$ required further modification.

Additionally, it was recognized that other parameters, although not influential during the 2006-2008 simulation, nevertheless are influential during the 20-year simulation period in

establishing dynamic equilibrium for groundwater concentration and mass loading to surface water. For example, analysis of the spin-up simulation revealed that $\lambda_{SeO_4}^{het}$ influences strongly the mass of Se discharged to surface water, particularly in the riparian zones along the Arkansas River and its tributaries (see Figure 6-1). Also, λ_{nit} was found to influence the command area-averaged C_{NO_3} in groundwater during the spin-up simulation. As such, λ_{nit} was varied according to command area. This process is shown in Figure 6-22, with the spin-up simulation re-run multiple times to investigate the influence of these parameters and to determine the final values of the model parameters.

Overall, parameter values were modified across multiple runs of the spin-up simulation until the final groundwater concentrations and mass loadings of the spin-up simulation and the values during the 2006-2008 simulation matched favorably with the observed values. For example, Figure 6-27 shows the daily mass loadings of SeO_4 to the Arkansas River during the 20-year spin-up simulation using four different values of $\lambda_{SeO_4}^{het}$: 0.008 d^{-1}, 0.02 d^{-1}, 0.04 d^{-1}, and 0.08 d^{-1}. As seen in the plot, lower values of $\lambda_{SeO_4}^{het}$ (e.g., 0.008 d^{-1}) allow more SeO_4 to enter the Arkansas River since less mass of SeO_4 is chemically reduced in the riparian areas along the river. The daily mass loadings at the end of the 20-year period were compared with the range of observed values during the 2006-2008 time period (see Figure 6-9) to determine the value of $\lambda_{SeO_4}^{het}$ that should be adopted for the system. As seen in the plot, the simulation using a value of 0.08 d^{-1} was not run for the 10-20 year time period since it became clear after a simulation of 10 years that the mass loadings were much lower than the observed values. The value of 0.02 d^{-1}, which in fact is the value used initially (see Table 6-14), was adopted.

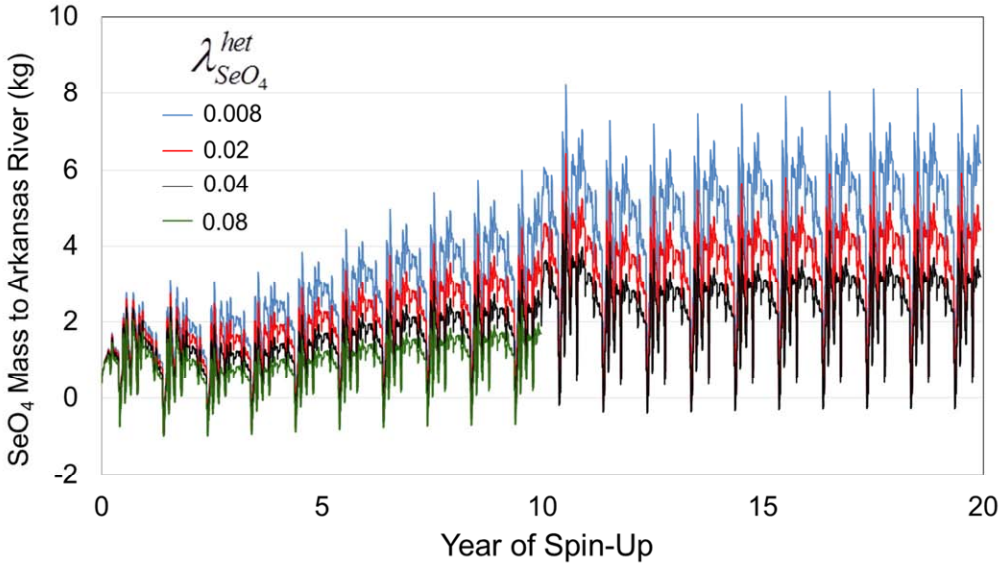

Figure 6- 27. Daily mass loadings of SeO_4 to the Arkansas River during the 20-year spin-up simulation, using four different values of $\lambda_{SeO_4}^{het}$ (0.008, 0.02, 0.04, 0.08).

Also, it was found that $\lambda_{O_2}^{auto}$ for the Holbrook command area and the Outside area needed to be lowered to preclude unrealistic large loadings of SeO_4 to the river. The value of $\lambda_{O_2}^{auto}$ for the Holbrook command and Outside area were decreased from 0.108 to 0.040 d^{-1} and from 0.491 to 0.01 d^{-1}, respectively. For the Outside, this decrease in $\lambda_{O_2}^{auto}$ lowered the resulting average C_{SeO_4} in groundwater from 123.1 µg L^{-1} to 65.5 µg L^{-1} when used in the 2006-2008 simulation. This is shown in Table 6-15. Although this lessened the match between the observed (123.4 µg L^{-1}) and simulated value, the decrease was necessary for providing reasonable values of SeO_4 mass loading. Hence, an interplay between $\lambda_{O_2}^{auto}$ (releasing SeO_4 into the groundwater and influencing the resulting mass loading to surface water) and $\lambda_{SeO_4}^{het}$ (chemically reducing SeO_4 in the riparian zone and also influencing the mass loading to surface water) was required in parameter value modification.

The final set of parameter values are shown in Table 6-14. Values for $\lambda_{NO_3}^{auto}$ were not modified during the re-run of the spin-up simulation. As shown in the next section, the final set of parameter values were used for the 2006-2008 simulation to verify that model results compared reasonably well with observed values. In summary, although the squared difference between the concentration values are least for the case of using the PEST-derived parameter values, these concentration values were changed as parameter values were modified in the re-run of the spin-up simulation.

The plot shown in Figure 6-27 also shows that 20 years is adequate for the seasonal fluctuations of SeO_4 mass loading to reach a dynamic equilibrium. Figure 6-28 shows the daily mass loading for both SeO_4 and NO_3 during the spin-up simulation. Notice that NO_3 loading reaches a steady seasonal fluctuation after only about 5 years. Additional demonstrations of dynamic equilibrium and typical ranges of concentration fluctuations are shown in Figures 6-29 to 6-31. Figure 6-29 shows the fluctuation of C_{SeO_4} in groundwater for three different sets of grid cells. In Figure 6-29A, the selected grid cells are adjacent to shale, hence demonstrating the typically high concentrations resulting from oxidation of residual Se, and in Figures 6-29B and 6-29C the grid cells are in layers 1 and 4, respectively, for various crop types. Figure 6-30 shows the fluctation of C_{NO_3} in layers 1 and 4 for various crop type, and Figure 6-31 shows the fluctuation of L_N and L_{Se} in layer 1 for various crop types. The range of fluctuation of C_{NO_3} and L_N in layer 1 varies from year-to-year due to the stochastic perturbation of NH_4 fertilizer and stover mass that is applied each year. As seen in Figure 6-30A and Figure 6-31A, this affects primarily the cell with corn cultivation, since the fertilizer loading is higher than for other crops (see Table 6-9) and since the stover mass is approximatley ten time higher than for other crops (see Table 6-7).

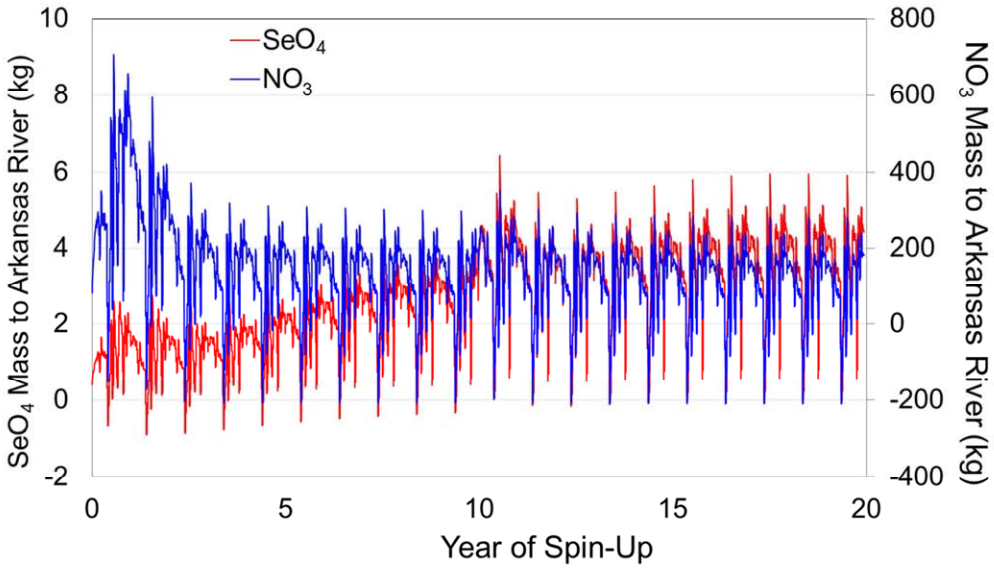

Figure 6- 28. Daily mass loadings of SeO_4 and NO_3 to the Arkansas River during the 20-year spin-up simulation. For Se, the value of $\lambda_{SeO_4}^{het}$ is 0.02 d^{-1}.

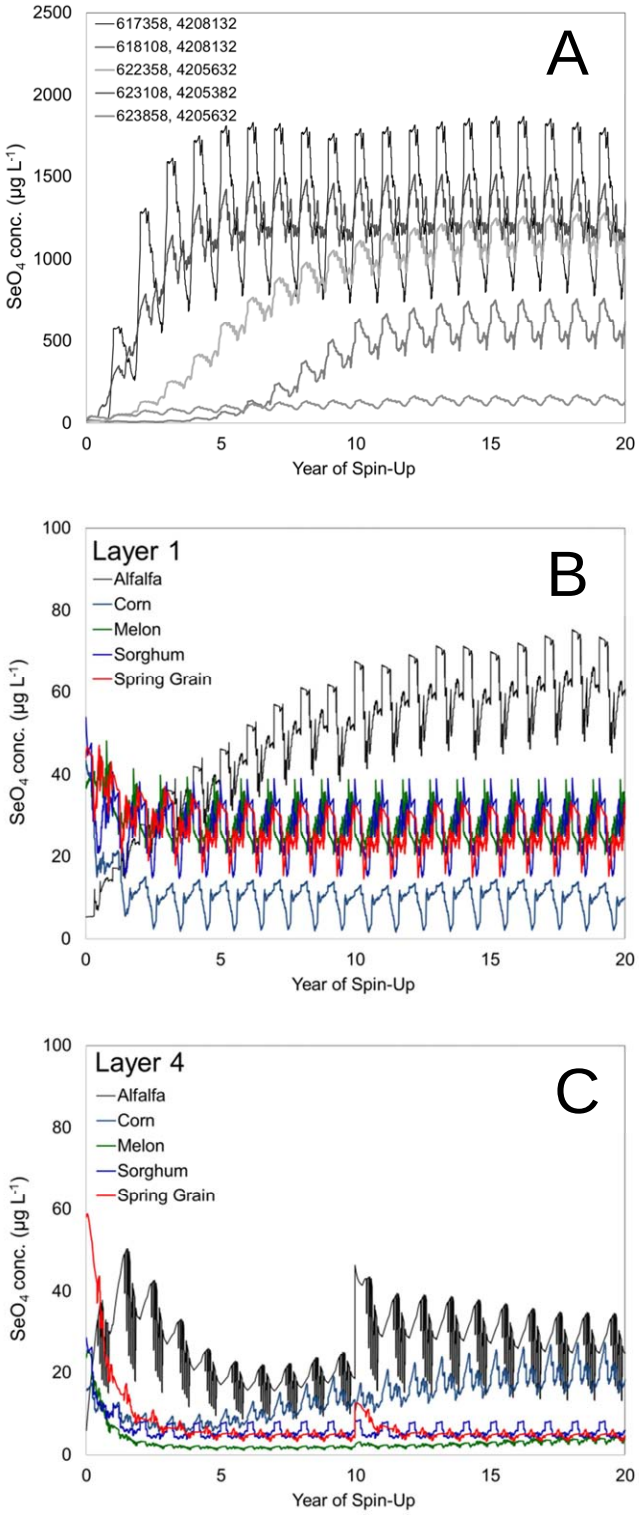

Figure 6- 29. Fluctuation of C_{SeO_4} in groundwater for selected individual grid cells (A) adjacent to shale, (B) underlying cultivated areas, in layer 1 of the model, and (C) underlying cultivated areas, in layer 4 of the model. For (A), coordinates correspond to UTM coordinates of the grid cell centers.

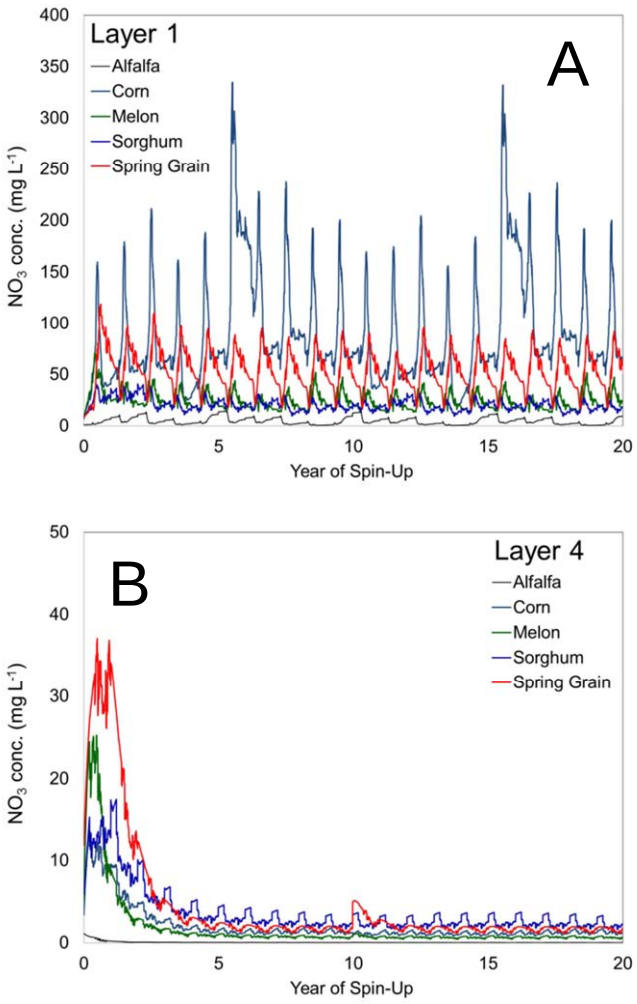

Figure 6- 30. Fluctuation of C_{NO_3} in groundwater for selected individual grid cells (A) underlying cultivated areas, in layer 1 of the model, and (B) underlying cultivated areas, in layer 4 of the model.

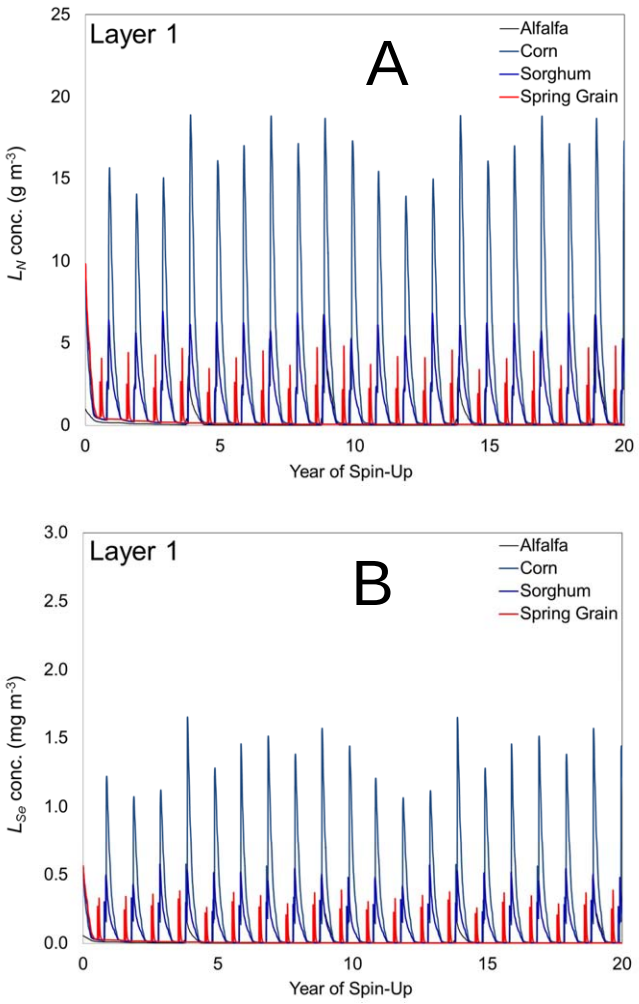

Figure 6- 31. Fluctuation of (A) L_N and (B) L_{Se} for selected individual grid cells underlying cultivated areas.

Figures 6-32 to 6-37 show contour plots of species concentration at the end of the 20-year spin-up simulation, as well as total mass transferred by selected chemical reactions during the simulation. The contour plots of species concentration correspond to the initial concentration used for the 2006-2008 simulation. Figure 6-32 shows the spatial distribution of L_N in layer 1; Figure 6-33 shows the spatial distribution of C_{O_2} in layer 4; Figure 6-34 shows the spatial distribution of C_{NO_3} in layer 4 as well as cumulative mass of denitrified NO_3 in layers 1 and 4; Figure 6-35 shows the spatial distribution of C_{SeO_4} in layer 4; Figure 6-36 shows the cumulative

mass of reduced SeO_4 in layers 1 and 4, and Figure 6-37 shows the spatial distribution of C_{SeO_3} in layer 4.

For C_{O_2}, a plot of water table depth for the same simulation time is shown in Figure 6-33B, to demonstrate the influence of the reaeration term. As can be seen in Figure 6-33, areas of shallow water tables have typically a high value of C_{O_2}, and vice versa, since areas with deep and shallow water tables are supplied via the reaeration term with small and large amounts of O_2 from the ground surface, respectively. Areas of high water table elevation also typically correspond to areas of cultivated and associated application of irrigation water, with O_2 mass also supplied in the irrigation water.

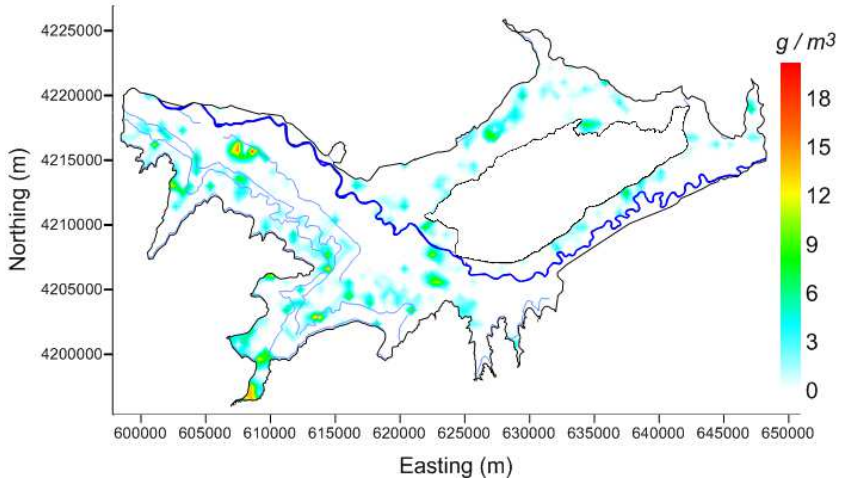

Figure 6- 32. Contour plot of spatial distribution of L_N in layer 1 of the model at the end of the 20-year spin-up simulation.

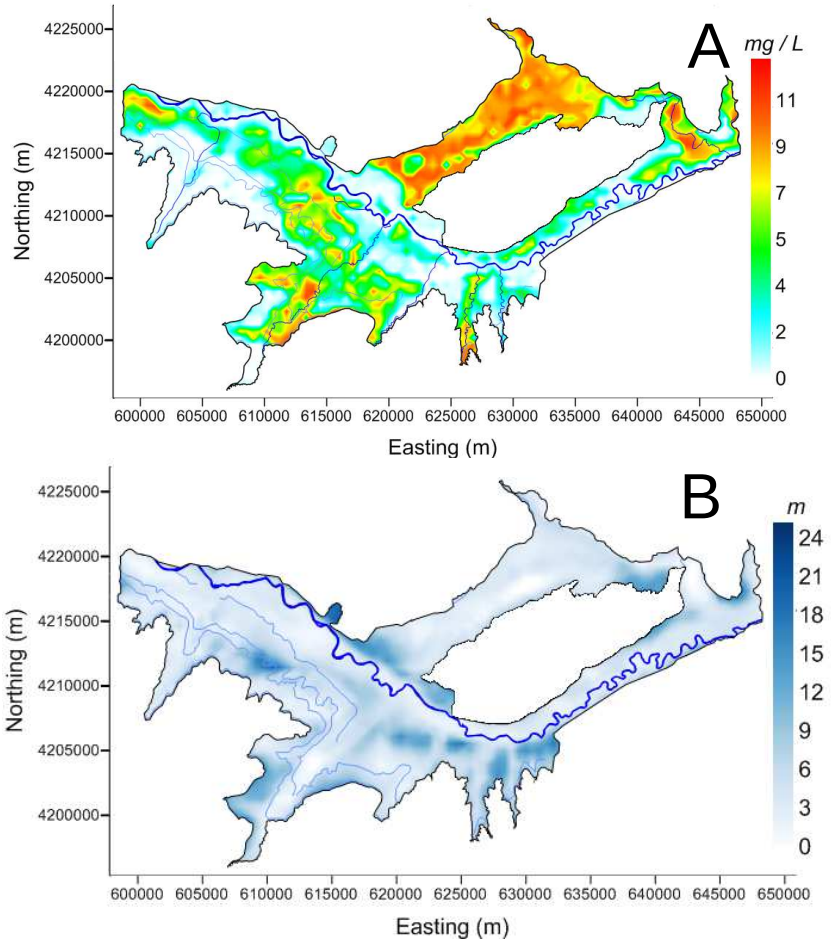

Figure 6- 33. (A) Contour plot of spatial distribution of C_{O_2} in groundwater at the end of the 20-year spin-up simulation and (B) depth from the ground surface to the water table at the end of the 20-year spin-up simulation.

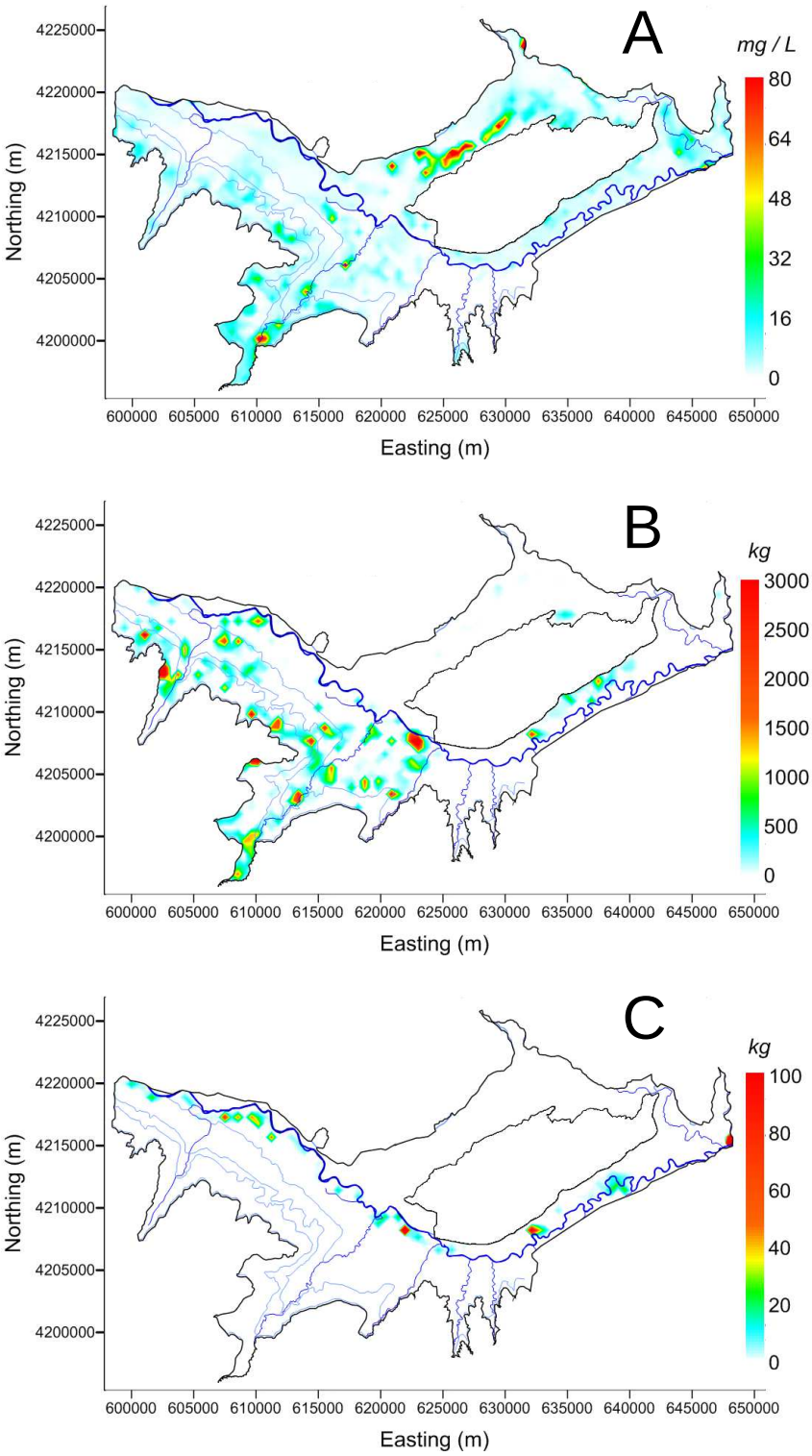

Figure 6- 34. Contour plot of spatial distribution of (A) C_{NO_3} in groundwater in layer 4 at the end of the 20-year spin-up simulation, (B) cumulative mass of denitrified NO_3 in layer 1 during the 20-year simulation, and (C) cumulative mass of denitrified NO_3 in layer 4 during the 20-year simulation.

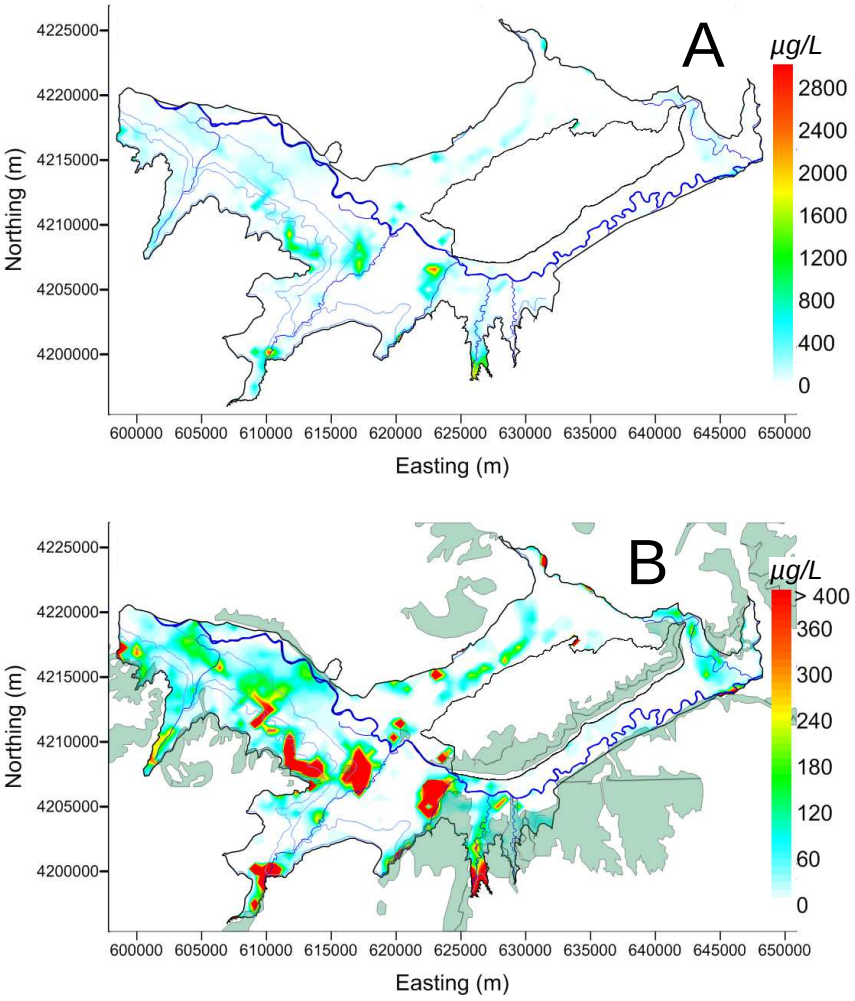

Figure 6- 35. Contour plot of spatial distribution of C_{SeO_4} in groundwater in layer 4 at the end of the 20-year spin-up simulation. (A) uses a color scale that is uniformly discretized, whereas (B) uses a color scale that is limited to below 400 µg L^{-1}, in order to show areas of low to medium concentration.

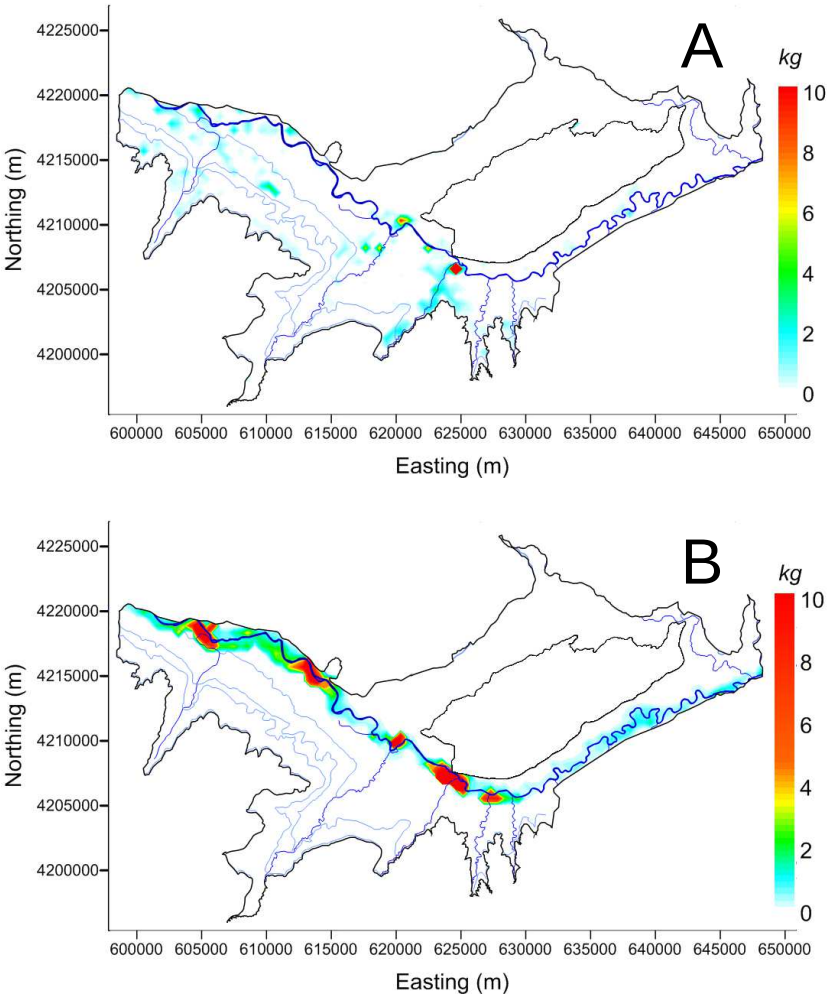

Figure 6- 36. Contour plot of spatial distribution of cumulative mass of reduced SeO_4 in (A) layer 1 and (B) layer 4 during the 20-year simulation.

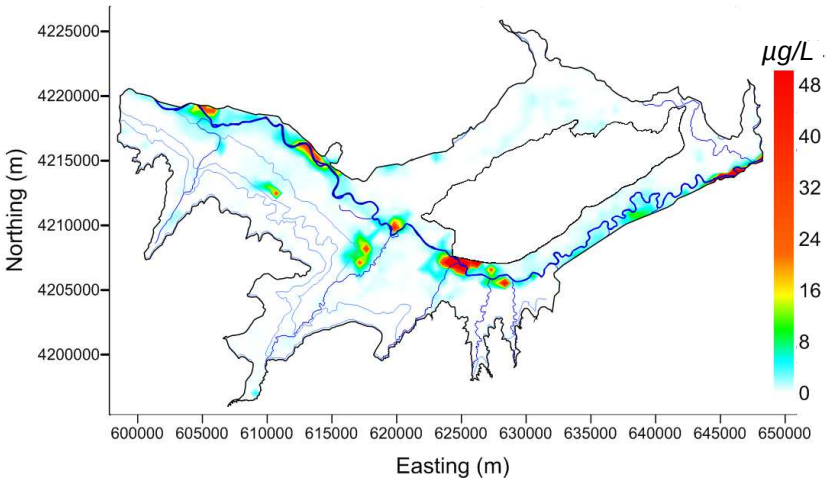

Figure 6- 37. Contour plot of spatial distribution of C_{SeO_3} in groundwater in layer 4 at the end of the 20-year spin-up simulation.

As can be seen in Figure 6-34A and Figure 6-34B, areas of denitrification in layer 1 correspond to cultivated areas whereas areas of denitrification in layer 4 correspond to riparian areas adjacent to the Arkansas River. The denitrification in layer 4 influences the mass of NO_3 loaded to the Arkansas River.

Figure 6-35A and Figure 6-35B show the same values of C_{SeO_4}, but Figure 6-35B uses a color limited to a maximum value of 400 µg L^{-1} in order to show areas with low values of C_{SeO_4}. As can be seen in Figure 6-35B, areas with high values of C_{SeO_4} correspond typically to areas adjacent to surface shale. Similar to the plots of denitrification shown in Figure 6-34B, the plots of cumulative mass of chemically reduced SeO_4 shown in Figure 6-36 demonstrate the correspondence of SeO_4 reduction to riparian zones. As discussed previously, the chemical reduction of SeO_4 in riparian zones has a strong influence on the amount of SeO_4 mass loaded to the Arkansas River. As seen in Figure 6-37 SeO_3, as a product of SeO_4 reduction, is present in the groundwater in locations of SeO_4 reduction.

6.4.2.1.5 Final Calibration Simulation and Model Testing

Using the final parameter values shown in Table 6-14, both the 2006-2008 calibration simulation and the 2008-2009 testing simulation were run, and model results were compared to observed values. Final command area average values of C_{SeO_4}, C_{NO_3}, and C_{O_2} in groundwater for the calibration period are contained in Tables 6-15, 6-16, and 6-17. Comparison of these values with observed values, as well as comparison of simulated and observed values for the testing period, is shown in Figure 6-38 for each of the command areas.

Before describing the results shown in Figure 6-38, it should be noted that error bars are associated with each observed concentration average. These are included to provide a practical comparison between point values (field-measured) and areal values (model-calculated), and account for the fact that the actual average of solute concentration in a 250 m by 250 m surface area is uncertain. In order to quantify the variability of solute concentration within a given cultivated field, and hence corresponding approximately to a spatial area of 250 m by 250 m, data were analyzed from field work in the Upstream Study Region in which salt concentration estimated by specific conductance, EC (electrical conductivity at 25^o C), was measured in multiple groundwater monitoring wells within the same field. Data from eight different fields were analyzed, and results are presented in Table 6-18. Data were collected from Fields 7, 17, and 40 during both 1999 and 2000, whereas data were collected from Fields 81, 100, 102, 103, and 104 only during 2000. At each sampling event, the number of wells sampled within each field is shown in column 3 of Table 6-18 and the number of sampling events during the year is shown in column 4. For each sampling day, the average EC measured in a field and the corresponding standard deviation of EC were used to calculate a CV value over the measurements for that sampling event, corresponding to the degree of variability of EC

measurements within a single field. The sampling event CV values during the year were then averaged for each field, and are shown in column 7. A table containing all results (average EC for each field, for each sampling event) is shown in Appendix B.

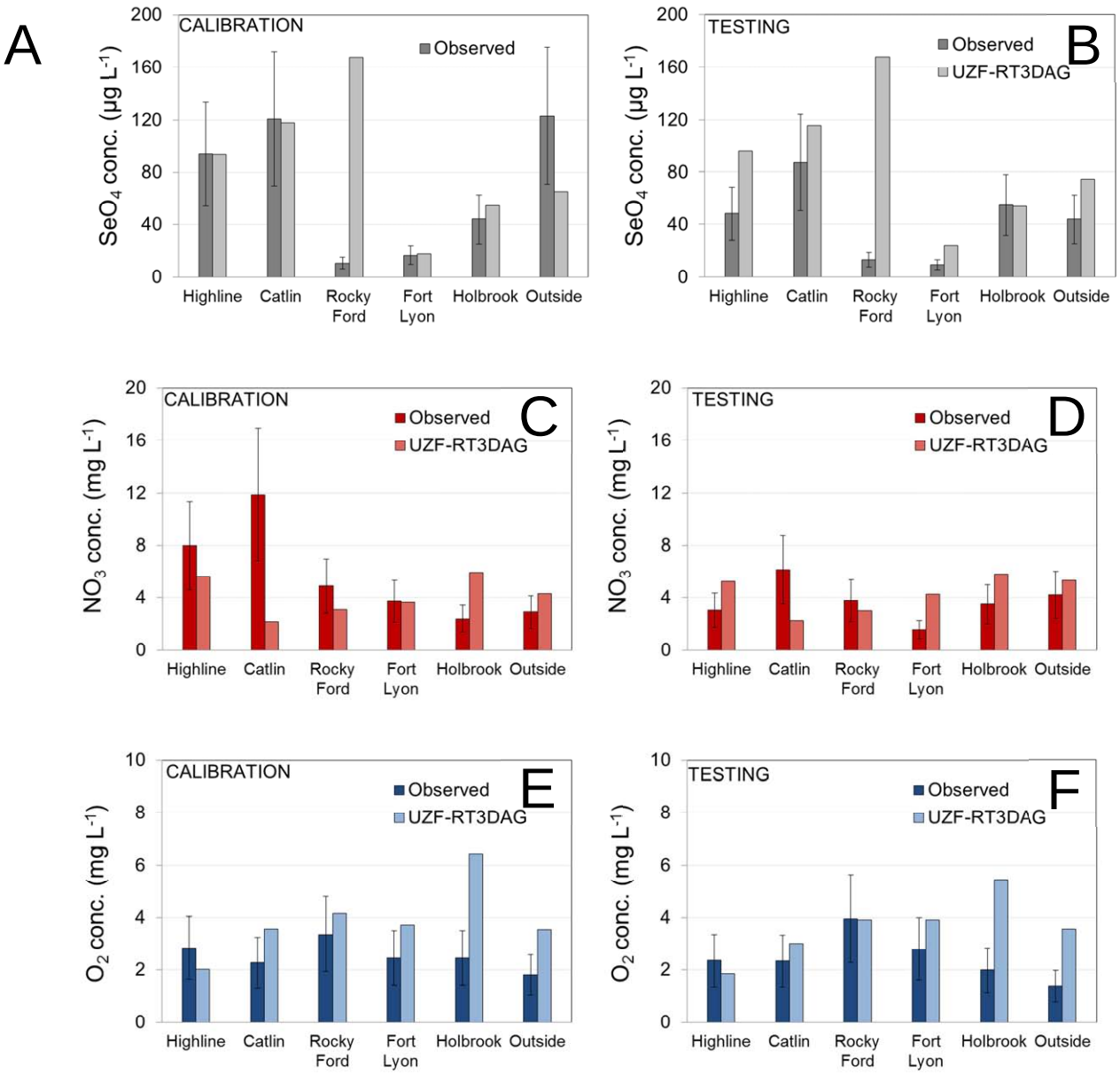

Figure 6- 38. Comparison between simulated and observed average C_{SeO4}, C_{NO_3}, and C_{O_2} for each command area, for the calibration period (A, C, E) and the testing period (B, D, F).

Taking into account the CV for each field and for each year, the average CV of EC within a field is calculated to be 0.42. This CV value is applied to the observed values shown in Figure 6-38. By plotting this variability in Figure 6-38, it is assumed that the fields considered in Table 6-18 have a spatial area of approximately 250 m by 250 m. It also is assumed that C_{SeO_4}, C_{NO_3}, and C_{O_2} have the same variability as salt concentration. EC-C_{SeO_4} and EC-C_{NO_3} relationships derived from data gathered in fields without multiple wells are both significant, with a Pearson correlation coefficient of 0.38 and 0.29, respectively.

Table 6- 18. Variability of groundwater EC measurements in cultivated fields, measured using the CV value of the measurements for each sampling day and for each field.

Field ID	Year	Number of Wells	Number of Sampling Events	Yearly Avg. EC (dS/m)	Average CV of EC for Field
7	1999	11	11	4.18	**0.46**
7	2000	13	15	3.73	**0.51**
17	1999	9	11	2.02	**0.55**
17	2000	9	14	2.69	**0.38**
40	1999	10	11	5.25	**0.68**
40	2000	10	13	6.20	**0.59**
81	2000	7	13	1.68	**0.26**
100	2000	7	13	3.93	**0.36**
102	2000	7	13	5.53	**0.25**
103	2000	10	12	5.56	**0.33**
104	2000	9	12	4.92	**0.30**

In analysis of the results presented in Figure 6-38A, comparison between the simulated and observed values for the Rocky Ford Ditch command area as well as the Outside area should be treated with caution as the number of samples is not high enough to provide reliable averages of groundwater concentration (see Tables 6-2, 6-4, and 6-6). Hence, for the Rocky Ford Ditch values, the simulated value of C_{SeO_4} (167.9 µg L^{-1}) is far higher than the observed value (10.9 µg L^{-1}) for the calibration period. This, however, could be an artifact of not having samples in areas of high C_{SeO_4}. In general, for command areas with a substantial number of samples (see Tables 6-

2, 6-4, and 6-6), the simulated values of C_{SeO_4} for the calibration period compare favorably with the observed values, particularly if the uncertainty in the observed values are taken into account. This is shown in Figure 6-38A. Excluding the Rocky Ford Ditch values, and treating the reported observed value as the true value and hence neglecting uncertainty, the R^2 value is 0.67.

As shown in Figure 6-38C, favorable matches occur for C_{NO_3} for all command areas expect for the Catlin command area (11.9 mg L^{-1} observed vs. 2.2 mg simulated mg L^{-1}). The high observed average, however, is a result of two groundwater samples with measured C_{NO_3} values of 66.0 mg L^{-1} and 45.6 mg L^{-1}, measured at Well 12 on October 6 2007 and Well 41 on May 23 2007, respectively. These concentrations constitute two of the four highest measured values of C_{NO_3} during the calibration period throughout the Upstream Study Region, and also are much higher than other measured concentrations at these same wells during the calibration period (10.3, 11.8, and 26.0 mg L^{-1} for Well 12 and 14.4 mg L^{-1} for Well 41). Hence, the high average of C_{NO_3} for the Catlin command area is a result of unusually high single-occurrence measurement concentrations that were not captured by the model. Overall, the sum of the squared differences between observed and simulated for C_{NO_3} is 22.7 (R^2 = 0.25).

As shown in Figure 6-38E, favorable matches occur also for C_{O_2} , except for the Holbrook command area where the simulated value (6.4 mg L^{-1}) is much higher than the observed value (2.5 mg L^{-1}). As seen in Figure 6-33, the shallow water tables in the Holbrook command area result in high C_{O_2} in the saturated zone. Hence, the reaeration term likely is overestimating the amount of O_2 supplied to the saturated zone for areas of shallow water tables. Overall, the sum of the squared differences between observed and simulated for C_{O_2} is 22.7 (R^2 = 0.003).

Results of the testing period are shown in Figures 6-38B, 6-38D, and 6-38F. As seen in the figures, favorable matches occur for C_{SeO_4}, C_{NO_3}, and C_{O_2}. For C_{SeO_4}, the simulated average for the Highline command area did not change considerably from the calibration period to the testing period (93.4 µg L^{-1} to 95.6 µg L^{-1}), whereas the observed concentration decreased by nearly half (93.9 µg L^{-1} to 48.2 µg L^{-1}). The observed and simulated values of C_{NO_3} for the Catlin command area are closer in value for the testing period due to the decrease in average observed concentration, and the overall match between the observed and simulated values for C_{O_2} is better for the testing period than for the calibration period. These results are reflected quantitatively, as the sum of squared differences for C_{SeO_4}, C_{NO_3}, and C_{O_2} increased to 4225.9 (R^2 = 0.75), decreased to 33.3 (R^2 = 0.25), and decreased to 18.6 (R^2 = 0.00) from the calibration period values of 3468.9, 114.6, and 22.7, respectively.

In regards to the high simulated C_{SeO_4} values in the Highline command area, the average C_{SeO4} in the groundwater did not decrease during the testing period due to the presence of high-concentration areas in the vicinity of surface shale. Although several observation wells in the Highline command area are located near surface shale, the average observed C_{SeO_4} likely would be higher if more samples were collected near shale. For example, Well 20 is located near shale and had an average of 266.8 µg L^{-1} over the 9 sampling events with a maximum concentration of 1350 µg L^{-1} measured for a sample collected on June 19 2006. As a further example, groundwater sampled from a piezometer well in the Highline command area (see Chapter 2, Section 2.3.1) had an average C_{SeO_4} value of 2508 µg L^{-1} for seven samples taken from August 2009 to December 2010 (values of 1620, 1520, 2870, 2650, 2860, 3300, and 2740 µg L^{-1}). The piezometer well had a screen located within yellow clay. High model-simulated averages of C_{SeO_4}

as compared to observed values is not a definite proof that the model yields inaccurate results, i.e., a higher average value of C_{SeO_4} in the Highline command area actually may exist in the actual aquifer system.

The observed and simulated mass loadings of Se during the 2006-2009 period are shown in Figure 6-39A, with the values simulated during the calibration and testing periods shown in green and red, respectively. It should be noted that the observed mass loadings correspond to total dissolved Se, where the simulated mass loadings correspond to SeO_4. Since total dissolved Se includes both SeO_4 and SeO_3, the simulated loading of total dissolved Se would be higher than what is indicated for SeO_4 in Figure 6-39A. The simulated loading of total dissolved Se will be included in future studies. Overall, the simulated daily mass loadings are similar to the observed values in regards to fluctuation pattern and range of values. This favorable match likely also would occur if SeO_3 loadings were added to the SeO_4 loadings, since SeO_3 only accounts for approximately 2-10% of the dissolved Se (see Figure 6-42 below). The simulated mass loadings track the observed loadings particularly well during the summer months of each year. Although observed loadings of NO_3 are not yet available, the simulated daily loadings are shown in Figure 6-39B for completeness.

6.4.2.2 Further Model Corroboration using Global Measures

Besides comparisons between simulated and observed species concentrations at the command area scale and mass loading to surface water, other comparisons are performed at the scale of the model domain to assess model corroboration. With these comparisons as well as comparisons performed in the previous section, it is shown that the model indeed captures the response of the aquifer system in regards to species concentration, species mass output to surface water, and inter-species relationships.

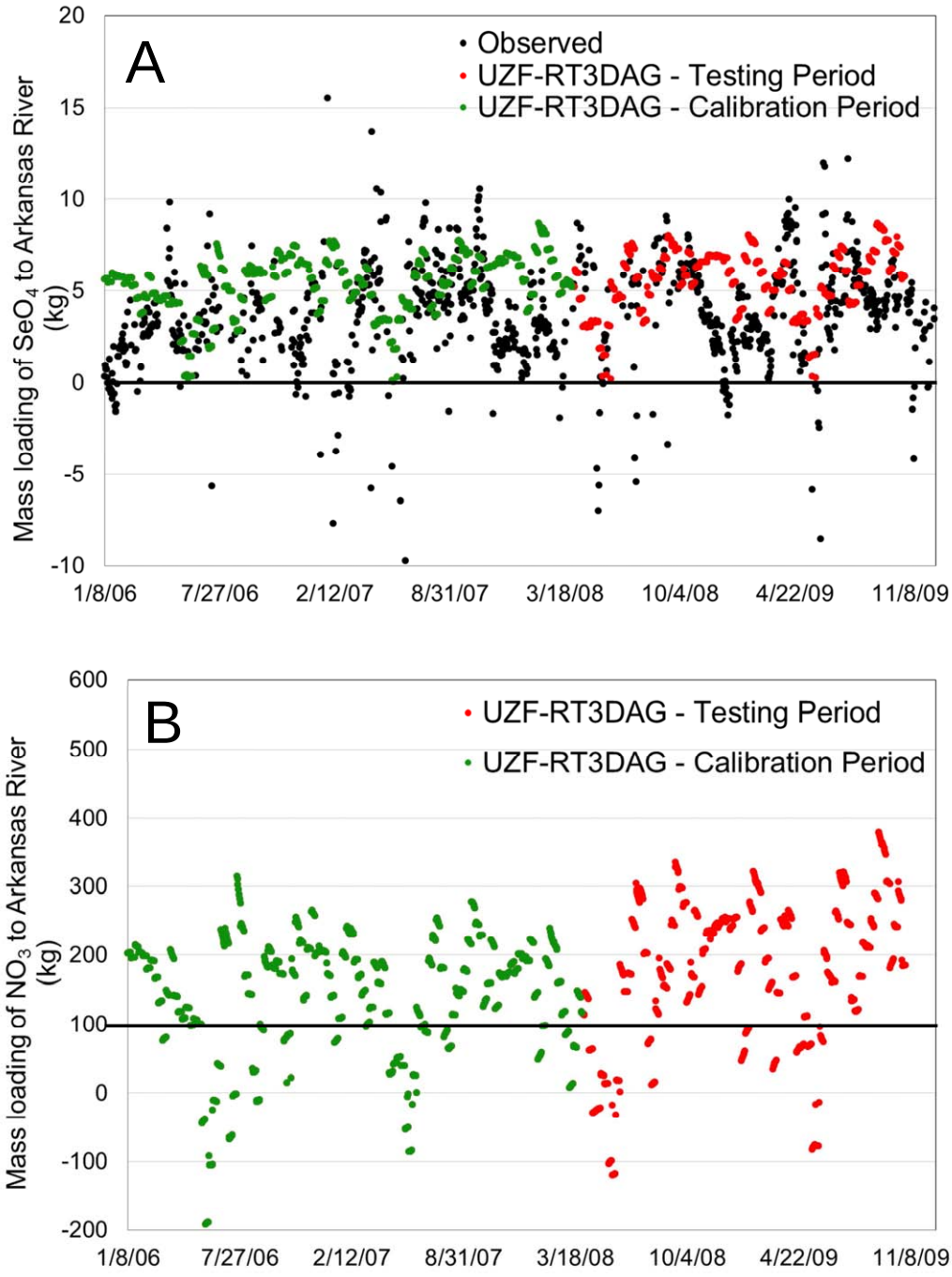

Figure 6- 39. Observed (black) and simulated daily mass loadings of (A) SeO_4 (kg) and (B) NO_3 (kg) from the aquifer to the Arkansas River for the entire reach of the river within the Upstream Study Region. The simulated values during the calibration period are shown in green, and the simulated values during the testing period are shown in red.

The first global comparison is the relationship between C_{NO_3} and C_{SeO_4} in groundwater. As was presented in Chapter 2, a significant relationship between C_{NO_3} and C_{SeO_4} has been recognized in agricultural-influenced groundwater systems, including the LARV (Wright, 1999; Gates et al., 2009; Bailey and Gates, 2012), with C_{SeO_4} positively correlated with C_{NO_3} due to (i) the oxidation of residual Se by NO_3 and (ii) the inhibition of SeO_4 reduction in the presence of NO_3. Figure 6-40 shows log-log plots of C_{NO_3} vs. C_{SeO_4} for observed and simulated values for both the calibration and testing periods. For the observed values, 141 data values are available for the four sampling events of the calibration period and 199 data values are available for the five sampling events of the testing period. For the simulated results, values of C_{NO_3} and C_{SeO_4} were taken from each grid cell in layer 4 for the simulation times corresponding to the dates of field sampling. This resulted in 30,374 and 38,140 simulated values for the calibration and testing periods, respectively. Also shown in Figure 6-40 are the C_{NO_3} and C_{SeO_4} detection limits for the groundwater samples analyzed in the laboratory (see Chapter 2). Data values shown at these limits likely have actual concentrations lower than the limit values, and hence would correspond more closely with simulated values.

As seen in Figure 6-40, the simulated values capture the main positive correlation between C_{NO_3} and C_{SeO_4}. For the calibration period, the Pearson correlation coefficient for the observed and simulated values is 0.56 and 0.36, respectively, and for the testing period the correlation coefficient for the observed and simulated values is 0.71 and 0.42, respectively. Hence, the enhanced correlation between C_{NO_3} and C_{SeO_4} for the observed values in the testing period also is captured in the model.

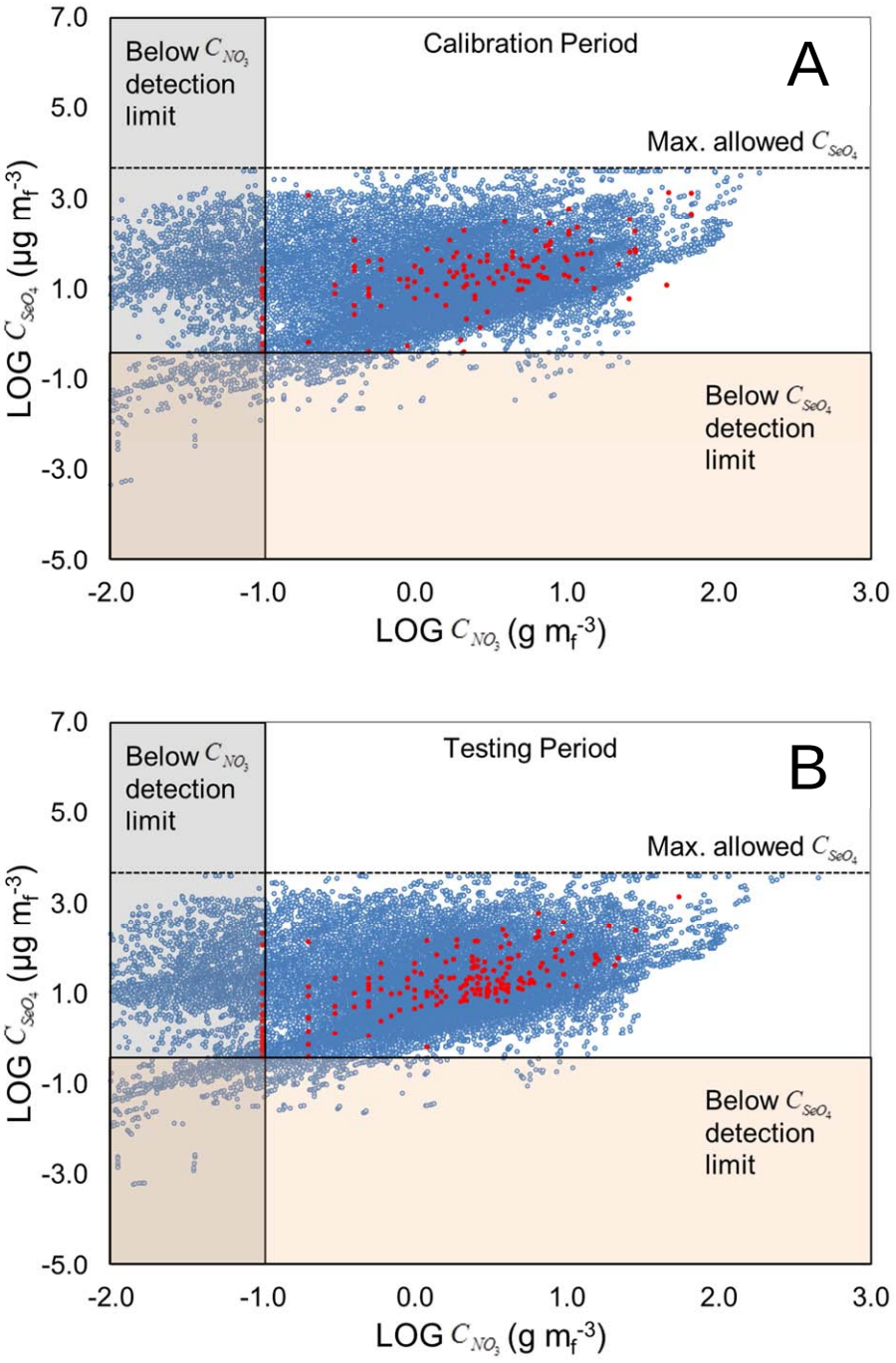

Figure 6- 40. Log-log plots of C_{NO_3} vs C_{SeO_4} for observed (red dots) and simulated (blue dots) values for both the (A) calibration and (B) testing periods. For the simulated results, values were taken from every grid cell in layer 4 of the model.

For both the calibration and testing periods, however, it can be seen in Figure 6-40 that simulated C_{SeO_4} values can be high (>10^2 µg L^{-1}) in grid cells where C_{NO_3} values are close to 0.0 mg L^{-1} (<10^{-1} mg L^{-1}), contrary to the expected positive relationship. This also occurs for the observed data and is seen particularly for the testing period results in Figure 6-40B, wherein many data points have values of C_{NO_3} at the detection limit, indicating that high values of C_{SeO_4} occur in groundwater samples that have low C_{NO_3} values. The high C_{SeO_4} values, however, likely are due to the presence of O_2 in the groundwater, which similar to NO_3 is able to oxidize residual Se from shale as well as inhibit SeO_4 reduction. This possibility is explored using a log-log plot of C_{NO_3} vs. C_{O_2} (Figure 6-41) for both observed and simulated values during the calibration period. As can be seen in the figure, high values of C_{O_2} (>$10^{0.5}$ mg L^{-1}) occur in grid cells where C_{NO_3} values are close to 0.0 mg L^{-1} (<10^{-1} mg L^{-1}), and hence may be the cause of high C_{SeO_4} values in grid cells where C_{NO_3} values are close to 0.0 mg L^{-1}. This occurrence likely would be seen also in the observed data if the detection limits were closer to 0.0 mg L^{-1}. If so, the data points lined along the C_{NO_3} detection limit in Figures 6-40B and 6-41 would have values of C_{NO_3} closer to 0.0 m mg L^{-1} and hence demonstrate that there are groundwater samples with high C_{O_2} and C_{SeO_4} values and low C_{NO_3} values.

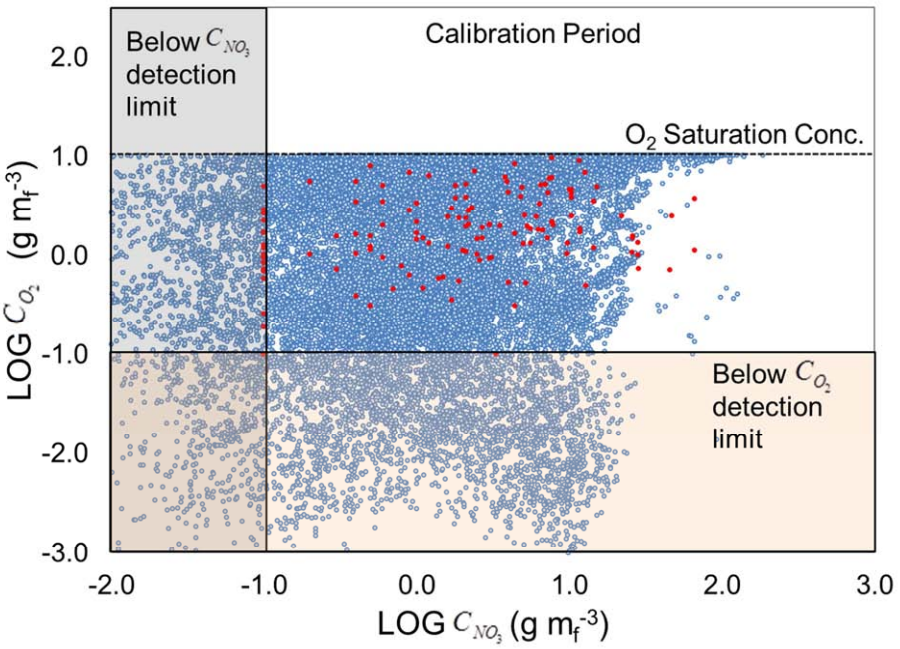

Figure 6- 41. Log-log plots of C_{NO_3} vs C_{O_2} for observed and simulated values for the calibration period. For the simulated results, values were taken from every grid cell in layer 4 of the model.

The second global measure is the portion of dissolved Se mass in groundwater accounted for by SeO_4, with remaining mass attributed to SeO_3. This measure determines if the model is able to capture the observed relationship between SeO_4 and SeO_3, with the latter species a product of SeO_4 chemical reduction. The measure thus also analyzes the ability of the model to simulate accurately the occurrence and rate of SeO_4 reduction.

To analyze the accuracy of the simulated SeO_4-SeO_3 relationship, the portion of dissolved Se mass accounted for by SeO_4 was calculated for both the observed and simulated values, with the simulated values of C_{SeO_4} and C_{SeO_3} taken from each grid cell in layer 4 of the model. Figure 6-42 shows the frequency distributions of these values for both the calibration and testing periods. As seen in the figure, the frequency distributions of the observed and simulated values have a close match for both the calibration and testing periods, with the vast majority of the observed and

simulated values having very high (>0.99) SeO_4 portions. These values also are consistent with other groundwater sampling studies in which SeO_4 has been found to account for approximately 90% to 95% of dissolved Se in agricultural waters (Masscheleyn et al., 1989; Gates et al., 2009).

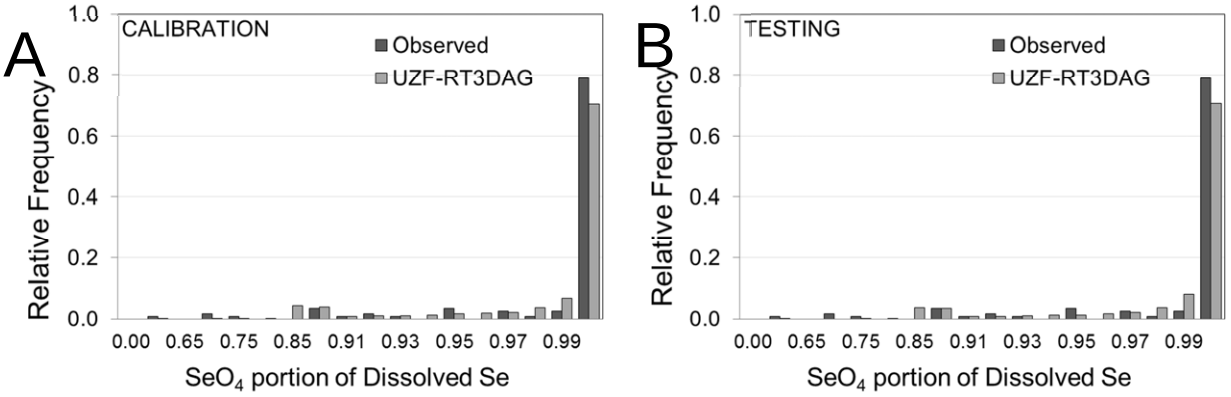

Figure 6- 42. Frequency distribution of SeO4 portion of dissolved Se for both the (A) calibration and (B) testing periods, with the simulated portion of SeO4 calculated for every grid cell in layer 4 of the model.

The third global comparison is between the observed and simulated frequency distributions of C_{SeO_4}, C_{NO_3}, and C_{O_2}, with frequency distributions constructed using every observed value in the Upstream Study Region and every simulated value from layer 4 of the model. Whereas previous comparisons between observed and simulated values were performed according to the mean of the concentration values (see Section 6.4.2.1.5), this comparison analyzes the ability of the model to represent accurately the spread of the concentration values as compared to observed values and the relative frequency of concentration values within a given concentration interval, i.e., to verify that the model captures the global statistics of the concentration value. First, the frequency distributions will be shown for both the calibration and testing periods. Second, the fitted statistical distributions to the frequency distributions are plotted and compared. For the latter, the Pearson 5 distribution was found to best fit (using Kolmogorov-Smirnov measure) the frequency distributions of observed and simulated C_{SeO_4}, C_{NO_3}, and C_{O_2}.

Figure 6-43 shows the frequency histograms of the observed and simulated C_{SeO_4} values for both the calibration (Figure 6-43A) and testing (Figure 6-43B) periods, as well as the fitted Pearson 5 distribution for both the calibration (Figure 6-43C) and testing (Figure 6-43D) periods. The parameter values for the Pearson 5 distributions (α, β, shift) are shown in Figures 6-43C and 6-43D. As can be seen from the figure, excellent matches occur between the distributions of the observed and simulated values, particularly for the testing period, indicating that the model produces the spread of C_{SeO_4} values as observed in the actual aquifer system.

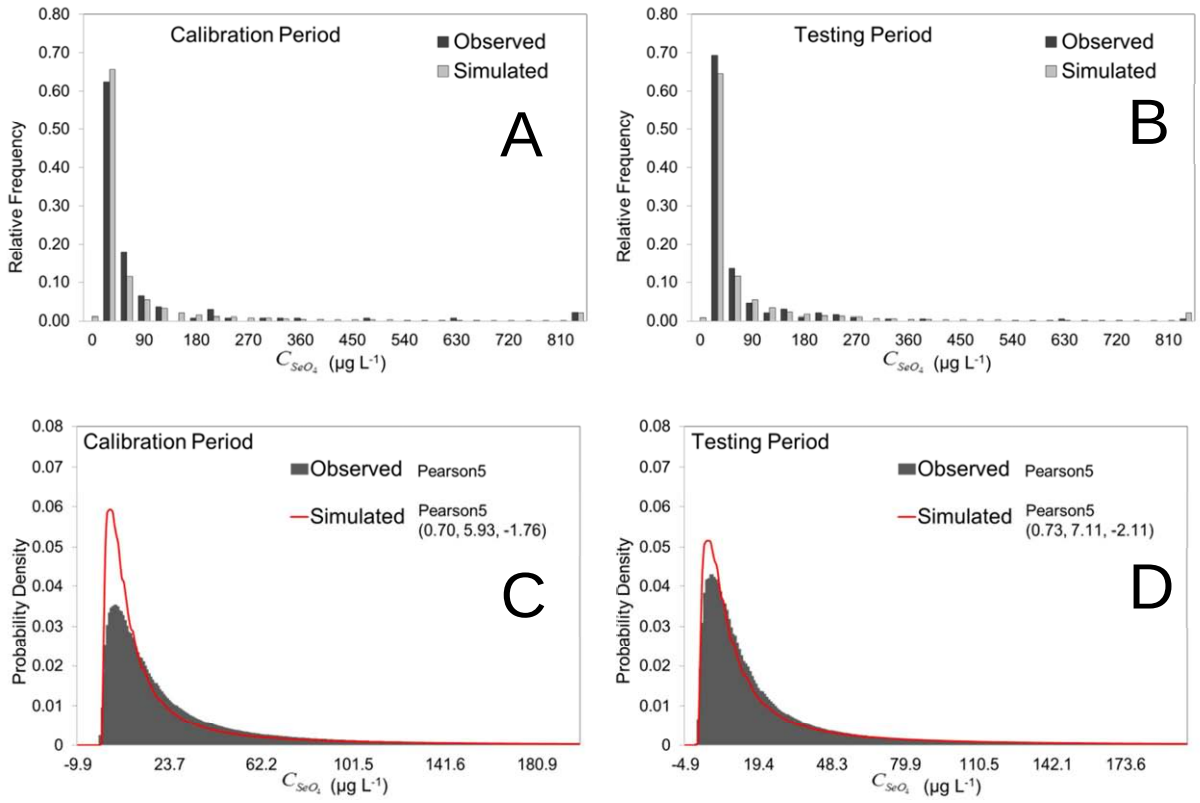

Figure 6- 43. Frequency distributions of observed and simulated values of C_{SeO_4} for the (A) calibration period and (B) testing period, and fitted Pearson 5 distributions for the (C) calibration period and (D) testing period.

Figures 6-44 and 6-45 show similar results for C_{NO_3} and C_{O_2}. Excellent matches occur for C_{NO_3}, particularly for the testing period. For the calibration period, the model produces relative more

values of low C_{NO_3} as compared to the observed values. Matches between the distributions of observed and simulated values of C_{O_2} are poor to good, with the model producing relatively more values of both low C_{O_2} and high C_{O_2} . The poor match at low values likely results from the increased uncertainty of the readings of the YSI instrument at low values of C_{O_2} , whereas the high values of C_{O_2} likely are a result of the inclusion of the reaeration term. For the former, the the confidence associated with readings decreases from 95% to 75% when the concentration is at or below 0.1 mg L^{-1}. Overall, however, the model seems to produce accurately both the observed spread of values and the observed relative frequency of concentration values within a given concentration interval for C_{SeO_4} , C_{NO_3} , and C_{O_2} .

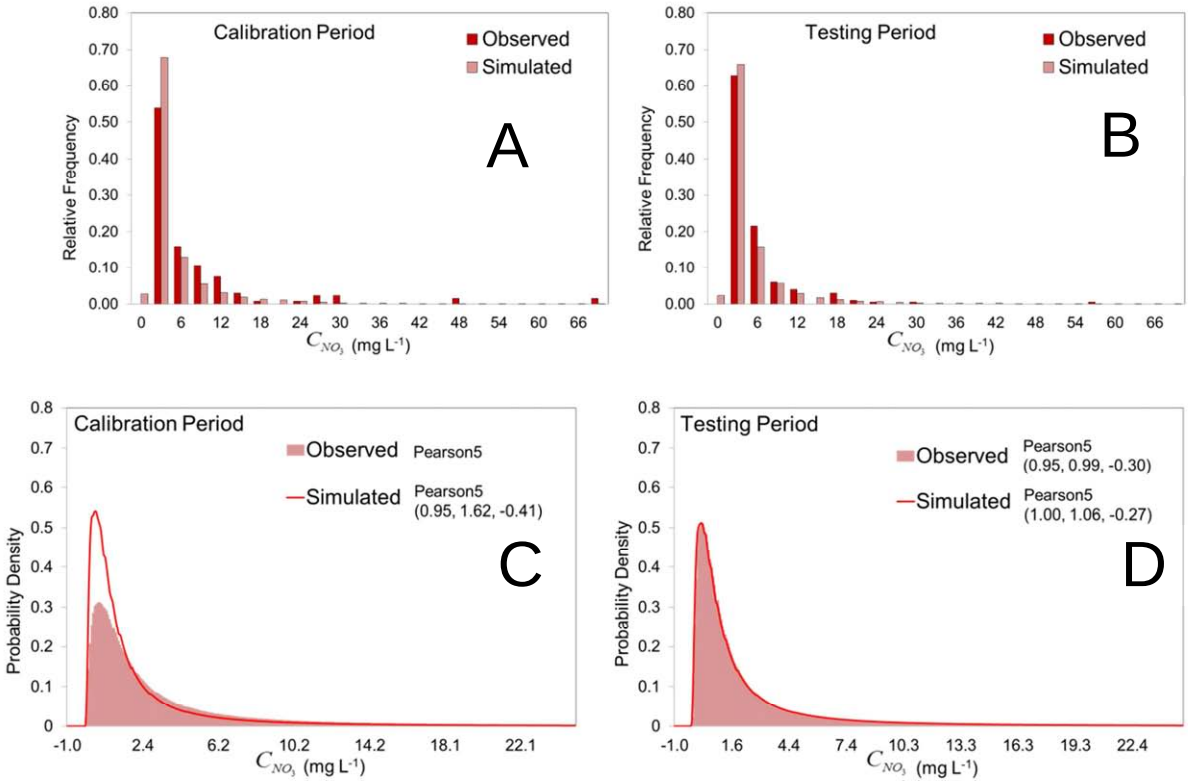

Figure 6- 44. Frequency distributions of observed and simulated values of C_{NO_3} for the (A) calibration period and (B) testing period, and fitted Pearson 5 distributions for the (C) calibration period and (D) testing period.

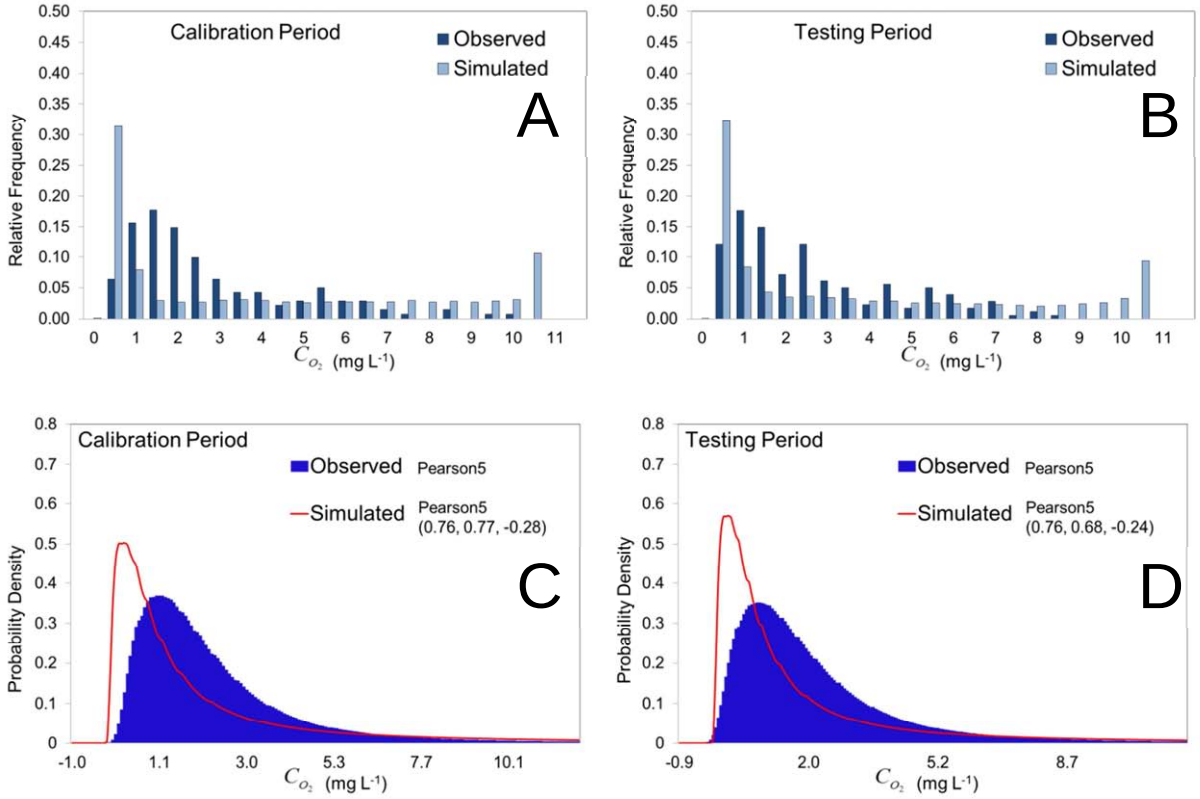

Figure 6- 45. Frequency distributions of observed and simulated values of C_{O_2} for the (A) calibration period and (B) testing period, and fitted Pearson 5 distributions for the (C) calibration period and (D) testing period.

6.4.2.3 Additional Model Results

Additional model results for the calibration and testing simulations are shown in Figures 6-46 to 6-55. Figures 6-46 and 6-47 show the fluctuation of C_{SeO_4} and C_{NO_3} during the 2006-2009 simulation, respectively, for selected grid cells, similar to the results shown in Figures 6-29 and 6-30 for the 20-year spin-up simulation. Several cells exhibit a dynamic equilibrium in species concentration whereas others demonstrate year-to-year variability as irrigation practices change. Figures 6-48, 6-49, 6-50, and 6-51 show contour plots of the spatial distribution of C_{O_2}, C_{NO_3},

C_{SeO_4} and C_{SeO_3}, respectively, for June 19 2006 and May 15 2009. Figure 6-51 demonstrates again the chemical occurrence of chemical reduction of SeO_4 and resulting production of SeO_3 mass in riparian areas. Figures 6-52 and 6-53 show the simulated mass exchange of NO_3 and SeO_4, respectively, between groundwater and surface water for December 2 2006, August 10 2008, and May 17 2009 for each of the 1,943 river cells in the model domain. Red bars indicate mass loading from groundwater to surface water, and green bars indicate mass loading from surface water to groundwater.

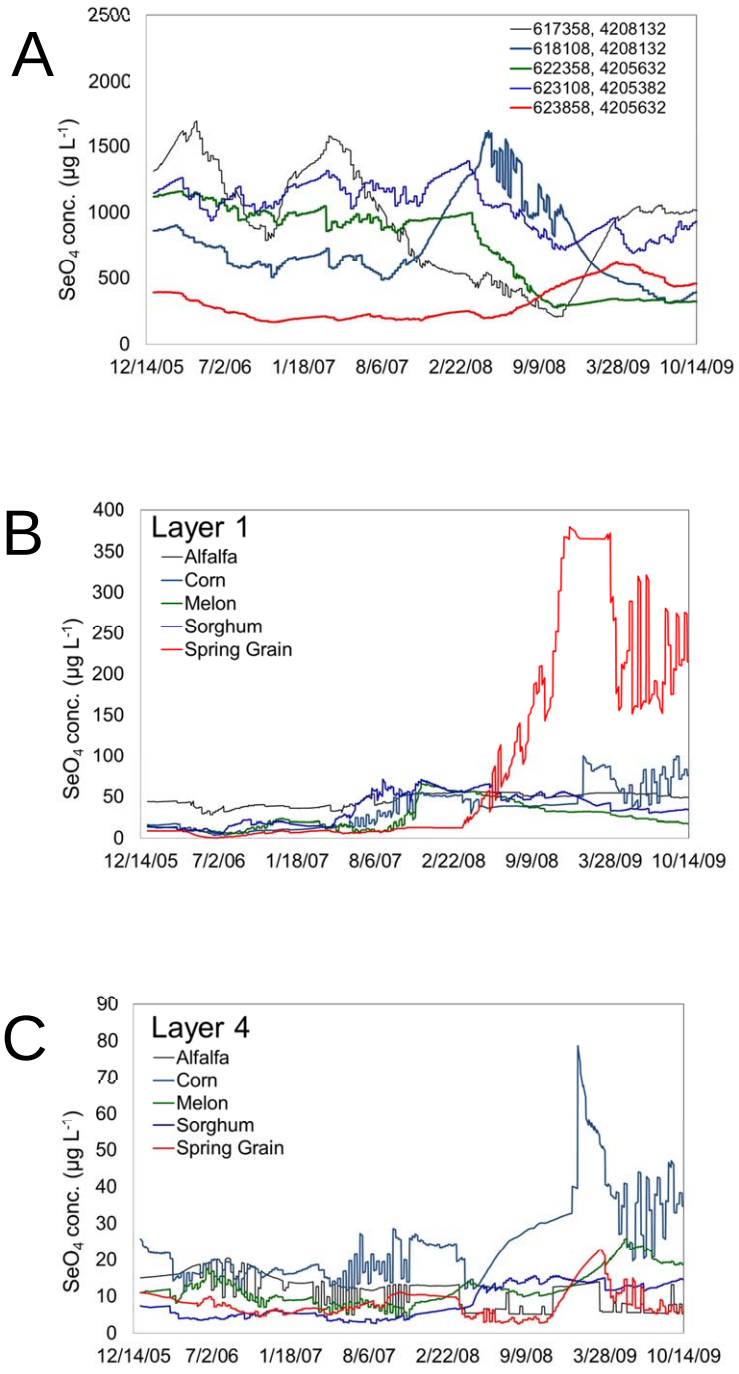

Figure 6- 46. Fluctuation of C_{SeO_4} in groundwater during 2006-2009 simulation for selected individual grid cells (A) adjacent to shale, (B) underlying cultivated areas, in layer 1 of the model, and (C) underlying cultivated areas, in layer 4 of the model.

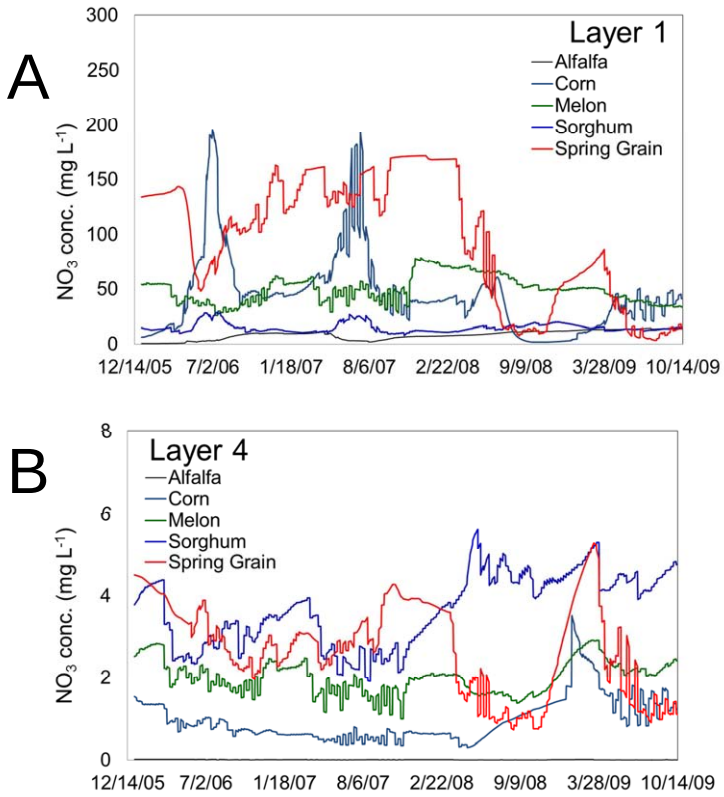

Figure 6- 47. Fluctuation of C_{NO_3} in groundwater during 2006-2009 simulation for selected individual grid cells (A) underlying cultivated areas, in layer 1 of the model, and (B) underlying cultivated areas, in layer 4 of the model.

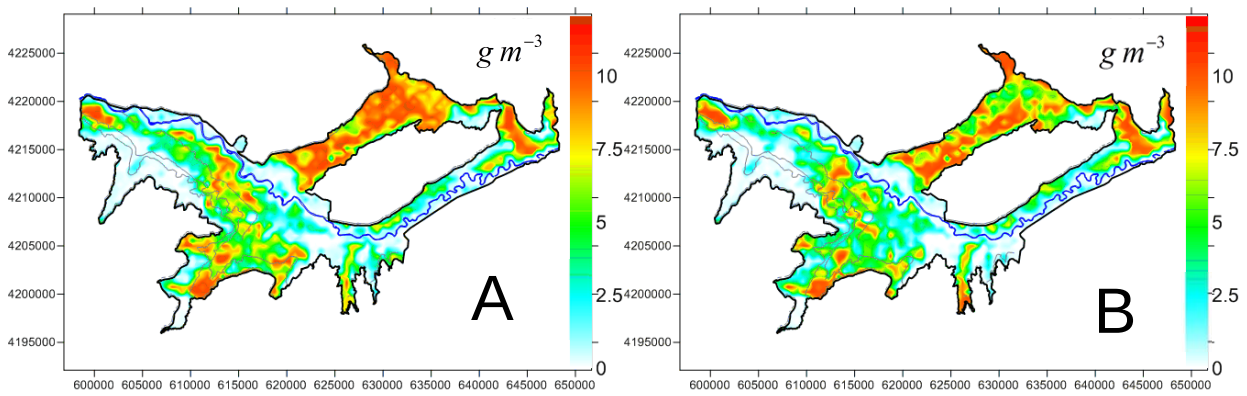

Figure 6- 48. Contour plot of spatial distribution of simulated C_{O_2} in groundwater in layer 4 of the model for (A) June 19 2006 and (B) May 15 2009.

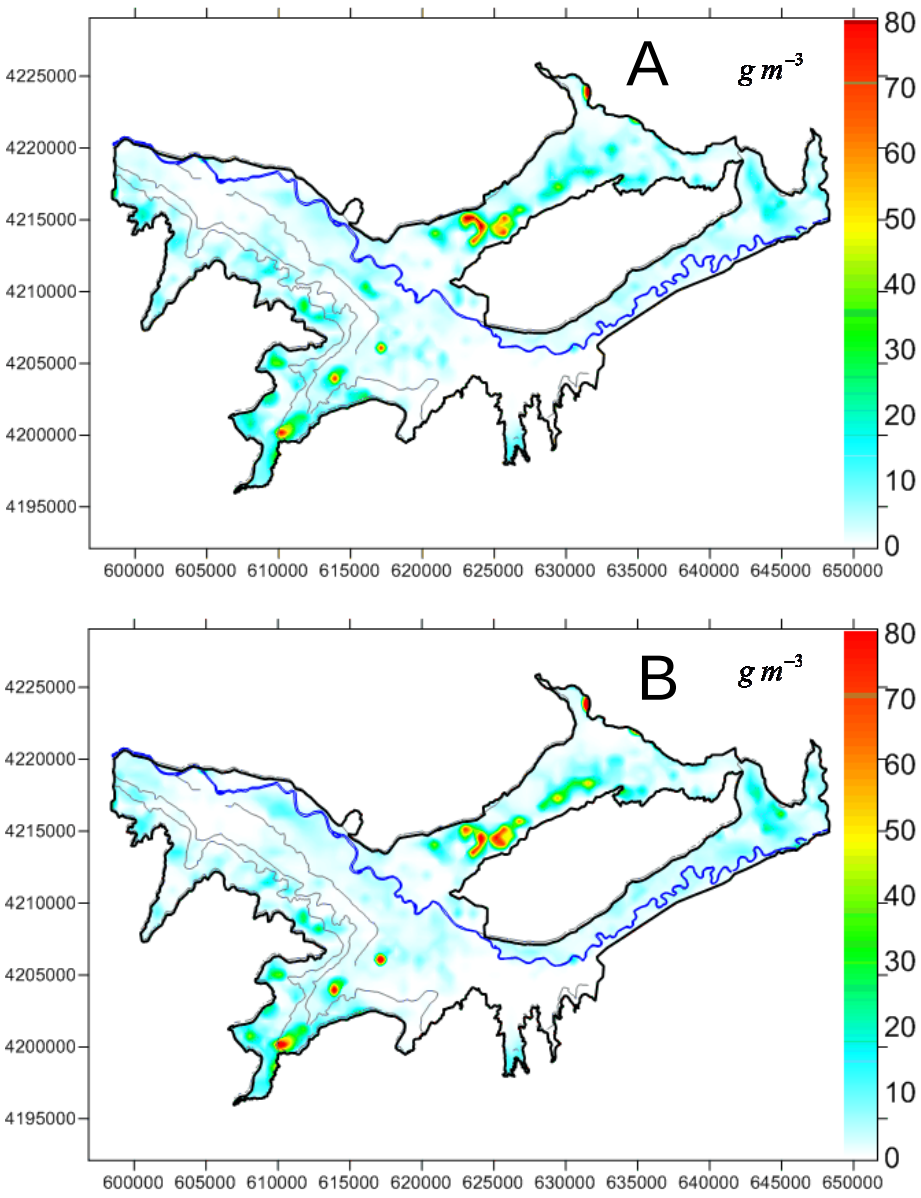

Figure 6- 49. Contour plot of spatial distribution of simulated C_{NO_3} in groundwater in layer 4 of the model at June 19 2006 and May 15 2009.

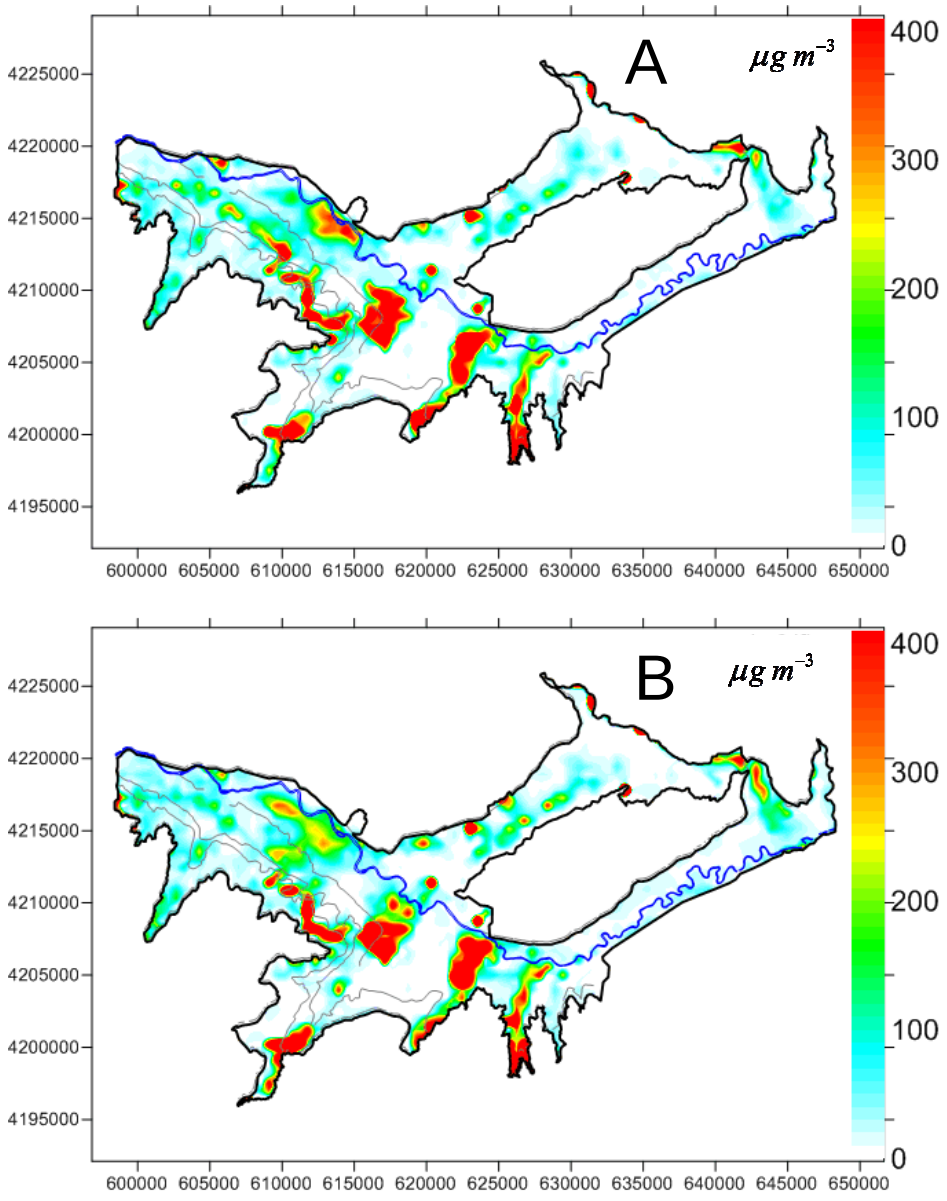

Figure 6- 50. Contour plot of spatial distribution of simulated C_{SeO_4} in groundwater in layer 4 of the model at June 19 2006 and May 15 2009.

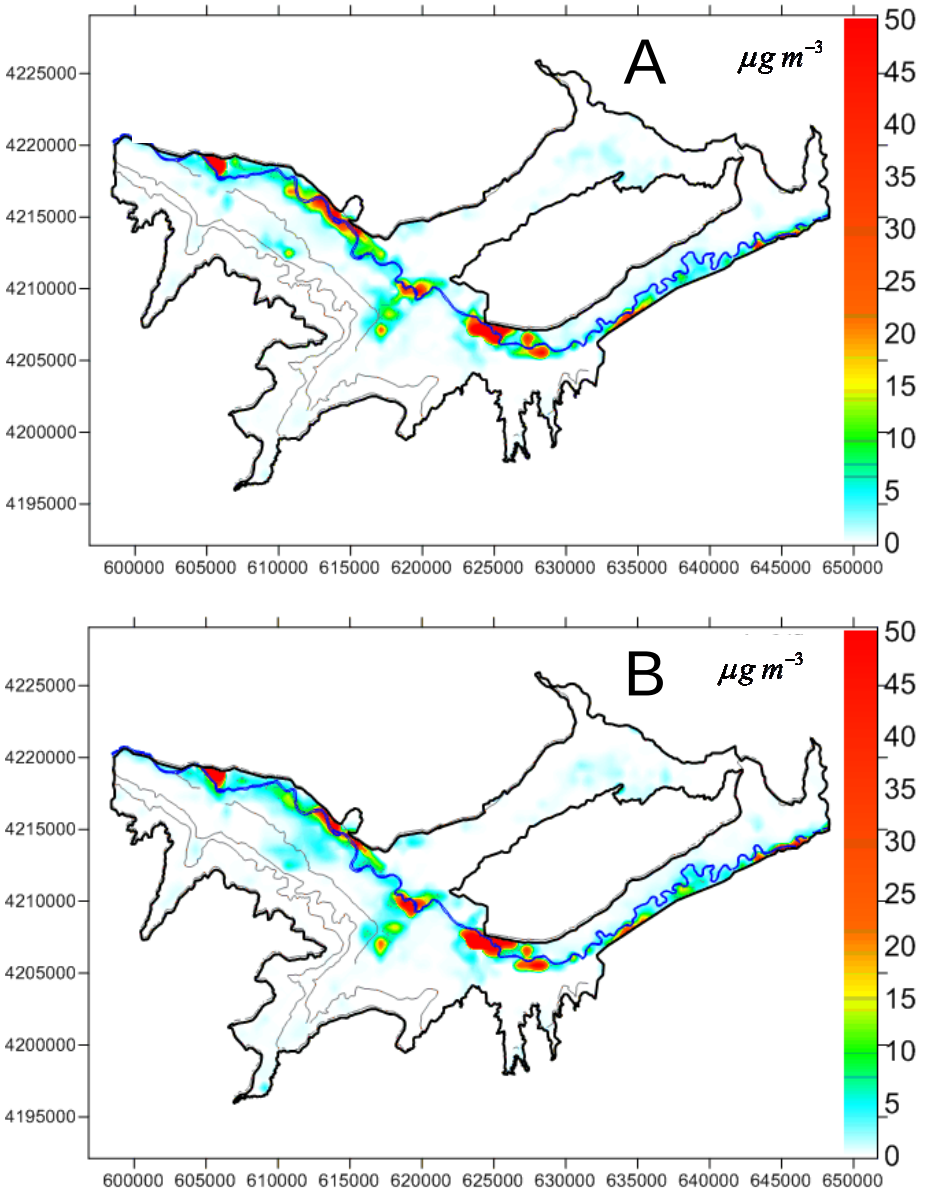

Figure 6- 51. Contour plot of spatial distribution of simulated C_{SeO_3} in groundwater in layer 4 of the model at June 19 2006 and May 15 2009.

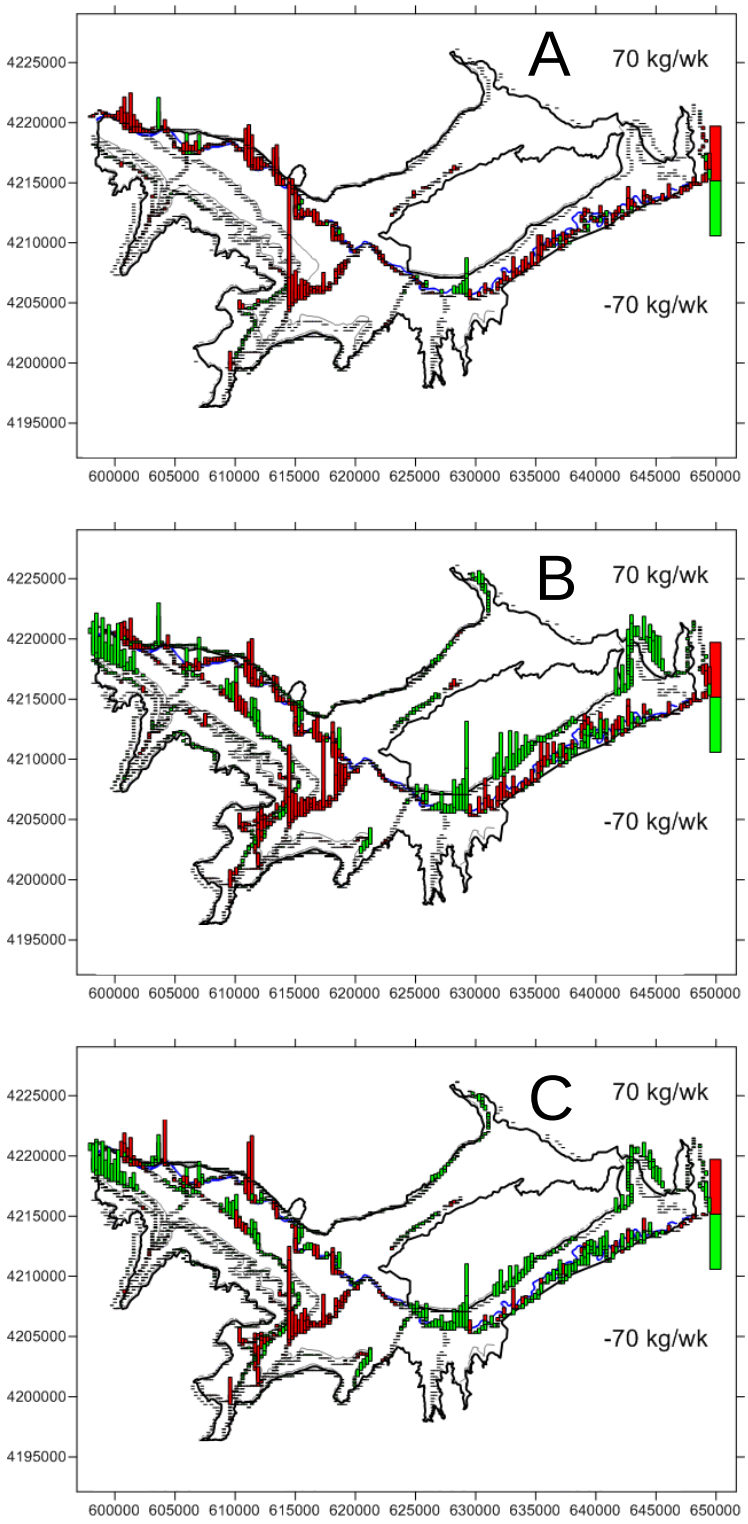

Figure 6- 52. Simulated mass exchange of NO_3 between groundwater and surface, in kg/wk for (A) December 2 2006, (B) August 10 2008, and (C) May 17 2009 for each of the 1,943 river cells in the model domain. Red bars indicate mass loading from groundwater to surface water, and green bars indicate mass loading from surface water to groundwater.

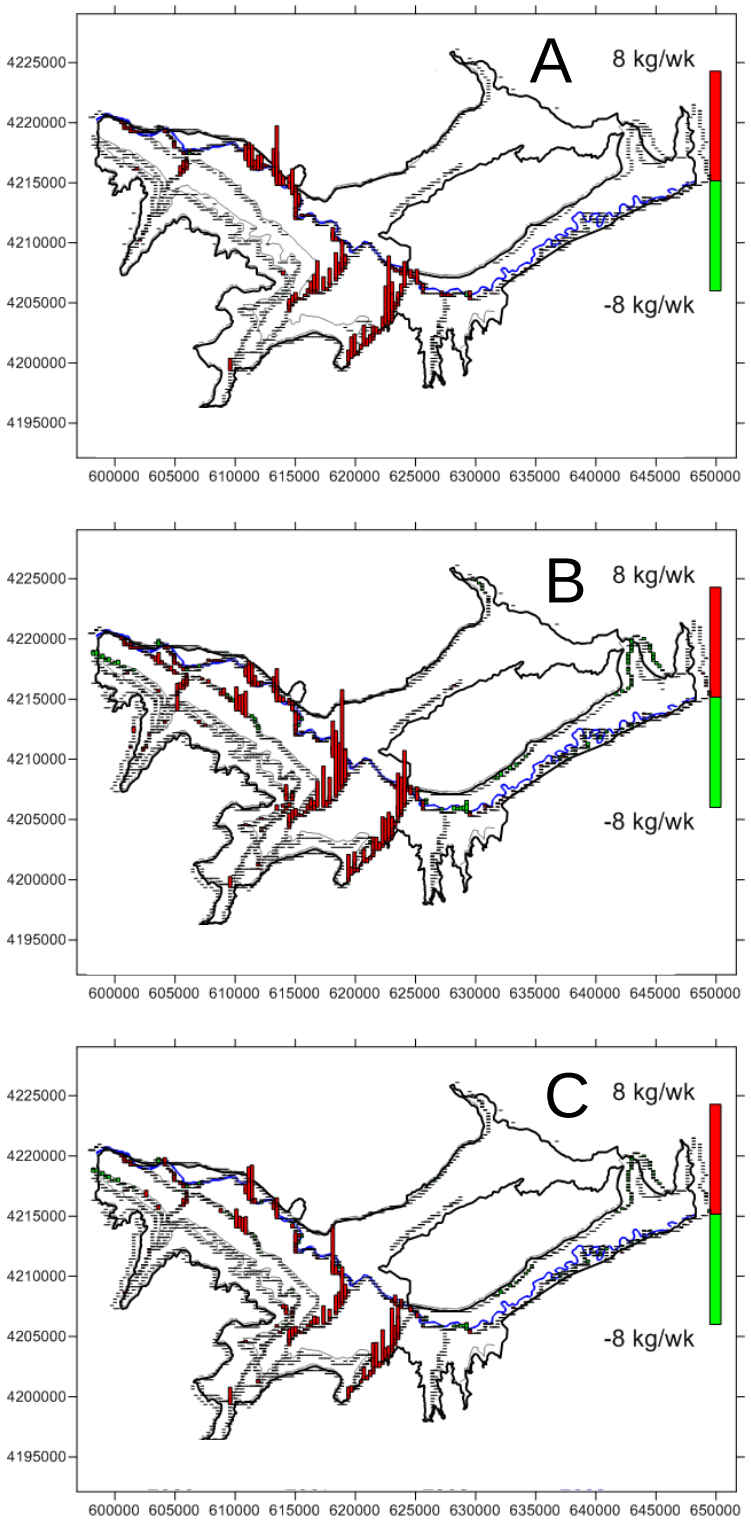

Figure 6- 53. Simulated mass exchange of SeO_4 between groundwater and surface, in kg/wk for (A) December 2 2006, (B) August 10 2008, and (C) May 17 2009 for each of the 1,943 river cells in the model domain. Red bars indicate mass loading from groundwater to surface water, and green bars indicate mass loading from surface water to groundwater.

Final model results shown (Figure 6-54) are the observed and simulated daily mass loadings of SeO_4 (kg) to Timpas Creek and Crooked Arroyo, the two main tributaries to the Arkansas River within the Upstream Study Region. As seen in Figure 6-54A, the model over-predicts the mass of Se discharged to Timpas Creek during the winter periods and under-predicts the mass of SeO_4 discharged during the summer months, except for the months during the summer of 2008. Under-prediction during the summer months is expected as the model does not account for surface runoff and drain input into surface water bodies, which is expected to be significant during the summer months. As seen in Figure 6-54B, the model greatly over-predicts the mass loading of SeO_4 to Crooked Arroyo for all but a few days during the 2006-2009 simulation period. The large loadings simulated by the model are due principally to the presence of shale along the length of Crooked Arroyo (see Figure 6-1) and resulting large amount of Se released from the shale through autotrophic reduction of both O_2 and NO_3. Also, the observed values are calculated using flow rates from a single gage within Crooked Arroyo and using measured C_{SeO_4} from a single sampling point, hence suggesting a considerable degree of uncertainty.

As model output within these areas does not affect significant portions of the aquifer, it was not deemed necessary to modify model parameters to match observed and simulated values during this modeling study. If coupling the model with surface transport processes, however, accurate simulation of mass loadings of the tributaries would become vastly more important. For such a case, chemical reduction rates assigned to the grid cells within the riparian areas of these two tributaries would be adjusted, similar to the process described in this chapter for matching observed and simulated loadings to the Arkansas River.

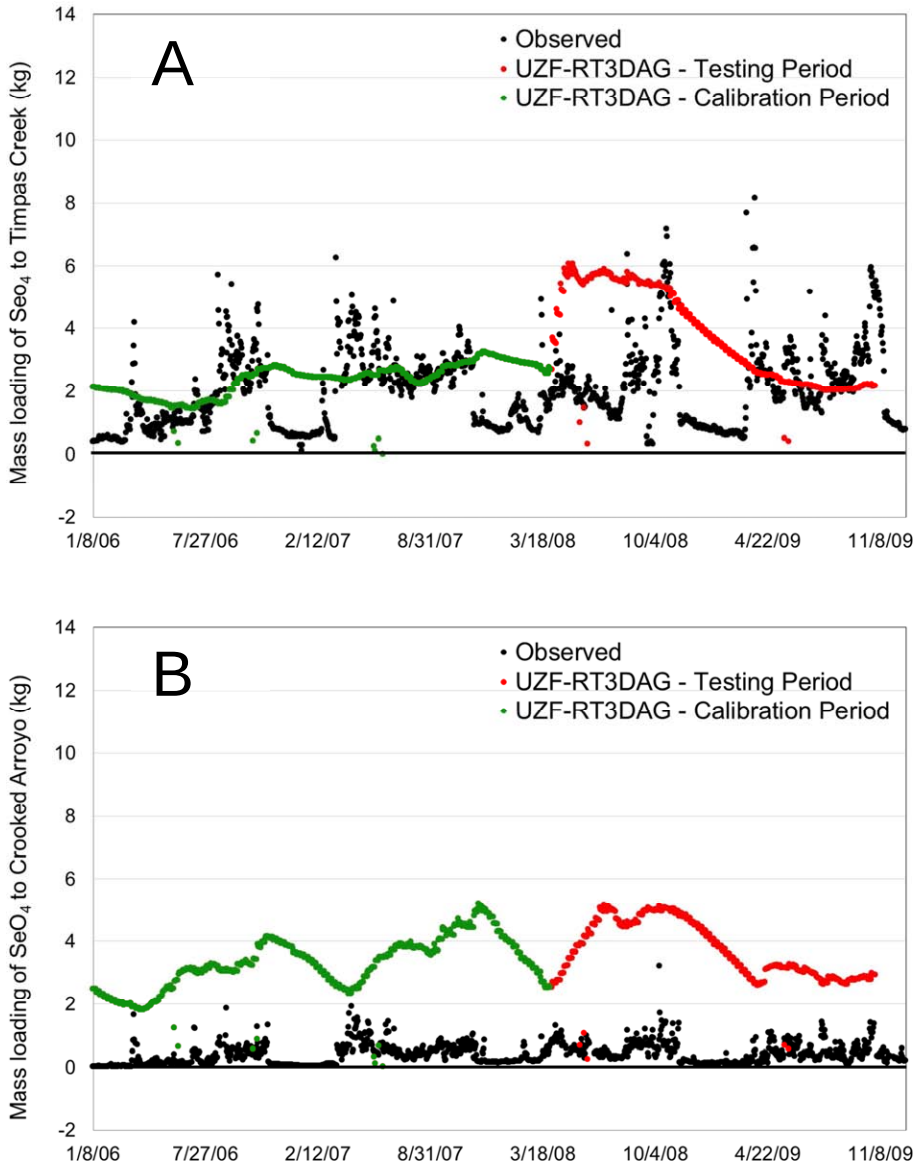

Figure 6- 54. Observed and simulated daily mass loadings of SeO_4 to (A) Timpas Creek and (B) Crooked Arroyo.

6.5 SUMMARY

This chapter summarized the application of the UZF-RT3DAG model to the 50,600-ha Upstream Study Region of the Lower Arkansas River Valley in southeastern Colorado, which has exhibited elevated concentrations of Se in the Arkansas River, the river tributaries, and

groundwater during recent decades. Following model calibration, achieved through comparison between observed and simulated average concentrations of O_2, NO_3, and SeO_4 in each command area and the daily mass loadings of Se to the Arkansas River for the January 1 2006 through March 31 2008, the model was tested for April 1 2008 through October 31 2009. Model parameters that required estimation are autotrophic reduction of O_2, $\lambda_{O_2}^{auto}$, autotrophic reduction of NO_3, $\lambda_{NO_3}^{auto}$, nitrification of NH_4, λ_{nit}, and heterotrophic reduction of SeO_4, $\lambda_{SeO_4}^{het}$, with the latter affecting mostly the mass loading of Se to the Arkansas River. Simulated concentrations and mass loadings compare favorably with observed values during both the calibration and testing period. Comparisons between observed and simulated values for other global comparisons (NO_3-SeO_4 relationship, SeO_4-SeO_3 relationship, frequency distribution of concentration values) also were very favorable. Chapter 7 presents the results of using the calibrated UZF-RT3AD model to explore BMP Scenarios within the Upstream Study Region to remediate elevated concentrations and mass loadings of SeO_4 and NO_3.

CHAPTER 7

INVESTIGATING BEST-MANAGEMENT PRACTICES OF SELENIUM AND NITROGEN REMEDIATION IN THE LOWER ARKANSAS RIVER VALLEY, SOUTHEASTERN COLORADO

7.1 INTRODUCTION

As discussed in Chapter 1, one important use of numerical models is analyzing the long-term impact of system changes on system-response variables. These changes are implemented into the system through alteration of system forcing terms or system parameters. For example, a key focus in agricultural watersheds may be the impact of system inputs such as nitrogen (N) fertilizer loading, rate of applied irrigation water, changes in land-use, and implementation of riparian buffer zones along streams, on calculated nutrient concentrations in groundwater and mass loadings of nutrients to streams. As discussed in Chapter 1, many field and modeling studies have addressed the impact of changes in one or more of these inputs (e.g., Heathwaite et al., 1998; Hefting and Klein, 1998; Chaplot et al., 2004). For modeling studies, models calibrated for certain study sites are run through a series of simulations, often 10 to 50 years in duration of simulation period, in which system inputs are systematically changed over a range of values. Although numerous models have explored alternatives for N remediation at both field-scale and watershed-scale, no known studies have been performed to explore alternatives for selenium (Se) remediation in agricultural watersheds.

In this study, the calibrated and tested Se reactive transport model presented in Chapter 6 is used to explore the impact of BMPs in the LARV in southeastern Colorado on C_{SeO_4} in groundwater and Se loading to the Arkansas River. Since the model also accounts for the fate and transport of N species, and due to the looming nutrient contamination problem in the LARV, the impact on C_{NO_3} and NO_3 loadings also will be presented. BMPs explored in this study include decreased N fertilizer loading, decreased values of C_{NO_3} and C_{SeO_4} in canal water derived from remediations upstream in the watershed, reduced irrigation application volumes, and the implementation of riparian buffer zones that are high in organic matter content. Results of these scenarios are compared against a Baseline ("do-nothing") Scenario. Consistent with other modeling studies (e.g., Chaplot et al., 2004; Ledoux et al., 2007; Lee et al., 2010) and with reports of quantified over-fertilization by farmers (Trachtenberg and Ogg, 1994), seasonal fertilizer loading reductions of 20% and 30% are explored. Canal concentrations are reduced by 20% and 30%, annual applied irrigation volumes are decreased by 10% and 20%, and first-order constants of heterotrophic denitrification and heterotrophic reduction of SeO_4, representing increased chemical activity in the riparian buffer zones due to higher contents of organic matter, are increased by 20% and 50%. For the irrigation scenarios, the groundwater flow model is re-run using the specified percentage of annual irrigation volume reduction.

Reduction in N fertilizer, besides the obvious impact on C_{NO_3} in groundwater and NO_3 loads to streams, was investigated due to the significant influence of NO_3 on SeO_4 in soil water and groundwater (see Chapter 2). The expected decreased values of C_{NO_3} will enable chemical reduction of SeO_4 to SeO_3, and hence eliminate SeO_4 from the system. Decreased values of C_{NO_3} also will decrease the amount of SeO_4 released from $FeSe_2$-bearing shale through autotrophic

denitrification, although the release of SeO_4 from shale through autotrophic reduction of O_2, a dominant process in the system (see Chapter 6), is not affected. The decrease in species concentrations assumes that remediation strategies have been implemented upstream of the canal diversion, and affects the species mass entering the root zone via applied irrigation water as well as the mass entering the subsurface via canal seepage. As explained further in Section 7.2, simulations are run for a 36-year period. It should be mentioned that no attempt is made herein to predict future species concentrations in groundwater and species mass loadings to surface water. Rather, the simulated concentrations and mass loadings of the BMP scenarios are compared against the Baseline Scenario in order to quantify potential changes in system behavior. Similarl to Chapters 5 and 6, NO_3 and SeO_4 throughout this chapter refer to NO_3-N and SeO_4-Se.

7.2 ALTERNATIVE LAND-MANAGEMENT SCENARIOS

The scenarios explored in this study are summarized in Table 7-1. Twelve scenarios, including one Baseline Scenario in which model inputs and parameters used in Chapter 6 are unchanged, are explored. For each scenario the targeted input is bolded and highlighted in gray. Scenarios 1 and 2 target fertilizer loading; Scenarios 3 and 4 target canal concentration; Scenarios 5 and 6 target irrigation volumes; Scenarios 7 and 8 target combinations of fertilizer loadings, canal concentration, and irrigation volumes; Scenarios 9 and 10 target first-order constants of chemical reduction reactions and hence implementation of riparian buffer zones; and Scenario 11 targets a combination of fertilizer loading, canal concentration, and riparian buffer zones. Throughout the remainder of this chapter, the scenarios will be identified using the label under the “Type” column in Table 7-1.

Percent decrease in annual fertilize loading is applied to each crop type within the Upstream Study Region (see Table 6-9); percent decrease in canal concentrations is applied to each canal within the Upstream Study Region (see Table 6-11); percent decrease in applied irrigation water volume is applied across the entire model domain; and percent increase in the rate constants of heterotrophic denitrification and heterotrophic reduction of SeO_4 is applied to the base values of 0.10 d^{-1} and 0.02 d^{-1}, respectively.

Table 7- 1. Summary of 11 scenario alternatives investigated using the calibrated model.

Scenario	Type	% Fert Reduction	% Canal Conc. Reduction	% Irrigation Reduction	% Increase in λ_x^{het}	$\lambda_{NO_3}^{het}$	$\lambda_{SeO_4}^{het}$
Baseline	Baseline	0	0	0	0	0.10	0.020
1	F20	**20**	0	0	0	0.10	0.020
2	F30	**30**	0	0	0	0.10	0.020
3	C20	0	**20**	0	0	0.10	0.020
4	C30	0	**30**	0	0	0.10	0.020
5	I10	0	0	**10**	0	0.10	0.020
6	I20	0	0	**20**	0	0.10	0.020
7	F30 C30	**30**	**30**	0	0	0.10	0.020
8	F30 C30 I20	**30**	**30**	**20**	0	0.10	0.020
9	HET20	0	0	0	**20**	**0.12**	**0.024**
10	HET50	0	0	0	**50**	**0.15**	**0.030**
11	F30 C30 HET50	**30**	**30**	0	**50**	**0.15**	**0.030**

As discussed in Chapter 1, many modeling studies investigating the effect of BMPs use simulation periods between one to several decades. This is done to (i) provide adequate time for the complete effect of the BMPs to register in mass loadings to streams, and (ii) incorporate the temporal variability in climate. For (i), the long time required to affect mass loadings is due to the long travel time of subsurface water from infiltration at the ground surface to points of aquifer-stream interaction.

To provide a quantification of the travel time in the LARV, the groundwater flow simulation used during 2006-2009, as described in Chapter 6, was used to calculate time of travel from each

point in the aquifer to surface water (i.e., Arkansas River and its tributaries). This would provide an indication of the time required for changes implemented in cultivated fields to impact mass loadings in the Arkansas River. For each week of the simulation, the distance and travel time to surface water was calculated for each grid cell in the aquifer using the current groundwater flow paths. The travel time at each grid cell was then averaged over the weeks of the simulation to get approximate spatial values.

This process is highly approximate since calculations for each week are performed assuming that the current groundwater flow paths are in dynamic equilibrium, which is not the case. Further studies will include particle tracking to provide a more accurate depiction of groundwater travel times. However, current results provide a rough approximation of travel time to surface water. Spatial contour plots of approximate travel time to surface water are shown in Figure 7-1, with the same results shown in Figures 7-1A, 7-1B, 7-1C using scales of 5, 20, and 50 years, respectively. For each plot, groundwater in areas shown in red will not reach surface water until the maximum time of the scale, e.g., for Figure 7-1B the groundwater in red areas will not reach surface water for at least 20 years. For Figure 7-1A, notice the small percentage of total land area that has groundwater that will reach surface water within 5 years. Furthermore, note that it appears that the groundwater in a significant spatial extent of the shale-affected zones takes more than 30 years to reach the tributaries and the Arkansas River.

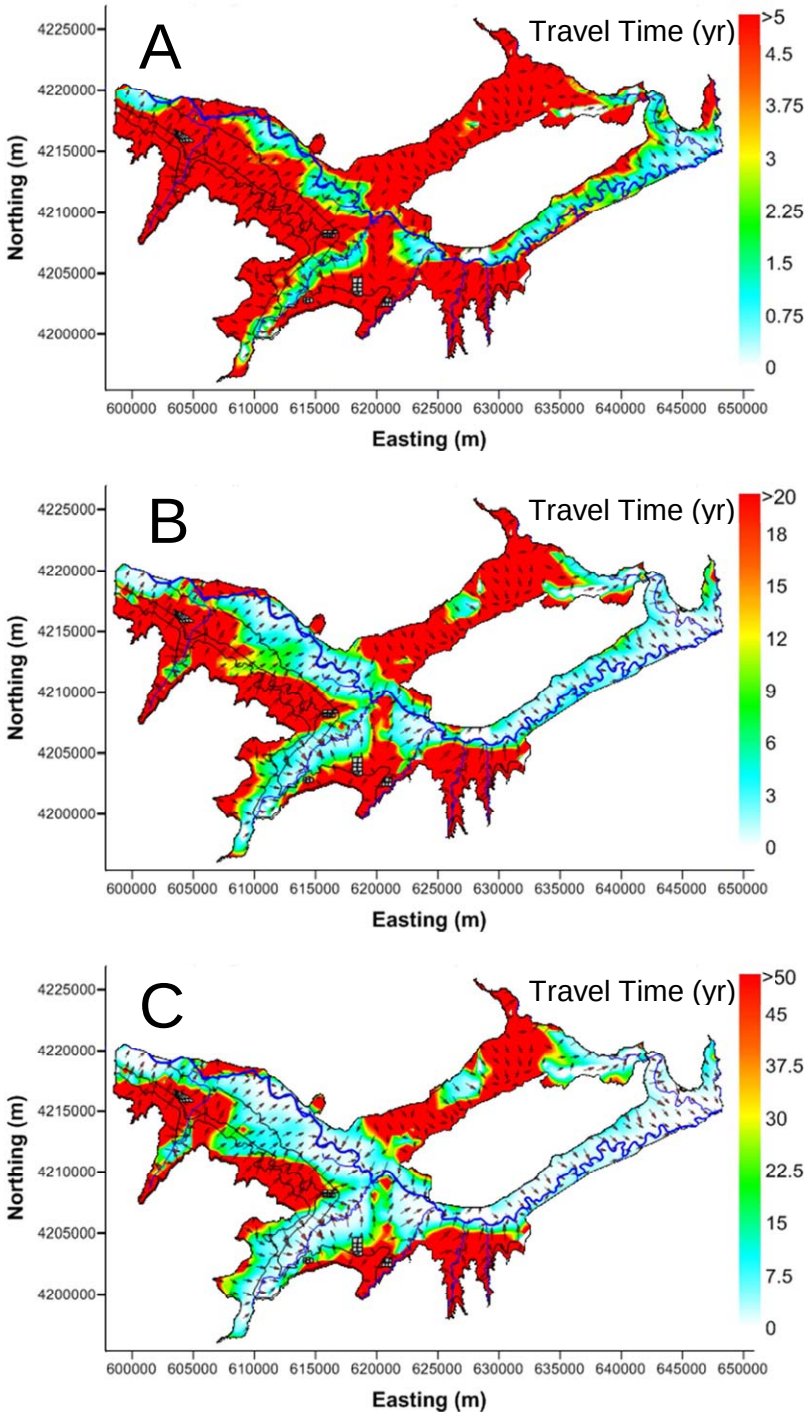

Figure 7- 1. Travel time to surface water for each point in the aquifer of the Upstream Study Region of the LARV, using a scale of (A) 5 years, (B) 20 years, and (C) 50 years. For each plot, groundwater in areas shown in red will not reach surface water until the maximum time of the scale.

Using the results of the travel time calculations and the results of other modeling studies, the following process is used to establish long-term simulations for the BMPs. In essence this involves establishing the groundwater flow field for several decades. First, each scenario simulation is run for the years 2006-2009 using the scenario features described in Table 7-1. Second, using the results of the 2006-2009 simulation as initial conditions, each scenario simulation is run for a 36-year simulation, using four cycles of the calibrated 8 ½-year groundwater flow simulation of Gates et al. (2012) for the Upstream Study Region for 1999-2007. For the irrigation scenarios (Scenario 5, 6, and 8), the groundwater flow field results from running the groundwater flow simulation for 1999-2007 using the specified percentage of reduced irrigation volumes. Compared to historical streamflow in the Arkansas River (see Figure 6-2), the 9-year period from 1999-2007 is representative of a 9-year pattern of streamflow, with a very wet year (1999) as well as very dry years (2002-2003). This is shown in a plot of streamflow for the Arkansas River at Catlin Dam for 1999-2009, normalized to the average streamflow of 18.3 $m^3 s^{-1}$ for 1965-2009 shown in red. As seen in the figure, 1999 is a very wet year, 2002-2003 are very dry years, and 2000, 2001, and 2004-2009 are average years. Hence, besides providing adequate time for groundwater under the majority of cultivated fields to discharge to surface water, the 36-year simulation provides also for temporal variability in climate.

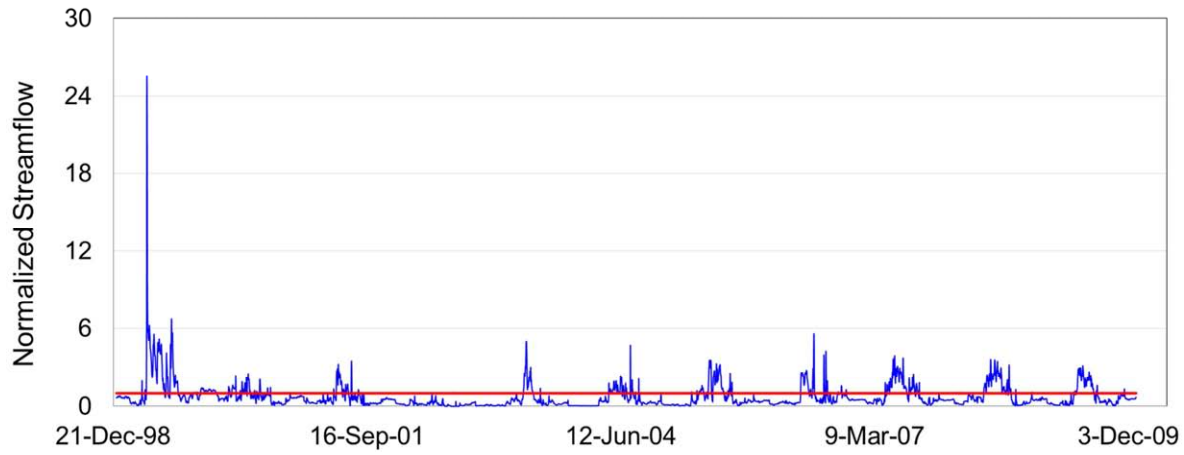

Figure 7- 2. Normalized stream discharge of the Arkansas River at Catlin Dam to average stream discharge for 1965-2009, for the years 1999-2009.

The results of each of the 11 scenarios are compared to the results of the Baseline Scenario, with the following two measures used to quantify the relative success of each scenario in decreasing concentrations and mass loadings of SeO_4 and NO_3:

(1) The difference in total daily mass loadings (summed over the reach of the Arkansas River within the Upstream Study Region) for the entire simulation period between the scenario simulation and the Baseline simulation, and

(2) The difference in groundwater concentration at the end of the simulation period between the scenario simulation and the Baseline simulation, using command-area averages.

The spatial patterns in mass loadings and groundwater concentration leading to the values calculated in (1) and (2) also are investigated, with changes in groundwater concentration and mass exchange between groundwater and surface water plotted for each grid cell and each River cell, respectively. For groundwater concentration, differences between the scenario simulation and the Baseline Scenario are shown for the last day of the simulation. For mass exchange between groundwater and surface water, differences are summed over the period of the simulation.

7.3 RESULTS

7.3.1 Average Command Area Concentrations in Groundwater

For the first analysis of the scenario simulation results, the average C_{SeO_4} and C_{NO_3} for each command area is calculated for each 3-month period and compared to the Baseline simulation values. Figure 7-3 shows the resulting time series of average C_{SeO_4} in groundwater for Scenarios 2, 4, 6, 7, 10, and 11 for each command area. Values were taken from layer 4 of the model, coinciding with the analysis performed in Chapter 6. Different scales of C_{SeO_4} are used for each command area figure in order to view the differences in concentration. As can be seen in the figure, C_{SeO_4} for the BMP scenarios are relatively unchanged from the Baseline simulation for the Highline, Otero, and Catlin command areas, but have a noteworthy decrease from the Baseline simulation for the Rocky Ford Ditch, Fort Lyon, and Holbrook command areas as well as for the Outside Area. For all command areas the Scenario with fertilizer, canal concentration, and riparian area implementations (Scenario 11) had the lower average C_{SeO_4} through the 36-year period.

The decrease in concentration also is reflected in Table 7-2, which shows the percent reduction for each scenario and command area from the Baseline simulation, using the concentration values at the end of the simulation. The two fertilizer scenarios (Scenarios 1 and 2) had minimal impact on C_{SeO_4}, with the highest percent change occurring for the Holbrook command area (2.8%). The two canal concentration scenarios (3 and 4) had a noteworthy impact for the Fort Lyon command area (11.7% and 17.7%), likely due to the high proportion of cultivated fields adjacent to the canal. The two riparian area scenarios (9 and 10) also had minimal impact. Overall, the Fort Lyon command area had the highest percent decrease in C_{SeO_4}

due to its sensitivity to canal concentration. The irrigation scenarios (5 and 6) actually had increased values of C_{SeO_4}. This is due not only to the decreased water content, and hence an increase in solute concentration for a given mass of SeO_4, but also due to hyper-concentration of SeO_4 in the upper soil layers due to a decrease in infiltration rates and corresponding leaching.

Average C_{SeO_4} for layers 1-6 for the Fort Lyon command area are shown in Figure 7-4, to demonstrate the variability in C_{SeO_4} through the thickness of the aquifer. The cell-by-cell values of C_{SeO_4} will be presented in Section 7.3.3 to provide insights into the areas within each command area that contribute to the decrease in average C_{SeO_4}.

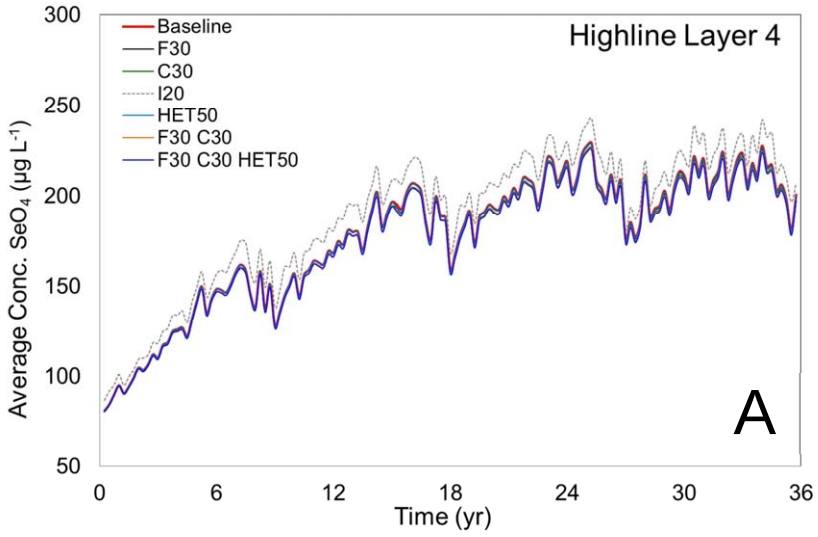

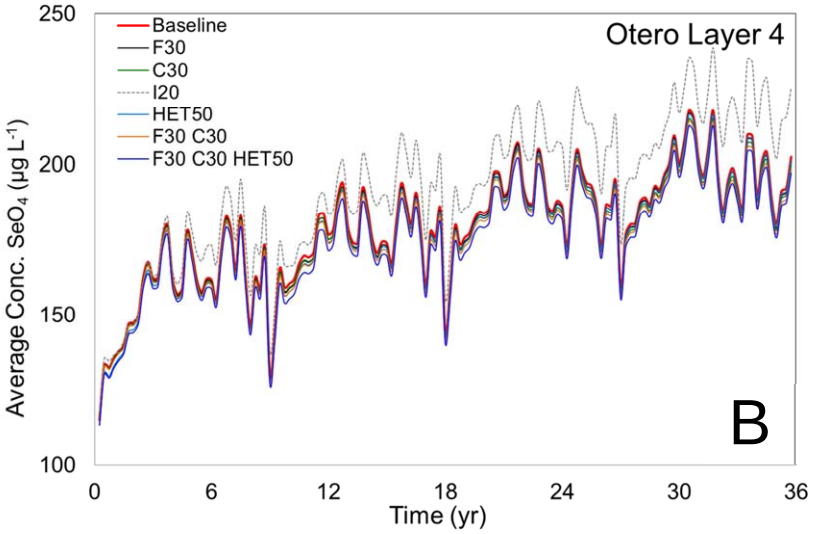
Otero Layer 4
Baseline
F30
C30
I20
HET50
F30 C30
F30 C30 HET50
Average Conc. SeO4 (µg L-1)
Time (yr)
B

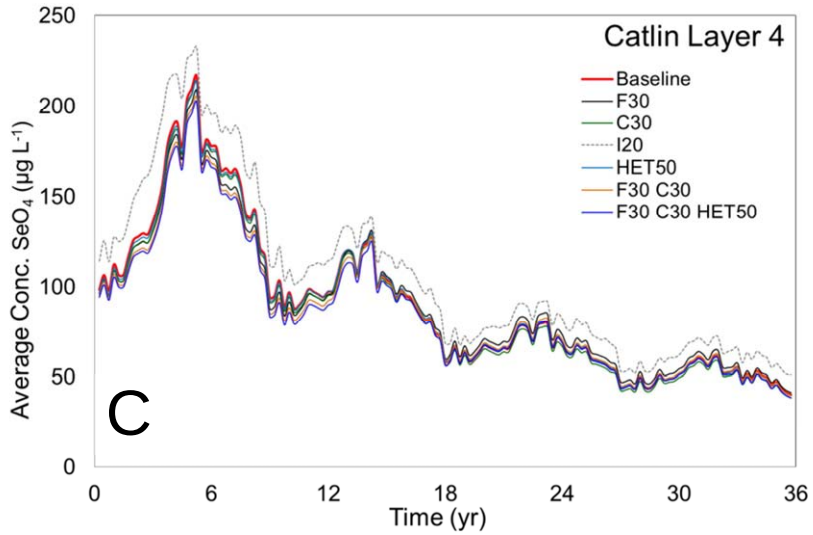
Catlin Layer 4
Baseline
F30
C30
I20
HET50
F30 C30
F30 C30 HET50
Average Conc. SeO4 (µg L-1)
Time (yr)
C

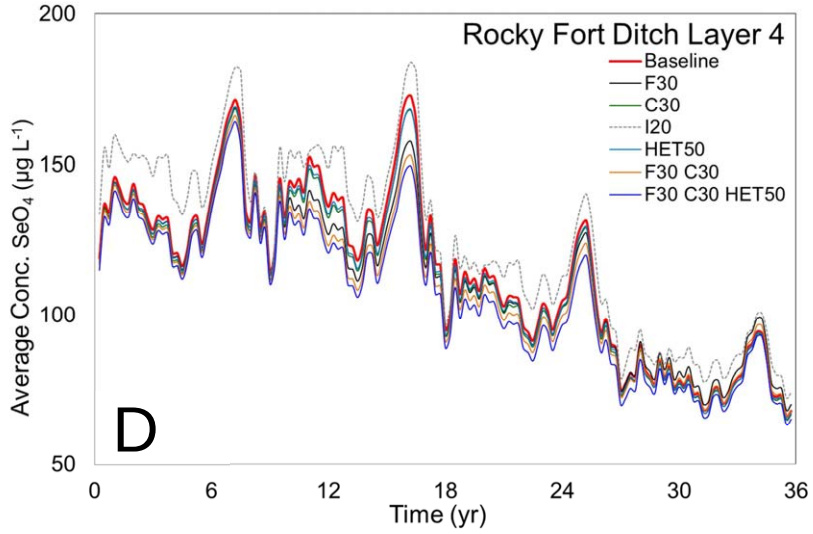
Rocky Fort Ditch Layer 4
Baseline
F30
C30
I20
HET50
F30 C30
F30 C30 HET50
Average Conc. SeO4 (µg L-1)
Time (yr)
D

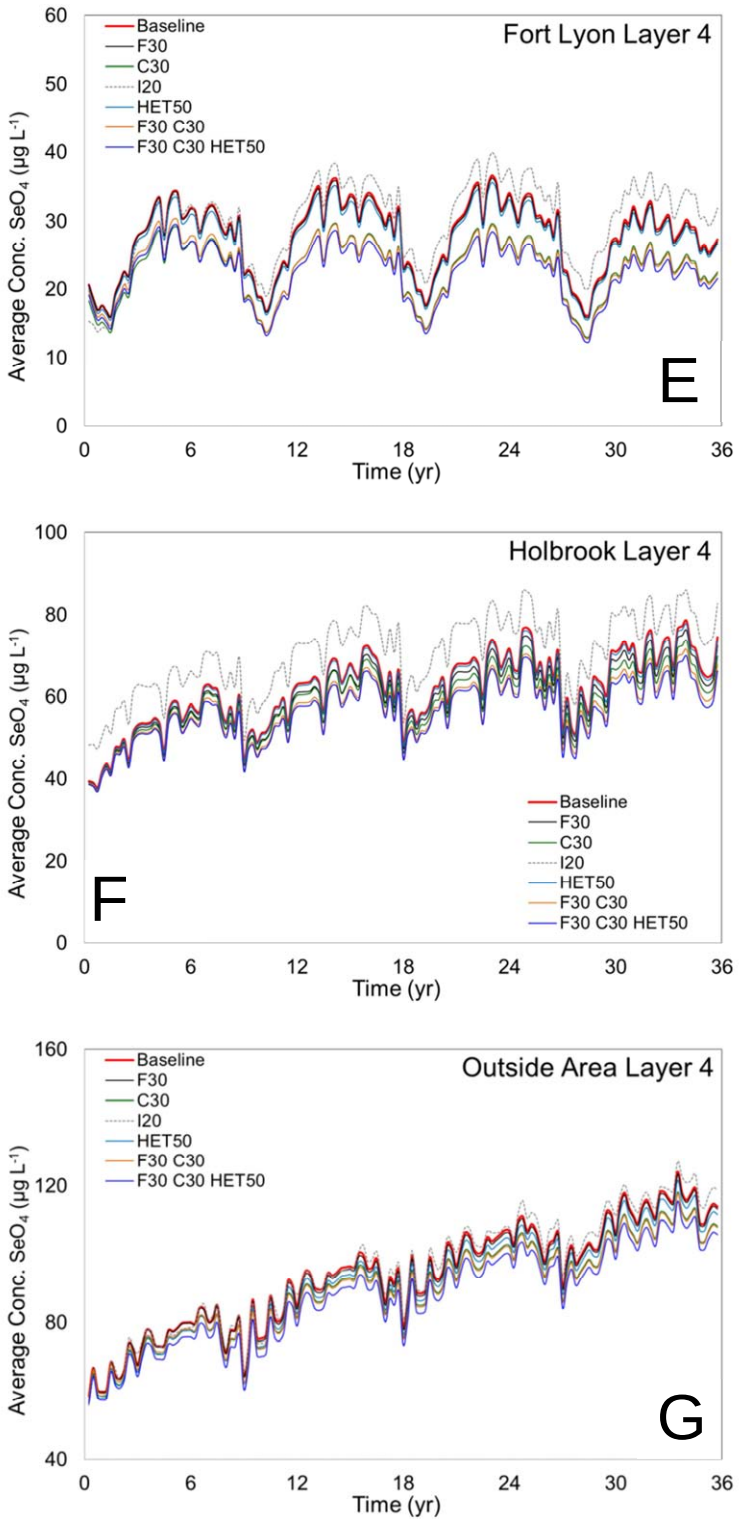

Figure 7- 3. Average C_{SeO_4} in layer 4 for the (A) Highline, (B) Otero, (C) Catlin, (D) Rocky Ford Ditch, € Fort Lyon, and (F) Holbrook command areas, for each 3-month period of the 36-year scenario simulations. (G) shows the average C_{SeO_4} for the Outside Area.

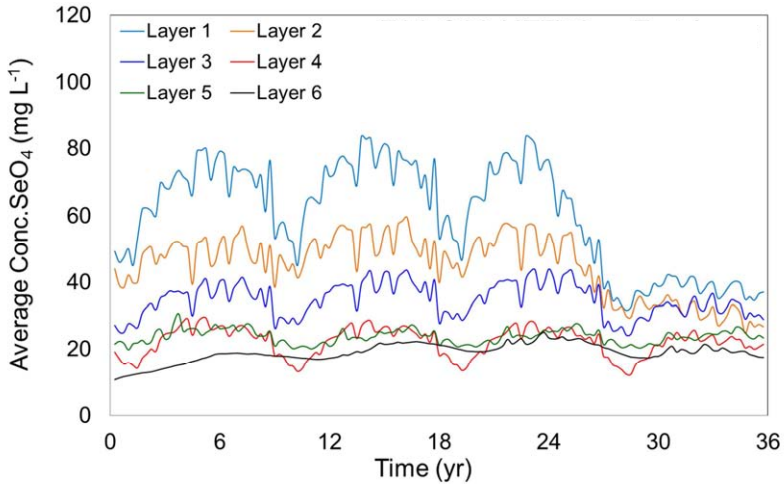

Figure 7- 4. Average C_{SeO_4} for each model layer for the Fort Lyon command area for Scenario 11.

Table 7- 2. Percent reduction in average C_{SeO_4} for each command area at the end of the 36-year scenario simulation with layer 4 of the model, as compared to the Baseline Scenario.

Scen.	Type	Highline	Otero	Catlin	RF Ditch	Fort Lyon	Holbrook	Outside
1	F20	0.3%	0.5%	-2.5%	-2.3%	1.0%	1.6%	0.4%
2	F30	0.4%	0.8%	-2.9%	-3.1%	1.4%	2.8%	0.6%
3	C20	0.7%	0.8%	2.9%	1.6%	11.7%	4.2%	3.3%
4	C30	1.1%	1.3%	4.3%	1.9%	17.7%	6.3%	4.9%
5	I10	1.2%	-4.6%	-13.5%	-4.5%	-7.8%	-9.3%	-2.3%
6	I20	-3.2%	-11.5%	-27.0%	-9.1%	-16.7%	-11.1%	-4.3%
7	F30 C30	1.4%	2.0%	1.4%	-0.1%	18.8%	9.0%	5.3%
8	F30 C30 I20	-1.5%	-9.6%	-25.1%	-7.8%	5.9%	-3.1%	0.7%
9	HET20	0.1%	0.3%	0.5%	0.5%	1.1%	0.5%	0.9%
10	HET50	0.3%	0.6%	1.1%	1.2%	2.5%	1.1%	2.0%
11	F30 C30 HET50	1.7%	2.6%	4.2%	4.3%	21.1%	11.1%	7.0%

Comparisons between the BMP scenarios and the Baseline scenario also were performed for NO_3 in terms of command area average concentrations. These results are shown in Figure 7-5 for each command area. Similar to the SeO_4 results shown in Figure 7-3, the lowest values of C_{NO_3} occur for Scenario 11. However, changes in average C_{NO_3} values during the 36-year period as

compared to the Baseline simulation are much greater than for C_{SeO_4}. This can be seen in Table 7-3, with percent reductions of 40%, 33%, 49%, 41%, and 31% for Scenario 11 for the Highline, Otero, Catlin, Rocky Ford Ditch, and Fort Lyon command areas, respectively. These changes are due primarily to the influence of the fertilizer scenarios (1 and 2) on C_{NO_3} throughout the aquifer, with percent reductions of 35%, 28%, 41%, 31%, and 12% for Scenario 2 for the same command areas. These results are expected, as sensitivity results in Chapter 6 and Appendix C indicate that nitrification of NH_4 is the most influential process in governing C_{NO_3} in the saturated zone. The cell-by-cell values of C_{NO_3} will be presented in Section 7.3.3 to provide insights into the areas within each command area that contribute to the decrease in average concentration

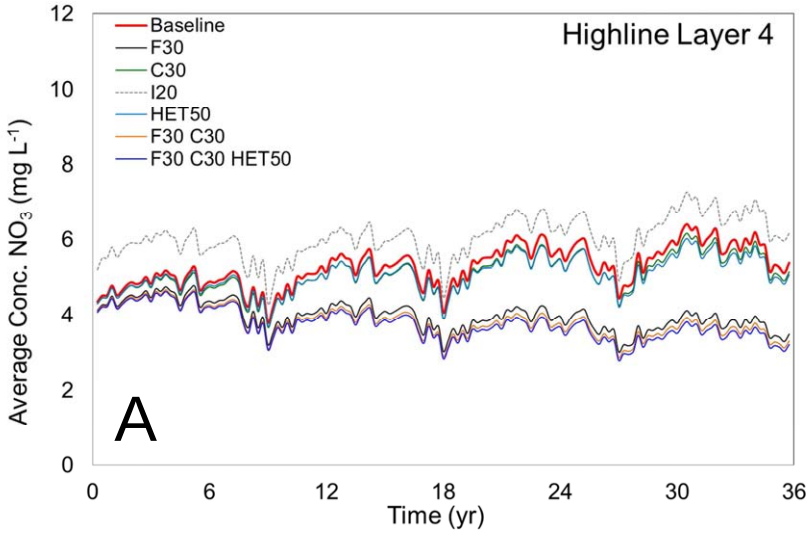

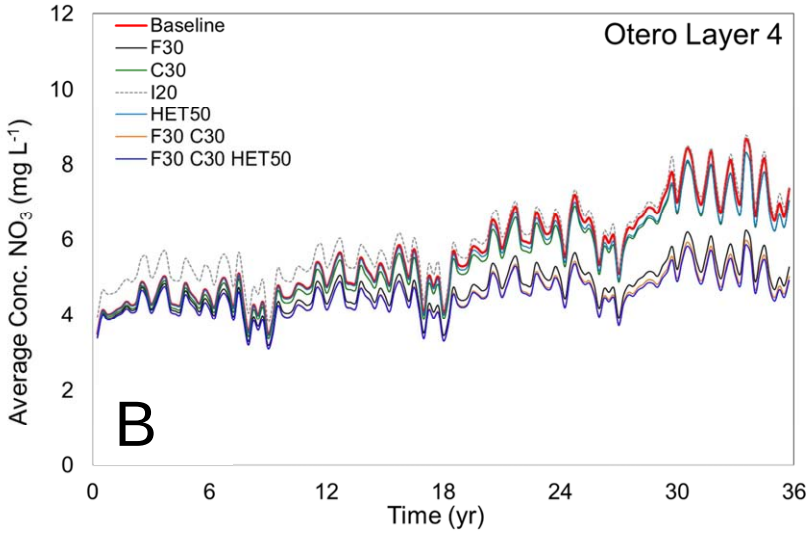
Baseline
F30
C30
I20
HET50
F30 C30
F30 C30 HET50
Otero Layer 4
B
Average Conc. NO_3 (mg L^{-1})
Time (yr)
0
2
4
6
8
10
12
0
6
12
18
24
30
36

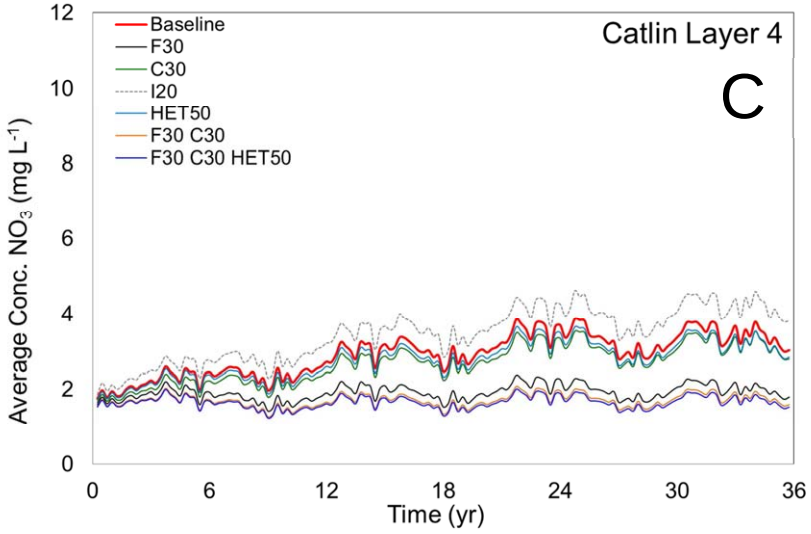
Baseline
F30
C30
I20
HET50
F30 C30
F30 C30 HET50
Catlin Layer 4
C
Average Conc. NO_3 (mg L^{-1})
Time (yr)
0
2
4
6
8
10
12
0
6
12
18
24
30
36

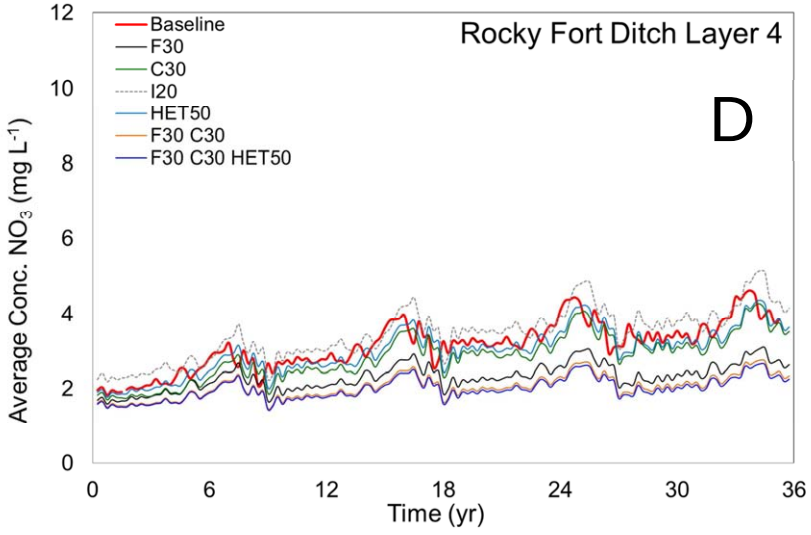
Baseline
F30
C30
I20
HET50
F30 C30
F30 C30 HET50
Rocky Fort Ditch Layer 4
D
Average Conc. NO_3 (mg L^{-1})
Time (yr)
0
2
4
6
8
10
12
0
6
12
18
24
30
36

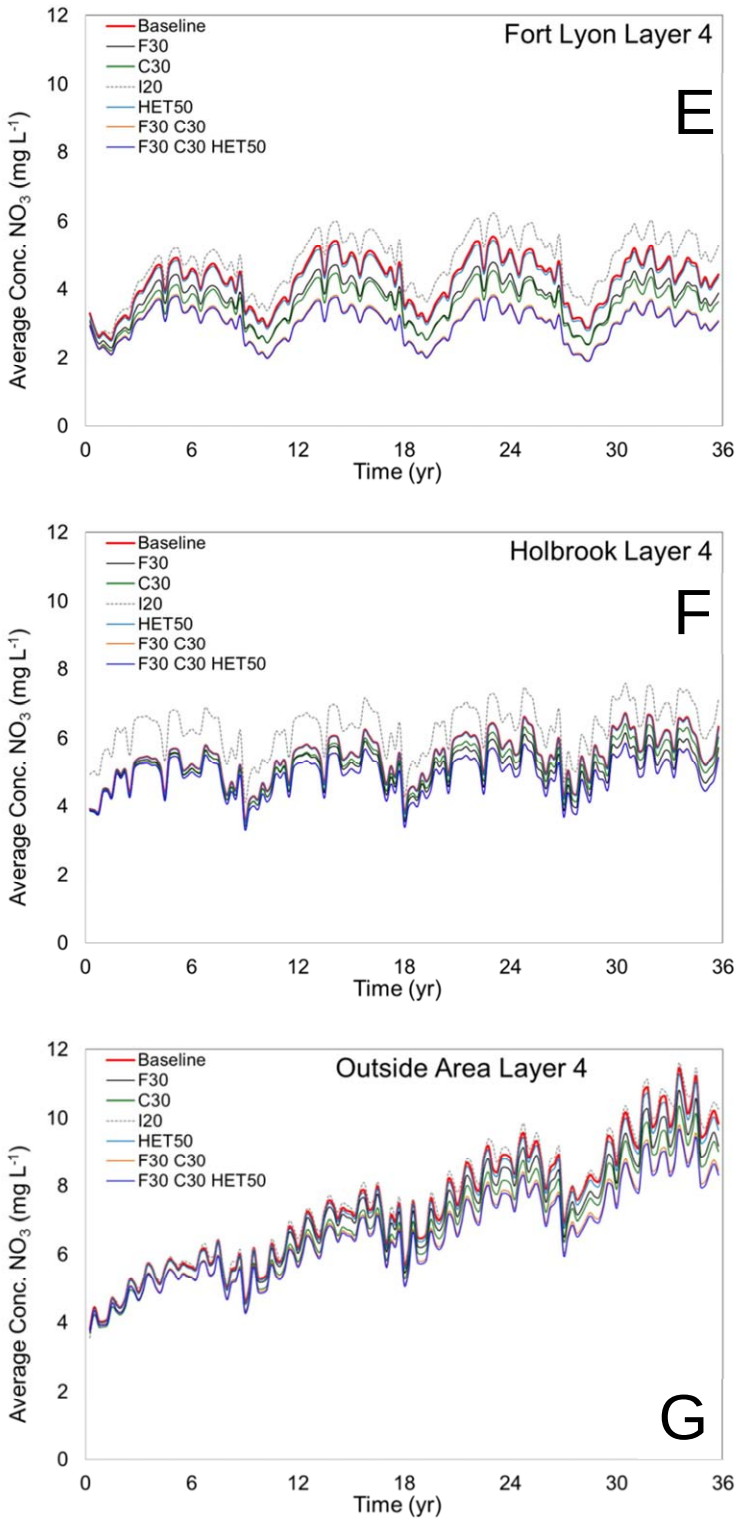

Figure 7- 5. Average C_{NO_3} in layer 4 for the (A) Highline, (B) Otero, (C) Catlin, (D) Rocky Ford Ditch, (E) Fort Lyon, and (F) Holbrook command areas, for each 3-month period of the 36-year scenario simulations. (F) shows the average concentration for the Outside Area.

Table 7- 3. Percent reduction in average C_{NO_3} for each command area at the end of the 36-year scenario simulation, as compared to the Baseline Scenario.

Scen.	Type	Highline	Otero	Catlin	RF Ditch	Fort Lyon	Holbrook	Outside
1	F20	27%	22%	31%	24%	9%	7%	5%
2	F30	35%	28%	41%	31%	12%	9%	7%
3	C20	3%	3%	5%	6%	12%	3%	6%
4	C30	4%	4%	8%	8%	18%	5%	8%
5	I10	-8%	1%	-13%	-4%	-9%	-11%	-4%
6	I20	-15%	-1%	-26%	-8%	-19%	-13%	-4%
7	F30 C30	39%	32%	47%	39%	30%	14%	14%
8	F30 C30 I20	30%	29%	35%	35%	18%	2%	9%
9	HET20	2%	2%	3%	2%	1%	0%	1%
10	HET50	6%	4%	6%	5%	2%	1%	2%
11	F30 C30 HET50	40%	33%	49%	41%	31%	14%	16%

Further analysis was performed to examine the assumption that 36 years is an adequate length of time for the BMP simulations to reach a new dynamic equilibrium. Figure 7-6 shows the percent reduction in both C_{SeO_4} and C_{NO_3} through the 36-year period for each command area, with the percent reduction (i.e., the decrease in concentration as compared to the Baseline simulation) becoming steady during the last two decades of the simulation. Figure 7-7 shows the percent reduction in both C_{SeO_4} and C_{NO_3} for layers 1-6 of the model, with results for the Fort Lyon and Catlin command areas shown for C_{SeO_4} and C_{NO_3}, respectively. Again, values of percent reduction become steady in time during the last two decades of the simulation. These results demonstrate that, in regards to average groundwater concentrations calculated in both the lateral dimensions (by command area) and the vertical dimension (aquifer depth), 36 years is an adequate length of time for the aquifer system to adjust to the BMP implementations and reach a new dynamic equilibrium.

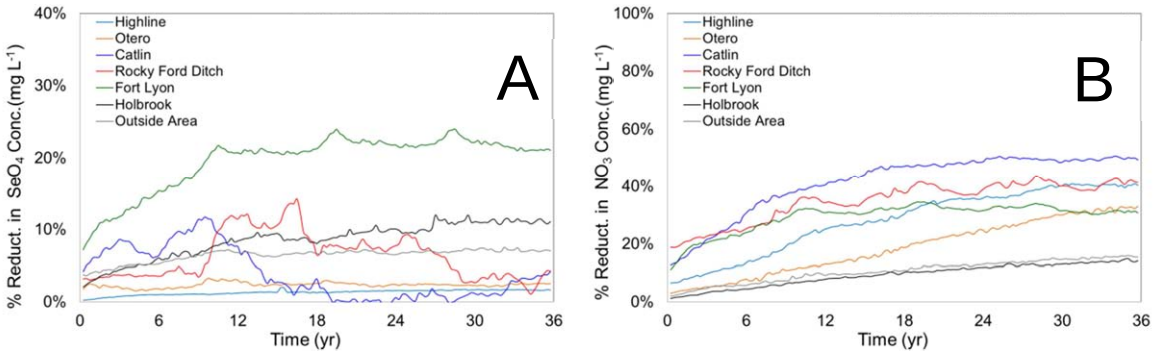

Figure 7- 6. Percent reduction in average concentration for each command area for (A) SeO_4 and (B) NO_3 for each command area for Scenario 11, as compared to the Baseline scenario.

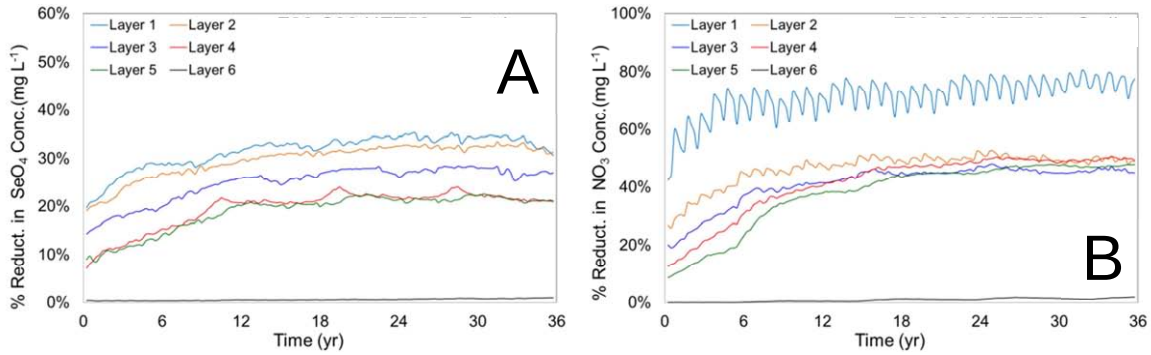

Figure 7- 7. Percent reduction in average concentration for model layers 1-6 for (A) SeO_4 for the Fort Lyon command area and (B) NO_3 for the Catlin command area for Scenario 11, as compared to the Baseline scenario.

7.3.2 Total Change in Daily Mass Loading to Arkansas River

For the second analysis of the scenario simulation results, the total mass loadings to the Arkansas River, as calculated using all River cells along the reach of the Arkansas River in the Upstream Study Region, are compared with the Baseline simulation results for each BMP scenario. Figure 7-8 shows the time series of daily mass loadings of SeO_4 to the Arkansas River from the aquifer for Scenarios 2, 4, and 6 (Figure 7-8A), Scenarios 9 and 10 (Figure 7-8B), and the multi-practice Scenarios 8 and 11. As can be seen in Figure 7-8C, the multi-practice Scenarios have the largest impact in reducing the mass loadings of SeO_4 to the Arkansas River, with Scenario 11 having the greatest impact of the two. As seen in Figures 7-8A and 7-8B, the

riparian area implementation Scenarios have a greater impact in reducing SeO_4 loads than the fertilizer, canal concentration, and reduced irrigation Scenarios. In future studies the loading of SeO_3 to the Arkansas River will be added to the loading of SeO_4 to obtain the loading of total dissolved Se. However, since SeO_4 comprises approximately 90-100% of total dissolved Se in groundwater (see Figure 6-42), the results shown here are an adequate approximate of Se loadings.

These results are reflected in Figure 7-9, which shows the total percent reduction of SeO_4 loads for each Scenario as compared to the Baseline simulation. Scenario 11 has the highest percent reduction with 34.5%, followed by Scenario 10 with 20.5%, Scenario 8 with 19.1%, and Scenario 7 with 15.5%. These results indicate that the single-practice BMP of riparian area implementation has a larger impact for Se load reduction than the combined practices of fertilizer, canal concentration, and irrigation volume reduction, and that the riparian area implementation causes the majority of the load reduction for Scenario 11.

Of the single-practice BMPs, riparian area implementation had the highest degree of impact (9.4% and 20.5% for Scenarios 9 and 10, respectively), followed by the canal concentration (5.7% and 8.7% for Scenarios 3 and 4), fertilizer (4.5% and 7.1% for Scenarios 1 and 2), and irrigation reduction (3.6% and 7.4% for Scenarios 5 and 6), although the latter three are not significantly different. The cell-by-cell values will be presented in Section 7.3.4 to provide insights into the areas along the River that contribute to the load reduction.

Similar to Figures 7-6 and 7-7, which show the attainment of steady conditions for the Scenarios in regards to groundwater concentrations, Figure 7-10 shows the percent reduction of SeO_4 loads for Scenario 11 as compared to the Baseline Scenario. As can be seen in the figure, the values of percent reduction become steady within the first two decades of the simulation,

indicating that the mass exchange between the aquifer and the River has responded adequately to the impacts of the BMP implementations during the 36-year period.

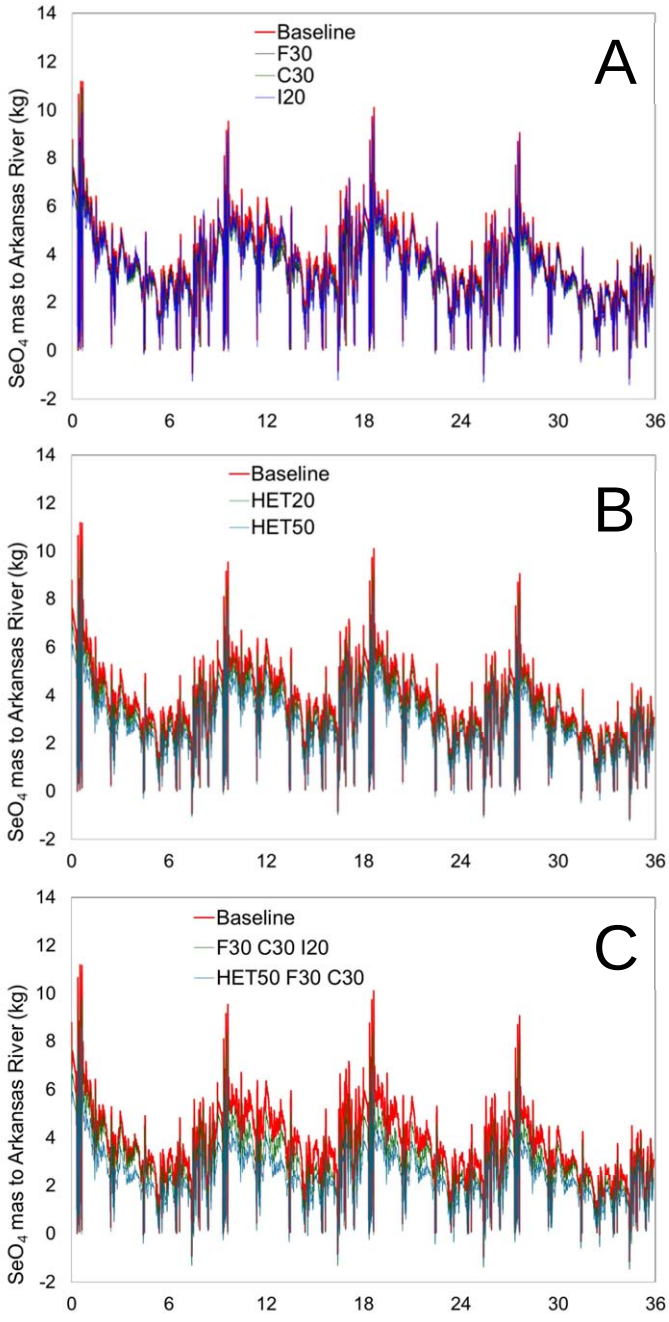

Figure 7- 8. Daily mass loadings of SeO_4 (kg) to the Arkansas River during the 36-year scenario simulation for (A) the single-approach scenarios (2,4,6), (B) the riparian area scenarios (9,10) and (C) the multi-approach scenarios (8,11) . For each figure, the daily mass loadings of the Baseline Scenario also are included for comparison.

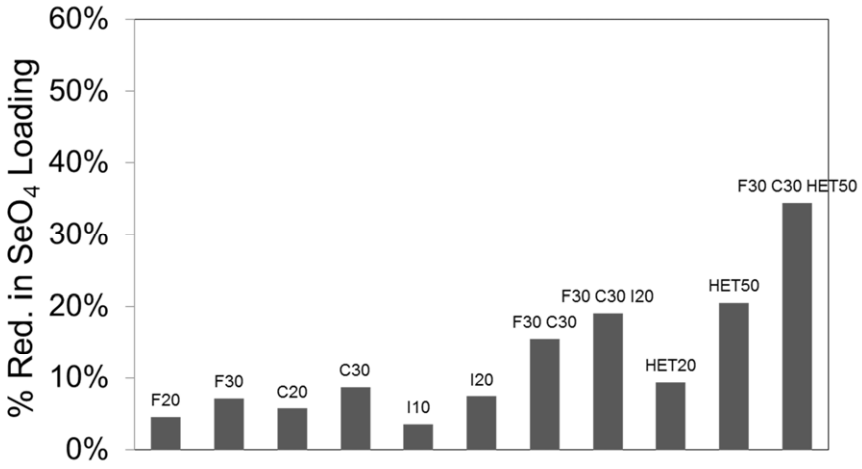

Figure 7- 9. Total percent reduction in mass loadings of SeO_4 to the Arkansas River for each Scenario during the 36-year simulation, as compared to the Baseline Scenario.

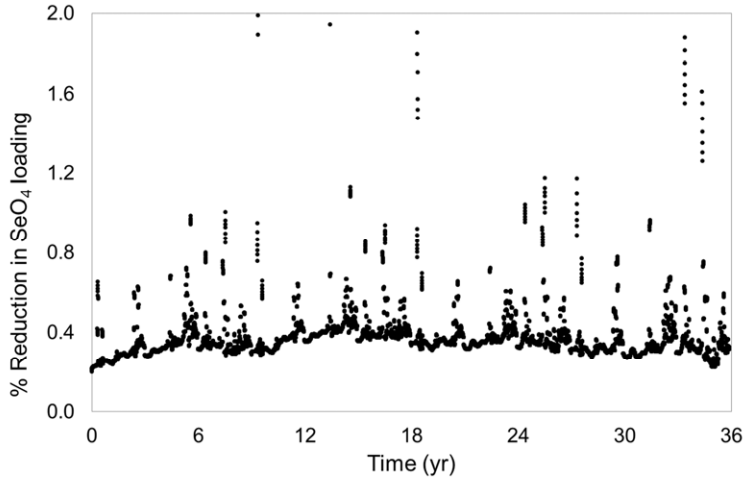

Figure 7- 10. Percent reduction in mass loading of SeO_4 to the Arkansas River during the 36-year scenario simulation for Scenario 11, as compared to the Baseline Scenario.

Comparisons between the BMP scenarios and the Baseline scenario also were performed for NO_3 loads to the Arkansas River. Figure 7-11 shows the daily mass loadings for the single-practice scenarios (Figures 7-11A, 7-11B, and 7-11C) and the multi-practice scenarios (Figure 7-11D). Similar to the results for Se loading, the largest decrease in mass loading of NO_3 occurs for the multi-practice scenarios, as shown in Figure 7-11D. This is reflected in Figure 7-12,

which shows the total percent reduction of NO_3 loads for each scenario as compared to the Baseline simulation. Scenario 11 has the highest percent reduction with 52.0%, followed by Scenario 8 with 48.2% and Scenario 7 with 42.5%, all of which are multi-practice scenarios. However, going from the three-practice Scenario 8 to the four-practice Scenario 11 only increased the load reduction from 48.2% to 52.0%, demonstrating the small effect of the riparian area implementation on the NO_3 loads to the River. This is in contrast to the results for SeO_4 loading, which showed a strong dependency on the chemical activity of the riparian zone.

Of the single-practice BMPs, fertilizer reduction had the highest degree of impact (17.7% and 24.2% for Scenarios 1 and 2, respectively), followed by the canal concentration (13.2% and 19.9% for Scenarios 3 and 4), riparian area implementation (6.3% and 13.7% for Scenarios 9 and 10), and irrigation reduction (4.4% and 9.5% for Scenarios 5 and 6). The cell-by-cell values will be presented in Section 7.3.4 to provide insights into the areas along the River that contribute to the load reduction.

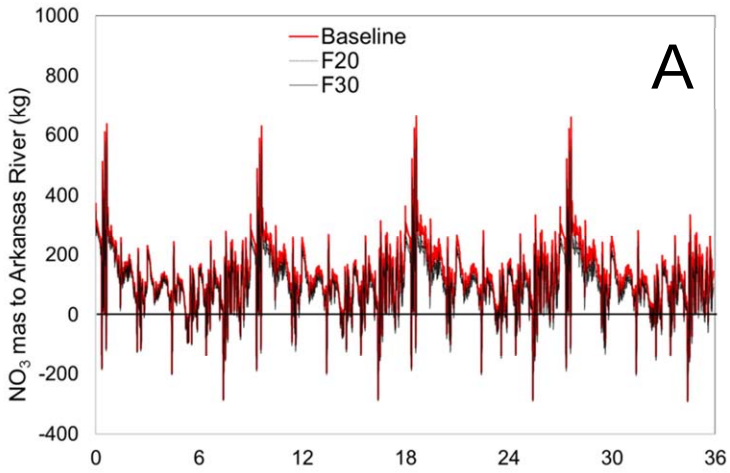

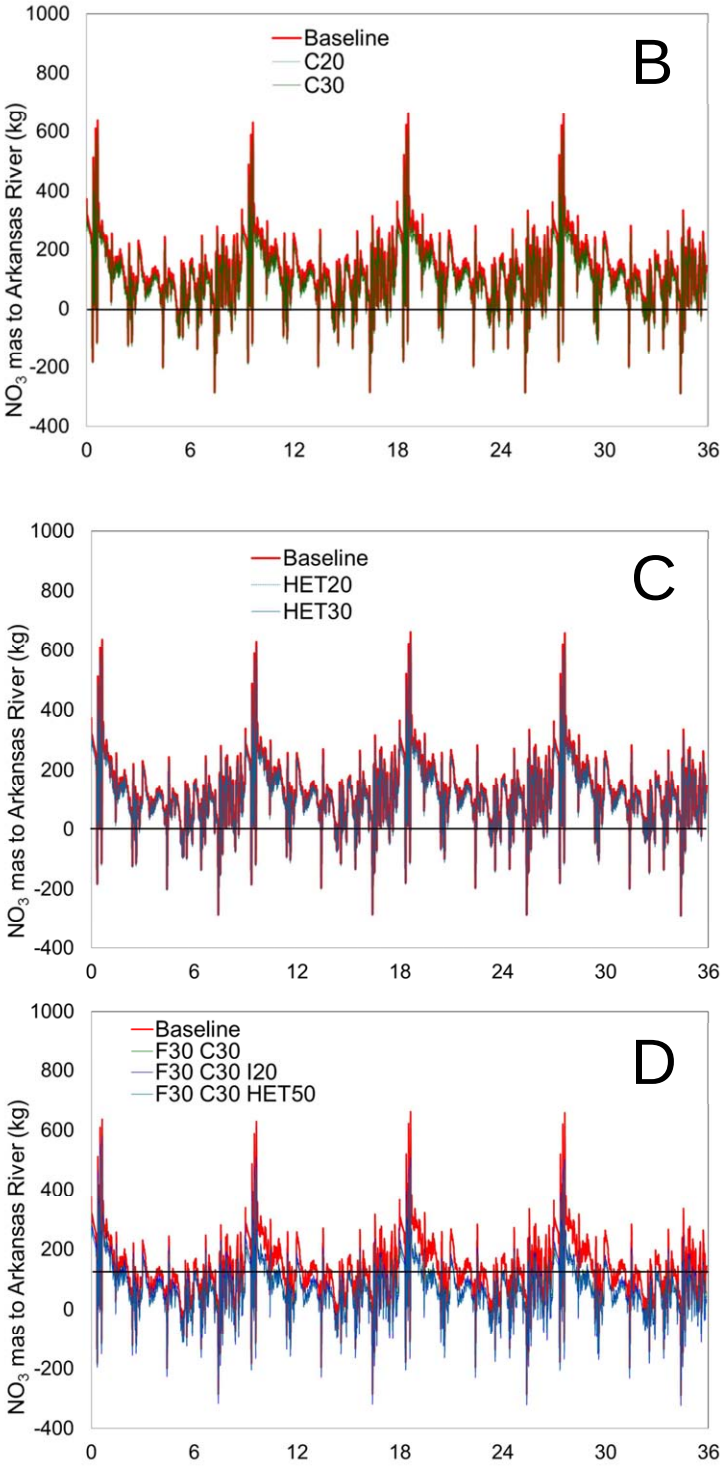

Figure 7- 11. Daily mass loadings of NO_3 (kg) to the Arkansas River during the 36-year scenario simulation for (A) the fertilizer scenarios (1, 2), (B) the canal concentration scenarios (3, 4), (C) the riparian area scenarios (9, 10) and (D) the multi-approach scenarios (7, 8, 11) . For each figure, the daily mass loadings of the Baseline Scenario also are included for comparison.

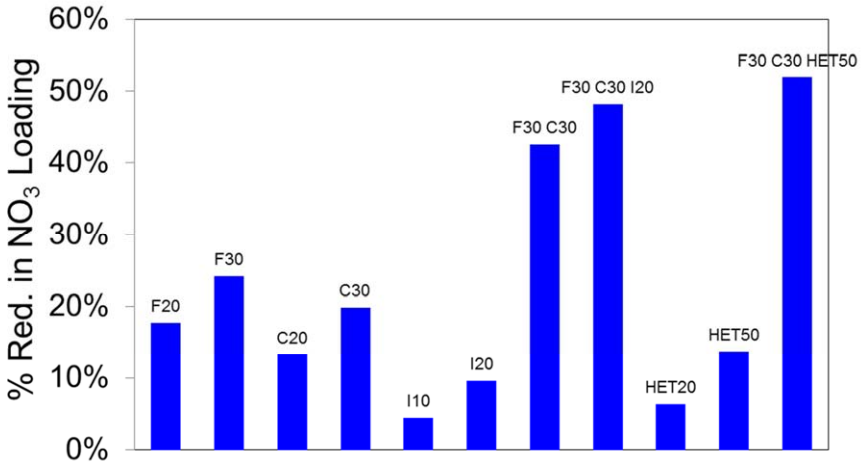

Figure 7- 12. Total percent reduction in mass loadings of NO_3 to the Arkansas River for each Scenario during the 36-year simulation, as compared to the Baseline Scenario.

The results shown in Figures 7-8 to 7-12 consider only the River cells along the Arkansas River, i.e., they consider only the mass exchange between the aquifer and the Arkansas River. However, there are two main tributaries, Timpas Creek and Crooked Arroyo (see Figure 6-1) that contribute flow, and hence mass loadings of SeO_4 and NO_3, to the Arkansas River. To provide a more complete description of the loading of SeO_4 and NO_3 to the Arkansas River, the loading from the aquifer to these two tributaries also must be taken into account. Although the loading to the tributaries was not treated as a calibration target in model calibration, and hence there is significant disparity between observed and simulated values during the model calibration and model testing periods (see Figure 6-54), it is expected that the percentage increase or decrease of mass loadings as compared to the Baseline Scenario would remain the same if parameter estimation were performed for the two tributaries.

Figure 7-13 shows the simulated daily mass loadings of SeO_4 to Timpas Creek and Crooked Arroyo through the 36-year period for Scenarios 7, 8, and 11 as compared to the Baseline Scenario, and Figure 7-14 shows the loadings of NO_3 to Timpas Creek and Crooked Arroyo.

Table 7-4 shows the total percent reduction of SeO_4 and NO_3 loads to Timpas Creek and Crooked Arroyo for each scenario, as compared to the Baseline Scenario, using the combined load to Timpas Creek and Crooked Arroyo. For SeO_4, Scenario 6 (I20) has the highest percent of load reduction, indicating that reducing the irrigation in cultivated fields near the two tributaries has a large impact on SeO_4 loading. Fertilizer reduction and implementing riparian buffer zones has negligible impact. This also is seen in the multi-practice scenarios, with increase in load reduction from Scenario 7 to Scenario 8 (2.0% to 11.8%) due to the inclusion of the I20 practice in Scenario 8, and the small load reduction for Scenario 11 (2.9%) due to the exclusion of the I20 practice. For NO_3, fertilizer reduction (33.7% and 33.8% for Scenarios 1 and 2, respectively) has the largest impact on NO_3 load reduction.

For a more complete accounting of the actual loading of SeO_4 and NO_3 to the Arkansas River, i.e. through both aquifer-river mass exchange along the length of the river as well as the mass loadings entering the Arkansas River via the tributaries, the percent reduction in loading is re-calculated using the combined loadings to the Arkansas River, Timpas Creek, and Crooked Arroyo. The results of these calculations, and their comparison to the case when only the loadings to the Arkansas River from the aquifer are considered (see Figure 7-12), are shown in Figure 7-15. As seen in the figure, the percent reduction for the NO_3 loads remains relatively the same as the case that considers only loadings to the Arkansas River, but the percent reduction for the SeO_4 loads is significantly lower except for the I10 and I20 scenarios. Whereas the percent reduction in NO_3 loading to the tributaries is similar in magnitude to the percent reduction in loading to the Arkansas River, the percent reduction in SeO_4 for the tributaries is low compared to the Arkansas River, hence offsetting the reduction in loads from the aquifer to the Arkansas River. These results for both SeO_4 and NO_3 are discussed in more detail in 7.3.4.

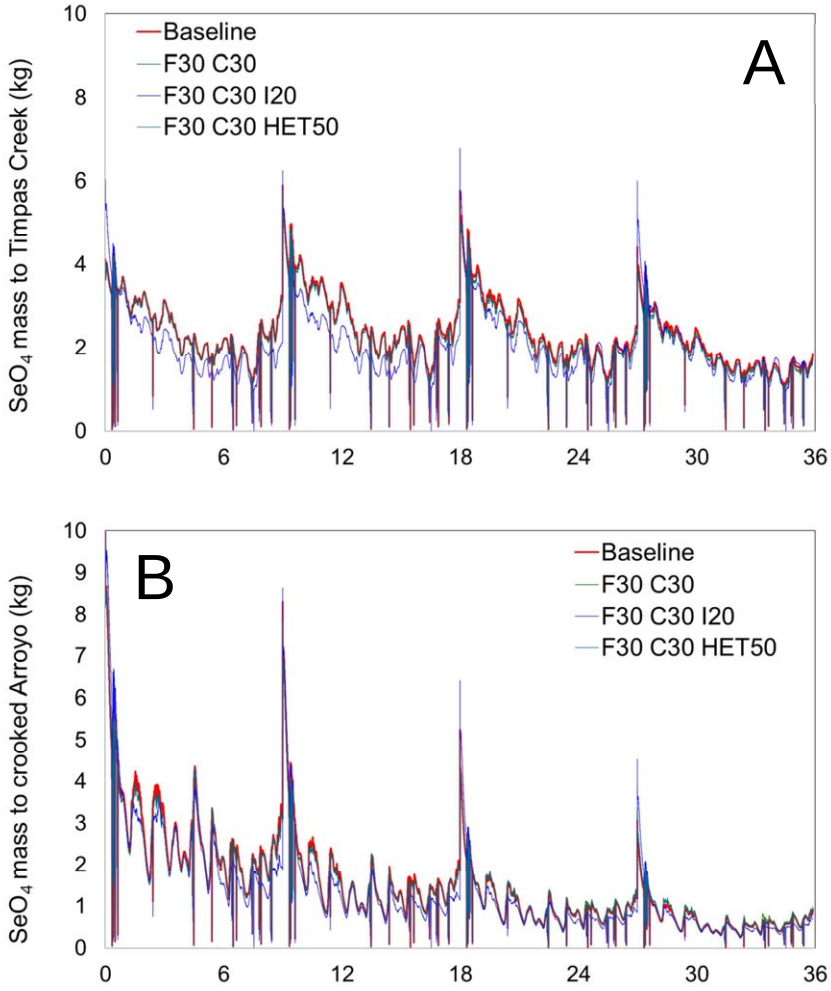

Figure 7- 13. Daily mass loadings of SeO_4 (kg) to (A) Timpas Creek and (B) Crooked Arroyo during the 36-year scenario simulation for Scenarios 7, 8, and 11.

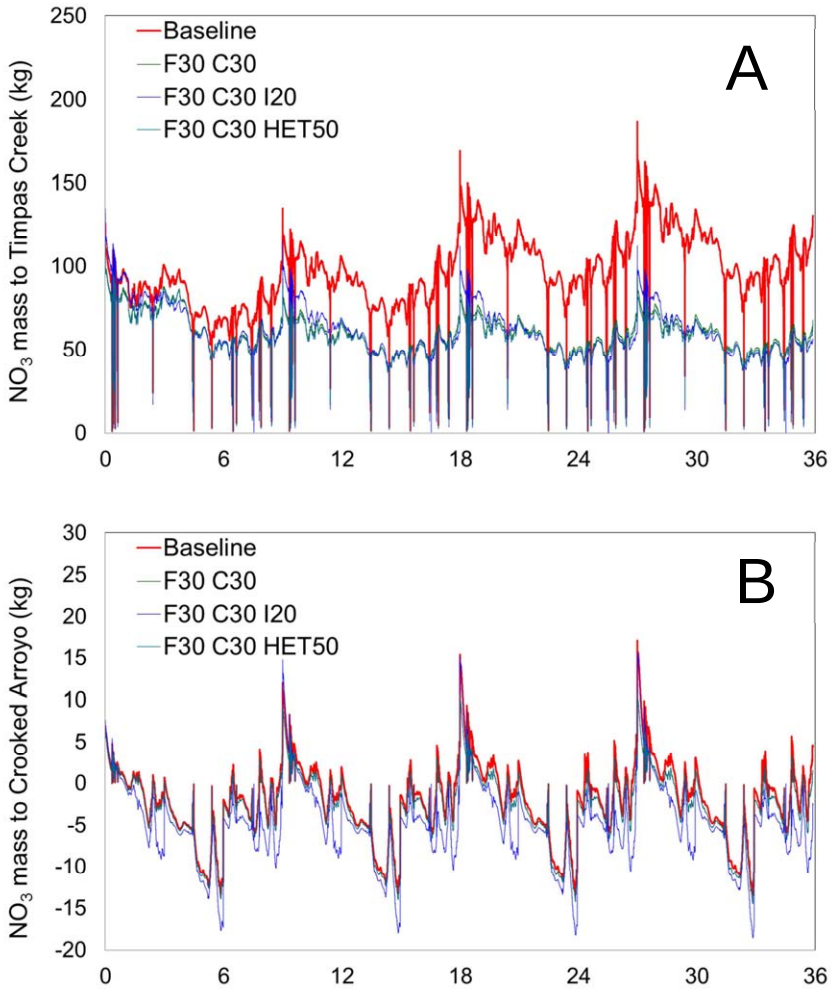

Figure 7- 14. Daily mass loadings of NO_3 (kg) to (A) Timpas Creek and (B) Crooked Arroyo during the 36-year scenario simulation for Scenarios 7, 8, and 11.

Table 7- 4. Total percent reduction in mass loadings of SeO_4 and NO_3 to Timpas Creek and Crooked Arroyo during the 36-year scenario simulation, as compared to the Baseline Scenario.

Scenario	Type	% Reduction SeO_4 Loading	% Reduction NO_3 Loading
1	F20	-0.3%	33.7%
2	F30	0.0%	33.8%
3	C20	1.3%	5.3%
4	C30	2.0%	7.9%
5	I10	6.6%	0.4%
6	I20	10.4%	5.5%
7	F30 C30	2.0%	40.1%
8	F30 C30 I20	11.8%	40.8%
9	HET20	0.1%	2.0%
10	HET50	0.1%	4.6%
11	F30 C30 HET50	2.9%	41.7%

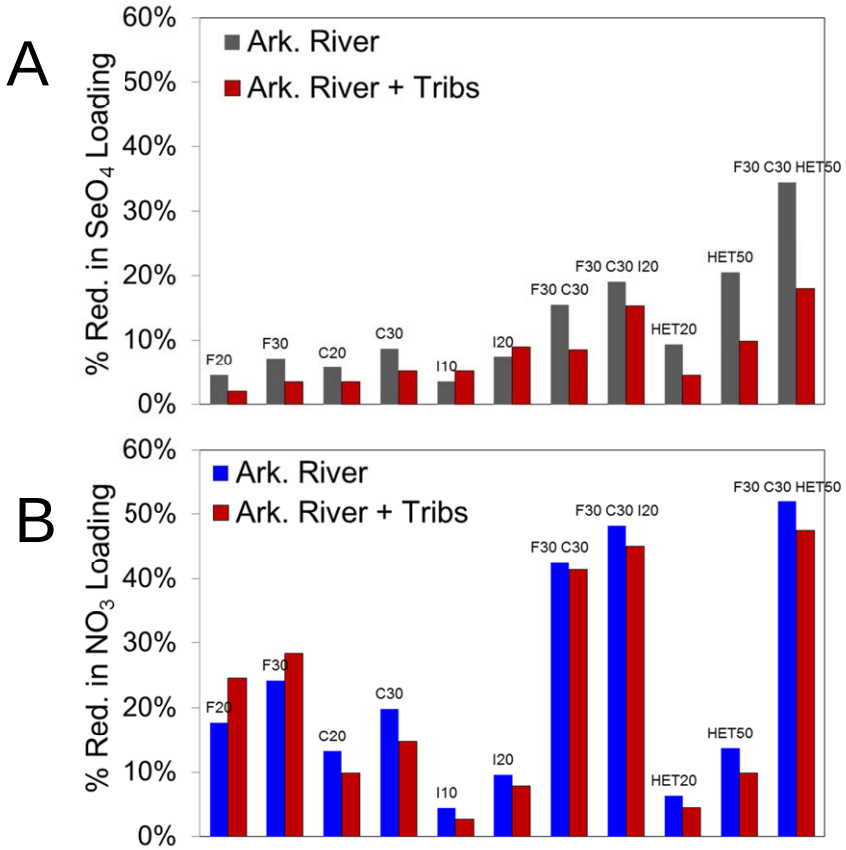

Figure 7- 15. Total percent reduction in mass loadings of (A) SeO_4 and (B) NO_3 the Arkansas River during 36-year scenario simulation, as compared to the Baseline Scenario. For both (A) and (B), the series "Ark. River" only uses River cells along the reach of the Arkansas River, and the series "Ark. River + Tribs" includes the mass entering the tributaries Timpas Creek and Crooked Arroyo, and hence also loading mass to the Arkansas River.

7.3.3 Spatial Change in Species Concentration and Total Mass Loading

Results showing the spatial changes in groundwater concentration and total mass loadings are shown in this section to analyze further the results presented in Sections 7.3.1 and 7.3.2. The change in average concentration for command areas and the total mass loading along the Arkansas River and its tributaries provides key measures of the overall impact of selected single-practice and multi-practices scenarios as compared to the Baseline Scenario. However, these global measures do not lend insight into the spatial variation of changes throughout the study region. In contrast, cell-by-cell results depict the reduction in concentration and mass loadings for each local area of the aquifer, and hence localized region within the aquifer sensitive to changes in land-management practices can be identified and targeted for field implementation.

The difference in C_{SeO_4} between the BMP Scenarios and the Baseline Scenario for the last day of the 36-year simulation is shown in Figure 7-16, for Scenarios 2, 4, 6, 10, 8, and 11. For each scenario, the difference in total mass loadings for each River cell also is shown, with the red and green bars indicating a decrease and increase in loading, respectively. For the irrigation canals, the red bars indicate a decrease in mass loading to the aquifer via seepage. As seen for the global comparisons in Sections 7.3.1 and 7.3.2, the fertilizer (Figure 7-16A_1), canal concentration (Figure 7-16B_1), and reduced irrigation scenarios (Figure 7-16C_1) have minimal impact for C_{SeO_4}, although several locations in the Holbrook command area and along Timpas Creek have differences of > 20 µg L^{-1} for Scenario 4 (Figure 7-16B_1), and several locations in the Highline command area have differences of > 50 µg L^{-1} for Scenario 6 (Figure 7-16C_1). The values of C_{SeO_4} in Scenario 10 (Figure 7-16D_1) are decreased along the central-southeast section of the Arkansas River. These effects are combined in Scenarios 8 (Figure 7-16E_1) and 11 (Figure 7-16F_1).

Scenario 2 (Figure 7-16A_2) and Scenario 4 (Figure 7-16B_2) have load reductions in the northwest section of the Arkansas River, whereas the I20 scenario (Figure 7-16C_2) also has high load reductions along Timpas Creek and Crooked Arroyo, which also was seen in Table 7-4. For Scenario 10 (Figure 7-16D_2), the loadings receive a significant reduction at several locations along the Arkansas River, in particular along the central-southeast section of the River, which was not affected by Scenarios 2 and 4. This is reflected by the decrease in concentration along the same section of river (Figure 7-16D_1). However, the mass loadings along the tributaries are not affected. For Scenario 8 (Figure 7-16E_2) the influences of Scenarios 2 and 4, i.e. the load reduction along the northwest section of the River, and the influence of Scenario 6, i.e. the load reduction for Timpas Creek and Crooked Arroyo, are included. For Scenario 11 (Figure 7-16F_2) the influence of Scenario 6 is not included, but the impact of Scenario 10, i.e., the large load reduction along the central-southeast section of the River, is included. If the Scenario 6 practice were included in Scenario 11, large load reductions along Timpas Creek and Crooked Arroyo also would occur, thus greatly reducing the load to the Arkansas River.

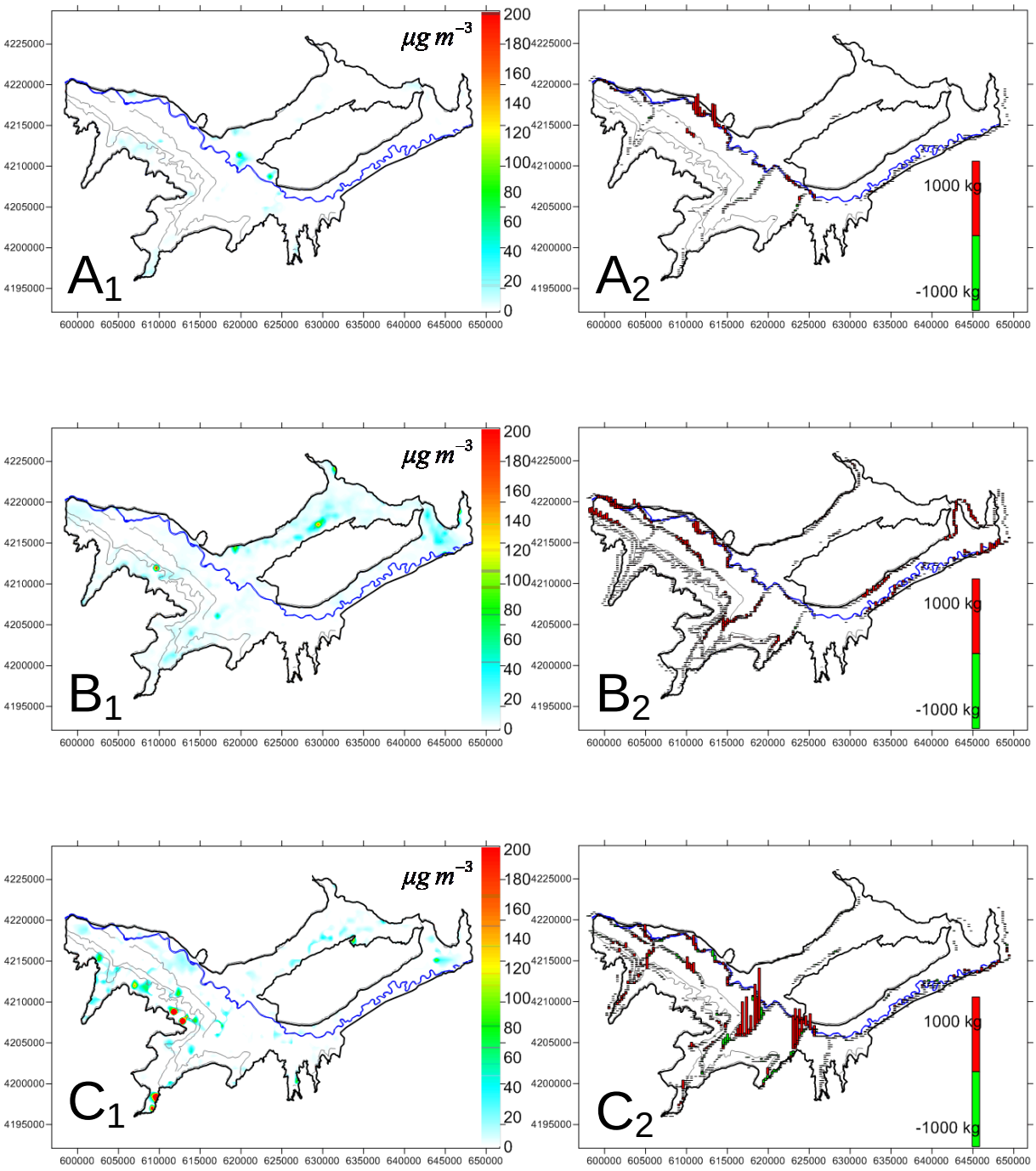
$\mu g\ m^{-3}$
200
180
160
140
120
100
80
60
40
20
0
A1
A2
B1
B2
C1
C2
1000 kg
-1000 kg
4225000
4220000
4215000
4210000
4205000
4200000
4195000
600000 605000 610000 615000 620000 625000 630000 635000 640000 645000 650000

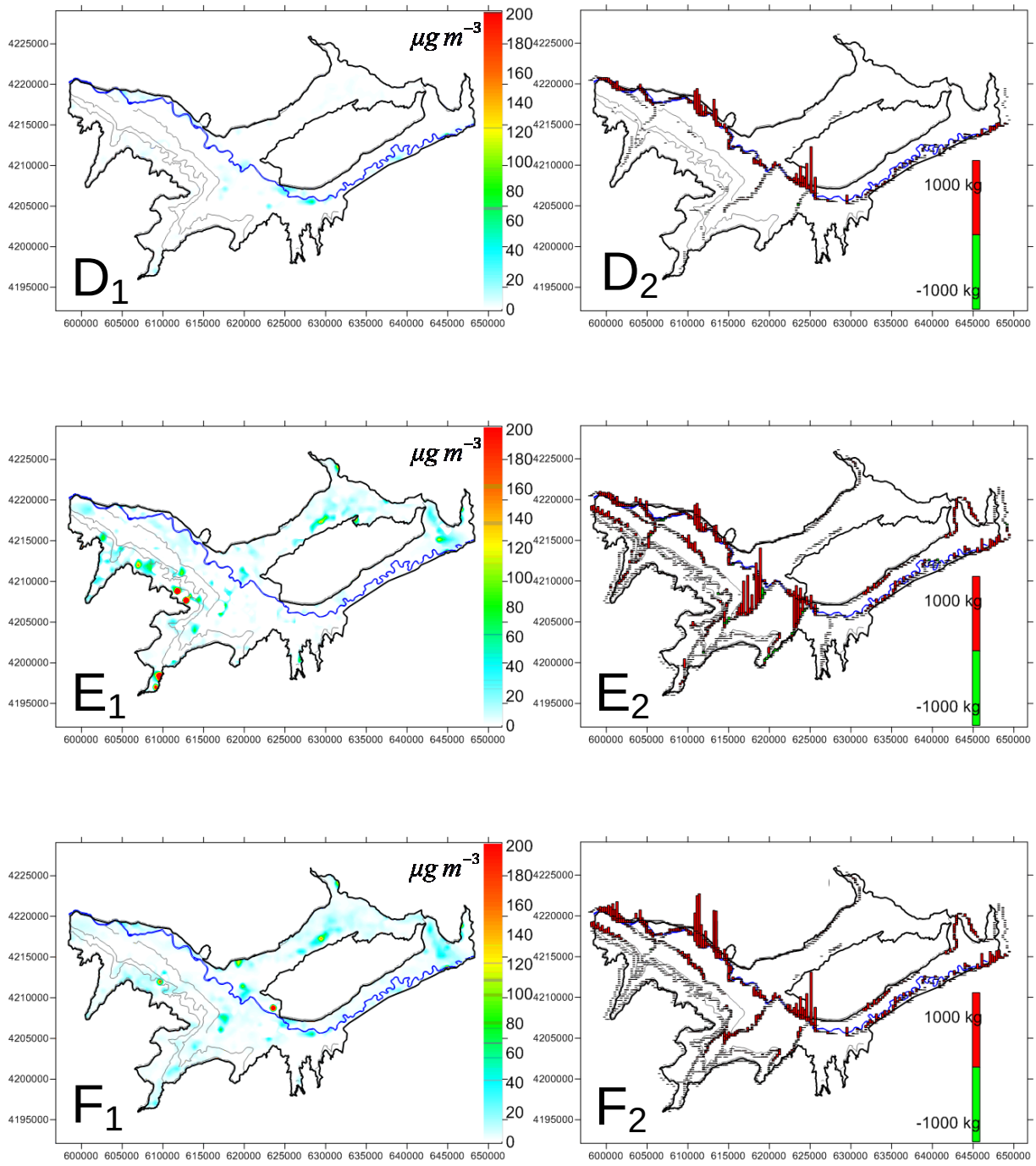

Figure 7- 16. Difference in C_{SeO_4} between the Baseline Scenario and scenario simulation in layer 4 of the model and associated change in total mass loadings for each River cell for Scenarios (A) 2, (B) 4, (C) 5, (D) 7, (E) 10, and (F) 11.

The difference in C_{NO_3} between the BMP scenarios and the Baseline Scenario for the last day of the 36-year simulation is shown in Figure 7-17, for Scenarios 2, 4, 6, 10, 8, and 11. For each scenario, the difference in total mass loadings for each River cell also is shown, with the red and green bars indicating a decrease and increase in loading, respectively. For the irrigation canals, the red bars indicate a decrease in mass loading to the aquifer via seepage As seen for the global comparisons in Sections 7.3.1 and 7.3.2, the fertilizer reduction scenario (Figure 7-17A) by far has the greatest impact on groundwater concentration and NO_3 loading to the Arkansas River, with the latter particularly impacted by the decreased loading to Timpas Creek. Scenario 4 (Figure 7-17B_2) also has an impact on mass loadings along the Arkansas River as well as in a reduction of loading from the irrigation canals, mainly the Catlin Canal, Rocky Ford Ditch, and Fort Lyon Canal, to the aquifer via seepage. Scenario 6 (Figure 7-17C) and Scenario 10 (Figure 7-17D) have minimal impact on concentration and loadings.

The results for the multi-practice Scenario 8 (Figure 7-17E) and Scenario 11 (Figure 7-17F) largely are influenced by the inclusion of the Scenario 2 practice, with numerous areas within the aquifer receiving a decrease in C_{NO_3} of > 10 mg L^{-1} and significant load reductions occurring along both the Arkansas River and Timpas Creek. The decrease in seepage mass along the Catlin Canal, Rocky Ford Ditch, and Fort Lyon Canal are a result of including the Scenario 4 practice.

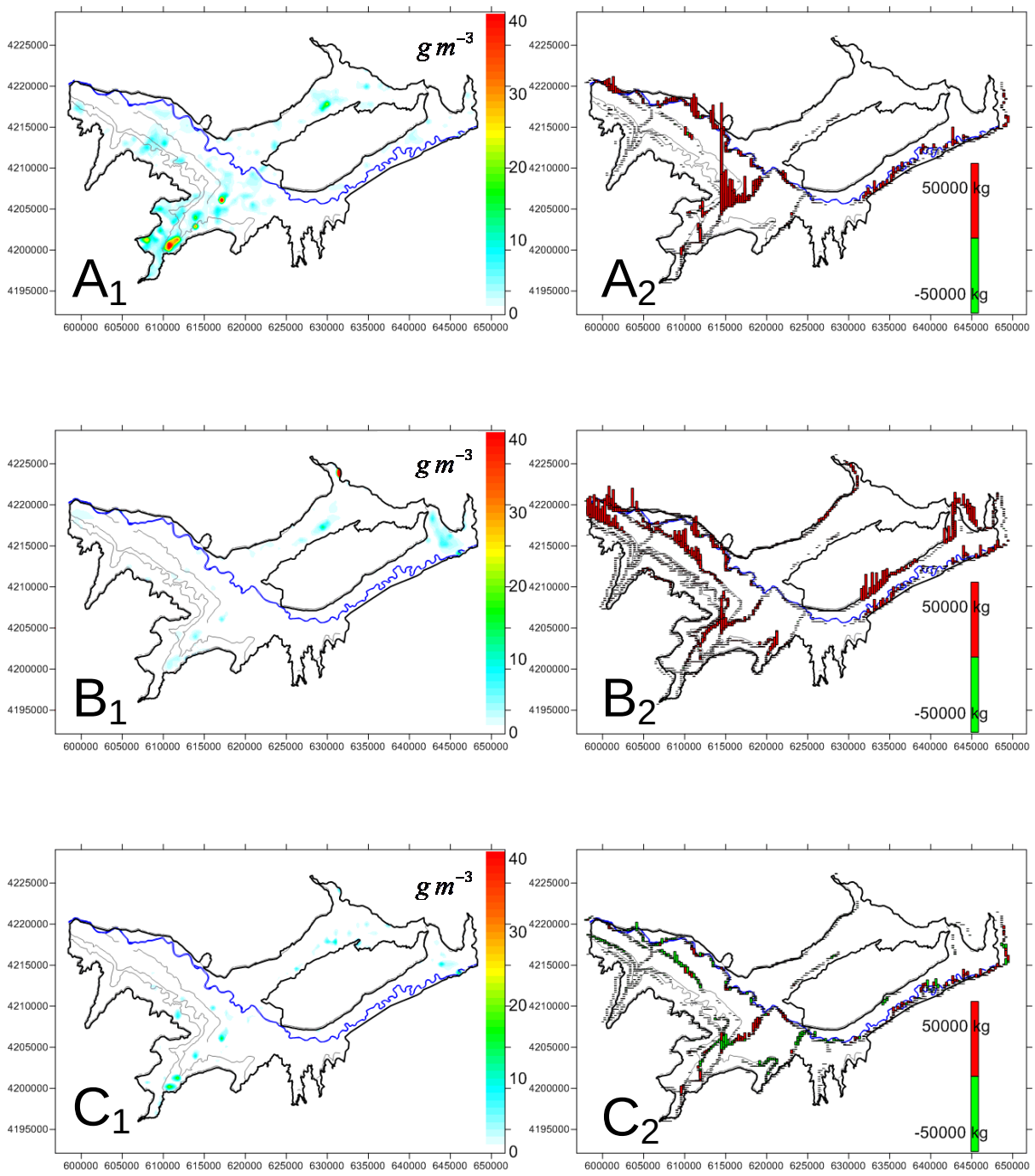
A1
A2
B1
B2
C1
C2
g m⁻³
0
10
20
30
40
50000 kg
-50000 kg
4225000
4220000
4215000
4210000
4205000
4200000
4195000
600000 605000 610000 615000 620000 625000 630000 635000 640000 645000 650000

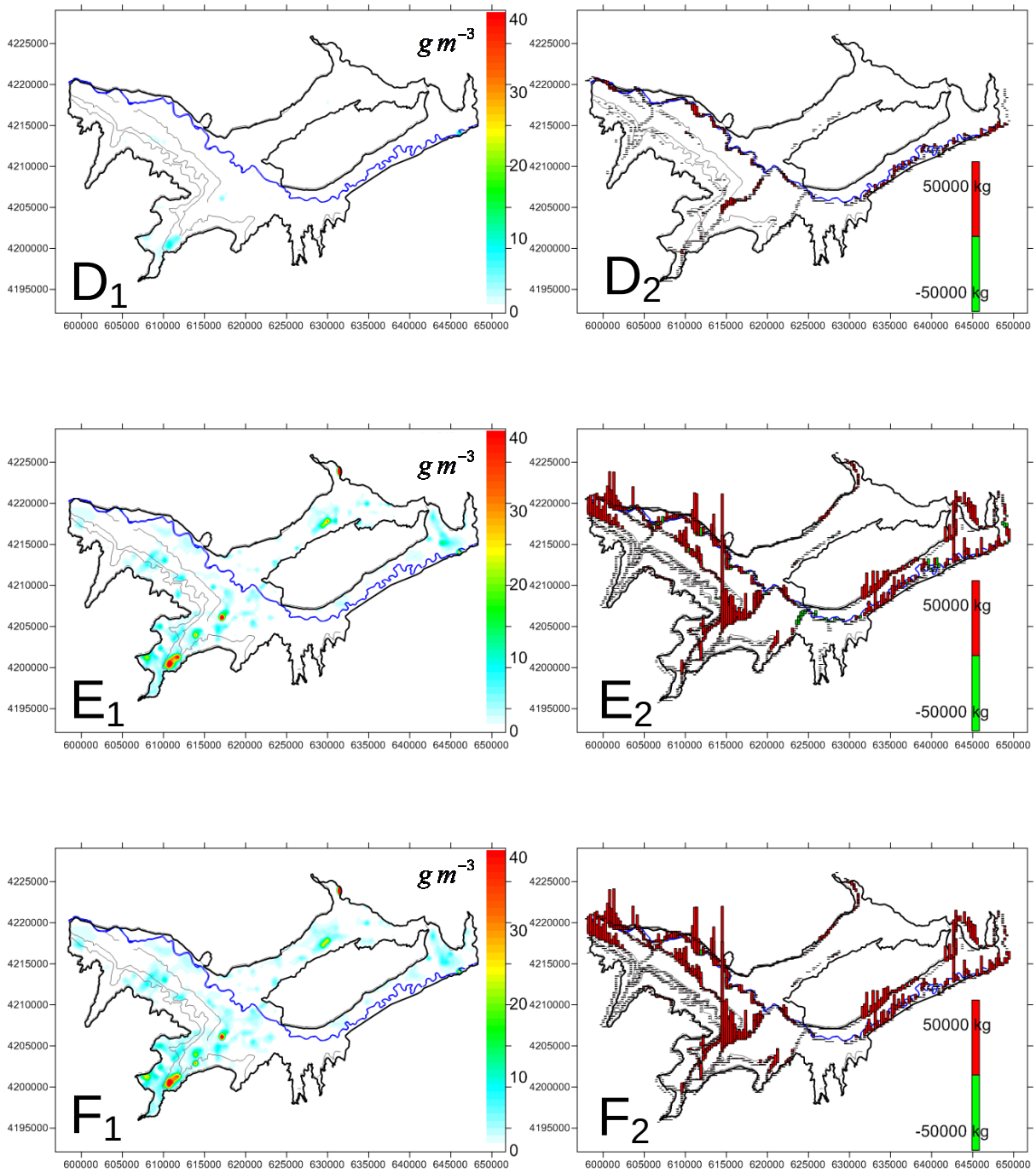

Figure 7- 17. Difference in C_{NO_3} between the Baseline Scenario and scenario simulation in layer 4 of the model and associated change in total mass loadings for each River cell for Scenarios (A) 2, (B) 4, (C) 6, (D) 7, (E) 10, and (F) 11.

7.4 SUMMARY

The calibrated UZF-RT3DAG model for the Upstream Study Region in the Lower Arkansas River Valley in southeastern Colorado was used to investigate BMPs for remediation of Se and, by virtue of the scenarios, NO_3. Practices investigated include reduction in N fertilizer (20% and 30%), reduction in canal concentration for both SeO_4 and NO_3 (20% and 30%), reduction in volume of applied irrigation water (10% and 20%), enhancement of riparian buffer zones via an increase in rate of heterotrophic chemical reduction of SeO_4 and denitrification (20% and 50%), and several combinations of these practices.

Overall, the practices had minor impact on the resulting C_{SeO_4} in groundwater, but mass loadings of SeO_4 to the Arkansas River and its tributaries was significant when implementing riparian buffer zones and when combining this practice with the fertilizer and canal concentration reduction scenarios. Load reductions were concentrated along certain sections of the Arkansas River and Timpas Creek. For NO_3, significant decreases in groundwater concentration were realized through the fertilizer reduction practices, with small decreases resulting from the canal concentration and riparian buffer zone practices. NO_3 loadings were impacted mostly by fertilizer reduction, followed by canal concentration reduction, riparian buffer zone implementation, and irrigation volume reduction.

Results indicate that combining the practices of decreasing fertilizer loading, decreasing canal concentration, and enhancing riparian buffer zones could decrease the mass loading of SeO_4 and NO_3 to the Arkansas River by approximately 20-30% and 40-50%, respectively. Analysis of spatial variations in concentration and load reduction suggests further that local areas within the aquifer and along the Arkansas River and its tributaries can be targeted for changes in

land-management practices and subsequent reduction in groundwater concentration and mass loadings.

CHAPTER 8

CONCLUSIONS AND RECOMMENDATIONS

The research presented herein summarizes efforts towards conceptualizing and simulating the chemical fate and reactive transport of selenium (Se) in regional-scale irrigated agricultural groundwater systems. These efforts included field sampling of soil, soil water, groundwater, and shale bedrock material; laboratory methods to determine the dependency of Se on dissolved oxygen (O_2) and nitrate (NO_3) in soil and aquifer systems; the development and testing of a numerical model, UZF-RT3D, capable of simulating the reactive transport of multiple interacting chemical species in variably-saturated transport systems; the development of Se and nitrogen (N) reaction modules for UZF-RT3D and subsequent testing of the modules at small scales (soil profiles); and the application of the model to a 50,600-ha region within the Lower Arkansas River Valley (LARV) in southeastern Colorado. When the Se and N reaction modules are activated for UZF-RT3D, the model is referred to as UZF-RT3DAG due to its design for agricultural groundwater systems. However, the model could be applied to non-agricultural groundwater systems as well.

The latter application consisted of model calibration and model testing using an extensive set of field data, and subsequent use of the model in best-management-practice (BMP) scenarios to explore possible land- and water-management practices for remediation of Se. Due to the strong relationship between selenate (SeO_4) and nitrate (NO_3), and since NO_3 also is a contaminant in the LARV, all modeling applications and remediation scenarios also included N cycling and NO_3 fate and transport.

The major conclusions from the field studies, laboratory studies, and the development and testing of UZF-RT3D and UZF-RT3DAG are contained in Chapters 2-5. Only a description of

the model limitations and the conclusions from the application of the model to the regional study site will be presented here.

8.1 LIMITATIONS OF UZF-RT3DAG

The limitations of the UZF-RT3DAG model were described in Chapters 4 and 6. They are summarized as follows:

(i) The UZF1 package for MODFLOW uses a kinematic-wave approximation for unsaturated flow that neglects the diffusive terms in the Richards equation. Hence, the model can be used primarily for large-scale systems in which this approach is reasonable, i.e., capillary-pressure gradients can be neglected and soil parameters can be treated as homogeneous.

(ii) Surface water flow and chemical transport (e.g., overland flow, channel flow in canals, rivers, and tributaries) capabilities are not currently available in the model. Mass exchange between the aquifer and surface water is calculated using the *River* package in MODFLOW, specified species concentrations for the surface water, and simulated groundwater concentrations. Hence, species concentrations in surface water currently cannot be estimated from the model.

(iii) Growth of crops is not simulated explicitly. Rather, average crop parameters for each crop type are supplied to the model to simulate root growth, daily uptake of N and Se, dead root mass at the end of the growing season, and the amount of above-ground stover that is incorporated into the soil layers at plowing. This approach assumes that climatic and land-management practices for a given crop type remain the same throughout the

model simulation. The parameter values, however, are perturbed stochastically for each grid cell in the model domain, thus providing heterogeneity in the system.

(iv) Growth and death of microbial populations are simulated. Hence, the model assumes that microbial populations required for oxidation-reduction reactions are present in limitless supply, and does not take into account the various microbial species responsible for different reaction types.

(v) The influence of phosphate (PO_4) and sulfate (SO_4) is not taken into account. PO_4 is a strong sorbent, and typically competes with SeO_3 for soil surface sites and even can displace SeO_3 from soil surface sites. Crop uptake of SO_4 may limit the crop uptake of SeO_4.

Points (ii) and (iii) have a direct influence on the analysis of the scenario testing results in Chapter 7. Since mass loadings to surface water are not coupled with resulting surface water concentrations, and since these concentration influence seepage of species mass into the aquifer that may occur in downstream locations along the canal, tributary, or river, the influence of BMPs cannot be assessed completely.

Other cautions in using the model are the same as with the use of any numerical model. That is, the realization that the physical and chemical processes depicted in the model are gross approximations of the actual processes, and also that models are more useful as investigatory tools than as prediction tools (Pilkey and Pilkey-Jarvis, 2007). This is especially true for reactive transport models, which are comprised of numerous transport and chemical reaction parameters that provide concentrations that can range over orders of magnitude. The aim of such models is not to duplicate species concentrations at field observation wells and predict their exact values during the coming decades; rather, the objectives should be to investigate the governing

processes on species concentration and to capture the principal spatial and temporal trends (Konikow, 2011) and inter-species relationships within the aquifer system.

For the application of the UZF-RT3DAG model to the Upstream Study Region, a final caution should be mentioned regarding the adopted schemes of temporal and spatial discretization. As discussed in Chapter 6, weekly time steps used in the groundwater flow model provide weekly average inputs of hydrologic stresses (rainfall, applied irrigation, canal seepage) and hence prevent the model from accurately simulating the influence of short-duration (hourly or daily) events. This also is the case for the spatial discretization scheme, which often results in portions of multiple fields residing within a single grid cell, and hence requiring a composite value of infiltration rates and crop parameters (e.g., fertilizer loading, rooting depth) based on the fields within the cell. Consequently, the adopted schemes of temporal and spatial discretization smooth out localized system stresses in time and space. However, these schemes are consistent with the aim of the study, which is to capture the regional hydrologic and chemical trends of the aquifer system rather than provide point-by-point predictions.

8.2 CONCLUSIONS FROM MODEL CALIBRATION AND TESTING

In regards to the objectives of chemical reactive transport models as discussed in Section 8.1, the UZF-RT3DAG was successful in its application to the 50,600-ha study site within the LARV, as presented in Chapter 6. Following the general theory of Konikow (2011) for calibration of groundwater mass transport models, the simulated and observed concentrations of O_2, NO_3, and SeO_4 during 2006-2009 were compared using time-averaged and space-averaged values, with averages calculated according to canal command area. The simulated and observed daily mass loadings of Se from the aquifer to the Arkansas River also were compared, although

once again the major patterns in mass loading were sought rather than exact duplication of observed values.

A combination of automated calibration (using PEST) and manual calibration was used to reproduce the principal spatial trends in species concentration and mass loading. During the calibration process it became evident that the 20-year spin-up simulation, used to provide initial concentrations for the 2006-2008 model calibration simulation, also was essential in estimating parameters that were not sensitive during the 2006-2008 simulation period. Overall, values of the rate of autotrophic reduction of O_2, $\lambda_{O_2}^{auto}$, and the rate of autotrophic reduction of NO_3, $\lambda_{NO_3}^{auto}$, for each command area were estimated primarily using automated calibration for the 2006-2008 simulation period, while values of the rate of heterotrophic reduction of SeO_4, $\lambda_{SeO_4}^{het}$, and the rate of nitrification, λ_{nit}, were estimated using the 20-year spin-up simulation. Values of $\lambda_{O_2}^{auto}$, $\lambda_{NO_3}^{auto}$, and , λ_{nit} affected primarily the concentration of SeO_4 and NO_3 within the aquifer, whereas the value of $\lambda_{SeO_4}^{het}$ affected the loadings of Se to the Arkansas River. Overall, the spin-up simulation was crucial in establishing dynamic equilibrium within the system.

In general, favorable matches occurred between the command area-averaged groundwater concentrations and the mass loadings to the Arkansas River. Comparisons between observed and simulated mass loadings of Se to Timpas Creek and Crooked Arroyo, tributaries to the Arkansas River, were not improved during the calibration process through parameter value modification, but will be pursued in future work. Other global comparisons yielded excellent matches between field data and simulated values. The NO_3-SeO_4 relationship, the portion of dissolved Se attributed to SeO_4, and the global frequency distribution for SeO_4 and NO_3 each were able to be captured by the model to a satisfactory degree. The frequency distribution of simulated O_2 concentration, in comparison to the frequency distribution of observed O_2 concentration, can be

improved upon. Discrepancies for O_2 likely result from the rough approximation of reaeration used to calculate the mass of O_2 supplied to the saturated zone via gaseous diffusion and from the uncertain in-situ measurement of O_2 at low concentrations.

Finally, it should be noted that the influence of shale, and particularly an accurate depiction of the spatial distribution of shale in both the lateral and vertical dimensions of the aquifer, is vital for the simulation of SeO_4 fate and transport. Throughout the model calibration exercise it became evident that the presence of shale, through autotrophic reduction of O_2 and NO_3, governed the concentration of SeO_4 in groundwater and hence also influenced the loading of SeO_4 to surface water.

8.3 CONCLUSIONS FROM SCENARIO TESTING

Scenario testing included the following land-management practices:

- Decrease in seasonal loading of N fertilizer
- Decrease in concentration of SeO_4 and NO_3 in the canal water
- Decrease in volume of applied irrigation water
- Increase in rate of chemical reduction of SeO_4 and NO_3 in the riparian areas along the tributaries and the Arkansas River (representing installing of riparian buffer zones)

Alternative levels of these practices were included either individually or in combinations. Simulations were run for 2006-2009 and then for an additional 36 years, with the 9-year hydrologic period of 1999-2007 repeated four times. This duration was deemed necessary to allow the land-management practices to adequately impact the mass loadings of N and Se to

surface water, due to the long travel time of groundwater. When compared with a Baseline Scenario, results of scenario simulations indicate that:

- Practices generally had only a small influence on SeO_4 concentration in groundwater (< 10% reduction).
- Decrease in mass loadings of Se to the Arkansas River and its tributaries is significant when implementing riparian buffer zones (5-20%), and when combining this practice with a decrease in N fertilizer loading and canal concentrations (15-30%).
- Decrease in concentration of NO_3 in groundwater (20-30%) and NO_3 loading to surface water (20-30%) is significant when decreasing N fertilizer loading. Percent reductions increase to 30-50% and ~45% for groundwater concentration and mass loadings, respectively, when combined with a decrease in canal concentrations and implementation of riparian buffer zones.
- There is a high degree of spatial variability in concentration and mass loading changes, suggesting that localized sections of the aquifer can be targeted for implementation of land- and water-management practices.

As noted in Section 8.1, these results should be tempered by an understanding of the limitations of the model. Even with these limitations, however, there is obvious overall decrease in groundwater concentrations and mass loadings when employing these management practices. Results from the sensitivity analysis, shown in Appendix C, indicate further that decreasing the loading of N fertilizer will positively impact the concentration of both NO_3 and SeO_4 in the groundwater. For SeO_4, the decrease in groundwater concentration occurs due to less NO_3 available for autotrophic reduction in the presence of shale and resulting release of SeO_4.

8.4 AVENUES OF FUTURE RESEARCH

Possible areas of future research fall into one of two categories: ways in which the current research could be improved, and which were not pursued do to limitation of time and resources; and general avenues of research that can provide insight into the cycling and transport of Se at the watershed scale. Items within the first category include:

- **Better model calibration for areas adjacent to tributaries**. This would include matching the observed and simulated mass loadings of Se to Timpas Creek and Crooked Arroyo through modification of chemical reaction parameters.
- **Comparing the observed and mass loading of NO_3** to the Arkansas River and its tributaries, and performing additional parameter estimation to provide favorable matches. Observed loadings of NO_3 currently are being calculated for the model domain.
- **Refinement of the Reaeration Term** for simulating the diffusive transport of O_2 through the unsaturated zone from the ambient atmosphere to the saturated zone of the aquifer. As discussed in Chapter 6, the current scheme for incorporating reaeration seems to result in an over-prediction of O_2 in the groundwater, particularly in the case of shallow water table. The inclusion of reaeration will be refined in future studies, and likely will involve modifying the parameters of the reaeration term or adopting a scheme that simulates both water and air transport in the groundwater flow model.
- **Incorporating of phosphorus (P) and sulfur (S) cycling** in order to include the influence of PO_4 and SO_4 on Se species. As P is generally a nutrient of focus in

agricultural systems and since SO_4 is the principal constituent of salt in the LARV, multiple benefits would be derived from including these cycles in UZF-RT3DAG.

- **Extending the chemical transport of Se species to surface water**. This would allow Se concentration to be simulated within the network of canals, tributaries, and the Arkansas River, as well as a more accurate depiction of mass exchange between the aquifer and surface water, and hence provide a more complete representation of Se transport in watersheds.
- **Apply the model to investigate a larger array of BMP scenarios.** These scenarios include irrigation efficiency improvement and canal seepage reduction, as well as more combinations of practices. These scenarios also will be analyzed over an extended period of simulation (~40 to 50 years).
- **Extending the calibration and application of the model to the Downstream Study Region** of the LARV. This study area is located downstream of John Martin Reservoir, and covers a total of about 55,200 ha, or which about 33,000 ha are irrigated. An extensive data set, including measurements of C_{O_2}, C_{SeO_4}, and C_{NO_3} is available for the period 2002-2011.

Items within the second category include:

- Developing a more complete description of Se mass exchange between the aquifer and streams. This applies also to other chemical species and nutrients, and requires extensive field work. Results of the field work can be used to develop processes for numerical models as well as provide field data for subsequent model testing.

- Investigating the cycling of organic matter in riparian areas, in order to more accurately simulate this cycling in numerical models. In relation to the previous point, an accurate depiction of this cycling is imperative in assessing the mass loading of Se and other species to streams and rivers.
- Consideration of the use of Se hyper-accumulator plants (Wan et al., 1988; Fernández-Martínez and Charlet, 2009; Freeman et al., 2010; Freeman and Bañuelos, 2011) in the riparian zone to remove Se from the soil water. This potentially could eliminate Se from the soil water before it is discharged to surface water.
- Investigating the concentration and overall presence of Se in the aquifer and Arkansas River during ambient, pre-irrigation conditions. This would help identify realistic targets for Se concentration and loading reduction.

8.5 CONCLUSIONS REGARDING THE SELENIUM PROBLEM

As discussed in Chapter 1, Se contamination affects both humans and animals and, due to the natural presence of Se in geologic formations and associated soils, occurs in regions around the world. Se is released into the hydrosphere and environment principally due to shale located in the soil-aquifer system, and hence such a system is the obvious focus of field and modeling studies. Results from this dissertation indicate that control of Se contamination is largely dependent on the control of other species such as NO_3 and O_2, which in turn are dependent on land- and water-management practices and land-use. Remediation in Se will be accomplished insofar as management practices and land-use patterns are optimized.

REFERENCES

Abrams, M. M., C. Shennan, R. J. Zasoski, and R. G. Burau (1990), Selenomethionine uptake by wheat seedlings, Agronomy Journal, 82, 4.

Afzal, S., M. Younas, and K. Ali. 2000. Selenium speciation sutides from Soan-Sakesar Valley, Salt Range, Pakistan. Water International. 25:425-436.

Ahlrichs, J. S., and L. R. Hossner. 1987. Selenate and selenite mobility in overburden by saturated flow. J Environ Qual. 16:95-98.

Ahmed, S., and G. de Marsily (1993), Cokriged Estimation of Aquifer Transmissivity as an Indirect Solution of the Inverse Problem: A Practial Approach. Water Resour. Res., 29(2), 521-530.

Ajwa, H. A., G. S. Bañuelos, and H. F. Mayland (1998), Selenium uptake by plants from soils amended with inorganic and organic materials, J Environ Qual, 27, 10.

Alemi, M.H., Goldhamer, D.A., and D.R. Nielsen (1988), Selenate transport in steady-state, water-saturated soil columns. J. Environ. Qual. 17(4), 608-613.

Alemi, M.H., Goldhamer, D.A., and D.R. Nielsen (1991), Selenate transport in steady-state, unsaturated soil columns. J. Environ. Qual. 20, 89-95.

Allen, R.G., Walter, I.A., Elliott, R., Howell, T., Itenfisu, D., and M. Jensen (2005), The ASCE standardized reference evapotranspiration equation. ASCE-Environmental and Water Resources Institute Task Committee Reporty, January, 2005.

Allen, R.G., and J.L. Wright (2002), Conversion of Wright (1981) and Wright (1982) alfalfa-based crop coefficients for use with the ASCE Standardized Penman-Monteith Reference Evapotranspiration Equation, Kimberly Crop Coefficient Conversion.

Alfthan, G., D. Wang, A. Aro, and J. Soveri. 1995. The geochemistry of selenium in groundwaters in Finland. Science of the Total Environment. 162:93-103.

Almasri, M.N., and J.J. Kaluarachchi (2007), Modeling nitrate contamination of groundwater in agricultural watersheds. J. Hydrol., 343, 211-229.

Anbumozhi, V., Radhakrishnan, J., and E. Yamaji (2005), Impact of riparian buffer zones on water quality and associated management considerations. Ecol. Engrg. 24, 517-523.

Aro, A., G. Alfthan, P. Ekholm, and P. Varo. 1998. Effects of selenium supplementation of fertilizers on human nutrition and selenium status. p. 81-98. In W. T. Frankenberger and R. A. Engberg (ed.) Enviromental Chemistry of Selenium. Marcel Dekker, New York, New York, USA.

Babcock, B.A., and A.M. Blackmer (1992), The value of reducing temporal input non-uniformities. J. Agric. Res. Econ. 17:335–347.

Bailey, R.T., and D.A. Baù (2010), Ensemble Smoother assimilation of hydraulic head and return flow data to estimate hydraulic conductivity, *Water Resour. Res.*, 46, W12543, doi:10.1029/2010WR009147.

Bailey, R.T., and D.A. Baù (2011), Estimating spatially-variable first-order rate constants in groundwater reactive transport systems, J. Cont. Hydrol., 122, 104-121.

Bailey, R.T., Hunter, W.J., and T.K. Gates (2012), The influence of nitrate on selenium in irrigated agricultural groundwater systems. J. Env. Qual. 41(3), 783-792.

Bailey, R.T., Morway, E.D., Niswonger, R.G., and T.K. Gates (2012), Modeling variably-saturated multi-species reactive transport with MODFLOW-UZF and RT3D. Ground Water, accepted.

Balistrieri, L. S., and T. T. Chao .1987. Selenium adsorption by Goethite. Soil Science Society of America Journal. 51:1145-1151.

Bañuelos, G. S., and D. W. Meek (1990), Accumulation of selenium in plants grown on selenium-trated soils, J Environ Qual, 19(4), 6.

Michael Bartolo, personal communication, October 2009.

Baú, D.A., and A.S. Mayer (2008), Optimal design of pump-and-treat systems under uncertain hydraulic conductivity and plume distribution, J. Cont. Hydrol., 100, 30-46.

Beck, M.A., Levander, O.A., and J. Handy (2003), Selenium deficiency and viral infection. J. Nutr. 133 (5 Suppl 1): 1463S-7S.

Benson, S.M. Influence of nitrate on the mobility and reduction kinetics of selenium in groundwater systems. p. 437-457. In W. T. Frankenberger and R. A. Engberg (ed.) Enviromental Chemistry of Selenium. Marcel Dekker, New York, New York, USA.

Birkinshaw, S.J., and J. Ewen (2000), Nitrogen transformation component for SHETRAN catchment nitrate transport modelling. J. Hydrol., 230, 1-17.

Birkinshaw, S. J., and J. Ewen (2000), Modelling nitrate transport in the Slapton Wood catchment using SHETRAN, Journal of Hydrology, 230, 16.

Bisbjerg, B., and G. Gissel-Nielsen (1969), The Uptake of Applied Selenium by Agricultural Plants, Plant and Soil, 31(2), 12.

Bixio, A.C., Orlandini, S., Paniconi, C., and Putti, M. (2000), Physically-based distributed model for coupled surface runoff and subsurface flow simulation at the catchment scale, in Computational Methods in Water Resources, vol. 2, Computational Methods, Surface Water systems and Hydrology, edited by L. R. Bentley et al., pp. 1115-1122, Balkema, Rotterdam, Netherlands.

Blankendaal, M., Hodgson, R. H., Davis, D. G., Haerauf, R. A. and Shimabukuro, R. H. 1972. Growing plants without soil for experimental use. U.S. Department of Agriculture Miscellaneous Publication. No. 1251, U.S. Government Printing Office, Washington, D.C. USA.

Boettcher, J., Strebel, O., and W.H.M. Duynisveld (1989), Kinetic und Modellierung gekoppelter Stoffeumsetzugen im Grundwasser eines Lockergesteinsaquifers. Geol. Jahrb., Ser. C, 51, 3-40.

Brady, N.C., and R.R. Weil (1996), The nature and properties of soils. 11th edition, Upper Saddle River, New Jersey, Prentice-Hall.

Brooks, R.H., and Corey, A.T. (1966), Properties of porous media affecting fluid flow. American Society of Civil Engineers, Journal of Irrigation and Drainage, 101, 85-92.

Brun, A., and P. Engesgaard (2002), Modelling of transport and biogeochemical processes in pollution plumes: literature review and model development. J. Hydrol., 256, 211-227.

Buchleiter, G. W., H. J. Farahani, and L. R. Ahuja. 1995 Model evaluation of groundwater contamination under center pivot irrigated corn in eastern Colorado. In: C. Heatwole (ed.): Proceedings of the International Symposium on Water Quality Modeling. Orlando, Florida. pp 41-50.

Bujdos, M., J. Kubova, and V. Stresko (2000), Problems of selenium fractionation in soils rich in organic matter, Analytica Chimica Acts, 408, 7.

Bureau of Reclamation (2006), Evaluation of Selenium remediation concepts for selected tributaries/drains in the Grand Valley of Western Colorado, U.S. Department of the Interior, Bureau of Reclamation.

Burgers, G., P.J. van Leeuwen, and G. Evensen (1998), Analysis scheme in the Ensemble Kalman Filter, Mon. Weather Rev., 126, 1719-1724.

Burkhalter, J. P., and Gates, T. K. 2005. "Agroecological impacts from salinization and waterlogging in an irrigated river valley". Journal of Irrigation and Drainage Engineering, 131(2): 197 - 209.

Bye, R., and W. Lund .1982. Determination of selenium in pyrite by the atomic absorption-hydride generate technique. Fresenius Z Anal Chem. 313:211-212.

Byers, H. G. (1937), The origin, distribution, and effects of selenium, edited by B. o. C. a. Soils, p. 326, Washington, D.C.

Calderone, S. J., W. T. Frankenberger, D. R. Parker, and U. Karlson. 1990. Influence of temperature and organic amendments on the mobilization of selenium in sediments. Soil Biology and Biochemistry. 22:615-620.

Camporese, M., Paniconi, C., Putti, M., and Salandin, P. (2009), Ensemble Kalman filter data assimilation for a process-based catchment scale model of surface and subsurface flow, Water Resour. Res., 45, W10421, doi:10.1029/2008WR007031

Chang, S-Y., and S.M.I. Latif (2010), Extended Kalman Filtering to Improve the Accuracy of a Subsurface Contaminant Transport Model. J. Envir. Eng., 136, 466-474.

Chaplot, V., Saleh, A., Jaynes, D.B., and J. Arnold (2004), Predicting water, sediment and NO_3-N loads under scenarios of land-use and management practices in a flat watershed., Water, Air, and Soil Pollution 154, 271-293.

Chen, Y., and D. Zhang (2006), Data assimilation for transient flow in geologic formations via Ensemble Kalman Filter. Adv. Water Resour., 29(8), 1107-1122.

Clement, T.P. (1997), RT3D – A modular computer code for simulating reactive multi-species transport in 3-dimensional groundwater aquifer. Draft report. PNNL-SA-28967. Richland, Washington: Pacific Northwest National Laboratory.

Clement, T.P., Peyton, B.M., Skeen, R.S., Jennings, D.A., and J.N. Petersen (1997), Microbial growth and transport in porous media under denitrification conditions: experiments and simulations. J. Contam. Hydrol., 24, 269-285.

Clement, T.P., Sun, Y., Hooker, B.S., and J.N. Peterson (1998), Modeling multispecies reactive transport in groundwater. Groundwater Mon. & Rem., 18, 79-92.

Combs, G.F., Jr., Q. Su, C.H. Liu and S. B. Combs. 1986. Effect of dietary selenite, copper and zinc on tissue trace mineral levels in chicks. Biol. Trace Elem. Res. 11:51-64.

Conan, E., Bouraoui, F., Turpin, N., Marsily, G. de, and G. Bidoglio (2003), Modeling flow and nitrate fate at catchment scale in Brittany (France). J. Envir. Qual., 32, 2026-2032.

Conde, J. E., and M. S. Alaejos (1997), Selenium concentrations in natural and environmental waters, Chemical Reviews, 97, 26.

Cukier, R., Fortuin, C.M., Schuler, K.E., Petschek, A.G., and J.H. Schaibly (1973), Study of the sensitivity of coupled reaction systems to uncertainties in rate coefficients. i theory. J. Chem. Physics 59, 3873-3878.

Deverel, S.J., and R. Fujii (1988), Processes affecting the distribution of selenium in shallow groundwater of agricultural areas, western San Joaquin Valley, California. Water Resour. Res. 24, 516-524.

Deverel, S.J., and S.P. Millard (1988), Distribution and mobility of selenium and other trace elements in shallow groundwater of the western San Joaquin Valley, California. Environ. Sci. Technol. 22:697.

Dhillon, S. K., B. K. Hundal, and K. S. Dhillon (2007), Bioavailability of selenium to forage crops in a sandy loam soil amended with Se-rich plant materials, Chemosphere, 66(9), 1734-1743.

Doherty, J. (2007), PEST user manual. 5th ed. Brisbane, Queensland, Australia: Watermark Numerical Computing.

Dowdle, P.R., and R.S. Oremland. 1998. Microbial oxidation of elemental selenium in soils and bacterial cultures. Environ. Sci. Technol. 32:3749-3755.

El-Sadek, A., M. Radwan and J. Feyen, 2001. Numerical analysis of the transport and fate of nitrate in the soil and nitrate leaching to drains. TheScientificWorldJournal, 1 (S2): 170-180.

Evensen, G. (1994), Sequential data assimilation with a nonlinear quasi-geostrophic model using Monte Carlo methods to forecast error statistics. J. Geophys. Res., 99(C5), 10, 143-10,162.

Evensen, G. (2003), The ensemble Kalman filter: theoretical formulation and practical implementation. Ocean Dynam., 53, 343-367.

Evensen, G., and P.J. van Leeuwen (2000), An ensemble Kalman smoother for nonlinear dynamics. Mon. Weather Rev., 128, 1852-1867.

Ewen, J., G. Parkin, and P. E. O'Connell (2000), SHETRAN: Distributed river basin flow and transport modeling system, Journal of Hydrologic Engineering, 9.

Fernández-Martínez, A., and L. Charlet. 2009. Selenium environmental cycling and bioavailability: a structural chemist point of view. Reviews in Environmental Science and Bio/Technology. 8:81-110.

Fio, J. L., R. Fujii, and S. J. Deverel. 1991. Selenium mobility and distribution in irrigated and nonirrigated alluvial soils. Soil Sci. Soc. Am. J. 55:1313-1320.

Flury, M., W. T. Frankenberger, and W. A. Jury. 1997. Long-term depletion of selenium frm Kesterson dewatered sediments. The Science of the Total Environment. 198:259-270.

Frankenberger, W. T., and M. Arshad. 2001. Bioremediation of selenium-contaminated sediments and water. BioFactors. 14:241-254.

Freeman, J.L., Tamaoki, M., Stushnoff, C., Devonshire, J., McGrath, S., Fakra, S., Marcus, M, Quinn, C.F., Van Hoewyk, D., and E.A.H. Pilon-Smits. 2010. Molecular mechanisms of selenium tolerance and hyperaccumulation in *Stanleya pinnata*. Plant Physiology 153, 1630-1652.

Freeman, J.L., and G.S. Bañuelos. 2011. Selection of salt and boron tolerant selenium hyperaccumulator genotypes and characterization of Se phytoremediation from agricultural drainage sediments. Environmental Science and Technology 45, 9703-9710.

Frind, E. O., W. H. M. Duynisveld, O. Strebel, and J. Boettcher. 1990. Modeling of multicomponent transport with microbial transformation in groundwater: the Fuhrberg case. Water Resources Research. 26:1707-1719.

Gailey, R.M., Crowe, A.S., and S.M. Gorelick (1991), Coupled process parameter estimation and prediction uncertainty using hydraulic head and concentration data. Adv. Water Resour., 14(5), 301-314.

Gambolati G., Pini G., Putti M., Paniconi C., Zannetti P. (1994), Finite element modeling of the transport of reactive contaminants in variably saturated soils with LEA and non-LEA sorption. In Environmental Modeling Vol. II: Computer Methods and Software for Simulating Environmental Pollution and its Adverse Effects, chapter 7: 173-212 Computational Mechanics Publications, Southampton, UK.

Gao, S., K. K. Tanji, D. W. Peters, and M. J. Herbel (2000), Water selenium speciation and sediment fractionation in a California flow-through wetland system, J Environ Qual, 29, 9.

Garcet J.D.P., Tilmant, A., and L. Bellefontaine (2002), Scenario analysis supporting fertilizer management strategies in the agricultural region of the Brusselean aquifer, Proceedings, Agricultural Effects on Ground and Surface Waters: Research at the Edge of Science and Society, Wageningen, October 2000. IAHS Publ. no. 273.

Gates, T. K., B. M. Cody, J. P. Donnelly, A. W. Herting, R. T. Bailey, and J. Mueller Price. 2009. Assessing selenium contamination in the irrigated stream-aquifer system of the Arkansas River, Colorado. J Environ Qual. 38:2344-2356.

Gates, T.K., Garcia, L.A., Hemphill, R.A., Morway, E.D., and A. Elhaddad (2012), Irrigation practices, water consumption, and return flows in Colorado's Lower Arkansas River Valley: Field and model investigations. Colorado Water Institute Completion Report No. 221, Colorado State University, Fort Collins, CO.

Gerla, P.J., Sharif, M.U., and S.F. Korom (2011), Geochemical process controlling the spatial distribution of selenium in soil and water, west central South Dakota, Environ. Earth Sci. 62, 1551-1560.

Giacobbo, F., Marseguerra, M., and E. Zio (2002), Solving the inverse problems of parameter estimation by genetic algorithms: the case of a groundwater contaminant transport problem. Ann. Nucl. Energy, 29, 967-981.

Gomez-Hernandez, J.J., Hendricks Franssen, H.-J., and A. Sahuquillo (2003) Stochastic conditional inverse modeling of subsurface mass transport: A brief review and the self-calibrating method. Stoch. Environ. Res. and Risk Assess. 17, 319-328.

Greenburg, A. E,, Clesceri, L. S,, and Eaton, A. D. (eds). 1992. Standard methods for the examination of water and wastewater, 18th edn. Section 8010 E. Prepairing organisms for toxicity tests. Washington, DC: American Public Health Association, American Water Works Association and Water Environmental Federation.

Guo, L., W. T. Frankenberger, and W. A. Jury. 1999. Evaluation of simultaneous reduction and transport of selenium in saturated soil columns. Water Resources Research. 35:663-669.

Guo, L., W. A. Jury, W. T. Frankenberger, and Y. Zhang. 2000. Characterizing kinetics of sequential selenium transformation in soil. J Environ Qual. 29:1041-1048.

Gusman, A.J., and M.A. Mariño (1999), Analytical modeling of nitrogen dynamics in soils and groundwater. J. Irrig. and Drain., 125(6), 330-337.

Halvorson, A.D., F.C. Schweissing, Bartolo, M.E., and C.A. Reule. 2005. Corn response to nitrogen fertilization in a soil with high residual nitrogen. Agron. J. 97:1222-1229.

Hamilton, S. J. 1998. Selenium effects on endangered fish in the Colorado River basin. p. 297-314. In W. T. Frankenberger and R. A. Engberg (ed.) Enviromental Chemistry of Selenium. Marcel Dekker, New York, New York, USA.

Hantush, M.M., and M.A. Marino (1997), Estimation of spatially variable aquifer hydraulic properties using Kalman filtering. J. Hydraul. Engrg. ASCE, 123(11), 1027-1035.

Harbaugh, A.W. (2005), MODFLOW-2005, the U.S. Geological Survey modular ground-water model – The Ground-Water Flow Process. U.S. Geological Survey Techniques and Methods 6-A16.

Healy, R.W. (1990), Simulation of solute transport in variably saturated porous media with supplemental information on modification of the U.S. Geological Survey's computer program VS2D: U.S. Geological Survey Water-Resources Investigations Report 90-4025.

Heathwaite, A.L., Griffiths, P., and R.J. Parkinsons (1998), Nitrogen and phosphorus in runoff from grassland and buffer strips following application of fertilizers and manures. Soil Use and Management 14, 142-148.

Heatwole, K.K., and J.E. McCray (2007), Modeling potential vadose-zone transport of nitrogen from onsite wastewater systems at the development scale. J. Cont. Hydrol., 91, 184-201.

Hefting, M.M., and J.J.M. de Klein (1998), Nitrogen removal in buffer strips along a lowland stream in the Netherlands: a pilot study. Environ. Pollut., 102, 521–526

Hefting, M.M., Clement, J.-C, Bienkowski, P., Dowrick, D., Guenat, C., Butturini, A., Topa, S., Pinay, G., and J.T.A. Verhoeven (2005), The role of vegetation and litter in the nitrogen dynamics of riparian buffer zones in Europe. Ecol. Engrg. 24(5), 465-482.

Hendricks Franssen, H. J., Gomez-Hernandez, J.J., and A. Sahuquillo (2003), Coupled inverse modeling of groundwater flow and mass transport and the worth of concentration data. J. Hydrol., 281, 281-295.

Hendricks Franssen, H. J., and W. Kinzelbach (2008), Real-time groundwater flow modeling with the Ensemble Kalman Filter: Joint estimation of states and parameters and the filter inbreeding problem. Water Resour. Res., 44, W09408, doi:10.1029/2007WR006505.

Hill, A.R. (1996), Nitrate removal in stream riparian zones. J. Envir. Qual., 25, 743-755.

Hunter et al., 1998

Hill, M. C., and C. R. Tiedeman (2007), Effective Groundwater Model Calibration: With Analysis of Data, Sensitivities, Predictions, and Uncertainty, Wiley.

Hudak, P. F. 2010. Nitrate, arsenic and selenium concentrations in The Pecos Valley Aquifer, West Texas, USA. Int. J. Environ. Res. 4:229-236.

Jacques, D., and J. Simunek (2005), User manual of the multicomponent variably-saturated flow and transport model HP1. Open Report of the Belgian Nuclear Research Centre, SCK-CEN-BLG-998, Waste & Disposal Department, Belgium.

Johnson, C.D., Truex, M.J., and T.P. Clement (2006), Natural and enhanced attenuation of chlorinated solvents using RT3D, Pacific Northwest National Laboratory, United States Department of Energy.

Johnsson, H., Bergström, L., Jansson, P., and K. Paustian (1987), Simulated nitrogen dynamics and losses in a layered agricultural soil. Agric. Ecosyst. Environ. 18, 333-356.

Johnsson, L. (1991), Selenium uptake by plants as a function of soil type, organic matter content and pH, Plant and Soil, 133, 8.

Kalman, R.E. (1960), A new approach to linear filtering and prediction problems. J. Basic Eng., 82, 35-45.

Keppenne, C. (2000), Data assimilation into a primitive-equation model with a parallel ensemble Kalman filter. Mon. Weather Rev., 128, 1971-1981.

Kim, J.-W., Kim, J., Choi, H., and F.W. Schwartz (2004), Modeling the fate and transport of organic and nitrogen species in soil aquifer treatment process. Water Science Tech., 50(2), 255-261.

Kindred, J.S., and M.A. Celia (1989),Contaminant transport and biodegradation 2. Conceptual model and test simulations. Water Resour. Res., 25(6), 1149-1159.

Kinzelbach, W. K. H., Dillon, P. J. & Jenson, K. H (1990), State of the art of existing numerical groundwater quality models of the saturated zone and experience with their application in agricultural problems. In: DeCoursey, D.D. (ed) . Proceedings of the International

Symposium on Water Quality Modelling of Agricultural Non-Point Sources, Part I. Report No. , ARS-81, . Agric. Res. Serv, US Dept of Agric, Beltsville, 307-325.

Kinzelbach, W., Schäfer, W., and J. Herzer (1991), Numerical modeling of natural and enhanced denitrification processes in aquifers. Water Resour. Res., 27(6), 1123-1135.

Kishchak, I. T. (1998), Supplementation of selenium in the diets of domestic animals, in Environmental Chemistry of Selenium, edited by W. T. Frankenberger and R. A. Engberg, Marcel Dekker, New York, New York.

Kleinman, P.J.A., Sharpley, A.N., Gartley, K., Jarrell, W.M., and S. Kuo (2001), Interlaboratory comparison of soil phosphorus extracted by various soil test methods. Commun. Soil Sci. Plant Anal. 32(15,16), 2325-2345.

Kollat, J.B., Reed, P.M., and D.M. Rizzo (2008), Addressing model bias and uncertainty in three dimensional groundwater transport forecasts for a physical aquifer experiment. Geoph. Res. Letters, 35, L17402, doi: 10.1029/2008GL035021.

Konikow, L.F. (2011), The secret to successful solute-transport modeling. Ground Water 49(2), 144-159.

Korom, S. F. 1992. Natural denitrification in the saturated zone: A review. Water Resources Research. 28:1657-1668.

Kubota, J., W. H. Allaway, D. C. Carter, E. E. Cary, and V. A. Lazar (1967), Selenium crops in the United States in relation to the selenium responsive diseases of livestock, Journal of Agricultural and Food Chemistry, 15, 6.

Kuisi, M. A., and A. Abdel-Fattah. 2010. Groundwater vulnerability to selenium in semi-arid environments: Amman Zarqa Basin, Jordan. Environ Geochem Health. 32:107-128.

Ledoux, E., Gomez, E., Monget, J.M., Viavattene, C., Viennot, P., Ducharne, A., Benoit, M., Mignolet, C., Schott, C., and B. Mary (2007), Agriculture and groundwater nitrate contamination in the Seine basin. The STICS-MODCOU modeling chain, Science of the Total Environment 275, 33-47.

Lee, M-S., Lee, K-K., Hyun, Y., Clement, T.P., and D. Hamilton (2006), Nitrogen transformation and transport modeling in groundwater aquifers. Ecol. Mod., 192, 143-159.

Lee, M., Park, G., Park, M., Park, J., Lee, J., and S. Kim (2010), Evaluation of non-point source pollution reduction by applying best management practices using a SWAT model and QuickBird high resolution satellite imagery. J. Environmental Sciences 22(6), 826-833.

Levander, O. A., and R. F. Burk. 2006. Update of human dietary standards for selenium. p. 399-410. In D. L. Hatfield, M. J. Berry and V. N. Gladyshev (ed.). Selenium its molecular biology and role in human helath. Springer, New York.

Liu, C.W. and T.N. Narasimhan (1994), Modeling of selenium transport at the Kesterson reservoir, California, U.S.A. J. Cont. Hydrol. 15, 345-366.

Liu, Y., and H.V. Gupta (2007), Uncertainty in hydrologic modeling: Toward an integrated data assimilation framework, Water Resour. Res., 43, W07401, doi:10.1029/ 2006WR005756.

Liu, G., Y. Chen, and D. Zhang (2008), Investigation of flow and transport processes at the MADE site using ensemble Kalman filter. Adv. Water Resour., 31, 975-986.

Logan, T. J., A. C. Chang, A. L. Page, and T. J. Ganje (1987), Accumulation of Selenium in Crops Grown on Sludge-treated Soil, J Environ Qual, 16, 4.

Losi, M. E., and W. T. Frankenberger. 1998. Microbial oxidation and solubilization of precipitated elemental selenium in soil. J Environ Qual. 27:836-843.

Lu, G., Clement, T.P., Zheng, C., and T.H. Wiedemeier (1999), Natural attenuation of BTEX compounds: Model development and field-scale application. Ground Water, 37(5), 707-717.

Ma, L., M. J. Shaffer, J. K. Boyd, R. Waskom, L. R. Ahuja, K. W. Rojas, and C. Xu (1998), Manure Management in an Irrigated Silage Corn Field: Experiment and Modeling. Soil Sci. Soc. Am. J. 62:1006-1017

Ma., L., Ahuja, L.R., Ascough II, J.C., Shaffer, M.J., Rojas, K.W., Malone, R.W., and M.R. Cameira (2000), Integrating system modeling with field research in agriculture: Applications of the Root Zone Water Quality Model (RZWQM). Adv. Agronomy 71, 233-292.

Macy, J. M., T. A. Michel, and D. G. Kirsch. 1989. Selenate reduction by a Pseudomonas species: a new mode of anaerobic respiration. FEMS Microbiology Letters. 61:195-198.

Martens, D. A., and D. L. Suarez (1997), Selenium speciation of marine shales, alluvial soils, and evaporation basin soils of California, J Environ Qual, 26, 9.

Masscheleyn, P. H., R. D. Delaune, and J. W. H. Patrick. 1989. Transformations of selenium as affected by sediment oxidation-reduction potential and pH. Environmental Science & Technology. 24:91-96.

Mayer, K.U., Frind, E.O., and D.W. Blowes (2002), Multicomponent reactive transport modeling in variably saturated porous media using a generalized formulation for kinetically controlled reactions, Water Resour. Res., 38(9), 1174-1194.

McDonald, M.G., and A.W. Harbaugh (1988), A modular three-dimensional finite-difference ground-water flow model. Techniques of Water-Resources Investigations, Book 6. U.S. Geological Survey.

McLaughlin, D. (2002), An integrated approach to hydrologic data assimilation: interpolation, smoothing, and filtering. Adv. Water Resour., 25, 1275-1286.

McMahon, P.B., J.K. Böhlke, and B.W. Bruce. 1999. Denitrification in marine shales in northeastern Colorado. Water Resources Research. 35:1629-1642.

McMahon, P. B., and F. H. Chapelle. 2008. Redox processes and water quality of selected principal aquifer systems. Ground Water. 46:259-271.

McNab Jr., W.W., and B.P. Dooher (1998), Uncertainty analysis of fuel hydrocarbon biodegradation signatures in ground water by probabilistic modeling. Ground Water, 36(4), 69-698.

Millington, R.J., and J.M. Quirk (1961), Permeability of porous solids. Trans. Faraday Soc. 57, 1200-1207.

Mirbagheri, S. A., K. K. Tanji, and T. Rajaee (2008), Selenium transport and transformation modelling in soil columns and ground water contamination prediction, Hydrological Processes, 22(14), 2475-2483.

Mishra, A.K., Gutjahr, A., and H. Rafaram (1999), Transport with spatially kinetic sorption: recursion formulation. Adv. Water Resour., 22, 549-555.

Mizutani, T., K. Kanaya, and T. Osaka. 2001. Map of selenium content in soil in Japan. Journal of Health Science, 47:407-413.

Molénat, J., and C. Gascuel-Odoux (2002), Modelling flow and nitrate transport in groundwater for the prediction of water travel times and of consequences of land use evolution on water quality. Hydrol. Proc., 16, 479-492.

Morway E.D., Niswonger R.G., Langevin, C.D., Bailey, R.T., and R.W. Healy (2012), Modeling variably saturated subsurface solute transport with MODFLOW-UZF and MT3DMS. Ground Water, in press.

Morway, E.D., Gates, T.K., and R.G. Niswonger (2012), Regional-scale appraisal of options to enhance groundwater flow conditions in an irrigated alluvial aquifer system. In preparation.

Moxon, A.L. (1937), Alkali disease or selenium poisoning. South Dakota State College of Agriculture and Mechanical Arts, Agric. Exp. Stn. Bull. No. 311.

Mueller Price, J., and T.K. Gates (2008), Assessing uncertainty in mass balance calculation of river nonpoint source loads. J. Env. Engr. 134(4) 247-258.

Neal, R. H., and G. Sposito. 1989. Selenate adsorption on alluvial soils. Soil Sci. Soc. Am. J. 53:70-74.

Neal, R. H., and G. Sposito (1991), Selenium mobility in irrigated soil columns as affected by organic carbon amendment, J Environ Qual, 20, 7.

Neale, C.N., Hughes, J.B., and C.H. Ward (2000), Impacts of unsaturated zone properties on oxygen transport and aquifer reaeration. Ground Water, 38(5), 784-794.

Neale, C.N., Holder, A.W., Ward, C.H., and J.B. Hughes (2002), Groundwater reaeration and hydrocarbon plume length: a modeling analysis. J. Env. Engrg., 128(1), 40-50.

Neitsch, S.L., Arnold, J.G., Kiniry, J.R., and J.R. Williams (2011), Soil and water assessment tool. Theoretical Documentation. Grassland, Soil and Water Research Laboratory, Agricultural Research Service, Temple, Texas.

Niswonger, R.G., Prudic, D.E., and R.S. Regan (2006), Documentation of the unsaturated-zone flow (UZF1) package for modeling unsaturated flow between the land surface and the water table with MODFLOW-2005, U.S. Geological Survey Techniques and Methods 6-A19.

Niswonger, R.G., Panday, Sorab, and Ibaraki, Motomu, 2011, MODFLOW-NWT, A Newton formulation for MODFLOW-2005: U.S. Geological Survey Techniques and Methods 6–A37, 44 p.

Oremland, R. S., J. T. Hollibaugh, A. S. Maest, T. S. Presser, L. G. Miller, and C. W. Culbertson. 1989. Selenate reduction to elemental selenium by anaerobic bacteria in sediments and culture: biogeochemical significance of a novel, sulfate-independent respiration. Appl Environ Microbiol. 55:2333-2343.

Oremland, R. S., N. A. Steinberg, A. S. Maest, L. G. Miller, and J. T. Hollibaugh. 1990. Measurement of in situ rates of selenate removal by dissimlatory bacterial reduction in sediments. Environ. Sci. Technol. 24:1157-1164.

Oremland, R. S., J.S. Blum, A.B. Bindi, P.R. Dowdle, M. Herbel, and J.F. Stolz. 1999. Simultaneous reduction of nitrate and selenate by cell suspensions of selenium-respiring bacteria. Appl. Environ. Microbiol. 65:4385-4392.

Panday S., Huyakorn P.S. (2008), MODFLOW SURFACT: A state-of-the-art use of vadose zone flow and transport equations and numerical techniques for environmental evaluations. Vadose Zone Journal 7:610.

Parkhurst, D.L., Kipp, K.L., Engesgaard, P., and S.R. Charlton (2004), PHAST – A program for simulating ground-water flow, solute transport, and multicomponent geochemical reactions. U.S. Geological Survey, Denver, Colorado.

Parkhurst D.L., Kipp K.L., Engesgaard P., Charlton S.R. (2010), PHAST Version 2 - A program for simulating groundwater flow, solute transport, and multicomponent geochemical reactions, U. S. Geological Survey Techniques and Methods 6-A35, 235 pg.

Parkin, T.B., and J.A. Robinson (1989), Stochastic models of soil denitrification. Appl. Environ. Micro., 55(1), 72-77.

Pauwels, H., W. Kloppmann, J.-C. Foucher, A. Martelat, and V. Fritsche. 1998. Field tracer test for denitrification in a pyrite-bearing schist aquifer. Applied Geochemistry. 13:767-778.

Peng, A., Z. Wang, P. D. Whanger, G. F. Combs, and J. Y. Yeh (1995), in Environmental Bioinorganic Chemistry of Selenium, edited by C. E. S. Technology, Beijing, China.

Pilkey, O.H., and L. Pilkey-Jarvis (2007), Useless arithmetic: why environmental scientists can't predict the future. Columbia University Press, United State of America.

Presser, T.S., Sylvester, M.A., and W.H. Low (1994), Bioaccumulation of selenium from natural geologic sources in Western States and its potential concequences. Environ. Manag. 18, 423-436.

Prommer, H., Barry, D.A., and C. Zheng (2003), MODFLOW/MT3DMS-based reactive multicomponent transport modeling. Ground Water, 41(2), 247-257.

RamaRao, B.S., LaVenue, A.M., Marsily, G. de, and M.G. Marietta (1995), Pilot point methodology for automated calibration of an ensemble of conditionally simulated transmissivity field 1. Theory and computational experiments. Water Resour. Res., 31(2), 475-493.

Ray, C., and R.K. Jain (1999), Nitrate pollution of wells: pollution prevention policy options. Environ. Engg. And Policy, 1, 165-173.

Rodell, M., Houser, P.R., Berg, A.A., Famiglietti, J.S. (2005), Evaluation of 10 methods for initializating a land surface model. J. Hydrometeorology 6, 146-155.

Rong, Y., and W. Xuefeng (2011), Effects of nitrogen fertilizer and irrigation rate on nitrate present in the profile of a sandy farmland in Northwest China. Procedia Environmental Sciences 11, 726-732.

Rubin, J. (1983), Transport of reacting solutes in porous media: Relation between mathematical nature of problem formulation and chemical nature of reactions. Water Resour. Res., 19(5), 1231-1252.

Ryser, A. L., Strawn, D. G., Marcus, M. A., Johnson-Maynard, J. L., Gunter, M. E., and Moller, G. 2005. Micro-spectroscopic investigation of selenium-bearing minerals from the Western US phosphate resource area. Geochem. Trans., 6(1): 1 – 11.

Sager, M. (2006), Selelnium in agriculture, food, and nutrition, Pure Applied Chemistry, 78(1), 23.

Sahu, M., and R.R. Gu (2009), Modeling the effects of riparian buffer zone and contour strips on stream water quality, Ecol. Engrg. 35, 1167-1177.

Schafer, W., and R. Therrien (1995), Simulating transport and removal of xylene during remediation of a sandy aquifer. J. Cont. Hydrol., 19, 205-236.

Schafer, D., Schafer, W., and W. Kinzelbach (1998), Simulation of reactive processes related to biodegradation in aquifer 1. Structure of the three-dimensional reactive transport model. J. Cont. Hydrol., 31, 167-186.

Schwarz, K., and C. M. Foltz (1957), Selenium as an integral part of factor 3 against dietary necrotic liver degeneration, Soc., 79, 2.

Scott, G. R. (1968), Geologic and structure contour map of the La Junta quadrangle, Colorado and Kansas, edited by U. S. G. Survey, Reston, Virginia.

Seiler, R. L. 1995. Prediction of areas where irrigation drainage may induce selenium contamination of water. J Environ Qual. 24:973-979.

Seiler, R. L. 1997. Methods to identify areas susceptible to irrigation-induced selenium contamination in the Western United States, edited by US Dept. of the Interior, USGS, Washington, D.C., p. 4. Fact Sheet FS-038-97.

Shamrukh, M., Corapcioglu, M.Y., and F.A.A. Hassona (2001), Modeling the effect of chemical fertilizers on ground water quality in the Nile Valley Aquifer, Egypt. Ground Water, 39(1), 59-67.

Sharps, J. A. (1976), Geologic map of the Lamar quadrangle, Colorado and Kansas, edited by U. S. G. Survey, Reston, Virginia.

Shrift, A. (1954), Sulfur-Selenium Antagonium. I. Antimetabolite Action of Selenate on the Growth of Chlorella vulgaris, American Journal of Botany, 41(3), 8.

Simunek, J., M. Sejna, and M. Th. van Genuchten (1998), The Hydrus-1D software package for simulating the one-dimensional movement of water, heat, and multiple solutes in variably saturated media. Version 2.0. IGWMC-TPS 70. Int. Ground Water Modeling Center, Colorado School of Mines, Bolder, CO.

Simunek J., Jacques D., van Genuchten M.T., Mallants D. (2006), Multicomponent geochemical transport modeling using the HYDRUS computer software packages. Journal of American Water Resources Association 42:1537-1547.

Skorupa, J. P. 1998. Selenium poisoning of fish and wildlife in nature: Lessons from twelve real-world experiences. p. 315-396. In W. T. Frankenberger and R. A. Engberg (ed.) Enviromental Chemistry of Selenium. Marcel Dekker, New York, New York, USA.

Sood, A. and W.F. Ritter (2010), Evaluation of best management practices in Millsboro Pond watershed using Soil and Water Assessment Tool (SWAT) model. J. Water Resource and Protection, 2(5), 403-412.

Sors, T. G., D. R. Ellis, and D. E. Salt (2005), Selenium uptake, translocation, assimilation and metabolic fate in plants, Photosynth Res, 86(3), 373-389.

Sposito, G., A. Yang, R. H. Neal, and A. Mackzum. 1991. Selenate reduction in an alluvial soil. Soil Sci. Soc. Am. J. 55:1597-1602.

Spruill, T.B. (2000), Statistical evaluation of effects of riparian buffers on nitrate and ground water quality, J. Env. Qual. 29, 1523-1538.

Stavridou, E., K. Thorup-Kristensen, and D. Young (2011), Assessment of selenium mineralization and availability from catch crops, Soil Use and Management.

Stillings, L. L., and M. C. Amacher. 2010. Kinetics of selenium release in mine waste from the Meade Peak phosphatic shale, Phosphoria formation, Wooley Valley, Idaho, USA. Chemical Geology. 269:113-123.

Stolz, J. F., P. Basu, and R. S. Oremland. 2002. Microbial transformation of elements: the case of arsenic and selenium. Int. Microbiol. 5:201-207.

Stork, A., W. A. Jury, and W. T. Frankenberger. 1999. Accelerated volatilization rates of selenium from different soils. Biological Trace Element Research. 69:217-234.

Tayfur, G., K. K. Tanji, and A. Baba (2010), Two-dimensional finite elements model for selenium transport in saturated and unsaturated zones, Environ Monit Assess, 169(1-4), 509-518.

Tokunaga, T. K., J. G. E. Brown, I. J. Pickering, S. R. Sutton, and S. Bajt (1997), Selenium redox reactions and transport between ponded waters and sediments, Environmental Science & Technology, 31, 7.

Trachtenberg, E., and C. Ogg (1994), Potential for reducing nitrogen pollution through improved agronomic practices. Water Resour. Bull. 30:1109–1118.

USEPA. 1983. Methods for chemical analysis of water and waste. EPA/600/4-79/020. USEPA, Washintong, D.C.

Vaché, K.B., Eilers, J.M., and M.V. Santelmann (2002), Water quality modeling of alternative agricultural scenarios in the U.S. Corn Belt, J. Amer. Water Res. Assoc. 38(3), 773-787.

Valstar, J.R., McLaughlin, D.B., te Stroet, C.B.M., and F.C. van Geer (2004), A representer-based inverse method for groundwater flow and transport application. Water Resour. Res., 40, W05116, doi:10.1029/2003WR002922.

van Breukelen, B.M., and J. Griffioen (2004), Biogeochemical processes at the fringe of a landfill leachate pollution plume: potential for dissolved organic carbon , Fe(II), Mn(II), NH_4, and CH_4 oxidation J. Contam. Hydrol. 73, 181-205.

van Genuchten, M. Th. (1980), A closed-form equation for predicting the hydraulic conductivity of unsaturated soils. Soil Sci. Soc. Am. Journal, 44(5), 892-898.

van Genuchten, M. Th. (1981). Analytical solutions for chemical transport with simultaneous adsorption, zero-order production and first-order decay. J. Hydrol. 49, 213-233.

van Genuchten, M.T., and Nielsen, D.R. (1985), On describing and predicting the hydraulic properties of unsaturated soils. Ann. Geophy., 3, 615-628.

van Veen, J.A., and E.A. Paul (1981), Organic carbon dynamics in grassland soils. (1) Background information and computer simulation. Can. J. Soil Sci., 61, 185-201.

Vanderborght J., Kasteel R., Herbst M., Javaux M., Thiery D., Vanclooster M., Mouvet C., Vereecken H. (2005), A set of analytical benchmarks to test numerical models of flow and transport in soils. Vadose Zone Journal 4:206.

von der Heide, C., Bottcher, J., Deurer, M., Weymann, D., Well, R., and W.H.M. Duijnisveld (2008), Spatial variability of N20 concentrations and of denitrification-related factors in the surficial groundwater of a catchment in Northern Germany. J. Hydrol., 360, 230-241.

Voss, C.I., and A.M. Provost (2003), SUTRA, A model for saturated-unsaturated variable-density ground-water flow with solute or energy transport. USGS Water-Resources Investigations Report 02-4231. Reston, Virginia: USGS.

Voss, C.I., and A.M. Provost (2010), SUTRA, A model for saturated-unsaturated, variable-density ground-water flow with solute or energy transport. USGS Water-Resources Investigations Report 02-4231. Reston, Virginia: USGS.

Vugrin, E.D., McKenna, S.A., and K.W. Vugrin (2007), Markov models and the Ensemble Kalman Filter for estimation of sorption rates. Sandia Report. SAND2007-5975. Albuquerque, New Mexico: Sandia National Laboratories.

Wagner, B.J. (1992), Simultaneous parameter estimation and contaminant source characterization for coupled groundwater flow and contaminant transport modelling. J. Hydrol., 135, 275-303.

Wan, H. F., R. L. Mikkelsen, and A. L. Page (1988), Selenium uptake by some agricultural crops from central California soils, J Environ Qual, 17, 4.

Wang, Z., and Y. Gao (2001), Biogeochemical cycling of selenium in Chinese envrionments, Applied Geochemistry, 16, 7.

Wang, D., Y. Chen, and X. Cai (2009), State and parameter estimation of hydrologic models using the constrained ensemble Kalman filter, Water Resour. Res., 45, W11416, doi:10.1029/2008WR007401.

Weres, O., H. R. Bowman, A. Goldstein, E. C. Smith, and L. Tsao. 1990. The effect of nitrate and organic matter upon mobility of selenium in groundwater and in a water treatment process. Water, Air, and Soil Pollution. 49:251-272.

White, A. F., S. M. Benson, A. W. Yee, J. H. A. Wollenberg, and S. Flexser. 1991. Groundwater contamination at the Kesterson Reservoir, California 2. Geochemical parameters influencing selenium mobility. Water Resources Research. 27:1085-1098.

Widdowson, M.A., Molz, F.J., and L.D. Benefield (1988), A numerical transport model for oxygen- and nitrate-based respiration linked to substrate and nutrient availability in porous media. Water Resour. Res., 24(9), 1553-1565.

Williams, M. C., and H. F. Mayland (1992), Selenium absorption by two-grooved milkvetch and western wheat grass from selenomethionine, selenocytine, and selenite, Journal of Range Management, 45, 5.

Winkel, L.H.E., Johnson, C.A., Lenz, M., Grundl, T., Leupin, O.X., Amini, M., and L. Charlet (2012), Environmental Selenium Research: From Microscopic Processes to Global Understanding. Env. Sci. Tech. 46, 571-579.

Wissmeier, L., and D.A. Barry (2010), Implementation of variably saturated flow into PHREEQC for the simulation of biogeochemical reactions in the vadose zone. Environ. Model. & Soft., 25(3), 526-538.

Wriedt, G., and M. Rode (2006), Modelling nitrate transport and turnover in a lowland catchment system. J. Hydrol., 328, 157-176.

Wright, W. G. 1999. Oxidation and mobilization of selenium by nitrate in irrigation drainage. J Environ Qual. 28:1182-1187.

Yang G.-Q., and Y.M. Xia (1995). Studies on human dietary requirements and safe range of dietary intakes of selenium in China and their application in the prevention of related endemic diseases. Biomed. Environ. Sci., 8, 187-201.

Yeh, G.T., and V.S. Tripathi (1989), A critical evaluation of recent developments in hydrogeochemical transport models of reactive multichemical components. Water Resour. Res., 25(1), 93-108.

Yeh, T.-C. J., Gutjahr, A.L., and M. Jin (1995), An iterative cokriging-like technique for ground-water flow modeling. Ground Water 33(1), 33-41.

Zawislanski, P. T., and M. Zavarin. 1996. Nature and rates of selenium transformations: a laboratory study of Kesterson Reservoir Soils. Soil Sci. Soc. Am. J. 60:790-800.

Zhang, Y., and J. N. Moore. 1997. Reduction potential of selenate in wetland sediment. J Environ Qual. 26:910-916.

Zhang, H. H., Z. F. Wu, C. L. Yang, B. Xia, D. R. Xu, and H. X. Yuan. 2008. Spatial distributions and potential risk analysis of total soil selenium in Guangdong Province, China. J Environ Qual. 37:780-787.

Zhang, P., Liu, Y., Pan, Y., and Z. Yu (2012), Land use pattern optimization based on CLUE-S and SWAT models for agricultural non-point source pollution control. Mathematical and Computer Modeling, doi:10.1016/j.mcm.2011.10.061.

Zheng C. and Wang P. (1999), MT3DMS: A modular three-dimensional multispecies transport model for simulation of advection, dispersion, and chemical reactions of contaminants in groundwater systems; Documentation and user's guide, Contract Report SERDP-99-1. Vicksburg, MS. U. S. Army Engineer Research and Development Center.

Zou, S., and A. Parr (1995), Optimal Estimation of Two-Dimensional Contaminant Transport, Ground Water, 33, 319-325.

APPENDICES

APPENDIX A: CODE DEVELOPMENT OF RT3DAG, A NUMERICAL MODEL FOR SIMULATING THE FATE AND TRANSPORT OF NUTRIENTS IN AGRICULTURAL GROUNDWATER SYSTEMS

APPENDIX B: DATA PERTAINING TO UZF-RT3DAG MODEL APPLICATION TO THE LOWER ARKANSAS RIVER VALLEY, SOUTHEASTERN COLORADO

APPENDIX C: RESULTS FROM SENSITIVITY TEST OF THE UZF-RT3DAG MODEL FOR THE LOWER ARKANSAS RIVER VALLEY, SOUTHEASTERN COLORADO

APPENDIX D: ENSEMBLE SMOOTHER ASSIMILATION OF HYDRAULIC HEAD AND RETURN FLOW DATA TO ESTIMATE HYDRAULIC CONDUCTIVITY DISTRIBUTION
(Published in *Water Resources Research*, 2010)

APPENDIX E: ESTIMATING GEOSTATISTICAL PARAMETERS AND SPATIALLY-VARIABLE HYDRAULIC CONDUCTIVITY WITHIN A CATCHMENT SYSTEM USING AN ENSEMBLE SMOOTHER (Published in *Hydrology and Earth System Sciences*, 2012)

APPENDIX F: ESTIMATING SPATIALLY-VARIABLE RATE CONSTANTS OF DENITRIFICATION IN IRRIGATED AGRICULTURAL GROUNDWATER SYSTEMS USING AN ENSEMBLE SMOOTHER (In Review in *Journal of Hydrology*, 2012)

APPENDIX A

CODE DEVELOPMENT OF UZF-RT3DAG, A NUMERICAL MODEL FOR SIMULATING THE FATE AND TRANSPORT OF NUTRIENTS IN AGRICULTURAL GROUNDWATER SYSTEMS

A1. SUMMARY OF RT3DAG

The numerical model RT3DAG is a derivative of the multi-species reactive transport model RT3D (Reactive Transport in 3 Dimensions) (Clement, 1997), which was designed for simulating the reactive transport of multiple species in the saturated zone of subsurface systems. When investigating the fate and transport of selenium (Se) and nitrogen (N) species in agricultural groundwater systems, however, physical and chemical processes occurring in the root zone and underlying zone between the rooting depth and the water table play a vital role in determining the loading (amount and timing) of species mass to the saturated zone. Furthermore, efficient methods of simulating the cycling of Se and N, as well as carbon (C) species and dissolved oxygen (O_2) are required for applications to regional-scale systems.

To meet these needs, three modeling packages were designed and implemented into the original RT3D modeling code. The first package is the Variably-Saturated Transport (VST) package, which links RT3D with output from MODFLOW-UZF simulations as well as modifies calculations within RT3D to handle volumetric water content rather than porosity. The UZF (Unsaturated Zone Flow) package (Niswonger et al., 2006) simulates the one-dimensional vertical flow of water in the unsaturated zone and was chosen due to its efficient solution to the 1D groundwater flow equation and hence potential application to large-scale systems. The VST package is described adequately in Chapter 4, and will not be discussed further in this appendix. The second package is the Nutrient Cycling (NTR) package, which accounts for the reading and processing of data required for the cycling of C, N, and Se species. These data include

parameters (discussed below) for crop cultivation and management, crop type for each cell of the model's surface grid, and species concentration of the infiltrating irrigation water. The third package is the Irrigation (IRG) package, which handles the accounting of the species mass entering the system via surface water irrigation, aquifer (pumped) water irrigation, and rainfall. Mathematical description of the processes is included in Chapters 5 and 6. This appendix is included to describe the framework of the NTR and IRG packages and to describe more fully the input files and developed subroutines. These are discussed in the following sections, followed by a description of the data flow in a typical RT3DAG simulation.

A2. NUTRIENT CYCLING (NTR) PACKAGE

As described in Chapter 5, the NTR package provides the framework for simulating the cycling and reactive transport of C, N, and Se species in variably-saturated subsurface systems. Cycling occurs in the root zone as species mass is introduced into the subsurface environment via fertilizer, irrigation, decaying plant mass (dead roots and after-harvest stover) and removed via crop uptake during the growing season. Throughout the year, species mass is either removed from the system or transferred to other forms via chemical reactions such as nitrification, denitrification, selenium reduction, volatilization, and mineralization/immobilization. Since the reactions are microbially-mediated, rates of reaction being are dependent on soil temperature and soil moisture. Oxidation-reduction reactions also are dependent on the presence of organic carbon, which is indicated by the amount of organic matter decomposition in the soil profile. Species mass that is not taken up by the crop roots is leached below the root zone, eventually loaded to the saturated zone and transported through the aquifer to surface water discharge points.

In order to incorporate these processes in the NTR package, two sets of parameters and other system data are required. The first set includes crop-specific parameters, with parameter values specified for each crop type included in the simulation; the second set includes chemical reaction parameters that can either be spatially-uniform or spatially-variable; and system data includes crop type for each irrigated field for each year of the simulation, amount and timing of fertilizer application for each crop type, measured air temperature for each day of the simulation period, and data points describing the rate of microbial activity as a function of soil moisture for various types of reactions. Certain parameters and data values are varied stochastically within RT3D to enable heterogeneity in the system.

An array of binary values (0, 1) is also included to specify whether each surface grid cell is within a surface water riparian zone (value = 1) or not (value = 0). The oxidation-reduction reaction rate laws are handled differently for riparian zone cells as opposed to cells underlying cultivated fields. Since the model accounts for the presence of organic carbon through organic matter decomposition, and since this process is only simulated in the model for cultivated fields, the dependence of reaction rate on the presence of organic carbon in the riparian zone has been relaxed.

The crop-specific parameters, amount and timing of fertilizer application, crop type of each field, daily air temperature, values of microbial activity dependence on soil moisture, and array of riparian zone indices are specified in the new NTR (.ntr) input file. Sections of the file are as follows:

A2.1 Specify Number of Crops and Crop Types

14
Alfalfa
Bean
Corn
Melon
Onion
Pasture
Pumpkin
Sorghum
SpringGrain
Squash
Sunflower
Vegetable
WinterWheat
Clear

A2.2 Specify Parameters for Each Crop Type

GENERAL CROP PARAMETERS

CROP	PLDY	HVTP	FYR	HVDY	PGDY	PGDP	RTHV	CBRT	STPG	CBST	FLR	MNMS	MNC
Alfalfa	120	5	3	273	293	1.0	500.0	0.4	561.6	0.4	0.8	0.0	0.40
Bean	140	1	1	273	293	0.8	500.0	0.3	561.6	0.3	0.0	0.0	0.40
Corn	121	1	1	298	318	1.0	500.0	0.4	5616.0	0.4	0.0	0.0	0.40
Melon	135	1	1	222	242	1.0	500.0	0.4	561.6	0.4	0.0	0.0	0.40
Onion	79	1	1	258	278	1.0	500.0	0.4	561.6	0.4	0.0	0.0	0.40
Pasture	242	5	3	273	293	1.0	500.0	0.4	0.0	0.4	0.8	0.0	0.40
Pumpkin	152	1	1	273	293	1.0	500.0	0.4	561.6	0.4	0.0	0.0	0.40
Sorghum	140	1	1	288	308	1.0	500.0	0.4	1684.8	0.4	0.0	0.0	0.40
SpringGrain	91	1	1	196	216	1.0	500.0	0.4	1684.8	0.4	0.0	0.0	0.40
Squash	140	1	1	206	226	1.0	500.0	0.4	561.6	0.4	0.0	0.0	0.40
Sunflower	152	1	1	283	303	1.0	500.0	0.4	561.6	0.4	0.0	0.0	0.40
Vegetable	115	1	1	242	262	1.0	500.0	0.4	561.6	0.4	0.0	0.0	0.40
WinterWheat	273	1	1	186	206	1.0	500.0	0.4	1684.8	0.4	0.0	0.0	0.40
Clear	0	0	0	0	0	0	0	0	0	0	0	0	0

Where:

PLDY Planting day (day index of the year)

HVTP Type of harvest cycle, either annual or perennial. If perennial, then HVTP refers to the number of years in the perennial cycle.

FYR	For perennial crops, FYR refers to the number of years at the beginning of the perennial cycle that the crop receives fertilizer.
HVDY	Harvest day (day index of the year). For perennial crops, HVDY refers to the harvest day in the last year of the perennial cycle.
PGDY	Plow day (day index of the year). For perennial crops, refers to the plowing day in the last year of the perennial cycle.
PGDP	The depth of plowing (m)
RTHV	The root mass at harvest time per unit land area (kg ha^{-1})
CBRT	Carbon mass fraction of the root mass (0 to 1)
STPG	The mass of after-harvest stover mass per unit land area (kg ha^{-1})
CBST	Carbon mass fraction of the stover mass (0 to 1)
FLR	Fraction of roots that is alive at harvest time (0 to 1). This specifies the fraction of root mass that is incorporated into the soil at harvest time (1-FLR) as opposed to the fraction of root mass that is incorporated into the soil at plowing time (FLR).
MNMS	Seasonal mass of manure applied, per unit land area (kg ha^{-1})
MNC	Carbon mass fraction of manure (0 to 1)

ROOT GROWTH PARAMETERS

CROP	RTDP	RTB	RTC	RBETA
Alfalfa	1.83	0.10	0.05	5.0
Bean	0.91	0.05	0.05	5.0
Corn	1.22	0.07	0.05	5.0
Melon	1.22	0.10	0.07	5.0
Onion	0.46	0.05	0.05	5.0
Pasture	0.91	0.05	0.05	5.0
Pumpkin	0.91	0.08	0.06	5.0
Sorghum	0.91	0.10	0.05	5.0
SpringGrain	0.91	0.10	0.07	5.0
Squash	0.91	0.05	0.10	5.0
Sunflower	0.91	0.05	0.06	5.0
Vegetable	0.91	0.05	0.06	5.0
WinterWheat	0.91	0.05	0.06	5.0
Clear	0.00	0.00	0.00	0.0

Where:

RTDP Maximum seasonal rooting depth (m)

RTB B shape parameter for defining seasonal root growth curve (-)

RTC C shape parameter for defining seasonal root growth cruve (-)

RBETA Depth distribution parameter for root mass, defining the variation of root mass with depth. (-)

NUTRIENT PLANT PARAMETERS

NITROGEN

CROP	CNRT	CNST	FNO3	FNH4	FUREA	NUP	NB	NC	NBETA	MNCN
Alfalfa	25.0	50.0	0.0	22.4	0.0	22.4	1.0	0.08	5.0	20.0
Bean	25.0	45.0	0.0	140.0	0.0	84.2	1.0	0.08	5.0	20.0
Corn	70.0	50.0	0.0	252.0	0.0	224.6	2.0	0.06	5.0	20.0
Melon	25.0	50.0	0.0	112.0	0.0	112.3	2.0	0.10	5.0	20.0
Onion	25.0	50.0	0.0	140.0	0.0	78.6	1.3	0.06	5.0	20.0
Pasture	70.0	50.0	0.0	0.0	140.0	112.3	1.2	0.06	5.0	20.0
Pumpkin	25.0	50.0	0.0	140.0	0.0	84.2	1.0	0.08	5.0	20.0
Sorghum	70.0	50.0	0.0	0.0	112.0	112.3	1.0	0.07	5.0	20.0
SpringGrain	70.0	50.0	0.0	0.0	112.0	112.3	2.0	0.09	5.0	20.0
Squash	25.0	50.0	0.0	140.0	0.0	84.2	3.0	0.12	5.0	20.0
Sunflower	25.0	50.0	0.0	140.0	0.0	84.2	2.0	0.11	5.0	20.0
Vegetable	25.0	50.0	0.0	140.0	0.0	84.2	2.0	0.11	5.0	20.0
WinterWheat	70.0	50.0	0.0	0.0	112.0	112.3	2.0	0.09	5.0	20.0
Clear	0.0	0.0	0.0	0.0	0.0	0.0	0.0	0.00	0.0	0.0

SELENIUM

CROP	SEST	SERT	FSE	SEUP	MNSE
Alfalfa	0.0001	0.00017	0	1.3	0.003
Bean	0.00005	8.3E-05	0	0.3	0.003
Corn	0.0013	0.00217	0	10.8	0.003
Melon	0.00005	8.3E-05	0	1.3	0.003
Onion	0.00005	8.3E-05	0	2.7	0.003
Pasture	0.0032	0.00533	0	10.7	0.003
Pumpkin	0.00005	8.3E-05	0	2.7	0.003
Sorghum	0.0013	0.00217	0	10.4	0.003
SpringGrain	0.0013	0.00217	0	8.7	0.003
Squash	0.00005	8.3E-05	0	2	0.003
Sunflower	0.00005	8.3E-05	0	0.1	0.003
Vegetable	0.00005	8.3E-05	0	2.7	0.003
WinterWheat	0.0013	0.00217	0	8.7	0.003
Clear	0	0	0	0	0

Where:

CNRT Carbon-Nitrogen ratio for crop root mass (-)

CNST Carbon-Nitrogen ratio for stover mass (-)

FNO3 Seasonal amount of applied NO_3 fertilizer (kg h^{-1})

FNH4 Seasonal amount of applied NH_4 fertilizer (kg h^{-1})

FUREA Seasonal amount of applied urea (kg h^{-1})

NUP Seasonal crop uptake of nitrogen (kg ha^{-1})

NB B shape parameter for curve defining daily uptake of nitrogen (-)

NC C shape parameter for curve defining daily uptake of nitrogen (-)

NBETA Depth distribution parameter for nitrogen uptake (-)

MNCN Carbon-nitrogen ratio for manure (-)

SEST Selenium mass fraction of stover mass (0 to 1)

SERT Selenium mass fraction of root mass (0 to 1)

FSE Seasonal amount of applied Se fertilizer (g ha^{-1})

SEUP Seasonal crop uptake of selenium (g ha^{-1})

MNSE Selenium mass fraction of manure (0 to 1)

FERTILIZER TIME ARRAYS

2	Number of NO_3 fertilizer application times
-14 42	Timing of application (number of days before or after planting day PLDY)
0.40 0.60	Fraction of seasonal fertilizer applied on each application day (must sum to 1.00)

The number of application times, timing of application, and fraction of seasonal application are specified for NO_3 fertilizer, NH_4 fertilizer, and Se fertilizer, and manure for each crop type.

A2.3 Specify Crop Type(s) for each grid cell, for each year of the simulation

The general, root, nitrogen, and selenium crop parameters are mapped to the cells of the surface grid using cell crop arrays:

CELL CROP INFORMATION
YEAR 2006

CELL	Alfalfa	Bean	Corn	Melon	Onion	Pasture	Pump	Sorgh	Grain	Squash	Sunfl	Veg	WWh	Clear
CELL 1	0.25	0.00	0.31	0.00	0.00	0.00	0.00	0.00	0.00	0.00	0.00	0.00	0.00	0.44
CELL 2	0.45	0.00	0.55	0.00	0.00	0.00	0.00	0.00	0.00	0.00	0.00	0.00	0.00	0.05
CELL 3	0.79	0.00	0.21	0.00	0.00	0.00	0.00	0.00	0.00	0.00	0.00	0.00	0.00	0.00
CELL 4	0.76	0.00	0.00	0.00	0.00	0.24	0.00	0.00	0.00	0.00	0.00	0.00	0.00	0.00
CELL 5	0.43	0.00	0.00	0.00	0.00	0.57	0.00	0.00	0.00	0.00	0.00	0.00	0.00	0.00
CELL 6	0.52	0.00	0.00	0.00	0.00	0.44	0.00	0.00	0.00	0.00	0.00	0.00	0.00	0.04
CELL 7	0.44	0.00	0.00	0.00	0.00	0.28	0.00	0.00	0.00	0.00	0.00	0.00	0.00	0.28
CELL 8	0.34	0.00	0.00	0.00	0.00	0.00	0.00	0.56	0.00	0.00	0.00	0.00	0.00	0.10
CELL 9	1.00	0.00	0.00	0.00	0.00	0.00	0.00	0.00	0.00	0.00	0.00	0.00	0.00	0.00
:														
:														
CELL N														

For each surface cell in the model grid, the portion of the grid cell occupied by each crop type is specified for each year of the simulation. A scenario with multiple fields residing in a single grid cell is shown in Figure A1. For example, CELL 1 contains portions of three fields, with one field growing alfalfa and occupying 25% of the cell area, another field growing corn and occupying 31% of the cell area, and a non-cultivated field occupying 44% of the cell area. CELL 9 is completely encompassed by a field growing alfalfa, and hence the Alfalfa term is given a value of 1.00. For cells encompassing more than one field, the subroutines within the NTR package apply a weighting scheme that calculates composite crop parameters for the grid cell depending on the crop type of the fields within the cell.

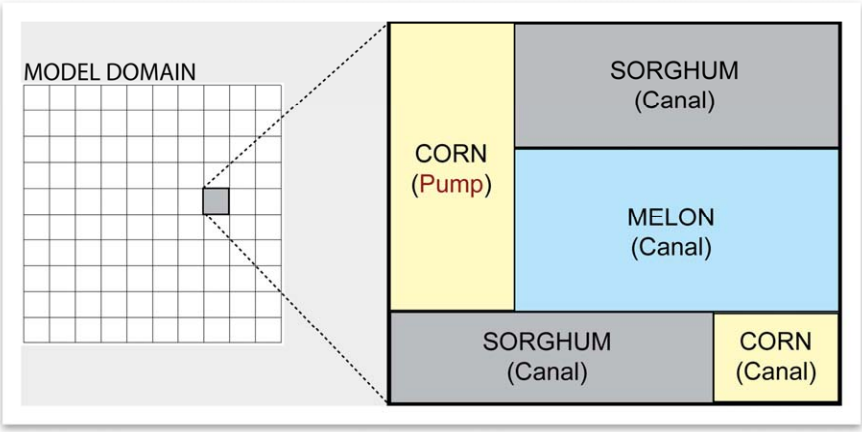

Figure A 1. Situation of multiple irrigated fields comprising a single grid cell. The fields also receive irrigation water from difference sources (canal vs. pumping well), and hence the species concentration associated with the infiltrating water also must be weighted.

A2.4 Air Temperature

Air temperature is specified for each day of the simulation. This is used to calculate daily soil temperature as described in Chapter 5.

```
TEMPERATURE DATA
YEAR 2006
   DAY 1      3.38
   DAY 2     -2.52
   DAY 3     -1.94
```

DAY 4	-3.14
DAY 5	-12.62
DAY 6	-13.16
DAY 7	-8.51
DAY 8	-0.25
DAY 9	11.02
DAY 10	1.53
DAY 11	-0.92
DAY 12	-2.02

A2.5 Microbial activity as a function of soil moisture

Microbial activity as a function of soil moisture θ is represented by data points that describe the fraction of maximum activity as a function of saturation. Data points are provided for any desired chemical reactions. In this example, mineralization (MIN) and denitrification (DEN) are represented. For a saturation of 0.70, mineralization and denitrification proceed at 60% and 72% of the maximum rate, respectively. For a saturation of 1.00, they proceed at 40% and 100% of the maximum rate.

SATURATION-MICROBIAL ACTIVITY DATA POINTS

21

SAT	MIN	DEN
0	0.000	0.000
5	0.010	0.000
10	0.020	0.000
15	0.060	0.000
20	0.120	0.000
25	0.230	0.000
30	0.320	0.000
35	0.450	0.000
40	0.560	0.000
45	0.700	0.000
50	0.800	0.000
55	0.920	0.000
60	0.940	0.010
65	0.850	0.020
70	0.720	0.030
75	0.600	0.090
80	0.540	0.170
85	0.470	0.350
90	0.440	0.550
95	0.410	0.800
100	0.400	1.000

A3. IRRIGATION (IRG) PACKAGE

The IRG package handles the accounting of the species mass entering the system via surface water irrigation, aquifer (pumped) water irrigation, and rainfall. The data required by IRG to perform this accounting is (i) concentration of species for canal water, pumped water, and rainfall, and (ii) the fraction of infiltration flux, for each week of the year, attributed to canal water, pumped water, and rainfall. The latter requirement arises due to the possibility of multiple irrigated fields residing in a single grid cell, each with a different source of irrigation water (canal water vs. pumped water). Such a situation is shown in Figure A1. The data for (i) and (ii) are read into RT3DAG through the .irg input file.

For (i), the species concentration in canal water is determined using field measurements. Concentration values are provided for each day of the simulation in which field measurements are available, and within the IRG package linear interpolation is used to calculate canal concentrations for simulation time steps between field measurements times. For example, the following input data shows the species concentrations for six canals for day 171 and day 509 of the simulation. Concentration values of canal irrigation water used by the model are calculated by linearly interpolating between the values specified for days 171 and 509.

Canal	O_2	NO_3	NH_4	N_2	SeO_4	SeO_3	SeMet
	171						
Highline	7.43	0.00	1.20	0.00	2.63	0.00	0.00
Otero	7.43	0.00	1.20	0.00	3.28	0.00	0.00
Catlin	7.78	0.00	0.67	0.00	3.60	0.00	0.00
Rocky Ford	7.40	0.00	0.86	0.00	4.17	0.00	0.00
Fort Lyon	7.43	0.00	1.20	0.00	3.92	0.00	0.00
Holbrook	7.43	0.00	1.20	0.00	4.83	0.00	0.00
	509						
Highline	9.57	0.00	1.33	0.00	4.50	0.00	0.00
Otero	9.57	0.00	1.33	0.00	4.99	0.00	0.00
Catlin	10.15	0.00	1.05	0.00	5.40	0.00	0.00
Rocky Ford	9.76	0.00	2.00	0.00	5.60	0.00	0.00
Fort Lyon	9.57	0.00	1.33	0.00	5.47	0.00	0.00
Holbrook	9.57	0.00	1.33	0.00	6.15	0.00	0.00

Solute concentration of pumped aquifer water is determined from concentrations calculated by RT3DAG at the simulation time at which irrigation is applied. The source cell of the groundwater well, and hence the cell that dictates the concentration of the applied irrigation water, is determined from a list of groundwater wells and associated pumping tracts, i.e., the surface grid cells that can receive water from each of the wells. For example, Figure A2 shows the pumping tracts for four selected wells, with the selected wells shown in dark gray and the cells to which they can provide irrigation water shown in light gray.

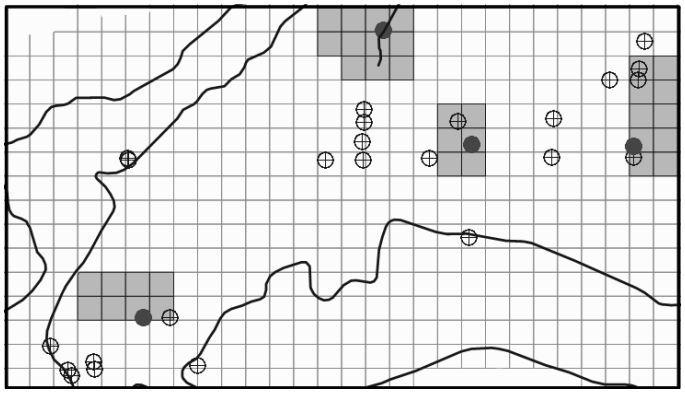

Figure A 2. Pump tracts (shown with light gray cells) associated with selected groundwater pumping wells (shown with dark gray circles). Any of the cells in the pump tract are candidate cells for receiving irrigation water from the pumping well.

The wells and associated pumping tracts are listed in the .irg input file as follows, with four wells listed as an example:

WELL ID	CELL	SURFCE CELLS IN TRACT				
1705057	12208	12209	12421	12422		
1705058	10484	10485	10486	10697	10698	10699
1705064	10484	10485	10486	10697	10698	10699
1705065	10697	10910	11123			

:

:

For each well, an ID is specified, along with the surface grid cell associated with the location of the well and the surface grid cells that reside within the pump tract. When a cell receives pumped irrigation water, the IRG subroutines search through the list of groundwater pump IDs and

associated pump tracts to find the pump that can give water to the cell. Then, the model-calculated species concentration within the grid cell associated with the screen of the groundwater pump is used as the concentration of the irrigation water. The layer of the model associated with the pump screens is specified in the .irg input file.

For (ii), a composite species concentration is calculated by specifying, for each week of the simulation, the fraction of infiltration water derived from canal water, pumped irrigation water, and rainwater. Then, using the species concentration as discussed in (i), the composite concentration for the k^{th} species is calculated by:

$$C_{k,INF} = \left(C_{k,S}F_{k,S}\right) + \left(C_{k,A}F_{k,A}\right) + \left(C_{k,R}F_{k,R}\right)$$

where *S*, *A*, and *R* represent surface water, aquifer water, and rainwater, and *F* is fraction (-), with $F_{k,S} + F_{k,A} + F_{k,R}$ summing to 1.0. The fractions are listed in the .irg for each surface grid cell that receives infiltration water. For example, for several selected cells for the first three weeks of a simulation:

CELL	CANAL	Week 1			Week 2			Week 3		
10895	1	0.000	0.000	1.000	0.000	0.000	0.000	0.000	0.000	0.000
10896	1	0.000	0.860	0.140	0.000	1.000	0.000	0.000	1.000	0.000
10897	1	0.000	0.948	0.052	0.000	1.000	0.000	0.000	1.000	0.000
10898	1	0.000	0.904	0.096	0.000	0.000	0.000	0.000	1.000	0.000
10899	1	0.000	0.792	0.208	0.000	0.000	0.000	0.000	1.000	0.000
10900	1	0.000	0.000	1.000	0.000	0.000	0.000	0.000	0.000	0.000

For each week, the first, second, and third columns are the fraction of infiltrated water attributed to aquifer water, canal water, and rainwater. For canal water, the source canal is specified for each cell. In this example, the source canal is Canal 1.

A4. CHANGES TO OTHER RT3D PACKAGES

A4.1 Changes to the BTN package

A key process in the fate and transport of Se species in groundwater systems is the oxidation of residual Se from shale by O_2 and/or NO_3. Hence, the location of shale must be specified in the model. To do so, a Geologic Material Type array is read in through the .btn input file, with the material type specified for each grid cell (for each grid layer) in the model domain. Material type currently can be specified as either alluvium or shale.

A4.3 Changes to the RCT package

The RCT package handles the change in species concentration due to chemical reactions. For RT3DAG, a new reaction package was designed and implemented, with the reactions described in Chapter 5. The reaction package is entitled AGRRXNS, and the reaction parameters (using spatially-uniform reaction rates) are specified in the modified .rct input file:

GENERAL	
0.25	kL
0.11	kM
0.003	kH
0.5	FE
0.2	FH
0.75	KCO2
1	KO2
2	kO2H
0.1	kO2A
NITROGEN	
1	IO2
0.5	INO3
8	CNMICR
12	CNHUM
0.8	kNIT
0.1	kVOL
10	KNO3
0.1	kDENH
0.01	kDENA
SELENIUM	
122.5	CSEMICR
175	CSEHUM

0.002	kSEO4
0.02	k1SEO3
0.02	k2SEO3
0.02	kSEVOL
1000	KSE

A5. DATA FLOW IN UZF-RT3DAG

Using the details described in Sections A1-A4, the flow of data in the RT3DAG model is shown in Figure A3. Text highlighted in red indicates features (e.g., input data, subroutines, output data) that were incorporated as part of the VST, NTR, and IRG packages.

The RT3DAG simulation begins by reading in the .btn, .ntr, .irg, and .rct input files. Immediately upon reading the crop parameters and crop types for each grid cell, the NTR subroutines map the crop parameters to the surface grid cell, weighting them if multiple fields comprise a grid cell, and stores the crop parameter arrays. The canal species concentrations, list of pumping wells and associated pump tracts, and infiltration fractions for each grid cell for each week of the simulation are read in and stored in arrays in the IRG package. Reaction parameters are read and stored in arrays in the RCT package.

Following data input and storage, the model loops through the stress periods, the flow time steps within each stress period, and the transport time steps within each flow time step. For a given stress period, during which time the concentration of sources and sinks remain constant, the concentrations associated with source-sink cells (e.g., river, canal cells) are read in and used to calculate the change in concentration at cells that either discharge water to surface water bodies or receive seepage from surface water bodies. At the beginning of each flow time step, the flow field and sources-sinks information are read from the UZF-MODFLOW linker file. These data consists of volumetric water content, infiltration flux and 1D percolation flux in the

unsaturated zone, flow rates in the vertical and lateral directions in the saturated zone, discharge to/from surface water bodies, pumping, and evapotranspiration from the saturated zone.

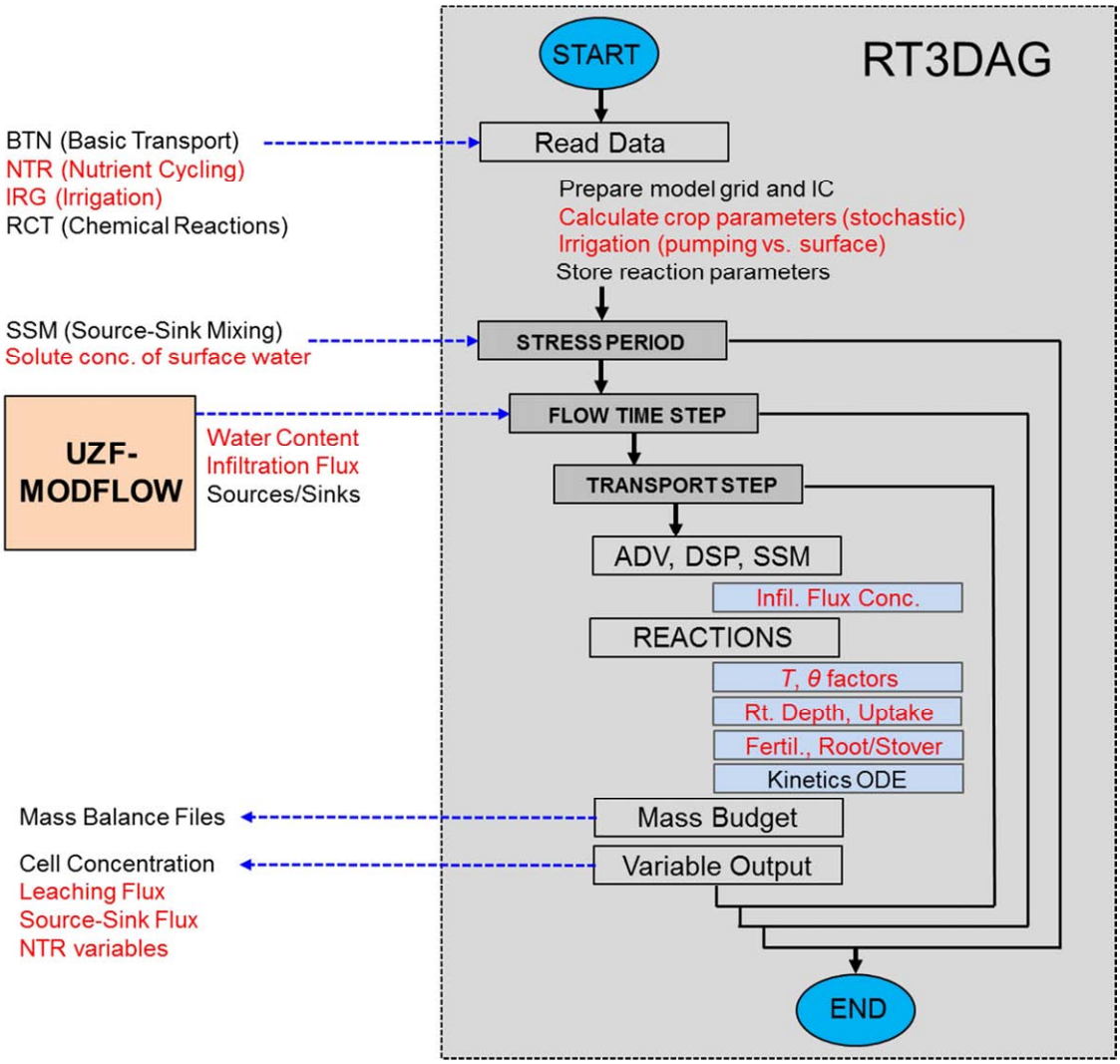

Figure A 3. Flow of data in RT3DAG. Data is input through the .btn, .ntr, .irg, and .rct files, and model output and mass-balance information is output either for each transport time step or upon request.

For each transport time step, the change in concentration in each grid cell due to advection, dispersion, and source-sink mixing is calculated first, followed by the change in concentration due to all chemical reactions. The change in concentration due to infiltrating water is calculated

within the SSM package using subroutines from the IRG package. Before calculating the change in concentration due to chemical reactions, the RCT package calls the NTR subroutines to calculate the following for each grid cell for the current time step: environmental reduction factor using soil temperature and soil saturation, rooting depth (if simulation time is during growing season), crop uptake (if simulation time is during growing season), fertilizer application (if specified), root mass additions (if harvest day) and stover mass additions (if plowing day). These values are then used in association with chemical reaction parameters to calculate the change in concentration of each species. Se oxidation (from shale material) occurs if the cell contains O_2 and/or NO_3 and if any of the six surrounding cells have a shale material type.

If the current simulation time is specified as an output time, then cell concentration, leaching flux, and source-sink flux are output for each cell in the model grid. For specified cells, mass associated with each NTR component (e.g., fertilizer, uptake, denitrification, mineralization/ immobilization) is output for each transport time step. This enables a detailed analysis of mass balance for individual cells, and provides insights into the processes that govern the resulting concentration of a given cell. Mass balance for each species is calculated and output at the end of each transport time step. Mass balance summaries also are output to the main RT3DAG output file, with examples shown here for SeO_4 (Figure A4) and the nitrogen litter pool (Figure A5):

```
FOR SPECIES NO.:   12  SEO4

              TOTAL CHANGE IN MASS USING CONCENTRATION (DMASS1)
                             TOTAL MASS =   DISSOLVED   +   SORBED   +   SOLID
                             INITIAL =   0.25332990E+12+ 0.74468321E+13+  0.0000000    = 0.77001618E+13
                             CURRENT =   0.34315928E+12+ 0.74468321E+13+  0.0000000    = 0.77899912E+13
                              DMASS1 =   0.89829409E+11

              TOTAL CHANGE IN MASS USING SOURCES/SINKS (DMASS2)
                                                        MASS IN            MASS OUT
                                   CONSTANT CONCENTRATION:    0.000000           0.000000
                                       CHEMICAL REACTIONS:   0.1168169E+12     -0.1918986E+11
                                            CONSTANT HEAD:    0.000000           0.000000
                                                    WELLS:    0.000000          -0.3342924E+10
                                                  RIVERS:   0.1657415E+10      -0.9974428E+10
                                         CANAL IRRIGATION:   0.1590566E+10       0.000000
                                       AQUIFER IRRIGATION:   0.3342924E+10       0.000000
                                              FERTILIZER:    0.000000           0.000000
                                             CROP UPTAKE:    0.000000          -0.1133579E+10
                                                                ---------------------------------
                                                    TOTAL:   0.1234078E+12     -0.3364079E+11
                             DMASS2 =   0.8976699E+11

              % DISCREPANCY (DMASS2 TO DMASS1) =   0.0008
```

Figure A 4. Mass balance summary for SeO_4 as output by UZF-RT3DAG.

```
FOR SPECIES NO.:    9  NLIT

              TOTAL CHANGE IN MASS USING CONCENTRATION (DMASS1)
                             TOTAL MASS =   DISSOLVED   +   SORBED   +   SOLID
                             INITIAL =    0.0000000    +  0.0000000    + 0.18860934E+09= 0.18860934E+09
                             CURRENT =    0.0000000    +  0.0000000    +  42084416.    =  42084416.
                              DMASS1 =  -0.14652493E+09

              TOTAL CHANGE IN MASS USING SOURCES/SINKS (DMASS2)
                                                        MASS IN            MASS OUT
                                   CONSTANT CONCENTRATION:    0.000000           0.000000
                                       CHEMICAL REACTIONS:   0.7702751E+09     -0.1612687E+10
                                                  MANURE:    0.000000           0.000000
                                                ROOT MASS:   0.1601225E+09       0.000000
                                              STOVER MASS:   0.5357661E+09       0.000000
                                                                ---------------------------------
                                                    TOTAL:   0.1466164E+10     -0.1612687E+10
                             DMASS2 =  -0.1465230E+09

              % DISCREPANCY (DMASS2 TO DMASS1) =  -0.0001
```

Figure A 5. Mass balance summary for the nitrogen litter pool as output by UZF-RT3DAG.

A6. NTR, IRG, AND RCT SUBROUTINES

A6.1 NTR Subroutines

AGRRP – Read and prepare data for NTR package

AGRALLOC – Allocate arrays required for NTR package

Parameter Weighting Subroutines – Weight crop parameters according to crop types

AGRVALUES – Determine agricultural-related sources-sinks for grid cell

- **AGRET** – Calculate soil temperature environmental reduction factor
- **AGRES** – Calculate soil moisture environmental reduction factor
- **AGRROOT** – Calculate rooting depth (if growing season)
- **AGRUPTAKE** – Calculate crop uptake (if growing season)
- **AGRRESMASS** – Calculate mass of crop residue added to soil organic matter
- **AGRRESCONC** – Calculate concentration of crop residue added to soil organic matter
- **AGRFERT** – Calculate mass of applied fertilizer
- **AGRMANURE** – Calculate mass of applied manure

AGRINIT – Initialize species concentration for the RT3DAG simulation

AGRBUDGET – Track and output mass balance components for specified observation cells

A6.2 IRG Subroutines

IRGRP – Read and prepare data for IRG package

IRGALLOC – Allocate arrays required for IRG package

IRGPUMPC – Retrieve species concentration from pumping cell, for specified surface grid cell

IRGCANALC – Calculate solute concentration from canal, for specified surface grid cell

A6.3 RCT Subroutines

AGRRXNS – Calculate change in species mass according to chemical reactions and agricultural-related sources-sinks

SEPRODUCE – Determine the mass of Se produced from adjacent shale cells

APPENDIX B

DATA PERTAINING TO UZF-RT3DAG MODEL APPLICATION TO THE LOWER ARKANSAS RIVER VALLEY, SOUTHEASTERN COLORADO

This appendix contains data and model results for the UZF-RT3DAG model application to the Upstream Study Region in the LARV that were not able to be included in Chapter 6 due to space limitations. These data and results include (i) aerial photos of selected portions of the Upstream Study Region, (ii) values of O_2, NO_3, and SeO_4 concentration from every observation in the Upstream Study Region during the years 2006-2009 (iii) values of salt concentration from multiple observation wells residing in the same cultivated field, (iv) comparison of observed and simulated values of NO_3 concentration for each observation well, and (v) comparison of observed and simulated values of SeO_4 concentration for each observation well.

Photos in (i) are included to show the outcrop of shale formations, a major source of selenium (Se), and their proximity to cultivated fields and irrigation canals. Values in (ii) were averaged according to command area to provide calibration targets during the parameter estimation process. Values in (ii) were used to quantify the degree of uncertainty of solute concentration within a single cultivated field and hence indicate how these values should be compared to grid cell values simulated by the model. For (iv) and (v), comparisons are made with simulated values from the cell corresponding to the location of the observation well. These comparisons were not used in model calibration, but are included here to demonstrate that the model produces cell-by-cell results that are similar in magnitude and range to observed point values.

B1. AERIAL PHOTOS OF SHALE OUTRCOPS IN THE UPSTREAM STUDY REGION

Figure B- 1. Aerial photos within the Upstream Study Region of the LARV showing shale outrcops.

B2. MEASURED CONCENTRATIONS IN OBSERVATION WELLS, 2006-2009

Table B- 1. Measured concentrations of O_2 in the Upstream Study Region observation wells, 2006-2009.

Name	6/19/06	5/23/07	10/6/07	3/20/08	6/23/08	8/14/08	1/15/09	5/14/09	7/22/09
6		5.02	0.26	0.95	0.73	0.43			
8	0.84	1.19	0.73	2.86	1.34	1.01	1.29	0.74	0.97
11	4.64	5.60	1.66	1.57	2.18	3.35	2.29	1.33	1.35
12	3.87	1.71	1.13	1.58	3.88	0.64		2.21	1.27
14					0.12				
15					0.41				
17		2.03	2.22	5.29	0.95	1.37	4.03	0.60	0.60
18					2.06	0.96			
20	2.53	0.59	1.08	2.51	1.79	1.94	1.92	0.73	0.51
21		2.46			4.28		1.69	1.43	1.21
22	4.31	2.18	1.31	3.05	0.64	2.19	2.59	1.01	1.08
23					1.97	3.12			
24	3.85	2.84	1.70	1.14	2.83	0.66	1.14		0.69
28	1.02	3.76	2.04	1.82	0.71	1.06	2.50	1.69	1.74
29	1.51	0.74	2.02	1.36		1.54	1.14	1.13	1.18
31	1.72	2.25	1.50	0.70				0.10	0.01
33	6.03	5.28	4.24	5.22	4.40		5.01	6.10	5.46
35		7.17			2.55	2.76			5.69
37	6.09	1.33	3.55	4.39	3.24		2.09	3.40	5.93
38	0.79	0.61	1.51	1.45		0.44	0.62	0.42	0.91
39	0.95	0.39	1.49	0.73	0.46	0.41	1.01	0.27	4.82
40					2.55				
41	0.95	0.72		1.20					
43		0.59	0.94		0.55	1.33		0.44	
45	9.09	4.94	3.93	2.56	6.38	5.78	3.42	6.86	5.25
48	2.49	3.33	4.67	9.66	2.08	3.26	5.56	6.15	5.59
49					5.26			8.15	5.24
52					2.39				
53					2.88				
55	0.55	0.36	0.53		0.94		0.80	0.41	0.42
59	0.63	0.47	2.07	1.33	2.26	0.47	0.63	1.16	
62					7.97				
64					2.44				
65	1.27	0.97		6.95		0.49	5.75		
67	0.50	1.86	2.52						
68	6.26	4.89	3.87		5.01	4.35	2.78	3.70	4.33
69					6.71				
71			5.26						
72	8.07	5.60	1.70						
73					3.53				
74	0.90	1.34	1.10	0.54	2.04	0.24		0.37	2.09
76					0.11				
77					5.90	6.88			
80	3.39	6.37	1.04	8.48	4.18	1.65	4.19	6.90	1.12
82					4.23				
83		5.62	1.62	5.58	2.08			2.55	2.15
84	5.13	3.01	2.39	2.39	2.42	0.32	1.89	1.46	
85					4.80				
90					4.39				

91					2.19				
92	6.88								
93	2.20	2.94	2.06		2.43	0.59	0.30	2.13	2.53
94					0.66				
95	1.97		1.04	1.79	1.06	2.09	2.58	0.87	0.55
96					3.06	0.43			
97					6.59				
98					5.28	7.27			
203	2.68								
204	1.99	0.96	1.87	1.51		0.81			
206					3.26				
208	0.31	0.31	1.03						
209	1.23	1.03	1.98	0.46	1.75	0.84	1.63	0.86	1.05
16A					0.71				
16B					4.19				
16C					0.78				
207B	0.19	1.23							
26A					5.45				
26B					5.18	3.44			
60A	3.50	5.11	2.86	1.57	4.74	2.41	3.56	7.72	2.53
87A	2.02	3.49	1.92	1.65	2.32	1.55	1.06	1.24	0.67
87B					1.36				
9A	1.03	1.19	1.12	0.85		0.02	1.25	0.82	
9B					0.69				

Table B- 2. Measured concentrations of NO_3 in the Upstream Study Region observation wells, 2006-2009.

Name	6/19/06	5/23/07	10/6/07	3/20/08	6/23/08	8/14/08	1/15/09	5/14/09	7/22/09
6		0.10	0.10	0.10	0.20	0.10		0.10	0.10
8		0.10	0.10	0.90	0.10	0.10	0.30	0.10	0.10
11	10.40	3.91	4.40	0.30	2.60	2.90	1.50	2.40	2.30
12	10.30	11.80	66.02	26.01	4.20	3.70	54.82	3.80	6.50
14					0.50				
15					3.50				
17		3.00		7.00	2.10	2.10	0.70	2.50	1.50
18					15.30	3.10			
20	46.92	0.10	25.81	10.40	2.50	1.20	1.90	1.40	9.60
21		1.60			1.50	4.10	0.10	3.00	0.10
22	7.30	7.70	5.00	2.30	2.50	2.60	4.10	4.30	2.50
23					4.80	10.90			
24	1.80	2.20	1.00	0.50	2.30	2.00	1.20		0.50
27									17.90
28	28.31	66.02	7.90	6.30	8.10	6.50	10.30	6.30	
29	26.11	28.51		28.11	21.81	20.81	15.51	15.71	15.60
31		0.10	2.70	0.10				0.10	0.10
33	7.40	7.00	10.40	6.50	5.80		5.90	5.70	5.20
35		2.40	3.30		2.20	2.60			3.80
37	7.70	9.80	14.50	4.00	2.90	8.50	7.40	4.00	3.30
38	0.80	1.50	1.10	1.00	2.60	2.80	2.40	1.10	0.90
39	0.60	0.40	2.50	0.30	0.80	1.20	1.40	1.00	0.70
40					0.10				
41		45.61		14.40					
43		1.40	3.00		0.80	2.00		3.10	
45	11.70	15.20	4.80	5.10	3.00	2.20	2.20	4.00	3.50
48	6.10	6.40	10.00	7.70	8.40	9.30	2.60	4.00	1.90
49					3.00			7.60	3.00
51					1.60				
52					9.60				
53					0.10				
55	1.90	1.70	5.20		4.20		6.90	4.10	3.70
59	0.90	1.10	3.00	1.20	0.60	1.00	0.20	0.90	
62					4.90				
64					0.30				
65		0.10		0.90	0.10	0.20	0.20	0.20	0.10
66					0.30				
67	12.90	11.80	22.11						
68	3.80	4.90	2.10		3.70	3.90	3.40	5.10	4.80
69					3.00				
71			2.10				1.20		
72	0.50	0.40	0.10						
73					3.80				
74	2.60	5.60	2.10	4.00	2.40	2.10		2.70	1.40
76					0.10				
77					3.40	4.10			
80	1.00	1.20	0.40	4.40	3.40	1.00	9.70	1.60	1.10
82					1.40				
83		0.20			0.10		0.20	19.01	6.70
84	0.60	1.70	2.10	1.90	10.70	6.50	28.41	16.21	
85					0.40				
88					2.60				
90					0.50				
91					0.10				

92	12.70								
93	1.00	0.10	2.20		1.00	11.70	1.40	1.50	0.60
94					3.00				
95	5.30		9.70	6.70	6.10	3.70	2.40	2.70	1.30
96					0.10	0.10			
97					5.00				
98					1.80	1.70			
203		0.10			0.20				
204	3.50	3.10	5.60	7.20	2.20	2.70			
206					0.20				
208	4.40	0.50	2.50						
209	0.50	0.20	2.10	0.70	0.10	0.10	0.10	0.10	0.10
16A					5.70				
16B					2.70				
16C					4.90				
207B		1.60							
26A					0.30				
26B					1.00	0.20			
60A	0.40	1.80	2.20	0.50	1.80	4.10	2.40	0.40	0.50
87A	0.60	0.60	2.70	0.40	0.60	0.50	0.50	0.60	0.50
87B					0.90				
9A		0.10	2.00	0.10	0.10	0.10	0.10	0.10	
9B					0.20				

Table B- 3. Measured concentrations of NO_3 in the Upstream Study Region observation wells, 2006-2009.

Name	6/19/06	5/23/07	10/6/07	3/20/08	6/23/08	8/14/08	1/15/09	5/14/09	7/22/09
6	8.22	15.80	0.40	2.36	0.74	0.55		1.48	0.40
8	1.09	9.12	0.40	11.40	1.02	0.40	1.34	2.56	1.19
11	187.00	310.00	65.00	12.00	55.00	49.60	23.40	37.00	23.00
12	602.00	228.00	1300.00	350.00	126.00	108.00	1410.00	264.00	238.00
14					1.16				
15					19.80				
17	6.28	55.00		30.20	15.40	8.38	3.28	9.92	6.80
18					45.60	16.60			
20	1360.00	9.45	6.04	158.00	147.00	150.00	110.00	73.50	387.00
21		13.20			11.30	15.70	120.00	8.78	5.62
22	88.30	95.60	45.80	51.80	41.40	39.40	59.40	60.00	38.80
23					70.20	76.20			
24	18.60	18.90	14.60	7.00	23.10	13.40	9.14		5.34
28	187.00	460.00	110.00	193.00	214.00	184.00	184.00	172.00	3.72
29	64.60	65.80		74.30	60.80	43.40	73.40	61.90	63.50
31	0.60	10.20	1.42	0.57				0.79	0.61
33	17.80	17.70	19.00	19.80	20.00		20.30	17.20	17.60
35		20.30	13.40		20.10	17.00			22.40
37	69.80	50.40	62.40	32.70	34.40	93.00	32.50	28.10	33.00
38	16.50	42.40	26.00	32.00	24.50	32.00	52.80	27.60	22.20
39	4.22	4.44	6.02	8.02	10.20	11.00	8.65	12.20	10.10
40					218.00				
41	0.56	12.00		116.00					
43		7.30	3.14		4.37	6.81		11.30	
45	15.60	10.40	9.66	9.88	9.56	7.10	10.20	6.94	7.28
48	43.30	49.20	42.80	284.00	66.40	54.20	146.00	198.00	153.00
49					13.40			15.40	10.60
51					50.00				
52					26.70				
53					2.54				
55	22.80	24.30	33.30		38.80		47.00	39.20	48.00
59	16.40	23.80	41.00	75.50	46.70	47.30	9.06	13.80	
62					13.60				
64					22.40				
65	0.40	1.33		0.54	0.40	0.40	0.40	1.46	0.40
66					5.32				
67	58.50	58.20	34.80						
68	17.40	15.40	11.10		13.60	12.70	10.60	12.40	13.50
69					21.80				
71			32.60				0.64		
72	41.90	118.00	1.37						
73					16.50				
74	13.60	31.80	26.00	26.90	21.70	7.18		22.50	14.50
76					1.72				
77					13.20	13.80			
80	6.32	9.81	2.75	51.20	10.40	4.66	138.00	8.85	5.34
82					19.50				
83		1200.00			27.60		3.03	321.00	39.20
84	28.20	117.00	194.00	64.20	196.00	628.00	253.00	56.10	
85					5.20				
88					12.60				
90					16.20				
91					3.42				
92	27.40								

93	32.00	28.70	12.60		8.13	14.80	5.73	11.60	2.48
94					11.30				
95	15.00		20.80	20.10	17.40	17.00	12.40	12.80	10.70
96					10.60	10.30			
97					22.00				
98					22.70	22.40			
203	8.22	16.90			2.81				
204	24.20	17.30	14.60	18.40	16.60	21.80			
206					142.00				
208	22.10	8.02	7.12						
209	0.40	0.65	0.40	0.40	0.40	0.40	0.40	0.40	1.06
16A					29.00				
16B					9.68				
16C					19.90				
207B	2.19	4.43							
26A					3.66				
26B					30.60	14.60			
60A	31.60	50.40	2.20	10.20	58.20	10.90	66.40	10.30	6.63
87A	27.10	43.80	40.00	25.00	12.70	12.40	22.20	23.20	14.70
87B					20.90				
9A	25.40	1.18	0.72	1.08	0.67	0.53	0.88	17.20	
9B					2.97				

B3. QUANTIFYING VARIABILITY FOR FIELD-SCALE SOLUTE CONCENTRATION

Results from field studies within the Upstream Study Region indicate that there is significant variability in solute concentration in the groundwater underlying cultivated fields. This variability is critical when comparing point measurements from small-diameter observation wells in the field to large spatial areas (e.g., 250 m by 250 m) of computational grid cells for numerical models. In such a comparison, it should be realized that the actual average concentration in the groundwater underlying a spatial area the size of the grid cell is not known, and hence uncertainty should be assigned the observed values of concentration.

Eight fields with multiple observation wells are used in the assessment of in-field solute concentration variability. Table B-4 summarizes the results. For each date of sampling, each well in each field is sampled for salt concentration (dS/m), with the average, standard deviation, and resulting coefficient of variation (CV) of salt concentration calculated for the field. For example, for Field 7 in 1999 the 11 observation wells were sampled on June 17, 1999, with an average concentration of 4.41 dS/m, a standard deviation of 1.82 dS/m, and a CV of 0.41. This process was repeated for each field, for each sampling event, and for each year, with the CVs of each sampling event averaged for a given field. These average field CV values were then averaged, for a combined CV value of 0.42. This value is used to provided 1-σ error bounds to the observed values shown in Chapter 6 and in Sections B4 and B5 in this Appendix.

Table B- 4. Coefficient of Variation (CV) of salt concentration for a single field (multiple wells within a single field)

Field ID	Year	Num Wells	Sample Date	Average Salt Conc. (dS/m)	σ of Salt Conc.	CV	Average CV for Field
7	1999	11	6/17/99	4.41	1.82	0.41	
		11	6/28/99	4.40	1.10	0.25	
		11	7/19/99	3.88	2.15	0.55	
		11	8/4/99	5.01	3.04	0.61	
		11	8/10/99	4.75	2.04	0.43	
		11	8/17/99	4.31	1.81	0.42	**0.46**
		11	9/8/99	4.12	1.61	0.39	
		11	9/13/99	4.16	1.69	0.41	
		11	10/6/99	3.70	1.80	0.49	
		11	11/4/99	3.68	1.85	0.50	
		11	12/18/99	3.59	2.03	0.57	
7	2000	13	2/2/00	5.39	2.71	0.50	
		13	5/7/00	3.59	1.65	0.46	
		13	5/14/00	4.35	2.64	0.61	
		13	5/23/00	4.33	2.01	0.47	
		13	5/30/00	3.60	1.79	0.50	
		13	6/5/00	3.61	1.79	0.50	
		13	6/12/00	3.56	1.87	0.53	
		13	6/20/00	3.36	1.35	0.40	**0.51**
		13	6/29/00	3.73	1.80	0.48	
		13	7/4/00	4.33	2.19	0.50	
		13	7/11/00	3.44	1.68	0.49	
		13	9/6/00	2.82	1.58	0.56	
		13	10/16/00	3.31	1.66	0.50	
		13	11/21/00	3.24	1.85	0.57	
		13	12/24/00	3.32	2.00	0.60	
17	1999	9	6/17/99	1.51	1.57	1.04	
		9	6/28/99	1.80	1.11	0.62	
		9	7/19/99	2.07	1.36	0.66	
		9	8/4/99	1.90	1.07	0.56	
		9	8/10/99	1.93	1.12	0.58	
		9	8/17/99	2.01	1.04	0.52	**0.55**
		9	9/8/99	1.88	0.96	0.51	
		9	9/13/99	1.82	0.92	0.51	
		9	10/6/99	2.21	0.68	0.31	
		9	11/4/99	2.29	0.65	0.29	
		9	12/18/99	2.80	1.13	0.41	
17	2000	9	5/7/00	2.36	1.26	0.53	
		9	5/14/00	2.43	1.23	0.51	
		9	5/23/00	3.06	1.39	0.45	
		9	5/30/00	2.60	1.11	0.43	
		9	6/5/00	2.54	1.11	0.44	
		9	6/12/00	2.62	1.08	0.41	**0.38**
		9	6/19/00	2.64	1.06	0.40	
		9	6/29/00	2.66	1.13	0.43	
		9	7/4/00	3.21	1.12	0.35	
		9	7/11/00	2.77	0.90	0.32	
		9	9/6/00	2.52	0.60	0.24	
		9	10/16/00	2.79	0.63	0.23	

		9	11/21/00	2.75	0.90	0.33	
		9	12/24/00	2.73	0.73	0.27	
40	1999	10	6/17/99	5.86	4.14	0.71	
		10	6/28/99	5.45	3.78	0.69	
		10	7/19/99	4.48	3.90	0.87	
		10	8/4/99	6.53	4.70	0.72	
		10	8/10/99	5.91	3.92	0.66	
		10	8/17/99	4.44	1.80	0.40	**0.68**
		10	9/8/99	4.91	3.50	0.71	
		10	9/13/99	5.20	4.22	0.81	
		10	10/6/99	3.11	1.53	0.49	
		10	11/4/99	4.69	3.51	0.75	
		10	12/18/99	7.20	4.62	0.64	
40	2000	10	2/2/00	8.91	6.02	0.68	
		10	5/8/00	6.03	2.84	0.47	
		10	5/24/00	9.06	6.68	0.74	
		10	5/29/00	6.84	4.62	0.68	
		10	6/5/00	5.24	3.41	0.65	
		10	6/19/00	5.51	3.08	0.56	
		10	6/29/00	5.22	2.61	0.50	**0.59**
		10	7/4/00	5.94	2.70	0.45	
		10	7/10/00	7.11	4.58	0.64	
		10	9/6/00	4.83	3.00	0.62	
		10	10/16/00	5.18	2.77	0.54	
		10	11/23/00	5.31	2.52	0.47	
		10	12/24/00	5.41	3.79	0.70	
81	2000	7	5/2/00	1.62	0.58	0.36	
		7	5/23/00	1.99	0.55	0.28	
		7	5/29/00	1.72	0.49	0.28	
		7	6/14/00	1.86	0.46	0.25	
		7	6/19/00	1.77	0.39	0.22	
		7	7/3/00	2.15	0.44	0.20	
		7	7/10/00	2.10	0.43	0.21	**0.26**
		7	7/17/00	2.30	0.85	0.37	
		7	7/24/00	1.85	0.53	0.29	
		7	8/1/00	1.19	0.23	0.19	
		7	8/7/00	0.95	0.29	0.31	
		7	8/22/00	1.37	0.27	0.20	
		7	12/24/00	0.96	0.23	0.24	
100	2000	7	5/16/00	5.28	1.89	0.36	
		7	5/24/00	3.84	1.62	0.42	
		7	5/29/00	4.03	1.52	0.38	
		7	6/4/00	3.76	0.81	0.21	
		7	6/12/00	4.14	1.48	0.36	
		7	6/19/00	3.72	1.97	0.53	
		7	6/28/00	3.85	1.67	0.43	**0.36**
		7	7/3/00	4.53	1.89	0.42	
		7	7/10/00	4.56	2.02	0.44	
		7	9/5/00	3.26	1.04	0.32	
		7	10/17/00	3.25	0.75	0.23	
		7	11/23/00	3.64	1.30	0.36	
		7	12/23/00	3.27	0.91	0.28	
102	2000	7	5/16/00	7.36	2.05	0.28	
		7	5/24/00	6.25	1.34	0.21	**0.25**
		7	5/29/00	4.73	1.04	0.22	

		7	6/4/00	5.00	0.75	0.15	
		7	6/12/00	5.43	1.59	0.29	
		7	6/19/00	4.96	0.89	0.18	
		7	6/28/00	4.75	1.90	0.40	
		7	7/3/00	6.48	1.34	0.21	
		7	7/10/00	5.96	1.16	0.19	
		7	9/5/00	4.49	1.15	0.26	
		7	10/17/00	5.79	1.33	0.23	
		7	11/23/00	5.33	1.58	0.30	
		7	12/23/00	5.30	1.66	0.31	
103	2000	10	5/16/00	6.49	1.62	0.25	
		10	5/24/00	6.48	1.35	0.21	
		10	5/29/00	4.91	1.08	0.22	
		10	6/4/00	5.23	1.20	0.23	
		10	6/12/00	5.64	1.87	0.33	
		10	6/19/00	5.28	1.65	0.31	
		10	6/28/00	5.13	1.60	0.31	**0.33**
		10	7/3/00	5.88	1.71	0.29	
		10	9/5/00	5.48	2.20	0.40	
		10	10/17/00	5.27	1.39	0.26	
		10	11/23/00	5.53	3.48	0.63	
		10	12/23/00	5.36	2.70	0.50	
104	2000	9	5/24/00	5.83	0.93	0.16	
		9	5/29/00	4.56	0.85	0.19	
		9	6/4/00	4.96	1.35	0.27	
		9	6/13/00	4.45	0.84	0.19	
		9	6/19/00	4.84	1.35	0.28	
		9	6/28/00	5.58	2.00	0.36	
		9	7/3/00	6.12	1.86	0.30	**0.30**
		9	7/10/00	5.97	2.27	0.38	
		9	9/5/00	3.62	1.69	0.47	
		9	10/17/00	4.77	1.47	0.31	
		9	11/23/00	4.30	1.39	0.32	
		9	12/23/00	4.07	1.28	0.31	

B4. COMPARISONS OF SIMULATED AND OBSERVED NO_3 CONCENTRATION AT OBSERVATION WELLS

Figures B-2 and B-3 contain the time series plots of simulated and observed concentrations of NO3 and SeO4, respectively, for each observation well during 2006-2009. Simulated values are taken from grid cells in layer 4 of the model that coincide with the location of the observation well. Red dots indicate observed measurements of concentration. Error bars are included to indicate the variability of the observed value for a representative cultivated field, as determined from the results presented in Section C3.

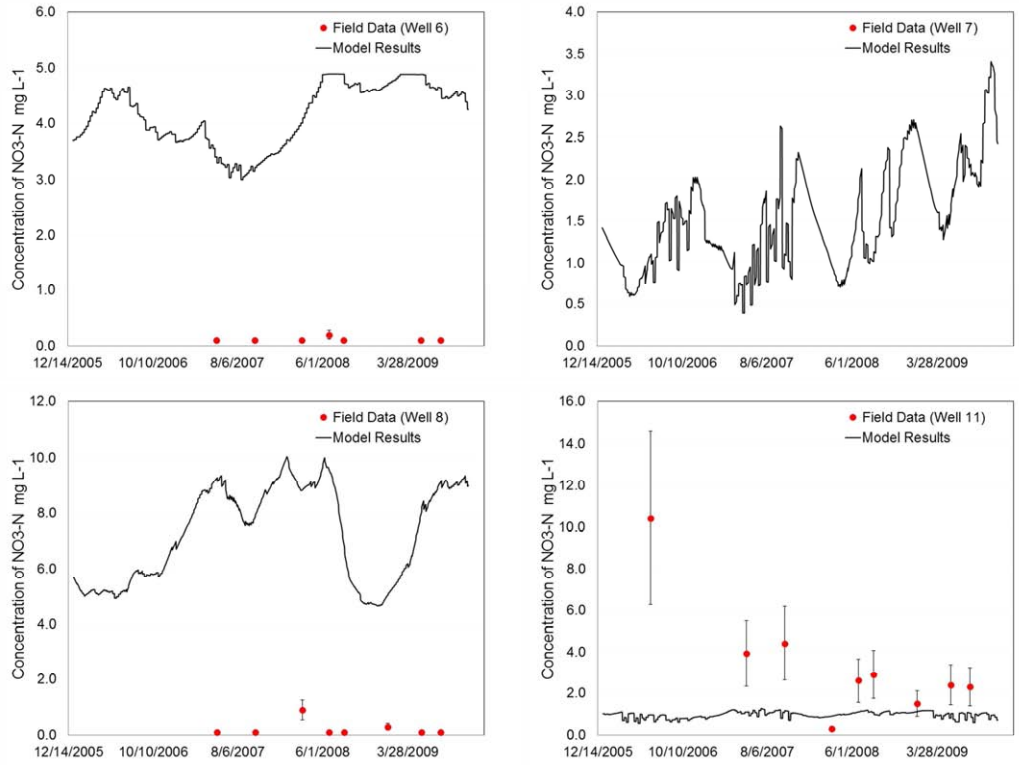

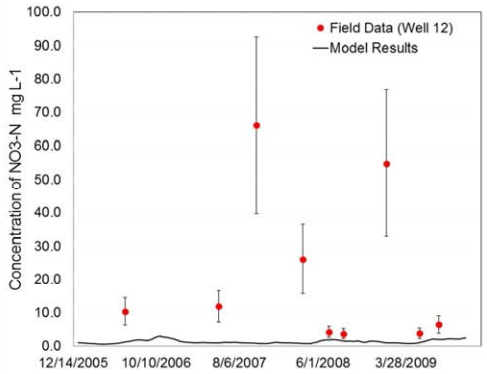
Field Data (Well 12)
Model Results
Concentration of NO3-N mg L-1
100.0
90.0
80.0
70.0
60.0
50.0
40.0
30.0
20.0
10.0
0.0
12/14/2005
10/10/2006
8/6/2007
6/1/2008
3/28/2009

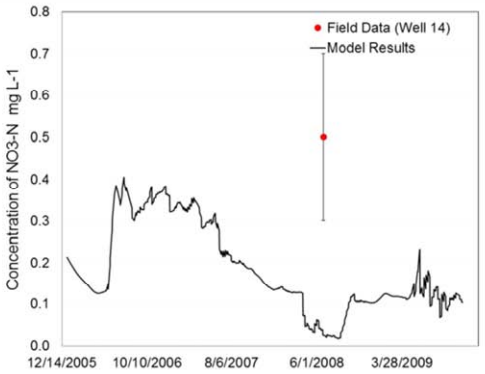
Field Data (Well 14)
Model Results
Concentration of NO3-N mg L-1
0.8
0.7
0.6
0.5
0.4
0.3
0.2
0.1
0.0
12/14/2005
10/10/2006
8/6/2007
6/1/2008
3/28/2009

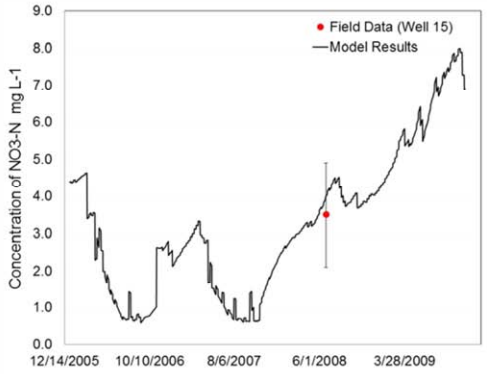
Field Data (Well 15)
Model Results
Concentration of NO3-N mg L-1
9.0
8.0
7.0
6.0
5.0
4.0
3.0
2.0
1.0
0.0
12/14/2005
10/10/2006
8/6/2007
6/1/2008
3/28/2009

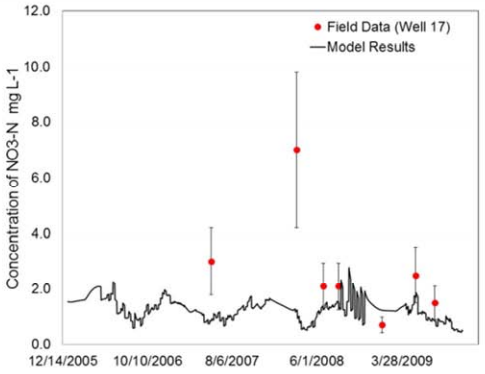
Field Data (Well 17)
Model Results
Concentration of NO3-N mg L-1
12.0
10.0
8.0
6.0
4.0
2.0
0.0
12/14/2005
10/10/2006
8/6/2007
6/1/2008
3/28/2009

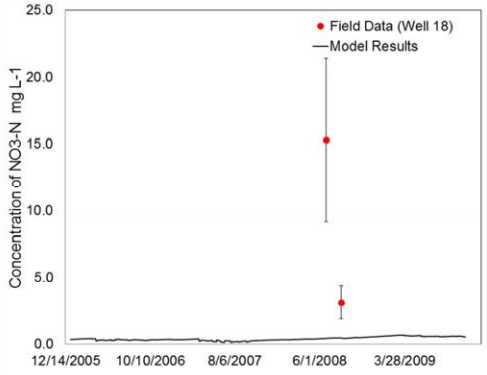
Field Data (Well 18)
Model Results
Concentration of NO3-N mg L-1
25.0
20.0
15.0
10.0
5.0
0.0
12/14/2005
10/10/2006
8/6/2007
6/1/2008
3/28/2009

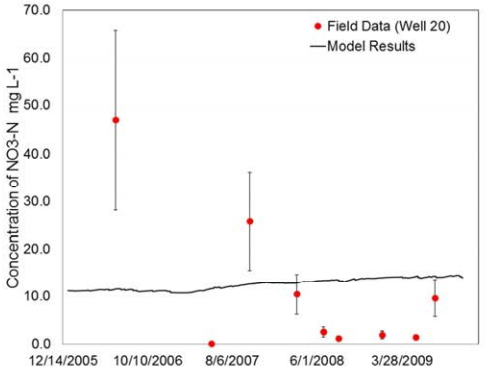
Field Data (Well 20)
Model Results
Concentration of NO3-N mg L-1
70.0
60.0
50.0
40.0
30.0
20.0
10.0
0.0
12/14/2005
10/10/2006
8/6/2007
6/1/2008
3/28/2009

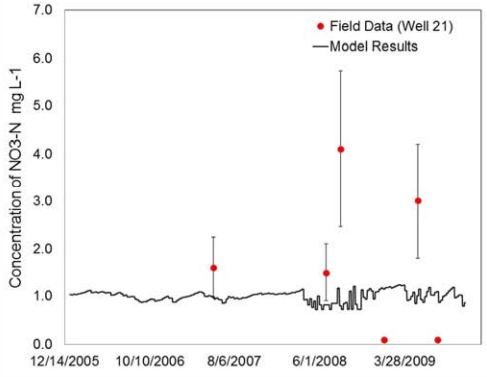
Field Data (Well 21)
Model Results
Concentration of NO3-N mg L-1
7.0
6.0
5.0
4.0
3.0
2.0
1.0
0.0
12/14/2005
10/10/2006
8/6/2007
6/1/2008
3/28/2009

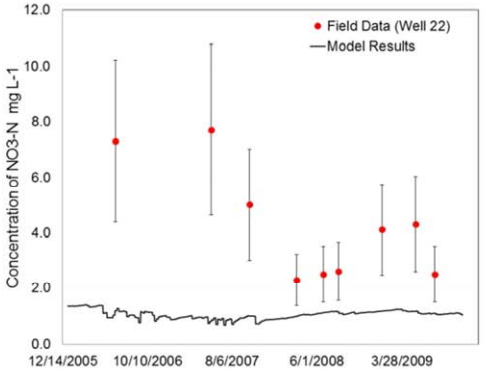
Field Data (Well 22)
Model Results
Concentration of NO3-N mg L-1
12.0
10.0
8.0
6.0
4.0
2.0
0.0
12/14/2005
10/10/2006
8/6/2007
6/1/2008
3/28/2009

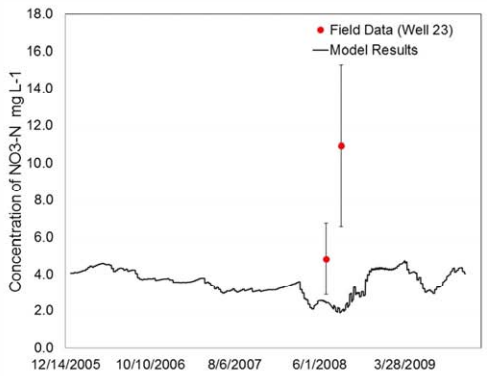
Field Data (Well 23)
Model Results
Concentration of NO3-N mg L-1
18.0
16.0
14.0
12.0
10.0
8.0
6.0
4.0
2.0
0.0
12/14/2005
10/10/2006
8/6/2007
6/1/2008
3/28/2009

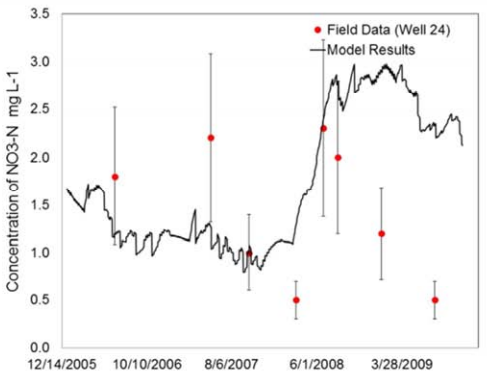
Field Data (Well 24)
Model Results
Concentration of NO3-N mg L-1
3.5
3.0
2.5
2.0
1.5
1.0
0.5
0.0
12/14/2005
10/10/2006
8/6/2007
6/1/2008
3/28/2009

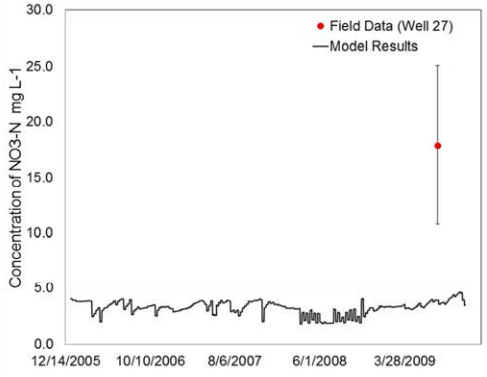
Field Data (Well 27)
Model Results
Concentration of NO3-N mg L-1
30.0
25.0
20.0
15.0
10.0
5.0
0.0
12/14/2005
10/10/2006
8/6/2007
6/1/2008
3/28/2009

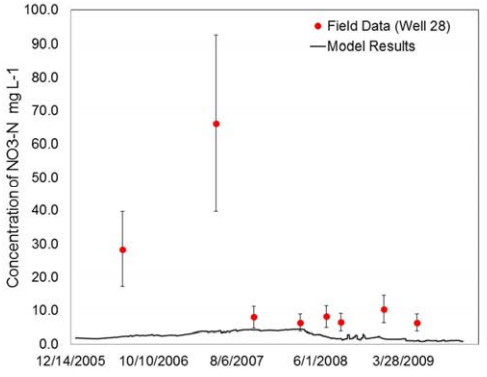
Field Data (Well 28)
Model Results
Concentration of NO3-N mg L-1
100.0
90.0
80.0
70.0
60.0
50.0
40.0
30.0
20.0
10.0
0.0
12/14/2005
10/10/2006
8/6/2007
6/1/2008
3/28/2009

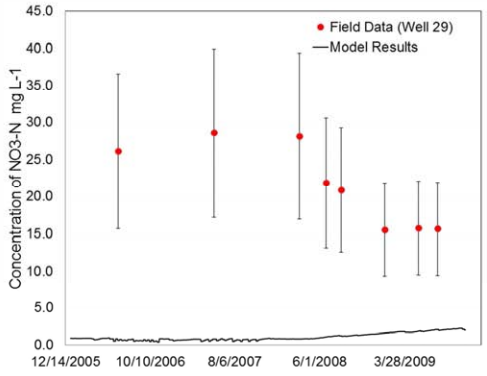
Field Data (Well 29)
Model Results
Concentration of NO3-N mg L-1
45.0
40.0
35.0
30.0
25.0
20.0
15.0
10.0
5.0
0.0
12/14/2005
10/10/2006
8/6/2007
6/1/2008
3/28/2009

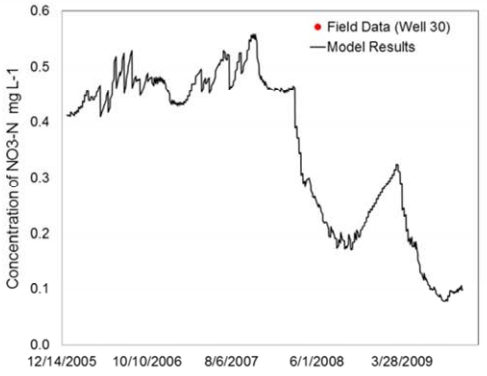
Field Data (Well 30)
Model Results
Concentration of NO3-N mg L-1
0.6
0.5
0.4
0.3
0.2
0.1
0.0
12/14/2005
10/10/2006
8/6/2007
6/1/2008
3/28/2009

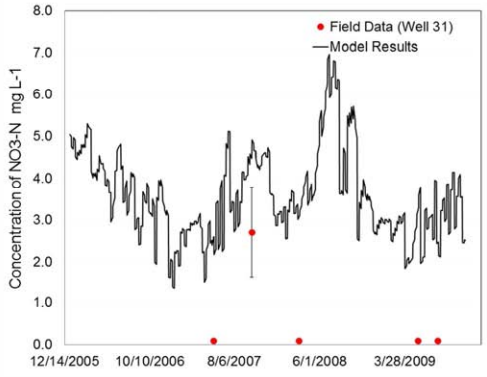
Field Data (Well 31)
Model Results
Concentration of NO3-N mg L-1
8.0
7.0
6.0
5.0
4.0
3.0
2.0
1.0
0.0
12/14/2005
10/10/2006
8/6/2007
6/1/2008
3/28/2009

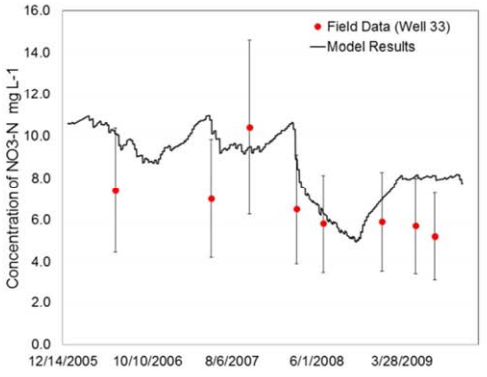
Field Data (Well 33)
Model Results
Concentration of NO3-N mg L-1
16.0
14.0
12.0
10.0
8.0
6.0
4.0
2.0
0.0
12/14/2005
10/10/2006
8/6/2007
6/1/2008
3/28/2009

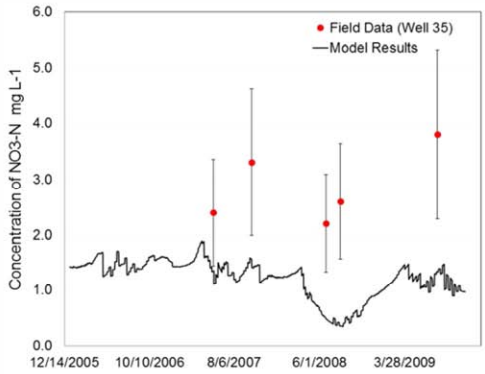
Field Data (Well 35)
Model Results
Concentration of NO3-N mg L-1
6.0
5.0
4.0
3.0
2.0
1.0
0.0
12/14/2005
10/10/2006
8/6/2007
6/1/2008
3/28/2009

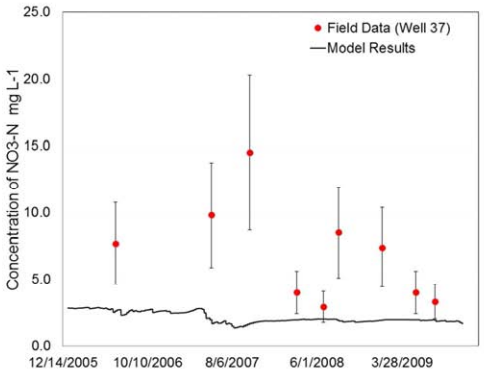
Field Data (Well 37)
Model Results
Concentration of NO3-N mg L-1
25.0
20.0
15.0
10.0
5.0
0.0
12/14/2005
10/10/2006
8/6/2007
6/1/2008
3/28/2009

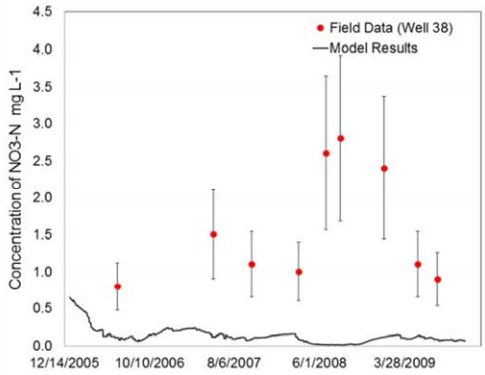
Field Data (Well 38)
Model Results
Concentration of NO3-N mg L-1
4.5
4.0
3.5
3.0
2.5
2.0
1.5
1.0
0.5
0.0
12/14/2005
10/10/2006
8/6/2007
6/1/2008
3/28/2009

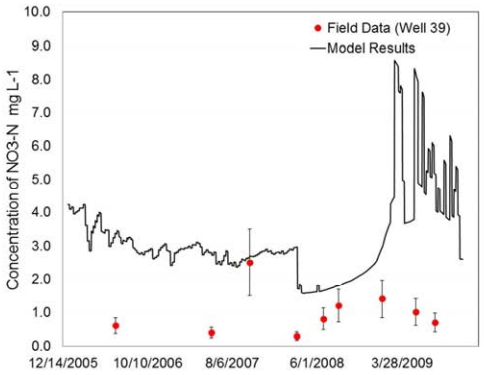
Field Data (Well 39)
Model Results
Concentration of NO3-N mg L-1
10.0
9.0
8.0
7.0
6.0
5.0
4.0
3.0
2.0
1.0
0.0
12/14/2005
10/10/2006
8/6/2007
6/1/2008
3/28/2009

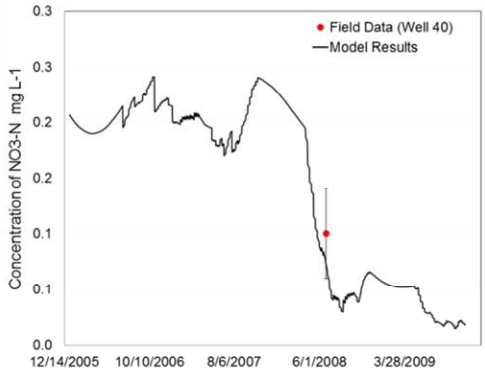
Field Data (Well 40)
Model Results
Concentration of NO3-N mg L-1
0.3
0.3
0.2
0.2
0.1
0.1
0.0
12/14/2005
10/10/2006
8/6/2007
6/1/2008
3/28/2009

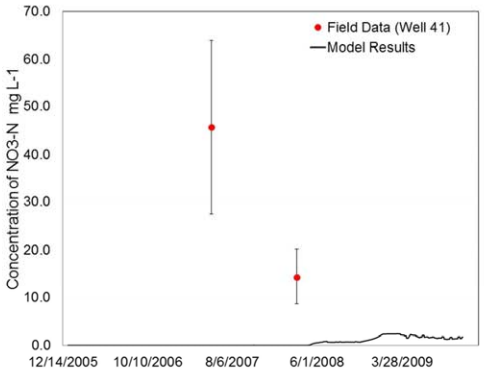
Field Data (Well 41)
Model Results
Concentration of NO3-N mg L-1
70.0
60.0
50.0
40.0
30.0
20.0
10.0
0.0
12/14/2005
10/10/2006
8/6/2007
6/1/2008
3/28/2009

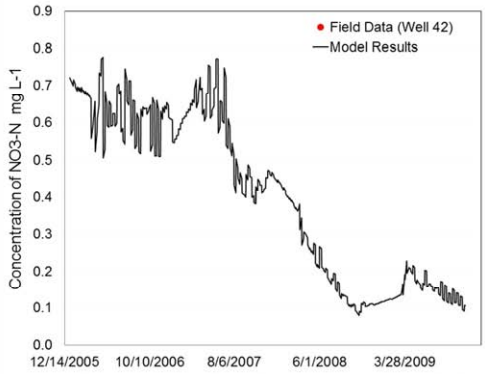
Field Data (Well 42)
Model Results
Concentration of NO3-N mg L-1
0.9
0.8
0.7
0.6
0.5
0.4
0.3
0.2
0.1
0.0
12/14/2005
10/10/2006
8/6/2007
6/1/2008
3/28/2009

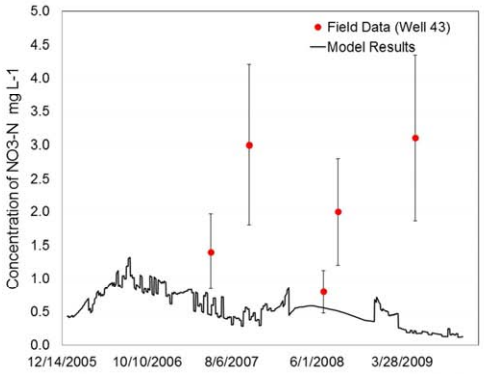
Field Data (Well 43)
Model Results
Concentration of NO3-N mg L-1
5.0
4.5
4.0
3.5
3.0
2.5
2.0
1.5
1.0
0.5
0.0
12/14/2005
10/10/2006
8/6/2007
6/1/2008
3/28/2009

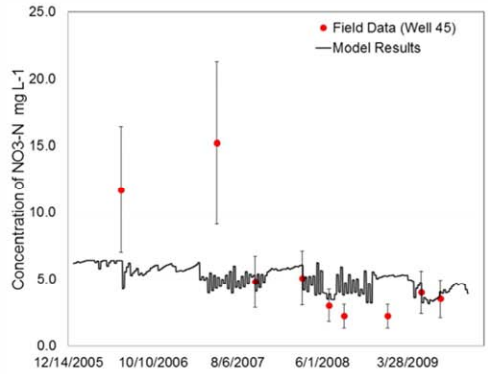
Field Data (Well 45)
Model Results
Concentration of NO3-N mg L-1
25.0
20.0
15.0
10.0
5.0
0.0
12/14/2005
10/10/2006
8/6/2007
6/1/2008
3/28/2009

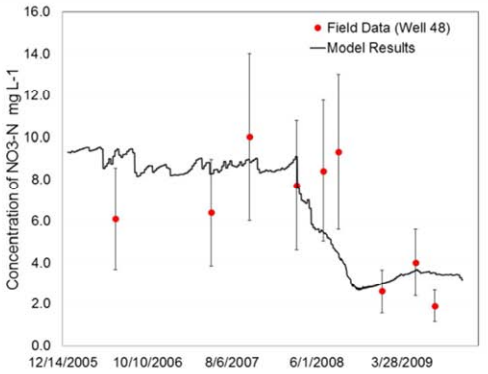
Field Data (Well 48)
Model Results
Concentration of NO3-N mg L-1
16.0
14.0
12.0
10.0
8.0
6.0
4.0
2.0
0.0
12/14/2005
10/10/2006
8/6/2007
6/1/2008
3/28/2009

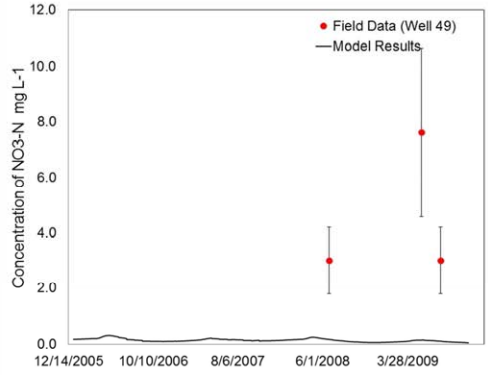
Field Data (Well 49)
Model Results
Concentration of NO3-N mg L-1
12.0
10.0
8.0
6.0
4.0
2.0
0.0
12/14/2005
10/10/2006
8/6/2007
6/1/2008
3/28/2009

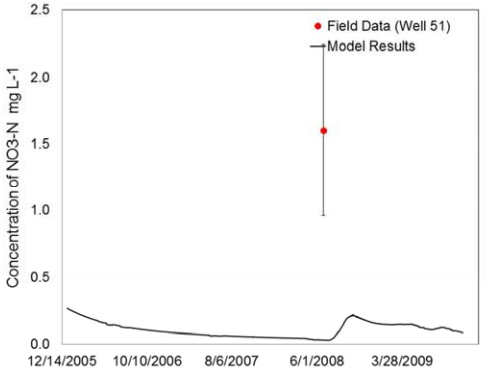
Field Data (Well 51)
Model Results
Concentration of NO3-N mg L-1
2.5
2.0
1.5
1.0
0.5
0.0
12/14/2005
10/10/2006
8/6/2007
6/1/2008
3/28/2009

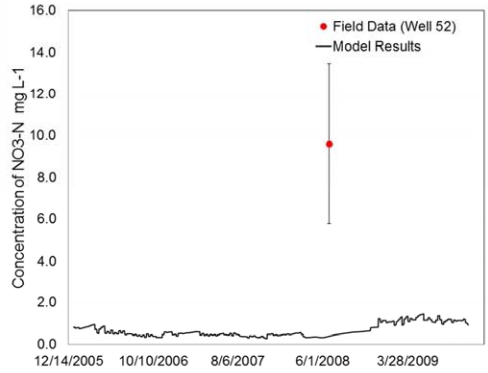
Field Data (Well 52)
Model Results
Concentration of NO3-N mg L-1
16.0
14.0
12.0
10.0
8.0
6.0
4.0
2.0
0.0
12/14/2005
10/10/2006
8/6/2007
6/1/2008
3/28/2009

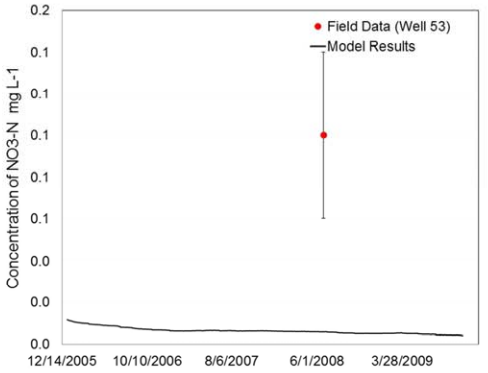
Field Data (Well 53)
Model Results
Concentration of NO3-N mg L-1
0.2
0.1
0.1
0.1
0.1
0.0
0.0
12/14/2005
10/10/2006
8/6/2007
6/1/2008
3/28/2009

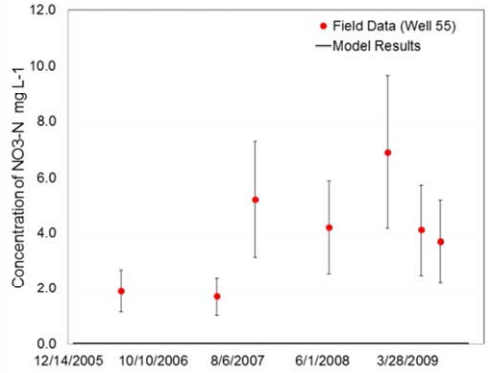
Field Data (Well 55)
Model Results
Concentration of NO3-N mg L-1
12.0
10.0
8.0
6.0
4.0
2.0
0.0
12/14/2005
10/10/2006
8/6/2007
6/1/2008
3/28/2009

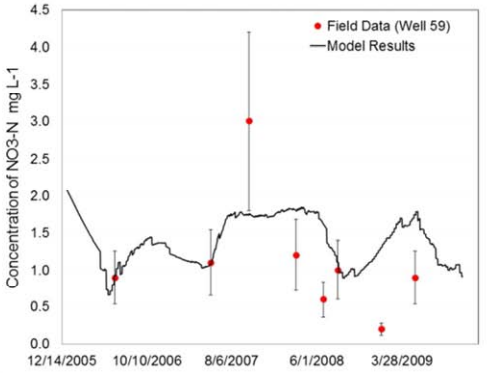
Field Data (Well 59)
Model Results
Concentration of NO3-N mg L-1
4.5
4.0
3.5
3.0
2.5
2.0
1.5
1.0
0.5
0.0
12/14/2005
10/10/2006
8/6/2007
6/1/2008
3/28/2009

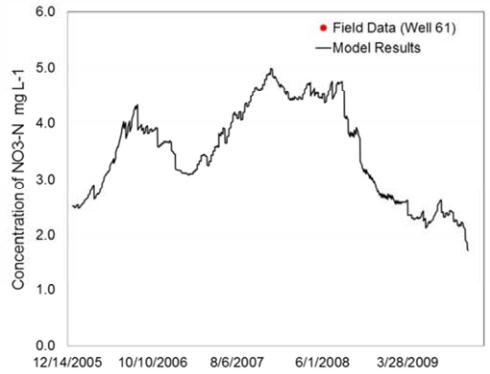
Field Data (Well 61)
Model Results
Concentration of NO3-N mg L-1
6.0
5.0
4.0
3.0
2.0
1.0
0.0
12/14/2005
10/10/2006
8/6/2007
6/1/2008
3/28/2009

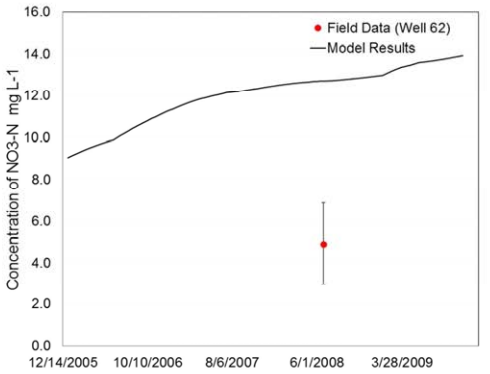
Field Data (Well 62)
Model Results
Concentration of NO3-N mg L-1
16.0
14.0
12.0
10.0
8.0
6.0
4.0
2.0
0.0
12/14/2005
10/10/2006
8/6/2007
6/1/2008
3/28/2009

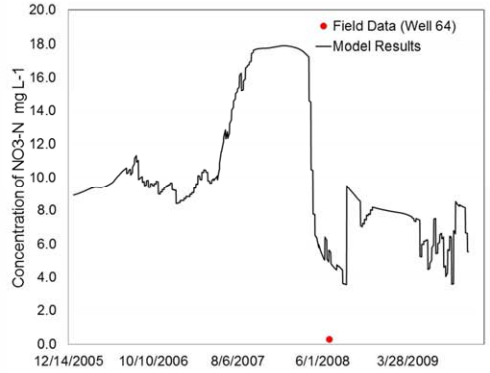
Field Data (Well 64)
Model Results
Concentration of NO3-N mg L-1
20.0
18.0
16.0
14.0
12.0
10.0
8.0
6.0
4.0
2.0
0.0
12/14/2005
10/10/2006
8/6/2007
6/1/2008
3/28/2009

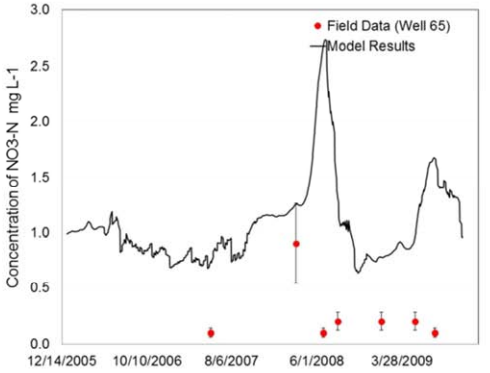
Field Data (Well 65)
Model Results
Concentration of NO3-N mg L-1
3.0
2.5
2.0
1.5
1.0
0.5
0.0
12/14/2005
10/10/2006
8/6/2007
6/1/2008
3/28/2009

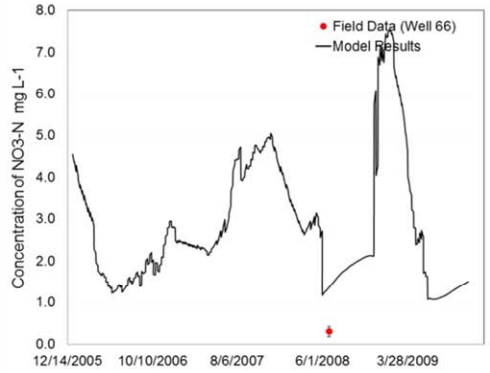
Field Data (Well 66)
Model Results
Concentration of NO3-N mg L-1
8.0
7.0
6.0
5.0
4.0
3.0
2.0
1.0
0.0
12/14/2005
10/10/2006
8/6/2007
6/1/2008
3/28/2009

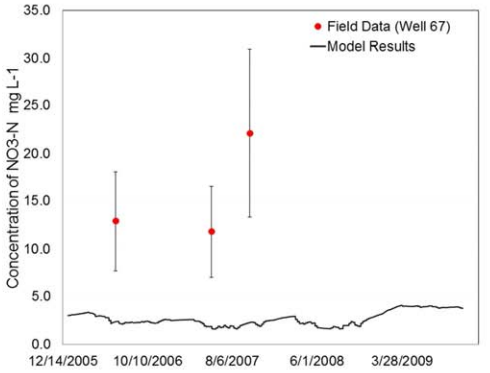
Field Data (Well 67)
Model Results
Concentration of NO3-N mg L-1
35.0
30.0
25.0
20.0
15.0
10.0
5.0
0.0
12/14/2005
10/10/2006
8/6/2007
6/1/2008
3/28/2009

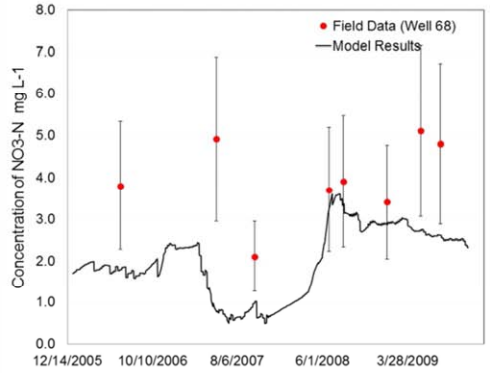
Field Data (Well 68)
Model Results
Concentration of NO3-N mg L-1
8.0
7.0
6.0
5.0
4.0
3.0
2.0
1.0
0.0
12/14/2005
10/10/2006
8/6/2007
6/1/2008
3/28/2009

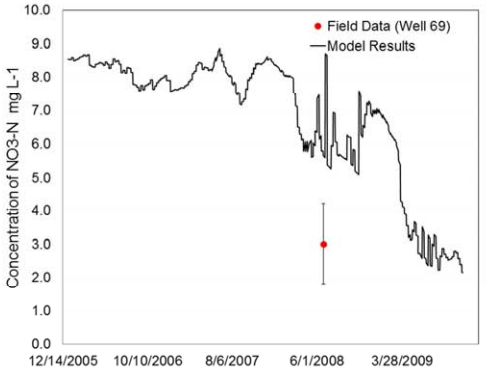
Field Data (Well 69)
Model Results
Concentration of NO3-N mg L-1
10.0
9.0
8.0
7.0
6.0
5.0
4.0
3.0
2.0
1.0
0.0
12/14/2005
10/10/2006
8/6/2007
6/1/2008
3/28/2009

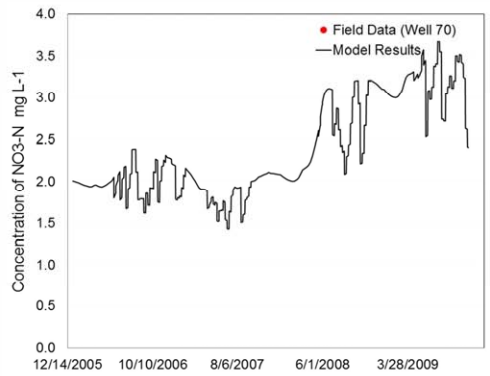
Field Data (Well 70)
Model Results
Concentration of NO3-N mg L-1
4.0
3.5
3.0
2.5
2.0
1.5
1.0
0.5
0.0
12/14/2005
10/10/2006
8/6/2007
6/1/2008
3/28/2009

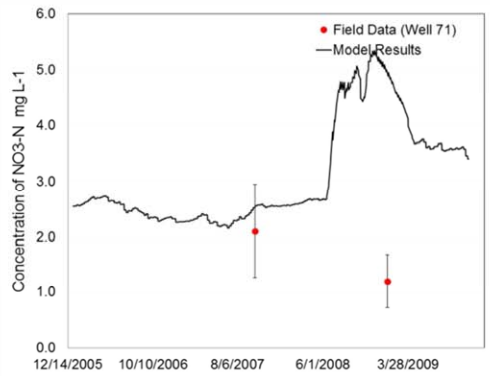
Field Data (Well 71)
Model Results
Concentration of NO3-N mg L-1
6.0
5.0
4.0
3.0
2.0
1.0
0.0
12/14/2005
10/10/2006
8/6/2007
6/1/2008
3/28/2009

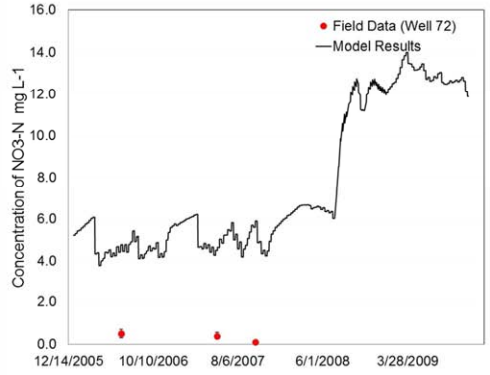
Field Data (Well 72)
Model Results
Concentration of NO3-N mg L-1
16.0
14.0
12.0
10.0
8.0
6.0
4.0
2.0
0.0
12/14/2005
10/10/2006
8/6/2007
6/1/2008
3/28/2009

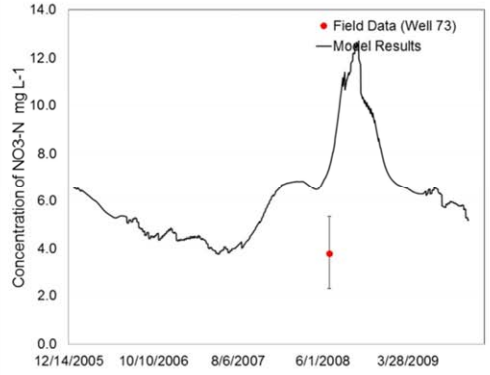
Field Data (Well 73)
Model Results
Concentration of NO3-N mg L-1
14.0
12.0
10.0
8.0
6.0
4.0
2.0
0.0
12/14/2005
10/10/2006
8/6/2007
6/1/2008
3/28/2009

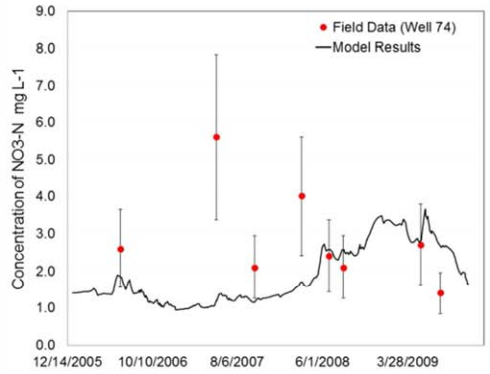
Field Data (Well 74)
Model Results
Concentration of NO3-N mg L-1
9.0
8.0
7.0
6.0
5.0
4.0
3.0
2.0
1.0
0.0
12/14/2005
10/10/2006
8/6/2007
6/1/2008
3/28/2009

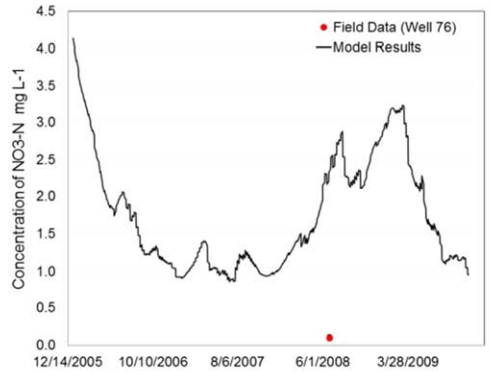
Field Data (Well 76)
Model Results
Concentration of NO3-N mg L-1
4.5
4.0
3.5
3.0
2.5
2.0
1.5
1.0
0.5
0.0
12/14/2005
10/10/2006
8/6/2007
6/1/2008
3/28/2009

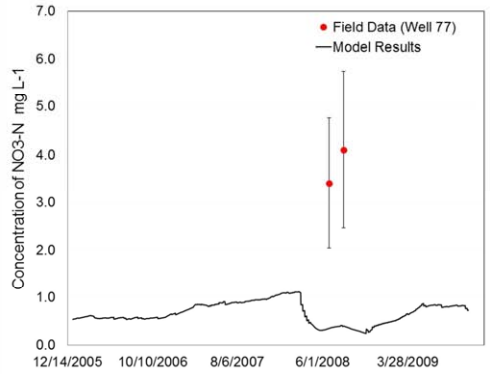
Field Data (Well 77)
Model Results
Concentration of NO3-N mg L-1
7.0
6.0
5.0
4.0
3.0
2.0
1.0
0.0
12/14/2005
10/10/2006
8/6/2007
6/1/2008
3/28/2009

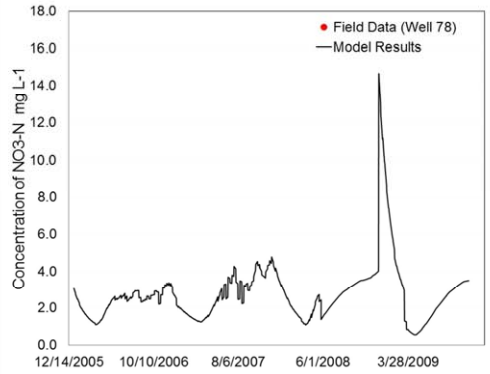
Field Data (Well 78)
Model Results
Concentration of NO3-N mg L-1
18.0
16.0
14.0
12.0
10.0
8.0
6.0
4.0
2.0
0.0
12/14/2005
10/10/2006
8/6/2007
6/1/2008
3/28/2009

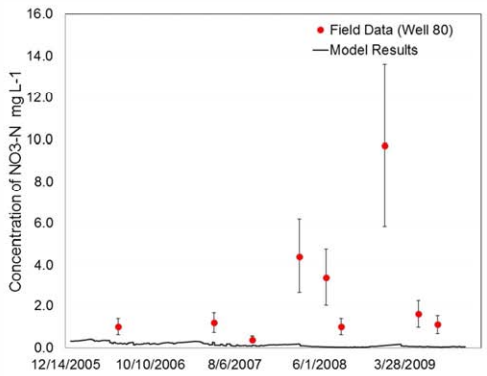
Field Data (Well 80)
Model Results
Concentration of NO3-N mg L-1
16.0
14.0
12.0
10.0
8.0
6.0
4.0
2.0
0.0
12/14/2005
10/10/2006
8/6/2007
6/1/2008
3/28/2009

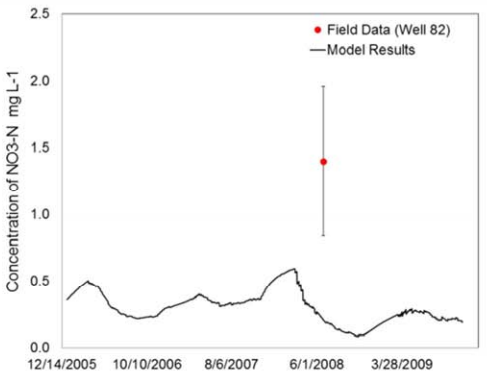
Field Data (Well 82)
Model Results
Concentration of NO3-N mg L-1
2.5
2.0
1.5
1.0
0.5
0.0
12/14/2005
10/10/2006
8/6/2007
6/1/2008
3/28/2009

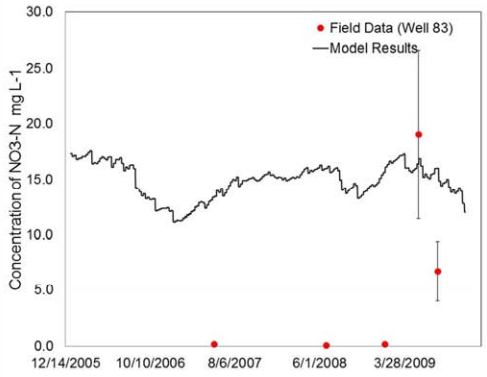
Field Data (Well 83)
Model Results
Concentration of NO3-N mg L-1
30.0
25.0
20.0
15.0
10.0
5.0
0.0
12/14/2005
10/10/2006
8/6/2007
6/1/2008
3/28/2009

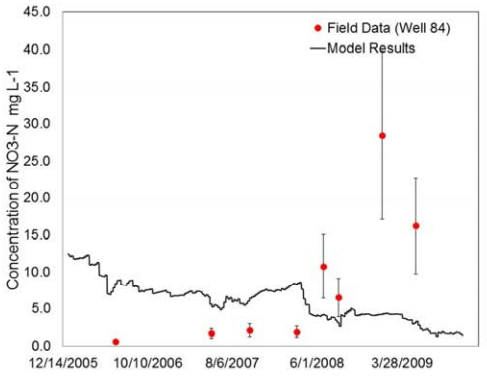
Field Data (Well 84)
Model Results
Concentration of NO3-N mg L-1
45.0
40.0
35.0
30.0
25.0
20.0
15.0
10.0
5.0
0.0
12/14/2005
10/10/2006
8/6/2007
6/1/2008
3/28/2009

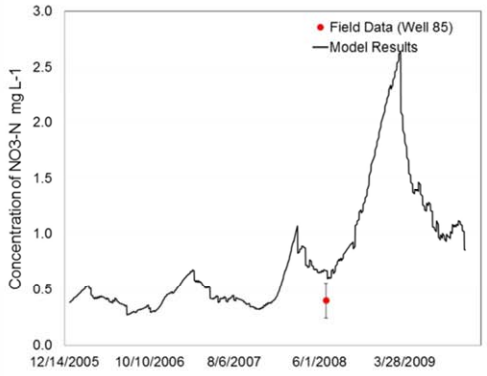
Field Data (Well 85)
Model Results
Concentration of NO3-N mg L-1
3.0
2.5
2.0
1.5
1.0
0.5
0.0
12/14/2005
10/10/2006
8/6/2007
6/1/2008
3/28/2009

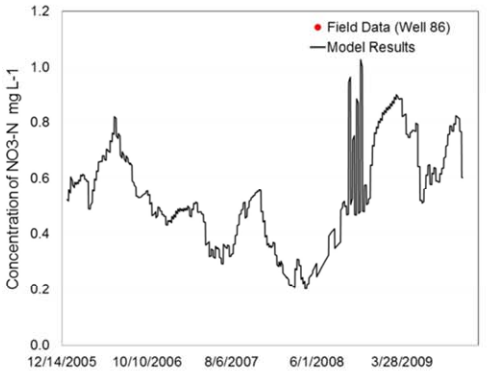
Field Data (Well 86)
Model Results
Concentration of NO3-N mg L-1
1.2
1.0
0.8
0.6
0.4
0.2
0.0
12/14/2005
10/10/2006
8/6/2007
6/1/2008
3/28/2009

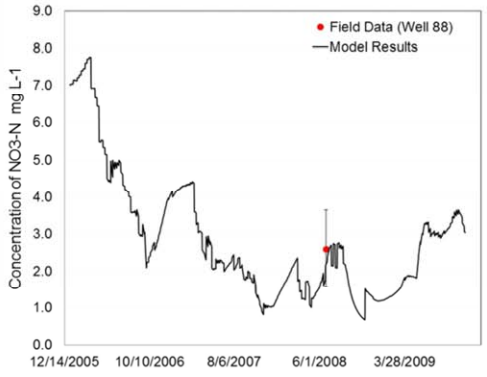
Field Data (Well 88)
Model Results
Concentration of NO3-N mg L-1
9.0
8.0
7.0
6.0
5.0
4.0
3.0
2.0
1.0
0.0
12/14/2005
10/10/2006
8/6/2007
6/1/2008
3/28/2009

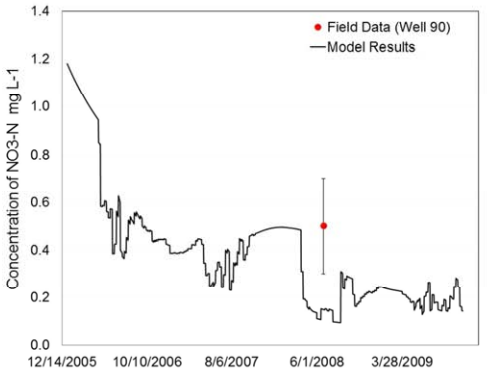
Field Data (Well 90)
Model Results
Concentration of NO3-N mg L-1
1.4
1.2
1.0
0.8
0.6
0.4
0.2
0.0
12/14/2005
10/10/2006
8/6/2007
6/1/2008
3/28/2009

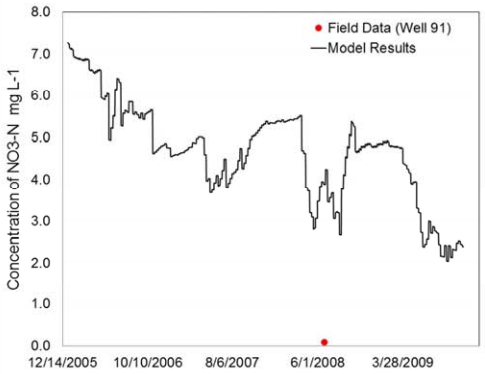
Field Data (Well 91)
Model Results
Concentration of NO3-N mg L-1
8.0
7.0
6.0
5.0
4.0
3.0
2.0
1.0
0.0
12/14/2005
10/10/2006
8/6/2007
6/1/2008
3/28/2009

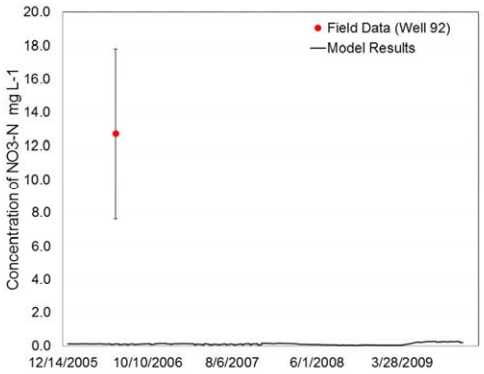
Field Data (Well 92)
Model Results
Concentration of NO3-N mg L-1
20.0
18.0
16.0
14.0
12.0
10.0
8.0
6.0
4.0
2.0
0.0
12/14/2005
10/10/2006
8/6/2007
6/1/2008
3/28/2009

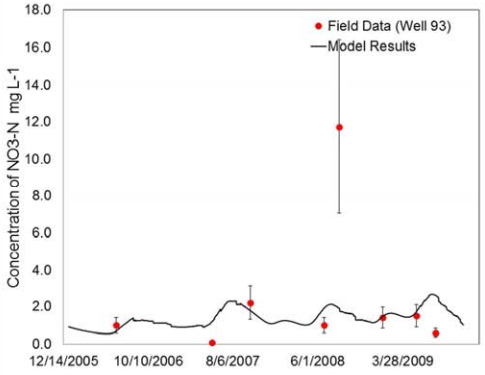
Field Data (Well 93)
Model Results
Concentration of NO3-N mg L-1
18.0
16.0
14.0
12.0
10.0
8.0
6.0
4.0
2.0
0.0
12/14/2005
10/10/2006
8/6/2007
6/1/2008
3/28/2009

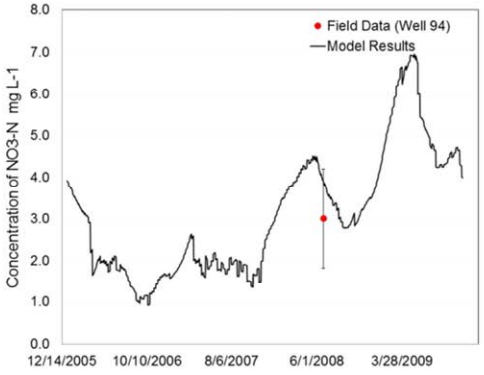
Field Data (Well 94)
Model Results
Concentration of NO3-N mg L-1
8.0
7.0
6.0
5.0
4.0
3.0
2.0
1.0
0.0
12/14/2005
10/10/2006
8/6/2007
6/1/2008
3/28/2009

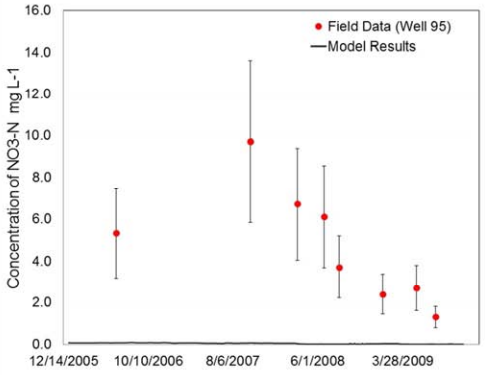
Field Data (Well 95)
Model Results
Concentration of NO3-N mg L-1
16.0
14.0
12.0
10.0
8.0
6.0
4.0
2.0
0.0
12/14/2005
10/10/2006
8/6/2007
6/1/2008
3/28/2009

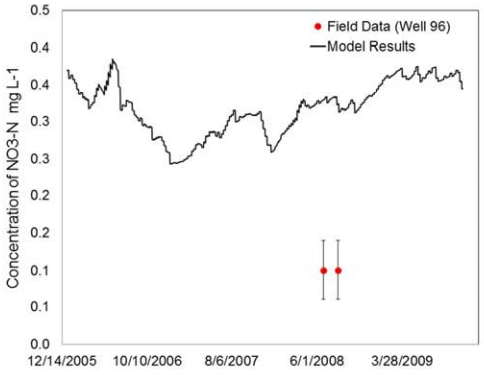
Field Data (Well 96)
Model Results
Concentration of NO3-N mg L-1
0.5
0.4
0.4
0.3
0.3
0.2
0.2
0.1
0.1
0.0
12/14/2005
10/10/2006
8/6/2007
6/1/2008
3/28/2009

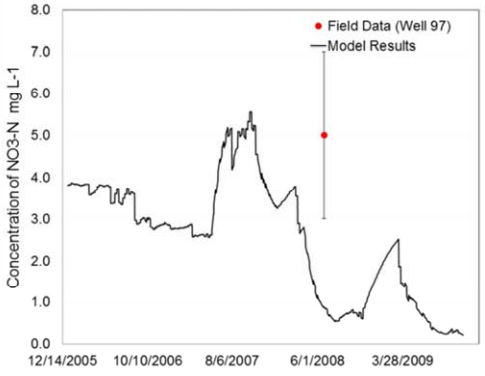
Field Data (Well 97)
Model Results
Concentration of NO3-N mg L-1
8.0
7.0
6.0
5.0
4.0
3.0
2.0
1.0
0.0
12/14/2005
10/10/2006
8/6/2007
6/1/2008
3/28/2009

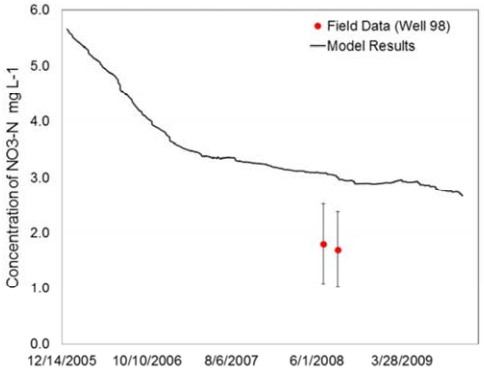
Field Data (Well 98)
Model Results
Concentration of NO3-N mg L-1
6.0
5.0
4.0
3.0
2.0
1.0
0.0
12/14/2005
10/10/2006
8/6/2007
6/1/2008
3/28/2009

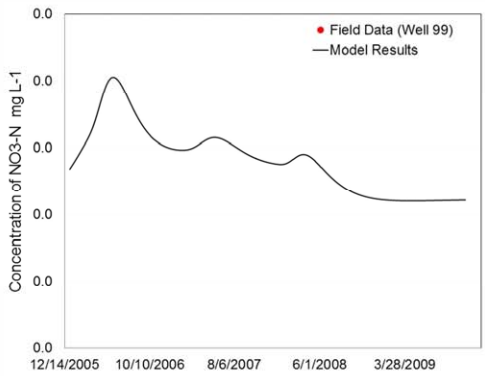
Field Data (Well 99)
Model Results
Concentration of NO3-N mg L-1
0.0
0.0
0.0
0.0
0.0
0.0
12/14/2005
10/10/2006
8/6/2007
6/1/2008
3/28/2009

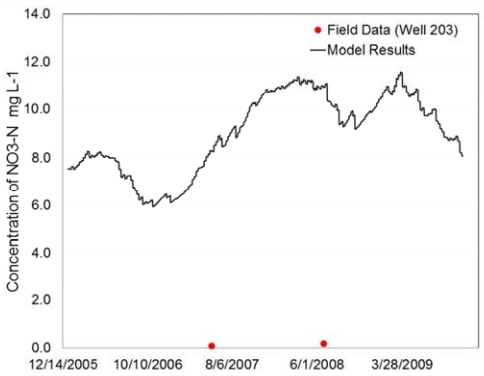
Field Data (Well 203)
Model Results
Concentration of NO3-N mg L-1
14.0
12.0
10.0
8.0
6.0
4.0
2.0
0.0
12/14/2005
10/10/2006
8/6/2007
6/1/2008
3/28/2009

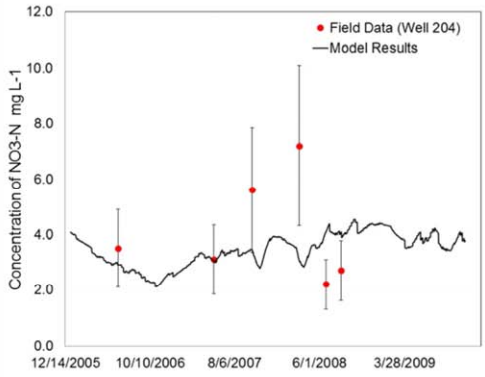
Field Data (Well 204)
Model Results
Concentration of NO3-N mg L-1
12.0
10.0
8.0
6.0
4.0
2.0
0.0
12/14/2005
10/10/2006
8/6/2007
6/1/2008
3/28/2009

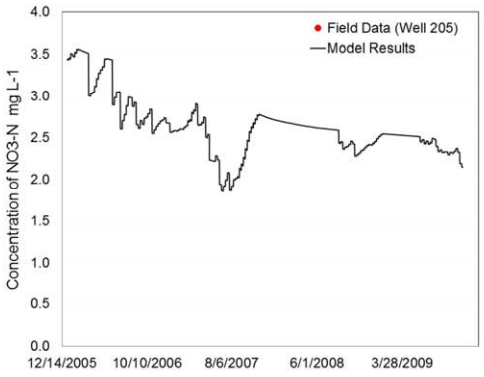
Field Data (Well 205)
Model Results
Concentration of NO3-N mg L-1
4.0
3.5
3.0
2.5
2.0
1.5
1.0
0.5
0.0
12/14/2005
10/10/2006
8/6/2007
6/1/2008
3/28/2009

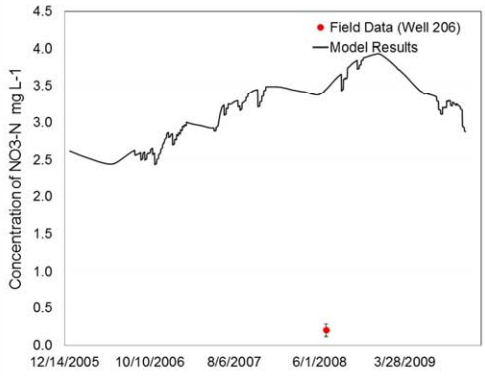
Field Data (Well 206)
Model Results
Concentration of NO3-N mg L-1
4.5
4.0
3.5
3.0
2.5
2.0
1.5
1.0
0.5
0.0
12/14/2005
10/10/2006
8/6/2007
6/1/2008
3/28/2009

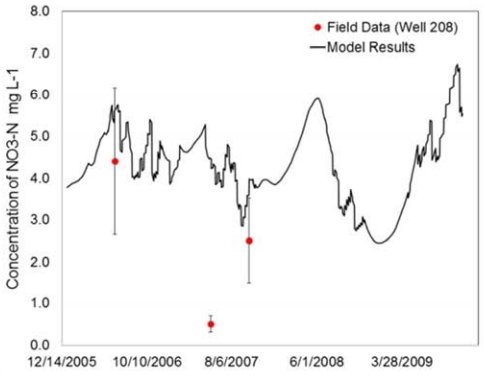
Field Data (Well 208)
Model Results
Concentration of NO3-N mg L-1
8.0
7.0
6.0
5.0
4.0
3.0
2.0
1.0
0.0
12/14/2005
10/10/2006
8/6/2007
6/1/2008
3/28/2009

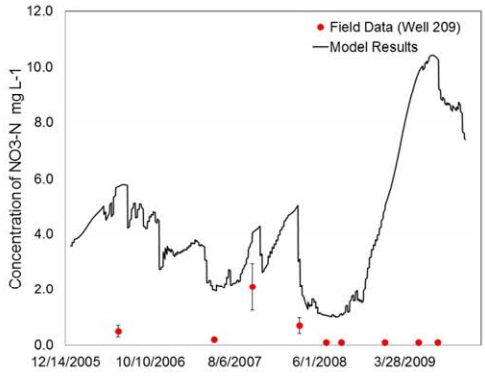
Field Data (Well 209)
Model Results
Concentration of NO3-N mg L-1
12.0
10.0
8.0
6.0
4.0
2.0
0.0
12/14/2005
10/10/2006
8/6/2007
6/1/2008
3/28/2009

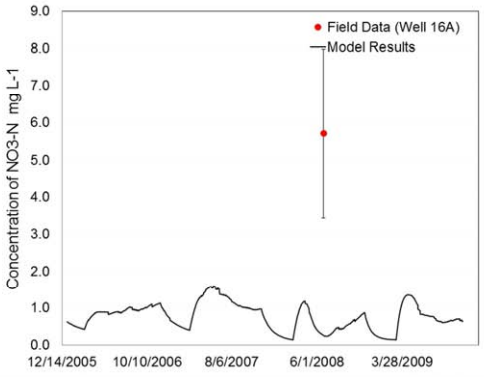
Field Data (Well 16A)
Model Results
Concentration of NO3-N mg L-1
9.0
8.0
7.0
6.0
5.0
4.0
3.0
2.0
1.0
0.0
12/14/2005
10/10/2006
8/6/2007
6/1/2008
3/28/2009

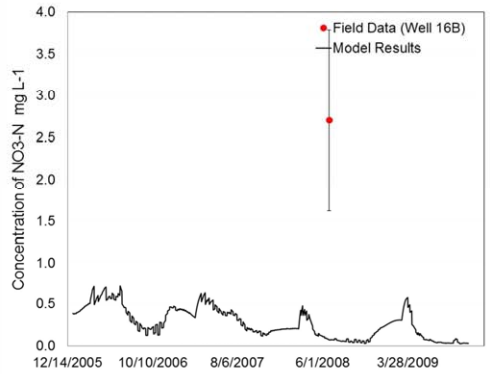
Field Data (Well 16B)
Model Results
Concentration of NO3-N mg L-1
4.0
3.5
3.0
2.5
2.0
1.5
1.0
0.5
0.0
12/14/2005
10/10/2006
8/6/2007
6/1/2008
3/28/2009

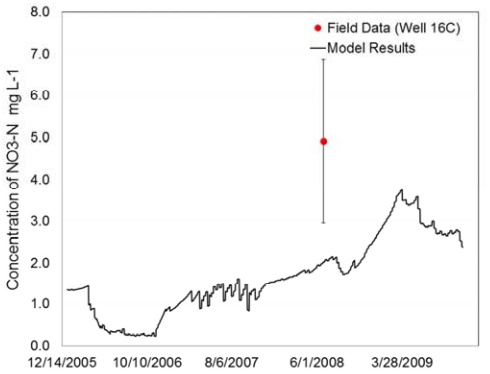
Field Data (Well 16C)
Model Results
Concentration of NO3-N mg L-1
8.0
7.0
6.0
5.0
4.0
3.0
2.0
1.0
0.0
12/14/2005
10/10/2006
8/6/2007
6/1/2008
3/28/2009

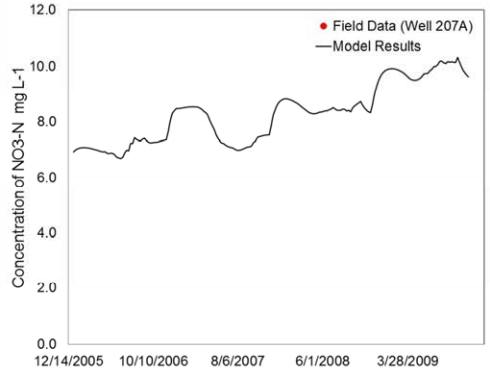
Field Data (Well 207A)
Model Results
Concentration of NO3-N mg L-1
12.0
10.0
8.0
6.0
4.0
2.0
0.0
12/14/2005
10/10/2006
8/6/2007
6/1/2008
3/28/2009

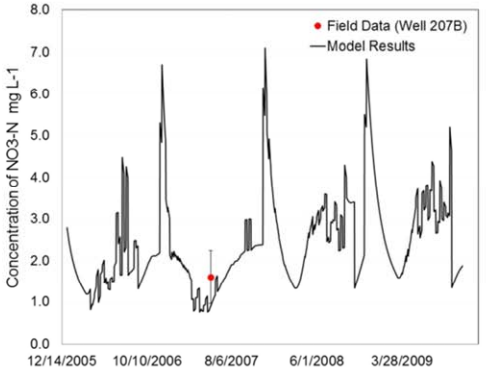
Field Data (Well 207B)
Model Results
Concentration of NO3-N mg L-1
8.0
7.0
6.0
5.0
4.0
3.0
2.0
1.0
0.0
12/14/2005
10/10/2006
8/6/2007
6/1/2008
3/28/2009

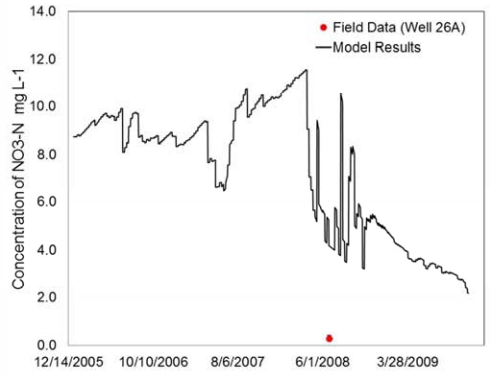
Field Data (Well 26A)
Model Results
Concentration of NO3-N mg L-1
14.0
12.0
10.0
8.0
6.0
4.0
2.0
0.0
12/14/2005
10/10/2006
8/6/2007
6/1/2008
3/28/2009

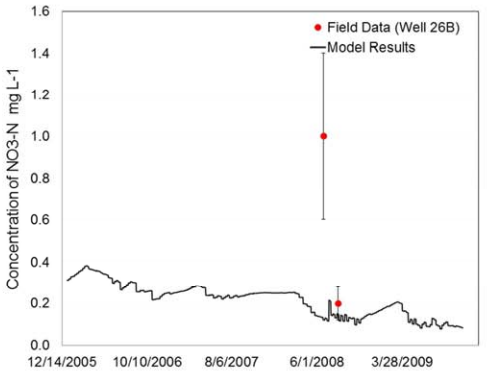
Field Data (Well 26B)
Model Results
Concentration of NO3-N mg L-1
1.6
1.4
1.2
1.0
0.8
0.6
0.4
0.2
0.0
12/14/2005
10/10/2006
8/6/2007
6/1/2008
3/28/2009

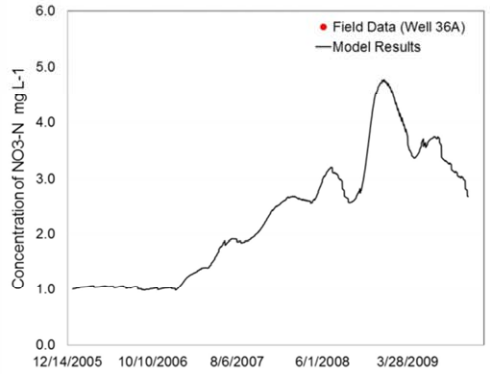
Field Data (Well 36A)
Model Results
Concentration of NO3-N mg L-1
6.0
5.0
4.0
3.0
2.0
1.0
0.0
12/14/2005
10/10/2006
8/6/2007
6/1/2008
3/28/2009

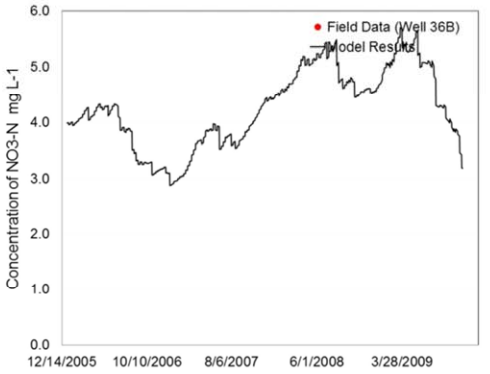
Field Data (Well 36B)
Model Results
Concentration of NO3-N mg L-1
6.0
5.0
4.0
3.0
2.0
1.0
0.0
12/14/2005
10/10/2006
8/6/2007
6/1/2008
3/28/2009

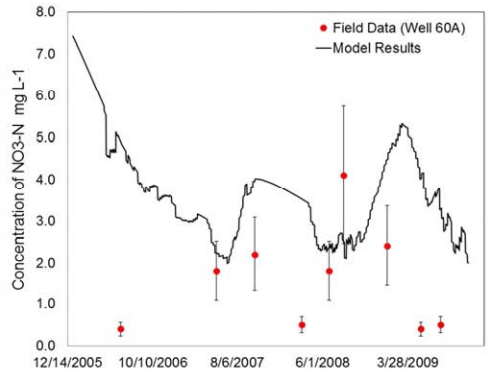
Field Data (Well 60A)
Model Results
Concentration of NO3-N mg L-1
8.0
7.0
6.0
5.0
4.0
3.0
2.0
1.0
0.0
12/14/2005
10/10/2006
8/6/2007
6/1/2008
3/28/2009

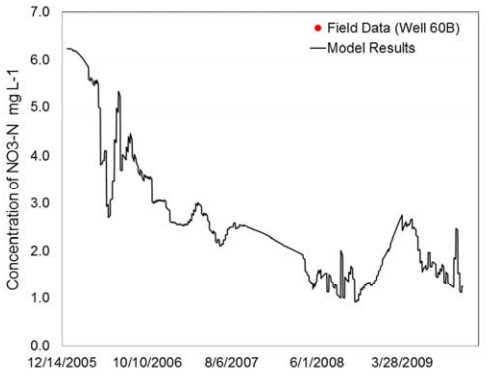
Field Data (Well 60B)
Model Results
Concentration of NO3-N mg L-1
7.0
6.0
5.0
4.0
3.0
2.0
1.0
0.0
12/14/2005
10/10/2006
8/6/2007
6/1/2008
3/28/2009

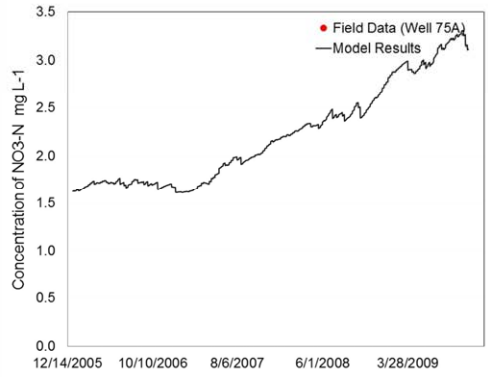
Field Data (Well 75A)
Model Results
Concentration of NO3-N mg L-1
3.5
3.0
2.5
2.0
1.5
1.0
0.5
0.0
12/14/2005
10/10/2006
8/6/2007
6/1/2008
3/28/2009

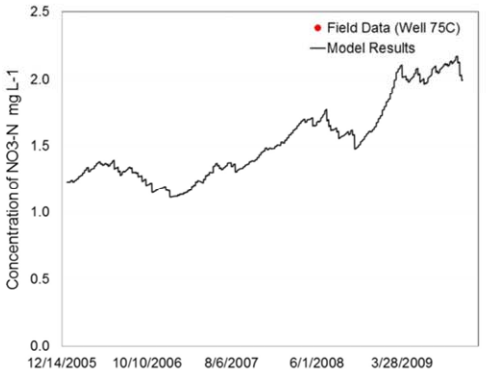
Field Data (Well 75C)
Model Results
Concentration of NO3-N mg L-1
2.5
2.0
1.5
1.0
0.5
0.0
12/14/2005
10/10/2006
8/6/2007
6/1/2008
3/28/2009

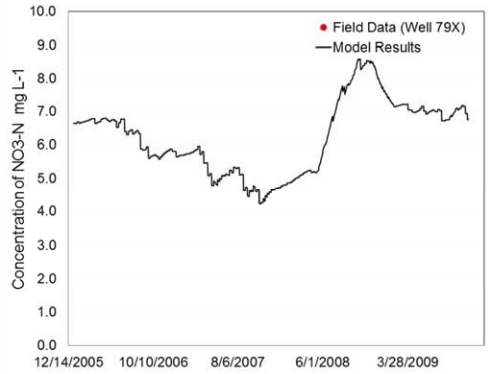
Field Data (Well 79X)
Model Results
Concentration of NO3-N mg L-1
10.0
9.0
8.0
7.0
6.0
5.0
4.0
3.0
2.0
1.0
0.0
12/14/2005
10/10/2006
8/6/2007
6/1/2008
3/28/2009

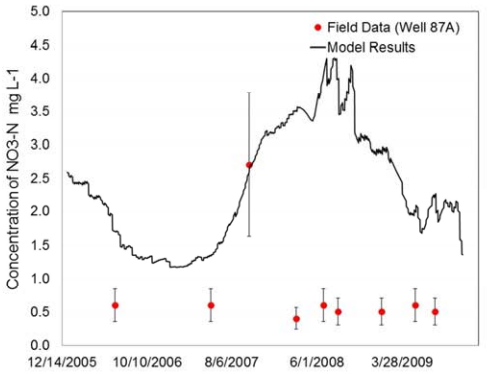
Field Data (Well 87A)
Model Results
Concentration of NO3-N mg L-1
5.0
4.5
4.0
3.5
3.0
2.5
2.0
1.5
1.0
0.5
0.0
12/14/2005
10/10/2006
8/6/2007
6/1/2008
3/28/2009

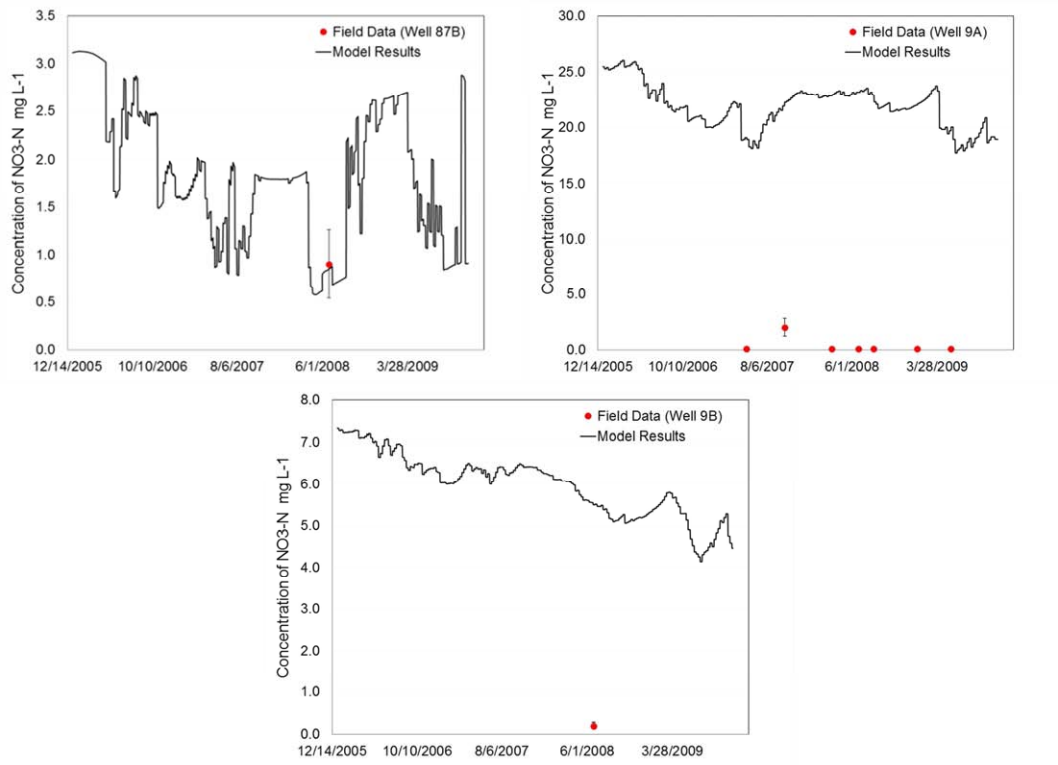

Figure B- 2. Comparison of simulated and observed NO_3 concentration at observation wells during 2006-2009. Simulated values are taken from grid cells in layer 4 of the model that coincide with the location of the observation well. Red dots indicate observed measurements of concentration. Error bars are included to indicate the variability of the observed value for a representative cultivated field.

B5. COMPARISONS OF SIMULATED AND OBSERVED SeO_4 CONCENTRATION AT OBSERVATION WELLS

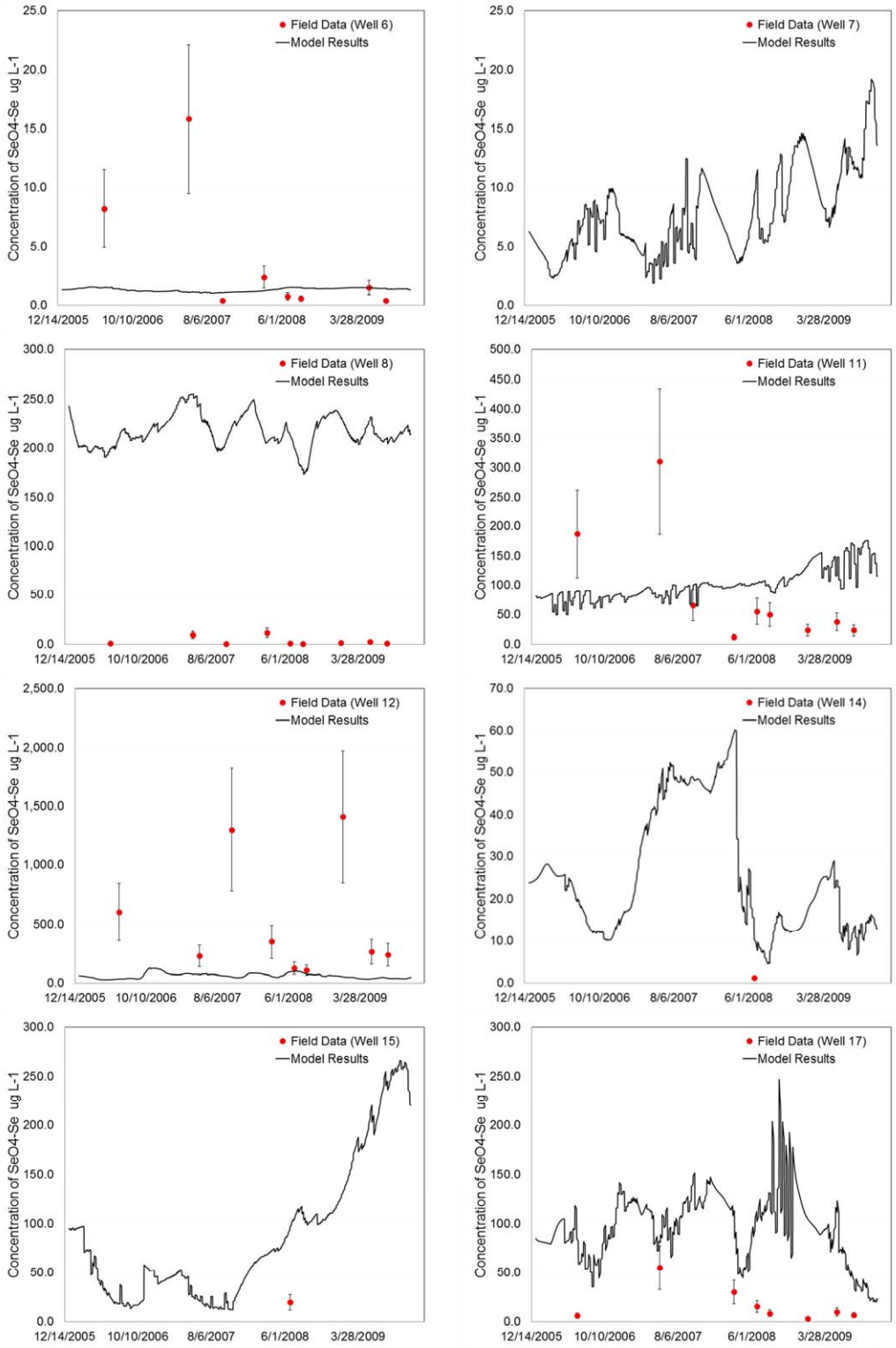

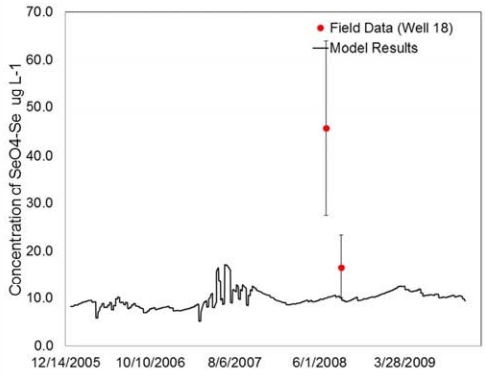
Field Data (Well 18)
Model Results
Concentration of SeO4-Se ug L-1
70.0
60.0
50.0
40.0
30.0
20.0
10.0
0.0
12/14/2005
10/10/2006
8/6/2007
6/1/2008
3/28/2009

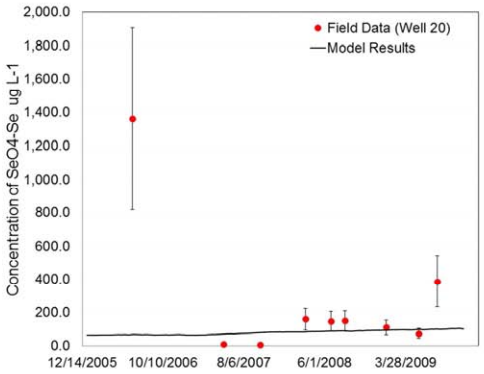
Field Data (Well 20)
Model Results
Concentration of SeO4-Se ug L-1
2,000.0
1,800.0
1,600.0
1,400.0
1,200.0
1,000.0
800.0
600.0
400.0
200.0
0.0
12/14/2005
10/10/2006
8/6/2007
6/1/2008
3/28/2009

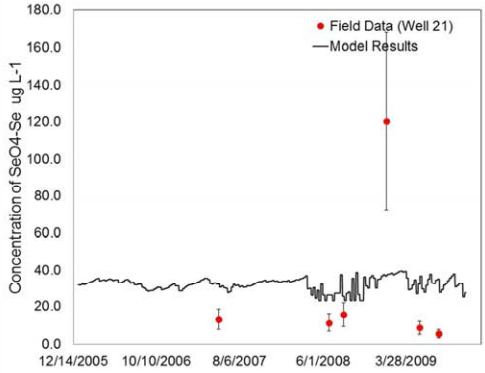
Field Data (Well 21)
Model Results
Concentration of SeO4-Se ug L-1
180.0
160.0
140.0
120.0
100.0
80.0
60.0
40.0
20.0
0.0
12/14/2005
10/10/2006
8/6/2007
6/1/2008
3/28/2009

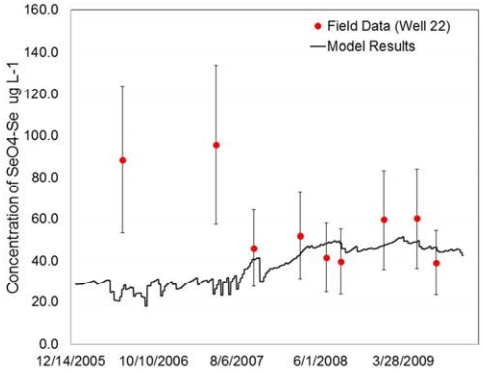
Field Data (Well 22)
Model Results
Concentration of SeO4-Se ug L-1
160.0
140.0
120.0
100.0
80.0
60.0
40.0
20.0
0.0
12/14/2005
10/10/2006
8/6/2007
6/1/2008
3/28/2009

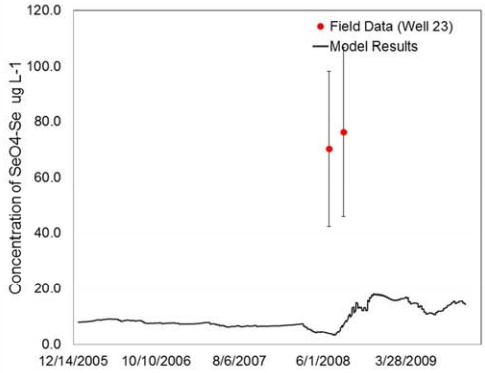
Field Data (Well 23)
Model Results
Concentration of SeO4-Se ug L-1
120.0
100.0
80.0
60.0
40.0
20.0
0.0
12/14/2005
10/10/2006
8/6/2007
6/1/2008
3/28/2009

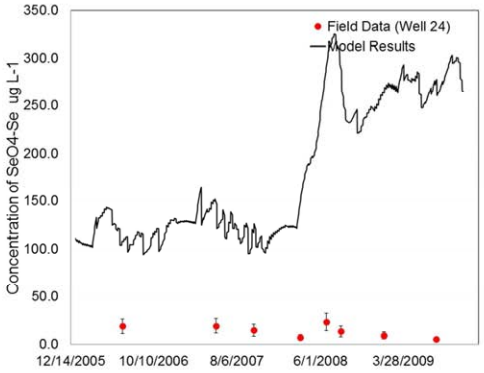
Field Data (Well 24)
Model Results
Concentration of SeO4-Se ug L-1
350.0
300.0
250.0
200.0
150.0
100.0
50.0
0.0
12/14/2005
10/10/2006
8/6/2007
6/1/2008
3/28/2009

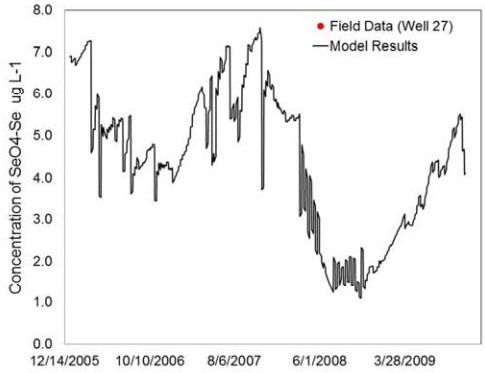
Field Data (Well 27)
Model Results
Concentration of SeO4-Se ug L-1
8.0
7.0
6.0
5.0
4.0
3.0
2.0
1.0
0.0
12/14/2005
10/10/2006
8/6/2007
6/1/2008
3/28/2009

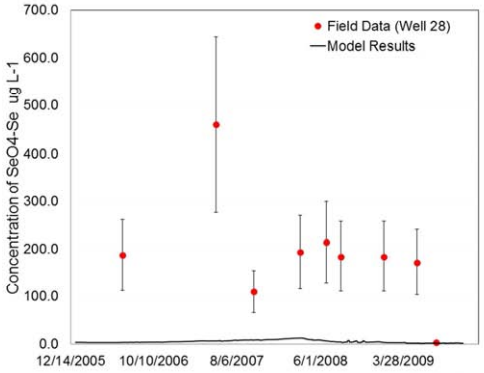
Field Data (Well 28)
Model Results
Concentration of SeO4-Se ug L-1
700.0
600.0
500.0
400.0
300.0
200.0
100.0
0.0
12/14/2005
10/10/2006
8/6/2007
6/1/2008
3/28/2009

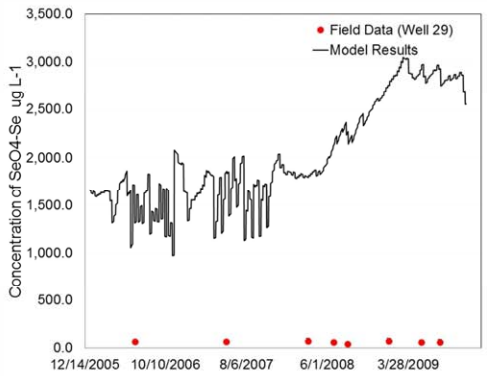
Field Data (Well 29)
Model Results
Concentration of SeO4-Se ug L-1
3,500.0
3,000.0
2,500.0
2,000.0
1,500.0
1,000.0
500.0
0.0
12/14/2005
10/10/2006
8/6/2007
6/1/2008
3/28/2009

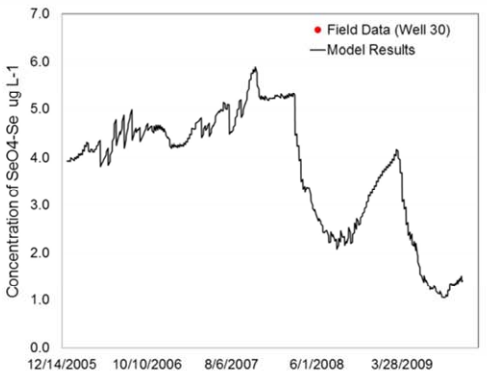
Field Data (Well 30)
Model Results
Concentration of SeO4-Se ug L-1
7.0
6.0
5.0
4.0
3.0
2.0
1.0
0.0
12/14/2005
10/10/2006
8/6/2007
6/1/2008
3/28/2009

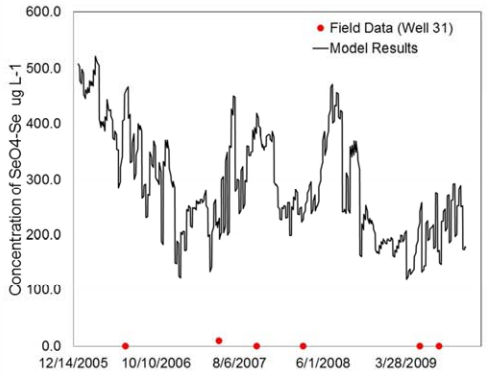
Field Data (Well 31)
Model Results
Concentration of SeO4-Se ug L-1
600.0
500.0
400.0
300.0
200.0
100.0
0.0
12/14/2005
10/10/2006
8/6/2007
6/1/2008
3/28/2009

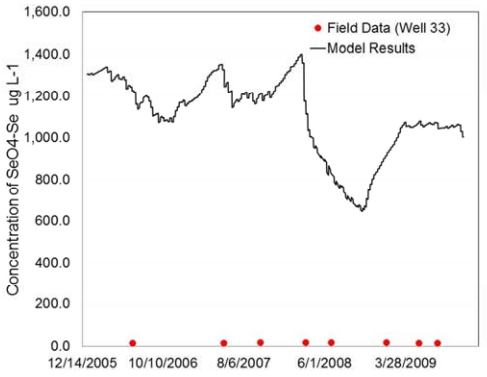
Field Data (Well 33)
Model Results
Concentration of SeO4-Se ug L-1
1,600.0
1,400.0
1,200.0
1,000.0
800.0
600.0
400.0
200.0
0.0
12/14/2005
10/10/2006
8/6/2007
6/1/2008
3/28/2009

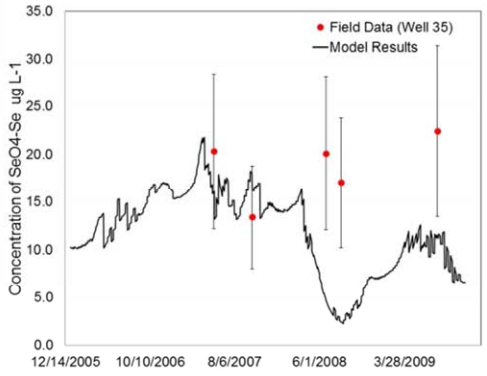
Field Data (Well 35)
Model Results
Concentration of SeO4-Se ug L-1
35.0
30.0
25.0
20.0
15.0
10.0
5.0
0.0
12/14/2005
10/10/2006
8/6/2007
6/1/2008
3/28/2009

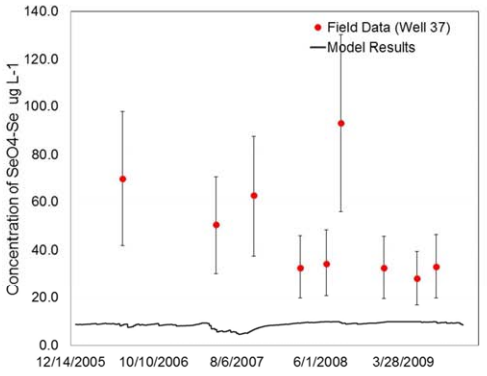
Field Data (Well 37)
Model Results
Concentration of SeO4-Se ug L-1
140.0
120.0
100.0
80.0
60.0
40.0
20.0
0.0
12/14/2005
10/10/2006
8/6/2007
6/1/2008
3/28/2009

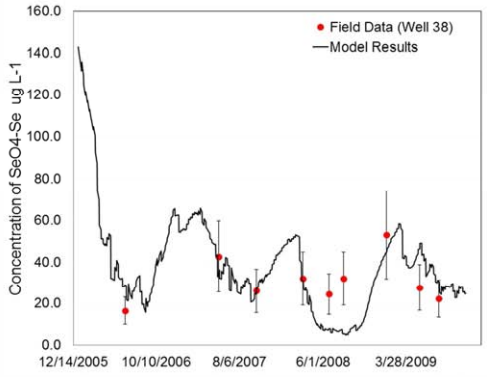
Field Data (Well 38)
Model Results
Concentration of SeO4-Se ug L-1
160.0
140.0
120.0
100.0
80.0
60.0
40.0
20.0
0.0
12/14/2005
10/10/2006
8/6/2007
6/1/2008
3/28/2009

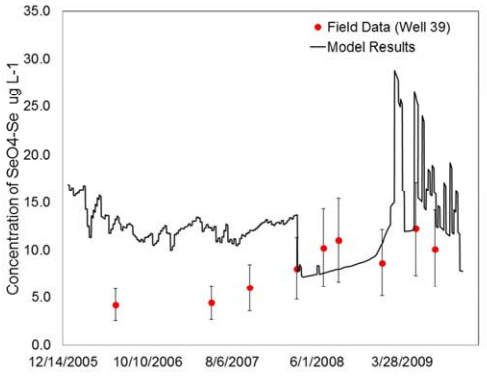
Field Data (Well 39)
Model Results
Concentration of SeO4-Se ug L-1
35.0
30.0
25.0
20.0
15.0
10.0
5.0
0.0
12/14/2005
10/10/2006
8/6/2007
6/1/2008
3/28/2009

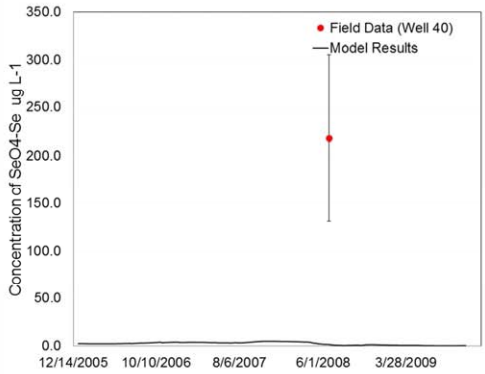
Field Data (Well 40)
Model Results
Concentration of SeO4-Se ug L-1
350.0
300.0
250.0
200.0
150.0
100.0
50.0
0.0
12/14/2005
10/10/2006
8/6/2007
6/1/2008
3/28/2009

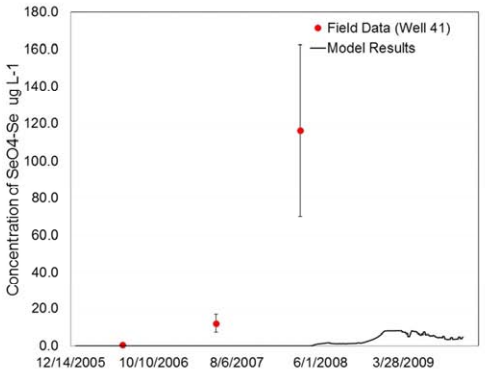
Field Data (Well 41)
Model Results
Concentration of SeO4-Se ug L-1
180.0
160.0
140.0
120.0
100.0
80.0
60.0
40.0
20.0
0.0
12/14/2005
10/10/2006
8/6/2007
6/1/2008
3/28/2009

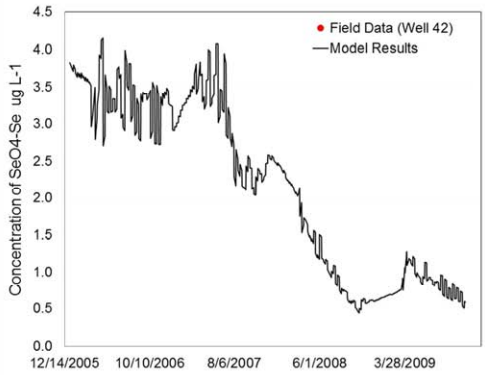
Field Data (Well 42)
Model Results
Concentration of SeO4-Se ug L-1
4.5
4.0
3.5
3.0
2.5
2.0
1.5
1.0
0.5
0.0
12/14/2005
10/10/2006
8/6/2007
6/1/2008
3/28/2009

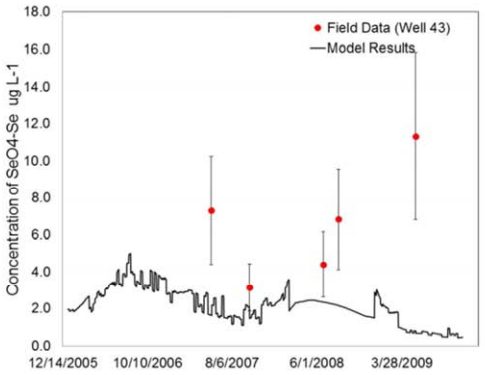
Field Data (Well 43)
Model Results
Concentration of SeO4-Se ug L-1
18.0
16.0
14.0
12.0
10.0
8.0
6.0
4.0
2.0
0.0
12/14/2005
10/10/2006
8/6/2007
6/1/2008
3/28/2009

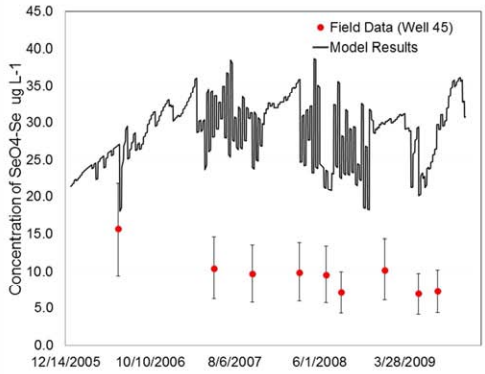
Field Data (Well 45)
Model Results
Concentration of SeO4-Se ug L-1
45.0
40.0
35.0
30.0
25.0
20.0
15.0
10.0
5.0
0.0
12/14/2005
10/10/2006
8/6/2007
6/1/2008
3/28/2009

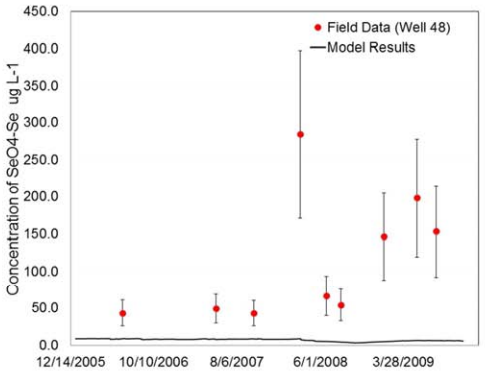
Field Data (Well 48)
Model Results
Concentration of SeO4-Se ug L-1
450.0
400.0
350.0
300.0
250.0
200.0
150.0
100.0
50.0
0.0
12/14/2005
10/10/2006
8/6/2007
6/1/2008
3/28/2009

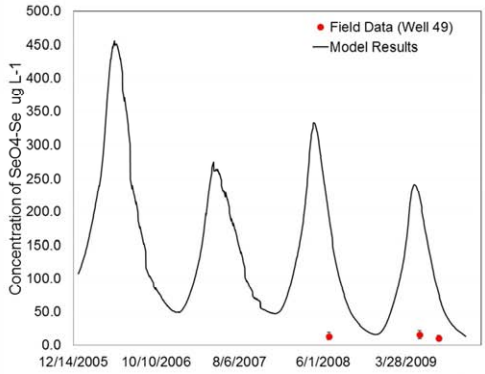
Field Data (Well 49)
Model Results
Concentration of SeO4-Se ug L-1
500.0
450.0
400.0
350.0
300.0
250.0
200.0
150.0
100.0
50.0
0.0
12/14/2005
10/10/2006
8/6/2007
6/1/2008
3/28/2009

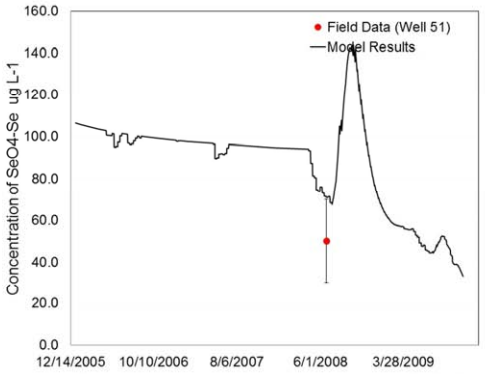
Field Data (Well 51)
Model Results
Concentration of SeO4-Se ug L-1
160.0
140.0
120.0
100.0
80.0
60.0
40.0
20.0
0.0
12/14/2005
10/10/2006
8/6/2007
6/1/2008
3/28/2009

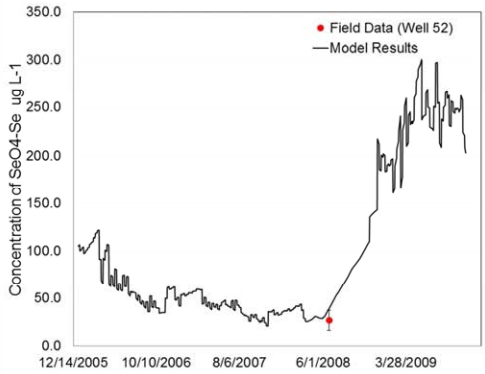
Field Data (Well 52)
Model Results
Concentration of SeO4-Se ug L-1
350.0
300.0
250.0
200.0
150.0
100.0
50.0
0.0
12/14/2005
10/10/2006
8/6/2007
6/1/2008
3/28/2009

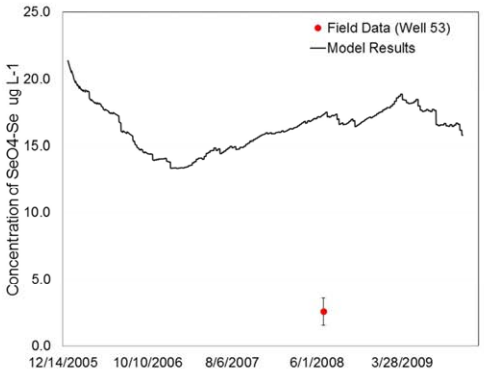
Field Data (Well 53)
Model Results
Concentration of SeO4-Se ug L-1
25.0
20.0
15.0
10.0
5.0
0.0
12/14/2005
10/10/2006
8/6/2007
6/1/2008
3/28/2009

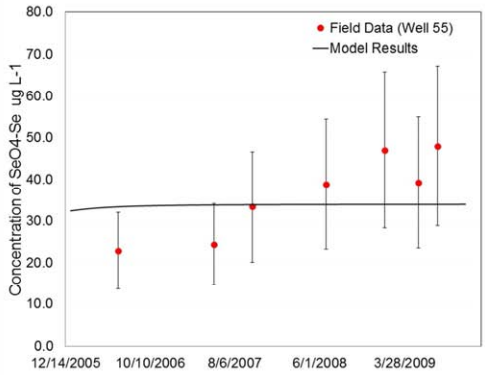
Field Data (Well 55)
Model Results
Concentration of SeO4-Se ug L-1
80.0
70.0
60.0
50.0
40.0
30.0
20.0
10.0
0.0
12/14/2005
10/10/2006
8/6/2007
6/1/2008
3/28/2009

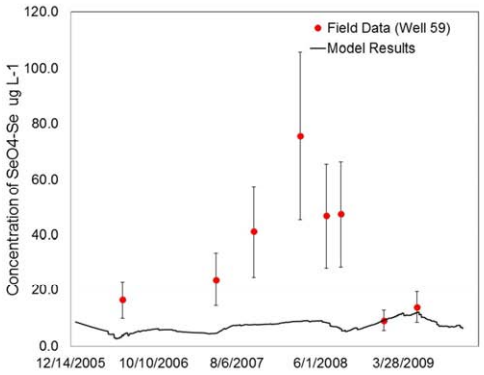
Field Data (Well 59)
Model Results
Concentration of SeO4-Se ug L-1
120.0
100.0
80.0
60.0
40.0
20.0
0.0
12/14/2005
10/10/2006
8/6/2007
6/1/2008
3/28/2009

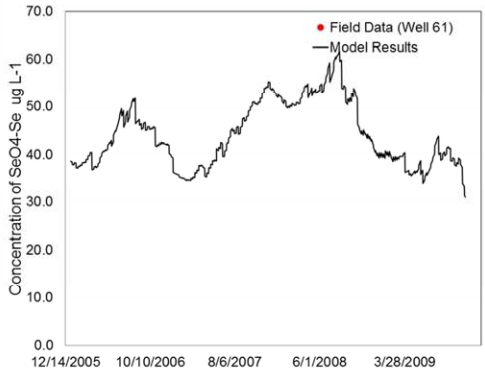
Field Data (Well 61)
Model Results
Concentration of SeO4-Se ug L-1
70.0
60.0
50.0
40.0
30.0
20.0
10.0
0.0
12/14/2005
10/10/2006
8/6/2007
6/1/2008
3/28/2009

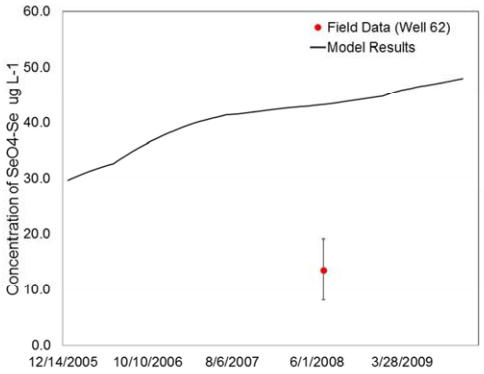
Field Data (Well 62)
Model Results
Concentration of SeO4-Se ug L-1
60.0
50.0
40.0
30.0
20.0
10.0
0.0
12/14/2005
10/10/2006
8/6/2007
6/1/2008
3/28/2009

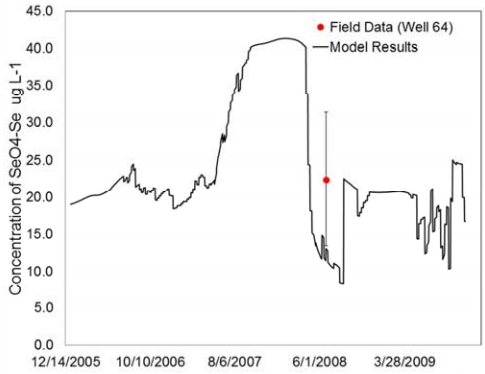
Field Data (Well 64)
Model Results
Concentration of SeO4-Se ug L-1
45.0
40.0
35.0
30.0
25.0
20.0
15.0
10.0
5.0
0.0
12/14/2005
10/10/2006
8/6/2007
6/1/2008
3/28/2009

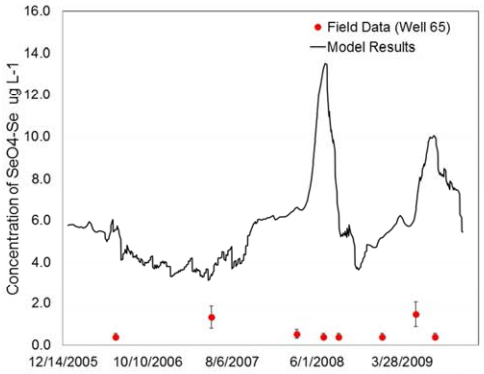
Field Data (Well 65)
Model Results
Concentration of SeO4-Se ug L-1
16.0
14.0
12.0
10.0
8.0
6.0
4.0
2.0
0.0
12/14/2005
10/10/2006
8/6/2007
6/1/2008
3/28/2009

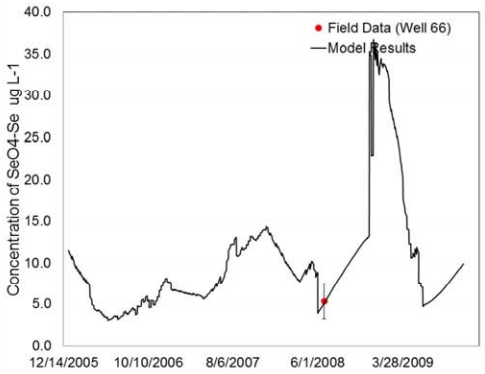
Field Data (Well 66)
Model Results
Concentration of SeO4-Se ug L-1
40.0
35.0
30.0
25.0
20.0
15.0
10.0
5.0
0.0
12/14/2005
10/10/2006
8/6/2007
6/1/2008
3/28/2009

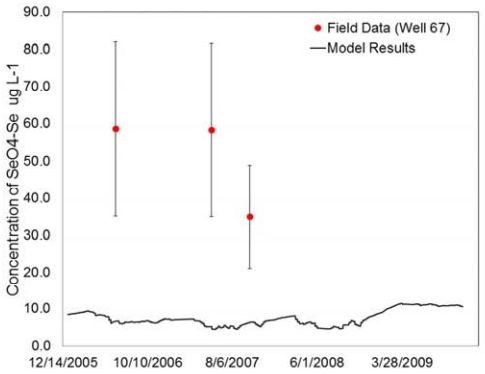
Field Data (Well 67)
Model Results
Concentration of SeO4-Se ug L-1
90.0
80.0
70.0
60.0
50.0
40.0
30.0
20.0
10.0
0.0
12/14/2005
10/10/2006
8/6/2007
6/1/2008
3/28/2009

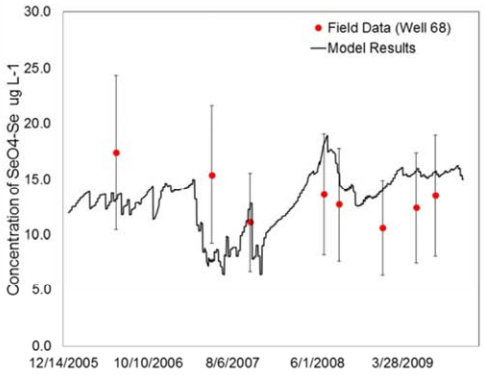
Field Data (Well 68)
Model Results
Concentration of SeO4-Se ug L-1
30.0
25.0
20.0
15.0
10.0
5.0
0.0
12/14/2005
10/10/2006
8/6/2007
6/1/2008
3/28/2009

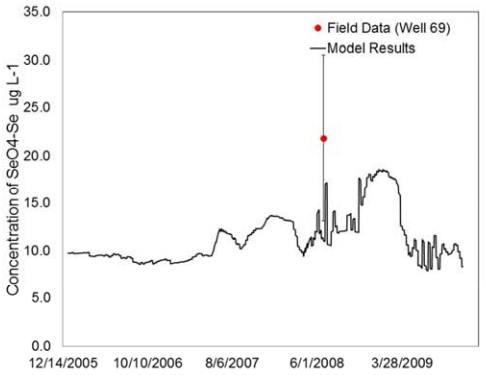
Field Data (Well 69)
Model Results
Concentration of SeO4-Se ug L-1
35.0
30.0
25.0
20.0
15.0
10.0
5.0
0.0
12/14/2005
10/10/2006
8/6/2007
6/1/2008
3/28/2009

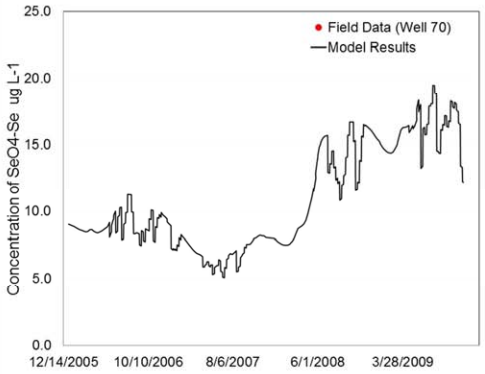
Field Data (Well 70)
Model Results
Concentration of SeO4-Se ug L-1
25.0
20.0
15.0
10.0
5.0
0.0
12/14/2005
10/10/2006
8/6/2007
6/1/2008
3/28/2009

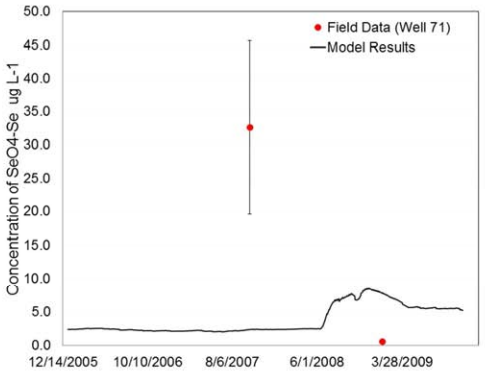
Field Data (Well 71)
Model Results
Concentration of SeO4-Se ug L-1
50.0
45.0
40.0
35.0
30.0
25.0
20.0
15.0
10.0
5.0
0.0
12/14/2005
10/10/2006
8/6/2007
6/1/2008
3/28/2009

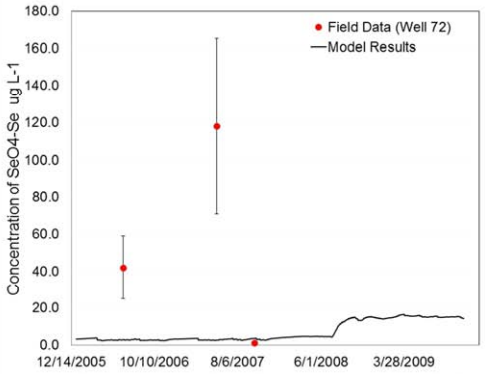
Field Data (Well 72)
Model Results
Concentration of SeO4-Se ug L-1
180.0
160.0
140.0
120.0
100.0
80.0
60.0
40.0
20.0
0.0
12/14/2005
10/10/2006
8/6/2007
6/1/2008
3/28/2009

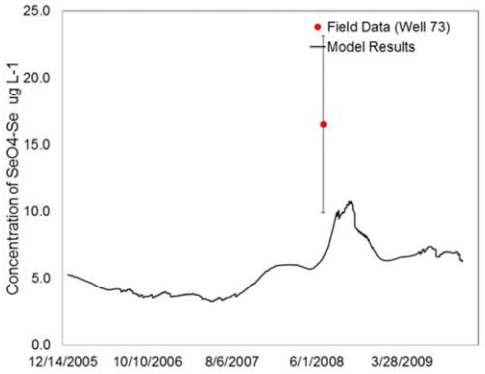
Field Data (Well 73)
Model Results
Concentration of SeO4-Se ug L-1
25.0
20.0
15.0
10.0
5.0
0.0
12/14/2005
10/10/2006
8/6/2007
6/1/2008
3/28/2009

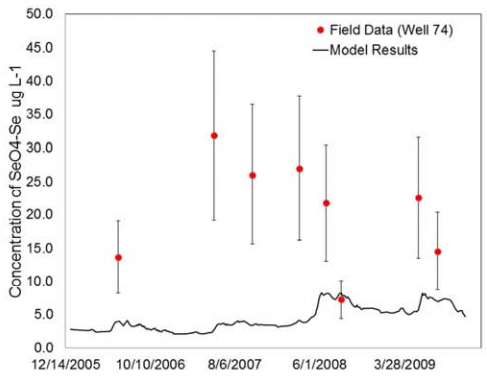
Field Data (Well 74)
Model Results
Concentration of SeO4-Se ug L-1
50.0
45.0
40.0
35.0
30.0
25.0
20.0
15.0
10.0
5.0
0.0
12/14/2005
10/10/2006
8/6/2007
6/1/2008
3/28/2009

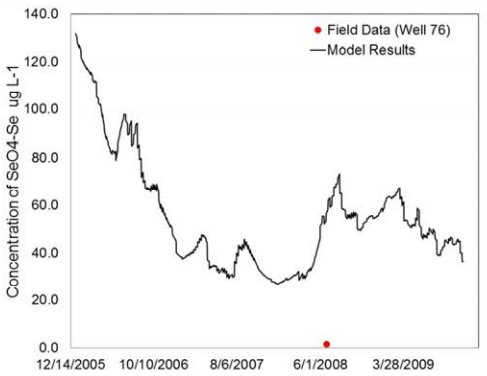
Field Data (Well 76)
Model Results
Concentration of SeO4-Se ug L-1
140.0
120.0
100.0
80.0
60.0
40.0
20.0
0.0
12/14/2005
10/10/2006
8/6/2007
6/1/2008
3/28/2009

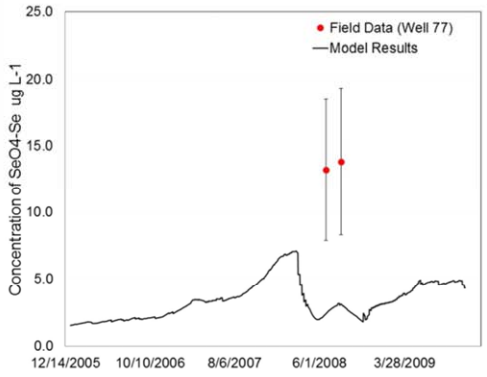
Field Data (Well 77)
Model Results
Concentration of SeO4-Se ug L-1
25.0
20.0
15.0
10.0
5.0
0.0
12/14/2005
10/10/2006
8/6/2007
6/1/2008
3/28/2009

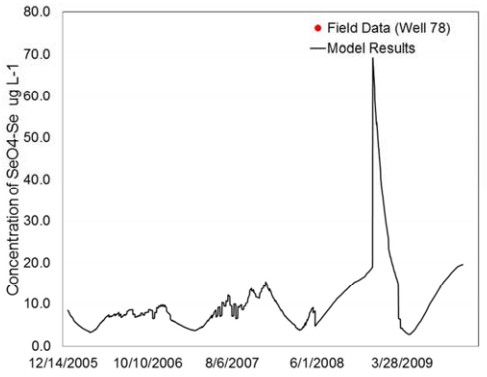
Field Data (Well 78)
Model Results
Concentration of SeO4-Se ug L-1
80.0
70.0
60.0
50.0
40.0
30.0
20.0
10.0
0.0
12/14/2005
10/10/2006
8/6/2007
6/1/2008
3/28/2009

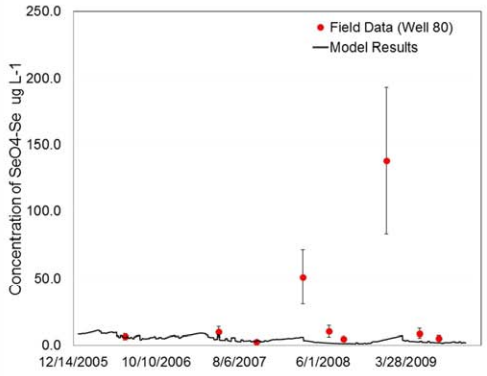
Field Data (Well 80)
Model Results
Concentration of SeO4-Se ug L-1
250.0
200.0
150.0
100.0
50.0
0.0
12/14/2005
10/10/2006
8/6/2007
6/1/2008
3/28/2009

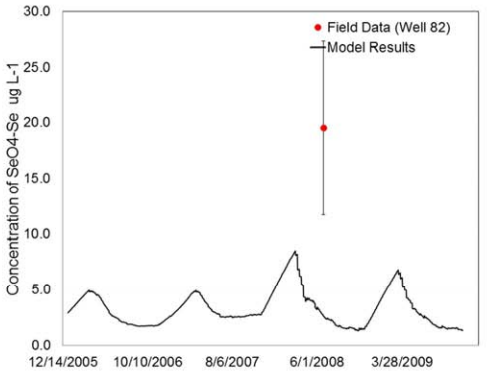
Field Data (Well 82)
Model Results
Concentration of SeO4-Se ug L-1
30.0
25.0
20.0
15.0
10.0
5.0
0.0
12/14/2005
10/10/2006
8/6/2007
6/1/2008
3/28/2009

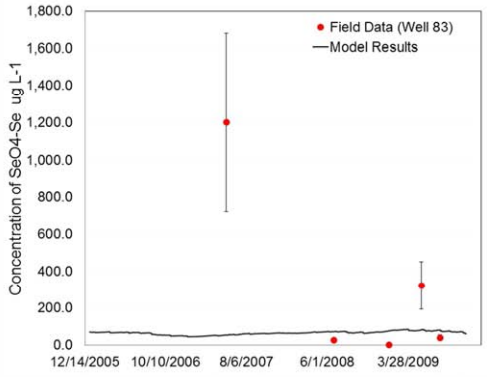
Field Data (Well 83)
Model Results
Concentration of SeO4-Se ug L-1
1,800.0
1,600.0
1,400.0
1,200.0
1,000.0
800.0
600.0
400.0
200.0
0.0
12/14/2005
10/10/2006
8/6/2007
6/1/2008
3/28/2009

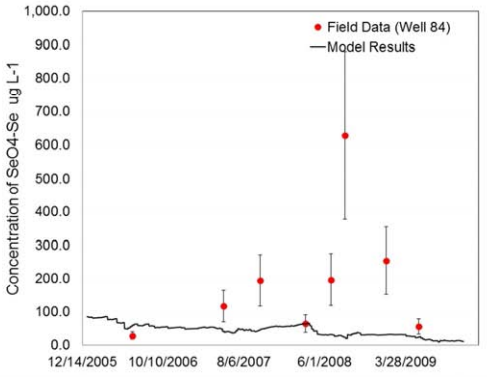
Field Data (Well 84)
Model Results
Concentration of SeO4-Se ug L-1
1,000.0
900.0
800.0
700.0
600.0
500.0
400.0
300.0
200.0
100.0
0.0
12/14/2005
10/10/2006
8/6/2007
6/1/2008
3/28/2009

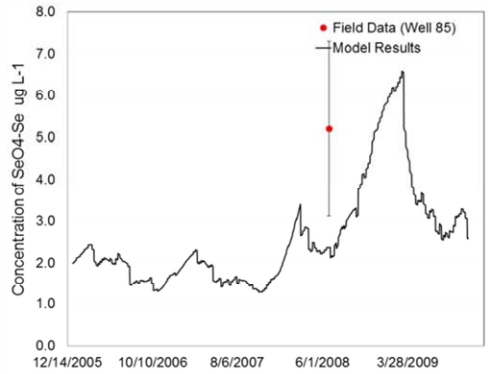
Field Data (Well 85)
Model Results
Concentration of SeO4-Se ug L-1
8.0
7.0
6.0
5.0
4.0
3.0
2.0
1.0
0.0
12/14/2005
10/10/2006
8/6/2007
6/1/2008
3/28/2009

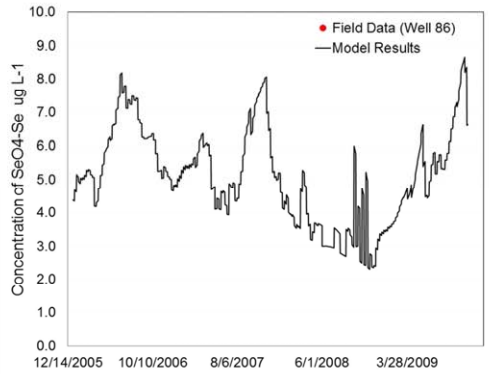
Field Data (Well 86)
Model Results
Concentration of SeO4-Se ug L-1
10.0
9.0
8.0
7.0
6.0
5.0
4.0
3.0
2.0
1.0
0.0
12/14/2005
10/10/2006
8/6/2007
6/1/2008
3/28/2009

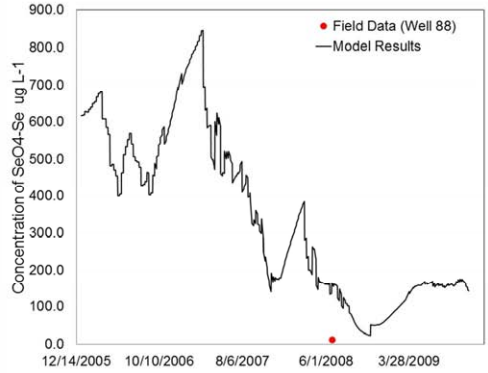
Field Data (Well 88)
Model Results
Concentration of SeO4-Se ug L-1
900.0
800.0
700.0
600.0
500.0
400.0
300.0
200.0
100.0
0.0
12/14/2005
10/10/2006
8/6/2007
6/1/2008
3/28/2009

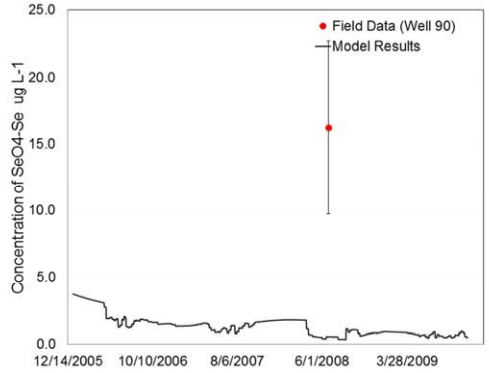
Field Data (Well 90)
Model Results
Concentration of SeO4-Se ug L-1
25.0
20.0
15.0
10.0
5.0
0.0
12/14/2005
10/10/2006
8/6/2007
6/1/2008
3/28/2009

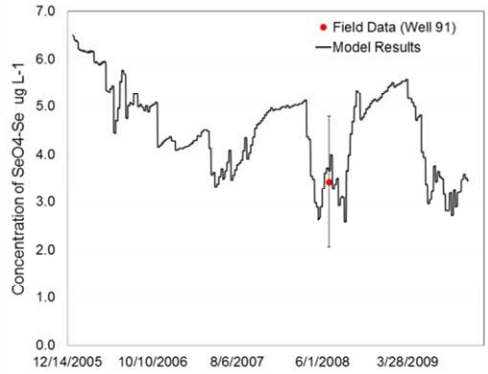
Field Data (Well 91)
Model Results
Concentration of SeO4-Se ug L-1
7.0
6.0
5.0
4.0
3.0
2.0
1.0
0.0
12/14/2005
10/10/2006
8/6/2007
6/1/2008
3/28/2009

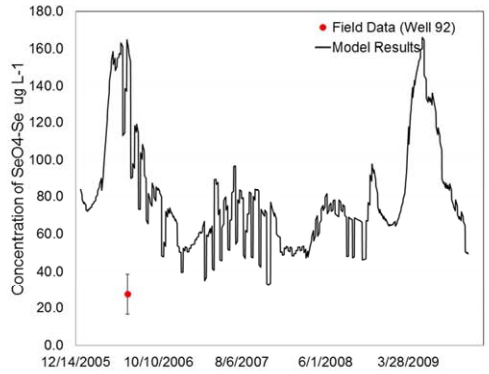
Field Data (Well 92)
Model Results
Concentration of SeO4-Se ug L-1
180.0
160.0
140.0
120.0
100.0
80.0
60.0
40.0
20.0
0.0
12/14/2005
10/10/2006
8/6/2007
6/1/2008
3/28/2009

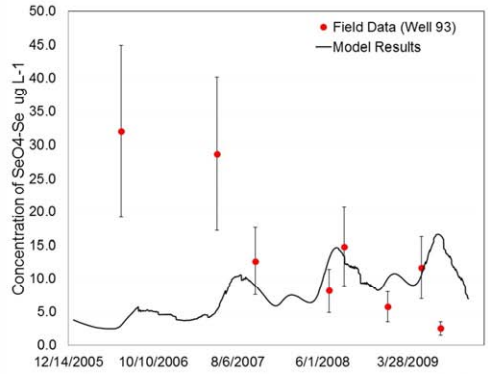
Field Data (Well 93)
Model Results
Concentration of SeO4-Se ug L-1
50.0
45.0
40.0
35.0
30.0
25.0
20.0
15.0
10.0
5.0
0.0
12/14/2005
10/10/2006
8/6/2007
6/1/2008
3/28/2009

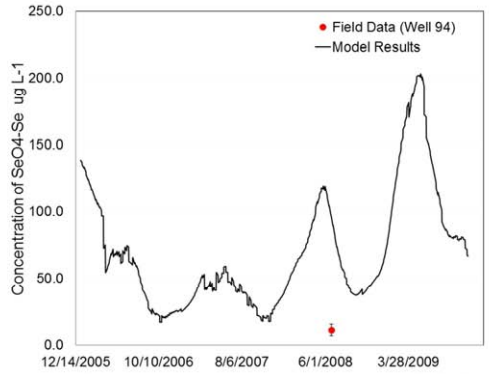
Field Data (Well 94)
Model Results
Concentration of SeO4-Se ug L-1
250.0
200.0
150.0
100.0
50.0
0.0
12/14/2005
10/10/2006
8/6/2007
6/1/2008
3/28/2009

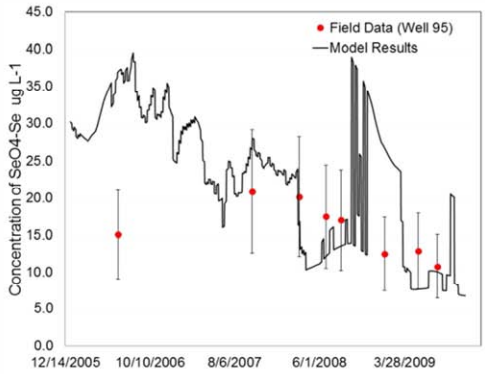
Field Data (Well 95)
Model Results
Concentration of SeO4-Se ug L-1
45.0
40.0
35.0
30.0
25.0
20.0
15.0
10.0
5.0
0.0
12/14/2005
10/10/2006
8/6/2007
6/1/2008
3/28/2009

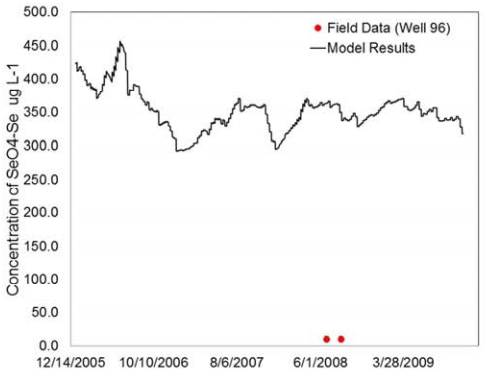
Field Data (Well 96)
Model Results
Concentration of SeO4-Se ug L-1
500.0
450.0
400.0
350.0
300.0
250.0
200.0
150.0
100.0
50.0
0.0
12/14/2005
10/10/2006
8/6/2007
6/1/2008
3/28/2009

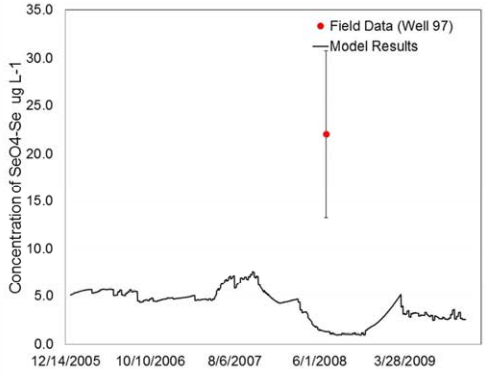
Field Data (Well 97)
Model Results
Concentration of SeO4-Se ug L-1
35.0
30.0
25.0
20.0
15.0
10.0
5.0
0.0
12/14/2005
10/10/2006
8/6/2007
6/1/2008
3/28/2009

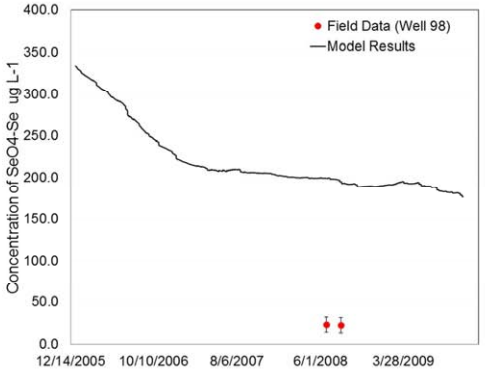
Field Data (Well 98)
Model Results
Concentration of SeO4-Se ug L-1
400.0
350.0
300.0
250.0
200.0
150.0
100.0
50.0
0.0
12/14/2005
10/10/2006
8/6/2007
6/1/2008
3/28/2009

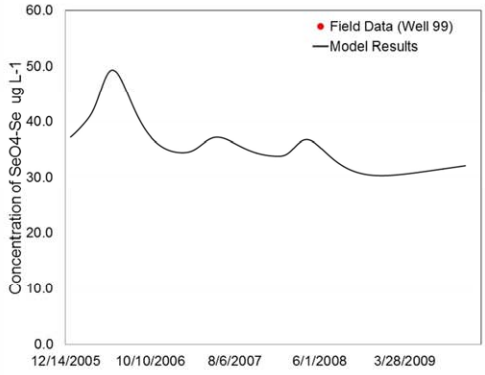
Field Data (Well 99)
Model Results
Concentration of SeO4-Se ug L-1
60.0
50.0
40.0
30.0
20.0
10.0
0.0
12/14/2005
10/10/2006
8/6/2007
6/1/2008
3/28/2009

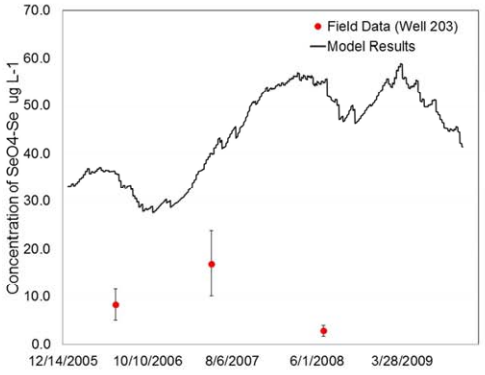
Field Data (Well 203)
Model Results
Concentration of SeO4-Se ug L-1
70.0
60.0
50.0
40.0
30.0
20.0
10.0
0.0
12/14/2005
10/10/2006
8/6/2007
6/1/2008
3/28/2009

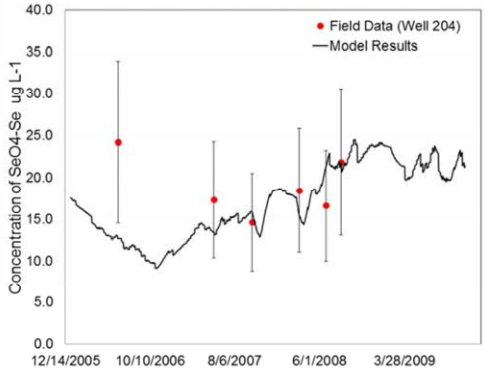
Field Data (Well 204)
Model Results
Concentration of SeO4-Se ug L-1
40.0
35.0
30.0
25.0
20.0
15.0
10.0
5.0
0.0
12/14/2005
10/10/2006
8/6/2007
6/1/2008
3/28/2009

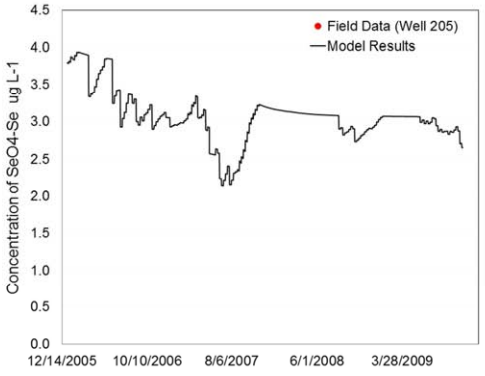
Field Data (Well 205)
Model Results
Concentration of SeO4-Se ug L-1
4.5
4.0
3.5
3.0
2.5
2.0
1.5
1.0
0.5
0.0
12/14/2005
10/10/2006
8/6/2007
6/1/2008
3/28/2009

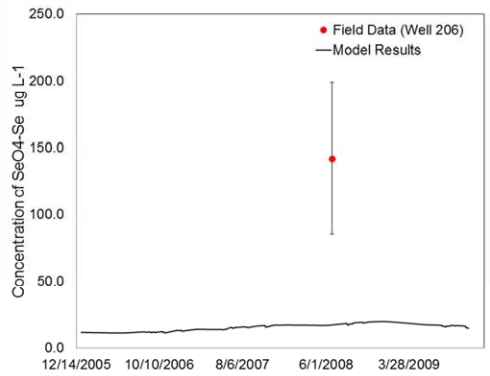
Field Data (Well 206)
Model Results
Concentration of SeO4-Se ug L-1
250.0
200.0
150.0
100.0
50.0
0.0
12/14/2005
10/10/2006
8/6/2007
6/1/2008
3/28/2009

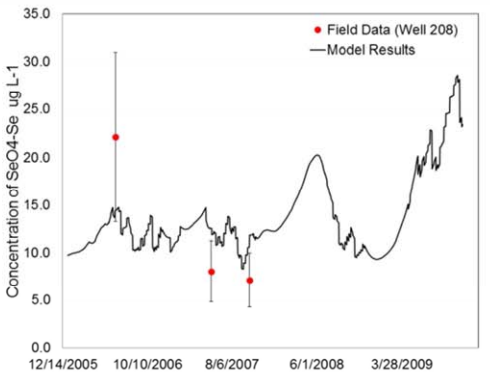
Field Data (Well 208)
Model Results
Concentration of SeO4-Se ug L-1
35.0
30.0
25.0
20.0
15.0
10.0
5.0
0.0
12/14/2005
10/10/2006
8/6/2007
6/1/2008
3/28/2009

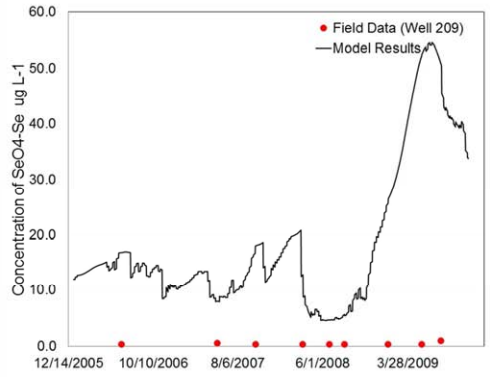
Field Data (Well 209)
Model Results
Concentration of SeO4-Se ug L-1
60.0
50.0
40.0
30.0
20.0
10.0
0.0
12/14/2005
10/10/2006
8/6/2007
6/1/2008
3/28/2009

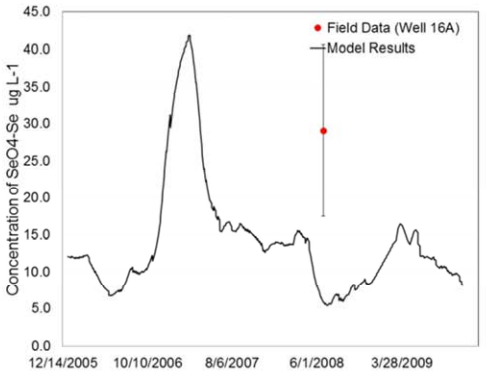
Field Data (Well 16A)
Model Results
Concentration of SeO4-Se ug L-1
45.0
40.0
35.0
30.0
25.0
20.0
15.0
10.0
5.0
0.0
12/14/2005
10/10/2006
8/6/2007
6/1/2008
3/28/2009

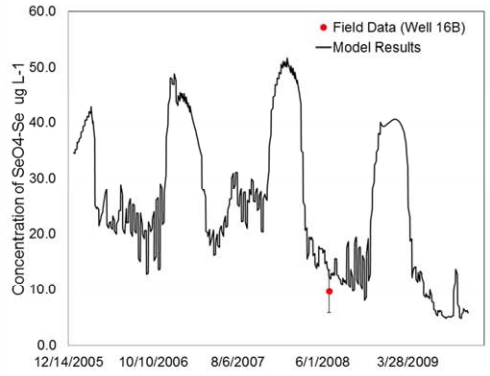
Field Data (Well 16B)
Model Results
Concentration of SeO4-Se ug L-1
60.0
50.0
40.0
30.0
20.0
10.0
0.0
12/14/2005
10/10/2006
8/6/2007
6/1/2008
3/28/2009

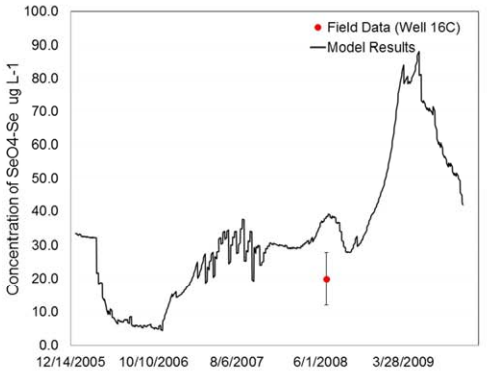
Field Data (Well 16C)
Model Results
Concentration of SeO4-Se ug L-1
100.0
90.0
80.0
70.0
60.0
50.0
40.0
30.0
20.0
10.0
0.0
12/14/2005
10/10/2006
8/6/2007
6/1/2008
3/28/2009

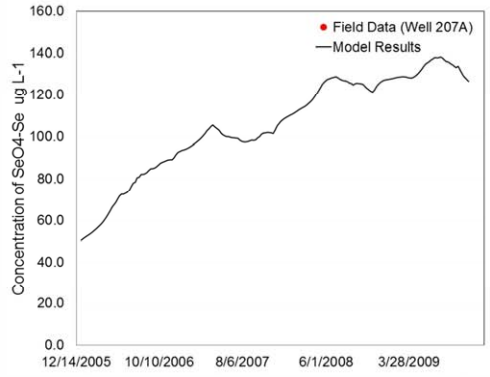
Field Data (Well 207A)
Model Results
Concentration of SeO4-Se ug L-1
160.0
140.0
120.0
100.0
80.0
60.0
40.0
20.0
0.0
12/14/2005
10/10/2006
8/6/2007
6/1/2008
3/28/2009

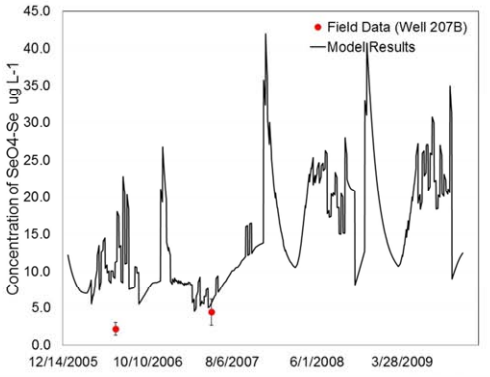
Field Data (Well 207B)
Model Results
Concentration of SeO4-Se ug L-1
45.0
40.0
35.0
30.0
25.0
20.0
15.0
10.0
5.0
0.0
12/14/2005
10/10/2006
8/6/2007
6/1/2008
3/28/2009

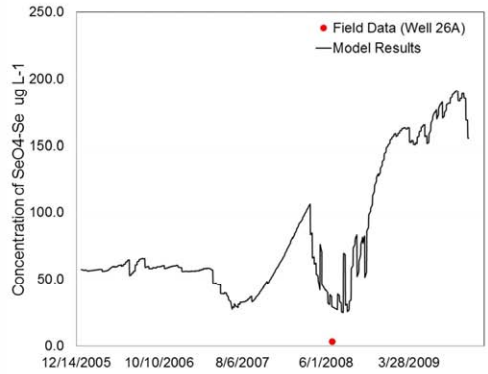
Field Data (Well 26A)
Model Results
Concentration of SeO4-Se ug L-1
250.0
200.0
150.0
100.0
50.0
0.0
12/14/2005
10/10/2006
8/6/2007
6/1/2008
3/28/2009

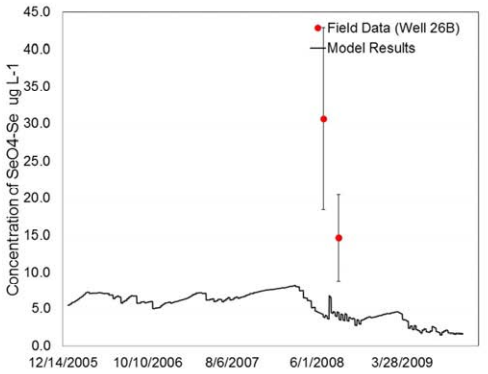
Field Data (Well 26B)
Model Results
Concentration of SeO4-Se ug L-1
45.0
40.0
35.0
30.0
25.0
20.0
15.0
10.0
5.0
0.0
12/14/2005
10/10/2006
8/6/2007
6/1/2008
3/28/2009

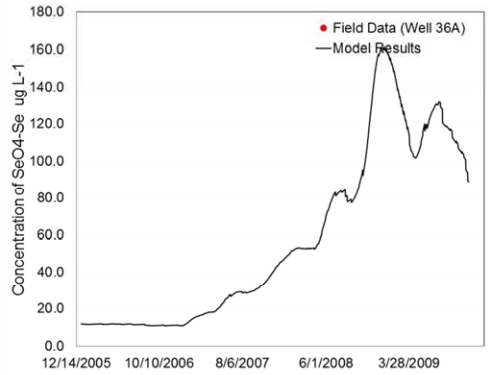
Field Data (Well 36A)
Model Results
Concentration of SeO4-Se ug L-1
180.0
160.0
140.0
120.0
100.0
80.0
60.0
40.0
20.0
0.0
12/14/2005
10/10/2006
8/6/2007
6/1/2008
3/28/2009

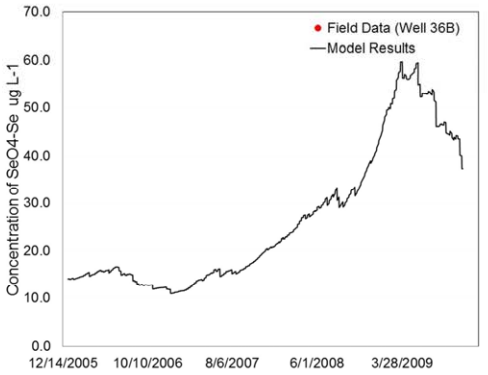
Field Data (Well 36B)
Model Results
Concentration of SeO4-Se ug L-1
70.0
60.0
50.0
40.0
30.0
20.0
10.0
0.0
12/14/2005
10/10/2006
8/6/2007
6/1/2008
3/28/2009

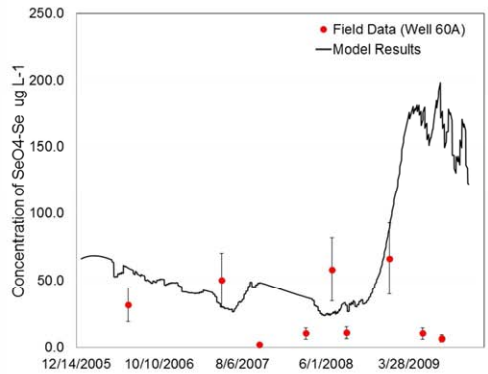
Field Data (Well 60A)
Model Results
Concentration of SeO4-Se ug L-1
250.0
200.0
150.0
100.0
50.0
0.0
12/14/2005
10/10/2006
8/6/2007
6/1/2008
3/28/2009

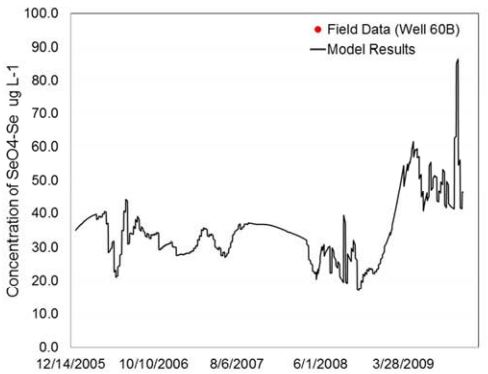
Field Data (Well 60B)
Model Results
Concentration of SeO4-Se ug L-1
100.0
90.0
80.0
70.0
60.0
50.0
40.0
30.0
20.0
10.0
0.0
12/14/2005
10/10/2006
8/6/2007
6/1/2008
3/28/2009

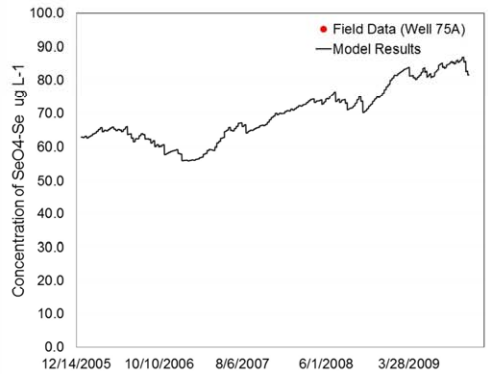
Field Data (Well 75A)
Model Results
Concentration of SeO4-Se ug L-1
100.0
90.0
80.0
70.0
60.0
50.0
40.0
30.0
20.0
10.0
0.0
12/14/2005
10/10/2006
8/6/2007
6/1/2008
3/28/2009

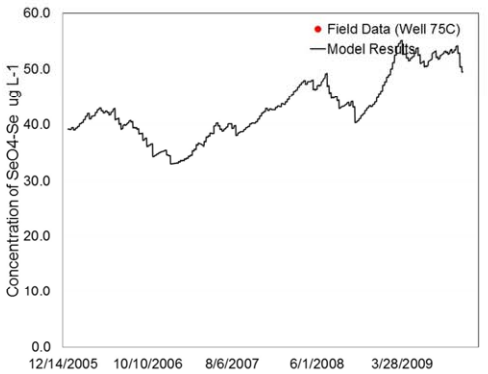
Field Data (Well 75C)
Model Results
Concentration of SeO4-Se ug L-1
60.0
50.0
40.0
30.0
20.0
10.0
0.0
12/14/2005
10/10/2006
8/6/2007
6/1/2008
3/28/2009

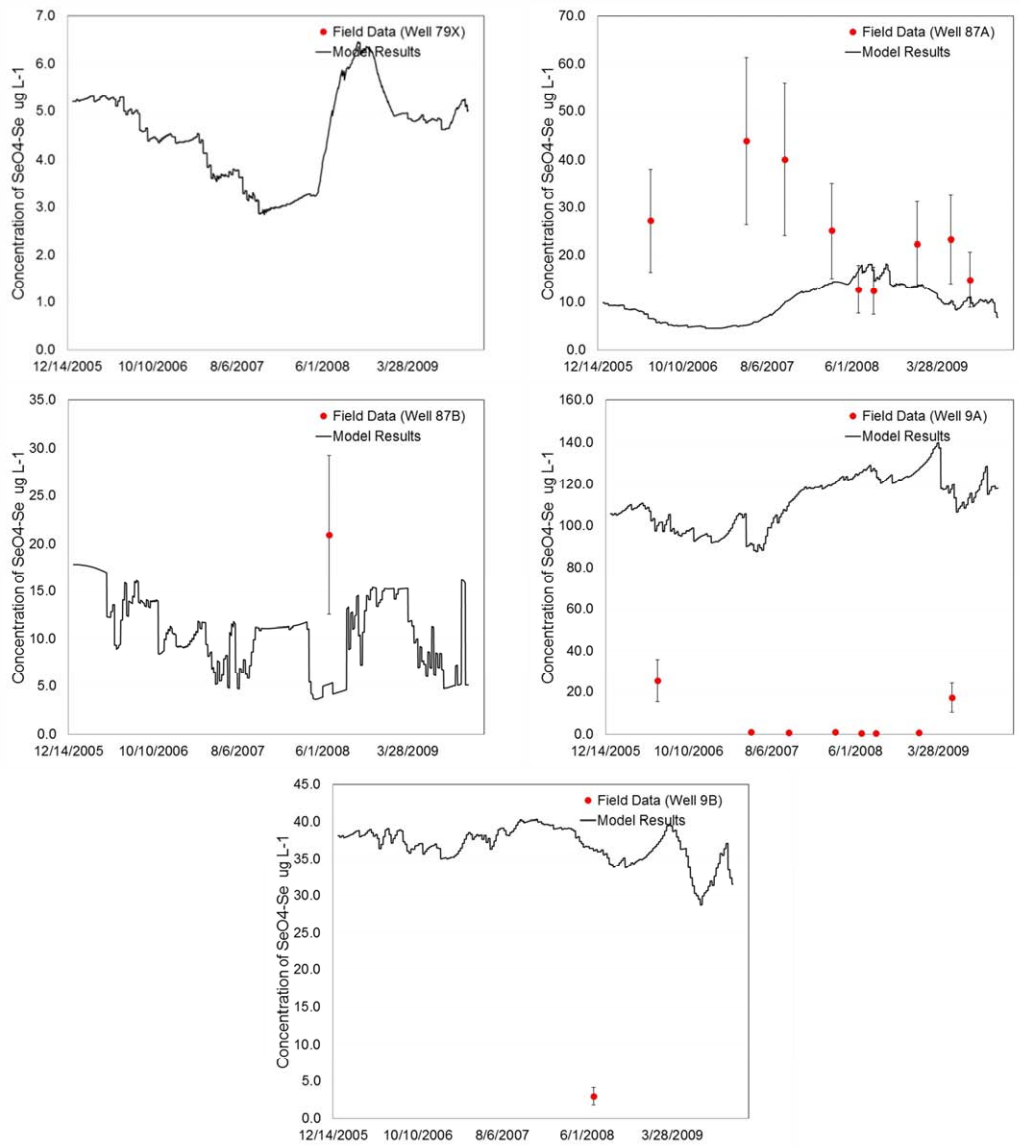

Figure B- 3. Comparison of simulated and observed SeO_4 concentration at observation wells during 2006-2009. Simulated values are taken from grid cells in layer 4 of the model that coincide with the location of the observation well. Red dots indicate observed measurements of concentration. Error bars are included to indicate the variability of the observed value for a representative cultivated field.

APPENDIX C

RESULTS FROM SENSITIVITY ANALYSIS OF THE UZF-RT3DAG MODEL FOR THE UPSTREAM STUDY REGION

This appendix contains results from the sensitivity test of the UZF-RT3DAG model for the Upstream Study Region study site that are too numerous to include in Chapter 6. These results provide important insights into the working of the model and the influence of system parameters, system inputs, command area, and crop type on resultant groundwater concentrations and mass loadings to surface. The FAST (Fourier Amplitude Sensitivity Test) (Cukier et al., 1973) method is used to determine the influence of parameters and system inputs/outputs on concentrations and loadings of NO_3 and SeO_4. The following parameters and system inputs/outputs were analyzed for impact on model results:

- Seasonal loading of NH_4 fertilizer F_{NH_4}
- Seasonal N uptake N_{up}
- Seasonal Se uptake Se_{up}
- C_{NO_3} in surface water
- C_{SeO_4} in surface water
- Rate of litter pool decomposition λ_L
- Rate of humus pool decomposition λ_H
- Rate of autotrophic reduction of O_2 in the presence of shale $\lambda_{O_2}^{auto}$
- Rate of autotrophic reduction of NO_3 in the presence of shale $\lambda_{NO_3}^{auto}$
- Rate of nitrification λ_{nit}
- Rate of NH_4 volatilization λ_{vol}

- Rate of heterotrophic denitrification $\lambda_{NO_3}^{het}$
- Rate of heterotrophic reduction of SeO_4 $\lambda_{SeO_4}^{het}$.

A total of 1053 simulations were run. Parameter values were perturbed using a coefficient of variation (CV) of 0.2 for all parameters except the concentrations of surface water, which were perturbed with a CV of 0.3. For each simulation, model results were processed with the aim of answering the following questions:

1. For the entire model domain, which parameters govern groundwater concentration and mass loading?
2. For each command area, which parameters govern C_{NO_3} and C_{SeO_4}?
3. For each crop type, which parameters govern C_{NO_3} and C_{SeO_4}?
4. For each crop type, which parameters govern leaching of NO_3 and SeO_4?

Providing answers for these questions can lend valuable insights into the system parameters that need to be quantified with more accuracy (either through field work or laboratory experiments), as well as the system inputs/outputs that can potentially be controlled in the field to remediate elevated concentrations and mass loadings. To address items (1) through (4), model results for each simulation were averaged according to (1) entire model domain, (2) each command area, and (3, 4) all cells corresponding to a certain crop type. Averages were calculated for C_{NO_3} and C_{SeO_4} in model layers 1, 2, 3, and 4, and the leaching flux of SeO_4 and NO_3 for model layers 2 (i.e., the leaching flux from layer 1 to layer 2), 3, and 4. For (1), the total mass loading from the aquifer to the Arkansas River also was calculated. The following sections show results for items (1) through (4) for both NO_3 and SeO_4. Results are presented using global sensitivity plots, with

the first-order sensitivity index (the main effect of the parameter on the change in model output) along the abscissa and the interaction effect (effect of the parameter on the change in model output due to interaction with other parameters) along the ordinate. The parameter labels in the global sensitivity plots can be interpreted as follows:

- **FNH4** = Seasonal loading of NH_4 fertilizer F_{NH_4}
- **NUP** = Seasonal N uptake N_{up}
- **kUPSE** = Seasonal Se uptake Se_{up}
- **CANALNO3** = C_{NO_3} in surface water
- **CANALSEO4** = C_{SeO_4} in surface water
- **kL** = Rate of litter pool decomposition λ_L
- **kH** = Rate of humus pool decomposition λ_H
- **kO2A** = Rate of autotrophic reduction of O_2 in the presence of shale $\lambda_{O_2}^{auto}$
- **kDENA** = Rate of autotrophic reduction of NO_3 in the presence of shale $\lambda_{NO_3}^{auto}$
- **kNIT** = Rate of nitrification λ_{nit}
- **kVOL** = Rate of NH_4 volatilization λ_{vol}
- **kDENH** = Rate of heterotrophic denitrification $\lambda_{NO_3}^{het}$
- **kSEO4** = Rate of heterotrophic reduction of SeO_4 $\lambda_{SeO_4}^{het}$.

C1. PARAMETERS GOVERNING NO_3

C1.1 Parameter governing global concentration and loading of NO_3

Figure C-1 shows the sensitivity indices for the parameters for C_{NO_3} in layers 1-4, leaching in layer 2-4, and mass loading of NO_3 to the Arkansas River. As seen in Figures C-1A to C-1D, λ_{nit} has the strongest influence on resulting C_{NO_3} in layers 1-4, with F_{NH_4} and N_{up} having a small influence in layers 1-3 and the C_{NO_3} in canal water having a moderate influence in layer 4, likely due to canal seepage. The C_{NO_3} in layer 4 is also influenced to a small degree by $\lambda_{NO_3}^{auto}$, due to the presence of shale and subsequent occurrence of autotrophic denitrification in certain areas of the aquifer. As seen in Figures C-1E to C-1G, λ_{nit} also governs the leaching in the lower layers of the model, although $\lambda_{NO_3}^{het}$ govern the leaching from layer 1 to layer 2, which correspond to the lower half of the root zone. As seen in Figure C-1H, mass loading of NO_3 is governed by both λ_{nit} and the C_{NO_3} in canal water.

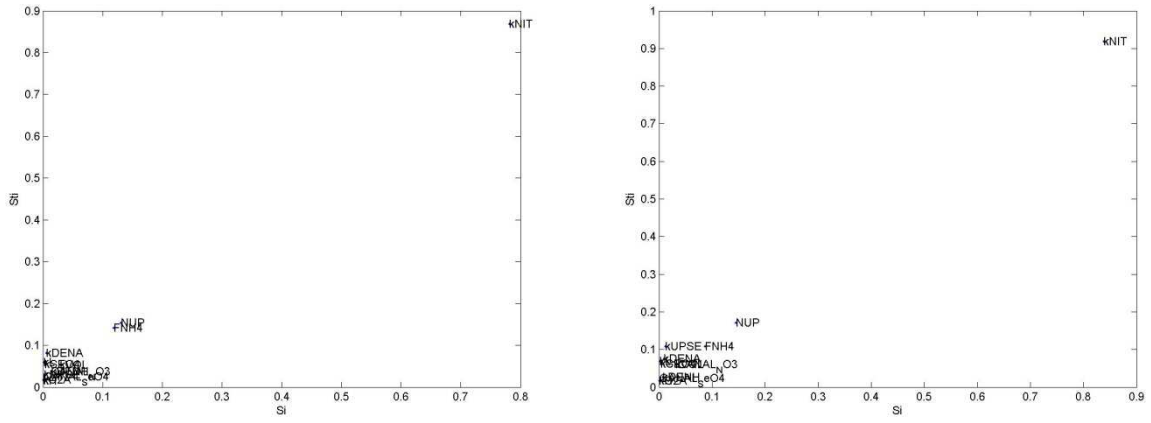

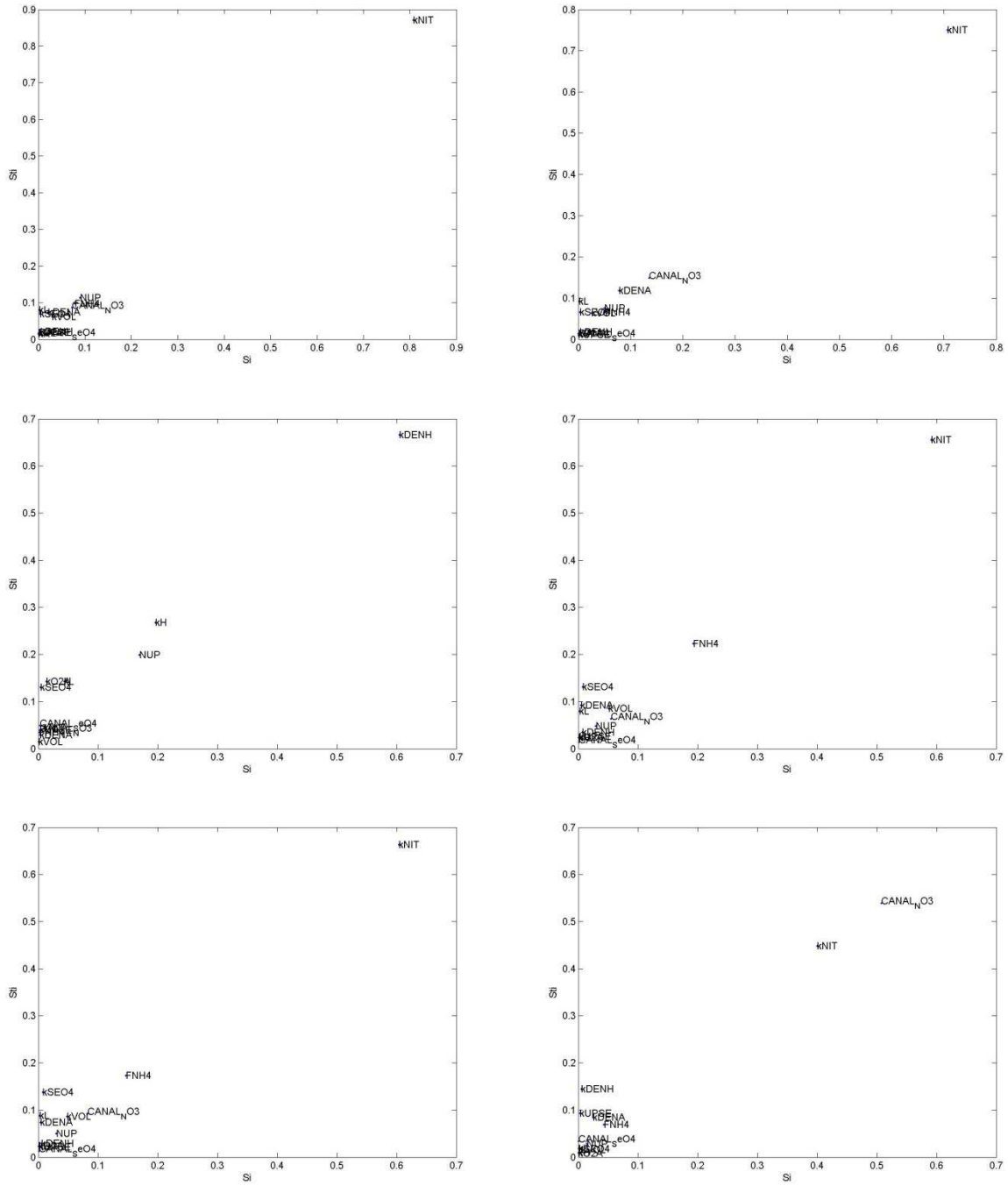

Figure C- 1. Sensitivity indices indicating the degree of parameter influence on C_{NO_3} in (A) layer 1, (B) layer 2, (C) layer 3, and (D) layer 4, NO_3 leaching from (E) layers 1 to 2, (F), layers 2 to 3, and (G) layers 3 to 4, and (H) NO_3 mass loading to the Arkansas River.

C1.2 Parameter governing C_{NO_3} in command areas

Figure C-2 shows the sensitivity indices for the parameters for C_{NO_3} in layer 4 for each of the six command areas. The results show important differences between the command areas, with a mixture of λ_{nit}, canal C_{NO_3}, N_{up}, and $\lambda_{NO_3}^{auto}$ providing noteworthy impacts on C_{NO_3}. For example, C_{NO_3} in the Catlin command area (Figure C-2A) is influenced mostly by $\lambda_{NO_3}^{auto}$ due to the presence of shale within the spatial extent of the command area, both the Fort Lyon and Highline command areas are influenced strongly by λ_{nit}, and the other command areas influence mostly by canal C_{NO_3}. These results suggest that different best-management practices should be implemented based on the command area. For example, C_{NO_3} in the Fort Lyon and Highline command areas may be controlled by reducing the loading of fertilizer N and hence the amount of NO_3 that is produced via nitrification.

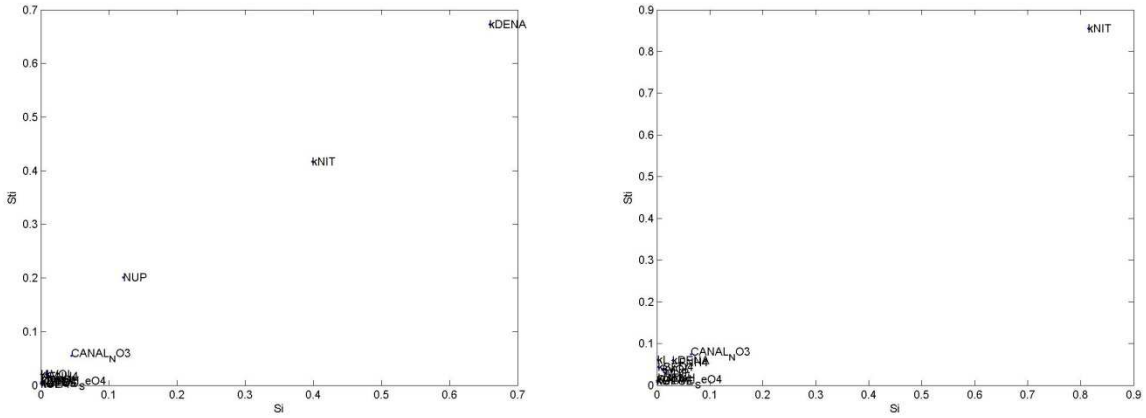

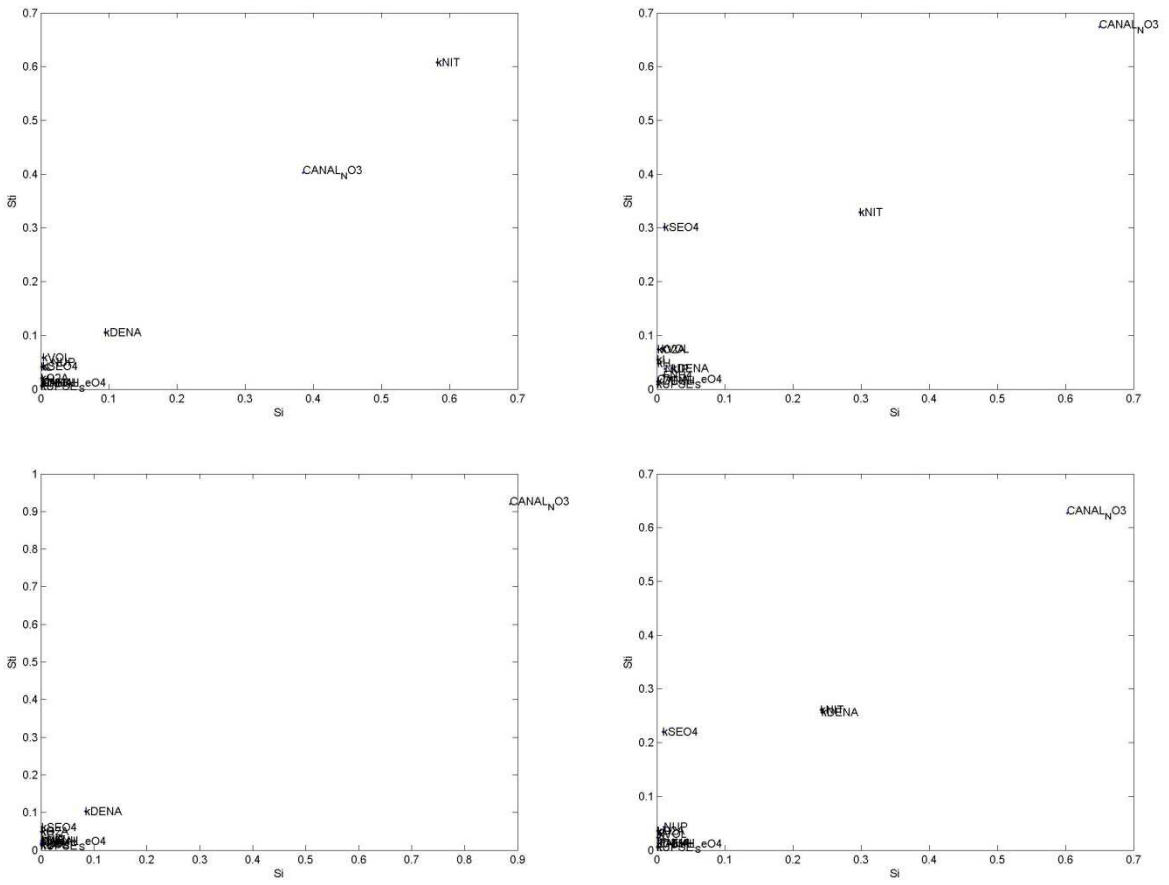

Figure C- 2. Sensitivity indices indicating the degree of parameter influence on C_{NO_3} in the (A) Catlin, (B) Fort Lyon, (C) Highline, (D) Holbrook, (E) Otero, and (F) Rocky Ford Ditch command areas.

C1.3 Parameter governing C_{NO_3} for each crop type

Figure C-3 shows the sensitivity indices for the parameters for C_{NO_3} in layer 4 for each of the crop types, i.e., the groups of cells that are associated with each crop type. As expected, λ_{nit} has a large influence on C_{NO_3} for a majority of the crop types. However, it is interesting to note that crops that receive small loadings of N fertilizer, such as alfalfa (Figure C-3A) and pasture (Figure C-3G) have are governed mostly by canal C_{NO_3} rather than λ_{nit}. The non-cultivated areas (Figure C-3C) also are governed by canal C_{NO_3} rather than knit, since there is no N fertilizer

loading. It is also interesting to note that crop types with a combined cultivated area that comprises a large portion of the model domain also are influenced by parameters besides λ_{nit}. Due to the large area of cultivation across the model domain, it is likely that a number of fields are adjacent to shale, and hence C_{NO_3} is influenced by $\lambda_{NO_3}^{auto}$. This occurs for corn (Figure C-3D), onion (Figure C-3F), Sorghum (Figure C-3I), and Spring Grain (Figure C-3J)

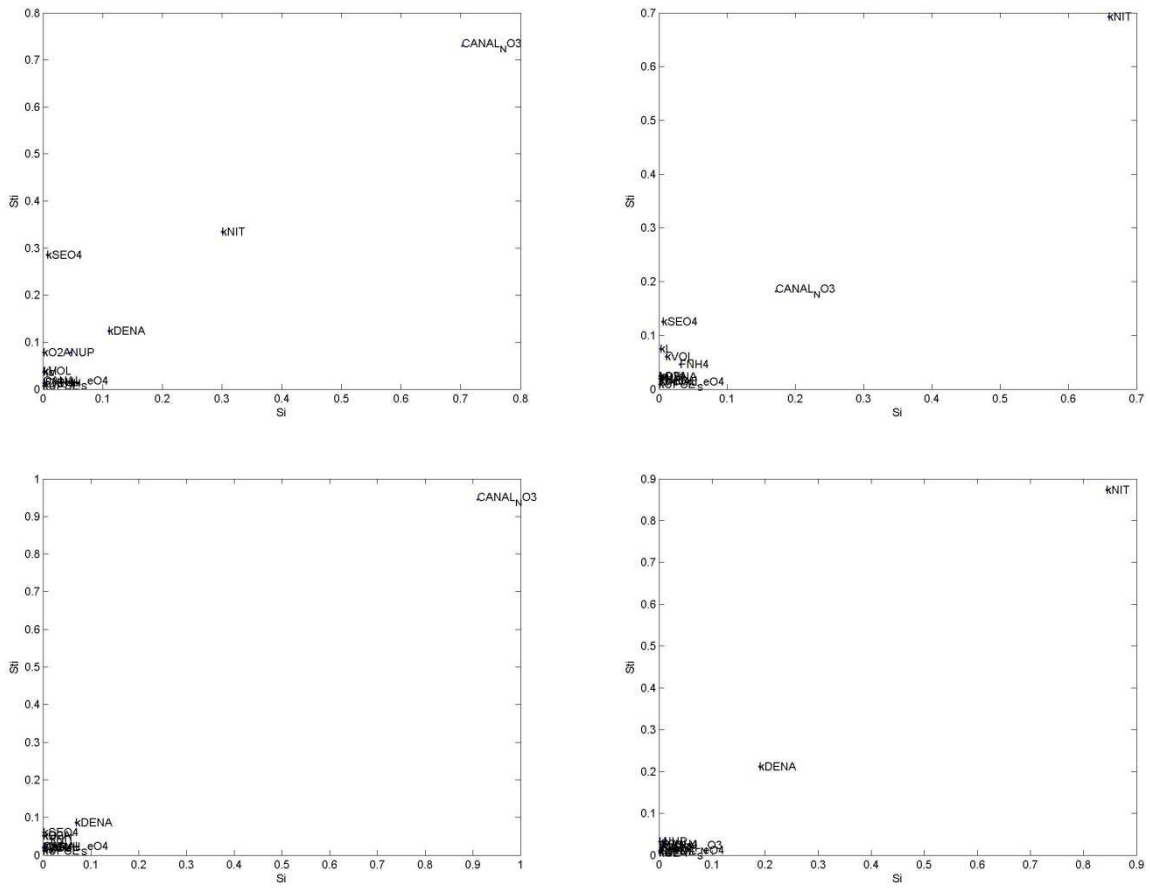

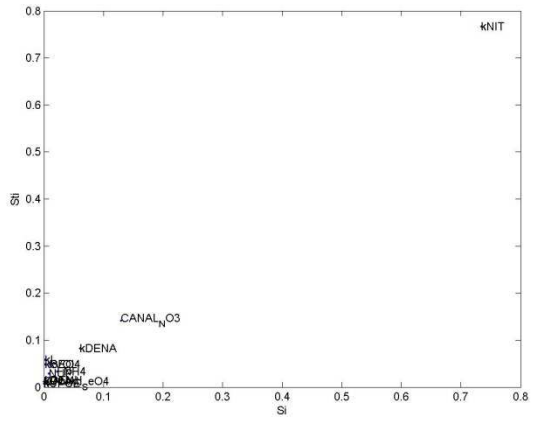
kNIT
kCANAL_NO3
kDENA
STi
Si

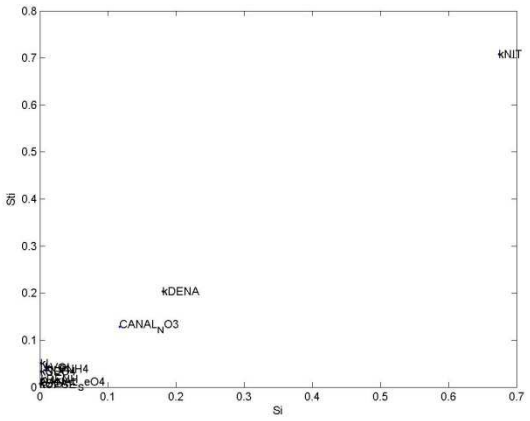
kNIT
kDENA
kCANAL_NO3
STi
Si

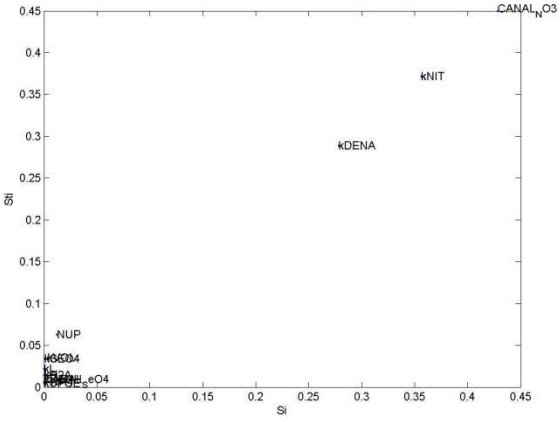
kCANAL_NO3
kNIT
kDENA
kNUP
STi
Si

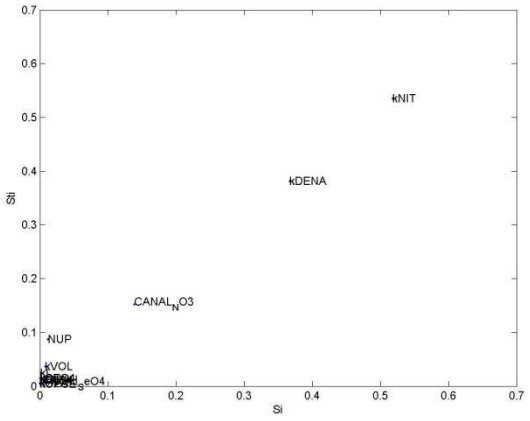
kNIT
kDENA
kCANAL_NO3
kNUP
kVOL
STi
Si

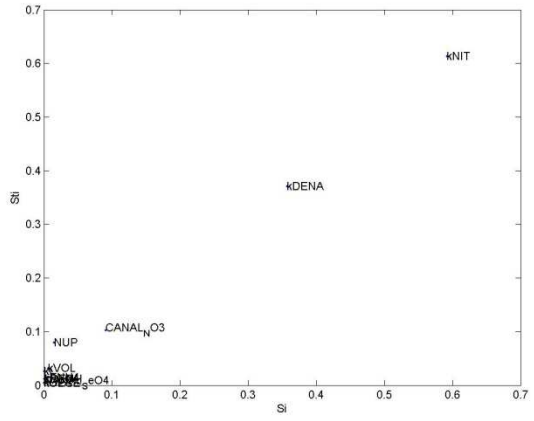
kNIT
kDENA
kCANAL_NO3
kNUP
kVOL
STi
Si

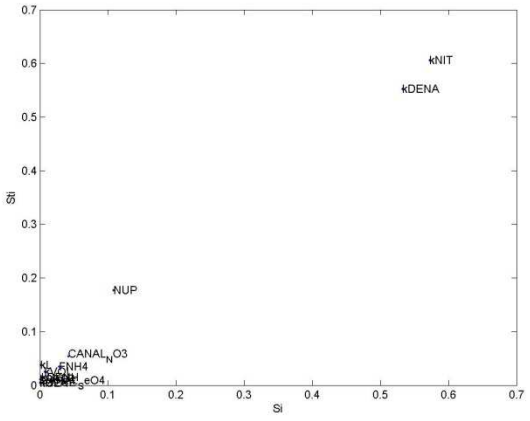
kNIT
kDENA
kNUP
kCANAL_NO3
STi
Si

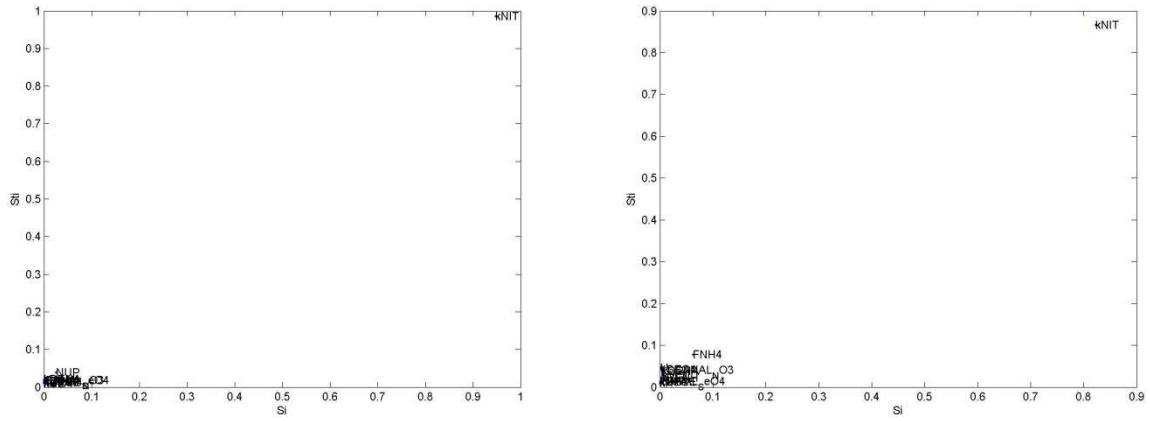

Figure C- 3. Sensitivity indices indicating the degree of parameter influence on C_{NO_3} for cells underlying (A) Alfalfa, (B) Bean, (C) Clear, (D) Corn, (E) Melon, (F) Onion, (G) Pasture, (H) Pumpkin, (I) Sorghum, (J) Spring Grain, (K) Sunflower, and (M) Vegetable.

C1.4 Parameter governing leaching flux of NO_3 for each crop type

Figure C-4 shows the sensitivity indices for the parameters for the leaching flux of NO3 from layers 3 to 4 for each of the crop types, i.e., the groups of cells that are associated with each crop type. As such, the results correspond to the leaching of NO_3 mass below a depth of 2.0 m. As seen in the figure, the leaching of NO_3 mass under the cultivated area of each crop type except for alfalfa (Figure C-4A) is governed by λ_{nit}, with the N fertilizer loading of alfalfa not enough to produce a governing influence of λ_{nit}. The non-cultivated areas (Figure C-4C) are governed by canal C_{NO_3}.

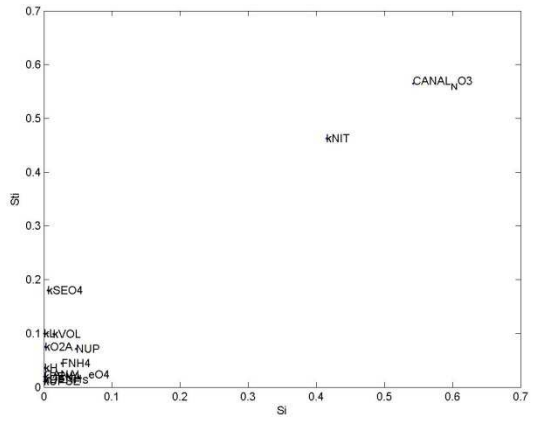
kNIT
kSEO4
klkVOL
kO2A
NUP
FNH4
Si
Sti

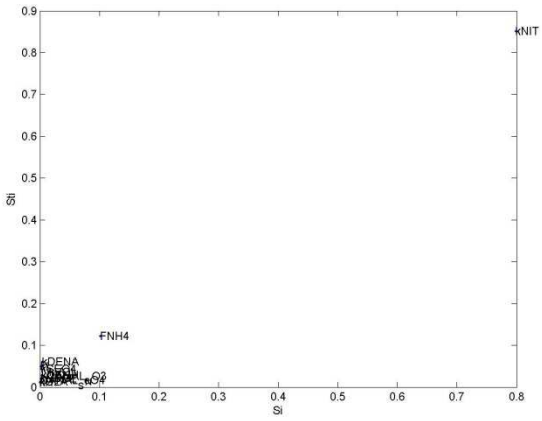
kNIT
FNH4
Si
Sti

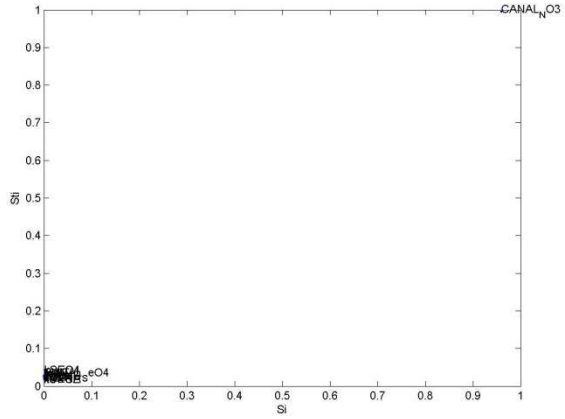
Si
Sti

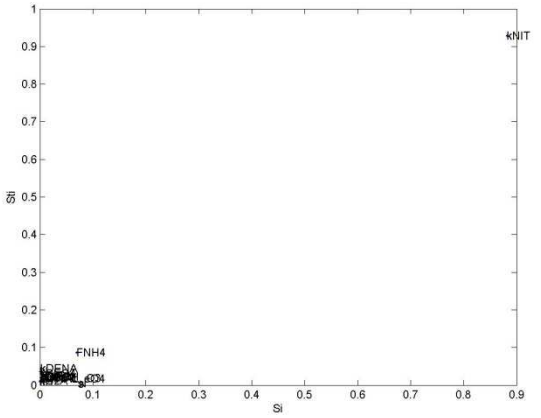
kNIT
FNH4
Si
Sti

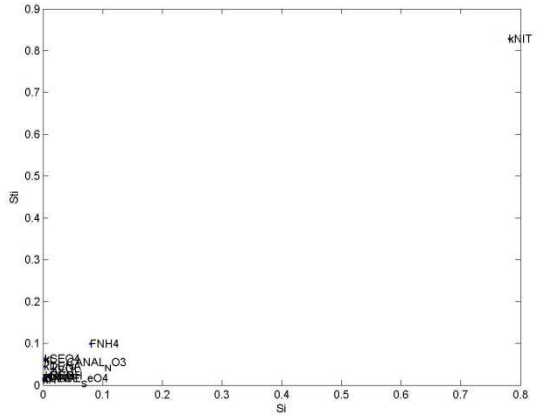
kNIT
FNH4
Si
Sti

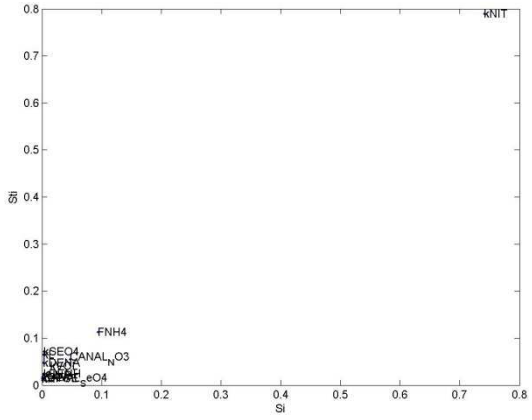
kNIT
FNH4
Si
Sti

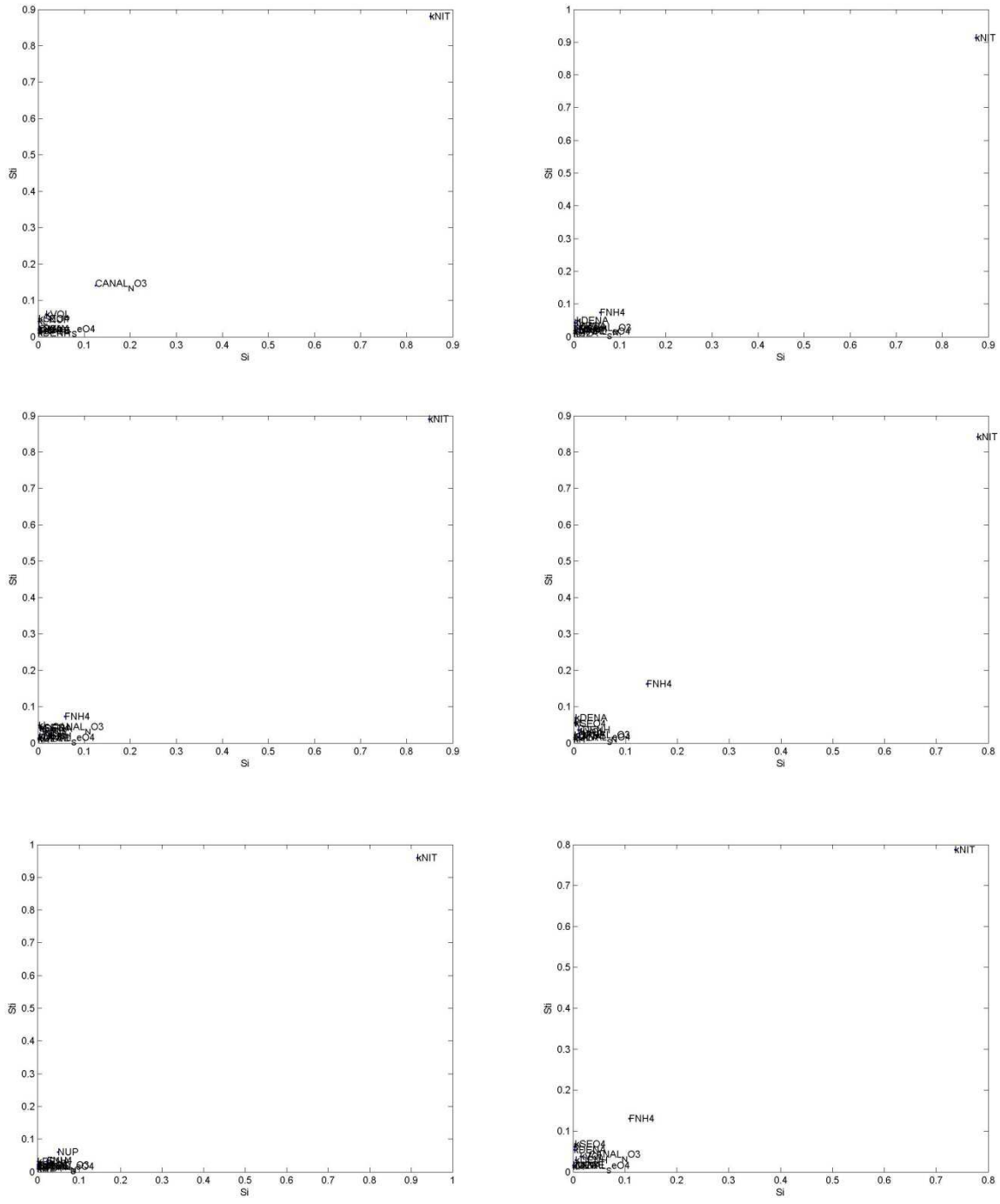

Figure C- 4. Sensitivity indices indicating the degree of parameter influence on leaching flux of NO_3 for cells underlying (A) Alfalfa, (B) Bean, (C) Clear, (D) Corn, (E) Melon, (F) Onion, (G) Pasture, (H) Pumpkin, (I) Sorghum, (J) Spring Grain, (K) Sunflower, and (M) Vegetable.

C2. PARAMETERS GOVERNING SeO_4

C2.1 Parameter governing global concentration and loading of SeO_4

Figure C-5 shows the sensitivity indices for the parameters for C_{SeO_4} in layers 1-4, leaching in layer 2-4, and mass loading of SeO_4 to the Arkansas River. As seen in Figures C-5A to C-5D, $\lambda_{O_2}^{auto}$ has the strongest influence on resulting C_{SeO_4} in layers 2-4, with λ_L the governing influence in layer 1. The strong influence of $\lambda_{O_2}^{auto}$ on simulated C_{SeO_4} also was seen in Chapter 6, and $\lambda_{O_2}^{auto}$ was a key parameter for estimation during the calibration process. As seen in Figures C-1E to C-1G, Se_{up} governs leaching of SeO_4 mass from layer 1 to layer 2, canal C_{SeO_4} governs the leaching from layer 2 to layer 3, $\lambda_{O_2}^{auto}$ governs the leaching from layer 3 to layer 4, and $\lambda_{O_2}^{auto}$ governs the mass loading of SeO_4 to the Arkansas River.

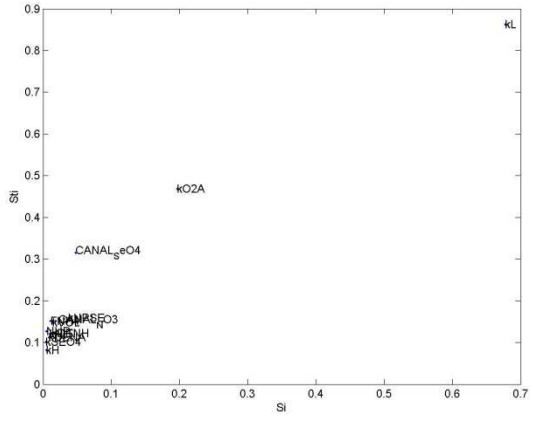

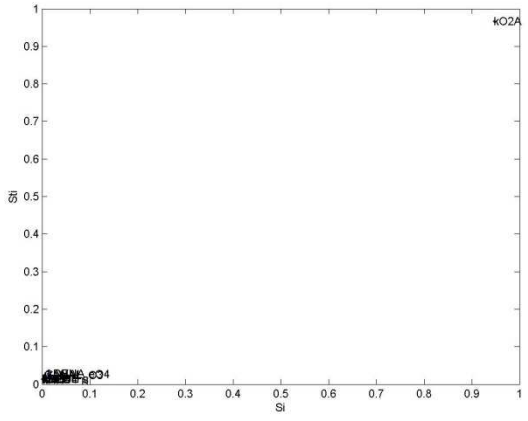

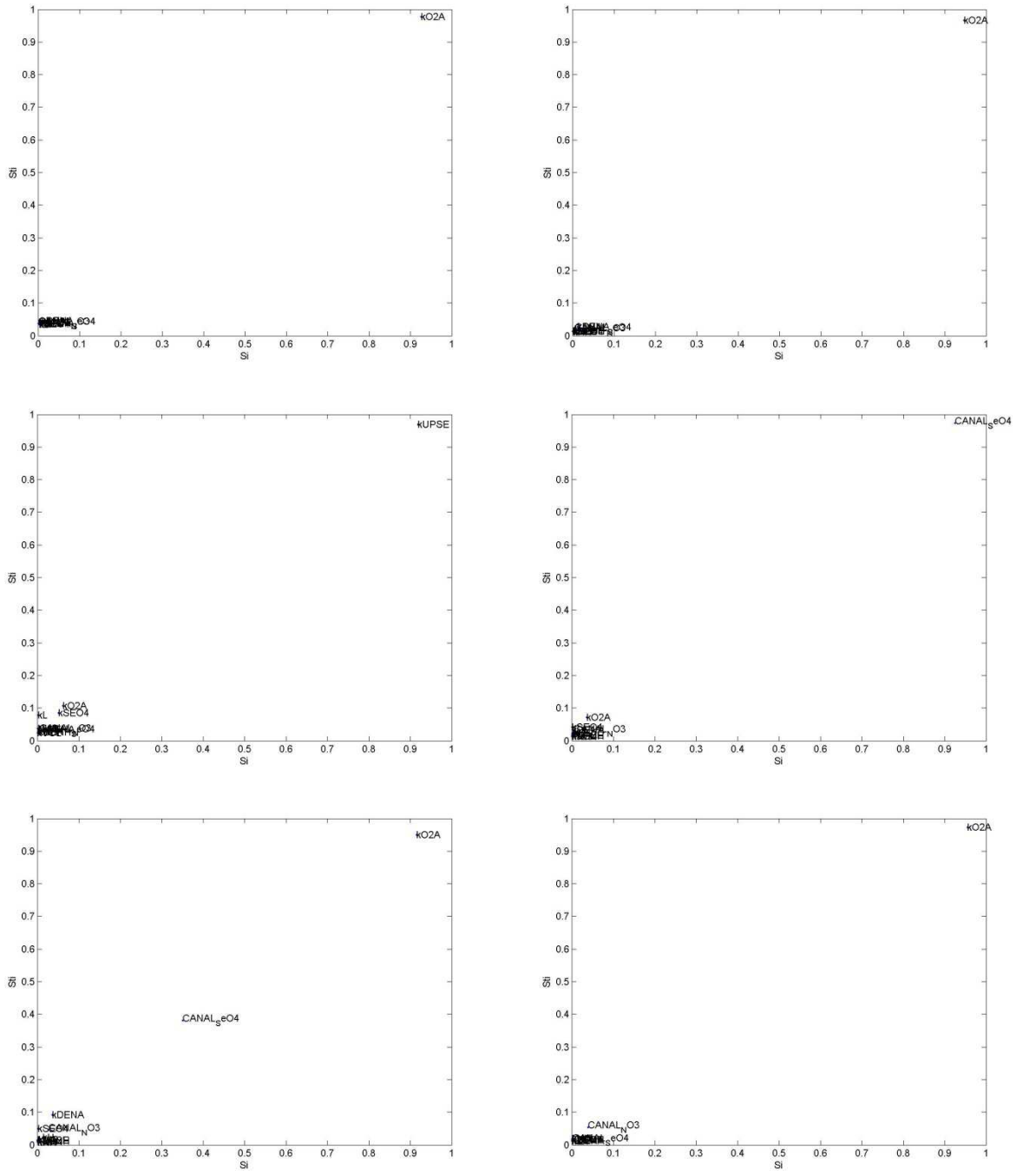

Figure C- 5. Sensitivity indices indicating the degree of parameter influence on C_{SeO_4} in (A) layer 1, (B) layer 2, (C) layer 3, and (D) layer 4, NO_3 leaching from (E) layers 1 to 2, (F), layers 2 to 3, and (G) layers 3 to 4, and (H) NO_3 mass loading to the Arkansas River.

C2.2 Parameter governing C_{SeO_4} in command areas

Figure C-6 shows the sensitivity indices for the parameters for C_{SeO_4} in layer 4 for each of the six command areas. Besides the Catlin command area, in which $\lambda_{NO_3}^{auto}$ has the strongest impact on C_{SeO_4} followed by $\lambda_{O_2}^{auto}$, C_{SeO_4} in each command area is governed by $\lambda_{O_2}^{auto}$. Again, this strong influence of $\lambda_{O_2}^{auto}$ was seen in Chapter 6 during the process of model calibration.

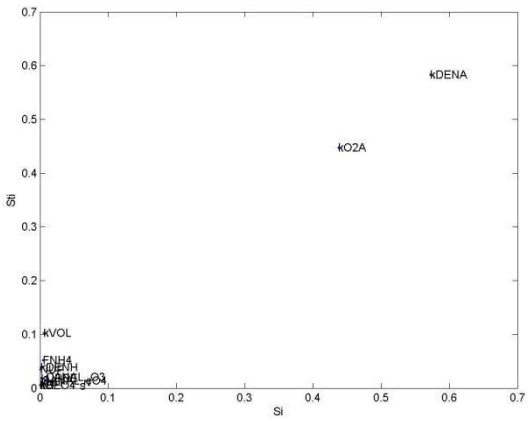

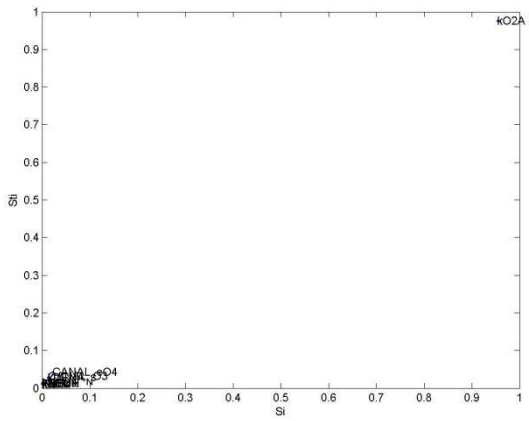

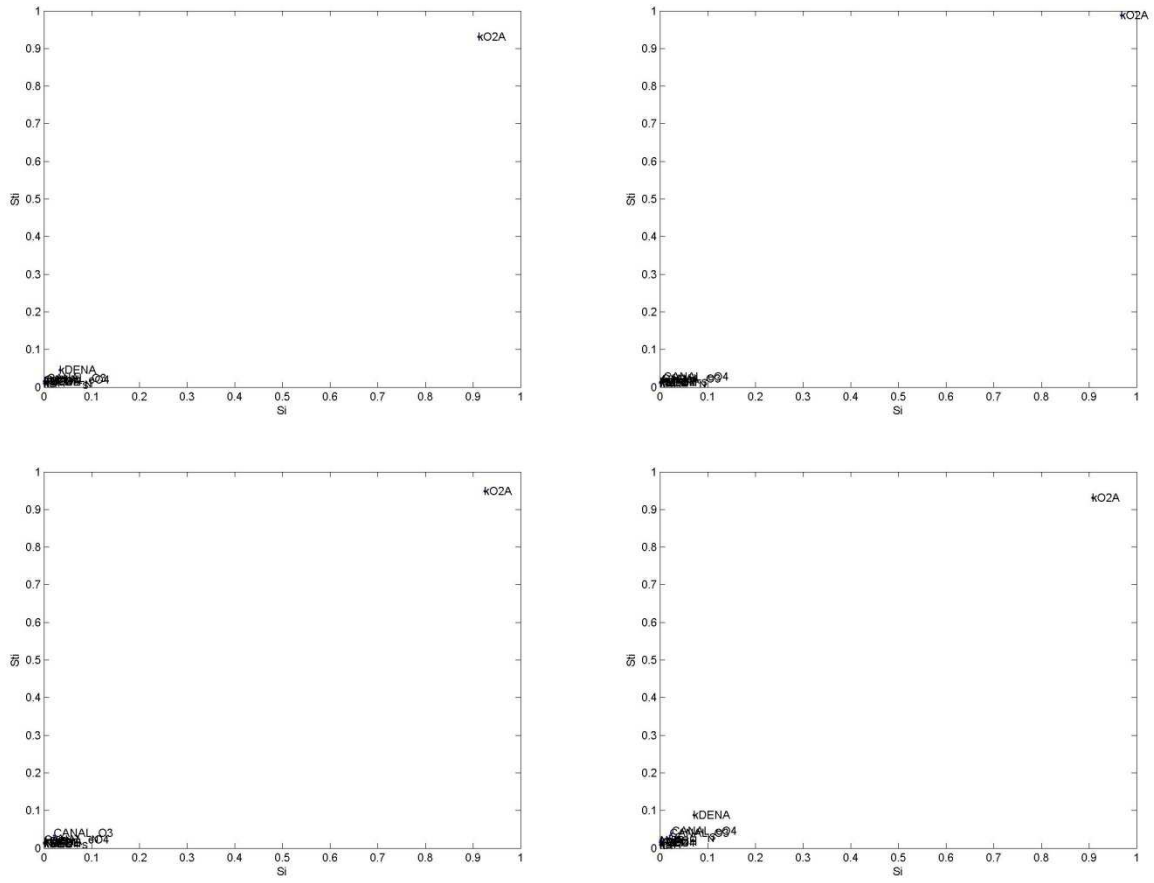

Figure C- 6. Sensitivity indices indicating the degree of parameter influence on C_{SeO_4} in the (A) Catlin, (B) Fort Lyon, (C) Highline, (D) Holbrook, (E) Otero, and (F) Rocky Ford Ditch command areas.

C2.3 Parameter governing C_{SeO_4} for each crop type

Figure C-7 shows the sensitivity indices for the parameters for C_{SeO_4} in layer 4 for each of the crop types, i.e., the groups of cells that are associated with each crop type. Similar to the findings in the previous two sections, $\lambda_{O_2}^{auto}$ governs C_{SeO_4} in layer 4 of the model. Exceptions to this rule, however, occur for the areas cultivated by corn (Figure C-7D), for which C_{SeO_4} is governed by $\lambda_{NO_3}^{auto}$, and for the areas cultivated by sorghum (Figure C-7I) and spring grain (Figure C-7J), in which $\lambda_{NO_3}^{auto}$ also plays a role in determining the simulated values of C_{SeO_4}. This is due to the high

seasonal loading of N fertilizer for these crop types and the subsequent high C_{NO_3} in the groundwater, thus leading to autotrophic denitrification in the presence of shale and the resulting production of SeO_4.

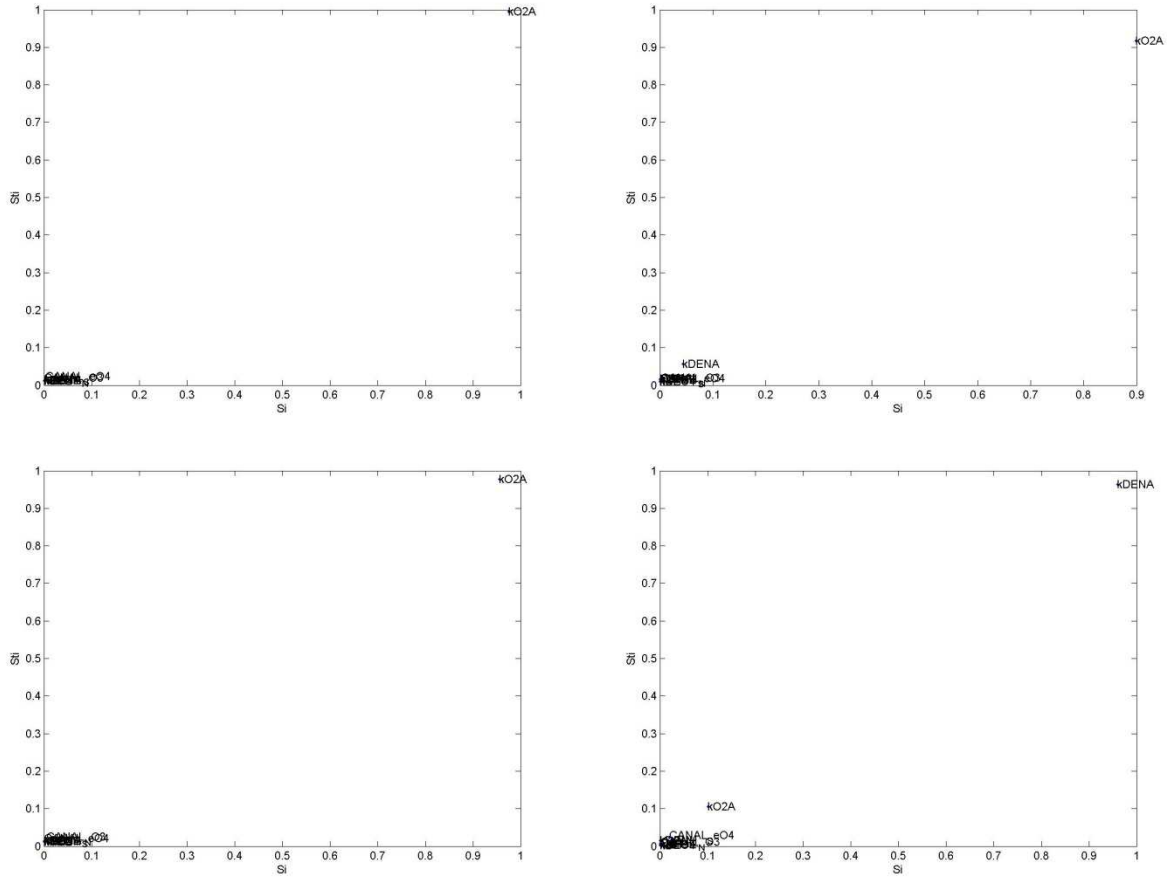

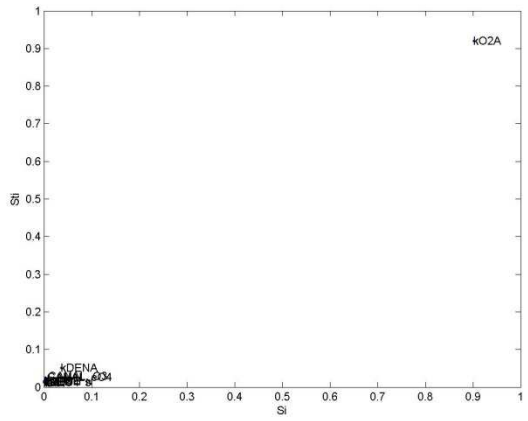
kO2A
kDENA
Sti
Si

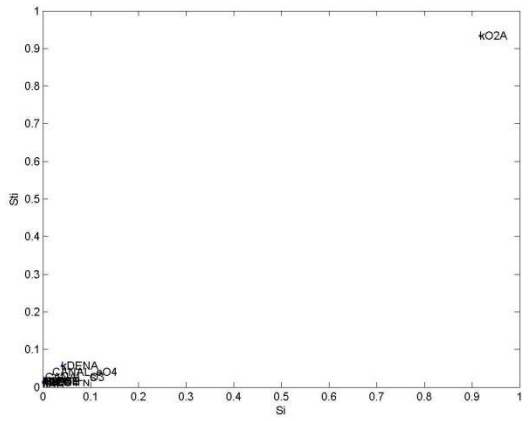
kO2A
kDENA
Sti
Si

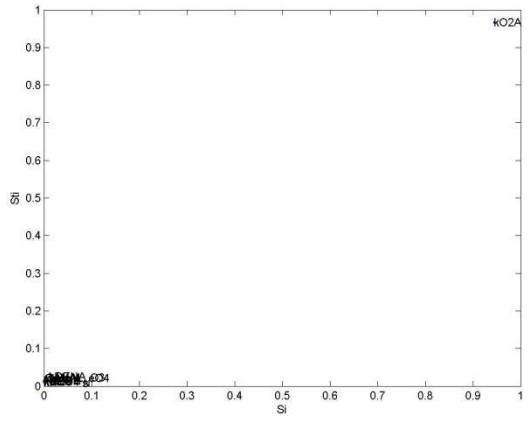
kO2A
Sti
Si

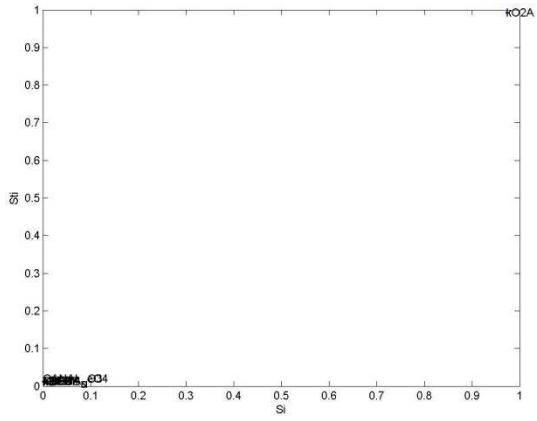
kO2A
Sti
Si

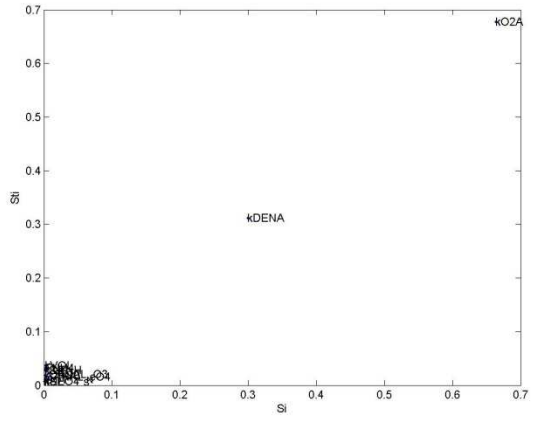
kO2A
kDENA
Sti
Si

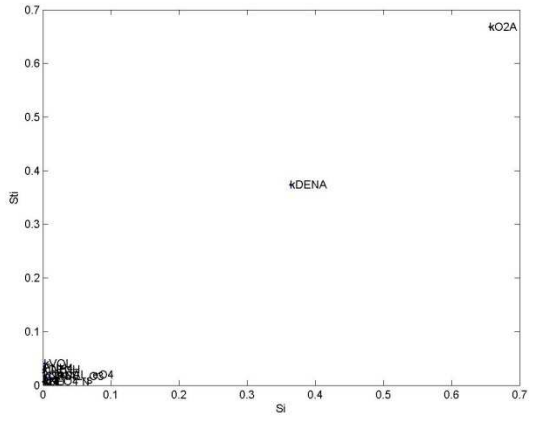
kO2A
kDENA
Sti
Si

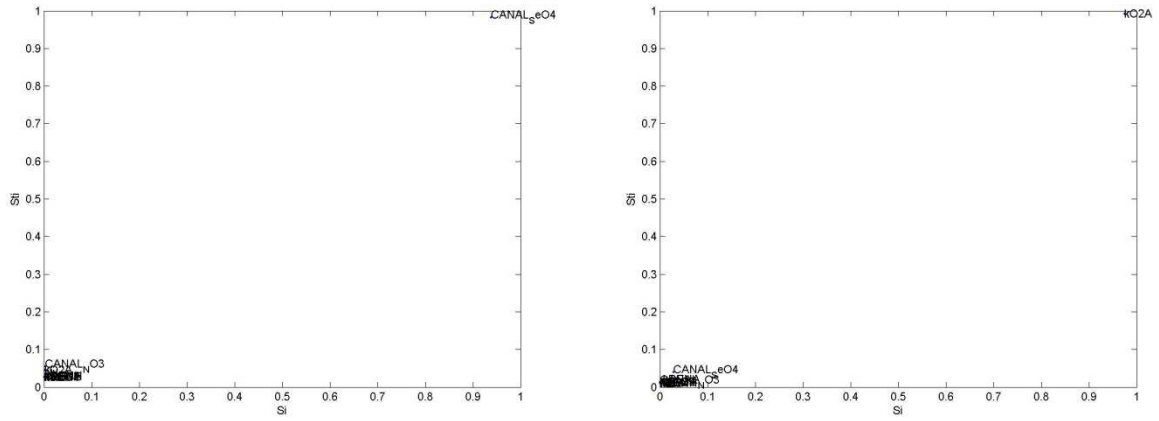

Figure C- 7. Sensitivity indices indicating the degree of parameter influence on C_{SeO_4} for cells underlying (A) Alfalfa, (B) Bean, (C) Clear, (D) Corn, (E) Melon, (F) Onion, (G) Pasture, (H) Pumpkin, (I) Sorghum, (J) Spring Grain, (K) Sunflower, and (M) Vegetable.

C2.4 Parameter governing leaching flux of SeO_4 for each crop type

Figure C-8 shows the sensitivity indices for the parameters for the leaching flux of SeO_4 from layers 3 to 4 for each of the crop types, i.e., the groups of cells that are associated with each crop type. As such, the results correspond to the leaching of SeO_4 mass below a depth of 2.0 m. The leaching SeO_4 mass is largely governed by $\lambda_{O_2}^{auto}$, although similarly to the results shown in C2.3 the areas cultivated by corn (Figure C-8D), sorghum (Figure C-8I) and spring grain (Figure C-8J) are also influenced by $\lambda_{NO_3}^{auto}$ due to the high seasonal loading of N fertilizer for these crop types.

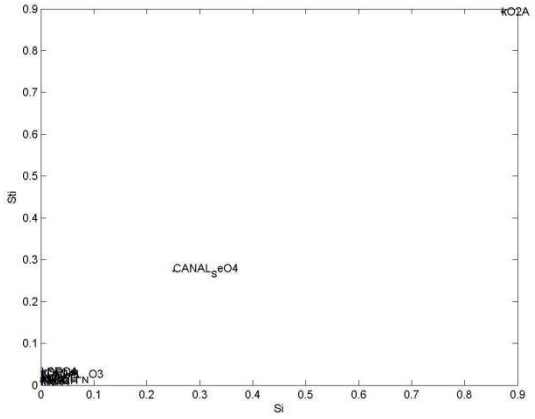
kO2A
CANALSeO4
Sti
Si

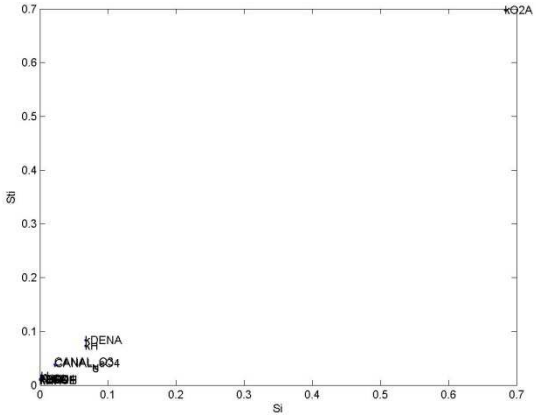
kO2A
kDENA
CANALSeO4
Sti
Si

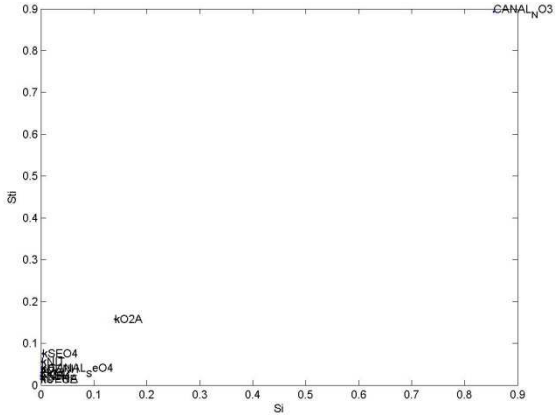
CANALNO3
kO2A
kSEO4
CANALSeO4
Sti
Si

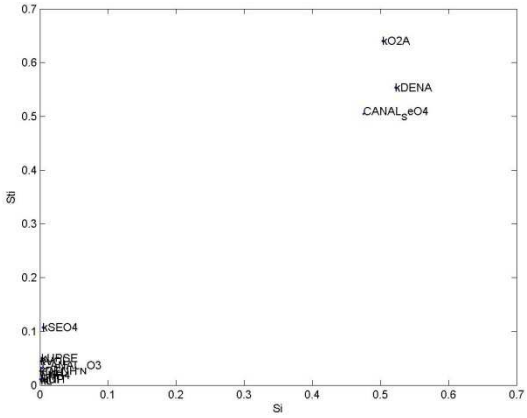
kO2A
kDENA
CANALSeO4
kSEO4
Sti
Si

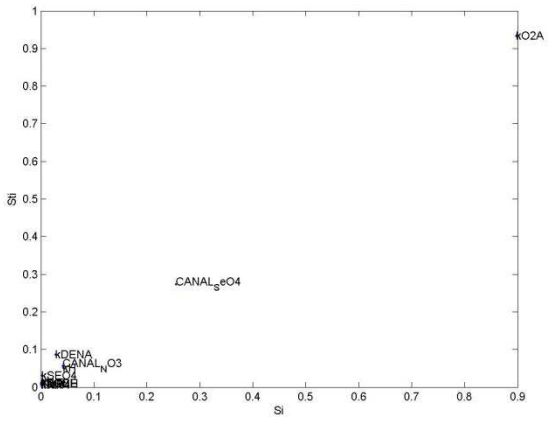
kO2A
CANALSeO4
kDENA
CANALNO3
Sti
Si

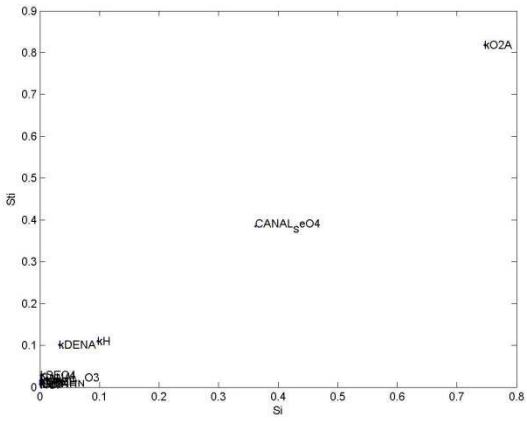
kO2A
CANALSeO4
kDENA
kH
Sti
Si

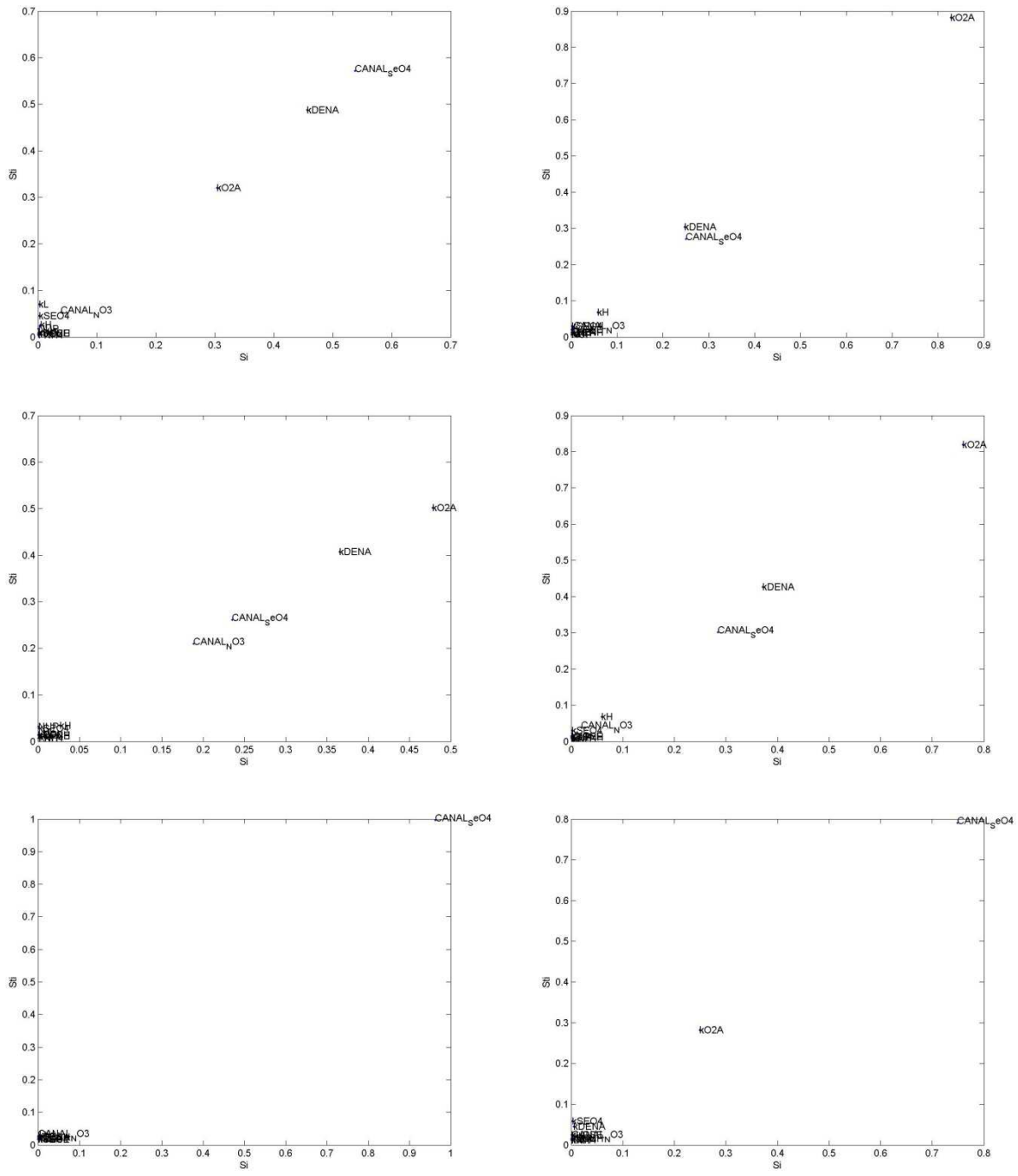

Figure C- 8. Sensitivity indices indicating the degree of parameter influence on leaching flux of SeO_4 for cells underlying (A) Alfalfa, (B) Bean, (C) Clear, (D) Corn, (E) Melon, (F) Onion, (G) Pasture, (H) Pumpkin, (I) Sorghum, (J) Spring Grain, (K) Sunflower, and (M) Vegetable.

APPENDIX D

ENSEMBLE SMOOTHER ASSIMILATION OF HYDRAULIC HEAD AND RETURN FLOW DATA TO ESTIMATE HYDRAULIC CONDUCTIVITY DISTRIBUTION[3]

D.0 Summary

Numerical groundwater models, frequently used to enhance understanding of the hydrologic and chemical processes in local or regional aquifers, are often hindered by an incomplete representation of the parameters which characterize these processes. In this study, we present the use of a data assimilation algorithm that incorporates all past model results and data measurements, an ensemble smoother (ES), to provide enhanced estimates of aquifer hydraulic conductivity (*K*) through assimilation of hydraulic head (*H*) and groundwater return flow volume (*RFV*) measurements into groundwater model simulation results. Based on the Kalman Filter methodology, residuals between forecasted model results and measurements, together with covariances between model results at measurement locations and non-measurement locations, are used to correct model results. Parameter estimation is achieved by incorporating model parameters into the algorithm, thus allowing the correlation between *H*, *RFV*, and *K* to correct the *K* fields. The applicability of the ES is demonstrated using a synthetic two-dimensional transient groundwater modeling simulation. Sensitivity analyses are carried out to show the performance of the ES in regards to measurement error, number of measurements, number of assimilation times, correlation length of the *K* fields, and the number of stream gage locations. Results show that the departure of the *K* fields from a reference *K* field is greatly reduced

[3] As published in Water Resources Research 46, W12543, doi:10.1029/2010WR009147 (2010), Ryan T. Bailey, Domenico A. Baù

through data assimilation, and demonstrate that the ES scheme is a promising alternative to other inverse modeling techniques due to low computational burden and the ability to run the algorithm entirely independent of the groundwater model simulation.

D.1 Introduction

Deterministic, numerical models, such as groundwater flow and transport models, can be powerful tools to enhance understanding of the hydrologic and chemical processes in a given watershed or geographic region. However, there are several inherent reasons why deterministic models are not fully capable of simulating the response of the system they are designed to represent [*Van Geer et al.*, 1991]. First, the processes that are included in most numerical models are usually represented in a simplistic fashion, and hence only approximate the actual system processes, such as the insertion of Darcy's law into groundwater flow models. And second, the parameters which define these processes and hence dictate the response of a dynamic system, are often not known with certainty.

As a means to reduce the uncertainty attached to system parameters, numerous parameter estimation methodologies have been proposed in the hydrologic literature, with the normal procedure of pinpointing parameter values that, when used in simulation models, yield an observed field response. In subsurface hydrology studies, the usual objective of these inverse modeling techniques is to identify values of transmissivity, hydraulic conductivity, or storativity in an aquifer system given measurements of hydraulic head.

In stochastic approaches, the parameter estimation procedure is to, first, establish an initial, *a priori* state of the aquifer system by generating an ensemble of spatially-variable parameter fields and subsequent flow fields using a groundwater model, and, second, determine the final, *a posteriori* ensemble of parameter fields that best honors measurement data collected from the

actual aquifer system. Parameter estimation methods differ principally in the solution methodology of the second step, many of which can be classified into the two broad categories of (1) Optimization and (2) Statistical Conditioning.

In Optimization methods, such as the pilot point method [*RamaRao et al.*, 1995], the self-calibrated method (SCM) [*Hendricks Franssen et al.*, 1999; *Gomez-Hernandez et al.*, 2003], and the representer method (RM) [*Bennett*, 1992; *Valstar et al.*, 2004], an objective function is defined and minimized in a least-squares optimization approach. In the RM, the objective function is minimized by first, establishing a set of nonlinear Euler-Lagrange equations that constitute the derivatives of the objective function; and second, setting the equations to zero and solving them using a set of unknown functions termed "representers". The representers are the cross covariances between the measurement data and the unknown system variables [*Valstar et al.*, 2004], and define the degree to which the measurement information at a given location will influence the correction of the nearby, unkown variables. A primary advantage of the RM, and one which is common among the methods in the Optimization class, is the built-in constraint that the state equations, such as the groundwater flow and transport equations, are satisfied, thus honoring the physical laws of the aquifer system and providing a realistic state estimation. Furthermore, the RM can act as a smoother, carrying information both forward and backward in time [*Evensen*, 2007]. However, the nonlinear nature of the Euler-Lagrange equations requires a computationally-intensive iterative procedure, with a computational effort equivalent to two simulation model runs for each additional measurement [*Valstar et al.*, 2004]. Furthermore, convergence is not always guaranteed.

In contrast to Optimization methods, Statistical Conditioning methods rely on the correlation between the system parameter and the system response variables to condition the system

parameter values. In the Cokriging Method (CM) [*Kitanidis and Vomvoris*, 1983; *Ahmed and De Marsily*, 1993; *Li and Yeh*, 1999], measurement data of primary and secondary variables are used in conjunction with their cross-correlation to interpolate predictions of variables between measurement locations. The covariance and cross covariance matrices are typically established using results of a flow model or a more simplistic relationship between the two variables [*Ahmed and De Marsily*, 1993]. In a similar procedure, the Ensemble Kalman Filter (EnKF), initially derived for use in oceanographic and meteorologic studies [e.g., *Evensen and van Leeuwen*, 1996; *Houtekamer and Mitchell*, 1998] and used extensively in hydrologic studies [e.g., *Reichle et al.* 2002; *Liu and Gupta*, 2007; *Camporese et al.*, 2009] uses data assimilation methods to provide a corrected system state [*Evensen*, 1994]. This method has been employed successfully in recent years in estimation of system parameters [e.g., *Moradkhani et al.*, 2005; *Aksoy et al.*, 2006], and offers an appealing alternative to optimization inverse methods, as computational burden is lower [*Camporese et al.*, 2009] and no iterative procedure is required. When comparing the RM and EnKF methods, *Reichle et al.* [2002] and *Ngodock et al.* [2006] found that the RM method could be more accurate than the EnKF but considerably more costly in terms of CPU (Central Processing Unit) time, and *Hendricks Franssen and Kinzelbach* [2009], when comparing the SCM and the EnKF methods, found that both methods produced similar results in conditioning transmissivity fields, although the EnKF method requires less CPU time. Although state equations are not always satisfied in both the CM and the EnKF, derivatives of the CM [*Yeh et al.*, 1995] and the EnKF [*Hendricks Franssen and Kinzelbach*, 2008; *Wang et al.*, 2009] have been proposed that preserve the laws inherent in the groundwater flow equation.

Derived from the original Kalman Filter (KF) [*Kalman*, 1960], a Bayesian-based framework in which prior information is merged with actual system data to produce a corrected, posterior

system estimate [*Evensen*, 1994], the EnKF is a Monte Carlo method designed to meet demands of large, nonlinear systems by using an ensemble of realizations to represent numerically the covariance of the model and measurement error statistics [*Evensen*, 2003]. Following the methodology of the KF, the model and measurement errors are assumed to be unbiased and uncorrelated. As such, the EnKF is a best linear unbiased estimator when applied to linear systems. If these errors are further constrained to be normally-distributed, than the KF and the EnKF are also maximum likelihood estimators [*Evensen and van Leeuwen*, 2000]. Merging of prior data from model simulations with observed, measured data is performed through a statistical update routine that spreads information from measurement locations to non-measurements locations according to the spatial covariance of simulation results. In this sense, each measurement assimilated into the simulate results acts in a similar fashion to the Representer in the RM method. In fact, *Evensen and van Leeuwen* [2000] demonstrate that the correction provided to each model value through the update routine is in fact defined by a representer, or influence function, of similar expression to the one presented in RM studies [*Bennett*, 1992; *Valstar et al.*, 2004]. However, the derivation and application of the representer is much more straightforward in the EnKF approach, and computational burden is much less.

Additional derivatives of the KF scheme are the Ensemble Smoother (ES) [*van Leeuwen and Evensen*, 1996] and the Ensemble Kalman Smoother (EnKS) [*Evensen and van Leeuwen* 2000]. In contrast to the EnKF, which incorporates all previous measurements to provide an updated model state at only the current time, a smoother analysis incorporates all previous measurements and model states to compute an updated model state estimate at all previous measurement times, using the spatial and temporal covariance of model results [*Evensen*, 2007]. In this way, previous

model states continue to be updated at each measurement assimilation time, and thus the method can be used to reconstruct historical conditions [*McLaughlin*, 2002].

The EnFK and EnKS schemes, in which updates are made sequentially through the time of model simulation, require either the embedding of the update routine algorithm into the modeling code or the need to stop the simulation, run the update routine, and re-start the simulation with the updated values. In contrast, the ES update routine is run once using all previous model states and measurement data, and as such can be applied exclusive of the model simulation, making it an appealing approach for estimation of time-independent parameters.

As discussed by *van Leeuwen*, [2001], a smoother gives superior results compared to a filter at earlier times, since the model states can be updated back in time, but provides identical estimates of the system state at the current assimilation time as the EnKF [*Evensen and van Leeuwen* 2000]. As such, these schemes have similarities with the RM. In fact, *Evensen and van Leeuwen* [2000] state that for linear model dynamics the ES provides the same solution as the RM, although CPU time for the RM is more costly.

Both the ES [*Dunne and Entakhabi*, 2005; *Pauwels and Lannoy*, 2006] and the EnKS [*Dunne and Entakhabi*, 2006; *Ngodock et al.*, 2006; *Durand et al.*, 2008] have been used in hydrologic modeling applications. For strongly nonlinear dynamical models, *Evensen and van Leeuwen* [2000] suggest that the EnKS provides a better system estimate than both the EnKF and the ES methods. However, applying the EnKF and ES to highly nonlinear hydrologic systems such as a coupled surface and variably-saturated flow model [*Camporese et al.*, 2009] and a land surface model [*Dunne and Entakhabi*, 2005] has proven successful.

Dual response-parameter variable estimation using the EnKF is performed by including the parameter values in the update routine with the system response variables, creating a cross

covariance matrix used in conditioning the parameter values by assimilation of system response measurement data. *Hantush and Marino* [1997], using random fields of aquifer properties and assimilating hydraulic head measurements into the KF routine, conditioned transmissivity and storativity fields within a two-dimensional (2D) groundwater model framework. *Chen and Zhang* (2006) used the EnKF scheme within a 2D and three-dimensional (3D) groundwater modeling framework to update pressure head hydraulic conductivity using principally head measurements; *Liu et al.* [2008] assimilated hydraulic head and tritium concentrations into a groundwater flow and transport model to estimate hydraulic conductivity and longitudinal dispersivity; and *Hendricks Franssen and Kinzelbach* [2008] used hydraulic head assimilation under uncertain recharge and transmissivity conditions within a 2D saturated, transient groundwater flow model to estimate the transmissivity field. The ES method has yet to be used in a parameter estimation framework in a hydrologic model application.

In most inverse modeling studies, only one set of system response measurement data, such as hydraulic heads, is used to estimate the system parameter in question. However, uncertainty associated with the estimated parameter can be greatly reduced if two dissimilar sets of system response data are used, as each set of data retains distinct information used in conditioning the parameter. For example, *Gailey et al.* [1991] used both hydraulic head and solute concentration data to estimate hydraulic conductivity, with the conclusion that using both sets of measurement data provided better estimates of the parameter than when only head data were used. Similar conclusions were drawn by *Hendricks Franssen et al.* [2003], *Gomez-Hernandez et al*. [2003] and *Liu et al.* [2008] using head and concentration data to condition transmissivity. Of particular note is the work performed by *Fu and Gomez-Hernandez* [2009], who used groundwater travel time data, calculated in a synthetic experiment by tracking the time of arrival of a tracer on the

edge of the aquifer system, as well as head data to reduce uncertainty on hydraulic conductivity. Using travel time data is of particular interest since it departs from the point measurements of head and concentration data, and hence provides global information on the patterns of hydraulic conductivity distribution in the aquifer.

In this paper, the applicability of the Ensemble Smoother scheme to condition aquifer parameters is explored using a synthetic two-dimensional transient groundwater flow simulation. The ES method was selected due to low computational intensity, its ability to reconstruct past flow fields of the aquifer system, its flexibility in running independent of the groundwater model simulation, and the fact that it is a promising tool that has not yet been explored in estimation of hydrologic parameters. The importance of assimilating two sets of system response measurement data is also explored. Specifically, hydraulic head measurements and calculated volumes of groundwater return flows to a stream, labeled return flow volumes in this paper, are used to condition the hydraulic conductivity field within a simplified aquifer-stream system. Measurements are taken from one or more simulation times. Both sets of data can be collected during field work, although return-flow volumes are not quite as straightforward as hydraulic head data due to the requirement of a mass-balance calculation between two stream gages. In numerical model results, hydraulic heads are immediate results of the groundwater flow simulations, while groundwater return flow volumes are calculated by summing flows leaving the model domain at constant-head boundary nodes. Sensitivity analyses are undertaken to gain insights into the influence of measurement errors, the number of assimilated measurements, the number of assimilation times, the correlation length used in generating the K fields, and the number of stream gage locations. Upscaling issues, in which point measurements from field

sampling represent model grid cell values, are discussed in conjunction with error of the assimilated measurements.

D.2 Data Assimilation Theory and Parameter Estimation

D.2.1 Kalman Filter Methology

The basic recursive data assimilation algorithm, based on the Kalman Filter methodology [*Kalman*, 1960] and its Bayesian framework, follows the sequential forecast-update (predictor-corrector) cycle, with updates of the system processed whenever measurement are available:

Forecast Step:

The model state $\boldsymbol{X}$ is run forward (forecasted) to time $t+\Delta t$ based on the model state at the current time $\boldsymbol{X}_t$, parameters $\boldsymbol{P}$, forcing terms $\boldsymbol{q}$, boundary conditions $\boldsymbol{b}$, and solution to the mathematical model $\boldsymbol{\Phi}$, generating the prior system information $\boldsymbol{X}^f_{t+\Delta t}$:

$$\boldsymbol{X}^f_{t+\Delta t} = \boldsymbol{\Phi}(\boldsymbol{X}_t; \boldsymbol{P}; \boldsymbol{q}_t; \boldsymbol{b}_t) \tag{1}$$

If this step occurs at the beginning of the model simulation, then $\boldsymbol{X}_t$ is equal to the initial model state $\boldsymbol{X}_0$.

Update Step:

At time $t+\Delta t$, measurement data $\boldsymbol{y}_{t+\Delta t}$ from the true state are collected, perturbed with a Gaussian error $\boldsymbol{v}$ to create the perturbed measurement vector $\boldsymbol{D}_{t+\Delta t}$, thus representing measurement error, and assimilated into the model forecast results $\boldsymbol{X}^f_{t+\Delta t}$ to generate a posterior state estimate, $\boldsymbol{X}^u_{t+\Delta t}$, where the *u* represents *update*:

$$\boldsymbol{X}^u_{t+\Delta t} = \boldsymbol{X}^f_{t+\Delta t} + \boldsymbol{K}_{t+\Delta t}\left(\boldsymbol{D}_{t+\Delta t} - \boldsymbol{H}\boldsymbol{X}^f_{t+\Delta t}\right) \tag{2}$$

The matrix $\boldsymbol{H}$ maps model results at measurement locations to actual measurements, creating a residual at measurement locations. A residual equal to 0 signifies complete agreement between the model state and true state. $\boldsymbol{H}$ is composed of binary constants (0 or 1) if the measurement

locations coincide with cell centers and if the measurement data correspond to state variables that are directly produced by the simulation model. The matrix $\boldsymbol{K}$ is termed the Kalman Gain (KG) matrix, with the following structure developed by *Kalman* [1960] to minimize the error covariance of the updated model state:

$$\boldsymbol{K} = \boldsymbol{C}^{f}\boldsymbol{H}^{T}(\boldsymbol{H}\boldsymbol{C}^{f}\boldsymbol{H}^{\boldsymbol{T}} + \boldsymbol{R})^{-1} \tag{3}$$

where $\boldsymbol{C}^{\boldsymbol{f}}$ is the forecast error covariance matrix associated with the model forecast $\boldsymbol{X}^{f}_{t+\Delta t}$ and $\boldsymbol{R}$ is the measurement error covariance matrix associated with the perturbed measurements $\boldsymbol{D}$.

The formulation of $\boldsymbol{K}$ performs two principal roles in the update routine. First, the information contained in $\boldsymbol{K}$ allows for information from measurement locations to be spread to non-measurement locations. Spatial correlation between node values at each model location and each measurement location, contained in $\boldsymbol{K}$, when multiplied by the residual matrix ($\boldsymbol{D}_{t+\Delta t}$ - $\boldsymbol{H}\boldsymbol{X}^{f}_{t+\Delta t}$) provides a correction term for each node in the model domain, thus blending model forecast values and measurement data throughout the entire model domain. Second, $\boldsymbol{K}$ acts as a weighting term that scales these correction terms according to model and measurement error. As $\boldsymbol{R}$ approaches zero, signifying low error in the measurement data, the influence of $\boldsymbol{K}$ increases and the residual is weighted more heavily. The model forecast values thus approach the measurement values. In contrast, as $\boldsymbol{C}^{\boldsymbol{f}}$ approaches 0, signifying low uncertainty in the model forecast, or if $\boldsymbol{R}$ is large, signifying high uncertainty in the measurement data, then the influence of $\boldsymbol{K}$ decreases, and the residual is weighted less heavily. The model forecast values thus receive little to no correction from the measurement data [*Maybeck*, 1979]. It is worth mentioning that the update routine presented in Equations (2) and (3) is obtained from maximizing the likelihood function $f\left(\boldsymbol{X}_{t+\Delta t}|\boldsymbol{D}_{t_1}, \boldsymbol{D}_{t_2}, \ldots, \boldsymbol{D}_{t+\Delta t}\right)$, representing the conditional probability of the state $\boldsymbol{X}$ at time $t+\Delta t$ given the measurements collected until that time [*Evensen and van Leeuwen*, 2000].

D.2.2 Ensemble Smoother (ES)

In ensemble methods of the Kalman Filter, such as the EnKF [*Evensen*, 1994] and the ES [*van Leeuwen and Evensen*, 1996], an ensemble of realizations is used to define $\boldsymbol{X}$. The ensemble is obtained with a Monte Carlo simulation and is used to approximate the mean and the variance of the model error, with the mean as the best estimate and the spread of the ensemble as the error variance. In the forecast-update scheme, the ensemble of model states, with each model realization defined by a different set of model parameters, is run forward in time and updated whenever measurement data are available. Measurement data are also represented by an ensemble, with the mean and the variance represented by the actual measurement and a normally-distributed measurement error, respectively. As all error statistics are assumed to follow a normal frequency distribution, all model values must be transformed to fit a normal distribution before use in the update routine.

Denoting n as the number of model nodes, N_{MC} as the number of realizations in the ensemble, and m as the number of measurements at each assimilation time, and referring to the matrices in Equations (2) and (3), the model forecast matrix $\boldsymbol{X}^f$ [n x N_{MC}] in the EnKF scheme holds the model results at the current time step for all realizations; $\boldsymbol{X}^u$ [n x N_{MC}] holds the updated model results for all realizations; the ensemble mean at each model node is stored in each column of the matrix $\overline{\boldsymbol{X}}$ [n x N_{MC}], computed by multiplying $\boldsymbol{X}^f$ by a N_{MC} x N_{MC} matrix where each element is equal to 1/ N_{MC}, and is used to calculate the deviation of the model values for all N_{MC} realizations:

$$\boldsymbol{X}^{Dev} = \boldsymbol{X}^f - \overline{\boldsymbol{X}} \tag{4}$$

Where $\boldsymbol{X}^{Dev}$ [n x N_{MC}] holds the deviation of each nodal value from the nodal ensemble mean. $\boldsymbol{C}^f$ [n x n], the forecast model error covariance matrix, is then calculated by:

$$\boldsymbol{C}^f = \frac{\boldsymbol{X}^{Dev} * \boldsymbol{X}^{Dev^T}}{N_{MC} - 1} \tag{5}$$

where *T* refers to the transpose of the matrix. The matrix $\boldsymbol{D}$ [*m* x N_{MC}] holds the perturbed measurements, with each measurement assigned an ensemble of errors randomly selected from a Gaussian distribution characterized by a measurement error assigned by the modeler. These perturbations are stored in a matrix $\boldsymbol{E}$ [*m* x N_{MC}] and used to calculate the measurement error covariance matrix $\boldsymbol{R}$ [*m* x *m*]:

$$\boldsymbol{R} = \frac{\boldsymbol{E} * \boldsymbol{E}^T}{N_{MC} - 1} \tag{6}$$

In contrast to the EnKF update routine, which updates only the current model state, the ES scheme includes all previous model states by maximizing the likelihood function $f\left(\boldsymbol{X}_{t_1}, \boldsymbol{X}_{t_2}, \ldots, \boldsymbol{X}_{t+\Delta t} | \boldsymbol{D}_{t_1}, \boldsymbol{D}_{t_2}, \ldots, \boldsymbol{D}_{t+\Delta t}\right)$, representing the conditional probability of all model states up to time $t+\Delta t$ given all measurements collected until that time [*Evensen and van Leeuwen*, 2000]. All measurements are applied to condition all model states, and thus the model states from previous measurement assimilation times are improved upon by the acquisition of new measurements. As such, the ES update routine can be run just once when, at the final collection time t_F, all model results and measurements have been made.

At time t_F, The forecast model state holds model state ensembles from all data collection times (t_1, t_2, …, t_F):

$$\widetilde{\boldsymbol{X}}_{t_F}^{\boldsymbol{f}} = \left[\boldsymbol{X}_{t_1}, \boldsymbol{X}_{t_2}, \ldots, \boldsymbol{X}_{t_F}\right]^T \quad \left(n * n_{t_F}\right) \text{ x } N_{MC} \tag{7}$$

In Equation (7), n_{tF} is the total number of times at which measurements are collected, and $\left[\boldsymbol{X}_{t_1}, \boldsymbol{X}_{t_2}, \ldots, \boldsymbol{X}_{t_F}\right]^T$ is the ensemble of model states at collection times. The calculated covariance matrix $\widetilde{\boldsymbol{C}}^f$ is composed of spatial covariance terms between nodes at the same simulation time, as

well as space-time covariance terms between nodes from different times. For instance, the space-time ensemble covariance between model states at times t_1 and t_2 is:

$$\boldsymbol{C}^f(\boldsymbol{X}_{t_1}, \boldsymbol{X}_{t_2}) = \frac{\boldsymbol{X}_{(t_1)}^{Dev} * \boldsymbol{X}_{(t_2)}^{Dev^T}}{N_{MC} - 1} \tag{8}$$

where $\boldsymbol{X}_{(t_1)}^{Dev}$ [n x N_{MC}] holds the deviation of each nodal value from the nodal ensemble mean at time t_1, and $\boldsymbol{X}_{(t_2)}^{Dev}$ [n x N_{MC}] holds the deviation of each nodal value from the nodal ensemble mean at time t_2. The measurement matrix $\boldsymbol{D}$ now holds perturbed measurements from all previous data collection times:

$$\widetilde{\boldsymbol{D}} = \left[\boldsymbol{D}_{t_1}, \boldsymbol{D}_{t_2}, \dots, \boldsymbol{D}_{t_F}\right]^{\boldsymbol{T}} \quad \left(m * n_{t_F}\right) \text{ x } N_{MC} \tag{9}$$

Where $\left[\boldsymbol{D}_{t_1}, \boldsymbol{D}_{t_2}, \dots, \boldsymbol{D}_{t_F}\right]^{\boldsymbol{T}}$ is the ensemble of perturbed measurements at data collection times. Using $\widetilde{\boldsymbol{X}}_{t_F}^f$ (Equation (7))**,** $\widetilde{\boldsymbol{C}}^f$ (Equation (8))**,** and $\widetilde{\boldsymbol{D}}$ (Equation (9)) in Equation (2), $\widetilde{\boldsymbol{X}}_{t_F}^u$ contains updated model states at the current and each previous measurement time.

Algorithms to solve the update routine of Equation (2) are given by *Burgers et al.* [1998] and *Keppenne* [2000], and can be implemented via a concise and efficient computer program. The solution strategy presented by *Keppenne* [2000] employs techniques to preclude the assemblage of $\boldsymbol{C}^f$, hence saving on computer memory and preventing numerical issues that arise from calculating its inverse, to provide a method that can be used for high-resolution real-world climate numerical models. For this study, the Keppenne algorithm was adapted to the ES scheme to allow the inclusion of forecast ensemble from all assimilation times. Even with these modifications the computational effort is very affordable, as discussed later.

D.2.3 Parameter Estimation using the Ensemble Smoother

The state matrix $\boldsymbol{X}$ can be augmented to include model parameter values, allowing the spatial covariance between parameter and state variables to correct not only the state, but also the parameters, of a model-estimated system. By doing so, the model itself is corrected to more precisely imitate the workings of the real-world system. In this work, both state variables (hydraulic head *H*, return flow volumes *RFV*) and parameters (hydraulic conductivity *K*) of a groundwater flow model are updated, using *H* and *RFV* measurements. In the ES format, the model forecast state matrix $\widetilde{\boldsymbol{X}}^{f}_{t_F}$ is comprised of either or both state variables *H* and *RFV*, and augmented to include the *K* values:

$$\widetilde{\boldsymbol{X}}^{f}_{t_F} = \left[\boldsymbol{X}_{(H)t_1}, \dots, \boldsymbol{X}_{(H)t_F}; \boldsymbol{X}_{(RFV)t_1}, \dots, \boldsymbol{X}_{(RFV)t_F}; \boldsymbol{X}_{(K)}\right] \qquad \left\{\left[(n+g) * n_{t_F}\right] + e\right\} \text{ x } N_{MC} \tag{10}$$

where *n* is the number of nodes in the system, *g* is the number of stream gages used to calculate the *RFV* measurements, and *e* is in general the number of parameters that characterize the system, e.g. the number of elements in a finite element discretization. Upon completion of the update routine, $\widetilde{\boldsymbol{X}}^{u}_{t_F}$ holds the updated state for *H*, *RFV*, and *K*. The forecast covariance matrix $\boldsymbol{C}^{f}$ now contains spatial cross-covariance submatrices between *H*, *RFV*, and *K* where, for example, the *H*-*K* cross-covariance submatrix at a time t_i is defined by:

$$\boldsymbol{C}^{f}{}_{t_i}(\boldsymbol{X}_{(H)t_i}, \boldsymbol{X}_{(K)t_i}) = \frac{\boldsymbol{X}^{Dev}{}_{(H)t_i} * \boldsymbol{X}^{Dev}{}_{(K)t_i}{}^{\boldsymbol{T}}}{N_{MC} - 1} \tag{11}$$

Where $\boldsymbol{X}^{Dev}{}_{(H)t_i}$ [n x N_{MC}] holds the deviation of each *H* nodal value from the *H* nodal ensemble mean, and $\boldsymbol{X}^{Dev}{}_{(K)t_i}$ [e x N_{MC}] holds the deviation of each *K* parameter value from the *K* ensemble mean. The *H*-*K* covariance submatrix defines the correlation between *H* and *K* forecast

values at all model locations, allowing *H* measurement information to correct the *K* values throughout the model domain.

Initially, only *H* and *RFV* measurements are used to condition the ensemble of *K* fields, and thus the measurement matrix $\boldsymbol{D}$ remains unchanged. However, *K* measurement data can also be added to $\boldsymbol{D}$ in order to further condition the *K* ensemble:

$$\widetilde{\boldsymbol{D}} = \left[\boldsymbol{D}_{(H)t_1}, \dots, \boldsymbol{D}_{(H)t_F}; \boldsymbol{D}_{(RFV)t_1}, \dots, \boldsymbol{D}_{(RFV)t_F}; \boldsymbol{D}_{(K)}\right] \qquad \left\{\left[(m+s) * n_{t_F}\right] + e\right\} \text{ x } N_{MC} \tag{12}$$

where *m* and *s* are the number of *H* and *RFV* measurements, respectively, per assimilation time .When employed in parameter estimation, the ES is a *K* field generator, given uncertain model formulation and measurement data.

D.2.4 Parameter Estimation in a Ground Water Modeling Framework

In this work, a synthetic 2D transient state groundwater flow problem is used to test the ES update routine to condition *K* fields using *H* and *RFV* measurement data. The overall forecast-update process using groundwater flow simulations is shown in Figure D-1. The forecast stage consists of initializing an ensemble of groundwater flow simulations with an ensemble of *K* fields and *H* initial conditions. The *K* fields are generated using a sequential Gaussian simulation algorithm similar to that proposed by *Deutsch and Journel* [1998]. This algorithm, called SKSIM, was developed by *Baú and Mayer* [2008] and uses known geostatistical parameters, mean, variance, and correlation length as the prior information in the Bayesian framework. According to this model, the spatial distribution of hydraulic conductivity is characterized by a normal distribution using an exponential covariance model in the log domain:

$$\log K = Y_k = N\left(\mu_{Y_K}; \sigma_{Y_K}\right); \tag{13}$$

$$cov_{Y_K,Y_K}(\boldsymbol{d}) = \sigma_Y^2 . \exp\left(\sqrt{\sum_{i=1}^{3} \frac{d_i^2}{\lambda_i^2}}\right)$$

where μ_{Y_K} and σ_{Y_K} are the mean and standard deviation of the log-*K* distribution, d_i are the components of the distance vector **d**, and λ_is are the spatial correlation scales in the coordinate directions. Boundary conditions and forcing terms are then applied throughout the duration of the simulation; system response variables (hydraulic head *H*, and return flow volumes *RFV*) are also generated throughout the simulation. An additional *K* field and groundwater flow simulation, from which measurements could be taken during the update step, are used to provide a "true" reference state against which the updated model states could be compared. For the majority of the scenarios presented in this paper, this "true" reference state was generated using the same geostatistical parameters as the *K* forecast ensemble. Several update scenarios, however, assimilate measurements taken from reference states generated using different geostatistical parameters than the forecast ensemble, with the recognition that the true set of geostatistical parameters is generally not known for a given aquifer system. Conditioning of the *K* ensemble in these scenarios, when compared with the conditioning that occurs when the reference state uses the same geostatistical parameters as the forecast ensemble, would provide insights as to how the method would perform when applied to real hydrologic systems.

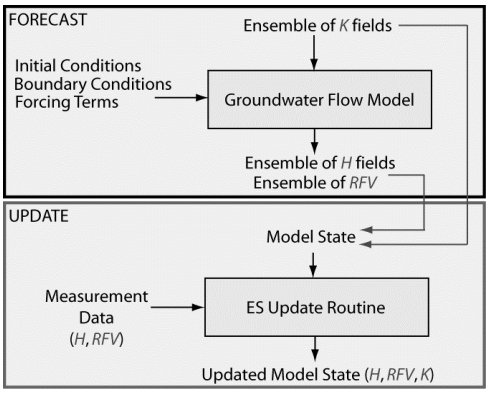

Figure D- 1. Forecast-update routine process for the ensemble smoother in a groundwater modeling framework. The Forecast stage consists of generating the initial ensemble of *K* fields and the resulting simulated *H* fields and return flow volumes. The Update stage consists of merging the forecast and measurement data via the ensemble smoother update routine to produce updated estimates of the variables.

The update stage consists of populating the forecast model state matrix with system response variables and the ensemble of *K* fields, taking measurements from the true state, and running the ES update routine to provide an updated estimate of the model states given the collected measurements. A coefficient of variation value represents measurement error and is used to perturb each measurement value. The performance of the update routine is analyzed by comparing the updated model state to the reference state via the following two performance parameters [*Hendricks Franssen and Kinzelbach*, 2008]:

$$AE(\boldsymbol{X}) = \frac{1}{N_{MC} * n} \sum_{j=1}^{N_{MC}} \sum_{i=1}^{n} \left| X_{i,j} - X_{i,true} \right| \tag{14}$$

$$AES(\boldsymbol{X}) = \frac{1}{N_{MC} * n} \sum_{j=1}^{N_{MC}} \sum_{i=1}^{n} \left| X_{i,j} - \bar{X}_i \right| \tag{15}$$

The average absolute error (*AE*) takes into account every value in each ensemble model, comparing the model values to the true value at each location in the model domain, and the average ensemble spread (*AES*) takes into account the deviation of the model values from the

ensemble mean at each location, providing an indication of the spread of the values at a given model location. Hence, *AE* is a measure of the algorithm to predict the true *K* field, and *AES* is a measure of the ensemble spread, or the confidence in the predicted values. The ensemble mean at each model grid cell can also be calculated and plotted to compare against the reference state. Similarly, the ensemble spread at each model grid cell can be calculated for the forecast and update ensembles to show improvement in the spread of the ensemble values. By computing the *AE* and *AES* values for both the forecast model state and the updated model state, it is possible to quantify the improvement in the model estimate provided by the update routine. Low values of *AE* indicate an ensemble state close to the true state, and low values of *AES* indicate small spread and high confidence in the ensemble. It should be noted that in applications to real-world systems Equation (14) would not be used, since the true state is not known. It is used in this study in order to test the accuracy of the ES scheme.

Although the purpose of this paper is to demonstrate the conditioning of the *K* field, the ability of the *H* measurements to condition the *H* ensemble will also be shown to demonstrate the accuracy of the ES scheme and its principal advantages over filtering methods, namely the ability to allow measurements collected at the current time to correct system states from past measurement times.

D.3 Ground Water Flow Simulations and Parameter Estimation

D.3.1 Forecast of Transient Flow Problem

The two-dimensional transient flow problem consists of an areal aquifer 2000 m west-east by 4000 m north-south (Figure D-2). Constant-head boundaries of 32 m and 28 m were placed on the west and east ends of the aquifer, respectively, with an average saturated thickness *b* of 30 m. The mesh was discretized using right-angled 50 m x 50 m isosceles triangular elements, resulting

in 6400 elements and 3321 nodes. The flow problem was solved using the finite element code SAT2D [*Gambolati et al.*, 1999], which solves the following governing equation for two-dimensional saturated transient groundwater flow:

$$\frac{\partial}{\partial x}\left(T_x \frac{\partial h}{\partial x}\right) + \frac{\partial}{\partial y}\left(T_y \frac{\partial h}{\partial y}\right) = S\frac{\partial h}{\partial t} + q \tag{16}$$

where T is transmissivity [L^2T^{-1}] and is related to K through $T = Kb$, h is hydraulic head [L], t is time [T], S is storativity [-], and q represents sources and sinks [LT^{-1}], with q represented by a monthly series of areally-distributed recharge (Figure D-2). Unconfined conditions were simulated by setting S to 0.20 to represent specific yield, with the assumption that the change in head throughout space and time in the simulation is much less than the average saturated thickness of the aquifer [*Polubarinova-Kochina*, 1962].

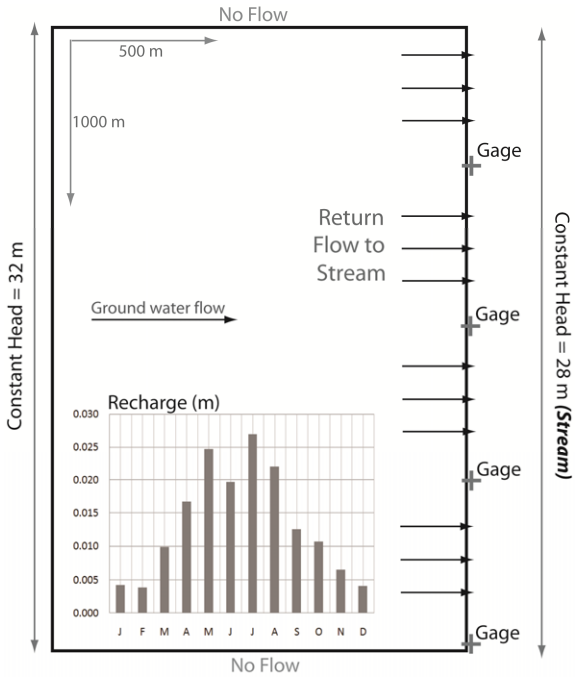

Figure D- 2. Plan view of the conceptual model for the 2D transient groundwater flow problem.

An ensemble of N_{MC} = 100 2D K fields was generated using SKSIM [*Baú and Mayer*, 2008] with mean μ_{Y_K} of -4.30 (log m sec^{-1}), standard deviation σ_{Y_K} of 0.434 (log m sec^{-1}), and

correlation length λ ($\lambda_x = \lambda_y$) of 1000 m, with each block of 2 triangular elements in the flow model mesh assigned a different *K* value. These *K* fields were used to simulate an ensemble of 100 flow fields, with each realization first run to steady-state to provide initial conditions for the 365-day transient simulation. Each transient simulation was run for t_F=365 days using a time step of 1 day. Using an Intel® Core™2 Duo CPU @ 3.00GHz desktop computer, overall CPU time to generate the forecast ensembles was approximately 22 minutes, with 16.5 minutes used in running SKSIM and 5.5 minutes in running the ensemble of SAT2D simulations.

Hydraulic heads were recorded at the end of each month to produce monthly *H* fields. The constant-head boundary on the east side of the aquifer was treated as a stream, with the flows leaving the model domain at the constant-head nodes along this boundary treated as groundwater return flows to the stream. *RFV*s were calculated by summing flows between designated stream gage locations between two moments in time. The following linear regression was carried out to identify the statistical distribution of the *RFV* values sampled by the stochastic simulation:

$$\left[f_\Phi(RFV_i), \Phi^{-1}\left(\frac{\mathrm{i}-0.5}{N_{MC}}\right)\right] \qquad i = 1,2,\ldots,N_{MC} \tag{17}$$

where Φ^{-1} is the inverse of the theoretical cumulative distribution function (CDF), numerically computed, and f_Φ is a transformation of *RFV* that depends on the type of CDF Φ under consideration. The analysis is performed by testing different types of model distributions Φ. The "goodness" of fit of the sampled distribution to Φ is assessed from the value of the coefficient of determination, r^2, which provides an estimate of the goodness of fit in terms of the average sum of residuals, and the Kolmogorov-Smirnov statistics, *KS*, which represents the maximum difference between the data and the regression. A value of r^2 approaching one and a low value of *KS* generally indicate a good fit. Using *RFV* values between two stream gages for the first 14 days of each of the 100 simulations, the inverse CDF of a lognormal fit is shown in Figure D-3.

The values of r^2 (0.988) and *KS* (0.054) suggest that the *RFV* values fit well to a lognormal distribution. As such, the *RFV* values were log-transformed for use in the ES update routine.

An additional *K*-*H* field combination (Figure D-4) was created to provide reference fields from which measurements are collected and against which update ensembles could be compared. Locations of *H* and *K* measurements, along with locations of stream gages to calculate *RFV* values, are shown in Figure D-4C. For most scenarios, *K* measurements were not included. *AE* and *AES* values for the forecast ensemble of *K* fields are 0.485 and 0.347, respectively, while *AE* and *AES* values for the resulting forecast ensemble of *H* fields are 0.361 and 0.262, respectively.

Additional *K* ensembles were created using SKSIM to determine the influence of correlation length on the ability of the *H* and *RFV* measurements to condition the *K* ensemble. Besides the initial correlation length of 1000 m, lengths of 300 m, 500 m, and 1500 m were used.

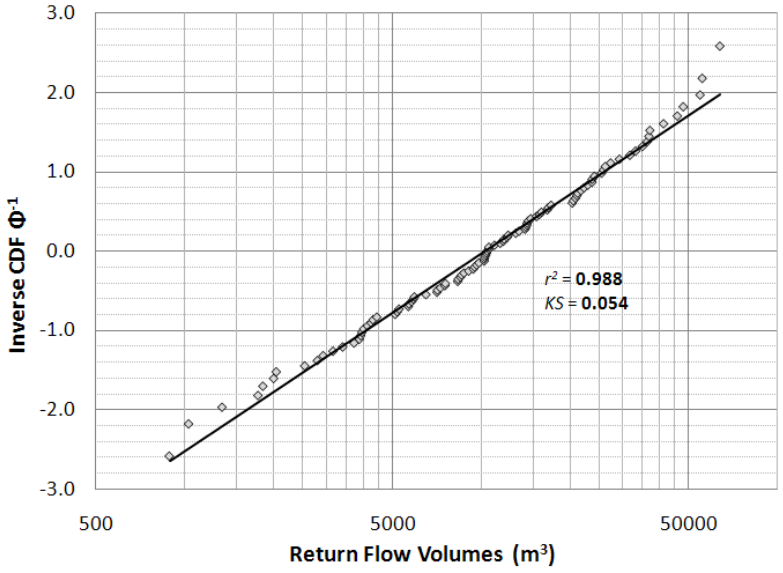

Figure D- 3. Inverse CDF of the return flow volumes, demonstrating the log-distributed behavior.

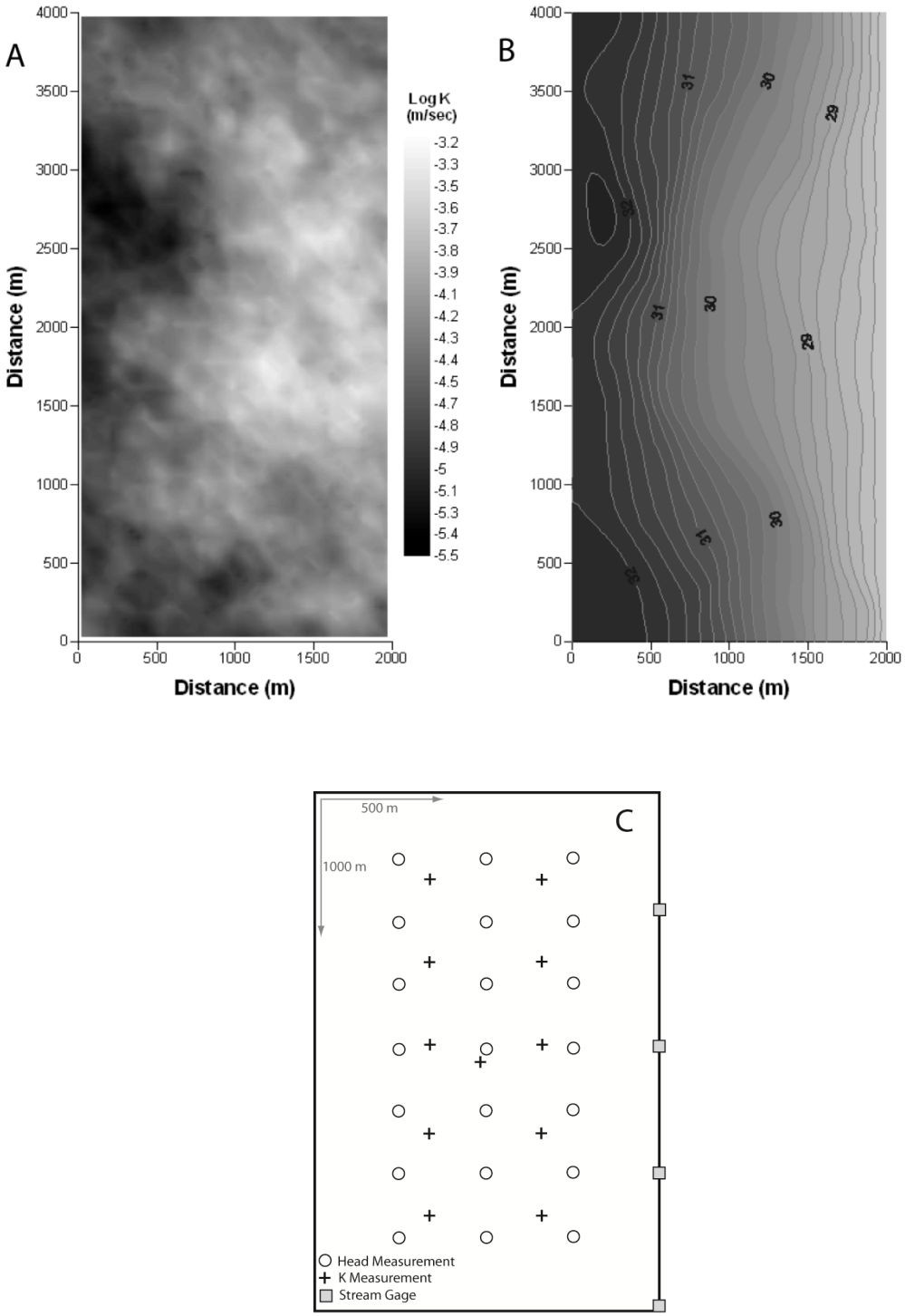

Figure D- 4. (A) Reference field for *K*, (B) Reference field for *H*, at simulation time = 365 days, and (C) Location of the hydraulic head measurements (open circles), hydraulic conductivity measurements (black crosses) and stream gages (gray boxes) used in the ES update routine.

D.3.2 Update of System State

D.3.2.1 Update of *H* Ensemble

Using monthly *H* measurements at the 21 locations shown in Figure D-4C, the considerable improvement in the updated *H* ensemble is demonstrated by the closeness of the updated *H* ensemble mean (Figure D-5A) to the reference state (Figure D-4B) and the decreased spread in the ensemble values at every node location (Figure D-5B). Notice also the minimized spread near the *H* measurement locations. Improvement in the ensemble is also demonstrated in the values of the performance parameters, with update values of 0.094 and 0.058 for *AE* and *AES*, respectively, a decrease of 74.0% and 77.9% with respect to the forecast.

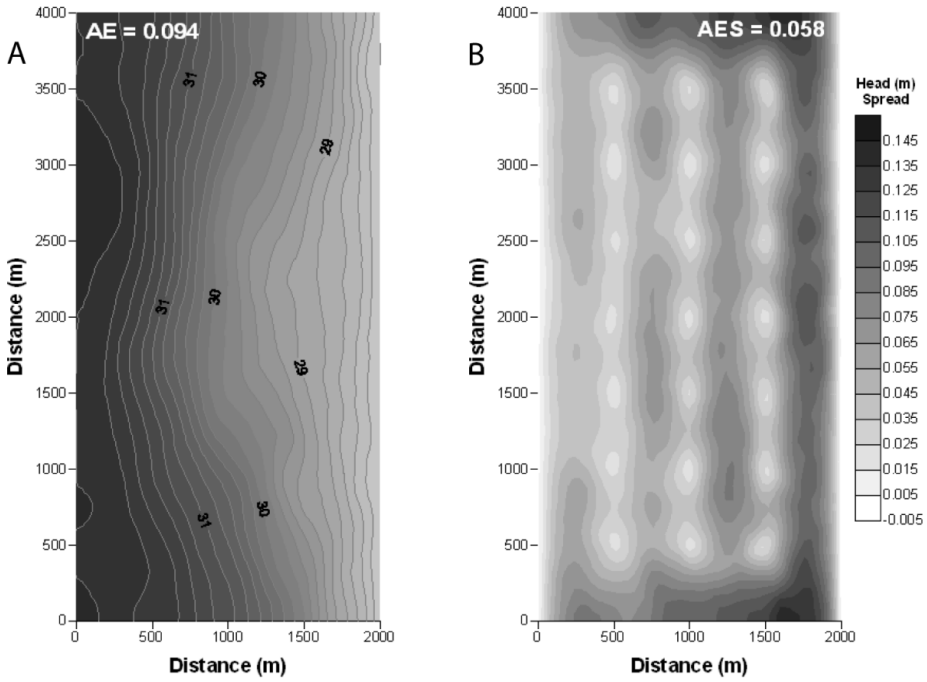

Figure D- 5. (A) *H* update ensemble mean at time = 365 days and (B) *H* update ensemble spread at every location in the model domain, conditioned by 21 *H* measurements. Compare (A) with the reference *H* state in Figure 4B. Coefficient of variation of *H* measurements was set to 0.00.

To demonstrate the ability of the ES routine to update previous model states using current measurements, the *H* ensemble at the end of the first month of the simulation was updated using measurements from each month of the 1-year simulation (Figure D-6). For this demonstration,

the correlation length of the *K* fields was 300 m. When measurements from only the first month were used, *AE* and *AES* were 0.313 and 0.228, respectively, an improvement of 13.1% and 12.3% from the forecast values. However, when measurements from both the first and second months were assimilated, the *AE* and *AES* values were 0.279 and 0.199, an improvement of 22.5% and 23.5%, respectively, from the forecast values. As measurements from additional months are assimilated, the improvement in the performance parameters increases, with an improvement of 63.9% and 71.2% for *AE* and *AES*, respectively, when measurements from the first 7 months are used to condition the *H* ensemble of the first month (Figure D-6). Any additional measurements (from months 8 to 12) provide no improvement in the *H* ensemble of the first month, indicating that the temporal correlation between the *H* values of months 8 to 12 and the first month are not strong enough to further influence the *H* ensemble of the first month.

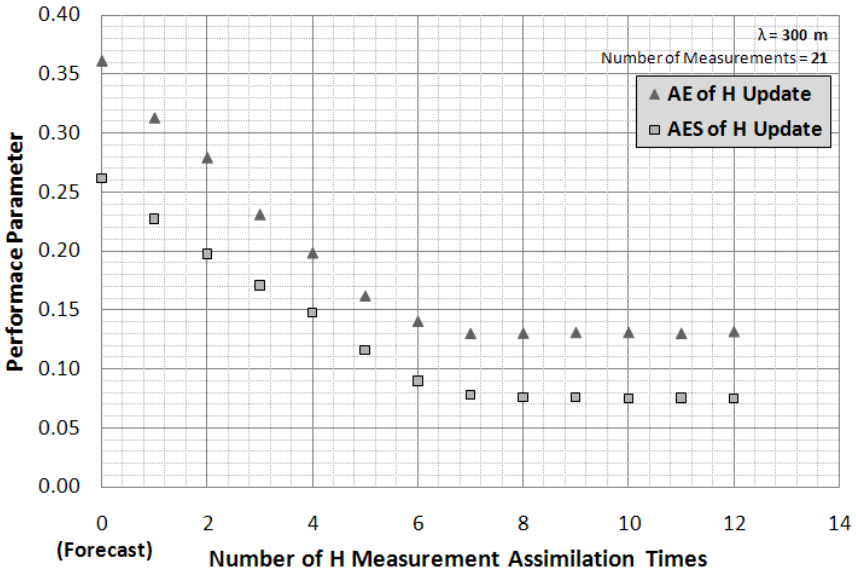

Figure D- 6. Influence of the number of measurement assimilation times on the updated *H* ensemble at time = 31 days, demonstrating the ability of the ES scheme to propagate information backwards in time.

D.3.2.2 Update of *K* Ensemble using Head Measurements

Hydraulic head measurements from the end of each of the 12 months were used to condition the *K* ensemble. Figure D-7 shows the ensemble means of the *K* fields from two update

scenarios, one using only one *H* measurement from the center of the flow field (Figure D-7A) and the second using 21 *H* measurements from the locations shown in Figure D-4C (Figure D-7B). In comparison to the reference *K* field (Figure D-4A), the first scenario is able to capture the general trend of a low *K* region in the western portion of the aquifer and a high *K* region in the eastern portion of the aquifer, whereas the second scenario captures the major patterns within each of the regions, although the updated fields underestimate the *K* values in the east-northeast region of the aquifer. Improvement gained from the update is also reflected in the performance parameters, with the *AE* for the first scenario decreased from 0.485 to 0.393, a reduction of 19.0%, and the *AE* for the second scenario decreased to 0.313, a reduction of 35.5%. The spread of the ensemble values in the second scenario was also decreased considerably (Figure D-8), with the *AES* reduced by 44.7%, from 0.347 for the forecast ensemble spread (Figure D-8A) to 0.192 for the updated ensemble spread (Figure D-8B).

The sensitivity analysis focused on number of *H* measurement assimilation times (1 to 12), the coefficient of variation of the *H* measurements (0 to 0.30), the correlation length used to generate the forecast *K* ensemble (300 m to 1500 m), and the number of *H* measurements assimilated. Results are presented in Table D-1 and Figure D-9. In Table D-1, the columns to the right of the *AE* and *AES* columns hold the percent reduction from the forecast values, with a higher percent reduction signifying an approach to the reference state.

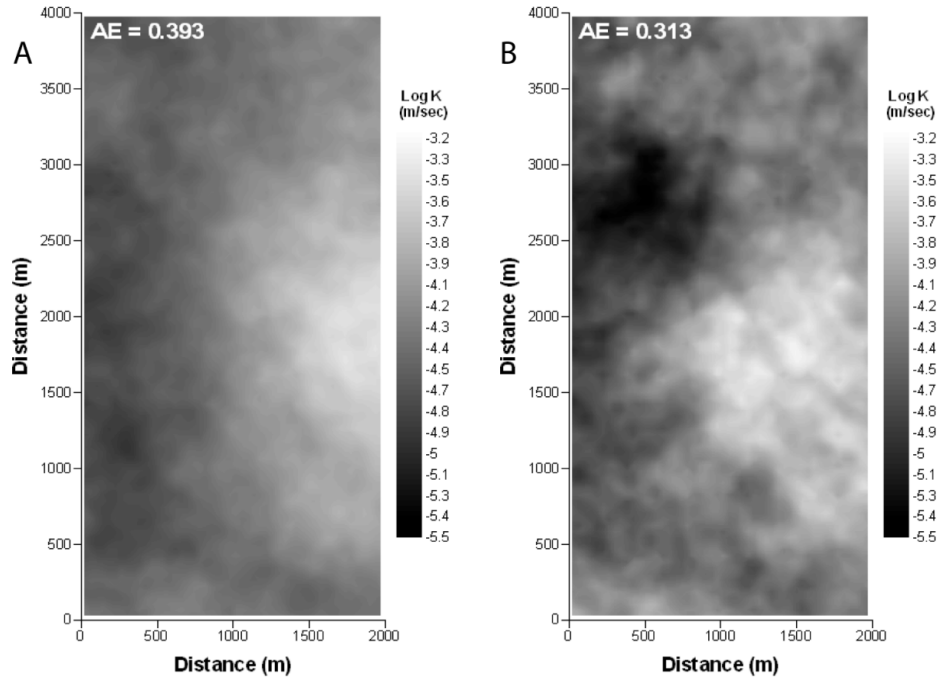

Figure D- 7. Updated ensemble mean at every model node when (A) 1 *H* measurement is assimilated, and (B) 21 *H* measurements are assimilated. Compare to the reference *K* field in Figure 4A.

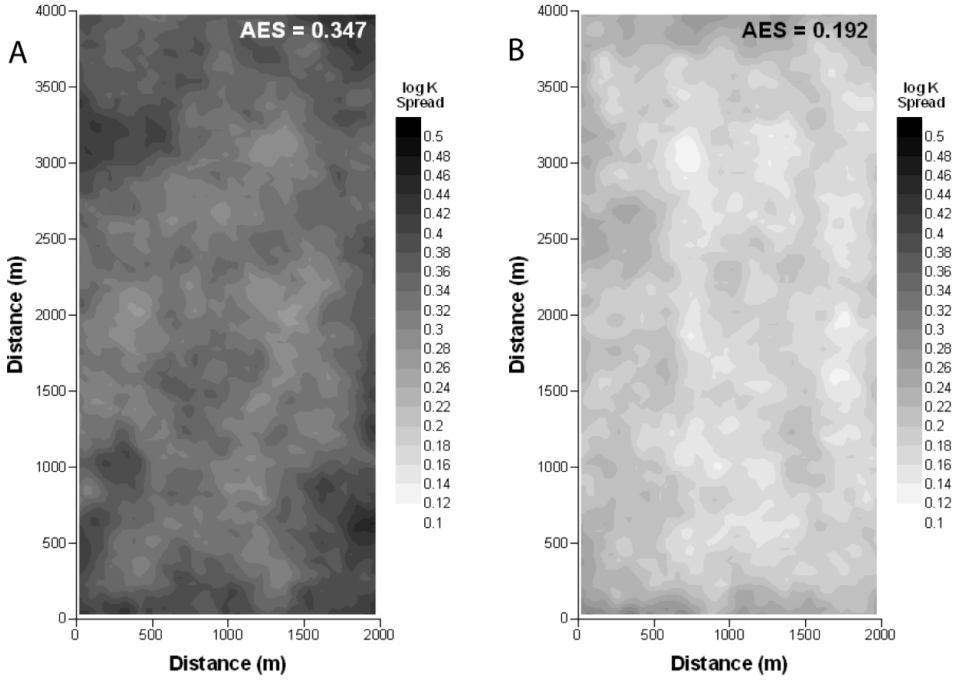

Figure D- 8. Ensemble spread at every model node of (A) the forecast *K* ensemble generated using SKSIM, and (B) the updated *K* ensemble conditioned by 21 *H* measurements.

Table D- 1. Sensitivity of performance parameters to number of assimilation times, measurement coefficient of variation, and *K* field correlation length, when only *H* measurements are used to condition the *K* fields.

						AE *(K)*		***AES*** *(K)*	
Scenario	**Analysis**	**Num Meas** *H*	**Num AT** *H*	**Corr Length** λ	**Coeff Var** *H*	***AE*** *K*	**% Reduct**	***AES*** *K*	**% Reduct**
Forecast	-	-	-	300	-	**0.482**	-	**0.346**	-
Forecast	-	-	-	1000	-	**0.485**	-	**0.347**	-
1	*H* Assimilation Times	21	**1**	300	0.000	**0.422**	12.8%	**0.296**	14.8%
2		21	**2**	300	0.000	**0.414**	14.6%	**0.285**	17.9%
3		21	**4**	300	0.000	**0.410**	15.4%	**0.273**	21.3%
4		21	**6**	300	0.000	**0.408**	15.8%	**0.268**	22.8%
5		21	**8**	300	0.000	**0.405**	16.4%	**0.263**	24.3%
6		21	**12**	300	0.000	**0.404**	16.6%	**0.258**	25.6%
7	*H* Measurement Error	21	12	1000	**0.000**	**0.313**	35.5%	**0.192**	44.8%
8		21	12	1000	**0.025**	**0.320**	34.0%	**0.206**	40.6%
9		21	12	1000	**0.050**	**0.343**	29.1%	**0.225**	35.2%
10		21	12	1000	**0.100**	**0.362**	25.3%	**0.253**	27.0%
11		21	12	1000	**0.200**	**0.370**	23.5%	**0.295**	15.0%
12		21	12	1000	**0.300**	**0.451**	6.9%	**0.323**	7.0%
13	*K* Correl. Length	21	12	**300**	0.000	**0.403**	16.8%	**0.256**	26.3%
14		21	12	**500**	0.000	**0.372**	23.5%	**0.217**	37.2%
15		21	12	**1000**	0.000	**0.313**	35.5%	**0.192**	44.8%
16		21	12	**1500**	0.000	**0.298**	38.4%	**0.183**	47.6%

Scenarios 1 through 6 analyzed the effect of the number of assimilation times on the performance parameters. Using a correlation length of 300 m, assimilating measurements from 12 months instead of 1 month reduced the *AE* value from 0.422 to 0.404, a moderate decrease, and the *AES* value from 0.296 to 0.258.

In regards to the error assigned to the *H* measurements (Scenarios 7 through 12), conditioning of *K* ceases when the coefficient of variation assigned to the *H* measurement is approximately 0.30 (Scenario 12). For an *H* measurement value of 31.2 m, this corresponds to measurement perturbations that range from approximately 6% to 90%, or 1.87 m to 28.1 m, from the measurement value, with 69 of the 100 measurement ensemble members within 25% of 31.2 m. In contrast, the perturbations assigned to the measurement value when the coefficient of variation is set to 0.025 (Scenario 8) range from 0.5% to 7.5%, or 0.16 m to 2.3 m, from the measurement value, with 69 of the 100 measurement ensemble members within 2.15% of 31.2 m.

The results from Scenarios 13 through 16 show that the correlation length of the *K* fields has a strong influence on the ability of the *H* measurements to condition the *K* ensemble, with the *AE* reduced from 0.403 to 0.298 when using correlation lengths of 300 m and 1500 m, respectively. The number of *H* measurements assimilated also has a strong influence (Figure D-9), although the *AE* reduces from only 0.319 to 0.313 when 14 and 21 measurements are used, respectively.

The CPU time to run the update routine, with monthly *H* ensembles and the *K* ensemble resulting in a $\boldsymbol{X}^{f}{}_{t_F}$ matrix of dimension [43052 x 100], was approximately 20 seconds, or 1.53% of the CPU time required to generate the forecast ensembles.

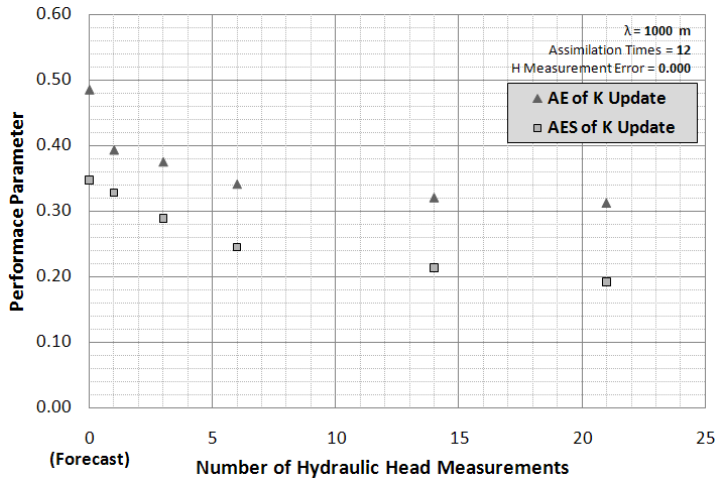

Figure D- 9. Sensitivity of the *K* ensemble performance parameters to the number of *H* measurements assimilated.

D.3.2.3 Conditioning to Dissimilar Geostatistical Frameworks

Further analysis was performed to assess the usefulness of the ES scheme when applied to real aquifer systems. In recognizing that the aquifer system from which the *H* measurements are collected in all probability has a different geostatistical formulation than that of the *K* ensemble used in the forecast step, six scenarios were tested that use reference *K* fields generated using modified geostatistical parameters from those used to generate the forecast *K* ensemble (μ_{Y_K} = -4.30; σ_{Y_K} = 0.434; λ = 1000 m). The results of these tests are presented in Table D-2. In

scenarios 1 and 2, μ_{Y_K} was increased to -3.80 and decreased to -4.80, respectively; in scenarios 3 and 4, σ_{Y_K} was decreased to 0.363 and increased to 0.495; and in scenarios 5 and 6, λ was 500 m and 1500 m.

Table D- 2. Ability of ES scheme to condition to reference *K* fields that have different geostatistical parameters than the *K* forecast ensemble.

	Reference State		***AE** (K)*		
Scenario	**Parameter Varied***	**Parameter Value**	**Forecast**	**Update**	**% Reduction**
1	μ_{YK}	-3.80	0.654	**0.587**	10.2%
2	μ_{YK}	-4.80	0.640	**0.595**	7.1%
3	σ_{YK}	0.132	0.456	**0.389**	14.8%
4	σ_{YK}	0.245	0.531	**0.421**	20.8%
5	λ	500	0.485	**0.339**	30.0%
6	λ	1500	0.484	**0.304**	37.2%

* Parameter values used in the forecast for each scenario were μ_{YK} = -4.30; σ_{YK} = 0.434; λ = 1000 m
Each scenario was conditioned using 21 *H* measurements from 12 assimilation times.
All *AES* forecast values were 0.347 and all *AES* update values were 0.192.

The reduction in *AE* from the forecast to update steps was greatest for the scenarios in which the true correlation length was different than the forecasted correlation length (scenarios 5 and 6), with the *AE* of the *K* ensemble reduced by 30.0% and 37.2%. The smallest reduction in *AE* (10.2% and 7.1%) occurred in scenarios 1 and 2, signifying that the update scheme has difficulties conditioning to the true *K* field when the true *K* values are shifted up or down from those assumed in the forecasted, prior aquifer system state. If the variance in the true *K* field is either lower or higher than that assumed in the forecast step, as in scenarios 3 and 4, the update scheme provides moderate improvement, with a reduction of 14.8% and 20.8%, respectively.

D.3.2.4 Update of *K* Ensemble using Return Flow Measurements

Return flow volumes were calculated from the ensemble of flow fields and assimilated into the model results to produce an updated *K* ensemble. Figure D-10 shows the ensemble mean and ensemble spread of the updated *K* fields from a scenario using 26 assimilation times (bi-weekly collection of measurements) and 4 stream gages. In comparison to the reference *K* field (see

Figure D-4A), the updated *K* ensemble captures the principal spatial patterns, although the updated fields overestimate the *K* values in the west-northwest region of the aquifer, due to the lack of influence of the *RFV* measurements on the opposite side of the aquifer, and underestimates the *K* values in the north-central region.

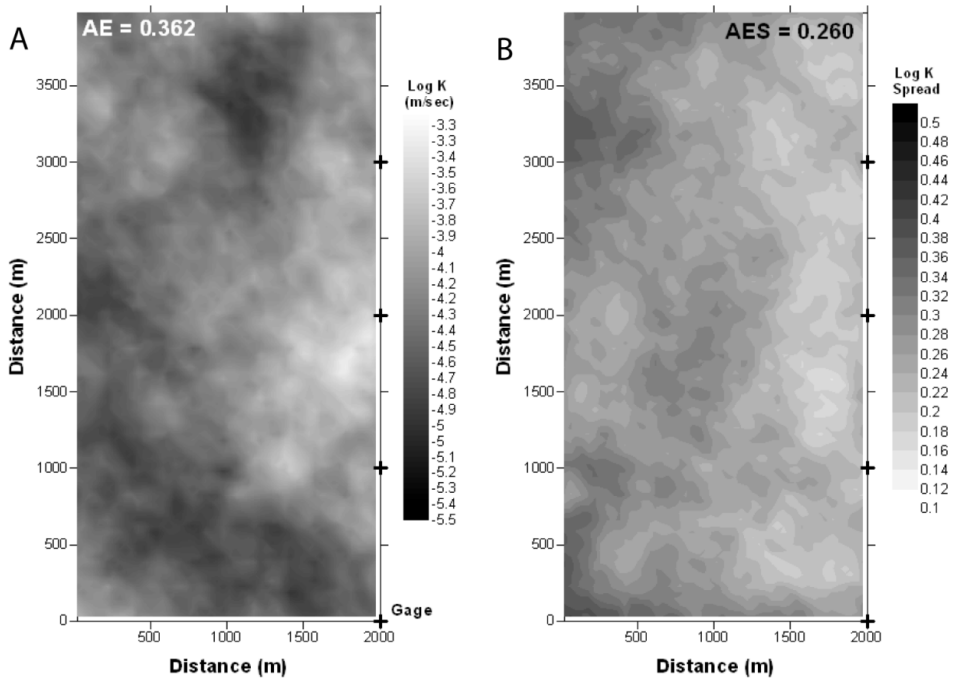

Figure D- 10. (A) Updated ensemble mean and (B) Updated ensemble spread at every model location, by assimilating bi-weekly return flow volumes calculated using four stream gages. Compare (A) to reference *K* field in Figure 4A; Compare (B) to forecast ensemble spread shown in Figure 8A.

The improvement gained from the update is also reflected in the performance parameters, with the *AE* decreased from 0.485 to 0.362, a reduction of 25.4%, and the *AES* decreased to 0.260, a reduction of 25.1%. A note of interest involves the spatial variation of the ensemble spread (Figure D-10B), with the lowest values occurring on the eastern edge of the aquifer, nearest the *RFV* measurement locations. CPU time to run the update routine, with bi-weekly *RFV* ensembles and the *K* ensemble resulting in a $\boldsymbol{X}^{f}{}_{t_F}$ matrix of dimension [3248 x 100], was approximately 1 second, or 0.08% of the CPU time required to generate the forecast ensembles.

The sensitivity analysis of the performance parameters is similar to the *H* measurement conditioning study, consisting of *RFV* measurement coefficient of variation, the number of assimilation times, the correlation length used in generating the forecast *K* ensemble, and the the number of stream gages. The coefficient of variation ranged from 0.00 to 3.00 (Scenarios 1 through 6); the number of assimilation times ranged from 1 (measurements taken only at 365 days) to 52 (weekly measurements) (Scenarios 7 through 12); *K*-field correlation lengths used were 300 m, 500 m, 1000 m, and 1500 m (Scenarios 13 through 16); and the number of gage locations ranged from 1 (gage located at the south end of the stream) to 20 (gages located every 200 m). Results are shown in Table D-3 and Figure D-11.

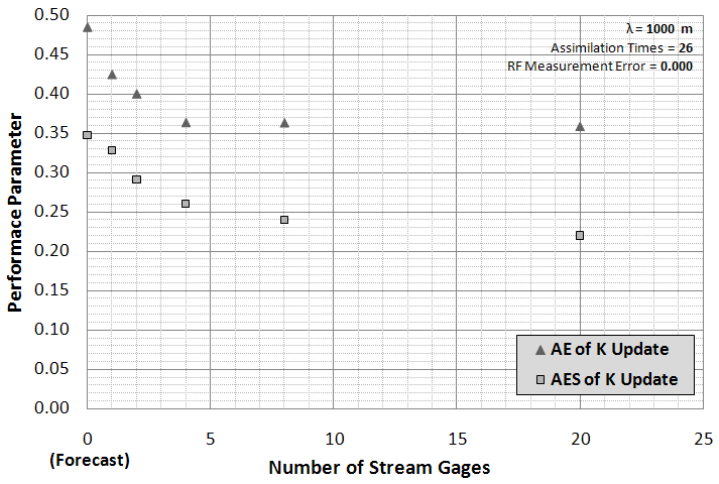

Figure D- 11. Sensitivity of the *K* ensemble performance parameters to the number of stream gages used to calculate ground water return flow volumes.

Assimilating measurements from every week instead of yearly improved the *AE* value from 0.384 to 0.362 and the *AES* value from 0.286 to 0.260, a reduction of 5.73% and 9.09%. In regards to *RFV* measurement error, improvement in performance parameters diminishes as the coefficient of variation approaches 3.00. Similar to the scenarios when *H* measurements were used to condition the *K* ensemble, the correlation length used also dramatically influences the *K*

update, with *AE* and *AES* improvements of only 7.9% and 14.0% when a length of 300 m is used, as opposed to an improvement of 29.1% and 28.9% when a length of 1500 m is used. Increasing the number of gages from 1 to 4 (Figure D-11) improved the *AE* and *AES* values from 0.425 to 0.362 and 0.338 to 0.260, a reduction of 14.8% and 23.1%, respectively.

Table D- 3. Sensitivity of performance parameters to measurement coefficient of variation, number of assimilation times, and *K* field correlation length, when only *RFV* measurements are used to condition the *K* fields.

						***AE** (K)*		***AES** (K)*	
Scenario	**Analysis**	**Num Gages** *RF*	**Num AT** *RF*	**Corr Length** *λ*	**Coeff Var** *RF*	***AE*** *K*	**% Reduct**	***AES*** *K*	**% Reduct**
Forecast*	-	-	-	1000	-	**0.485**	-	**0.347**	-
1	*H* Measurement Error	4	26	1000	**0.000**	**0.363**	25.0%	**0.260**	25.1%
2		4	26	1000	**0.300**	**0.372**	23.3%	**0.285**	18.1%
3		4	26	1000	**0.600**	**0.387**	20.1%	**0.293**	15.7%
4		4	26	1000	**1.250**	**0.415**	14.4%	**0.309**	11.0%
5		4	26	1000	**2.000**	**0.435**	10.3%	**0.323**	6.9%
6		4	26	1000	**3.000**	**0.452**	6.6%	**0.337**	3.0%
7	*H* Assimilation Times	4	**1**	1000	0.000	**0.384**	20.7%	**0.286**	17.7%
8		4	**2**	1000	0.000	**0.360**	25.7%	**0.266**	23.6%
9		4	**6**	1000	0.000	**0.356**	26.6%	**0.264**	24.0%
10		4	**12**	1000	0.000	**0.362**	25.2%	**0.260**	25.1%
11		4	**26**	1000	0.000	**0.363**	25.0%	**0.260**	25.1%
12		4	**52**	1000	0.000	**0.362**	25.2%	**0.260**	25.0%
13	*K* Correl. Length	4	26	**300**	0.000	**0.446**	7.9%	**0.299**	14.0%
14		4	26	**500**	0.000	**0.414**	14.7%	**0.283**	18.1%
15		4	26	**1000**	0.000	**0.363**	25.0%	**0.260**	25.1%
16		4	26	**1500**	0.000	**0.343**	29.1%	**0.248**	28.9%

D.3.2.5 Update of *K* Ensemble using Head and Return Flow Measurements

Further update scenarios were performed using both *H* and *RFV* measurements to jointly condition the *K* ensemble. Assimilating monthly 21 *H* measurements and bi-weekly *RFV* measurements using 4 stream gages resulted in an updated *K* ensemble (Figure D-12) that approaches the reference *K* field more closely than the scenarios in which only *H* measurements (Figure D-7B) or only *RFV* measurements (Figure D-10A) were assimilated. In terms of the performance parameters, *AE* value for the joint update was 0.301, reduced from 0.313 for the *H* measurement assimilation scenario and 0.362 for the *RFV* measurement assimilation scenario, an

improvement of 3.83% and 16.9%, respectively. As seen in Figure D-12, the updated *K* ensemble no longer underestimates the *K* values in the east-northeast region, as occurs when assimilating only *H* measurements (Figure D-7B), nor overestimates the *K* values in the west-northwest region, as occurs when assimilating only *RFV* measurements (Figure D-10A).

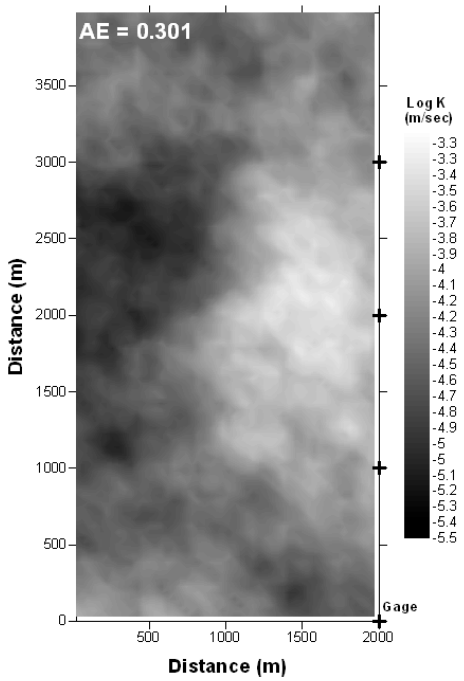

Figure D- 12. Updated *K* ensemble mean at every model location, by assimilating monthly 21 *H* measurements and bi-weekly *RFV* calculated using four stream gages. Compare to reference *K* field in Figure 4A.

Update scenarios using both *H* and *RFV* measurements were also run across the four correlation lengths of 300 m, 500 m, 1000 m, and 1500 m, using monthly assimilation times for both *H* and *RFV*. The results are shown in Figure D-13. Update scenarios using only *K* measurements, with the 10 measurement locations shown in Figure D-4C, were also run in order to compare the updated *K* ensemble with those when assimilating the system response variables. Of the four update routine scenarios of (a) 10 *K* measurements only, (b) monthly 21 *H* measurements only, (c) bi-weekly *RFV* measurements at 4 gaging stations only, and (d) both *H* and *RFV* measurements, (c) has the smallest influence on conditioning the *K* ensemble, followed by (a) and (c), with (d) having the largest influence (Figure D-13). However, it should be noted

that the coefficient of variation of measurements for all scenarios was set to 0.00, which is not very realistic in the case of *K* measurements. When a correlation length of 1000 m is used, and the coefficient of variation is set to 0.300 for each measurement, the *RFV* conditioning (*AE* = 0.372) provides a better estimate than the *K* conditioning (0.458), demonstrating that poor performance occurs when *K* measurements contain error. CPU time to run the update routine, with monthly *H* ensembles, bi-weekly *RFV* ensembles and the *K* ensemble resulting in a $\boldsymbol{X}^{f}{}_{t_F}$ matrix of dimension [43100 x 100], was approximately 21 seconds, or 1.61% of the CPU time required to generate the forecast ensembles.

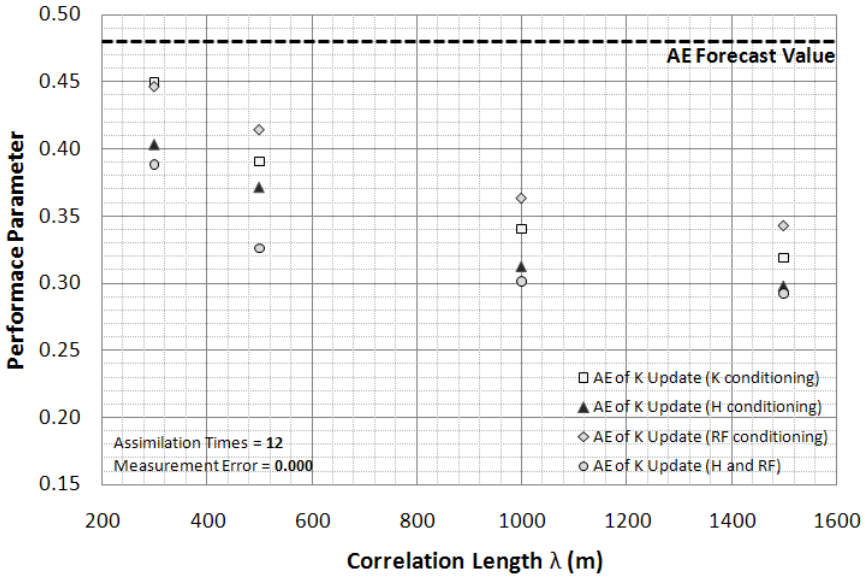

Figure D- 13. Influence of correlation length λ on the AE performance parameter for update scenarios of conditioning by (1) 10 *K* measurements, (2) 21 *H* measurements, (3) bi-weekly *RFV* measurements from 4 gaging stations, and both *H* and *RFV* measurements. Note: the AE forecast values for the various correlation lengths are: 0.482 (λ=300 m); 0.486 (λ=500 m); 0.485 (λ=1000 m); 0.484 (λ=1500 m).

A final set of scenarios was run in order to evaluate the influence of measurement placement when both sets of data, *H* and *RFV*, are used to condition the *K* ensemble. In departing from the measurement placement shown in Figure D-4C, 9 *H* measurements were placed in a north-south line near (1) the west edge of the aquifer with and without *RFV* measurement assimilation, for

scenarios 1 and 2 and (2) the east edge of the aquifer with and without *RFV* measurement assimilation, for scenarios 3 and 4.

As seen in Table D-4, there is considerable improvement in the fit to the reference state when both *H* and *RFV* measurements are assimilated (scenarios 2 and 4) as opposed to the situation when only *H* measurements are used (scenarios 1 and 3). The worst and best fits to the reference *K* field are scenarios 1 and 2, respectively, with *AE* values of 0.407 and 0.336 (Figure D-14), a reduction of 17.4%. As seen in Figure D-14, the updated *K* ensemble in scenario 2 more closely resembles the reference state (see Figure D-4A) than in scenario 1. The improvement between scenarios 3 and 4 is only 13.0% (0.399 to 0.347) . These results indicate that improvement in including *RFV* measurements, and the fit to the reference *K* field, is best when the *H* and *RFV* measurements data are collected from separate regions of the aquifer region as in scenario 2, since the *RFV* and *H* measurement data condition the *K* values in close proximity to the stream and in the western region of the aquifer, respectively. Collecting *H* data from the aquifer region near the stream, as in scenario 4, results in redundancy in conditioning the *K* values, and provides small influence on the *K* values in the western aquifer region.

Table D- 4. Results of measurement placement update scenarios, showing the improvement in performance parameters when both *H* and *RFV* measurements are assimilated.

					AE *(K)*		***AES*** *(K)*	
Scenario	***H*** **Meas. Placement**	**Num Gages**	**Num AT** *H*	**Num AT** *RF*	***AE*** *K*	**% Reduct**	***AES*** *K*	**% Reduct**
Forecast		-	-	-	**0.485**	-	**0.347**	-
1	**West**	0	12	12	**0.407**	16.0%	**0.247**	28.9%
2	**West**	4	12	12	**0.336**	30.7%	**0.21**	39.6%
3	**East**	0	12	12	**0.399**	17.7%	**0.256**	26.3%
4	**East**	4	12	12	**0.347**	28.3%	**0.22**	36.6%

Number of *H* measurements for each scenario = 9; λ = 1000 m; Measurement Error = 0.00

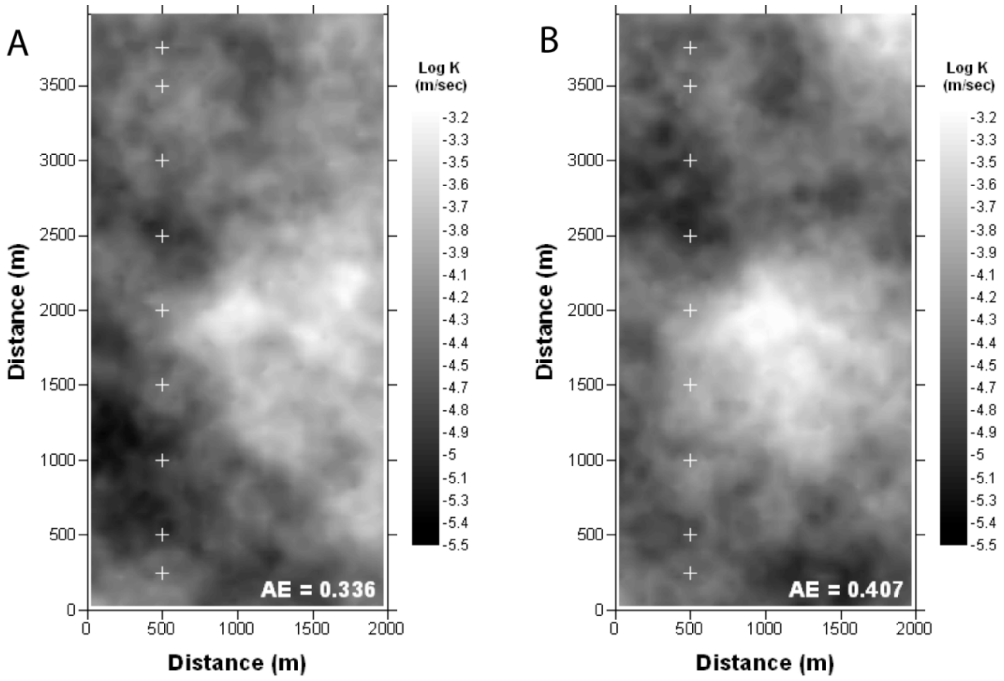

Figure D- 14. Updated *K* ensemble mean at every model location using (A) both *H* and *RFV* measurements (scenario 2), and (B) only *H* measurements (scenario 1).

D.4 Discussion

From results presented in Section 3, the ES update scheme is quite successful in using system response variables such as *H* and *RFV* measurements to condition the *K* fields to the reference *K* field. Sensitivity analyses demonstrate that conditioning the *K* ensemble is a function of (1) the number of assimilated measurements, (2) the error assigned to the measurements, (3) the number of measurement assimilation times, (4) the number of gaging locations along the stream, in the case of return flow volumes, and (5) the correlation length used in generating the initial ensemble of *K* fields.

Of these parameters, the correlation length of the *K* fields produces the greatest change in the *AE* value per change in the correlation length, with larger correlation lengths enhancing the ability of *H* and *RFV* measurements to provide an updated *K* ensemble that approaches the reference *K* field. This is inherent in the update routine (Equation (2)), since corrections to the

forecast values are dependent on the spatial covariance between *K* values, *H* and *K* values, and *RFV* and *K* values of the forecast ensembles. *K* fields that have highly spatially-correlated *K* values will, using the groundwater flow model, produce *H* fields that are also highly spatially-correlated. As such, information from *H* measurement locations will be spread further throughout the model domain, thus correcting *K* forecast values that otherwise would not be if a shorter correlation length were used. This feature of Kalman Filter methods, such as the ES scheme used in this study, is particularly important in the case of *RFV*, which are measured on only one side of the model domain. In order for spatial correlations to exist between the *K* values near the stream, which is strongly conditioned by the *RFV* measurements, and the *K* values at distances further from the stream, the *K* correlation lengths must be significant in order for *RFV* measurements to "reach" further west into the aquifer region. Hence, *K* ensembles conditioned by return flow volumes have much lower *AE* values when the correlation length is 1000 m or 1500 m, as opposed to 300 m or 500 m. This is also seen in the lower standard deviation of *K* values experienced on the side of the aquifer closest to the gage locations (Figure D-10B). Similar conclusions on the importance of correlation length were also drawn by *Chen and Zhang* [2006].

The issue of correlation length can also be seen in Figure D-13, where the improvement of *AE* when using both *H* and *RFV* measurements compared to the scenario when using only *H* measurements is slight for correlation lengths of 300 m, 1000 m, and 1500 m (reduction in *AE* of 3.7%, 3.6%, and 1.9%, respectively) but considerable (reduction in *AE* of 12.2%) when a correlation length of 500 m is used. For small correlation lengths there are no long conductivity paths in connection with the stream, and the localized *K* distribution patterns of the reference state are out of reach of the *RFV*. For large correlation lengths there are several long conductivity

paths in each forecasted *K* realization, including the reference state, in connection with the stream, and hence the *RFV* measurements provide no new additional information than what is already contained in the *H* measurement data. On the other hand, for intermediate correlation lengths, in which only a portion of the forecasted *K* fields contain long conductivity paths in connection with the stream, *RFV* measurements can be more informative on whether these measurements come from a reference state that contains no high conductivity paths, as opposed to one that has several high conductivity paths, and hence can provide information concerning the reference *K* state that is not available from the *H* measurements.

As measurement errors increase, the measurements have less and less influence on correcting the *K* forecast ensemble. *H* measurements cease to have an influence on the *K* ensemble when the coefficient of variation of the error is approximately 0.30. In reference to Equation (2), this situation equates to the variance of the measurements being sufficiently high to decrease the Kalman Gain matrix values to the point that the residuals at measurement locations receive very little weight. Hence, the forecast receives no correction. Of practical interest is the relation of the coefficient of variation with actual errors in field measurements. For example, a coefficient of variation of 0.025 assigned to an *H* measurement of 31.2 m corresponds to an ensemble of perturbation values in which the majority of the values are within 0.67 m, or 2.15%, of the assimilated measurement of 31.2 m. With this error assigned to the measurement value, the ability of the ES scheme to provide an accurate conditioning of the *K* ensemble only slightly diminishes (*AE* of 0.320) from the scenario in which no measurement error occurs (*AE* of 0.313) (Table D-1). This also has implications of scale, as errors arise when using point measurements of field data to represent model grid cell values. In this case, an error of 0.67 m represents the acceptable range in hydraulic head throughout an area represented by a model grid cell from

which a point measurement of hydraulic head is sampled, while still achieving a good fit to the reference *K* field. As such, the ES scheme is relatively insensitive to the measurement errors that occur in the field.

As seen in Table D-1, the improvement in *AE* of the *K* update ensemble shows negligible improvement when *H* measurements over more than 7 months are included in the update routine. This would be very valuable for systems containing a large number of variables, as the measurements and forecast ensembles from other assimilation times do not need to be included in the update routine, hence saving on CPU time. In terms of the general smoothing process, this same aspect can be seen in Figure D-6, where a cease in improvement of the system state at time = 31 days occurs when more than 7 months of measurement data are included in the update routine.

In the case of *RFV* measurement assimilation, the number of stream gaging stations have almost as strong of an influence on conditioning the *K* ensemble as the correlation length (see Table D-3 and Figure D-11). As the number of gages increases the calculated *RFV* values are more localized, and hence provide more information regarding the local *K* zones adjacent to the stream. However, the improvement in correcting the *K* ensemble is only valid up to a certain number of gaging stations, as the difference in having 4 gages (*K* ensemble *AE* = 0.363) and 20 gages (*K* ensemble *AE* = 0.358) is slight. Overall, the use of *RFV* measurements in conditioning *K* is promising , especially when used in conjunction with point measurements of *H*. The influence of the *RFV* measurements on the global *K* distribution in the aquifer is similar to the effect of groundwater travel times used by *Fu and Gomez-Hernandez* [2009], although calculating *RFV* measurements using flow measurements at stream gages may present a simpler, alternative method to installing wells required for tracer data collection. It should be noted that

the value of the *RFV* measurement data depends on the accuracy of the mass-balance along the stream reach. As such, the degree of measurement error assigned to the *RFV* data should be typically higher than that for *H* measurement data (see Table D-3 in Section 3.2.4).

As a side note, *K* measurements can also be assimilated directly into the *K* ensemble generated by SKSIM. When this was done, *AE* and *AES* values improved by a few percentage points compared to using the ES update routine to assimilate the *K* measurements. This would be of further interest in studies relying heavily on *K* measurements to condition the *K* ensemble.

For single-variable measurement assimilation, it is clear that *H* measurements have a stronger influence than *RFV* on producing a *K* ensemble that approaches the reference *K* field (see Figure D-13). However, adding *RFV* measurements to *H* measurements in a dual-variable measurement assimilation provides the best *K* ensemble estimate. The importance of having two sets of disparate system response data, such as *H* and *RFV*, to condition system parameters coincides with results from other inverse modeling studies [*Gailey et al.*,1991; *Franssen et al.*, 2003; *Gomez-Hernandez et al.*, 2003; *Fu and Gomez-Hernandez*, 2009], with the conclusion that information contained in one system response variable useful in conditioning a system parameter is distinct from the information contained in the other, resulting in an overall improved estimate of the parameter. For example, assimilating both *H* and *RFV* measurement data (section 3.2.4) is able to overcome the shortcomings when only *H* measurement data was assimilated (underestimation of *K* in some aquifer regions) and only *RFV* measurement data was assimilated (overestimation of *K* in some regions).

Furthermore, an analysis of the placement of *H* measurement locations demonstrates that the placement of observation wells, when stream gages are also used to calculate *RFV* measurements, can be placed far from the stream and still provide a reliable update of the *K*

ensemble, as the *H* and *RFV* data combine to condition *K* throughout the entire aquifer. Placement of observation wells is thus different if only *H* measurement data can be assimilated as opposed to the situation when both *H* and *RFV* data can be collected and used.

Lastly, computation burden of using the ES scheme is minimal, especially when compared with other inverse modeling methods, as the CPU time of the update routine is approximately 0.08 % of the CPU time required to run the simulation forecast ensemble when *RFV* measurements are assimilated, 1.5% when *H* measurements are assimilated, and 1.6 % when both *H* and *RFV* measurements are assimilated. The forecast/update CPU time ratio is not anticipated to be much higher when applying the ES scheme to real-world aquifer systems, as the longer CPU time of the update routine due to a larger number of cells is countered by the longer solution time of the more-complex, nonlinear state equations of the numerical models, such as catchment hydrology models [*Camporese et al.*, 2009].

D.5 Concluding Remarks

The Ensemble Smoother (ES), a statistical data assimilation routine that blends uncertain, model-produced values with measurement data within a Bayesian framework, was implemented and evaluated for synthetic groundwater flow simulations within a geostatistically uniform environment. Overall, using the ES scheme in an inverse modeling framework was successful in providing an updated ensemble that approaches the reference hydraulic conductivity (*K*) field. In the 2D transient flow simulations, both *H* measurements and return flow volumes (*RFV*) were used to condition the *K* ensemble, with stronger conditioning occurring with the *H* measurements for the correlation lengths used in this study. The ability of the scheme to condition to a reference *K* field generated using different geostatistical parameter than those used in generating the *K*

forecast ensemble further demonstrated the robustness of the method, especially when the correlation length of the reference *K* field was different than that of the forecast ensemble.

Sensitivity analyses demonstrated that for the scenarios addressed in this study the *K* ensemble conditioning was most sensitive to, in decreasing order, correlation length used in generating the *K* forecast ensemble, the number of measurements assimilated, and the error assigned to the assimilated measurements. The correlation length in the random *K* fields is of principal importance, as information from *H* measurement locations and stream gaging stations is able to be spread further throughout the model domain in correcting the *K* values.

The principal uniqueness of the ES scheme is the capability of including all past measurement data and model states into the update routine, thus allowing all assimilated measurements to condition all model states. In this way model states from previous times are improved upon by the assimilation of new measurements. With this structure, the ES update routine can be run once all model results and measurements have been collected, enabling the algorithm to be written and used independently from the model simulation, and allowing the code to be used for output from any model. Other advantages of the routine are shared with the Ensemble Kalman Filter (EnKF), namely the ability to (1) include a number of correlated system response variables and system parameters into the forecast system state matrix, (2) assimilate system response and system parameter measurements, (3) account for various sources of uncertainty in both model system and measurements and quantify this uncertainty, and (4) the low computational burden required by the update routine in comparison to other inverse modeling techniques. A disadvantage associated with the routine is the potential for producing corrected model values that are not consistent with the physical laws stipulated in the state equations, although this is of more

concern when updating system response variables rather than estimating parameters, as in this study.

Potential further research includes using three-dimensional, surface-subsurface coupled hydrologic models in the ES scheme, using the ES scheme in groundwater solute transport models, and applications to real-world modeling scenarios, such as in hydraulically-connected stream-aquifer systems.

Funding Source and Reviewers

The majority of this work has been made possible by a Colorado Agricultural Experiment Station (CAES) grant (Project No. COL00690). We would also like to acknowledge Harrie-Jan Hendricks-Franssen as well as two anonymous reviewers for their helpful comments and suggestions in improving the content of this paper.

References

Ahmed, S., and G. De Marsily (1993), Cokriged Estimation of Aquifer Transmissivity as an Indirect Solution of the Inverse Problem: A Practial Approach, *Water Resour. Res.*, 29(2), 521-530.

Aksoy, A., F. Zhang, and J.W. Nielsen-Gammon (2006), Ensemble-based simultaneous state and parameter estimation in a two-dimensional sea-breeze model, *Mon. Weather Rev.*, 134, 2951-2970.

Baú, D.A., and A.S. Mayer (2008), Optimal design of pump-and-treat systems under uncertain hydraulic conductivity and plume distribution, *J. Cont. Hydrol.*, 100, 30-46.

Bennett, A.F. (1992), *Inverse Methods in Physical Oceanography*, Cambridge Univ. Press, New York.

Burgers, G., P.J. van Leeuwen, and G. Evensen (1998), Analysis scheme in the Ensemble Kalman Filter, *Mon. Weather Rev.*, 126, 1719-1724.

Camporese, M., C. Paniconi, M. Putti, and P. Salandin (2009), Ensemble Kalman filter data assimilation for a processbased catchment scale model of surface and subsurface flow, *Water Resour. Res.*, 45, W10421, doi:10.1029/2008WR007031.

Chen, Y., and D. Zhang (2006), Data assimilation for transient flow in geologic formations via Ensemble Kalman Filter. *Adv. Water Resour.*, 29(8), 1107-1122.

Deutsch, C.V. and A.G. Journel (1998), GSLIB: Geostatistical software library. Oxford University Press.

Dunne, S. and D. Entekhabi (2005), An ensemble-based reanalysis approach to land data assimilation. *Water Resour. Res.*, 41, W02013, doi:10.1029/2004WR003449.

Dunne, S. and D. Entekhabi (2006), Land surface state and flux estimation using the ensemble Kalman smoother during the Southern Great Plains 1997 field experiment. *Water Resour. Res.*, *42*, W01407, doi:10.1029/2005WR004334.

Durand, M., N. P. Molotch, and S. A. Margulis (2008), A Bayesian approach to snow water equivalent reconstruction. *J. Geophys. Res.*, *113*, D20117, doi:10.1029/2008JD009894.

Evensen, G. (1994), Sequential data assimilation with a nonlinear quasi-geostrophic model using Monte Carlo methods to forecast error statistics. *J. Geophys. Res.*, 99(C5), 10, 143-10,162.

Evensen, G. (2003), The ensemble Kalman filter: theoretical formulation and practical implementation. *Ocean Dynam.*, 53, 343-367.

Evensen, G. Data assimilation. The Ensemble Kalman Filter. Springer-Verlag Berlin Heidelberg, 2007.

Evensen, G., and P.J. van Leeuwen (1996), Assimilation of Geosat altimeter data for the Agulhas Current using the ensemble Kalman filter with a quasigeostropic model. *Mon. Weather Rev.*, 124, 85-96.

Evensen, G., and P.J. van Leeuwen (2000), An ensemble Kalman smoother for nonlinear dynamics. *Mon. Weather Rev.*, 128, 1852-1867.

Fu, J., and J.J. Gomez-Hernandez (2009), Uncertainty assessment and data worth in groundwater flow and mass transport modeling using a blocking Markov chain Monte Carlo method, *J. Hydrol.*, 364, 328-341.

Gailey, R.M., Crowe, A.S., and S.M. Gorelick (1991), Coupled process parameter estimation and prediction uncertainty using hydraulic head and concentration data. *Adv. Water Resour.*, 14(5), 301-314.

Gambolati, G., M. Putti, and C. Paniconi (1999), Three-dimensional model of coupled density-dependent flow and miscible salt transport in groundwater, In J. Bear, A.H.D. Cheng, S. Sorek, D. Ouazar and I. Herrera Eds., *Seawater Intrusion in Coastal Aquifers: Concepts, Methods and Practices*, Kluwer Academic Publ., Dordrecht, The Netherlands, 10, 315-362.

Gomez-Hernandez, J.J., Hendricks Franssen, H.-J., and A. Sahuquillo (2003) Stochastic conditional inverse modeling of subsurface mass transport: A brief review and the self-calibrating method. *Stoch. Environ. Res. and Risk Assess*. 17, 319-328.

Hantush, M.M., and M.A. Marino (1997), Estimation of spatially variable aquifer hydraulic properties using Kalman filtering. *J. Hydraul. Engrg. ASCE*, 123(11), 1027-1035.

Hendricks Franssen, H. J., Gomez-Hernandez, J.J., Capilla, J.E., and A. Sahuquillo (1999), Joint simulation of transmissivity and storativity fields conditional to steady-state and transient hydraulic head data. *Adv. Water Resour.*, 23, 1-13.

Hendricks Franssen, H. J., Gomez-Hernandez, J.J., and A. Sahuquillo (2003), Coupled inverse modeling of groundwater flow and mass transport and the worth of concentration data. *J. Hydrol.*, 281, 281-295.

Hendricks Franssen, H. J., and W. Kinzelbach (2008), Real-time groundwater flow modeling with the Ensemble Kalman Filter: Joint estimation of states and parameters and the filter inbreeding problem. *Water Resour. Res.*, 44, W09408, doi:10.1029/2007WR006505.

Hendricks Franssen, H. J., and W. Kinzelbach (2009), Ensemble Kalman filtering versus sequential self-calibration for inverse modeling of dynamic groundwater flow systems. *J. Hydrol.*, 365, 261-274.

Houtekamer, P.L., and H.L. Mitchell (1998), Data assimilation using an ensemble Kalman filter technique. *Mon. Weather Rev.*, 126, 796-811.

Kalman, R.E. (1960), A new approach to linear filtering and prediction problems. *J. Basic Eng.*, 82, 35-45.

Keppenne, C. (2000), Data assimilation into a primitive-equation model with a parallel ensemble Kalman filter. *Mon. Weather Rev.*, 128, 1971-1981.

Kitanidis, P.K., and E.G. Vomvoris (1983), A geostatistical approach to the inverse problem in groundwater modeling (stead state) and one dimensional simulations, *Water Resour. Res.*, 19(3), 677-690.

Li, B. and T.-C. Jim Yeh (1999), Cokriging estimation of the conductivity field under variably saturated flow conditions, *Water Resour. Res.*, 35(12), 3663-3674.

Liu, Y., and H.V. Gupta (2007), Uncertainty in hydrologic modeling: Toward an integrated data assimilation framework, Water Resour. Res., 43, W07401, doi:10.1029/ 2006WR005756.

Liu, G., Y. Chen, and D. Zhang (2008), Investigation of flow and transport processes at the MADE site using ensemble Kalman filter. *Adv. Water Resour.*, 31, 975-986.

Maybeck, P.S. *Stochastic models, estimation, and control*. Volume 1. Academic Press, Inc. (London), 1979.

McLaughlin, D. (2002), An integrated approach to hydrologic data assimilation: interpolation, smoothing, and filtering. *Adv. Water Resour.*, 25, 1275-1286.

Moradkhani, H., S. Sorooshian, H.V. Gupta, and P.R. Houser (2005), Dual state-parameter estimation of hydrological models using ensemble Kalman filter. *Adv. Water Resour.*, 28, 135-147.

Ngodock, H.E., Jacobs, G.A., and M. Chen (2006), The representer method, the ensemble Kalman filter and the ensemble Kalman smoother: A comparison study using a nonlinear reduced gravity ocean model. *Ocean Modelling*, 12, 378-400.

Pauwels, V. R. N., and G. J. M. De Lannoy (2006), Improvement of modeled soil wetness conditions and turbulent fluxes through the assimilation of observed discharge. *J. Hydrometeorol.*, 7(3), 458–477.

Polubarinova-Kochina, P. Ya. Theory of Groundwater Movement. Princeton NJ: Princeton University Press, 1962

RamaRao, B.S., LaVenue, A.M., De Marsily, G., and M.G. Marietta (1995), Pilot point methodology for automated calibration of an ensemble of conditionally simulated transmissivity field 1. Theory and computational experiments. *Water Resour. Res.*, 31(2), 475-493.

Reichle, R.H., D.B. McLaughlin, and D. Entekhabi (2002), Hydrologic data assimilation with the ensemble Kalman filter. *Mon. Weather Rev.*, 130, 103-114.

Valstar, J.R., McLaughlin, D.B., te Stroet, C.B.M., and F.C. van Geer (2004), A representer-based inverse method for groundwater flow and transport application. *Water Resour. Res.*, 40, W05116, doi:10.1029/2003WR002922.

Van Geer, F.C., C.B.M. te Stroet, and Y. Zhou (1991). Using Kalman filtering to improve and quantify the uncertainty of numerical groundwater simulations, 1, The role of system noise and its calibration, *Water Resour. Res.*, 27(8), 1987-1994.

van Leeuwen, P.J. (2001), An ensemble smoother with error estimates. *Mon. Weather Rev.*, 129, 709-728.

van Leeuwen, P.J., and G. Evensen (1996), Data assimilation and inverse methods in terms of probabilistic formulation. *Mon. Weather Rev.*, 124, 2898-2913.

Wang, D., Y. Chen, and X. Cai (2009), State and parameter estimation of hydrologic models using the constrained ensemble Kalman filter, *Water Resour. Res.*, 45, W11416, doi:10.1029/2008WR007401.

Yeh, T.-C. J., Gutjahr, A.L., and M. Jin (1995), An iterative cokriging-like technique for ground-water flow modeling. Ground Water 33(1), 33-41.

APPENDIX E

ESTIMATING GEOSTATISTICAL PARAMETERS AND SPATIALLY-VARIABLE HYDRAULIC CONDUCTIVITY WITHIN A CATCHMENT SYSTEM USING AN ENSEMBLE SMOOTHER[4]

E.0 Summary

Groundwater flow models are important tools in assessing baseline conditions and investigating management alternatives in groundwater systems. The usefulness of these models, however, is often hindered by insufficient knowledge regarding the magnitude and spatial distribution of the spatially-distributed parameters, such as hydraulic conductivity (*K*), that govern the response of these models. Proposed parameter estimation methods frequently are demonstrated using simplified aquifer representations, when in reality the groundwater regime in a given watershed is influenced by strongly-coupled surface-subsurface processes. Furthermore, parameter estimation methodologies that rely on a geostatistical structure of *K* often assume the parameter values of the geostatistical model as known or estimate these values from limited data.

In this study, we investigate the use of a data assimilation algorithm, the Ensemble Smoother, to provide enhanced estimates of *K* within a catchment system using the fully-coupled, surface-subsurface flow model CATHY. Both water table elevation and streamflow data are assimilated to condition the spatial distribution of *K*. An iterative procedure using the ES update routine, in which geostatistical parameter values defining the true spatial structure of *K* are identified, is also presented. In this procedure, parameter values are inferred from the updated ensemble of *K* fields and used in the subsequent iteration to generate the *K* ensemble, with the process

[4] As published in Hydrology and Earth System Sciences 16, 287-304 (2012), Ryan T. Bailey, Domenico A. Baù

proceeding until parameter values are converged upon. The parameter estimation scheme is demonstrated via a synthetic three-dimensional tilted v-shaped catchment system incorporating stream flow and variably-saturated subsurface flow, with spatio-temporal variability in forcing terms. Results indicate that the method is successful in providing improved estimates of the *K* field, and that the iterative scheme can be used to identify the geostatistical parameter values of the aquifer system. In general, water table data have a much greater ability than streamflow data to condition *K*. Future research includes applying the methodology to an actual regional study site.

E.1 Introduction

E.1.1 Inverse Modeling in Groundwater Applications

Hydrologic models are important tools in assessing baseline conditions and investigating best-management practices in groundwater and catchment-scale systems. Before reliable hydrologic assessments can be made, however, parameter values that drive the response of the model must be appropriately chosen for a specific aquifer or catchment. Direct measurements of hydrologic parameters, however, are scarce and fraught with uncertainty, and typically only apply locally due to the spatial variability of parameter values.

To address this problem of parameter uncertainty, hydrologic models can be used in applications “opposite” or “inverse” to their original use, i.e., parameter values are treated as system unknowns and are determined by extracting information from observations of system-response variables (Kitanidis and Vomvoris, 1983). The general approach consists of determining the set of parameter values that yields adequate matches between model results and observations from the true hydrologic system. The treatment of parameter values as unknowns that need to be identified constitutes the inverse problem of groundwater modeling (Kitanidis

and Vomvoris, 1983), and in most cases must be incorporated in the modeling process (Carrera et al., 2005).

In recent decades numerous methodologies have been proposed and applied to the inverse modeling problem in groundwater modeling, with the general aim to estimate the spatial distribution of hydraulic conductivity (*K*) or transmissivity (*T*) in an aquifer system. An excellent review of early inverse methods is provided by Carrera and Neuman (1986). A review of more recently-proposed methods is given by Carrera et al. (2005). Broadly, parameter estimation is accomplished either through (i) optimization procedures, in which an objective function is defined (typically minimizing the error between model results and measurements) and minimized in a least-squares approach, and (ii) statistical conditioning, in which covariance between the parameters and system-response variables is utilized to condition the parameter values using measurement information. It should be noted that conditioning methods also incorporate a sense of optimization, although the optimization occurs in the derivation of the conditioning algorithm, e.g., through minimizing the trace of the *a posteriori* error estimate covariance matrix (e.g., Kalman, 1960).

For the optimization classification, methods include zonation, the pilot point method (e.g., RamaRao et al., 1995), the represent method (RM) (Bennett, 1992; Valstar et al., 2004), and the self-calibrated method (SCM) (Hendricks Franssen et al., 1999; Gómez-Hernández et al., 2003). For the statistical conditioning classification, methods include Cokriging (e.g., Ahmed and De Marsily, 1993; Li and Yeh, 1999) and data assimilation techniques, such as the family of Kalman Filter (Kalman, 1960) methods, including the Extended Kalman Filter (EKF) (Evensen, 1992), the Ensemble Kalman Filter (EnKF) (Evensen, 1994; Evensen, 2003), the Ensemble Kalman Smoother (EnKS) (Evensen and van Leeuwen 2000), and the Ensemble Smoother (ES) (van

Leeuwen and Evensen, 1996). The EnKF has particularly been used in recent years to estimate state parameters. Comparisons between the RM and EnKF methods are given by Reichle et al. (2002) and Ngodock et al. (2006). A comparison between the SCM and EnKF methods is provided by Hendricks Franssen and Kinzelbach (2009).

Proposed methodologies are demonstrated typically using simplified hydrologic systems. For applications to groundwater systems, the majority of methodologies are demonstrated using two-dimensional (2D) confined groundwater flow models (e.g., Gailey et al., 1991; Hantush and Mariño, 1997; Hendricks Franssen et al., 1999; Gómez-Hernández et al., 2003; Drécourt et al., 2006; Hendricks Franssen and Kinzelbach, 2008; Fu and Gómez-Hernández, 2009; Bailey and Baù, 2010). Several studies have employed three-dimensional steady-state flow models (Chen and Zhang, 2006; Liu et al., 2008), and several have estimated hydraulic parameters in variably-saturated flow conditions (Yeh and Zhang, 1996; Zhang and Yeh, 1997; Li and Yeh, 1999), although for the latter applications were limited to small 2D vertical-plane systems. In general, however, critical components of hydrology in watershed systems, e.g., infiltration and percolation in variably-saturated porous media, ponding and overland flow, and stream channel flow have been neglected. Catchment models such as CATHY (CATchment HYdrology), based on the 3D Richards equation for variably-saturated porous media and a diffusion wave approximation for overland and channel flow, have been used in data assimilation studies (Camporese et al., 2009; Camporese et al., 2010), but not yet in parameter estimation. Estimation of parameters in land-surface models has been performed (e.g., Boulet et al., 2002; Xie and Zhang, 2010), although the models treat groundwater flow using simplified approaches.

In recognition that improved parameter estimation occurs when system-response data from more than one governing equation is used (Gailey et al., 1991), with the implication that each

data type contains unique information regarding the parameter, numerous studies have employed two or more sets of dissimilar data to condition the parameter values. Such data sets typically include hydraulic head data as well as another data type such as solute concentration data (Gailey et al., 1991; Li and Yeh, 1999; Hendricks Franssen et al., 2003; Gómez-Hernández et al., 2003; Liu et al., 2008), groundwater temperature (Woodbury and Smith, 1988), groundwater travel time (Fu and Gómez-Hernández, 2009), groundwater discharge to surface water (Bailey and Baù, 2010), and tracer breakthrough data at observation wells (Wen et al., 2002). Streamflow data, which carries information regarding the spatial structure of aquifer *K* due to groundwater-surface water interactions, has been used in data assimilation to improve model performance (Schreider et al., 2001; Aubert et al., 2003; Clark et al., 2008; Camporese et al., 2009; Camporese et al., 2010), although as yet has not been used to condition *K*.

E.1.2 Kalman Filter Methods

In Kalman Filtering methods, *a priori* information, i.e., model parameters and associated model results, are merged with observation data from the true system to produce an *a posteriori* system estimate honoring the true system data at observation points, while still incorporating physically-based information from the numerical model. The resulting algorithm is used to merge model and measurement data whenever measurement data become available during the course of the model simulation.

In contrast to a filter, which assimilates data sequentially as they become available, a smoother incorporates all past model and measurement information in a single assimilation step. The EnKF, EnKS, and ES all use an ensemble of realizations to represent numerically the measurement error statistics (Evensen, 2003), and are designed for large, nonlinear systems. The EKF, EnKF, EnKS, and ES have all been used in hydrologic modeling applications in both

system-response updating (e.g., Schreider et al.,2001; Aubert et al., 2003; Dunne and Entakhabi, 2005; Clark et al., 2008; Durand et al., 2008; Camporese et al., 2009; Camporese et al., 2010) and system parameter conditioning (Hantush and Mariño, 1997; Boulet et al., 2002 ; Chen and Zhang, 2006; Hendricks Franssen and Kinzelbach, 2008; Liu et al., 2008; Bailey and Baù, 2010; Xie and Zhang, 2010). Application of the EnKF and ES to highly nonlinear hydrologic systems such as a land surface model (Dunne and Entakhabi, 2005) and a coupled surface and variably-saturated subsurface flow model (Camporese et al., 2009) has proven successful.

E.1.3 Geostatistics in Parameter Estimation

Many parameter estimation studies employ geostatistical models (GMs) to define the *a priori* estimate of the spatial distribution of *log-K* or *log-T* (e.g., Kitanidis and Vomvoris, 1983; Hantush and Mariño, 1997; Chen and Zhang, 2006; Hendricks Franssen and Kinzelbach, 2008), under the assumption that aquifer *K* in regional systems can generally be described using such models (Kitanidis and Vomvoris, 1983; Hoeksema and Kitanidis, 1985; Carrera et al., 2005). The values of the parameter (e.g.,, *log-K* mean, *log-K* variance, correlation length) that characterize these GMs often have a strong influence on the response of a groundwater model and parameter estimation results (Jafarpour and Tarrahi, 2011), and yet in practice are estimated from limited geologic information and hence are not known with a high degree of certainty (Gautier and Nœtinger, 2004; Jafarpour and Tarrahi, 2011).

As a consequence, several methodologies have aimed at estimating the values of GM parameters, with the general approach of (i) performing “structural analysis”, in which the form of the GM is selected, followed by (ii) an estimation of the values of the parameters defining the GM using observation data from the aquifer system. For example, Kitanidis and Vomvoris (1983) and Hoeksema and Kitanidis (1984) used maximum likelihood estimation to estimate

values for a two-parameter GM using measurements of *log-T* and hydraulic head in 1D and 2D steady-state flow systems, respectively, in their approach to estimating the spatial distribution of *log-T*. A more recent review of the technique is given in Kitanidis (1996). More recent studies in the field of petroleum-reservoir engineering (e.g., Yortsos and Al-Afaleg, 1997; Gautier and Noetinger, 2004) have used well test data to estimate parameter values of the permeability variogram. For example, Gautier and Noetinger (2004) expanded on the work of Kitanidis and Vomvoris (1983) to develop a methodology for transient flow.

E.1.4 Objectives of this Study

The objectives of this study are three-fold. The first objective is to apply the Kalman Filter parameter estimation methodology within a fully-coupled surface and variably-saturated subsurface flow model to provide more realistic simulation of water table elevation, as well as allow for streamflow to be simulated. To accomplish this, the CATHY model is used in a tilted v-catchment setting, similar in design to the v-catchment used by Camporese et al. (2009), with uncertain initial conditions (i.e., water table elevation) and uncertain patterns of applied water at the ground surface in space and time in a 365-day simulation. An ES is used to assimilate water table elevation data from a reference system to provide an updated estimate of the spatial distribution of *log-K*. Using uncertain initial conditions and forcing terms provides a stiff test for estimating *K* (Hendricks Franssen and Kinzelbach, 2008) since values of water table elevation and streamflow are not influenced solely by *K*. The second objective is to exploit the functionality of CATHY to explore the possibility of using streamflow measurements, solely and jointly with water table elevation data, to condition *K*.

The third objective is to use the ES in an iterative scheme to identify the parameters of a geostatistical model through assimilation of water table elevation data, and hence provide a new

methodology for estimating the value of these parameters. In this study, the ability of the scheme to assess the log-mean and log-variance of a geostatistical model is investigated. Uncertainty in correlation scales is not addressed in this study, but is left to future work. Assessment of the true correlation scale for a given aquifer will likely require the direct assimilation of *K* measurements, whereas in this study only the model response variables are assimilated.

For the first and second objectives, the influence of the number of measurements and the uncertainty assigned the measurement data on the ability of the ES to provide accurate updates is investigated. Overall, with uncertainty in initial conditions, forcing terms, and geostatistical model parameters, the complexity of real-world systems is approached, providing a key liaison between theory and real-world application.

E.2 Methodology

In this section, the theoretical development of the ES update algorithm is presented within the context of estimating the spatial distribution of *K* using observed water table elevation (*WT*) and streamflow (*Q*) data from a reference catchment system. The general forecast and update steps of the Kalman Filter are first discussed, followed by a modification of these steps for the ES scheme.

E.2.1 Forecast of System State

Using an ensemble of n_{MC} system realizations to establish the uncertainty in the system, the state of the system is estimated using the *model forecast* step:

$$\boldsymbol{X}_t^f = \Phi_t\left(\boldsymbol{P};\boldsymbol{X}_0;\boldsymbol{q};\boldsymbol{b}\right) \tag{1}$$

where *f* indicates *forecast*, $\boldsymbol{X}_t^f$ contains the ensemble of realizations of the forecasted estimate of the system at time *t*, $\boldsymbol{\Phi}_t$ represents the solution to the numerical model, and $\boldsymbol{P}$, $\boldsymbol{X}_0$, $\boldsymbol{q}$, and $\boldsymbol{b}$

represent the system parameters, initial conditions, forcing terms, and boundary conditions, respectively. The numerical model employed in this study is the CATHY model, and is used to generate values of *WT* and *Q* as well as establish relationships between the system parameter (i.e., *K*) and the system response variables (i.e., *WT* and *Q*).

CATHY simulates subsurface, overland, and channel flow by coupling the 3D Richards equation for variably saturated porous media with a 1D diffusion wave approximation of the de Saint Venant equation for surface flow (Bixio et al., 2000; Camporese et al., 2010). The groundwater flow equation is given by Camporese et al. (2010):

$$S_w S_s \frac{\partial \psi}{\partial t} + \phi \frac{\partial S_w}{\partial t} = \nabla \cdot \left[\boldsymbol{K}_s K_r \left(\nabla \psi + \eta_z \right) \right] + q_{ss} \tag{2a}$$

where $S_w = \theta/\theta_s$, with θ and θ_s as volumetric water content [-] and saturated water content (porosity) [-], respectively, S_S is the specific storage coefficient [L^{-1}], ψ is pressure head [L], t is time [T], ∇ is the spatial gradient operator [L^{-1}], $\boldsymbol{K}_s$ is the saturated hydraulic conductivity tensor [LT^{-1}] with $\boldsymbol{K}_s$ treated as a scalar field when conditions of isotropy are hypothesized, $K_r(\psi)$ is the relative hydraulic conductivity function [-], η_z = (0, 0, 1), z is the vertical coordinate directed upward [L], and q_{ss} represents distributed source or sink terms [$L^3L^{-3}T^{-1}$].

Using a 1D coordinate system s [L] to describe the channel network, the surface water flow equation is given by (Camporese et al. 2010):

$$\frac{\partial Q}{\partial t} + c_k \frac{\partial Q}{\partial s} = D_h \frac{\partial^2 Q}{\partial s^2} + c_k q_s \tag{2b}$$

where Q is the discharge along the stream channel [L^3T^{-1}], c_k is the kinematic celerity [LT^{-1}], D_h is the hydraulic diffusivity [L^2T^{-1}], and q_s is the inflow or outflow rate from the subsurface to the surface [$L^3L^{-1}T^{-1}$].

In CATHY, Equation (2a) is solved using Galerkin finite elements (FE), whereas Equation (2b) is solved using an explicit time discretization based on the Muskingum-Cunge routing scheme (Orlandini and Rosso, 1996). In this study, the $K_r(\psi)$ and $S_w(\psi)$ relationships are specified using the formulation of van Genuchten and Nielsen (1985), although other capillary curves are available in CATHY (see Camporese et al., 2010). The channel network is identified using the terrain topography from a digital elevation model (DEM) and the hydraulic geometry concept used by Orlandini and Rosso (1996). The DEM cells are then triangulated to generate a 2D triangular FE mesh, which is replicated vertically to construct a 3D tetrahedral FE mesh for the subsurface system. Interaction between surface water and groundwater modeled in CATHY is described by Putti and Paniconi (2004).

As will be discussed further in Section 2.2, the resulting system state $\boldsymbol{X}$ (Equation (1)) is comprised of: 1) a *WT* value for each node of the triangular FE mesh, calculated using the vertical profile of ψ for each of these nodes; 2) a *K* value for each DEM cell in the horizontal direction; 3) a *Q* value for each DEM grid cell along a stream channel. If *e* and *n* denote the number of DEM cells and FE nodes in the horizontal direction, respectively, and *g* the number of DEM cells along the stream channel, then the dimension *d* of $\boldsymbol{X}$ is equal to $[n+e+g]$. The forcing terms $\boldsymbol{q}$ in Equation (1) are represented by q_{ss} in Equation (2a), and in this study correspond to rates of applied water at the ground surface, with uncertainty established by sampling values from a prescribed frequency distribution. Uncertainty in $\boldsymbol{X_0}$ is also included, as discussed in Section 3.1.

The spatially-variable values of $Y_K = \log K$ are generated using SKSIM (Baù and Mayer, 2008), a sequential Gaussian simulation algorithm, where the spatial distribution and correlation

is established by a normal distribution wherein the geostatistical model is a 2D exponential covariance model in the logarithmic domain:

$$\log K = Y_K = N\left(\mu_{Y_K}; \sigma_{Y_K}\right)$$

$$cov_{Y_K, Y_K}(d) = \sigma^2_{Y_K} . \exp\left(\sqrt{\sum_{i=1}^{2} \frac{d_i^2}{\lambda_i^2}}\right) \quad (3)$$

where μ_{Y_K} and σ_{Y_K}, and $\sigma^2_{Y_K}$ are the mean, standard deviation, and variance of the logarithmic distribution of the parameters, respectively, d_is are the components of the distance vector **d**, and λ_is are the spatial correlation scales in the coordinate directions.

E.2.2 Update of System State

Correction to the *a priori* estimate $\boldsymbol{X}_t^f$ is accomplished by assimilating observed system-response data from the true system, thereby merging the model-calculated and observed values. This correction depends on the uncertainty attached to both the *a priori* estimate (i.e., the model results) and the true values (i.e., the observations from the true system), with uncertainty in the model forecast provided by the spread in the ensemble values and uncertainty in the observed values specified according to data-sampling methods. The correction made to the model-calculated values by the observed values is dictated by the ratio of these uncertainties. If there is less uncertainty attached to the observed data, which is typically the case, then the model-calculated value at the observation location will be corrected to approach the observed value. Furthermore, model results can also receive correction from observed data if the model value is correlated with the model value at the observation location. In this way information from the true state at observation points can be "spread" to regions between observation locations, and hence throughout the model domain.

This correction procedure is carried out through the following Kalman Filter update equation, with the forecasted ensemble $\boldsymbol{X}^f_t$ corrected, or updated, at a time t using m observed data stored in a vector $\boldsymbol{M}_t$ [m]:

$$\boldsymbol{X}^u_t = \boldsymbol{X}^f_t + \boldsymbol{\kappa}_t \left(\boldsymbol{D}_t - \boldsymbol{H}\boldsymbol{X}^f_t \right) \tag{4}$$

where $\boldsymbol{X}^u_t$ [d x n_{MC}] is the updated ensemble with u denoting update; $\boldsymbol{D}_t$ [m x n_{MC}] holds the ensemble of perturbed values of the measurement data, with the ensemble of values for each measurement value calculated by adding a Guassian perturbation (stored in the matrix $\boldsymbol{E}$ [m x n_{MC}]) to each of the m observations stored in $\boldsymbol{M}_t$; $\boldsymbol{H}$ [m x d] contains binary constants (0 or 1) resulting in the matrix product $\boldsymbol{H}\boldsymbol{X}^f_t$ that holds model results at measurement locations, and $\boldsymbol{\kappa}_t$ [d x m] is the so-called "Kalman Gain" matrix. In this study, observation data are sampled from a known reference state to enable assessment of the ES scheme.

In Equation (4), the difference, or residual, between the model values and observed values is represented by $\left(\boldsymbol{D}_t - \boldsymbol{H}\boldsymbol{X}^f_t \right)$, with the weighting of the correction and the spatial spread of the information dictated by $\boldsymbol{\kappa}_t$, which holds the ratio of uncertainties as well as the covariance between model values at each model node (Bailey and Baù, 2011). The form of $\boldsymbol{\kappa}_t$ is:

$$\boldsymbol{\kappa} = \boldsymbol{C}^f \boldsymbol{H}^T \left(\boldsymbol{H}\boldsymbol{C}^f \boldsymbol{H}^T + \boldsymbol{R} \right)^{-1} \tag{5}$$

where $\boldsymbol{C}^f$ [d x d] and $\boldsymbol{R}$ [m x m] are the forecast error and observation error covariance matrices, respectively, and are defined as:

$$\boldsymbol{C}^f = \frac{\left(\boldsymbol{X}^f_{t+\Delta t} - \overline{\boldsymbol{X}} \right)\left(\boldsymbol{X}^f_{t+\Delta t} - \overline{\boldsymbol{X}} \right)^T}{nmc - 1} \tag{6a}$$

$$\boldsymbol{R} = \frac{\boldsymbol{E}\boldsymbol{E}^T}{nmc - 1} \tag{6b}$$

where each column of $\overline{\boldsymbol{X}}$ [n x n_{MC}] holds the average value of the ensemble at each location in the domain.

In a straightforward application of data assimilation to a catchment system, Equation (4) would correspond to merging observed values of *WT* (or *Q*) with the model-calculated *WT* field (or *Q* along a stream channel) in order to provide a *WT* field that honors the observed *WT* data. However, doing so only corrects the system response of the model – the structural difference between the *a priori* model state and the true state that yields differences in the system response will persist indefinitely. To temper these structural differences, it is essential to correct the parameters that drive the system response. This can be accomplished by utilizing the relationships between *K* and the resulting values of *WT* and *Q* as established through CATHY. For example, the cross-covariance submatrix between *WT* and Y_K is defined as:

$$\boldsymbol{C}_t^f\left(X_{(WT)}, X_{(Y_K)}\right) = \frac{\left[\left(\boldsymbol{X}_t^f - \overline{\boldsymbol{X}}\right)_{WT}\right]\left[\left(\boldsymbol{X}_t^f - \overline{\boldsymbol{X}}\right)_{Y_K}\right]^T}{n_{MC} - 1} \tag{7}$$

By including the expression for Equation (7) into Equation (5), the values of Y_K in $\boldsymbol{X}^f_t$ can be corrected by observation data in $\boldsymbol{D}_t$ through the spatial correlation between Y_K, *WT*, and *Q*.

E.2.3 Forecast-Update Scheme for the Ensemble Smoother

Whereas Equations (1) and (4) are run in a sequential manner in the KF and EnKF schemes, with correction via Equation (4) occurring whenever observation data are sampled from the true system, the ES algorithm includes all previous model state and observation data up to the final data sampling time t_{nF}, at which time the ES update routine is run to provide updated system

states at all previous collection times. At time t_{nF}, the forecast matrix $\widetilde{\boldsymbol{X}}_{t_F}{}^{f}$ and the observation matrix $\widetilde{\boldsymbol{D}}_{t_F}$ hold the model state ensembles and the perturbed observation data from all data sampling times (t_1, t_2,…, t_{nF}):

$$\widetilde{\boldsymbol{X}}_{t_F}{}^{f} = \left[\boldsymbol{X}_{t_1}, \boldsymbol{X}_{t_2}, \ldots, \boldsymbol{X}_{t_{nF}}\right]^{T} \qquad \left[\left(d\right)\left(nF\right)\right] \mathrm{x}\, n_{MC} \tag{8a}$$

$$\widetilde{\boldsymbol{D}}_{t_f} = \left[\boldsymbol{D}_{t_1}, \boldsymbol{D}_{t_2}, \ldots, \boldsymbol{D}_{t_{nF}}\right]^{T} \qquad \left[\left(m\right)\left(nF\right)\right] \mathrm{x}\, n_{MC} \tag{8b}$$

where nF is the number of times at which measurements are collected. Within the ES scheme, the forecast covariance matrix $\widetilde{\boldsymbol{C}}_{t_{nF}}^{f}$ contains both spatial covariance terms and temporal covariance terms between cell values from different collection times (*Evensen*, 2007). The measurement error covariance matrix $\widetilde{\boldsymbol{R}}_{t_{nF}}$ also is established using the perturbations for each of the measurement values for each of the nF collection times. By inserting $\widetilde{\boldsymbol{X}}_{t_{nF}}{}^{f}$ and $\widetilde{\boldsymbol{D}}_{t_{nF}}$ into Equation (4) and $\widetilde{\boldsymbol{C}}_{t_{nF}}^{f}$ and $\widetilde{\boldsymbol{R}}_{t_{nF}}$ into Equation (5), the updated system state matrix $\widetilde{\boldsymbol{X}}_{t_{nF}}{}^{u}$ contains the updated model state for each assimilation time.

The Keppenne (2000) algorithm, which provides an efficient numerical strategy for updating the system state for the EnKF scheme and designed for high-resolution real-world climate numerical models, was modified to include model states and observation data from each assimilation time (Bailey and Baù, 2010) and used to compute Equation (4) within the ES framework. The techniques employed by Keppenne (2000) and hence inherent in the update algorithm used in this study do not require the direct assemblage of $\boldsymbol{C}^{f}$, hence saving on computer memory and preventing numerical issues.

E.2.4 Evaluating the Updated System State

The ability of the ES algorithm to bring the forecasted ensemble into conformity with the true system state is quantified through two location-specific parameters *EE* (ensemble error) and *EP* (ensemble precision) and two global parameters *AE* (absolute error) and *AEP* (average ensemble precision) (Hendricks Franssen and Kinzelbach, 2008; Bailey and Baù, 2011):

$$EE_i = \left| \overline{X}_i - X_{i,true} \right| \quad \left(i = 1,\ldots,n \right) \tag{9a}$$

$$EP_i = \frac{1}{nmc} \sum_{j=1}^{nmc} \left| X_{i,j} - \overline{X}_i \right| \quad \left(i = 1,\ldots,n \right) \tag{9b}$$

$$AE(X) = \frac{1}{\left(nmc \right)\left(n \right)} \sum_{j=1}^{nmc} \sum_{i=1}^{n} \left| X_{i,j} - X_{i,true} \right| \tag{9c}$$

$$AEP(X) = \frac{1}{\left(nmc \right)\left(n \right)} \sum_{j=1}^{nmc} \sum_{i=1}^{n} \left| X_{i,j} - \overline{X}_i \right| \tag{9d}$$

where $\overline{X}_i$ is the ensemble mean of the i^{th} location (node in a FE discretization of the domain or cell of the surface DEM grid), $X_{i,true}$ is the reference "true" value of the i^{th} location, and $X_{i,j}$ is the variable value of the i^{th} location of the j^{th} ensemble realization. Equations (9a) and (9c) provide a measure of the deviation between the model state and the reference state, and Equations (9b) and (9d) provide a measure of the spread of the values around the ensemble mean of the model state. The performance of the update routine is measured by calculating the difference between performance parameters of the forecasted and updated ensembles. As a second type of performance measure, the ensemble of CATHY simulations can be rerun using the updated ensemble of Y_K fields to determine if the updated Y_K ensemble produces simulated results that match the observed data, i.e. to see if the model has been "calibrated" adequately. This latter method will be demonstrated in Section 3.3.2.

E.2.5 Iterative Method to Estimate Geostatistical Parameters

In the forecast step of Sections 2.1, it is assumed that the parameters defining the GM of Equation (3) are known, i.e., that the parameter values used to generate the ensemble of Y_K fields for the forecast simulations are the same as the reference system from which the observation data is sampled. In recognition that this is generally not the case, the ES scheme decribed in Sections 2.1 through 2.3 is employed in an iterative scheme to discover the geostatistical parameter values of the true system, as shown in Figure E-1. Beginning with a set of estimated GM parameter values, an ensemble of Y_K fields is generated using SKSIM and the corresponding ensemble of CATHY flow simulations is run. Upon assimilating observation data from the reference system and conditioning the Y_K ensemble, the GM parameter values of the updated Y_K ensemble are inferred from the updated ensemble and used to produce the forecast Y_K ensemble for the subsequent iteration. This process proceeds until GM parameter values are converged upon. At each iteration the model-calculated values of *WT* can also be compared to the observed *WT* data from the true aquifer system, to verify that the estimated GM parameter values from the previous iteration yield a spatial structure of Y_K that furnishes the system response of the true system. It should be noted that estimation of the correlation scale λ was not pursued extensively in this study, as it became evident during initial uses of the iterative approach that λ could not be estimated using only a model-response variable such as water table elevation. As discussed in Section 4, the direct assimilation of Y_K values are likely required to provide information regarding λ, and will be pursued in future work.

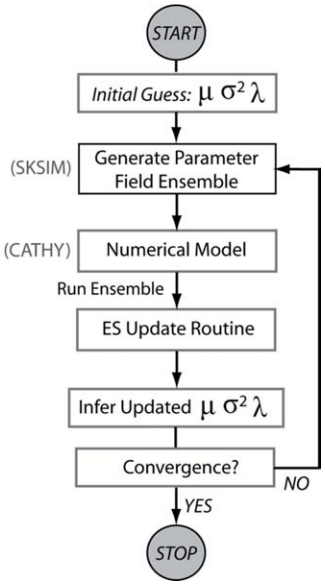

Figure E- 1. Flow chart for the iterative approach using an Ensemble Smoother to estimate geostatistical parameter values.

E.3 Parameter Estimation of Spatially-Variable *K*

E.3.1 Forecast Ensemble of *K, WT*, and *Q*

The catchment system used for the numerical experiment in this study is a 4.05 km by 4.05 km tilted v-shaped catchment, as shown in Figure E-2, with a stream flowing north to south along the central depression of the catchment. The DEM of the surface terrain, discretized using 50 m by 50 m grid cells for a total of e = 81 x 81 = 6561 grid cells, is shown in Figure E-3A with a contour plot of the ground surface elevation. Aquifer thickness varies between 7.5 m and 15.5 m, with the thickest portion under the central depression, as shown in Figures E-2 and E-3B. The subsurface is discretized by n_L = 10 layers of varying thickness, with thicknesses ranging from 0.375 m near the ground surface to 3.0 m near the aquifer base.

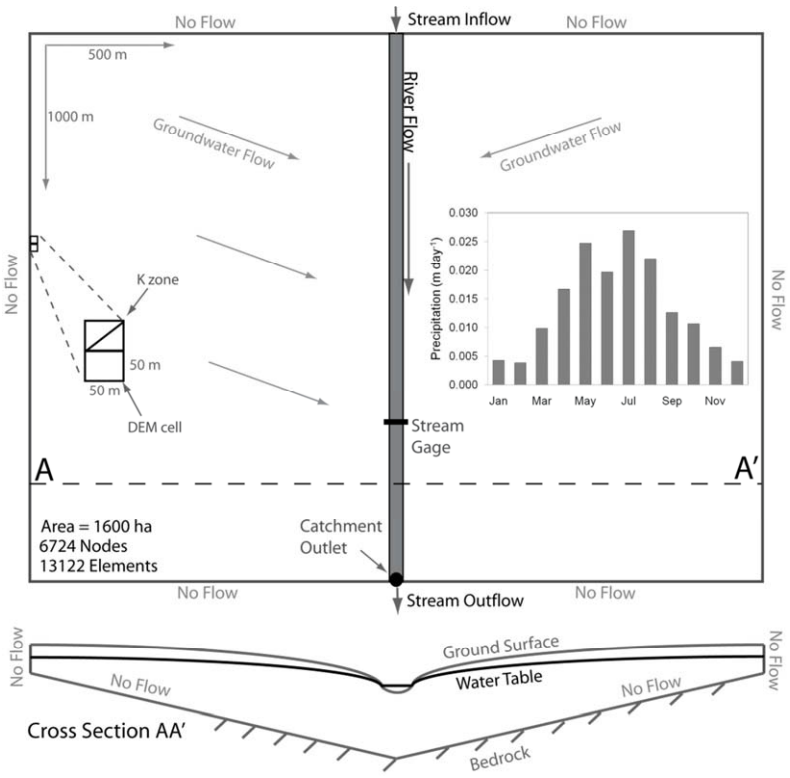

Figure E- 2. Conceptual model of tilted v-shaped catchment, with groundwater feeding the river flowing out of the basin through the catchment outlet. The monthly depth of precipitation applied to the ground surface is also shown.

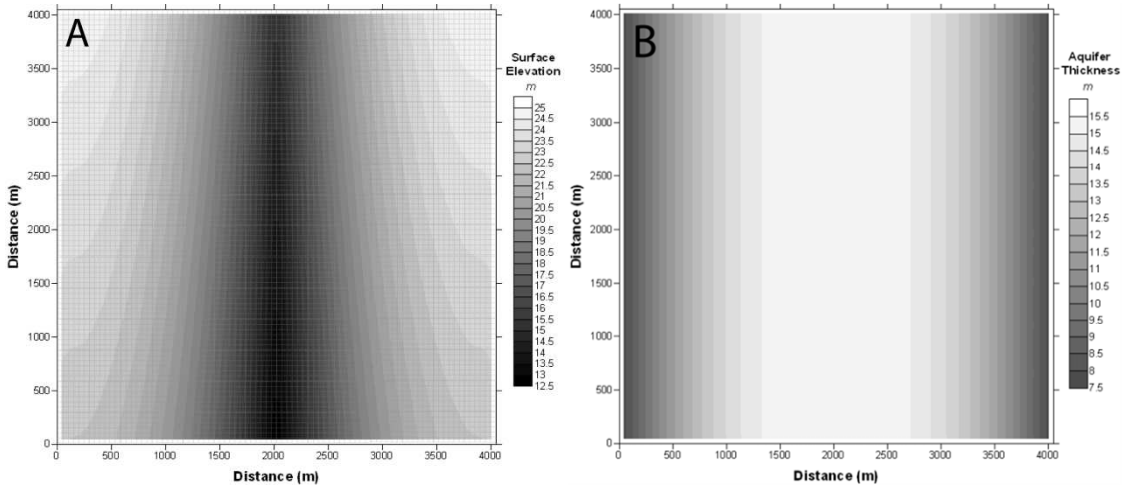

Figure E- 3. Contour representation of (A) ground surface elevation and (B) aquifer thickness. Both datasets are used to create the three-dimensional subsurface finite-element mesh.

The characteristics of the DEM, the 3D mesh, and the parameters of the model are summarized in Table E-1. The number of nodes in the 2D surface FE mesh is n = 82 x 82 = 6724. The 3D mesh is obtained from replicating the 2D FE mesh through the vertical extent of the subsurface and contains 3 x n_L x 2e = 393,660 tetrahedral elements and n x (n_L + 1) = 73,964 nodes. Lateral spatial distribution of Y_K for the forecast ensemble is generated using mean μ_{Y_K} = 1.301 log m day^{-1} (K = 20 m day^{-1}), standard deviation $\sigma^2_{Y_K}$ = (0.250 log m day^{-1})^2, and correlation length (λ_x=λ_y) = 1000 m, resulting in K values ranging from approximately 0.2 m day^{-1} to 1500 m day^{-1}. In this study, n_{MC} = 100 realizations are used for the ensemble. Values of Y_K are calculated for each DEM cell, resulting in a value of Y_K assigned to each 3D FE under the cell. In other words, the spatial distribution of Y_K is the same for each of the 10 layers in the 3D mesh. Vertical hydraulic conductivity, K_v, is set equal to one-third the value of horizontal K.

The simulation period is one year, from January to December. No-flow boundaries are assigned for every edge of the aquifer (see Figure E-2). Forcing terms q_{ss} consist of uniformly-distributed net infiltration from precipitation during the months of January through March and November through December, and spatially-varying rates of net infiltration from applied water (e.g., irrigation water) in addition to net infiltration from precipitation during the months of April through October. For the latter, rates are applied according to the cultivation pattern depicted in Figure E-4A, with cells shown in blue receiving monthly values randomly sampled from an exponential distribution (rate parameter γ = 0.75).

Table E- 1. Attributes of the DEM and three-dimensional mesh, and system parameters used in the CATHY V-Catchment simulations.

DEM Attributes	
Cells in x direction	81
Cells in y direction	81
Grid spacing *m*	50
Number of cells	6561
Mesh Attributes	
Aquifer Thickness	7.5 to 15.5
Number of Layers	10
Number of Surface Nodes	6724
Number of 3D Mesh Nodes	73964
Number of Tetrahedral Elements	393660
System Parameters	
Saturated hydraulic conductivity K_s	GM: Equations (3)
Mean μ of K fields	log 1.30 (m d^{-1})
Variance σ^2 of K fields	log 0.25 (m d^{-1})^2
Correlation Length λ of K fields	1000 m
Specific storage S_s	0.01 m^{-1}
Porosity *n*	0.35
Residual moisture content θ_r	0.061
van Genuchten parameters	α = 0.43 m^{-1}, *n* = 1.70
Simulation Details	
Monte Carlo Ensemble Size	100
Simulation period *days*	730.0

The pattern of cultivation shown in Figure E-4A is the same for each realization, but monthly rates vary across the realizations. The resulting rates are not intended to represent particular irrigation practices, but rather to provide a spatio-temporal variation in the forcing terms of the catchment system. As an example, the rates of net infiltration from combined precipitation and applied water for the month of July for one realization are shown in Figure E-4B, with values ranging from 0.000355 m day^{-1} to 0.006 m day^{-1} (represented by white and black, respectively). The depth of monthly net infiltration is presented in Figure E-2.

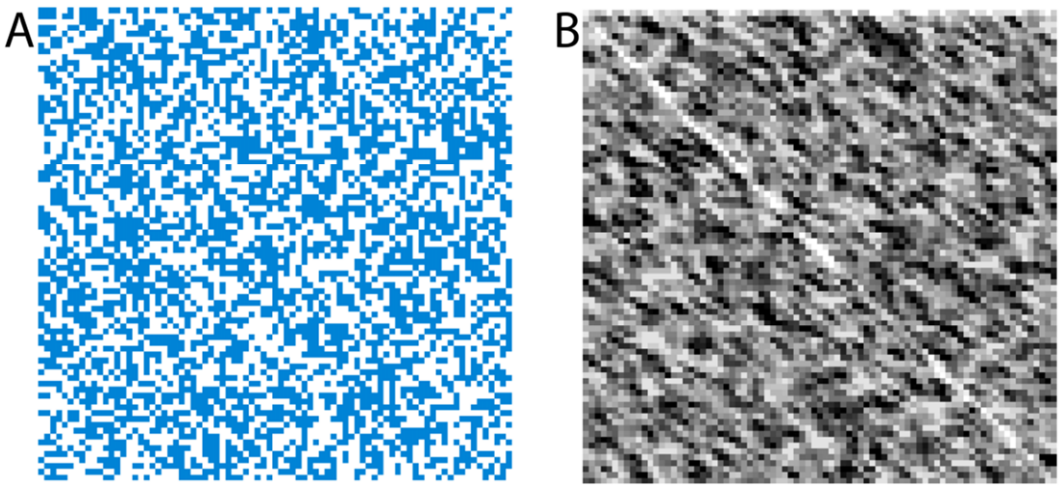

Figure E- 4. (A) Cultivated (blue) and non-cultivated fields (white), with cultivated fields receiving additional applied water during the months of April through October, and (B) Infiltration in the month of July (of the second year) for the true system, with values ranging from 0.000355 m day^{-1} to 0.006 m day^{-1} (represented by white and black, respectively).

Initial conditions for each simulation are achieved as follows. First, a 10,000-day spin-up simulation with a uniform net infiltration rate of 0.0012 m day^{-1} and isotropic, homogeneous aquifer with K = 30 m day^{-1} is run in order to achieve steady-state conditions in the catchment as determined by water table elevation and streamflow rate. Second, each realization of the ensemble is run for 365 days using a different anisotropic Y_K field and infiltration pattern to eliminate the bias due to the initial conditions. The results of this 365-day simulation are then used as initial conditions for the final 365-day simulation period for each realization, with time steps ranging between approximately 0.10 to 1.0 day. Stream inflow (Figure E-2) is set to 0.

An additional CATHY simulation representing the true catchment system is run, with the true Y_K field and resulting true *WT* field (at 365 days) depicted in Figure E-5. The streamflow rate at the outlet cell of the catchment is shown in Figure E-5B, indicating the increased discharge during the months of April through October due to increased rates of net infiltration from precipitation as well as applied water. In comparing the Y_K forecast ensemble to the true Y_K field using Equations (9c) and (9d), the AE and AEP values are 0.619 and 0.388, respectively.

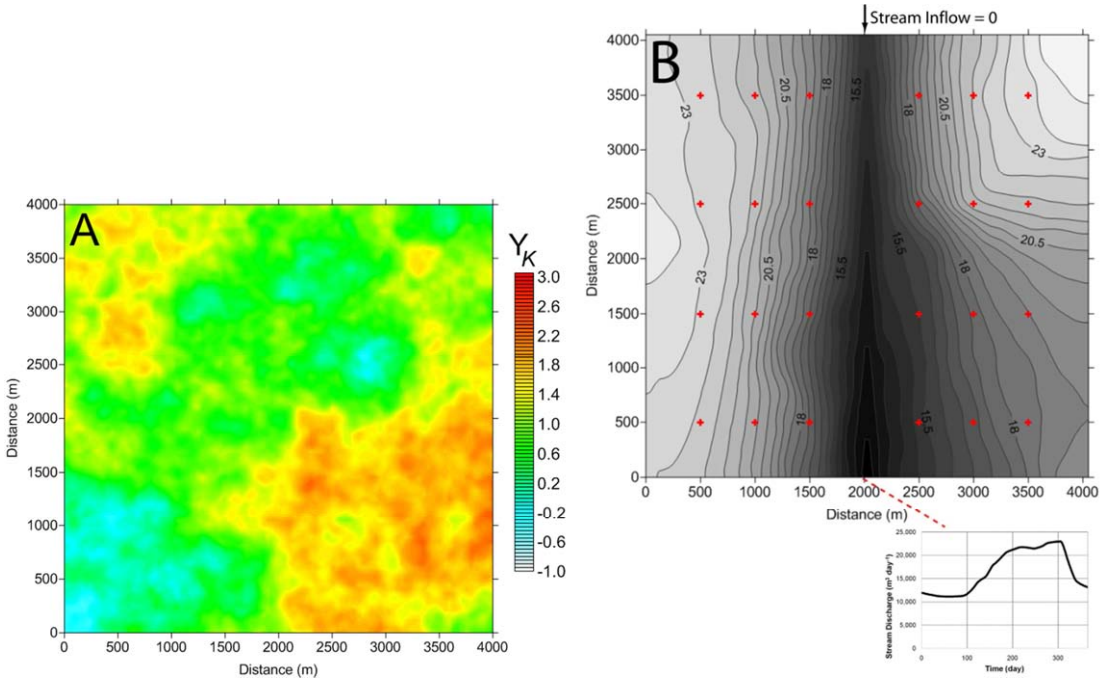

Figure E- 5. (A) Reference field of "true" Y_K and (B) corresponding *WT* field at time = 365 days as calculated by CATHY. In (B), red crosses indicate the location of 24 observation wells. The streamflow at the outlet cell during the 365-day simulation is shown in the subpanel.

The GM parameter values used to generate the Y_K field are the same as used for the forecast ensemble. This assumption will be relaxed in Section 3.3.2, when the iterative approach presented in Section 2.5 is used to estimate the true GM parameter values. The ability of the ES scheme to recover the spatial distribution of the true Y_K field by assimilating *WT* and *Q* measurements into the forecast ensemble results is explored in Section 3.2.

WT data and *Q* data are collected from observation wells (Figure E-5B) and stream gaging points (Figure E-2), respectively. CPU (Central Processing Unit) time to run a single realization on an Intel® Core™2 Duo CPU @ 3.00GHz desktop computer range from approximately 20 minutes to 180 minutes, depending on the spatial distribution of Y_K.

E.3.2 Update of *K* Ensemble

Observation data from the true catchment system are collected tri-monthly, resulting in four assimilation times during the year. As such, forecast ensemble model results are also saved every three months for use in the ES algorithm. The first set of update scenarios consists of conditioning the forecast Y_K ensemble using *WT* data from the 24 observation wells shown in Figure E-5B, with variations on (i) the number of assimilation times and (i) the error, defined using coefficient of variation (CV) of *WT* data, assigned to the observed *WT* data. For these scenarios, the CPU run-time of the ES update routine is approximately 30 seconds.

For the scenario where four assimilation times are used and the observation data are assumed to be error-free, the ensemble mean at each computational point for the updated Y_K ensemble is shown in Figure E-6A. The AE value of the updated Y_K ensemble, measuring the absolute error from the true Y_K field, is 0.380, a reduction of 38.6% from the forecast value of 0.619. In comparison with the true Y_K field shown in Figure E-5A, the mean of the updated Y_K ensemble in Figure E-6A captures the overall spatial pattern of the true field, with high values of Y_K in the northwest and southeast sections of the aquifer and low values in the north-central and southwest portions. The updated AEP value, measuring the spread of the updated Y_K ensemble, is 0.203, a reduction of 47.7% from the forecast value of 0.388. The spatial distribution of EP for the updated Y_K ensemble, as calculated by Equation (9b), is shown in Figure E-7. Notice that the spread of the ensemble values is lowest at and around the locations of the 24 observation wells.

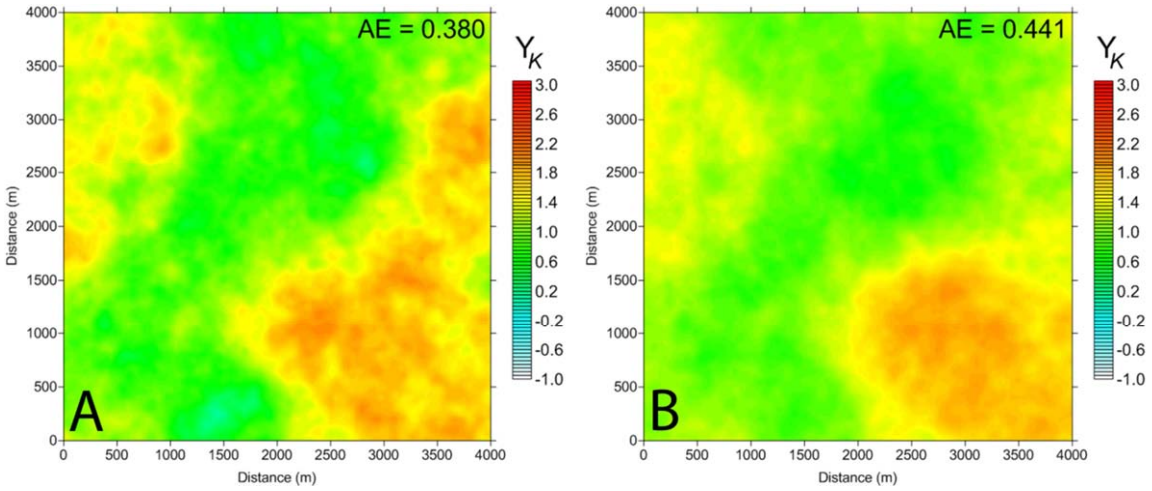

Figure E- 6. Spatial distribution of the updated Y_K ensemble using data from 24 observation wells sampled 4 times during the 365-day period, with the CV of observation data set to (A) 0.0 and (B) 0.3. Compare to the true state shown in Figure 5A.

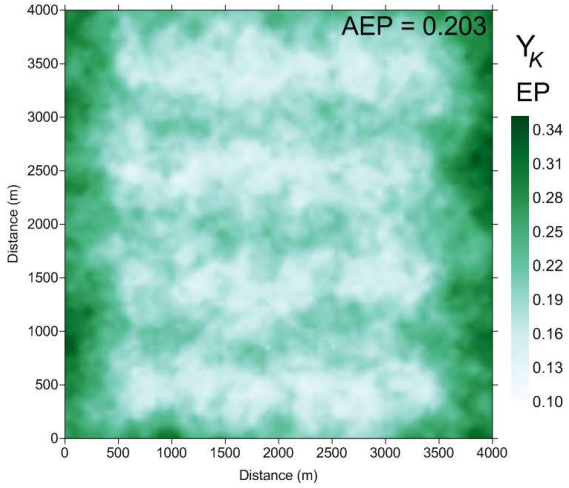

Figure E- 7. Spatial distribution of EP for the updated Y_K ensemble using data from 24 observation wells sampled 4 times during the 365-day period, with the CV of observation data set to 0.0.

When a CV value of 0.10 is assigned to the *WT* observation data, the AE and AEP values of the updated Y_K ensemble are 0.405 and 0.246, respectively, reductions of 34.5% and 36.6% from the forecast values. When a CV value of 0.30 is assigned, the AE and AEP values are 0.441 and 0.284, reductions of 28.8% and 26.8% from the forecast values. The ensemble of perturbed values for a data value collected from the observation well located at location (X = 2500 m, Y = 3500 m) for these two cases is shown in Figure E-8. For the latter case, the ensemble mean of the

updated Y_K ensemble is shown in Figure E-6B. In comparison to the case of CV = 0.00 (Figure E-6A), the spatial distribution of Y_K does not resemble as well the true Y_K field shown in Figure E-5A.

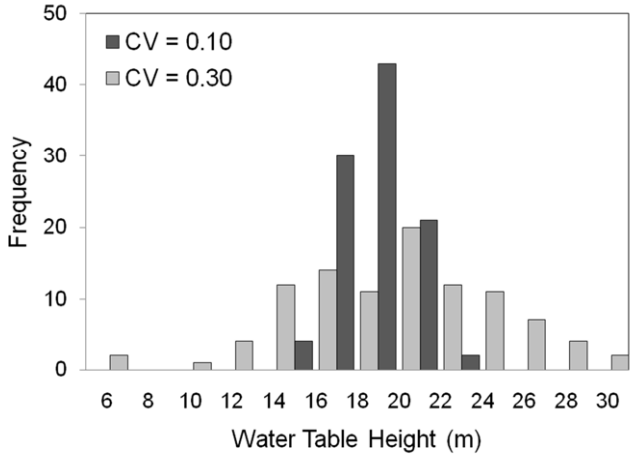

Figure E- 8. Frequency distribution of the ensemble of perturbed values for the observed *WT* value of 18.5 m collected on day 91 at location (X=2500 m, Y = 3500 m) of the "true aquifer", for CV values of 0.10 and 0.30.

When observation data from only one assimilation time (time = 365 days) is assimilated, the AE value of the updated Y_K ensemble is 0.408; when observation data from two assimilation times are used (time = 181 days and 365 days), the AE value is 0.385. In comparison to the AE value of 0.380, when four assimilation times are used, the improvement of the updated Y_K ensemble with respect to the true Y_K field is not considerable. The usefulness of additional assimilation times, however, is seen in the context of observation data error. Figure E-9 shows the increase of AE (i.e., the increase in deviation from the true Y_K field) with increasing values of CV of the *WT* observation data, for the cases when one, two, and four assimilation times are used. Notice that the increase of AE is lessened when observation data from multiple times are assimilated, with the best results occurring when 4 assimilation times are used. The use of additional assimilation times yielded no improvement. For the case of CV = 0.50, the AE value using one, two, and four assimilation times is 0.594, 0.563, and 0.471, respectively.

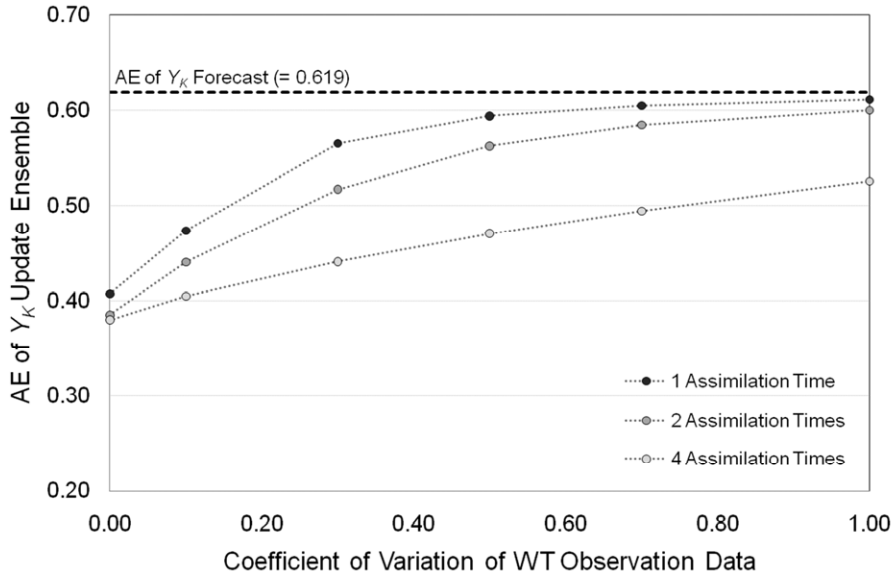

Figure E- 9. The increase of AE (i.e., the decrease in conditioning to the true Y_K field) with increasing values of CV of the *WT* observation data, for the cases when one, two, and four assimilation times are used.

The second set of update scenarios consists of assimilating observed values of *Q* from the reference system. The ensemble of values of *Q* for a given surface grid cell are found to be close to lognormally-distributed (Clark et al., 2008), with the coefficient of determination r^2 = 0.702 and the Kolmogorov-Smirnov statistics *KS* = 0.270 for a lognormal fit. This requires both the *Q* observation data and *Q* forecast ensemble to be log-transformed before use in the ES update routine.

When Y_Q = log *Q* data from 4 gaging stations along stream channel from the four measurement times are assimilated into the forecast ensembles of Y_Q and Y_K, the resulting AE and AEP values of the updated Y_K ensemble are 0.512 and 0.305, providing reductions of 17.3% and 21.3% from the forecast values. The ensemble mean for the updated Y_K ensemble for this scenario is shown in Figure E-10. When compared with the updated Y_K ensemble in Figure E-6A, it is clear that observation data from the 24 wells provide an updated Y_K ensemble that fits more closely with the true Y_K field than using Y_Q data. Still, the Y_K ensemble mean in Figure E-

10 captures the principal features of the spatial pattern of the true field. However, when error is assigned to the observed Y_Q data, the ability of the Y_Q data to condition the Y_K ensemble is reduced dramatically. Table E-2 shows the values of AE and AEP of the updated Y_K ensemble for scenarios in which the CV of the Y_Q data ranges from 0.00 to 1.00. When CV = 0.1, the reduction in the AE value from the forecast ensemble is 7.3%; for CV = 0.30, the reduction is only 2.0%.

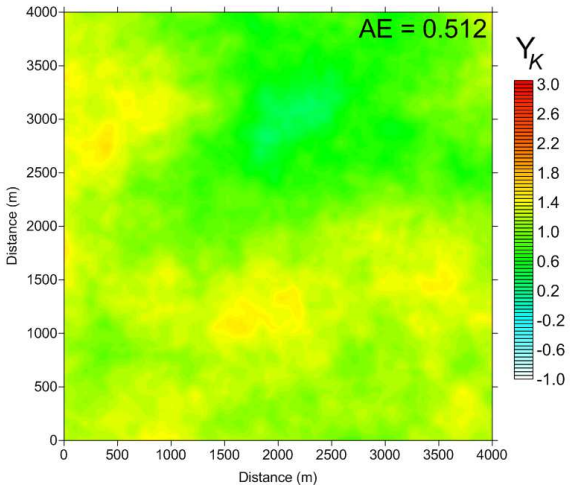

Figure E- 10. Spatial distribution of the mean of the updated Y_K ensemble using Y_Q data from four gaging stations along the stream channel sampled four times during the 365-day period, with the CV of observation data set to 0.0. Compare to the true state shown in Figure 5A.

Table E- 2. Performance measures of the updated Y_K ensemble for CV of Y_Q data ranging from 0.00 to 1.00, with the number of assimilation times (AT) equal to four.

Scenario	Num Gage *Q*	Num AT *Q*	CV *Q*	AE *K*	% Reduct	AEP *K*	% Reduct
FORECAST	-	-	-	0.619	-	0.388	-
UPDATE							
1	4	4	0.00	0.512	17.3%	0.305	21.3%
2	4	4	0.10	0.574	7.3%	0.368	5.0%
3	4	4	0.30	0.607	2.0%	0.384	1.0%
4	4	4	0.50	0.614	0.9%	0.386	0.4%
5	4	4	0.70	0.616	0.5%	0.387	0.2%
6	4	4	1.00	0.617	0.3%	0.387	0.1%

Table E-3 presents results of scenarios wherein *WT* and Y_Q data are jointly assimilated, with the number of observation wells ranging from 2 to 24. In each case, the observation wells are positioned in a grid network. In order to assess the influence of assimilating Y_Q data, four scenarios (1-4) are run with only *WT* observation data, with the same four scenarios rerun (scenarios 5-8) with the inclusion of assimilating Y_Q data from 4 gaging stations. Results indicate that the inclusion of Y_Q data only provides enhanced conditioning of the Y_K ensemble when the number of observation wells used is less than 8. For example, when 4 observation wells are used, the AE value for the scenarios with and without Y_Q data is 0.455 and 0.434, respectively; when two wells are used, the AE value with and without Y_Q data is 0.545 and 0.482, respectively. Hence, when sparse *WT* data are available, the additional Y_Q data are able to provide information regarding the spatial distribution of Y_K and hence partially maintain the value of AE.

Table E- 3. Performance measures of the updated Y_K ensemble as a result of assimilating (i) *WT* data, and (ii) *WT* and Y_Q data jointly

Scenario	Assim Var	Num Meas *WT*	Num Gage *Q*	Num AT *WT*	Num AT *Q*	CV *WT*	CV *Q*	AE Y_K	% Reduct	AEP Y_K	% Reduct
FORECAST								0.619	-	0.388	-
UPDATE											
1	*WT*	24	0	4	-	0.00	-	0.380	38.6%	0.203	47.7%
2		8	0	4	-	0.00	-	0.447	27.8%	0.261	32.6%
3		4	0	4	-	0.00	-	0.455	26.4%	0.297	23.3%
4		2	0	4	-	0.00	-	0.545	11.9%	0.334	13.9%
5	*WT, Q*	24	4	4	4	0.00	0.00	0.380	38.6%	0.203	47.7%
6		8	4	4	4	0.00	0.00	0.440	29.0%	0.252	35.0%
7		4	4	4	4	0.00	0.00	0.434	29.9%	0.284	26.9%
8		2	4	4	4	0.00	0.00	0.482	22.1%	0.301	22.3%

E.3.3 Case of Uncertain Geostatistical Parameter Values

E.3.3.1 Log-Mean of True Y_K field is Uncertain

In this section, the ability of the ES update routine to condition the ensemble of Y_K using *WT* observation data sampled from a catchment system where μ_{Y_K} is different from the one used in generating the forecast ensemble is explored. In the first scenario, μ_{Y_K} of the true Y_K field is 1.801 log m day^{-1} (K = 63.2 m day^{-1}, one-half order of magnitude higher than the forecast value of 20 m day^{-1}); for the second scenario, μ_{Y_K} of the true Y_K field is 0.801 log m day^{-1} (K = 6.3 m day^{-1}, one-half order of magnitude lower than the forecast value of 20 m day^{-1}). The value of $\sigma^2_{Y_K}$ in the true systems and the forecast ensemble is the same [(0.250 log m day^{-1})^2]. In Section 3.3.2, a more severe test is used to demonstrate the iterative approach described in Section 2.5.

The true Y_K field for the first and second scenarios are shown in Figures E-11A and E-11B, respectively. For the two scenarios, the AE of the forecast Y_K ensemble is 0.690 and 0.692, respectively. By assimilating *WT* data from 24 observation wells for four assimilation times, the AE of the updated Y_K ensemble for the two scenario is 0.365 and 0.395, respectively, resulting in reductions of 47.1% and 43.0% from the forecast AE values. The spatial distribution of the updated Y_K ensemble mean for the two scenarios is shown in Figures E-11C and E-11D. For both scenarios, the updated ensembles capture the general magnitude and spatial distribution of the true Y_K field.

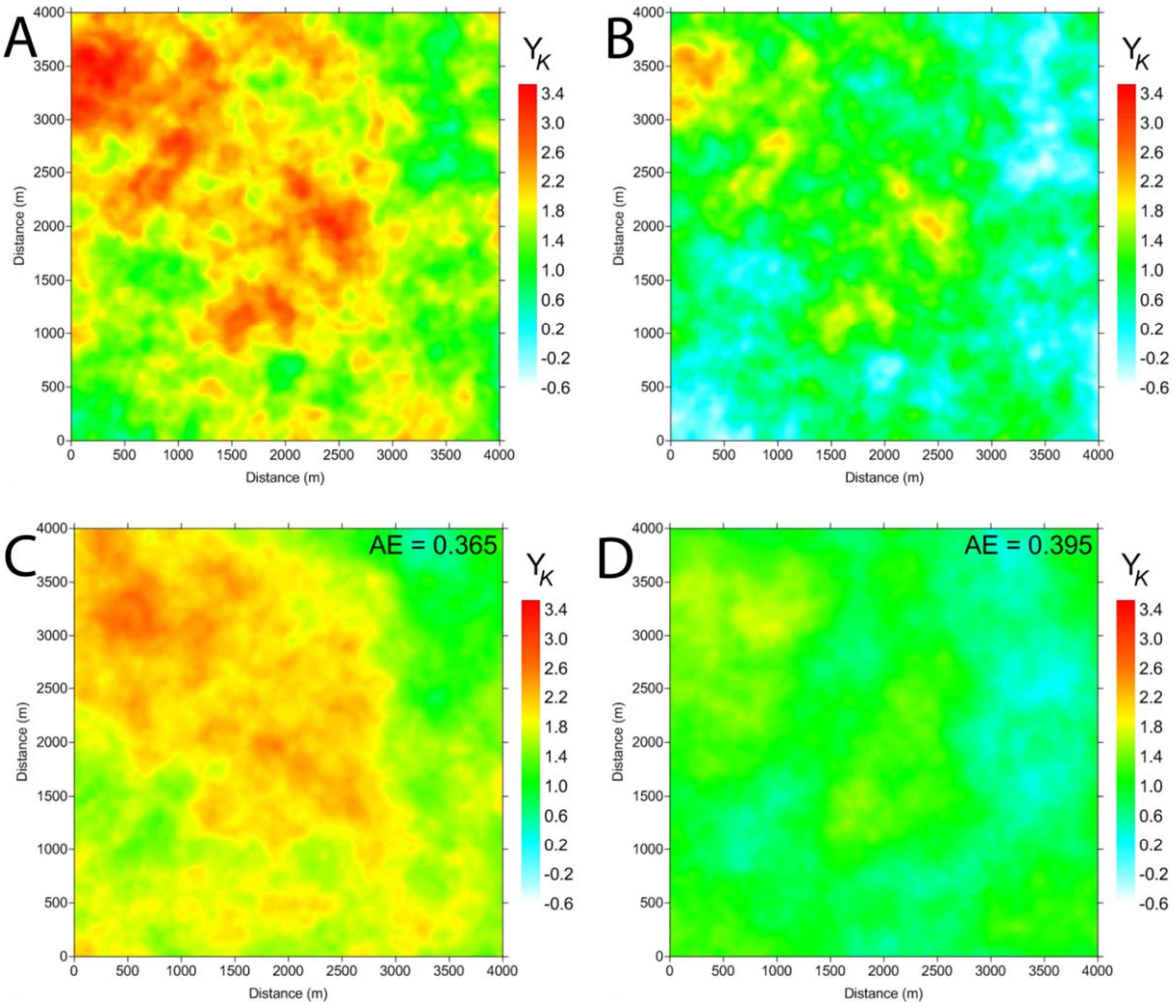

Figure E- 11. (A) True Y_K field using μ_{Y_K} = 1.801 log m day^{-1} (K = 63.2 m day^{-1}), (B) True Y_K field using μ_{Y_K} = 0.801 log m day^{-1} (K = 6.3 m day^{-1}), (C) mean distribution of the updated Y_K ensemble for the first scenario (μ_{Y_K} = 1.801), and (D) mean distribution of the updated Y_K ensemble for the second scenario (μ_{Y_K} = 0.801). For both scenarios scenario, 24 *WT* data from four assimilation times are used.

For the first scenario, the initially too-low (compared to the true system) values of Y_K are conditioned to the higher values present in the true system; for the second scenario, the initially too-high values are conditioned to the lower values. The same effect is observed through a comparison between the reference, forecast, and updated values of Y_K across a west-east transect located at Y = 2000 m, as shown in Figure E-12. In both scenarios, the forecast Y_K values along

the transect are approximately equal to the forecast μ_{Y_K} value of 1.301, whereas the updated Y_K values have been conditioned to resemble the true profiles.

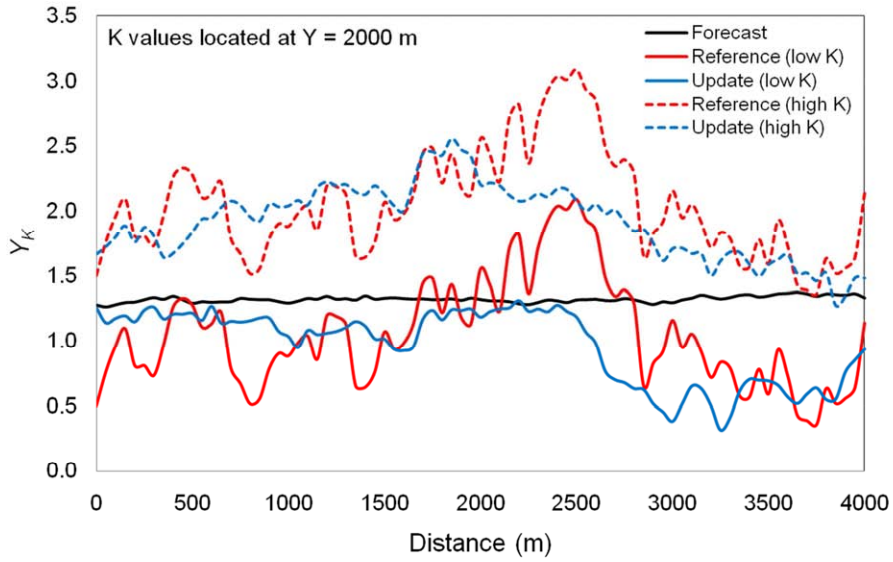

Figure E- 12. Comparison of reference and updated values of Y_K along the Y = 2000 m transect where the true μ_{Y_K} is higher (1.801 log m day^{-1}) and lower (0.801 log m day^{-1}) than the μ_{Y_K} of the forecast ensemble (1.301 log m day^{-1}). The values from the reference state are shown in red, and the updated values are shown in blue. For both scenarios, 24 WT measurements are assimilated.

E.3.3.2 Iterative Approach to Discover Geostatistical Parameter Values

To demonstrate the iterative approach, the true aquifer system has μ_{Y_K} and $\sigma^2_{Y_K}$ values of 0.301 log m day^{-1} (K = 2.0 m day^{-1}) and 0.500 (log m day^{-1})^2. The resulting true Y_K field is shown in Figure E-13. For each iteration, observation data from 24 observation wells and four assimilations are used to condition the Y_K ensemble. Beginning with a forecast Y_K ensemble generated using μ_{Y_K} = 1.301 log m day^{-1} and $\sigma^2_{Y_K}$ = 0.250 (log m day^{-1})^2, eight iterations are performed, with the μ_{Y_K} and $\sigma^2_{Y_K}$ values of the updated Y_K ensemble after each iteration shown

in Figure E-14. As seen in Figure E-14, the value of μ_{Y_K} reaches the parameter value from the true system within three iterations, but eight iterations are required to determine if convergence has been achieved. For $\sigma^2_{Y_K}$, the value from the updated Y_K decreases during the first several iterations, but eventually converges upon a value (0.580) slightly higher than the true value of 0.500 (log m day^{-1})^2. If the GM parameter values of the true system were unknown, then it would be assumed that μ_{Y_K} is just under 0.300 log m day^{-1} and $\sigma^2_{Y_K}$ is equal to 0.580 (log m day^{-1})^2.

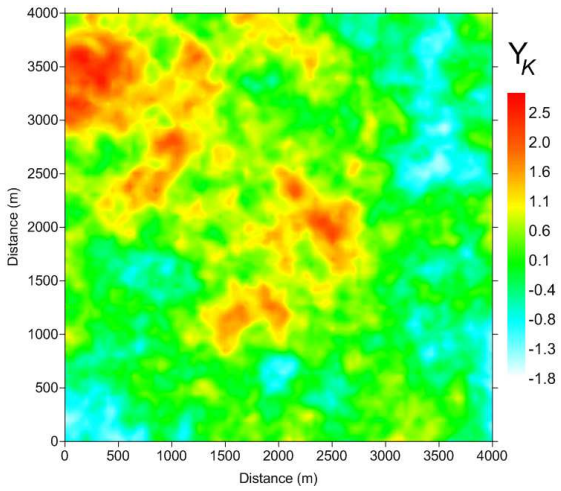

Figure E- 13. Reference Y_K field with μ_{Y_K} = 0.301 log m day^{-1} (2.0 m day^{-1}) and $\sigma^2_{Y_K}$ = 0.500 (log m day^{-1})^2.

Besides the convergence to the true GM parameter values, the approach of the updated Y_K ensemble to the spatial distribution of the true Y_K field is demonstrated in Figures E-15 and E-16. The ensemble mean of the updated Y_K ensemble for iterations 1 through 4 is shown in Figures E-15A-15D, with the AE value generally decreasing from the forecast value of 1.106 (0.755, 0.565, 0.507, and 0.518, respectively), although a slight increase occurs between iterations 3 and 4. The structure of the Y_K spatial distribution, however, progressively approaches the pattern of the true Y_K field shown in Figure E-15 with each successive iteration.

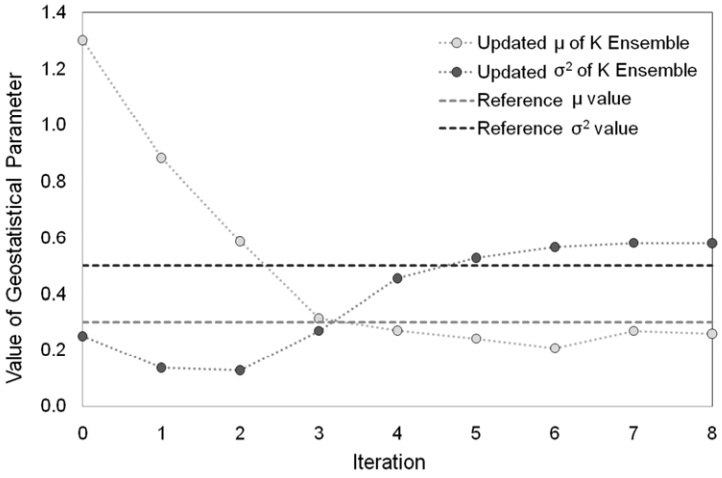

Figure E- 14. Progression of the estimated GM parameters μ_{Y_K} and $\sigma^2_{Y_K}$, demonstrating the convergence of the parameter values to ~0.300 log m day^{-1} and 0.580 (log m day^{-1})^2, respectively.

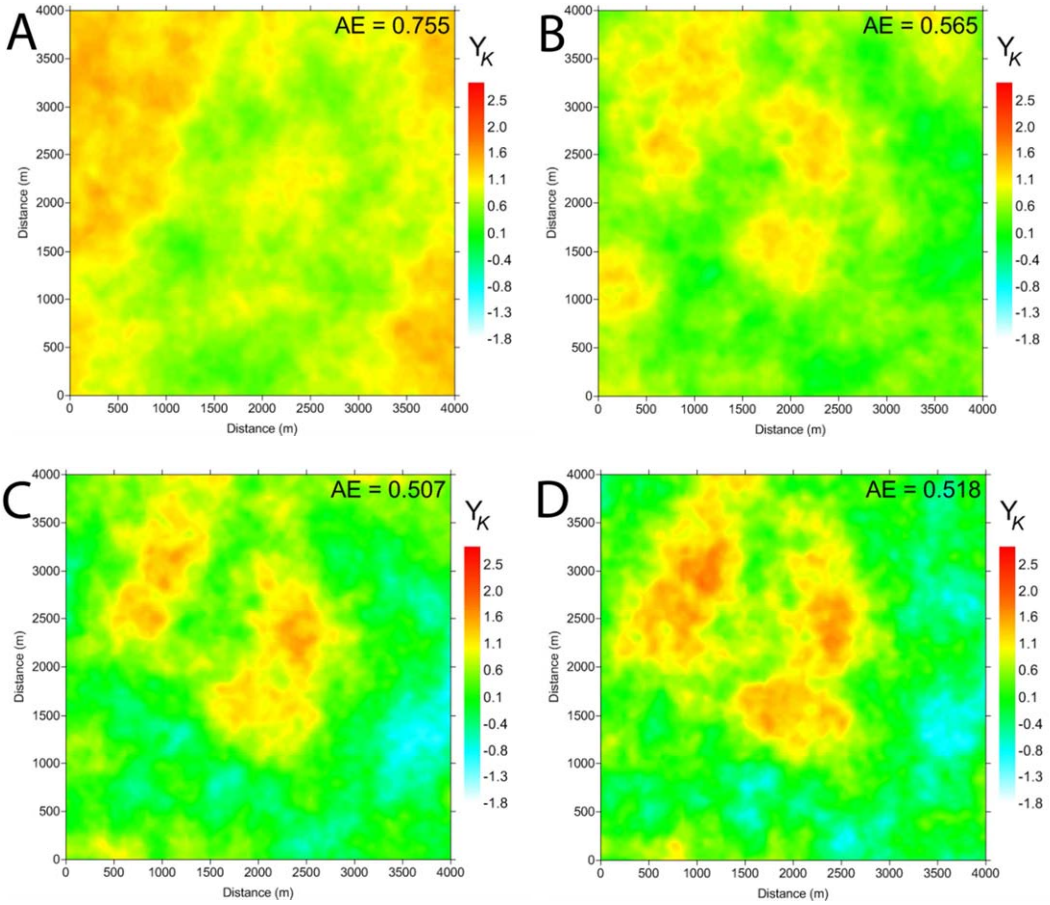

Figure E- 15. Ensemble mean of updated Y_K ensemble for the (A) 1st iteration, (B) 2nd iteration, (C) 3rd iteration, and (D) 4th iteration, for the case where the true values of μ_{Y_K} and $\sigma^2_{Y_K}$ are 0.301 log m day^{-1} and 0.500(log m day^{-1})^2, respectively. Compare to the true state in Figure 13.

Figure E-16 shows the true Y_K values, forecast Y_K values, and the updated values of Y_K for the 1st and 3rd iterations at the Y = 2000 west-east transect. Dramatic improvement in the updated Y_K values in relation to the true Y_K values occurs from the forecast to the 1st iteration, and from the first iteration to the third iteration.

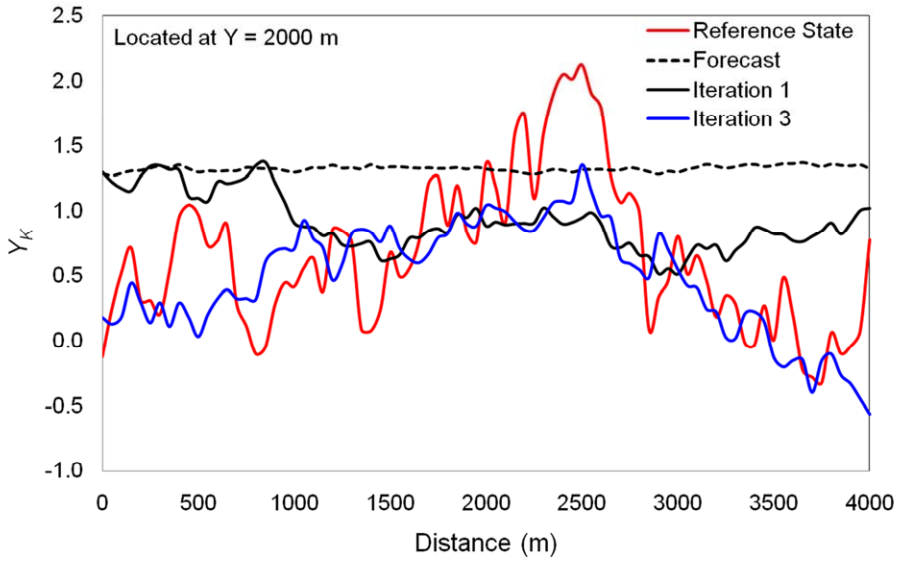

Figure E- 16. Value of Y_K along the Y = 2000 m transect for the reference state (red), the foreacast ensemble mean (dotted black line) and the update ensemble mean for the 1st (solid black line) and 2nd (solid blue line) iteration, for the case where the true values of μ_{Y_K} and $\sigma^2_{Y_K}$ are 0.301 log m day^{-1} and 0.500(log m day^{-1})^2, respectively.

Finally, comparisons are made between observed *WT* data from the true system and model-calculated *WT* values generated by CATHY using the updated values of μ_{Y_K} and $\sigma^2_{Y_K}$ from the previous iteration. This is especially important since such a comparison, i.e., re-running the numerical model using the estimated parameter values and comparing model results with observed data at observation locations, is generally the only means by which the parameter estimation method can be verified. Figure E-17 shows the comparison between observed *WT* data and model-calculated *WT* values from the forecast ensemble, the *WT* ensemble generated using the updated GM parameter values from the first iteration, and the *WT* ensemble using the

updated GM parameters from the second iteration. Comparisons for times = 273 days and 365 days are shown in Figures E-17A and E-17B, respectively.

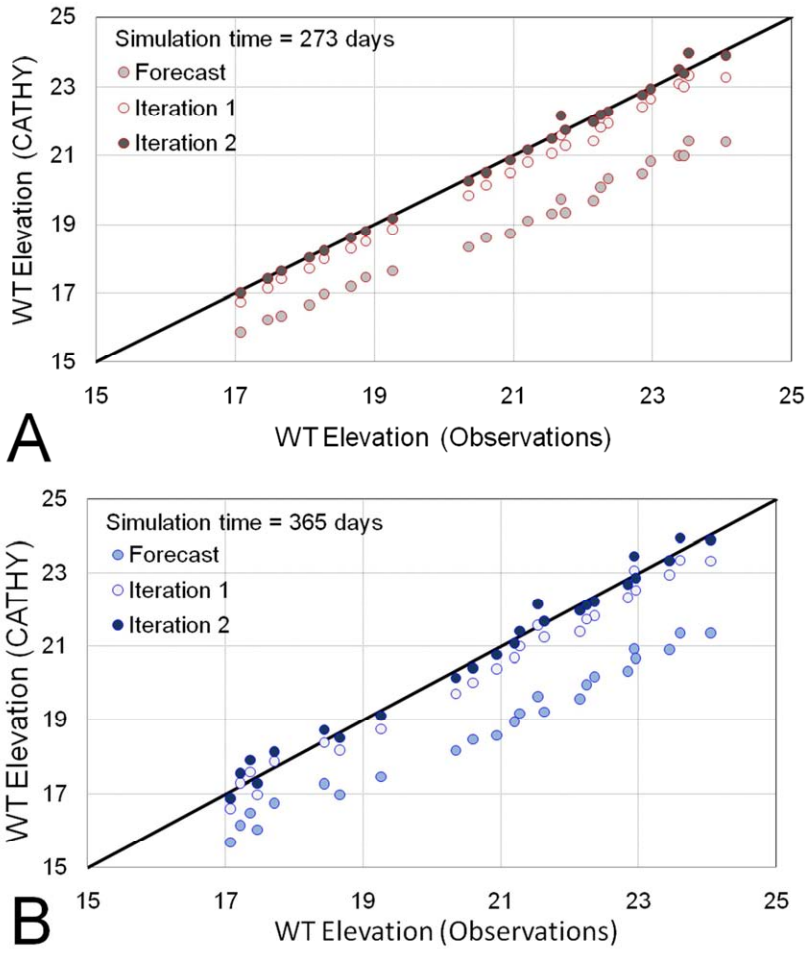

Figure E- 17. Comparison between model-calculated *WT* values and observed *WT* data from the true system for the forecast *WT* ensemble, the *WT* ensemble generated using the updated GM parameter values from the 1st iteration, and the *WT* ensemble using the updated GM parameters from the 2nd iteration. Comparison are made for (A) time = 273 days and (B) time = 365 days.

The match between the forecast values and the true value is much improved upon using the results from the first iteration, and an excellent match occurs using the results from the second iteration. Quantitatively, the sum of squared differences between the model results and true system values is 95.32, 4.29, and 0.59, respectively for time = 273 days, and 99.16, 4.98, and 1.83, respectively for time = 365 days. Notice that the forecasted *WT* values are lower than the observed *WT* values from the true aquifer system, since the forecast Y_K values are generated

using a higher value of μ_{Y_K} . However, using the lower updated value of μ_{Y_K} from the first and second iterations, the *WT* values become higher and more in accordance with the observed *WT* values.

E.4 Conclusions

The ES update routine, a derivative of the Kalman Filter approach, has been evaluated for the estimation of spatially-variable *K* in a catchment system using the fully-coupled, surface-subsurface flow model CATHY. A 4.05 km by 4.05 km tilted v-catchment was used in demonstration, with spatio-temporal variability in forcing terms to provide increased uncertainty in the system and to strive to mimic real-world conditions.

Both *WT* data and *Q* data were collected from a reference catchment system and assimilated into the ensemble of model results to condition the spatial distribution of *K* to approach the reference *K* field. Assimilating *WT* from a network of observation wells provided a distinct improvement in the *K* ensemble in relation to the true *K* field, with sets of data from multiple collection times tempering the decrease in improvement when error was assigned to the observed *WT* data. Assimilating *Q* data only slightly improved the *K* ensemble in relation to the true *K* field. Jointly assimilating *Q* and *WT* data only improved the estimate of *K* when data from a small number (2,4) of observation wells were assimilated. This is due to the region of influence of *Q*, i.e., the regions of the aquifer where the *K* values directly influence *Q* and hence can be conditioned by observed values of *Q*, being small compared to the collective region of influence of *WT* values at the observation wells.

For cases in which the parameter values defining the geostatistical structure of the aquifer system are uncertain to a small degree (i.e., mean of true *K* field is one-half order of magnitude

different than the assumed mean), the methodology is still able to condition adequately the forecast *K* ensemble to approach the magnitude and spatial structure of the true aquifer system. For more severe cases, i.e. the true and assumed means are different by an order of magnitude and the true and assumed variance of the *K* field is different, an iterative process using the ES is used to converge upon the true geostatistical parameter values. Results indicate that the process is successful in approximating the true values.

For the present study uncertainty in the correlation length of the *K* field is not investigated, and an amendment to the iterative scheme to converge upon unknown correlation length is left to future research, with assimilation of measurements of *K* likely necessary. Future studies also include an application of the methodology to an actual catchment system in order to estimate the geostatistical parameter values as well as the spatial distribution of *K*.

Funding Source and Reviewers

The majority of this work has been made possible by a Colorado Agricultural Experiment Station (CAES) grant (Project No. COL00690). We kindly thank Gaisheng Liu and an anonymous reviewer for for their helpful comments and suggestions in improving the content of this paper

References

Ahmed, S., and de Marsily, G.: Cokriged Estimation of Aquifer Transmissivity as an Indirect Solution of the Inverse Problem: A Practial Approach, Water Resour. Res., 29(2), 521-530, 1993.

Aubert, D., Loumagne, C., and Oudin, L.: Sequential assimilation of soil moisture and streamflow data in a conceptual rainfall-runoff model. J. Hydrol., 280, 145-161, 2003.

Bailey, R.T., and Baù, D.A.: Ensemble Smoother assimilation of hydraulic head and return flow data to estimate hydraulic conductivity, Water Resour. Res., 46, W12543, doi:10.1029/2010WR009147, 2010.

Bailey, R.T., and Baù, D.A.: Estimating spatially-variable first-order rate constants in groundwater reactive transport systems, J. Cont. Hydrol., 122, 104-121, 2011.

Baú, D.A., and Mayer, A.S.: Optimal design of pump-and-treat systems under uncertain hydraulic conductivity and plume distribution, J. Cont. Hydrol., 100, 30-46, 2008.

Bennett, A.F.: Inverse Methods in Physical Oceanography, Cambridge Univ. Press, New York, 1992.

Bixio, A.C., Orlandini, S., Paniconi, C., and Putti, M.: Physically-based distributed model for coupled surface runoff and subsurface flow simulation at the catchment scale, in Computational Methods in Water Resources, vol. 2, Computational Methods, Surface Water systems and Hydrology, edited by L. R. Bentley et al., pp. 1115-1122, Balkema, Rotterdam, Netherlands, 2000.

Boulet, G., Kerr, Y., and Chehbouni, A.: Deriving catchment-scale water and energy balance parameters using data assimilation based on extended Kalman filtering. Hydrol. Sci., 47, 449-467, 2002.

Camporese, M., Paniconi, C., Putti, M., and Salandin, P. :Ensemble Kalman filter data assimilation for a process-based catchment scale model of surface and subsurface flow, Water Resour. Res., 45, W10421, doi:10.1029/2008WR007031, 2009.

Camporese, M., Paniconi, C., Putti, M., and Orlandini, S.: Surface-subsurface flow modeling with path-based runoff routing, boundary condition-based coupling, and assimilation of multisource observation data, Water Resour. Res., 46, W02512, doi:10.1029/2008 WR007536, 2010.

Carrera, J., and Neuman, S.P.: Estimation of aquifer parameters under transient and steady-state conditions: 1. Maximum likelihood method incorporating prior information. Water Resour. Res., 22(2), 199-210, 1986.

Carrera, J., Alcolea, A., Medina, A., Hidalgo, J., and Slooten, L.J.: Inverse problem in hydrogeology. Hydrogeol. J., 13, 206-222, 2005.

Chen, Y., and Zhang, D.: Data assimilation for transient flow in geologic formations via Ensemble Kalman Filter. Adv. Water Resour., 29(8), 1107-1122, 2006.

Clark, M.P., Rupp, D.E., Woods, R.A., Zheng, X., Ibbitt, R.P., Slater, A.G., Schmidt, J., and Uddstrom, M.J.: Hydrological data assimilation with the ensemble Kalman filter: Use of streamflow observations to update states in a distributed hydrological model. Adv. Water Resourc., 31, 1309-1324, 2008.

Drécourt, J-P., Madsen, H., and Rosbjerg, D.: Calibration framework for a Kalman filter applied to a groundwater model. Adv. Water Resourc., 29, 719-734, 2006.

Dunne, S. and Entekhabi, D.: An ensemble-based reanalysis approach to land data assimilation. Water Resour. Res., 41, W02013, doi:10.1029/2004WR003449, 2005.

Durand, M., Molotch, N.P., and Margulis, S.A.: A Bayesian approach to snow water equivalent reconstruction. J. Geophys. Res., 113, D20117, doi:10.1029/2008JD009894, 2008.

Evensen, G.: Using the extended Kalman filter with a multilayer quasi-geostrophic ocean model. J. Geophys. Res., 97(C11), 17905-17924, 1992.

Evensen, G.: Sequential data assimilation with a nonlinear quasi-geostrophic model using Monte Carlo methods to forecast error statistics. J. Geophys. Res., 99(C5), 10, 143-10,162, 1994.

Evensen, G.: The ensemble Kalman filter: theoretical formulation and practical implementation. Ocean Dynam., 53, 343-367, 2003.

Evensen, G.: Data assimilation. The Ensemble Kalman Filter. Springer-Verlag Berlin Heidelberg, 2007.

Evensen, G., and van Leeuwen, P.J., An ensemble Kalman smoother for nonlinear dynamics. Mon. Weather Rev., 128, 1852-1867, 2000.

Fu, J., and Gómez-Hernández, J.J.: Uncertainty assessment and data worth in groundwater flow and mass transport modeling using a blocking Markov chain Monte Carlo method. J. Hydrol., 364, 328-341, 2009.

Gailey, R.M., Crowe, A.S., and Gorelick, S.M.: Coupled process parameter estimation and prediction uncertainty using hydraulic head and concentration data. Adv. Water Resour., 14(5), 301-314, 1991.

Gautier, Y., and Nœtinger, B.: Geostatistical parameters estimation using well test data, Oil & Gas Science Technology, 59(2), 167-183, 2004.

Gómez-Hernández, J.J., Hendricks Franssen, H.-J., and Sahuquillo, A.: Stochastic conditional inverse modeling of subsurface mass transport: A brief review and the self-calibrating method. Stoch. Environ. Res. and Risk Assess, 17, 319-328, 2003.

Hantush, M.M., and Mariño, M.A.: Estimation of spatially variable aquifer hydraulic properties using Kalman filtering. J. Hydraul. Engrg. ASCE, 123(11), 1027-1035, 1997.

Hendricks Franssen, H. J., Gómez-Hernández, J.J., Capilla, J.E., and Sahuquillo, A.: Joint simulation of transmissivity and storativity fields conditional to steady-state and transient hydraulic head data. Adv. Water Resour., 23, 1-13, 1999.

Hendricks Franssen, H. J., Gómez-Hernández, J.J., and Sahuquillo, A. Coupled inverse modeling of groundwater flow and mass transport and the worth of concentration data. J. Hydrol., 281, 281-295, 2003.

Hendricks Franssen, H. J., and Kinzelbach, W.: Real-time groundwater flow modeling with the Ensemble Kalman Filter: Joint estimation of states and parameters and the filter inbreeding problem. Water Resour. Res., 44, W09408, doi:10.1029/2007WR006505, 2008.

Hendricks Franssen, H. J., and Kinzelbach, W.: Ensemble Kalman filtering versus sequential self-calibration for inverse modeling of dynamic groundwater flow systems. J. Hydrol., 365, 261-274, 2009.

Hoeksema, R.J., and Kitanidis, P.K.: An application of the geostatistical approach to the inverse problem in two-dimensional groundwater modeling. Water Resour. Res., 20, 1003-1020, 1984.

Hoeksema, R.J., and Kitanidis, P.K.: Analysis of the spatial structure of properties of selected aquifers. Water Resour. Res., 21, 563-572, 1985.

Jafarpour, B., and Tarrahi, M.: Assessing the performance of the ensemble Kalman filter for subsurface flow data integration under variogram uncertainty. Water Resour. Res., 47, W05537, doi: 10.1029/2010WT009090, 2011.

Kalman, R.E.: A new approach to linear filtering and prediction problems. J. Basic Eng., 82, 35-45, 1960.

Keppenne, C.: Data assimilation into a primitive-equation model with a parallel ensemble Kalman filter. Mon. Weather Rev., 128, 1971-1981, 2000.

Kitanidis, P.K.: On the geostatistical approach to the inverse problem. Adv. Water Resour., 19, 333-342, 1996.

Kitanidis, P.K., and Vomvoris, E.G.: A geostatistical approach to the inverse problem in groundwater modeling (steady state) and one-dimensional simulations. Water Resour. Res., 19(3), 677-690, 1983.

Li, B. and Yeh, T.-C. J.: Cokriging estimation of the conductivity field under variably saturated flow conditions, Water Resour. Res., 35(12), 3663-3674, 1999.

Liu, G., Chen, Y., and Zhang, D.: Investigation of flow and transport processes at the MADE site using ensemble Kalman filter. Adv. Water Resour., 31, 975-986, 2008.

Ngodock, H.E., Jacobs, G.A., and Chen, M.: The representer method, the ensemble Kalman filter and the ensemble Kalman smoother: A comparison study using a nonlinear reduced gravity ocean model. Ocean Modelling, 12, 378-400, 2006.

Orlandini, S., and Rosso, R.: Diffusion wave modeling of distributed catchment dynamics, J. Hydraul. Eng. ASCE, 1(3), 103-113, 1996.

Putti, M., and Paniconi, C.: Time step and stability control for a coupled model of surface and subsurface flow, in Proceedings of the XV International Conference on Computational Methods in Water Resources (CMWR XV), vol. 2, pp. 1391-1402, Elsevier, New York, 2004.

RamaRao, B.S., LaVenue, A.M., de Marsily, G., and Marietta, M.G.: Pilot point methodology for automated calibration of an ensemble of conditionally simulated transmissivity field 1. Theory and computational experiments. Water Resour. Res., 31(2), 475-493, 1995.

Reichle, R.H., McLaughlin, D.B., and Entekhabi, D.: Hydrologic data assimilation with the ensemble Kalman filter. Mon. Weather Rev., 130, 103-114, 2002.

Schreider, S.Y., Young, P.C., and Jakeman, A.J.: An application of the Kalman filtering technique for streamflow forecasting in the Upper Murray Basin. Math. And Computer Model., 33, 733-743, 2001.

Valstar, J.R., McLaughlin, D.B., te Stroet, C.B.M., and van Geer, F.C.: A representer-based inverse method for groundwater flow and transport application. Water Resour. Res., 40, W05116, doi:10.1029/2003WR002922, 2004.

van Genuchten, M.T., and Nielsen, D.R.: On describing and predicting the hydraulic properties of unsaturated soils. Ann. Geophy., 3, 615-628, 1985.

van Leeuwen, P.J., and Evensen, G.: Data assimilation and inverse methods in terms of probabilistic formulation. Mon. Weather Rev., 124, 2898-2913, 1996.

Wen, W.-H., Deutsch, C.V., and Cullick, A.S.: Construction of geostatistical aquifer models integrating dynamic flow and tracer data using inverse technique. J. Hydrol., 255, 151-168, 2002.

Woodbury, A.D., and Smith, L.: Simultaneous inversion of hydrogeologic and thermal data 2. Incorporation of thermal data. Water Resour. Res., 24, 356-372, 1988.

Xie, X. and Zhang, D.: Data assimilation for distributed hydrological catchment modeling via ensemble Kalman filter. Adv. Water Resour., 33, 678-690, 2010.

Yeh, T.-C. J. and Zhang, J.: A geostatistical inverse method for variably saturated flow in the vadose zone. Water Resour. Res., 32, 2757-2766, 1996.

Yortsos, Y.C. and Al-Afaleg, N.: The permeability variogram from pressure transients of multiple wells: Theory and 1-D application. Society of Petroleum Engineers Journal, 2, 328-337, 1997

Zhang, J. and Yeh, T.-C. J.: An iterative geostatistical inverse method for steady flow in the vadose zone. Water Resour. Res., 33, 63-71, 1997.

APPENDIX F

ESTIMATING SPATIALLY-VARIABLE RATE CONSTANTS OF DENITRIFICATION IN IRRIGATED AGRICULTURAL GROUNDWATER SYSTEMS USING AN ENSEMBLE SMOOTHER

F.0 Summary

Groundwater contaminant transport models increasingly are being used to simulate the fate and transport of reactive solutes, particularly nitrate, within aquifer systems. These models, however, often are hindered due to a lack of information regarding parameters, such as kinetic decay rates, that govern the subsistence of the solute within the groundwater. In an overall effort to provide accurate estimates of spatially-variable parameters in numerical reactive transport modeling we employ a data assimilation scheme, the Ensemble Smoother (ES), which yields improved estimates of spatially-variable denitrification rates within an irrigated agricultural river-aquifer system using measurements of (i) nitrate concentration in the groundwater and (ii) mass of nitrate entering the river from the aquifer via groundwater flows. Based on the Kalman Filter methodology, in which distributed, uncertain model results are corrected by assimilating measurement data from a reference system, the ES incorporates uncertain parameter values, associated model results, and measurement data into an update algorithm to provide an updated, corrected model state that approaches the reference system state. As an important step in eventually employing the methodology to real-world systems, this study evaluates the parameter estimation scheme for a synthetic aquifer system approaching hydrologic (heterogeneous hydraulic conductivity, cropping patterns, canal seepage) and chemical (denitrification, leaching concentrations) complexities expected in aquifers influenced by agricultural practices. Sensitivity

analyses are conducted to investigate the influence of (i) the number of measurement data assimilated and (ii) the error assigned to the measurement data. Results indicate that the spatial distribution of denitrification rates can be estimated to a satisfying degree, and when implemented in additional model runs produce (i) simulated values that coincide favorably with measurement values from the reference state, and (ii) spatial distribution of nitrate concentration comparable to that of the reference state.

F.1 Introduction

The contamination of agriculturally-influenced aquifers and adjacent surface water bodies with nitrate (NO_3) is an ongoing problem world-wide, with adverse effects including eutrophication in surface water and methemoglobinema, or "blue-baby syndrome", for ecosystems and human populations, respectively [*Spalding and Exner*, 1993]. The presence of NO_3 in agricultural groundwater systems also can contribute to the oxidative dissolution and inhibition of chemical reduction of other dissolved environmental pollutants, such as sulfate (SO_4) and selenate (SeO_4) [e..g, *Frind et al.*, 1990; *Wright*, 1999; *Zhang et al.*, 2009]. Accumulation of NO_3 in saturated groundwater systems typically results from application of inorganic or organic fertilizers on cropped fields, with the NO_3 derived from either NO_3-based inorganic nitrogen (N) fertilizers, inorganic ammonium (NH_4) –based fertilizers that undergo nitrification in shallow soil layers, or organic N from organic fertilizers such as manure.

NO_3 not used by the crop rooting system is leached below the root zone via percolating irrigation water and rain water, eventually reaching the water table, followed by transport through the saturated zone according to advection-dispersion processes while undergoing denitrification, and finally discharged to surface water bodies. Denitrification can be heterotrophic, wherein the bacteria mediating the reaction acquire energy through the oxidation

of an organic electron (e^-) donor such as organic carbon (OC), as well as autotrophic, wherein the bacteria acquire energy through the oxidation of inorganic e^- donors such as ferrous iron (Fe^{2+}) or reduced sulfur (S) [*Korom,* 1992]. Heterotrophic denitrification occurs mainly in shallow unsaturated or saturated zones, where OC is present due to decaying crop material and leaching from the soil profile, respectively. Autotrophic denitrification occurs in the presence of pyrite (FeS_2), found in many regions of the world in weathered shale or bedrock shale underlying alluvial aquifers [e.g., *Pauwels et al.*, 1998; *McMahon et al.*, 1999; *Zhang et al.*, 2009]. A number of factors influence the rate of denitrification (e.g., soil water content, soil temperature, presence of microbial populations, concentration of e^- donors, competition from dissolved oxygen, etc.) [*Korom,* 1992].

In order to characterize the movement of NO_3 within aquifer systems both underlying and adjacent to agricultural areas, with the end goal of establishing baseline conditions and investigating mitigation scenarios, physically-based distributed numerical models have been used with increasing frequency in recent years for catchment-size regions [e.g., *Conan et al.*, 2003; *Carle et al.*, 2006; *Wriedt and Rode,* 2006]. These models, however, often are implemented rather simplistically in regards to model parameters, such as the rate constant assigned to the process of denitrification, which can be affected by local environmental conditions and hence be spatially-variable [*Hill,* 1996; *Groffman et al.*, 2009; *Almasri and Kaluarachchi,* 2007]. This is especially true in agricultural settings where factors effecting reaction kinetics, such as microbial population density and presence of organic carbon, can be highly temporally- and spatially-variable. Furthermore, simulations employing reaction kinetics often are most sensitive to the rate constant assigned to the reactive solute [e.g., *Lu et al.*, 1999; *Heatwole and McCray,* 2007].

Several studies [e.g., *McNab and Dooher*, 1998; *Heatwole and McCray*, 2007] have addressed uncertainty in rate constants by employing Monte Carlo schemes, in which first-order kinetic rate constant values are sampled from a log-normal distribution assembled from the literature. The rate constant value, however, is assigned as a homogeneous parameter within the model domain, hence neglecting possible heterogeneities.

To address the spatial heterogeneity of model parameters, numerous hydrologic studies have implemented parameter estimation methodologies, with the goal of systematically determining the spatially-variable parameter field that yields the observed measurements of system variables. These inverse modeling methods usually are classified as either (1) Markovian simulation-optimization methods, in which an iterative simulation-optimization procedure is used until a specified objective function has been satisfied under certain constraints [*RamaRao et al.*, 1995; *Gomez-Hernandez et al.*, 2003; *Valstar et al.*, 2004], or (2) statistical conditioning, in which a conditioning algorithm, developed through a least-squares optimization analysis [e.g., *Kalman*, 1960], uses the established correlation between the parameter and system-response variable to correct the parameter values using measured values of the system-response variable [*Ahmed and Marsily*, 1993; *Yeh et al.*, 1995].

In hydrological and contaminant transport studies, estimated parameters have included hydraulic conductivity, transmissivity, storativity, longitudinal and transverse dispersivity, and sorption coefficients, with measurement data consisting of hydraulic head, groundwater travel time, groundwater flow to rivers, and solute concentration [e.g., *Hantush and Marino*, 1997; *Hendricks Franssen et al.*, 2003; *Chen and Zhang*, 2006; *Liu et al.*, 2008; *Vugrin et al.*, 2007; *Bailey and Baù*, 2010]. In each instance, behavior of the measured system provides key information regarding parameters since parameter values at a given location dictate, partially or

wholly, the response of the system (i.e., the variable being measured). Several studies have employed two sets of disparate measurement data to condition the parameter field, with each type of measured variable providing unique information concerning the parameter. For example, both hydraulic head and solute concentration data have been used to estimate spatially-variable hydraulic conductivity and transmissivity [*Gailey et al.*, 1991; *Gomez-Hernandez et al*., 2003; *Hendricks Franssen et al.*, 2003, *Liu et al.*, 2008]. *Fu and Gomez-Hernandez* [2009] used hydraulic head data coupled with groundwater travel time data to provide information regarding hydraulic conductivity; more recently, *Bailey and Baù* [2010] used hydraulic head data and groundwater flows to a river to estimate hydraulic conductivity. In each instance, the inclusion of the second measured variable was necessary to overcome problems of undetermination of the parameter field.

A subset of the statistical conditioning methods includes inversion techniques based on the Kalman Filter [*Kalman*, 1960], a linear data assimilation algorithm that merges forecasted, uncertain model results with measurement data through an update algorithm to provide an updated system state that optimally honors the measurement data by minimizing the variance of the estimation error. Methods within this set include the Ensemble Kalman Filter (EnKF) [*Evensen*, 1994] and the Ensemble Smoother (ES) [*van Leeuwen and Evensen*, 1996]. In each scheme, an ensemble of simulations, with each simulation assigned a unique deterministic set of initial conditions, boundary conditions, forcing terms, and system parameters, is used to establish uncertainty in the aquifer system, with updates to the ensemble carried out by assimilating measurement data from the true aquifer system. Correction to aquifer parameters is achieved by incorporating the system parameter – system state variable cross-covariance structure into the update routine, thereby allowing the system variable measurement data to correct not only the

system state variables, e.g. hydraulic head, solute concentration, but also the parameters to which these variables are correlated.

Whereas the EnKF is sequential in nature, i.e., updates to the ensemble are made through simulated time sequentially whenever measurement data become available, the ES incorporates all previous measurements and model ensembles to compute a single updated model state estimate at all previous measurement times [*van Leeuwen and Evensen*, 1996], using both the spatial and temporal covariance of model results [*Evensen*, 2007]. This allows all previous model states to benefit from newly-acquired measurement data. Furthermore, the ES update routine is run only once, when model states have been simulated and all sets of measurement data have been collected.

The EnKF scheme has been used to estimate hydrologic parameters [e.g., *Hantush and Marino*, 1997; *Hendricks Franssen and Kinzelbach*, 2008] and contaminant transport parameters such as dispersivity [*Wagner*, 1992; *Giacobbo et al.*, 2002; *Liu et al.*, 2008]. More recently, the EnKF was used by *Bailey and Baù* [2011] to estimate the spatial-variability of a solute decay constant in a simplified aquifer system. The ES scheme has been used in hydrologic modeling applications [*Dunne and Entakhabi*, 2005; *Pauwels and Lannoy*, 2006; *Bailey and Baù*, 2010], but has yet to be employed in contaminant transport problems.

In this paper, we present the applicability of the ES scheme to provide improved estimates of spatially-variable denitrification rate constants within an irrigated agricultural river-aquifer system through assimilation of two sets of measurement data: concentration of NO_3 in the groundwater (C_{NO_3}), and mass of NO_3 entering the river from the aquifer through groundwater flow. The latter is referred to as *return mass* (*RM*) throughout the remainder of this paper. The ES scheme is used due to its computational efficiency [*Bailey and Baù*, 2012], a particular

requirement when dealing with physically-based distributed, data-intensive models such as reactive transport models. The methodology is applied to a one-year transient simulation for a synthetic aquifer system characterized by a comprehensive suite of hydrological and chemical forcing terms, processes, and system parameters that approaches a real-world setting. In doing so, we provide a liaison between the work presented by *Bailey and Baù* [2011] and the actual application of the methodology to actual aquifer systems. To the extent possible, model formulation, boundary conditions, and forcing term data are representative of the alluvial aquifer system in the Lower Arkansas River Valley (LARV) in southeastern Colorado, the site of future methodology application.

The sources of uncertainty considered here include rate of deep percolation (i.e., recharge to the water table from the unsaturated zone) in time and space, rate of canal seepage, C_{NO_3} of both deep percolation water and canal seepage water, dissolved organic carbon (DOC) concentration of deep percolation water, spatially-variable hydraulic conductivity of both the alluvium and bedrock shale material, spatially-variable heterotrophic denitrification rate constants within the alluvium, and, since the LARV is underlain by bedrock shale [*Gates et al.*, 2009], spatially-variable autotrophic denitrification rate constants. Deep percolation, canal seepage, and leaching of NO_3 and DOC are based on field monitoring studies performed in the LARV. Monod kinetics is used to simulate heterotrophic and autotrophic denitrification, with the reaction rate dependent on the relative presence of reactants, in order to reproduce the full complexity of the reaction. Measurement data from a reference aquifer system state are collected at the end of each month, and used in the ES scheme to provide improved estimates of the distribution of denitrification rates. In the case of assimilating measurements of C_{NO_3}, the ensemble of reactive transport simulations is rerun to determine if the updated ensemble of denitrification rate fields provides a

parameter structure that produces simulated results that match the measurements from the reference state, i.e., to see the effectiveness of the ES scheme in calibrating the model to a reasonable degree. Sensitivity analyses are performed to determine the influence of (i) measurement data errors, and (ii) uncertain reactivity of the reference heterotrophic denitrification rate field.

F.2 Estimation of Aquifer Parameters using the Ensemble Smoother

The ES update routine is based on the Kalman Filter algorithm [*Kalman*, 1960], a Bayesian statistical routine that optimally merges a theoretical state with measurements from the presumed true state to obtain a corrected state that is brought into conformity with the true state. The following sections describe the establishment of the theoretical, or model state in the *model forecast* step, followed by the correction of the model state in the *model update* step, according to the general Kalman Filter scheme. Both steps will then be discussed in terms of the ES framework. Terms used in each step will be described in relation to the synthetic aquifer system described in Section 3.

F.2.1 General Forecast Step

Using an ensemble scheme, in which the uncertainty of the state is established using an ensemble of simulations, the state of the system is estimated using the following *model forecast* step:

$$\boldsymbol{X}_t^f = \Phi_t\left(\boldsymbol{P};\boldsymbol{X}_0;\boldsymbol{q};\boldsymbol{b}\right) \tag{1}$$

where $\boldsymbol{\Phi}_t$ represents the solution to the mathematical model, *f* signifies forecast, and $\boldsymbol{P}$, $\boldsymbol{X}_0$, $\boldsymbol{q}$, and $\boldsymbol{b}$ represent the parameters, initial conditions, forcing terms, and boundary conditions, respectively, for the simulation members of the ensemble. The parameters $\boldsymbol{P}$ are assumed to be time-independent, whereas $\boldsymbol{q}$ and $\boldsymbol{b}$ can be time-dependent. The system state $\boldsymbol{X}$ represents the

model values at every cell of the grid discretizing the model domain, and $\boldsymbol{X}_t^f$ [*n* x *nmc*] is the forecasted estimate of the state, with *n* denoting the number of grid cells and *nmc* the number of realizations in the ensemble.

For the aquifer system considered in this study, and which is discussed in detail in Section 3, the reactive transport of NO_3 and DOC was simulated using RT3D [*Clement*, 1997], with the solution $\boldsymbol{\Phi}_t$ achieved by solving the following two advection-dispersion-reaction equations, written in tensorial notation:

$$R_{NO_3}\frac{\partial C_{NO_3}}{\partial t} = -\frac{\partial}{\partial x_i}\left(v_i C_{NO_3}\right) + \frac{\partial}{\partial x_i}\left(D_{ij}\frac{\partial C_{NO_3}}{\partial x_i}\right) + \frac{q_s}{\phi}C_{s_{NO_3}} + r_{Het} + r_{Auto} \tag{2}$$

$$R_{DOC}\frac{\partial C_{DOC}}{\partial t} = -\frac{\partial}{\partial x_i}\left(v_i C_{DOC}\right) + \frac{\partial}{\partial x_i}\left(D_{ij}\frac{\partial C_{DOC}}{\partial x_i}\right) + \frac{q_s}{\phi}C_{s_{DOC}} + r_{DOC} \tag{3}$$

where D_{ij} is the hydrodynamic dispersion tensor [L^2T^{-1}]; v is the pore velocity [LT^{-1}], ϕ is the porosity of the porous medium [$L_f^3L_b^{-3}$]; q_s is the volumetric flux of water entering the aquifer, representing sources and sinks of the species [$L_f^3L_b^{-3}T^{-1}$] where *b* represents the bulk volume]; C_s is the concentration of the sources and sinks [ML^{-3}]; r_{Het} and r_{Auto} represent the rate of heterotrophic and autotrophic denitrification [$ML^{-3}T^{-1}$], respectively; and r_{DOC} represents the rate of DOC consumption during the heterotrophic reaction [$ML^{-3}T^{-1}$]. The chemical reactions of heterotrophic and autotrophic denitrification are given as:

$$5CH_2O + 4NO_3 \rightarrow 5CO_3^{2-} + 2N_2 + 2H_2O + 6H^+ \tag{4}$$

$$5FeS_2 + 14NO_3 + 4H^+ \rightarrow 5Fe^{2+} + 10SO_4^{2-} + 7N_2 + 2H_2O \tag{5}$$

where in Equation (4) a generic organic compound denoted as CH_2O represents DOC. First-order kinetics is assumed to govern the decay of NO_3 according to the following dual-Monod rate law for heterotrophic denitrification and the Monod rate law for autotrophic denitrification:

$$r_{Het} = -\lambda_{Het} C_{NO_3} \left(\frac{C_{NO_3}}{k_{NO_3} + C_{NO_3}} \right) \left(\frac{C_{DOC}}{k_{DOC} + C_{DOC}} \right) \tag{6}$$

$$r_{Auto} = -\lambda_{Auto} C_{NO_3} \left(\frac{C_{NO_3}}{k_{NO_3} + C_{NO_3}} \right) \tag{7}$$

where k_j is the Monod half-saturation constant for reactant j [ML^{-3}], or the concentration of the reactant at which the reaction proceeds at half of the maximum rate, and λ_{Het} and λ_{Auto} are the rate constants of heterotrophic and autotrophic denitrification, respectively. The heterotrophic reaction occurs in the alluvium material where DOC is typically plentiful, whereas the autotrophic reaction occurs in the presence of FeS_2-bearing shale. The rate of DOC consumption, r_{DOC}, is based on the stoichiometric relationship between DOC and NO_3 in Equation (4) where the mass of DOC (150 g mol^{-1}) and NO_3 (248 g mol^{-1}) consumed results in a 150/248 = 0.6048 stoichiometric constant for DOC consumption, and hence $r_{DOC} = 0.6048\ r_{Het}$.

Principal parameters $\boldsymbol{P}$ governing the fate of NO_3 and DOC include λ_{Het} and λ_{Auto}; initial conditions $\boldsymbol{X}_0$ consist of values of C_{NO_3} and C_{DOC} at each location at the beginning of the simulation period; and forcing terms $\boldsymbol{q}_t$ include time-varying values of C_{NO_3} and C_{DOC} in deep percolation resulting from applied irrigation water and in seepage water from unlined irrigation canals.

Inter-cell pore velocities $\boldsymbol{v}$ in Equations (2) and (3) are provided by an ensemble of flow simulations predicted by the MODFLOW [*Harbaugh*, 2005] groundwater flow model and thus

are influenced by boundary conditions (specified head values and time-dependent river stage) and forcing terms (time- and space-varying values of deep percolation and canal seepage). Values of deep percolation and canal seepage comprise the term q_s in Equations (2) and (3).

Uncertainty in the model state is established by providing time- and/or space-variable values of $\boldsymbol{P}$, $\boldsymbol{X}_0$, $\boldsymbol{q}$, and $\boldsymbol{b}$ for each simulation member of the reactive transport simulation ensemble. For $\boldsymbol{P}$, ensembles of random log-λ_{Het} and log λ_{Auto} –fields are generated using SKSIM [*Baú and Mayer*, 2008], a sequential kriging Gaussian simulation algorithm, where the spatial distribution is established by a normal distribution using a two-dimensional exponential covariance model in the log domain:

$$\log \lambda = Y_\lambda = N\left(\mu_{Y_\lambda}; \sigma_{Y_\lambda}\right)$$

$$cov_{Y_\lambda, Y_\lambda}\left(\boldsymbol{d}\right) = \sigma^2_{Y_\lambda} . \exp\left(\sqrt{\sum_{i=1}^{2} \frac{d_i^2}{I_i^2}}\right) \tag{8}$$

where μ_{Y_p} and σ_{Y_p} are the mean and standard deviation of the logarithmic distribution of the parameters, d_i are the components of the distance vector **d**, and l_is are the spatial correlation scales in the coordinate directions. Lognormality of first-order reactions has been reported in the literature [e.g., *Parkin and Robinson*, 1989; *McNab and Dooher*, 1998], and is evidenced here for denitrification rate constants through a fit analysis of rate constant values (62 values for λ_{Het} and 13 values for λ_{Auto}) gathered from the literature, as shown in Figure F-1. The lognormal fit of λ_{Het} is superior to that of λ_{Auto} in both the coefficient of determination r^2 (0.97 compared to 0.86) and the Kolmogorov-Smirnov statistics (*KS*) (0.11 compared to 0.22) values, although acquiring more values for λ_{Auto} would likely improve these values. Rate constant values were assembled from field studies, laboratory studies, and modeling studies. It is assumed that the statistics

inferred from the collection of studies reported in the literature are reasonably descriptive of the uncertainty across the spatial domain of the problem analyzed in this study, which likely results in an exaggeration in the level of uncertainty given the disparate sources from which values were collected. Spatial correlation of λ as defined by Equations (8) is assumed to result from spatially-varying environmental factors, and is discussed further in Section 3.2.

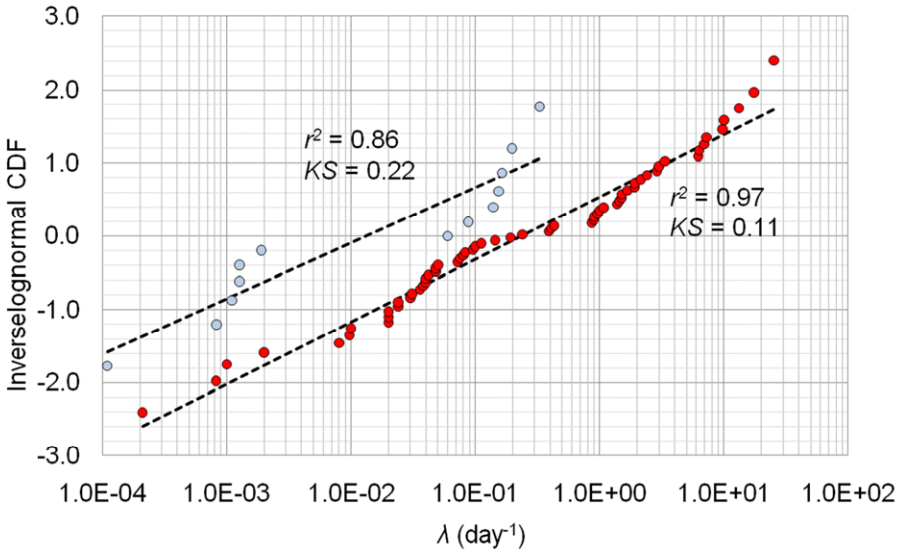

Figure F- 1. Fitting analysis for the statistical distributions of heterotrophic and autotrophic denitrification rate constants. These results show that λ_{het} and λ_{auto} typically fit well to a lognormal distribution (dashed lines).

Uncertainty in $\boldsymbol{X}_0$ is established by using an ensemble of steady-state solutions as initial conditions for the ensemble of transient simulations; as for $\boldsymbol{q}$, values of C_{NO_3} and C_{DOC} in the deep percolation and canal seepage water are sampled randomly from prescribed frequency distributions. Initial conditions, boundary conditions, and source and sink terms of the simulation ensemble of the flow model also are assigned uncertainty in order to provide a realistic hydrologic description of the system. Furthermore, hydraulic conductivity of the alluvium, K_A [LT^{-1}] and hydraulic conductivity of the bedrock shale, K_S [LT^{-1}] are assumed spatially-variable,

with random log-K_A and log-K_S fields generated using the same geostatistical model presented in Equation (8).

F.2.2 General Update Step for System-Response Variables

The forecasted ensemble $\boldsymbol{X}^f_t$ established through Equation (1) is corrected, or updated, at a time t using m measurement data from the true state through the following update equation:

$$\boldsymbol{X}^u_t = \boldsymbol{X}^f_t + \boldsymbol{\kappa}_t \left(\boldsymbol{D}_t - \boldsymbol{H}\boldsymbol{X}^F_t \right) \tag{9}$$

where $\boldsymbol{X}^u_t$ [$n \times nmc$] is the updated ensemble with u denoting update, $\boldsymbol{D}_t$ [$m \times nmc$] holds the ensemble of perturbed measurement data collected at time t, $\boldsymbol{H}$ [$m \times n$] contains binary constants (0 or 1) resulting in the matrix product $\boldsymbol{H}\boldsymbol{X}^u_t$ that holds model results at measurement locations, and $\boldsymbol{\kappa}_t$ [$n \times m$] is the so-called "Kalman Gain" matrix. Errors are assigned to the measurement data by adding an ensemble of Gaussian perturbations, stored in a matrix $\boldsymbol{E}$ [$m \times nmc$], to each of the m measurements, resulting in nmc values for each measurement data. If measurements are considered to be error-free, all nmc values are the same for each measurement. The ensemble of perturbed measurement data $\boldsymbol{D}_t$ is compared against the model results $\boldsymbol{H}\boldsymbol{X}^f_t$ at measurement locations, resulting in an ensemble of residuals that defines the deviation between the forecasted state and the true state at these locations.

These residuals form the basis for correcting the forecasted ensemble. The degree to which the correction occurs is dependent upon the uncertainty inherent in both the forecast ensemble and the measurement data and contained in $\boldsymbol{\kappa}_t$ through the forecast error covariance matrix $\boldsymbol{C}^f$ [$n \times n$] and the measurement error covariance matrix $\boldsymbol{R}$ [$m \times m$], respectively:

$$\boldsymbol{\kappa} = \boldsymbol{C}^f \boldsymbol{H}^T \left(\boldsymbol{H}\boldsymbol{C}^f \boldsymbol{H}^T + \boldsymbol{R} \right)^{-1} \tag{10}$$

where $\boldsymbol{C}^f$ and $\boldsymbol{R}$ are defined as:

$$\boldsymbol{C}^f = \frac{\left(\boldsymbol{X}^f_{t+\Delta t} - \overline{\boldsymbol{X}}\right)\left(\boldsymbol{X}^f_{t+\Delta t} - \overline{\boldsymbol{X}}\right)^T}{nmc - 1} \tag{11}$$

$$\boldsymbol{R} = \frac{\boldsymbol{E}\boldsymbol{E}^T}{nmc - 1} \tag{12}$$

In Equation (11), each column of $\overline{\boldsymbol{X}}$ [$n \times nmc$] holds the average value of the ensemble at each location in the domain. The matrices $\boldsymbol{C}^f$ and $\boldsymbol{R}$ hence describe the spread of the model values and the measurement values, respectively. In regards to Equation (10), if the spread of the measurement values is small compared to the spread of the model values, i.e., the measurement value is "trusted" more, then the values contained in $\boldsymbol{\kappa}$ approach 1.0, and the residual between the model values and the measurement values is weighted more heavily in correcting the model value to approach the measurement value. Conversely, if the spread of the measurements is large compared to the spread of the model values, than the residual receives little weight in correcting the model value. The latter condition, however, is not encountered frequently in dynamic systems, as typically higher confidence is placed in measurement data as compared to model results. Since $\boldsymbol{C}^f$ contains not only a measure of spread but also the spatial correlation of model results between model domain locations, information from measurements can be spread from measurement locations to non-measurement locations. A more thorough investigation on the correction procedure using $\boldsymbol{\kappa}$ can be found in *Bailey and Baù* [2011].

In this study, data placed in $\boldsymbol{D}_t$ consist of values of C_{NO_3} in the groundwater as well as *RM*, which are assumed to be measured using water samples from observation wells and sites along the river, respectively. For the latter, C_{NO_3} in the water samples at stream gauges are used to calculate the mass of NO_3 entering the river between two gauges during a period of time, with inflow of surface water into the stream (if any) and storage changes within the stream reach

assumed to be accounted for. The perturbations stored in $\boldsymbol{E}$ for both data types represent the error in acquiring the true value of C_{NO_3} in the observation well and in the river, respectively.

F.2.3 Coupled Update of System-Response Variables and System Parameters

As values of C_{NO_3} and *RM* are partially dependent on the rate constant of denitrification within the aquifer system, each contains important information regarding these rates. This information can be used to condition the rate constants using the update routine by including the cell-by-cell values of $Y_{\lambda_{Het}}$ into the forecast matrix $\boldsymbol{X}_t^f$. Doing so yields a covariance matrix $\boldsymbol{C}^f$ that contains not only spatial autocovariance of system-response variables such as C_{NO_3}, but also spatial cross-covariance submatrices between C_{NO_3} and $Y_{\lambda_{Het}}$. For example, the cross-covariance submatrix between C_{NO_3} and $Y_{\lambda_{Het}}$ is defined as:

$$\boldsymbol{C}_t^f\left(X_{(C_{NO_3})}, X_{(Y_{\lambda_{Het}})}\right) = \frac{\left[\left(\boldsymbol{X}_t^f - \overline{\boldsymbol{X}}\right)_{C_{NO_3}}\right]\left[\left(\boldsymbol{X}_t^f - \overline{\boldsymbol{X}}\right)_{Y_{\lambda_{Het}}}\right]^T}{nmc-1} \tag{13}$$

The correlation between the system-response variable and the parameter, established through model simulations, allows for measurements of the system-response variable to correct the parameter values. The conditioning of the parameters is dictated by the dependency of the values of the system-response variables upon the parameter values. In this study, a number of hydrologic and chemical boundary conditions and forcing terms are included to establish a condition wherein the values of C_{NO_3} and *RM* are dependent on many factors.

Testing of the results of parameter estimation are two-fold: first, the updated ensemble of spatially-variable $Y_{\lambda_{Het}}$ fields are compared qualitatively and quantitatively against the reference

$Y_{\lambda_{Het}}$ field (i.e., the system from which the measurements of C_{NO_3} and *RM* are taken); and second, the ensemble of reactive transport simulations are re-run using the updated ensemble of $Y_{\lambda_{Het}}$ fields, to determine if the simulated values of C_{NO_3} at measurement locations match to a suitable degree the measured values from the reference system. The latter is the definitive test, since the real goal of parameter estimation is whether the use of the estimated parameters can accurately simulate the system-response variables in the aquifer system, in this case C_{NO_3}.

F.2.4 Forecast and Update within the ES Framework

In contrast to sequential data assimilation methods, such as the EnKF, the ES includes all previous model states and measurement data up until the final measurement collection time t_F, at which time the ES update routine is run to provide updated system states at all previous collection times. This allows the update algorithm to be run once the model simulation has ended, rather than the need to either embed a sequential update routine into the modeling code or stop the simulation, assimilate measurement data, and restart the simulation using updated states and parameters. At time t_F, the forecast matrix $\widetilde{\boldsymbol{X}}_{t_F}^{\ f}$ holds model state ensembles from all measurement collection times ($t_{m_1}, t_{m_2}, ,\ldots, t_F$):

$$\widetilde{\boldsymbol{X}}_{t_F}^{\ f} = \left[\boldsymbol{X}_{t_{m_1}}, \boldsymbol{X}_{t_{m_2}}, \ldots, \boldsymbol{X}_{t_F} \right]^T \qquad \left[(n)\left(n_{t_m}\right) \right] \times nmc \tag{14}$$

Where n_{t_m} is the number of times at which measurements are collected. Within the ES approach, the forecast covariance matrix $\widetilde{\boldsymbol{C}}_{t_F}^{f}$ contains both spatial covariance terms and temporal covariance terms between cell values from different collection times. In turn, the measurement matrix $\widetilde{\boldsymbol{D}}_{t_F}$ holds perturbed measurements from each of the collection times:

$$\widetilde{D}_{t_f} = \left[D_{t_{m_1}}, D_{t_{m_2}}, \ldots, D_{t_F} \right]^T \quad \left[(m)\left(n_{t_m}\right) \right] \times nmc \tag{15}$$

The measurement error covariance matrix $\widetilde{R}_{t_F}$ also is established using the perturbations for each of the measurement values for each of the n_{t_m} collection times.

By inserting $\widetilde{X}_{t_F}^{\ f}$ and $\widetilde{D}_{t_F}$ into Equation (9) and $\widetilde{C}_{t_F}^{f}$ and $\widetilde{R}_{t_F}$ into Equation (10), the updated system state matrix $\widetilde{X}_{t_F}^{\ u}$ contains the updated model state for each measurement time. If parameters are included in the update algorithm, then these also are included in the forecast matrix $\widetilde{X}_{t_F}^{\ f}$. For the situation where both C_{NO_3} and *RM* measurements are used to condition $Y_{\lambda_{Het}}$ and $Y_{\lambda_{Auto}}$:

$$\begin{aligned} \widetilde{X}_{t_F}^{f} = & \left[X_{(C_{NO_3})t_{m1}}, \ldots, X_{\left(C_{NO_3}\right)t_F}; X_{(RM)t_1}, \ldots, X_{(RM)t_F}; X_{(Y_{\lambda_{Het}})}; X_{(Y_{\lambda_{Auto}})} \right] \\ & \left[\left(n+g\right)\left(n_{t_F}\right) + n \right] \times nmc \end{aligned} \tag{16}$$

where the C_{NO_3}, $Y_{\lambda_{Het}}$, and $Y_{\lambda_{Auto}}$ values from each location in the model domain are included for each ensemble member, and the number of *RM* values is equal to the number of stream gauges *g* used to calculate *RM*. The matrix $\widetilde{D}_{t_F}$ for this situation is:

$$\widetilde{D}_{t_F} = \left[D_{(C_{NO_3})t_{m1}}, \ldots, D_{\left(C_{NO_3}\right)t_F}; D_{(RM)t_{m1}}, \ldots, D_{(RM)t_F} \right] \quad \left[\left(m+g\right)\left(n_{t_F}\right) \right] \times nmc \tag{17}$$

where *m* is the number of observation wells placed in the aquifer.

The algorithm used to compute Equation (9) within the ES framework is based on the procedure presented by *Keppenne* [2000], who provided an efficient numerical strategy for updating the system state within an EnKF scheme. In this study, the Keppenne algorithm was

modified to include the model states and measurement data from each measurement collection time, similar to the work by *Bailey and Baù* [2010]. Computational effort is very affordable, as will be discussed in later sections.

F.2.5 Evaluating Uncertainty in the Updated System States

In order to quantify the effectiveness of the ES routine in updating the forecasted model states, a procedure is followed whereby measurement data are collected from a known reference state. This allows for calculations of deviation from the "true" system state on a location-by-location basis for both the forecasted and updated system states to provide an indication of the degree to which the forecasted state was corrected. This correction is analyzed by the two location-by-location parameters *EE* (ensemble error) and *EP* (ensemble precision) and the two associated global parameters *AE* (absolute error) and *AEP* (average ensemble precision) [*Hendricks Franssen and Kinzelbach*, 2008; *Bailey and Baù*, 2011]:

$$EE_i = \left| \overline{X}_i - X_{i,true} \right| \quad \left(i = 1,\ldots,n \right) \tag{18}$$

$$EP_i = \frac{1}{nmc} \sum_{j=1}^{nmc} \left| X_{i,j} - \overline{X}_i \right| \quad \left(i = 1,\ldots,n \right) \tag{19}$$

$$AE(X) = \frac{1}{\left(nmc \right)\left(n \right)} \sum_{j=1}^{nmc} \sum_{i=1}^{n} \left| X_{i,j} - X_{i,true} \right| \tag{20}$$

$$AEP(X) = \frac{1}{\left(nmc \right)\left(n \right)} \sum_{j=1}^{nmc} \sum_{i=1}^{n} \left| X_{i,j} - \overline{X}_i \right| \tag{21}$$

Where $\overline{X}_i$ is the ensemble mean of the i^{th} location (grid cell in a finite difference discretization of the domain), $X_{i,true}$ is the reference "true" value of the i^{th} location, and $X_{i,j}$ is the variable

value of the i^{th} location of the j^{th} ensemble realization. Equations (18) and (20) provide a measure of the deviation between the model state and the reference state, and Equations (19) and (21) provide a measure of the spread of the values around the ensemble mean of the model state. Lower values of *EE* and *AE* correspond to a model state that is approaching the "true" reference state, whereas lower values of *EP* and *AEP* signify reduced uncertainty in the model state. The performance of the update routine is measured by calculating the difference between performance parameters of the forecasted and the updated model states.

F.3 Flow and Reaction Transport Simulations and Estimation of $Y_{\lambda_{Het}}$

F.3.1 Conceptual Model of Aquifer System

The conceptual model of the boundary conditions and forcing terms for the synthetic aquifer system is shown in Figure F-2. The model domain is 4000 m north-south by 2000 m west-east, and is discretized by 100 by 100 (m × m) finite-difference grid cells in the horizontal direction and six layers in the vertical direction, with the top five layers representing the alluvial material and the bottom layer representing the bedrock shale. The five alluvium layers are each 3 m in thickness, resulting in an alluvial aquifer thickness of 15 m suitable to the LARV. The thickness of the shale layer was set to 2 m in thickness. The elevation of the ground surface is 115 m, whereas the elevation of the interface between the alluvium and the bedrock shale is 100 m. Sections of grid cells were assigned as either cropped or fallow (Figure F-2), with cropped grid cells receiving irrigation water during the growing season. The time period of assessment for this study was one year, with irrigation applied during the months of April through October.

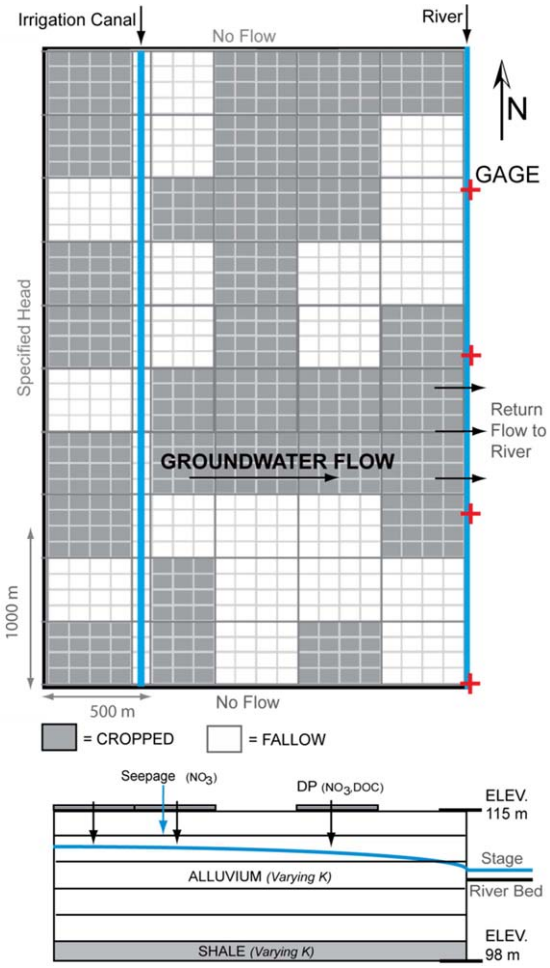

Figure F- 2. Conceptual model of the irrigated agricultural aquifer system. A river running north-south is located on the eastern edge of the aquifer and an irrigation canal running north-south is situated in the western portion of the aquifer. Deep percolation (DP) and associated values of $\boldsymbol{C_{NO_3}}$ and $\boldsymbol{C_{DOC}}$ are applied to cropped fields throughout the growing season. Canal seepage and associated values of $\boldsymbol{C_{NO_3}}$ contributes to the recharge for cells underlying the canal. K_A and K_S are spatially-variable, as are λ_{Het} and λ_{Auto}.

Lateral spatial distribution of the hydraulic conductivity of the alluvium material (K_A) was generated using SKSIM, with the ensemble of Y_{K_A} fields generated using mean $\mu_{Y_{K_A}}$ = -3.33 log m s^{-1}, standard deviation $\sigma_{Y_{K_A}}$ = 0.170 log m s^{-1}, and correlation length (l_x=l_y) = 750 m, resulting in K_A values ranging from 5.3 m day^{-1} to 314.6 m day^{-1}, which are representative of values observed in the LARV. K_A was assumed to not vary with depth. Spatial distribution of the hydraulic conductivity of the shale material (K_S) was generated using $\mu_{Y_{K_S}}$ = -6.00 log m s^{-1},

$\sigma_{Y_{K_S}}$ = 0.100 log m s^{-1}, and $l_x = l_y$ = 750 m, with resulting K_S values ranging from 0.03 m day^{-1} to 0.28 m day^{-1}, representative of shale material [e.g., *Molénat and Gascuel-Odoux,* 2002]. The Y_{K_A} field for the reference aquifer system used in this study is shown in Figure F-3A. No vertical correlation was assumed between K_A and K_S.

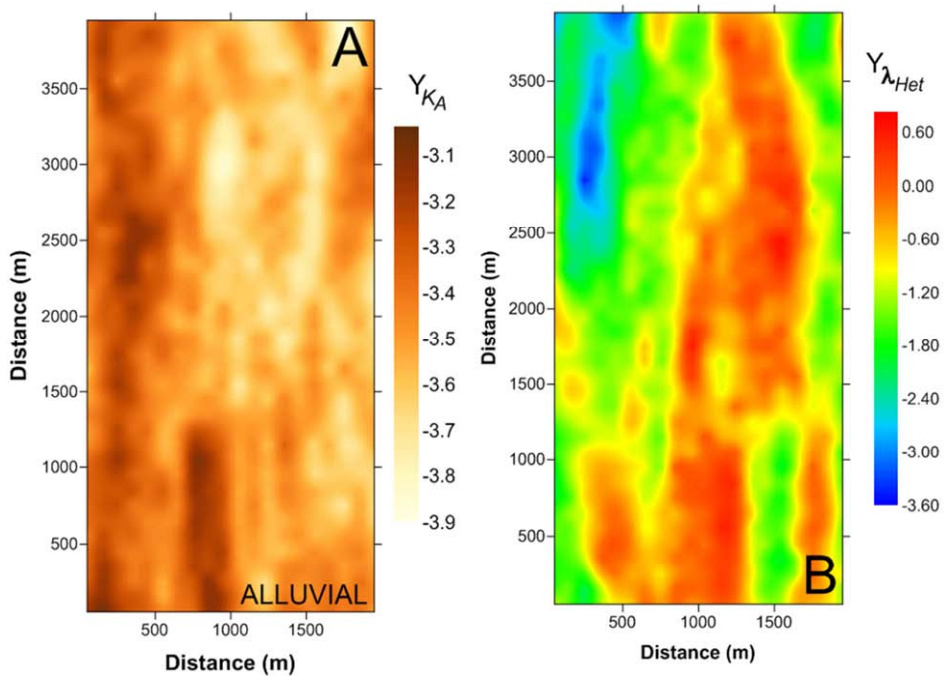

Figure F- 3. Reference system state of (A) $\boldsymbol{Y_{K_A}}$ and (B) $\boldsymbol{Y_{\lambda_{Het}}}$

The hydraulic head on the western edge of the aquifer was fixed at 111 m, representing average water levels in the region, and a river with a bed elevation of 107 m was situated along the eastern edge of the aquifer (Figure F-2). Month-averaged river flow depth values were acquired from data for the Arkansas River at Catlin Dam in southeastern Colorado. Data from 2006 were used, with minimum and maximum month averages of 0.6 m and 1.1 m occurring in January and May, respectively. The River package in MODFLOW was used to simulate groundwater flow interaction between the aquifer and the river, with the conductance of the river

bed assigned a value of 5,000 m^2 day^{-1}, typical of groundwater flow models used in the LARV (Burkhalter and Gates, 2005).

The groundwater flow field was further influenced by recharge water originating from (i) applied irrigation water and (ii) seepage from an un-lined canal situated in the western portion of the aquifer (Figure F-2). Recharge due to rainfall was neglected because of its reduced intensity in the LARV in relation to irrigation water and canal seepage. Deep percolation, i.e. applied irrigation water that does not contribute to soil water storage and is not used by the crops, but percolates below the root zone to recharge the water table, was assigned values based on field monitoring of irrigation studies conducted during the 2004-2008 irrigation seasons within the LARV [*Gates et al.*, 2012]. The empirical probability distribution of weekly deep percolation depths (m) based on 118 irrigation events from 22 field units over the 5 seasons within the study period was modeled using an exponential distribution (rate parameter $\gamma = 0.63$). For the model simulations described in Section 3.2, values were randomly sampled from the distribution and assigned to cells residing within the cropped sections during the irrigation months of April through October, with the distribution assumed to be valid for any month of the irrigation season. Values were spatially- and temporally-variable, with each cell receiving a unique deep percolation depth differing from every other cell, and with new values generated for each week of the irrigation season. Upflux from the water table was assumed negligible and not directly addressed in this study.

Recharge for cells underlying the irrigation canal is supplemented by canal seepage water, also occurring during the months of April through October with rates randomly selected from a normal distribution with mean of 1.50 m^3 day^{-1} m^{-1} and standard deviation of 0.50 m^3 day^{-1} m^{-1}. These rates are based on a field monitoring study of canal seepage in the LARV [*Susfalk et al.*,

2008], wherein rates of seepage from unlined canals ranged from 0.86 to 5.18 $m^3d^{-1}m^{-1}$. Cell-by-cell total recharge for the month of July for one of the simulations of the ensemble is shown in Figure F-4. Notice that in areas other than the irrigation canal, recharge is present only under cropped portions, and also that high recharge rates occur for cells containing the irrigation canal.

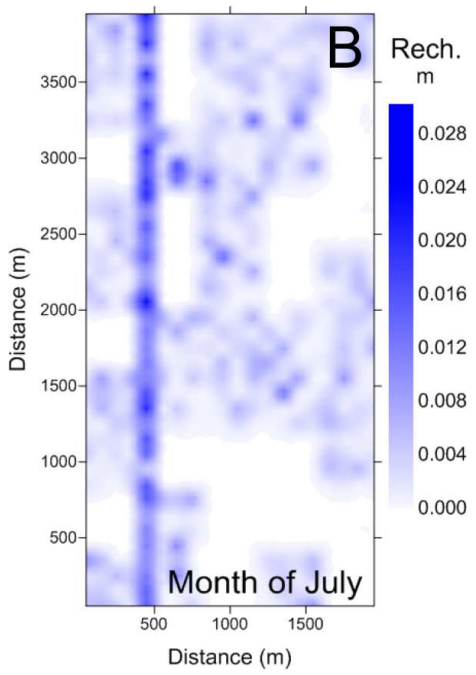

Figure F- 4. Spatial distribution of recharge for the month of July for the flow simulation combining deep percolation and canal seepage, with higher recharge values occurring under the canal due to canal seepage.

Spatial distribution of λ_{Het} within the alluvium material was generated using SKSIM, with $\mu_{Y_{\lambda_{Het}}}$ = -1.70 log day^{-1} and $\sigma_{Y_{\lambda_{Het}}}$ = 0.71 log day^{-1} based on the rate constants for heterotrophic denitrification shown in Figure F-1. The resulting values of λ_{Het} range between 5 x 10^{-6} day^{-1} and 90.7 day^{-1}, similar to the range shown in Figure F-1. Similarly for $\lambda_{Auto,}$ $\mu_{Y_{\lambda_{Auto}}}$ = -3.00 log day^{-1} and $\sigma_{Y_{\lambda_{Auto}}}$ = 0.71 log day^{-1} were based on the autotrophic denitrification rate constants shown in Figure F-1, with generated values ranging from 2.5 x 10^{-7} day^{-1} to 4.5 day^{-1}. The $Y_{\lambda_{Het}}$ field for the reference aquifer system is shown in Figure F-3B. The values of λ_{Het} are assigned to the top

four layers of the grid for the reactive transport simulations, whereas the values of λ_{Auto} are assigned to the alluvium-shale interface in layers 5 and 6. Vertical variation in the rate of heterotrophic denitrification is achieved through the use of Equations (6) and (7), wherein the rate is dependent on both C_{NO_3} and C_{DOC}.

Correlation length ($l_x = l_y$) for both λ_{Het} and λ_{Auto} was set to 750 m, resulting in patches of similarly-valued rate constants that vary in space on the order of the dimensions of the cropped and fallow sections of the land surface (see Figure F-3B). This was done under the assumption that field-to-field environmental conditions (e.g., development of soil organic matter and resulting leached DOC, development and subsistence of microbial populations) influence the values of λ_{Het} within the irrigated agricultural system. Longitudinal and transverse dispersivities [L] were set to 20 m and 4 m, respectively.

Values of $C_{s_{NO_3}}$ were assigned to both deep percolation water and canal seepage water, whereas values of $C_{s_{DOC}}$ were assigned only to deep percolation water. Similar to the forcing terms in the flow model regime, values were assigned only during the irrigation months of April through October, and were spatially- and temporally-variable, with each cell receiving a unique value differing from every other cell, with new values generated for each week of the irrigation season. Values of $C_{s_{NO_3}}$ for deep percolation water were selected randomly from a normal distribution with a mean equal to 25.0 g m^{-3}, corresponding to the mean of C_{NO_3} measured in a regional assessment of groundwater solutes in the LARV [*Gates et al.*, 2009], and a mean of $C_{s_{DOC}}$ equal to 20.0 g m_f^{-3} based on samples of groundwater solutes in the LARV. Standard deviations for both distributions were set to 1.5, producing a spread of values (e.g., 17.0 to 33.0 g

m_f^{-3} for $C_{s_{NO_3}}$) large enough to take into account differences in N cycling (fertilizer application timing and loading, crop uptake, nitrification) in the root zone between locations, yet within the range expected from land management practices that are assumed to be fairly consistent in a spatial area of 4 km by 2 km. The value of $C_{s_{NO_3}}$ for canal seepage water was set equal to 8.0 g m_f^{-3}, typical for the LARV [*Gates et al.*, 2009].

F.3.2 Reference State and Measurement Collection

A reference state of the aquifer system was established to (i) provide a system state from which measurement data can be collected and (ii) provide a system state against which both the forecasted and updated ensemble of model states can be compared, in order to assess the performance of the ES update routine. The reference fields for Y_{K_A} and $Y_{\lambda_{Het}}$ are shown in Figure F-3. Corresponding fields of Y_{K_S} and $Y_{\lambda_{Auto}}$ (now shown) also were used in the reference system. Initial conditions for the reference state simulation were achieved for the flow regime through a steady-state solution of the flow model, whereas for the solute regime the reactive transport simulation was run for 1000 days using the steady flow regime in order to achieve time-invariant solute transport conditions. The transient flow and transport simulation was then run for one year, using daily time steps.

The resulting head and log-C_{NO_3} ($Y_{C_{NO_3}}$) distributions at time = 365 days (Dec. 31), are shown in Figure F-5. Groundwater flow is from east to west in the section west of the canal, whereas the flow is west to east between the canal and the river, with flows and associated mass of NO_3 entering the river at cells adjacent to the river. The plot of C_{NO_3} is log-based due to the observed lognormality of the model-calculated C_{NO_3} values (r^2 = 0.92; *KS* = 0.11).

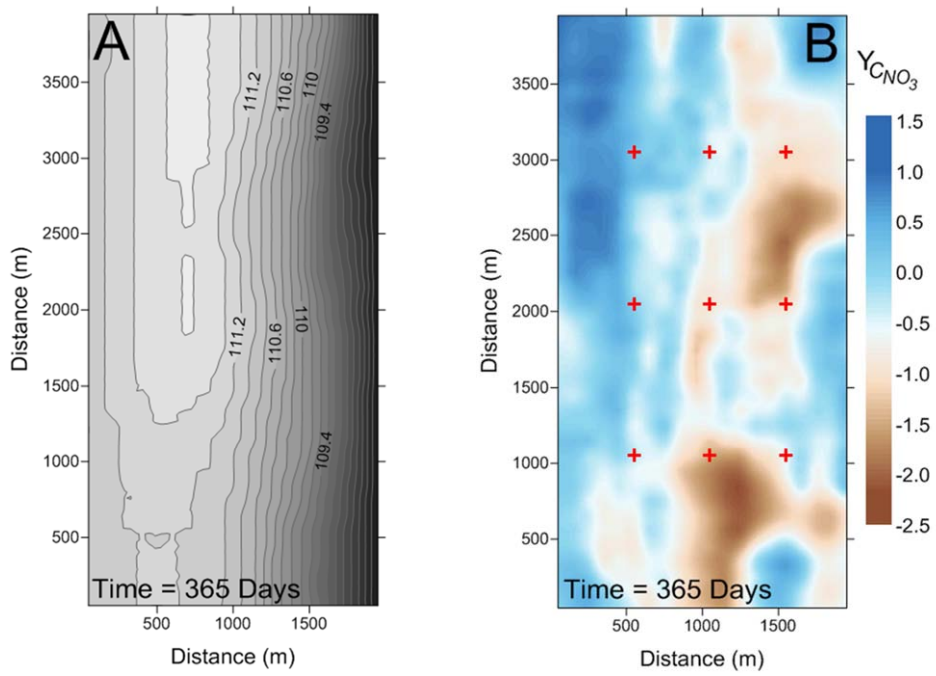

Figure F- 5. (A) Hydraulic head field (m) and (B) log-C_{NO_3}(log g m^{-3}) field of the reference aquifer system at time = 365 days. Locations of measurements for assimilation into the forecast model ensemble are shown by red crosses in (B).

For the head field, notice the mounding of water in the vicinity of the canal, with higher mounding occurring in the northern section due to higher randomly sampled seepage rate values for those cells. For the C_{NO_3} field, notice that high concentrations correspond to regions of low $Y_{\lambda_{Het}}$ values in Figure F-3B, and low concentrations correspond to regions of high $Y_{\lambda_{Het}}$ values, signifying an established correlation between the parameter and the system-response variable.

Measurements of C_{NO_3} in the groundwater were collected on a monthly basis from the nine locations shown in Figure F-5B, representing observation wells, for assimilation into forecasted model results. Measurements were collected from layer 4 of the model, which corresponds to the middle elevation of the saturated zone.

Four stream gages are installed along the river reach, as shown in Figure F-2, to measure the *RM* of NO_3 between two points in time. For example, the mass of NO_3 (kg) entering the stream

for the reference system during the month of December at each river grid cell is shown in Figure F-6A. The mass is summed up for the entire month of December, for the set of cells between two gauges. For example, the *RM* between the second and third gauges for the month of December is 90.2 kg. Notice that the *RM* values correspond to the reference $Y_{\lambda_{Het}}$ state shown in Figure F-3B.

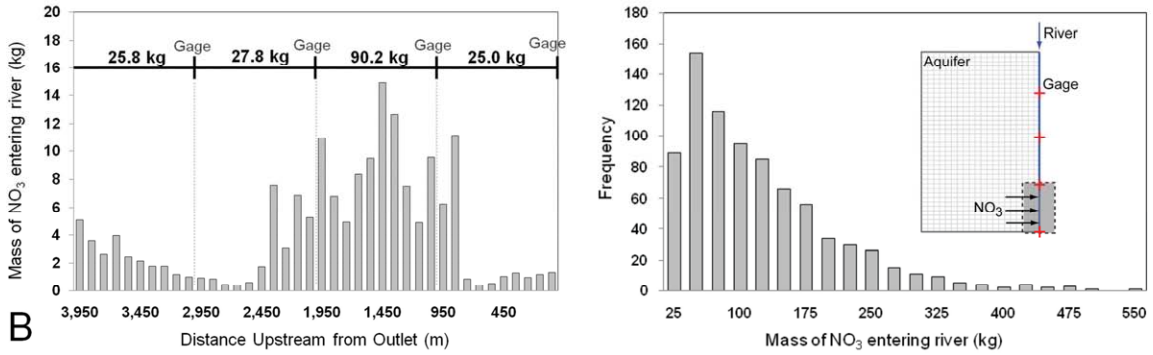

Figure F- 6. (A) Mass of NO_3 (kg) entering the river from the aquifer system for each cell located adjacent to the river, for the month of December for the reference state and (B) Frequency distribution of *RM* values between the 3rd and 4th stream gauges for the ensemble of simulations, for the month of December. *RM* values are calculated by summing the mass between stream gauges during the month.

High *RM* values, such as 90.2 kg., occur due to sections of low values of λ_{Het} next to the stream, whereas low *RM* values occur due to sections of high values of λ_{Het} next to the stream. As discussed in Section 3.4.2, this correlation is exploited to condition the values of $Y_{\lambda_{Het}}$ within vicinities next to the stream. Using more gauges would provide more localized estimates of *RM*, and hence would provide more information regarding the spatial variation of $Y_{\lambda_{Het}}$ in the sections next to the stream. The dependence of the update routine on the number of stream gauges is explored in Section 3.4.2.

F.3.3 Forecasted Ensemble of Model States

Using the information presented in Section 3.1, *nmc* = 800 simulations were run to establish the forecast ensemble of model states, with each simulation run for one year (from January 1 to December 31) and simulation results at the end of each month corresponding to a single model

state. Initial conditions for the transient MODFLOW simulations were achieved through a steady-state solution for each ensemble member. Each steady-state flow field was used in a corresponding spin-up 1000-day RT3D simulation to achieve a dynamic equilibrium in the reactive transport field. Fluxes from each transient MODFLOW simulation were then provided to a corresponding one-year RT3D simulation.

Total CPU (Central Processing Unit) time to run the ensemble on an Intel® Core™2 Duo CPU @ 3.00GHz desktop computer was 5663 minutes, with 144 minutes for the flow ensemble (41 minutes for steady-state and 103 minutes for transient simulations) and 5519 minutes for the reactive transport ensemble (4805 minutes for simulations to reach steady-state and 714 minutes for transient simulations).

The ensemble mean of $Y_{C_{NO_3}}$ at every grid cell is shown in Figure F-7A, with monthly values of C_{NO_3} shown for four locations. Notice that C_{NO_3} values are higher for cells that reside under cropped fields. Also notice that, for the two cells under fallow fields, the cell closest to the stream has higher values of C_{NO_3} since it is receiving NO_3 mass through groundwater transport from cells to the west that reside under cropped fields. The distribution of the ensemble of *RM* for the last stream gauge for the month of December is shown in Figure F-6B. The values are lognormally-distributed (r^2 = 0.93; *KS* = 0.097) and hence are log-transformed before use in the ES update routine.

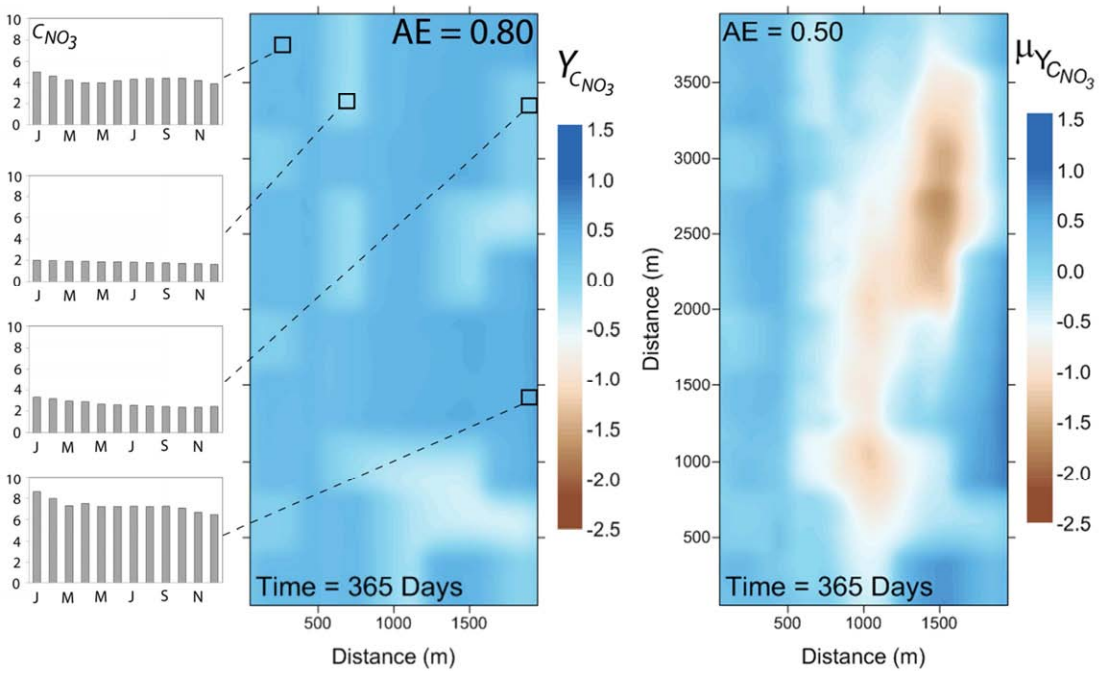

Figure F- 7. Ensemble mean of the (A) forecast $\boldsymbol{Y_{C_{NO_3}}}$(log g m^{-3}) ensemble and (B) updated $\boldsymbol{Y_{C_{NO_3}}}$(log g m^{-3}) ensemble for the last day of the simulation using the updated $\boldsymbol{Y_{\lambda_{Het}}}$ensemble in a re-run of the reactive transport simulation ensemble. For (A), the monthly time series of $\boldsymbol{Y_{C_{NO_3}}}$is shown for four selected cells, showing the difference in concentration between cells underlying cropped land as opposed to cells underlying fallow land.

The AE and AEP values for the forecast ensemble of $Y_{C_{NO_3}}$ fields for the model state at time = 365 days are 0.80 and 0.38, respectively, and provide a measure against which the values for the update ensemble can be compared to determine improvement in simulation results. The AE and AEP values for the forecast ensemble of $Y_{\lambda_{Het}}$ fields is 1.03 and 0.56, respectively. The spatial distribution of EE and EP for the $Y_{\lambda_{Het}}$ fields is shown in Figure F-8. Notice that the EE values, signifying the deviation between the ensemble mean and the reference value, are largest for areas of high and low reactivity (refer to Figure F-3B).

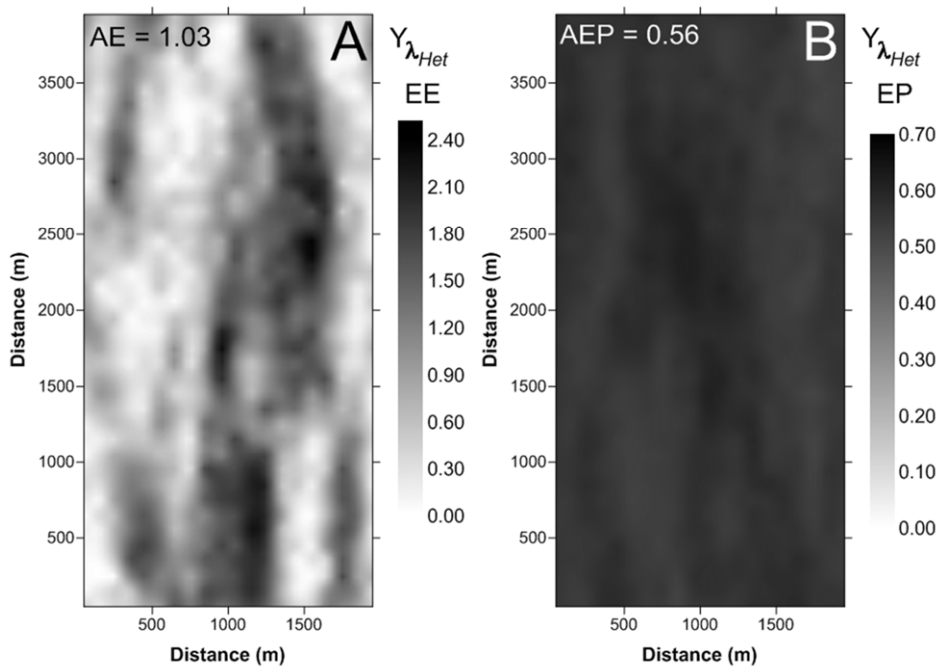

Figure F- 8. Spatial distribution of the (A) cell EE values and (B) cell EP values of the forecast $\boldsymbol{Y_{\lambda_{Het}}}$ (log day^{-1}) ensemble, as calculated using Equations (17) and (18).

F.3.4 Updated Ensembles and Sensitivity Analysis

F.3.4.1 Conditioning $Y_{\lambda_{Het}}$ using C_{NO_3} data

The first set of model update scenarios consists of updating the forecast ensemble of $Y_{\lambda_{Het}}$ using monthly measurements of $Y_{C_{NO_3}}$ from the 9 locations shown in Figure F-5B. For this scenario, CPU time to run the ES update routine was 2.2 minutes, or 0.04% of the CPU time required to produce the reactive transport forecast ensembles.

As a first test of the parameter estimation methodology, the updated $Y_{\lambda_{Het}}$ ensemble is compared to the reference $Y_{\lambda_{Het}}$ field. The update ensemble of the $Y_{\lambda_{Het}}$ fields is summarized in Figure F-9. Figure F-9A shows the updated ensemble mean at every grid cell, with the AE value reduced from 1.03 to 0.70, a reduction of 32.2%. Spatial distribution of the updated ensemble

error EE and ensemble precision EP, shown in Figures F-9B and Figure F-9C, shows in greater detail the accuracy of the updated ensemble in relation to the reference state of Figure F-3B. The AEP value was decreased from 0.56 to 0.40, a reduction of 28.6%. For the ensemble mean, the overall spatial patterns of the reference state, with high reactivity in the northeast, north-central, and southeast poritions of the aquifer and low reactivity in the northwest portion, are captured to some degree, although as evidenced by the EE plot in Figure F-9B, conditioning is least effective in the northwest and southeast portions. However, in comparison to the plot of forecast EE in Figure F-8A, much of the error has been reduced. The spread of the ensemble values also has been reduced, as shown in Figure F-9C, especially at and around the locations of the $Y_{C_{NO_3}}$ measurements, as compared to the plot of forecast EP in Figure F-8B.

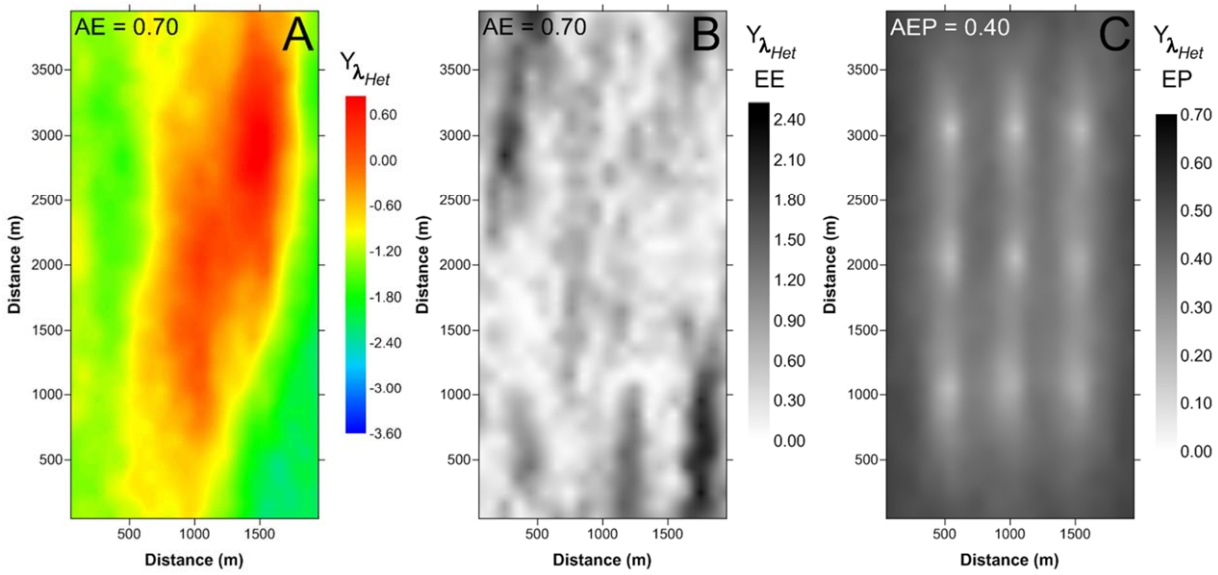

Figure F- 9. (A) Ensemble mean, (B) EE, and (C) EP of each grid cell of the updated $\boldsymbol{Y_{\lambda_{Het}}}$(log day^{-1}) ensemble through assimilation of 9 measurements of $\boldsymbol{Y_{C_{NO_3}}}$. Compare (A) to the reference state in Figure 3B, (B) to the forecast EE distribution in Figure 10A, and (C) to the forecast ES distribution in Figure 10B.

Supplementary measurement update scenarios were run to determine the influence of the error assigned to the $Y_{C_{NO_3}}$ measurements as well as the number of measurement sets assimilated on the updated $Y_{\lambda_{Het}}$ ensemble. The coefficient of variation (CV) of the $Y_{C_{NO_3}}$ measurements ranged from 0.00 to 3.00. For the measurement value of $Y_{C_{NO_3}}$ = 0.20 (C_{NO_3} = 1.58 g m_f^{-3}), which occurs at the northwestern-most measurement location at the end of January, the perturbed values using CV = 0.50 range from -0.08 to 0.47, which corresponds to C_{NO_3} values of 0.84 to 2.93 g m_f^{-3}, whereas for CV = 2.00, the values range from -0.91 to 1.27, which corresponds to C_{NO_3} values of 0.12 to 18.53 g m_f^{-3}. Even with a CV of 3.00 the updated AE value only increases to 0.76, still a decrease of 26.6% from the forecast AE value of 1.03. The steadiness of the AE value with increasing measurement error, however, is due to the assimilation of monthly measurement sets. When assimilating only two measurement sets, from months 6 and 12, the measurement error has a much stronger influence in preventing the measurement data from conditioning the $Y_{\lambda_{Het}}$ ensemble. For a CV equal to 3.00, the resulting AE value is 0.88.

Attempts were made to condition also the forecasted $Y_{\lambda_{Auto}}$ ensemble using measurements of C_{NO_3}, with values of C_{NO_3} from the reference state taken from layer 5 near the alluvium-shale interface. However, no improvement from the forecast ensemble was observed after data assimilation. This will be discussed further in Section 4.

F.3.4.2 Ensemble of $Y_{C_{NO_3}}$ using updated $Y_{\lambda_{Het}}$ ensemble

As a second, more definitive test of the parameter estimation methodology, the updated $Y_{\lambda_{Het}}$ ensemble is scrutinized to determine if it can produce simulated values of C_{NO_3} that correspond to

(i) the spatial distribution of C_{NO_3} of the reference aquifer system, and (ii) the assimilated measured values of C_{NO_3} from the 9 observation wells. To do so, each updated $Y_{\lambda_{Het}}$ field was used to re-run the reactive transport simulation and produce a corresponding C_{NO_3} field.

For item (i), the ensemble mean of each grid cell of the updated $Y_{C_{NO_3}}$ ensemble for the last day of the simulation (Dec. 31) is shown in Figure F-7B, with an AE value of 0.50, a reduction of 37.5% from the forecast ensemble value of 0.80. The spatial distribution of $Y_{C_{NO_3}}$ appears to follow quite closely the patterns of the reference state shown in Figure F-5B. For further analysis, the frequency distribution of the values of C_{NO_3} throughout the model domain for August 1 of the simulation is plotted for the reference state, the forecast C_{NO_3} ensemble mean, and the updated C_{NO_3} ensemble mean in Figure F-10. Notice that the values of the forecast ensemble (Figure F-10A) are mostly grouped within two intervals of concentrations (between 0.50 and 2.00 g m^{-3} and between 3.00 and 4.25 g m^{-3}), whereas the updated ensemble (Figure F-10B) more closely follows the distribution of the reference state, especially for low and high levels of concentration.

For item (ii), frequency distributions of the ensemble of forecasted and updated values at each of the 9 measurement locations were plotted, to determine if the updated ensemble values more closely approximated the reference value. Plots for three of the measurement locations are shown in Figure F-11, for the simulation results for August 1 of the simulation. In each case, the mean of the ensemble of updated values much more closely approximates the mean of the ensemble of forecasted values, and spread of the ensemble of updated values is much less than the spread of the forecasted values. The smallest improvement from the forecasted to updated

ensembles of the 9 measurement locations occurs at location (X=1550 m, Y=1050 m), which is shown in Figure F-11C.

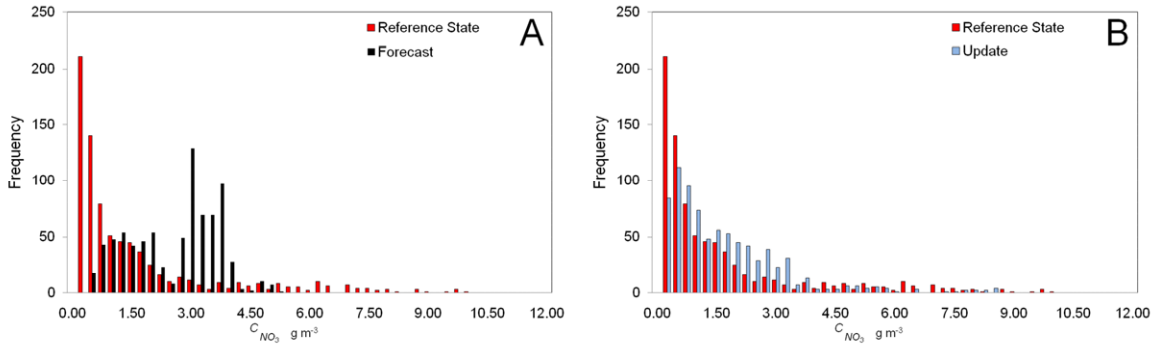

Figure F- 10. Frequency distribution of the values of $\boldsymbol{C_{NO_3}}$(g m^{-3}) throughout the model domain for (A) the reference state and the forecast ensemble mean, and (B) the reference state and the updated ensemble mean, using the updated $\boldsymbol{Y_{\lambda_{Het}}}$ensemble, for simulation results from the first day of August.

This is shown quantitatively in Table F-1, which contains the EE value for both the forecast and update ensembles at each measurement location. The EE value at the location corresponding to Figure F-11C (measurement No. 9) improves only from 0.64 to 0.45, a reduction of 28.8%. For all other measurement locations the smallest improvement is 75.2% (measurement No. 4), with an average EE reduction of 85.2%. A plot of the reference values (Column 4 in Table F-1) vs. the ensemble means of the forecasted and updated ensembles at the measurement locations (Columns 5 and 7) is shown in Figure F-12, with an obvious improvement in matching the simulated values with the observed values for the updated ensemble.

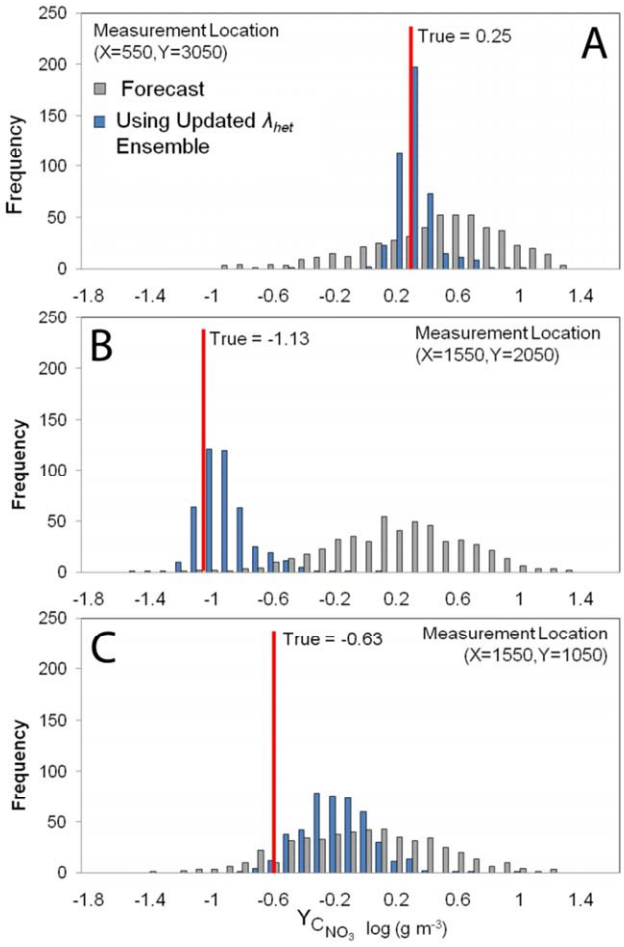

Figure F- 11. Frequency distributions of the ensemble of forecasted and updated values of $\boldsymbol{Y_{C_{NO_3}}}$(log g m^{-3}) as compared to the reference value, for the first day of August of the simulation.

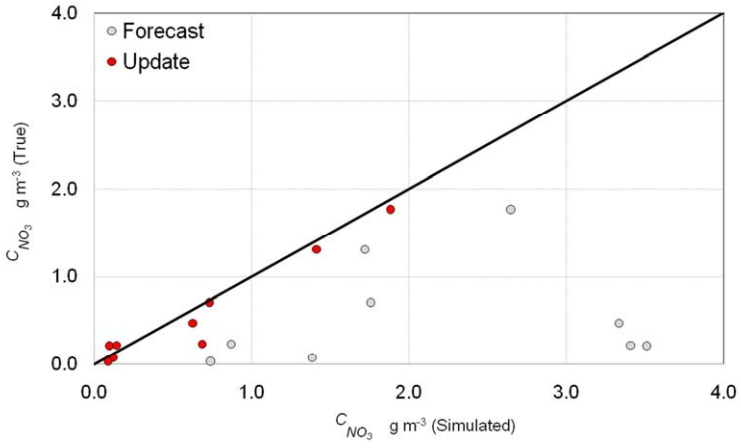

Figure F- 12. Plot of simulated vs. observed values of $\boldsymbol{C_{NO_3}}$(g m^{-3}) at the 9 measurement locations, for the ensemble mean of both the forecasted and updated ensembles.

Table F- 1. Comparisons of C_{NO_3} for the reference state, the forecast ensemble mean, and the update ensemble mean for the 9 measured values for the first day of August of the simulation.

				FORECAST		UPDATED*	
Meas.	**X**	**Y**	**TRUE**	**Mean**	**EE**	**Mean**	**EE**
1	550	3050	1.77	2.65	0.87	1.88	0.11
2	1050	3050	0.47	3.34	2.86	0.63	0.15
3	1550	3050	0.21	3.51	3.30	0.10	0.12
4	550	2050	1.31	1.72	0.41	1.41	0.10
5	1050	2050	0.22	3.41	3.19	0.14	0.07
6	1550	2050	0.07	1.39	1.31	0.12	0.05
7	550	1050	0.71	1.76	1.05	0.73	0.03
8	1050	1050	0.03	0.74	0.71	0.09	0.05
9	1550	1050	0.23	0.87	0.64	0.69	0.45

*Simulated using the updated λ_{Het} ensemble

F.3.4.3 Conditioning $Y_{\lambda_{Het}}$ using *RM* data

The second set of model update scenarios consists of updating the forecast ensemble of $Y_{\lambda_{Het}}$ fields using monthly measurements of *RM*. Figure F-13 shows the ensemble mean of the $Y_{\lambda_{Het}}$ ensemble at every grid cell for the situation where 4 stream gauges (Figure F-13A) and 10 gauges (Figure F-13B) are used to calculate *RM*. Using 10 gauges rather than 4 provides a more distinct definition of the spatial patterns present in the reference state. For example, the $Y_{\lambda_{Het}}$ values in the northwest section are more defined, with values approaching the low reactivity of the reference state. The values in the southeastern section also are more defined.

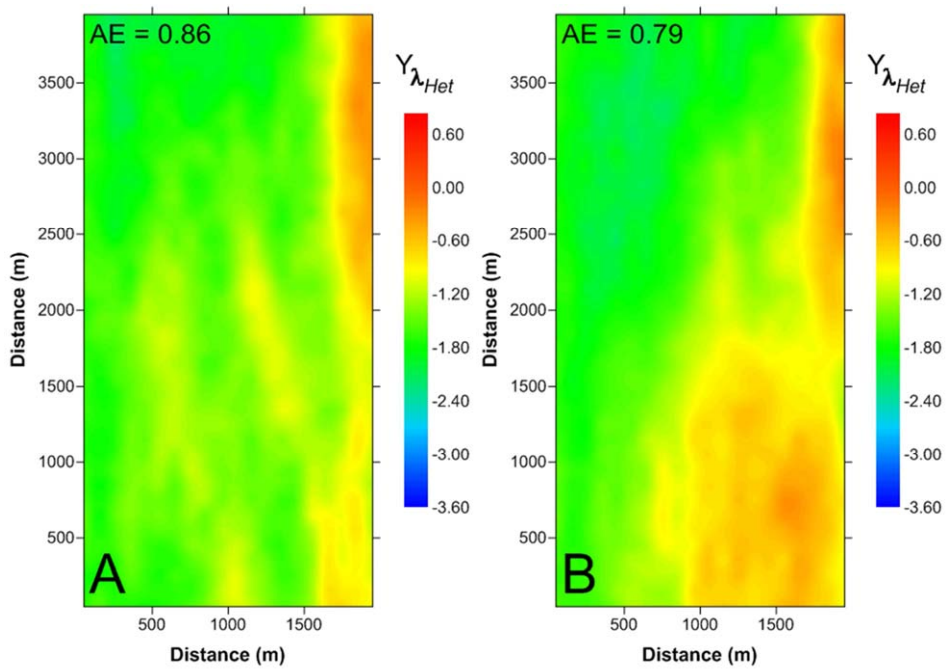

Figure F- 13. Ensemble mean of the updated $\boldsymbol{Y_{\lambda_{Het}}}$(log day^{-1}) ensemble by assimilating *RM* values using (A) 4 stream gauges and (B) 10 stream gauges. Compare to the reference state in Figure 3B.

The superiority of the 10-gauge scenario is further seen in an analysis of the AE values, with values of 0.86 and 0.79, respectively, a reduction of 16.6% and 23.1% from the forecast AE value. Both update ensembles, however, have much higher $Y_{\lambda_{Het}}$ values along the northern section of the stream than in the reference state. This is most likely due to the low values of *RM* along the northern section; along the mid-to-southern section, where the *RM* value is high (see Figure F-6A), the updated $Y_{\lambda_{Het}}$ values are very similar to those in the reference state.

A final scenario (not shown) was run in which both $Y_{C_{NO_3}}$ and *RM* measurements (using 4 gauges) were assimilated simultaneously, with a resulting AE value of 0.65 for the updated $Y_{\lambda_{Het}}$ ensemble, a reduction of 6.4% from the scenario of assimilating only $Y_{C_{NO_3}}$ measurements. Similar to the procedure in Section 3.4.1, update scenarios were run to determine the influence of error assigned to the *RM* measurements. Using CV values of 0.00 to 3.00, the AE values of the

updated $Y_{\lambda_{Het}}$ ensemble ranged linearly from 0.86 to 1.00, with the latter a decrease of only 3.2% from the forecast AE value.

F.3.4.4 Conditioning $Y_{\lambda_{Het}}$ in Aquifers of Uncertain Reactivity

In most cases, the value of $\mu_{Y_{\lambda_{Het}}}$ generally is not known with certainty, and hence there arises the possibility that the generated forecast ensemble of $Y_{\lambda_{Het}}$ has a range of values that do not correspond to those in the true aquifer system. In this section we explore the ability of the ES routine to condition the ensemble of $Y_{\lambda_{Het}}$ fields using $Y_{C_{NO_3}}$ data that are derived from a system where the reactivity is (i) one order of magnitude higher than expected, with $\mu_{Y_{\lambda_{Het}}}$ of the reference system equal to -0.85 log day^{-1} (0.14 day^{-1}) whereas $\mu_{Y_{\lambda_{Het}}}$ of the forecast ensemble is -1.70 log day^{-1}, and (ii) one order of magnitude lower than expected, with $\mu_{Y_{\lambda_{Het}}}$ of the reference system equal to -2.54 log day^{-1} (0.003 day^{-1}). For each scenario, monthly measurements were collected from the reference simulation and assimilated into the forecast ensemble. The forecast AE value of the $Y_{\lambda_{Het}}$ ensemble for both scenarios is 1.04 and 0.91, respectively. The corresponding forecast AE value of the $Y_{C_{NO_3}}$ ensemble are 0.81 and 0.47.

For the first scenario, the update AE value is 0.67, a reduction of 35.7% from the forecast value, indicating conditioning similar to the situation where the $\mu_{Y_{\lambda_{Het}}}$ is known with certainty, as in Sections 3.4.1. For the second scenario, however, the AE is only reduced by 2.3%, from 0.91 to 0.89. The conditioning for the first scenario is shown in Figure F-14, with the updated ensemble mean in the first scenario (Figure F-14B) approaching the reference system (Figure F-14A) much more thoroughly than for the second scenario (not shown).

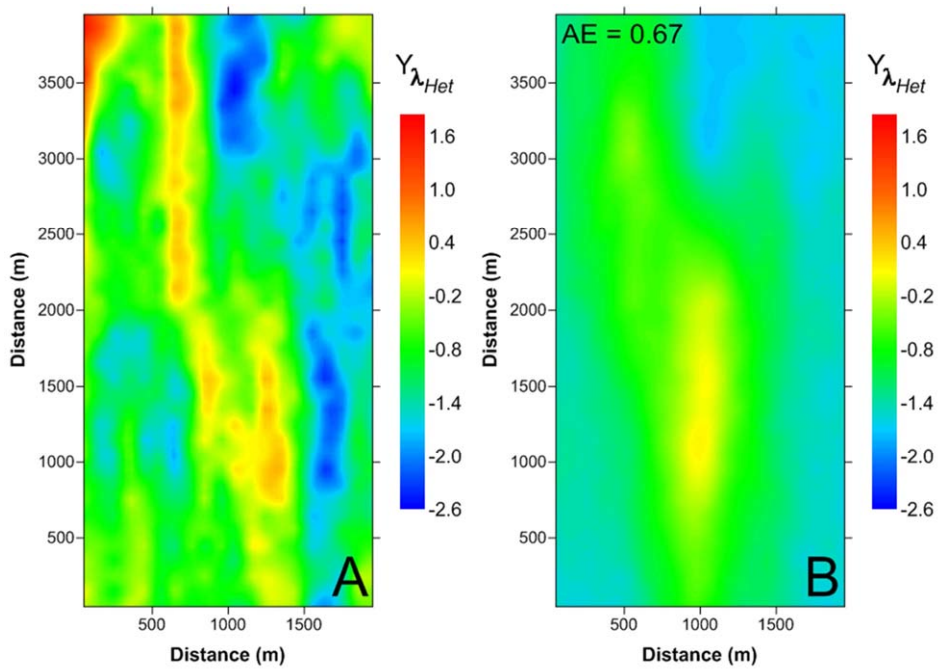

Figure F- 14. (A) Reference $\boldsymbol{Y_{\lambda_{Het}}}$ field (log day^{-1}) and (B) ensemble mean of the updated $\boldsymbol{Y_{\lambda_{Het}}}$ ensemble using 9 measurements of $\boldsymbol{Y_{C_{NO_3}}}$, when the reference state has rate constants that are on average an order of magnitude higher than prescribed in the forecast $\boldsymbol{Y_{\lambda_{Het}}}$ ensemble.

F.4 Discussion

Results presented in Sections 3.4 indicate that (i) even with the high degree of complexity established in the aquifer system (e.g., spatially- and temporally-variable forcing terms, the rate of heterotrophic denitrification dependent on both NO_3 and DOC) a strong correlation exists between the prescribed values of $Y_{\lambda_{Het}}$ and the model-calculated $Y_{C_{NO_3}}$ in the groundwater; and (ii) the ES update routine is successful in utilizing this correlation to condition the $Y_{\lambda_{Het}}$ ensemble to approach the reference $Y_{\lambda_{Het}}$ field using measurements of $Y_{C_{NO_3}}$ and *RM*. Re-running the simulation ensemble using the updated ensemble of $Y_{\lambda_{Het}}$ fields resulted in simulated values of C_{NO_3} that compared favorably with the measured values of C_{NO_3} at the observation wells in the reference

aquifer system. This is of particular significance since such a test is likely the sole method to test model results.

Outcomes reflect the nature of the measurements, as each type is allowed to condition values of $Y_{\lambda_{Het}}$ to which it is correlated. In the case of $Y_{C_{NO_3}}$, point measurements distributed throughout the spatial extent of the aquifer are able to condition values of $Y_{\lambda_{Het}}$ throughout the same spatial area, whereas measurements of *RM* only influence values of $Y_{\lambda_{Het}}$ adjacent to the stream. The ability of measurements calculated at one side of the aquifer, whether it be groundwater travel times, volumes of water entering the stream, or mass of a solute entering the stream, to condition aquifer parameters is a function of the correlation length of the parameter field [*Chen and Zhang*, 2006; *Bailey and Baù*, 2010]. For high correlation lengths, the influence of stream measurements can "reach" further into the spatial extent of the aquifer, and hence provide more information regarding the spatial distribution of the parameter. The correlation length of the $Y_{\lambda_{Het}}$ fields in this study, however, was constrained by the size of the cropped and fallow portions of the land surface.

The error assigned to the $Y_{C_{NO_3}}$ measurements had a significant effect on conditioning only when the coefficient of variation (CV) of the data exceeded 1.0. For values of CV higher than 1.0, including more sets of measurement data in the ES update routine (i.e., from several months throughout the year) allowed the ensemble of $Y_{\lambda_{Het}}$ fields to still receive significant correction from the measurement data.

The worth of jointly assimilating two disparate measurement types also was investigated, with both $Y_{C_{NO_3}}$ and *RM* measurements assimilated simultaneously, resulting in a reduction of

6.4% of the AE value from the scenario of assimilating only $Y_{C_{NO_3}}$ measurements. However, due to the decrease in the influence of *RM* measurements with increasing error, the results of this study cast doubts on the applicability of using *RM* data to effectively condition aquifer chemical parameters, unless (i) a high number of stream gauges can be employed to provide very localized estimates of *RM*, and (ii) measurements can be taken with a methodology that reduces error. Furthermore, measured C_{NO_3} in the stream may not always be a direct measure of the processes occurring within the aquifer, as denitrification during transport of NO_3 in the stream may also occur. If this is the case, the correlation between the calculated *RM* and the denitrification rate constant in the aquifer would be reduced, resulting in minimal conditioning.

In general, rate constants of low magnitude have a minimal affect on the resulting C_{NO_3} in a given location, and hence a significant correlation between the rate constant and the concentration value is not developed and conditioning of the rate constant values cannot occur. In this study, this is seen in (i) the poor conditioning of $Y_{\lambda_{Het}}$ when the reactivity in the true aquifer system is much lower than is stipulated in the forecast ensemble ( ), (ii) the poor conditioning of $Y_{\lambda_{Het}}$ in areas of low reactivity poor in sections of low reactivity, as shown in Section 3.4.1 and Figure F-9B, and (iii) the poor conditioning of $Y_{\lambda_{Auto}}$ by C_{NO_3}. For the latter, the low values of the λ_{Auto} rate constant (several orders of magnitude lower than for λ_{Het}, as shown in Figure F-1) prevent the autotrophic denitrification reaction from significantly altering C_{NO_3}.

Lastly, the computational burden of the ES update routine was found to be extremely affordable. As discussed in Section 3.4.1, CPU time to run the update routine with monthly $Y_{C_{NO_3}}$

ensembles and the $Y_{\lambda_{Het}}$ ensemble, resulting in a $\widetilde{X}_{t_F}^{f}$ matrix of dimension [10400 x 800], was approximately 2.2 minutes, or 0.04% of the CPU time required to generate the forecast ensembles through model simulation (5663 minutes). However, to test the methodology by re-running the reactive transport simulation ensemble, as discussed in Section 3.4.2, required the same CPU time as the 12-month reactive transport ensemble forecast (approximately 700 minutes).

F.5 Conclusions

Of prime importance in assessing the fate and transport of NO_3 in irrigated agricultural groundwater systems is a knowledge of the spatial distribution of denitrification rates within the aquifer. The purpose of this research is to show the usefulness of the Ensemble Smoother (ES) methodology in estimating this spatial distribution using system-response variables such as nitrate concentration and mass loadings of nitrate to streams, and to outline the approach when applying the methodology to real-world systems.

In applying the methodology, one must keep in mind that the determining factor in its effectiveness is the spatial and temporal correlation between the rate constant and the resulting solute concentration. Furthermore, using the updated parameter fields to re-run the simulation and obtain updated simulated values of solute concentration, to compare against observed values at measurement locations, is a vital step in exploring the applicability of parameter estimation methodologies.

Future work involves applying the methodology to a regional-scale study site within the LARV of southeastern Colorado in an overall effort to simulate the fate and transport of nutrients and associated constituents within the alluvial aquifer system.

Funding Source

The majority of this work has been made possible by grants from the Colorado Agricultural Experiment Station (CAES) (Project No. COL00690) and the Nonpoint Source Program of the Colorado Department of Public Health and Environment.

References

Ahmed, S., and G. de Marsily (1993), Cokriged estimation of aquifer transmissivity as an indirect solution of the inverse problem: A practical approach. *Water Resour. Res.*, 29(2), 521-530.

Almasri, M.N., and J.J. Kaluarachchi (2007), Modeling nitrate contamination of groundwater in agricultural watersheds. *J. Hydrol.*, 343, 211-229.

Bailey, R.T., and D.A. Baù (2010), Ensemble Smoother assimilation of hydraulic head and return flow data to estimate hydraulic conductivity, *Water Resour. Res.*, 46, W12543, doi:10.1029/2010WR009147.

Bailey, R.T., and D.A. Baù (2011), Estimating spatially-variable first-order rate constants in groundwater reactive transport systems, *J. Cont. Hydrol.*, 122, 104-121.

Bailey, R.T., and D.A. Baù (2012), Estimating geostatistical parameters and spatially-variable hydraulic conductivity within a catchment system using an ensemble smoother, *Hydrol. Earth Syst. Sci.*, 16, 287-304.

Baú, D.A., and A.S. Mayer (2008), Optimal design of pump-and-treat systems under uncertain hydraulic conductivity and plume distribution, *J. Cont. Hydrol.*, 100, 30-46.

Burkhalter, J.P., and T.K. Gates (2005), Describing agroecological impacts from salinization and waterlogging in an irrigated river valley, *J. Irrig. Drain. Engr.*, 131(2), 197-209.

Carle, S.F., Esser, B.K., and J.E. Moran (2006), High-resolution simulation of basin-scale nitrate transport considering aquifer system heterogeneity, *Geosphere*, 2, 195-209.

Chen, Y., and D. Zhang (2006), Data assimilation for transient flow in geologic formations via Ensemble Kalman Filter. *Adv. Water Resour.*, 29(8), 1107-1122.

Clement, T.P. (1997), RT3D – A modular computer code for simulating reactive multi-species transport in 3-dimensional groundwater aquifer. Draft report. PNNL-SA-28967. Richland, Washington: Pacific Northwest National Laboratory.

Conan, E., Bouraoui, F., Turpin, N., Marsily, G. de, and G. Bidoglio (2003), Modeling flow and nitrate fate at catchment scale in Brittany (France). *J. Envir. Qual.*, 32, 2026-2032.

Dunne, S. and D. Entekhabi (2005), An ensemble-based reanalysis approach to land data assimilation. *Water Resour. Res.*, 41, W02013, doi:10.1029/2004WR003449.

Evensen, G. (1994), Sequential data assimilation with a nonlinear quasi-geostrophic model using Monte Carlo methods to forecast error statistics. *J. Geophys. Res.*, 99(C5), 10, 143-10,162.

Evensen, G. Data assimilation. *The Ensemble Kalman Filter*. Springer-Verlag Berlin Heidelberg, 2007.

Frind, E.O., Duynisveld, W.H.M., Strebel, O., and J. Boettcher (1990), Modeling of multicomponent transport with microbial transformation in groundwater: the Fuhrberg case. *Water Resour. Res.*, 26(8), 1707-1719.

Fu, J., and J.J. Gomez-Hernandez (2009), Uncertainty assessment and data worth in groundwater flow and mass transport modeling using a blocking Markov chain Monte Carlo method, *J. Hydrol.*, 364, 328-341.

Gailey, R.M., Crowe, A.S., and S.M. Gorelick (1991), Coupled process parameter estimation and prediction uncertainty using hydraulic head and concentration data. *Adv. Water Resour.*, 14(5), 301-314.

Gates, T.K., Cody, B.M., Donnelly, J.P., Herting, A.W., Bailey, R.T., and J. Mueller-Price (2009), Assessing selenium contamination in the irrigated stream-aquifer system of the Arkansas River, Colorado. *J. Environ. Qual.*, 38, 2344-2356.

Gates, T.K., Garcia, L.A., Hemphill, R.A., Morway, E.D., and Elhaddad, A. (2011), Irrigation practices, water consumption, and return flows in Colorado's Lower Arkansas River Valley: Final report of field and model investigations 2004-2008." Colorado Water Institute Completion Report No. 221, Colorado State Univ., Fort Collins, CO.

Giacobbo, F., Marseguerra, M., and E. Zio (2002), Solving the inverse problems of parameter estimation by genetic algorithms: the case of a groundwater contaminant transport problem. *Ann. Nucl. Energy*, 29, 967-981.

Gomez-Hernandez, J.J., Hendricks Franssen, H.-J., and A. Sahuquillo (2003) Stochastic conditional inverse modeling of subsurface mass transport: A brief review and the self-calibrating method. *Stoch. Environ. Res. and Risk Assess*. 17, 319-328.

Groffman, P.M., Butterbach-Bahl, K., Fulweiler, R.W., Gold, A.J., Morse, J.L., Stander, E.K., Tague, C., Tonitto, C., and P. Vidon (2009), Challenges to incorporating spatially and temporally explicit phenomena (hotspots and hot moments) in denitrification models, *Biogeochemistry*, 93:49-77.

Hantush, M.M., and M.A. Marino (1997), Estimation of spatially variable aquifer hydraulic properties using Kalman filtering. *J. Hydraul. Engrg. ASCE*, 123(11), 1027-1035.

Harbaugh, A.W. (2005), MODFLOW-2005, the U.S. Geological Survey modular ground-water model – the Ground-Water Flow Process: U.S. Geological Survey Techniques and Methods 6-A16, variously paginated.

Heatwole, K.K., and J.E. McCray (2007), Modeling potential vadose-zone transport of nitrogen from onsite wastewater systems at the development scale. *J. Cont. Hydrol.*, 91, 184-201.

Hendricks Franssen, H. J., Gomez-Hernandez, J.J., and A. Sahuquillo (2003), Coupled inverse modeling of groundwater flow and mass transport and the worth of concentration data. *J. Hydrol.*, 281, 281-295.

Hendricks Franssen, H. J., and W. Kinzelbach (2008), Real-time groundwater flow modeling with the Ensemble Kalman Filter: Joint estimation of states and parameters and the filter inbreeding problem. *Water Resour. Res.*, 44, W09408, doi:10.1029/2007WR006505.

Hill, A.R. (1996), Nitrate removal in stream riparian zones. *J. Envir. Qual.*, 25, 743-755.

Hunter et al., 1998

Kalman, R.E. (1960), A new approach to linear filtering and prediction problems. *J. Basic Eng.*, 82, 35-45.

Keppenne, C. (2000), Data assimilation into a primitive-equation model with a parallel ensemble Kalman filter. *Mon. Weather Rev.*, 128, 1971-1981.

Korom, S.F. (1992), Natural denitrification in the saturation zone: a review. *Water Resour. Res.*, 28(6), 1657-1668.

Liu, G., Y. Chen, and D. Zhang (2008), Investigation of flow and transport processes at the MADE site using ensemble Kalman filter. *Adv. Water Resour.*, 31, 975-986.

Lu, G., Clement, T.P., Zheng, C., and T.H. Wiedemeier (1999), Natural attenuation of BTEX compounds: Model development and field-scale application. *Ground Water*, 37(5), 707-717.

McMahon, P.B., Böhlke, J.K., and B.W. Bruce (1999), Denitrification in marine shales in northeastern Colorado. *Water Resour. Res.,* 35(5), 1629-1642.

McNab Jr., W.W., and B.P. Dooher (1998), Uncertainty analysis of fuel hydrocarbon biodegradation signatures in groundwater by probabilistic modeling. *Ground Water*, 36(4), 69-698.

Parkin, T.B., and J.A. Robinson (1989), Stochastic models of soil denitrification. *Appl. Environ. Micro.*, 55(1), 72-77.

Pauwels, H., Kloppmann, W., Foucher, J-C., Martelat, A., and V. Fritsche (1998), Field tracer test for denitrification in a pyrite-bearing schist aquifer. *Appl. Geochem.,* 13(6), 767-778.

Pauwels, V. R. N., and G. J. M. De Lannoy (2006), Improvement of modeled soil wetness conditions and turbulent fluxes through the assimilation of observed discharge. *J. Hydrometeorol.*, 7(3), 458–477.

RamaRao, B.S., LaVenue, A.M., Marsily, G. de, and M.G. Marietta (1995), Pilot point methodology for automated calibration of an ensemble of conditionally simulated transmissivity field 1. Theory and computational experiments. *Water Resour. Res.*, 31(2), 475-493.

Spalding, R.F., and M.E. Exner (1993), Occurrence of Nitrate in Groundwater – A Review. *J. Envir. Qual.*, 22, 392-402.

Susfalk, R., Sada, D., Martin, C., Young, M., Gates, T., Rosamond, C., Mihevc, T., Arrowood, T., Shanafield, M., Epstein, B., Fitzgerlad, B., Lutz, A., Woodrow, J., Miller, G., and Smith, D. (2008), Evaluation of linear anionic polyacrylamide (LA-PAM) application to water delivery canals for seepage reduction. DHS Pub. No. 41245, Desert Research Institute, Reno, NV.

Valstar, J.R., McLaughlin, D.B., te Stroet, C.B.M., and F.C. van Geer (2004), A representer-based inverse method for groundwater flow and transport application. *Water Resour. Res.*, 40, W05116, doi:10.1029/2003WR002922.

van Leeuwen, P.J., and G. Evensen (1996), Data assimilation and inverse methods in terms of probabilistic formulation. *Mon. Weather Rev.*, 124, 2898-2913.

Vugrin, E.D., McKenna, S.A., and K.W. Vugrin (2007), Markov models and the Ensemble Kalman Filter for estimation of sorption rates. Sandia Report. SAND2007-5975. Albuquerque, New Mexico: Sandia National Laboratories.

Wagner, B.J. (1992), Simultaneous parameter estimation and contaminant source characterization for coupled groundwater flow and contaminant transport modelling. *J. Hydrol.*, 135, 275-303.

Wriedt, G., and M. Rode (2006), Modelling nitrate transport and turnover in a lowland catchment system. *J. Hydrol.*, 328, 157-176.

Wright, W. G. (1999), Oxidation and mobilization of selenium by nitrate by irrigation drainage, *J Environ Qual*, *28*(4).

Yeh, G.T., and V.S. Tripathi (1989), A critical evaluation of recent developments in hydrogeochemical transport models of reactive multichemical components. *Water Resour. Res.*, 25(1), 93-108.

Yeh, T.-C. J., Gutjahr, A.L., and M. Jin (1995), An iterative cokriging-like technique for ground-water flow modeling. Ground Water 33(1), 33-41.

Zhang, Y-C., Slomp, C.P., Broers, H.P., Passier, H.F., and P. Van Cappellen (2009), Denitrification coupled to pyrite oxidation and changes in groundwater quality in a shallow sandy aquifer. *Geoch. Et Cosm. Acta*, 73, 6716-6726.